

REPORT DOCUMENTATION PAGE

Form Approved OMB No. 0704-0188

Public reporting burden for this collection of information is estimated to average 1 hour per response, including the time for reviewing instructions, searching existing data sources, gathering and maintaining the data needed, and completing and reviewing the collection of information. Send comments regarding this burden estimate or any other aspect of this collection of information, including suggestions for reducing this burden to Washington Headquarters Services, Directorate for Information Operations and Reports, 1215 Jefferson Davis Highway, Suite 1204, Arlington, VA 22202-4302, and to the Office of Management and Budget, Paperwork Reduction Project (0704-0188), Washington, DC 20503.

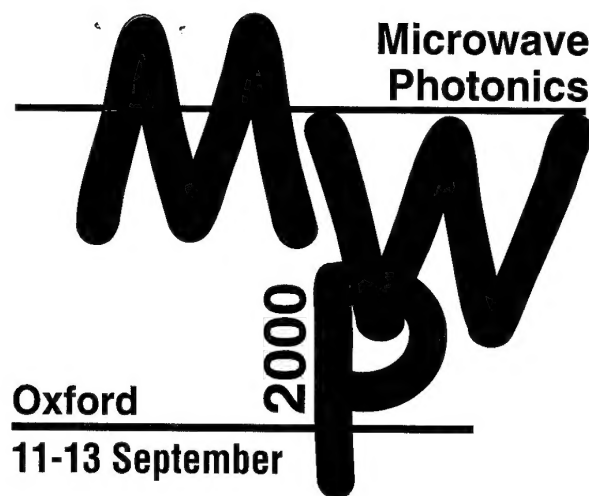
1. AGENCY USE ONLY (Leave blank)		2. REPORT DATE September 2000		3. REPORT TYPE AND DATES COVERED Conference Proceedings	
4. TITLE AND SUBTITLE Microwave Photonics 2000				5. FUNDING NUMBERS F61775-00-WF077	
6. AUTHOR(S) Conference Committee					
7. PERFORMING ORGANIZATION NAME(S) AND ADDRESS(ES) Institution of Electrical Engineers (IEE) Savoy Place London WC2R 0BL United Kingdom				8. PERFORMING ORGANIZATION REPORT NUMBER N/A	
9. SPONSORING/MONITORING AGENCY NAME(S) AND ADDRESS(ES) EOARD PSC 802 BOX 14 FPO 09499-0200				10. SPONSORING/MONITORING AGENCY REPORT NUMBER CSP 00-5077	
11. SUPPLEMENTARY NOTES					
12a. DISTRIBUTION/AVAILABILITY STATEMENT Approved for public release; distribution is unlimited.				12b. DISTRIBUTION CODE A	
13. ABSTRACT (Maximum 200 words) The Final Proceedings for Microwave Photonics 2000, 11 September 2000 - 13 September 2000 This was an interdisciplinary conference. Topics include: I Devices, Components and Techniques Ultra-fast lasers and detectors, ultra-fast optical modulators, microwave and millimeter-wave modulated optical signal generation techniques, analogue optical fiber links, optically controlled microwave devices, optical signal processors, ultra-fast optical probing and measurements, high-speed optical analogue to digital conversion, hybrid and chip level integration of photonic devices and circuits, microwave photonic device and circuit modeling. II Systems and Applications Fiber-fed wireless and cellular radio systems, optical control of array antennas, sub-carrier multiplexed and CATV systems, optically generated terahertz techniques and applications, satellite-based application, microwave aspects of digital optical fiber communication systems, system design and modeling, packaging, practical realization and field trials, novel microwave photonic systems and applications					
14. SUBJECT TERMS EOARD, Electromagnetics, Photonics, Microwave source				15. NUMBER OF PAGES 262	
				16. PRICE CODE N/A	
17. SECURITY CLASSIFICATION OF REPORT UNCLASSIFIED	18. SECURITY CLASSIFICATION OF THIS PAGE UNCLASSIFIED	19. SECURITY CLASSIFICATION OF ABSTRACT UNCLASSIFIED	20. LIMITATION OF ABSTRACT UL		

NSN 7540-01-280-5500

Standard Form 298 (Rev. 2-89)
Prescribed by ANSI Std. Z39-18
298-102

DTIC QUALITY INSPECTED 4

20010108 024



Technical Digest

International Topical Meeting on

Microwave Photonics MWP 2000



11-13 September 2000
St. John's College,
Oxford, UK

DISTRIBUTION STATEMENT A
Approved for Public Release
Distribution Unlimited



INTERNATIONAL TOPICAL MEETING ON MICROWAVE PHOTONICS MWP 2000

11-13 September 2000

St. John's College, Oxford, UK

Organised by:

Institution of Electrical Engineers

Co-sponsored by:

IEEE Lasers and Electro-optics Society

IEEE Microwave Theory and Techniques Society

We wish to thank the following for their contribution to the success of this conference:

**European Office of Aerospace Research and Development,
Air Force Office of Scientific Research,
United States Air Force Research Laboratory.**



CORNING
Discovering Beyond Imagination

Corning



SDL Integrated Optics Ltd



Agilent Technologies
Innovating the HP Way

Agilent



Marconi Caswell Ltd

AQ F01-04-0692

International Topical Meeting on

Microwave Photonics, MWP 2000

11-13 September 2000.

St. John's College, Oxford, UK

The papers in this book comprise the technical digest of the International Topical Meeting on Microwave Photonics - MWP2000. They reflect the authors' opinions and their inclusion in this publication does not necessarily constitute endorsement by the organisers or the IEEE.

Copyright and reprint permission: Abstracting is permitted with credit to the source. Libraries are permitted to photocopy beyond the limit of US Copyright law for private use of patrons those articles in this volume that carry a code at the bottom of the first page, provided the per-copy fee indicated in the code is paid through the Copyright Clearance Center, 222 Rosewood Drive, Danvers, MA 01923. For other copying, reprint or republication permission, write to IEEE Copyright Manager, IEEE Operations Center, 445 Hoes Lane, P O Box 1331, Piscataway, NJ 08855-1331. All rights reserved. Copyright ©2000 by the Institute of Electrical and Electronics Engineers, Inc

IEEE Catalog Number 00EX430

ISBN 0-7803-6455-4 (Softbound)

Library of Congress Number 00-03672

Additional Copies of this publication are available from:

IEEE Service Centre

445 Hoes Lane

Box 1331

Piscataway, NJ 08855-13331

Tel (+1) 908 981 0060

Fax (+1) 908 981 1721

Printed in Great Britain by Formara Ltd., Southend-on-Sea, Essex.

MWP 2000 COMMITTEES

CONFERENCE CHAIRMAN

Professor Alwyn Seeds

Dept. of Electronic and Electrical Engineering, University College London, UK. aseeds@ee.ucl.ac.uk

CONFERENCE CO-CHAIRMAN AND CHAIRMAN OF TECHNICAL PROGRAMME COMMITTEE

Professor Dieter Jaeger

Gerhard Mercator University, Germany. D.Jaeger@OE.Uni-Duisburg.de

CHAIRMAN OF MWP 2000 ORGANISING COMMITTEE

Dr Phil Lane,

Dept. of Electronic and Electrical Engineering, University College London, UK

p.lane@picard.ee.ucl.ac.uk

STEERING COMMITTEE

Dalma Novak, Australian Photonics CRC, Australia (Chair)

Charles Cox, MIT, USA

Nadir Dagli, UCSB, USA

Ronald Esman, Navel Research Lab, USA

Peter Herczfeld, Drexel University, USA

Dieter Jaeger, Gerhard Mercator University, Germany

Baheim Jalali, University of California, USA

Chi Lee, University of Maryland, USA

Robert Leheny, DARPA, USA

Mitsuru Naganuma, Teikyo University of Science & Technology, Japan

Hiroyo Ogawa, CRL, Japan

Alwyn Seeds, University College London, UK

Masahiro Tsuchiya, University of Tokyo, Japan

Paul Yu, University of California, USA

TECHNICAL PROGRAMME COMMITTEE

Dieter Jaeger, Gerhard Mercator University, Germany (Chair)

Masahiro Akiyama, Oki Electric Industry Co., Ltd, Japan

Arne Alping, Ericsson Microwave Systems AB, Sweden

Paul Biernacki, Naval Research Laboratory, USA

Charles Cox, Massachusetts Institute of Technology, USA

Nadir Dagli, University of California, USA

Phil Davies, University of Kent, UK

Didier Decoster, IEMN, France

Hans-Jorg Haisch, Alcatel SEL, Germany

Keizo Inagaki, ATR Adaptive Communications Research Laboratories, Japan

Tadao Ishibashi, NTT Photonics Laboratories, Japan

Ken-ichi Kitayama, Osaka University, Japan

Robert Minasian, The University of Sydney, Australia

John Payne, National Radio Astronomy Observatory, USA

Alwyn Seeds, University College London, UK

Michael Wale, Caswell Technology, UK

Paul Yu, University of California, USA

ORGANISING COMMITTEE

Phil Lane, University College London, UK

Joe Attard, University College London, UK

Izzat Darwazeh, UMIST, UK

John Mitchell, University College London, UK

Dave Wake, University College London, UK

TABLE OF CONTENTS

MWP 2000 Sessions		Page Number
MO1	Photonic Systems for Antennas 1	1
MO2	Photonic Systems for Antennas 2	20
TU1	Fibre Radio Networks	31
TU2	Microwave Photonic Devices	55
TU3	Optically Controlled Antenna Systems	78
TU4	Microwave to Optical Transduction	101
WE1	Microwave Photonic Links	125
WE2	Poster Session	152
WE3	Optical to Microwave Transduction	217
WE4	Novel Techniques	241
List of Authors		xvi

CONTENTS

Monday, 11 September

Page No.

11.00 hrs Registration opens

13.00 hrs Lunch

14.00 hrs **Welcome/Introductory Remarks**

A J Seeds (UCL)/ D Jaeger (Gerhard Mercator University)/
P M Lane (UCL)

14.10 hrs **Session MO1**

Photonic Systems for Antennas I

Co-Chairmen: C H Cox (MIT/Photonic Systems Inc.) /
M L Van Blaricum (Toyon Corpn.)

Invited

MO1.1 **Recent progress in dispersion-based photonic beamforming**

1

P J Matthews and P D Biernacki,
Naval Research Laboratory, USA

Invited

MO1.2 **BEAMTAP beam forming using a traveling fringes detector**

5

G Kriehn, G S Pati, PEX Silveria, F Schlottau and K Wagner,
University of Colorado, USA
D Dolphi and J P Huignard, Thomson CSF, France

Invited

MO1.3 **A brief history of photonic antenna reconfiguration**

9

M L Van Blaricum
Toyon Research Corporation, USA

MO1.4 **Range demonstration of a reconfigurable fiber-optic
time-steered 2D transmit beamformer**

13

D A Tulchinsky and P J Matthews
Naval Research Laboratory, USA

Invited

MO1.5 **Broadband nulling for conformal phased array antennas
using photonic processing**

17

H Zmuda
University of Florida, USA
E N Toughlian, ENSCO Inc., USA
P M Payson, AFRL/SNDR, USA

16.10 hrs Refreshment break

16.30 hrs **Special Session MO2**

Photonic Systems for Antennas II

Co-Chairmen: C H Cox (MIT/ Photonic Systems Inc.) / M L Van Blaricum (Toyon Corpn.)

Invited

MO2.1 **Technologies for optically controlled phased array antennas**

M J Wale

Caswell Technology, UK

(Not
Available)

Invited

MO2.2 **Photonic chip for steering a four element phased array antenna**

20

J Stulemeijer, D H P Maat and K Smit

Delft University of Technology, The Netherlands

R van Dijk and F E van Vliet,

TNO-Physics and Electronics Laboratory, The Netherlands

MO2.3 **Phased array antenna beamforming using a micromachined silicon spatial light modulator**

23

R A Wilson, P Sample, A Johnstone and M F Lewis

DERA, UK

Invited

MO2.4 **Efficient optical control of microwave circuits, antennas and arrays**

27

J Vian and Z Popovic

University of Colorado, USA

18.05 hrs Close of session

18.30 - 19.30 hrs Welcome drinks reception

(Followed by a free evening)

Tuesday, 12 September

08.30 hrs **Session TU1**

Fibre Radio Networks

Chairman: K Kitayama (Osaka University)

TU1.1 **400 Mbit/s BPSK data transmission at 60 GHz-band mm-wave using a two-mode injection-locked Fabry-Perot slave laser**

31

M Ogusu, K Inagaki and Y Mizuguchi

ATR Adaptive Communications Research Laboratories, Japan

		Page No.
TU1.2	Radio on fiber system for triple band transmission in mobile cellular communication Y Ito and Y Ebine NTT DoCoMo Inc., Japan	35
TU1.3	Penalty free W-CDMA radio signal transmission over fibre R E Schuh, B Verri and E Sundberg Telia Research AB, Sweden D Wake, BT, UK	39
TU1.4	Error-free transmission of radio QPSK signals in an optical subcarrier multiple access system suppressing optical beat interference with over-modulation I Seto, T Tomioka and S Ohshima Toshiba Corporation, Japan	43
TU1.5	Optical subcarrier multiplexing system using time sampling multiplexer to suppress optical beat interference Y Shoji and H Ogawa Ministry of Posts and Telecommunications, Japan	47
TU1.6	Impact of Optical Crosstalk in Fibre-Radio Systems incorporating WDM D Castleford, A Nirmalathas and D Novak Australian Photonics Cooperative Research Centre, Australia	51
10.30 hrs	Refreshment break	
11.00 hrs	Session TU2 Microwave Photonic Devices Chairman: D Decoster (IEMN)	
TU2.1	Invited paper Optical control of millimetre-wave p-HEMTs with applications to fibre radio S Iezekiel and N Bourhill University of Leeds, UK	55
TU2.2	Signal to noise ratio enhancement using heterojunction bipolar phototransistor by base current compensation S Dupont, M Fendler, F Jorge, S Maricot, J-P Vilcot and D Decoster Université des Sciences et Technologies de Lille, France	59
TU2.3	A two heterojunction bipolar photo-transistor configuration for millimeter wave generation and modulation J Lasri, A Bilenca, G Eisenstein, D Ritter, M Orenstein, V Sidorov, S P Goldgeier and S Cohen TECHNION, Israel	62

	Page No.
TU2.4 Multiple quantum well asymmetric Fabry-Perot modulators for RF-over-fibre applications R I Killey, J B Song, C P Liu and A J Seeds, University College London, UK J S Chadha, M Whitehead, P Stavrinou and G Parry, Imperial College, London, UK. C C Button, University of Sheffield, UK	66
TU2.5 Performance of the electroabsorption modulator as an integrated optoelectronic mixer for RF frequency conversion D S Shin, G L Li, W S C Chang and P K L Yu University of California, USA C K Sun and S A Pappert, SPAWAR Systems Ctr., USA	70
TU2.6 A 6 to 11 GHz all-optical image rejection microwave downconverter S J Strutz and K J Williams Naval Research Laboratory, USA	74
13.05 hrs Lunch	
14.00 hrs Session TU3 Optically Controlled Antenna Systems Chairman: P Biernacki (Naval Research Laboratory)	
TU3.1 Photonic true time delay beamformer demonstrator for an astronomical array antenna R van Dijk, A Roodnat and F E Vliet, TNO Physics and Electronics Laboratory, The Netherlands J D Bregman, ASTRON, The Netherlands	78
TU3.2 Photonic differential delay beam forming network for phased-array antennas C Bélisle, C Delisle and J Oldham Communications Research Centre, Canada	81
TU3.3 Broadband beamforming network using integrated optic RF phase shifters A Mitchell and R B Waterhouse Australian Photonics Cooperative Research Centre, Australia	85
TU3.4 Beam-steering of receiving array antenna using local signal beamformer by optical signal processing T Akiyama, K Inagaki and Y Mizuguchi	89

		Page No.
TU3.5	A novel two-element active antenna for varying the direction of microwave radiation by optical illumination Y Ueno, M Katsuragi and Y Yamamoto Osaka Sangyo University, Japan	93
TU3.6	Novel photonically controlled antenna for MMW communications G W Webb, S Angello, W Vernon, M Sanchez and S C Rose Innova Laboratories, Inc., USA	97
16.00 hrs	Refreshment break	
16.25 hrs	Session TU4 Microwave to Optical Transduction Chairman: N Dagli (University of California, Santa Barbara)	
	Invited	
TU4.1	Fast modulation performance of uncooled semiconductor lasers R V Penty, A B Massara, M Webster, K A Williams and I H White University of Bristol, UK	101
TU4.2	Enhanced direct modulation efficiency by FM to IM conversion H L T Lee and R J Ram Massachusetts Institute of Technology, USA O Kjebon and R Schatz Royal Institute of Technology, Sweden	105
TU4.3	Integrated tandem electroabsorption modulators for high speed OTDM applications V Kaman, Y-J Chiu, T Liljeberg and J E Bowers University of California, USA S Z Zhang, Agilent Technologies, USA	109
TU4.4	A folded-path GaAs travelling-wave modulator for phased-array receivers R G Walker and C Edge Caswell Technology, UK	113
TU4.5	Novel optical single-sideband suppressed-carrier modulator using a bidirectionally-driven electro-optic modulator A Loayssa, J M Salvade, D Benito and M J Garde Universidad Publica de Navarra, Spain	117
TU4.6	Effect of pilot tone -based modulator bias control on external modulation link performance E I Ackerman and C H Cox III Photonic Systems, Inc., USA	121

18.30 hrs Close of Session

19.00 hrs **Session PD**

Post-Deadline Session

Chairman: P K Yu (University of California, San Diego)

20.00 hrs Close of session

20.00 for 20.30 Conference dinner

Wednesday, 13 September

08.15 hrs **Session WE1**

Microwave Photonic Links

Chairman: P A Davies (University of Kent)

Invited

WE1.1 **Millimetre-wave bandwidth electroabsorption modulators and transceivers** 125

A Stöhr, R Heinzelmann and D Jäger
Gerhard-Mercator-Universität, Germany

WE1.2 **Millimetre-wave radio-over-fibre transmission using an optical injection phase-lock loop source** 129

L A Johansson and A J Seeds
University College London, UK

WE1.3 **Dispersion effects of optical filter in DWDM millimeter-wave fiber-radio systems** 133

K Kitayama, T Kamisaka and K Onohara
Osaka University, Japan
W Chujo, MPT, Japan

WE1.4 **156/Mb/s DPSK optical MM-wave Transmission employing a 60 GHz optoelectronic image rejection mixer** 137

Y Ozeki, K Nishikawa*, M Kishi and M Tsuchiya
University of Tokyo, Japan
*presently with Fujitsu Laboratories Ltd.

WE1.5 **Laser phase noise free optical heterodyne detection technique for 60-GHz-band radio-on-fiber systems** 141

T Kuri, MPT, Japan
K Kitayama, Osaka University, Japan

	Page No.
WE1.6 Electronic linearization and bias control for externally modulated fiber optic link B Jalali and V Magoon*, University of California, USA *presently with Conexant Systems, USA	145
WE1.7 Impact of ASE on phase noise in LMDS incorporating optical fibre backbones C Lim, A Nirmalathas, D Novak and R Waterhouse Australian Photonics Cooperative Research Centre, Australia	148
10.40 hrs Refreshment Break	
11.00 hrs Session WE2 Poster Session Chairman: P M Lane (University College London)	
WE2.1 A study of doped patch and dipole antenna arrays with photonic interactions D S Lockyer and J C Vardaxoglou Loughborough University, UK G J Ensell, University of Southampton, UK	152
WE2.2 Investigations in microwave optical links - accent on QAM I Frigyes, A Hilt and S Csernyin Budapest Technical University, Hungary	156
WE2.3 Theoretical consideration on transferring transparency for RF signal bandwidth on direct optical switching CDMA radio-on-fiber networks K Kumamoto, K Tsukamoto and S Komaki Osaka University, Japan	160
WE2.4 Increasing the channel number in WDM MM-wave systems by spectral overlap C G Schäffer, M Sauer, K Kojucharow and H Kaluzni Dresden University of Technology, Germany	164
WE2.5 Simultaneous baseband and RF modulations scheme in Gbit/s millimetre-wave wireless-fibre networks V Polo, A Martinez, J Marti, F Ramos, A Griol and R Llorente Universidad Politecnica di Valencia, Spain	168
WE2.6 An integrated fiber optics / broadband wireless access demonstrator for the next generation internet (NGI) network extension H Izadpanah, D J Gregoire, F A Dolezal, W Ng, D Yap and G Tangonan HRL Laboratories, USA	172

	Page No.
WE2.7 An optically amplified four-channel WDM downconverter for wideband microwave receiver applications S T Winnall, K L Mahady, D B Hunter and A C Lindsay Defence Science and Tehnology Organisation, Australia	175
WE2.8 Optical upconversion of 100 Mb/s BPSK microwave subcarrier signals using an unbalanced mach-zehnder interferometer G Maury, B Cabon and J-F Le Bigot LEMO, France A Hilt, BME-MHT, Hungary	179
WE2.9 Colliding pulse mode-locked lasers on semi-insulating substrate at 1.5μm H K Lee, M W Street, S D McDougall, E A Avrutin, A C Bryce and J H Marsh University of Glasgow, UK	183
WE2.10 Dependence of semiconductor laser intermodulation distortions on fiber length and its reduction by optical injection locking H-K Sung, Y-K Seo and W-Y Choi, Yonsei University, Korea	186
WE2.11 Nonlinear distortion suppression in dual parallel analog modulation of DFB-LD H-D Jung and S-K Han Yonsei University, Korea	190
WE2.12 Efficient photoreceivers for millimetre-wave cellular system base stations L Gomez-Rojas, X Wang, N J Gomes and P A Davies University of Kent at Canterbury, UK	194
WE2.13 An X-band balanced optical hybrid mixer for μ-wave optical interconnect in active phased array radar and communication systems S K Banerjee, U Goebel and P Nüchter DaimlerChrysler Aerospace AG, Germany	198
WE2.14 Experimental demonstration and modelling of optoelectronic mixing and digital modulation in a single InP photo heterojunction bipolar transistor A Bilenca, J Lasri, G Eisenstein, D Ritter, M Orenstein, V Sidorov, S Cohen and P Goldgeier TECHNION, Israel	203

	Page No.
WE2.15 High frequency and broadband signal measurements by ultrafast opto-microwave intermixing and sampling W-L Cao, M Du and C H Lee University of Maryland, USA N G Paulter, NIST, USA	207
WE2.16 Effect of modulation frequency and target depth on modulated laser line scanner performance in the Patuxent River Withdrawn L Mullen, V M Contarino, B Concannon and A Laux Naval Aviation Systems Team, USA	-
WE2.17 Two-dimensional field mapping of microstrip lines with a band pass filter or a photonic bandgap structure by fiber-optic EO spectrum Analysis System T Ohara, M Abe, S Wakana, M Kishi and M Tsuchiya, The University of Tokyo, Japan S Kawasaki, Tokai University, Japan	210
WE2.18 Synthesis of optical transversal filter with tap multiplexing G Yu, W Zhang and J A R Williams Aston University, UK	214
13.00 hrs Lunch Interval	
14.00 hrs Session WE3 Optical to Microwave Transduction Chairman: D Jaeger (Gerhard Mercator University)	
WE3.1 Velocity-matched distributed photodetectors with p-i-n photodiodes M S Islam, T Jung, S Murthy, T Itoh and M C Wu, University of California, USA D L Sivco and A Y Cho Lucent Technologies, USA	217
WE3.2 Photodiode compression due to current-dependent capacitance K J Williams Naval Research Laboratory, USA P G Goetz, Sachs-Freeman Associates, USA	221
WE3.3 A 120 - GHz integrated photonic transmitter T Nagatsuma, A Hirata, Y Royter and M Shinagawa NTT Telecommunications Energy Laboratories, Japan T Furuta, T Ishibashi and H Ito NTT Photonics Laboratories, Japan	225

	Page No.
WE3.4 Monolithically integrated millimeter-wave photonic emitter for 60-GHz fiber-radio applications K Takahata, Y Muramoto, S Fukushima, T Furuta and H Ito NTT Photonics Laboratories, Japan	229
WE3.5 Photonic modules for millimeter wave communication systems A C Paoletta and A Bauerle Lockheed Martin Communications & Power Centre, USA A M Joshi, Discovery Semiconductors, Inc., USA	233
WE3.6 High temperature superconducting MM-wave photomixers C J Stevens, D J Edwards Oxford University, UK	237
16.00 hrs Refreshment Break	
16.25 hrs Session WE4 Novel Techniques Chairman: A J Seeds (University College London)	
WE4.1 Invited Optical Processing of Microwave signals J Capmany, D Pastor, B Ortega and S Sales Universidad Politécnica de Valencia, Spain	241
WE4.2 Optical transversal filter employing high birefringence fibre bragg gratings W Zhang and J A R Williams Aston University, UK	245
WE4.3 A photonic wide band analog to digital converter E N Toughlian, ENSCO Inc., USA H Zmuda, University of Florida, USA	248
WE4.4 Ultra-low jitter mode-locking of Er-fiber laser at 10 GHz and its application in photonic analog-to-digital conversion W Ng, R Stephens and D Persechini HRL Laboratories, USA K V Reddy, Pritel Inc., USA	251
WE4.5 Shot-noise limited performance from an EDFA/FA/brillouin hybrid amplified photonic link S J Strutz and K J Williams Naval Research Laboratory, USA	255

**WE4.6 Optical generation of rapidly tunable millimeter
wave subcarrier**

259

Y Li, A J C Vieira, P Herczfeld, A Rosen and W Janton
Drexel University, USA

18.30 hrs Close of conference

List of Authors

Page No.

Abe, M210
Ackerman, E I121
Akiyama, T89
Angello, S97
Avrutin, E A183

Banerjee, S K198
Bauerle, A233
Bélisle, C81
Benito, D117
Biernacki, P D1
Bilenca, A62, 203
Bourhill, N55
Bowers, J E109
Bregman, J D78
Bryce, A C183
Button, C C66

Cabon, B179
Cao, W207
Capmany, J241
Castleford, D51
Chadha, J S66
Chang, W S C70
Chiu, Y-J109
Cho, A Y217
Choi, W Y186
Chujo, W133
Cohen, S62, 203
Cox III, C H121
Csernyin, S156

Davies, P A194
Decoster, D59
Dolezal, F A172
Dolphi, D5
Du, M207
Dupont, S59

Ebine, Y35
Edge, C113
Edwards, D L237
Eisenstein, G62, 203
Ensell, G J152

Fendler, M59
Frigyes, I156
Fukushima, S229
Furuta, T225, 229

Garde, M J117
Goebel, U198
Goetz, P221
Goldgeier, P62, 203
Gomes, N J194
Gomez-Rojas, L194
Gregoire, D J172
Griol, A168

Han, S K190
Herczfeld, P259
Hilt, A156, 179
Hirata, A225
Huignard, J P5
Hunter, D B175

Iezekiel, S55
Inagaki, K31, 89
Ishibashi, T225
Islam, M S217
Ito, Y35
Ito, H225, 229
Itoh, T217
Izadpna, H172

Jaeger, D125
Jalali, B145
Janton, W259
Johansson, L A129
Johnstone, A23
Jorge, F59
Joshi, A M233
Jung, T217
Jung, H D190

Kaluzni, H	164	Murthy, S.....	217
Kaman, V	109	Nagatsuma, T	225
Katsuragi, M.....	93	Ng, W.....	172, 251
Kawasaki, S.....	210	Nirmalathas, A	51, 148
Kennedy, K V.....		Nishikawa K.....	137
Killey, R I	66	Novak, D	51, 148
Kishi, M	137, 210	Nuchter, P.....	198
Kitayama, K I.....	133, 141		
Kjebon, O	105	Ogawa, H	47
Kojucharow, K	164	Ogusu, M.....	31
Komaki, S.....	160	Ohara, T.....	210
Kriehn, G.....	5	Ohshima, S.....	43
Kumamoto, K.....	160	Oldham, J	81
Kuri, T	141	Onohara, K.....	133
		Orenstein, M	62, 203
Lasri, J.....	62, 203	Ortega, B	241
Le Bigot, J-F	179	Ozeki, Y	137
Lee, H K.....	183		
Lee, H L T.....	105	Paoella, A C.....	233
Lee, C H.....	207	Pappert, S A	70
Lewis, M F.....	23	Parry, G	66
Li, Y	259	Pastor, D.....	241
Li, G L.....	70	Pati, G S	5
Liljeberg, T.....	109	Paulter, N G.....	207
Lim, C	148	Payson, P M	17
Lindsay, A C.....	175	Penty, R V	101
Liu, C P	66	Persechini, D	251
Llorente, R	168	Polo, V.....	168
Loayssa, A.....	117	Popovic, Z	27
Lockyer, D S	152		
		Ram, R J.....	105
Maat, D H P	20	Ramos, F	168
Magoon, V.....	145	Reddy, K V.....	251
Mahady, K L	175	Ritter, D.....	62, 203
Maricot, S.....	59	Roodnat, A	78
Marsh, J H.....	183	Rose, S C.....	97
Marti, J	168	Rosen, A.....	259
Martinez, A.....	168	Royter, Y	225
Massara, A B.....	101		
Matthews, P J.....	1, 13	Sales, S	241
Maury, G	179	Salvide, J M.....	117
McDougall, S D	183	Sample, P	23
Mitchell, A	85	Sanchez, M S	97
Mizuguchi, Y	31, 89	Sauer, M	164
Muramoto, Y	229		

Schäffer, C G.....	164	Wagner, K.....	5
Schatz, R.....	105	Wakana, S.....	210
Schlottau, F.....	5	Wake, D.....	39
Schuh, R E.....	39	Wale, M J.....	
Seeds, A J.....	66, 129	Walker, R G.....	113
Seo, Y K.....	186	Wang, X.....	194
Seto, I.....	43	Waterhouse, R B.....	85, 148
Shin, D S.....	70	Webb, G W.....	97
Shinagawa, M.....	225	Webster, M.....	101
Shoji, Y.....	47	White, I H.....	101
Sidorov, V.....	62, 203	Whitehead, M.....	66
Silveria, P E X.....	5	Williams, K J.....	74, 221, 255
Sivco, D L.....	217	Williams, J A R.....	214, 245
Smit, K.....	20	Williams, K A.....	101
Song, J B.....	66	Wilson, R A.....	23
Stavrinou, P.....	66	Winnall, S T.....	175
Stephens, R.....	251	Wu, M C.....	217
Stevens, C J.....	237		
Stöhr, A.....	125	Yamamoto, Y.....	93
Street, M W.....	183	Yap, D.....	172
Strutz, S J.....	74, 255	Yu, P K L.....	70
Stulemeijer, J.....	20	Yu, G.....	214
Sun, C K.....	70		
Sundberg, E.....	39	Zhang, S Z.....	109
Sung, H K.....	186	Zhang, W.....	214, 245
		Zmuda, H.....	17, 248
Takahata, K.....	229		
Tangonan, G.....	172		
Tomioka, T.....	43		
Toughlian, E N.....	17, 248		
Tsuchiya, M.....	137, 210		
Tsukamoto, K.....	160		
Tulchinsky, D A.....	13		
Ueno, Y.....	93		
van Dijk, R.....	20, 78		
van Vliet, F E.....	20		
van Blaricum, M L.....	9		
Vardaxoglou, J C.....	152		
Vernon, W.....	97		
Verri, B.....	39		
Vian, J.....	27		
Vieira, A J C.....	259		
Vilcot, J P.....	59		
Vliet, F E.....	78		

Welcome to Microwave Photonics 2000

On behalf of the Steering Committee for Microwave Photonics and the Technical Programme and Organising Committees for Microwave Photonics 2000, I would like to welcome you to Microwave Photonics 2000. This Conference will be the tenth in the series and it is satisfying to see how, over this period, Microwave Photonics has become a flourishing business area as well as an exciting field for interdisciplinary research.

This year's Conference, the first to be held in England, is organised by the Institution of Electrical Engineers, with technical co-sponsorship from the IEEE Microwave Theory and Techniques and IEEE Lasers and Electro-optics Societies. We have also received excellent support from our government and industrial financial sponsors, the US Air Force Office of Scientific Research, SDL Integrated Optics Ltd., Agilent Technologies Ltd., Marconi Caswell Ltd. and Corning Research Centre.

The programme for Microwave Photonics 2000 commences with a pair of special sessions organised by Dr. Charles Cox (MIT/Photonic Systems Inc.) and Dr. Mike Van Blaricum (Toyon Corpn.) on Photonic Systems for Antennas which include 7 invited papers. There then follow 7 regular sessions and a poster session spread over two days covering the full range of activities in microwave photonics, from new device results to systems experiments in broadband fibre-radio. Included in these sessions are a further 4 invited papers and 56 contributed papers selected by the Technical Programme Committee from over 80 submissions from 14 countries.

In addition to the formal technical sessions there will be a small technical exhibition and social events including a Drinks Reception on Monday evening and a Conference Dinner on Tuesday evening, immediately following the Post-deadline Papers Session.

All Conference events will be held within the beautiful and historic surroundings of St. John's College, Oxford, and I hope you will be able to find a little time to explore this remarkable city during your visit.

The Technical Programme and Organising Committees have worked hard to produce a programme reflecting the most exciting recent developments in Microwave Photonics. We look forward to your participation and contribution to making Microwave Photonics 2000 a success.

Alwyn Seeds

Chairman of Microwave Photonics 2000.

RECENT PROGRESS IN DISPERSION-BASED PHOTONIC BEAMFORMING (Invited)

Paul J. Matthews and Paul D. Biernacki

Naval Research Laboratory
Code 5651, Optical Sciences Division
Washington, DC 20375-5338

I. INTRODUCTION

The use of phased array antennas has increased rapidly over the last few years due to their many advantages over more traditional fixed or mechanically steered antennas. Some of these advantages include rapid beam steering, graceful degradation and the ability to dynamically shape the radiation pattern. The increased flexibility of array antennas enables the realization of more complex and advanced systems where an aperture is shared for many simultaneous functions. Such realizations are not possible using traditional methods.

Despite the increased use of electronically steered arrays and the large amount of research into this area, most systems still suffer from numerous drawbacks. Some of the more generic drawbacks include cost, complexity, size, weight and EMI susceptibility. Limitations in microwave signal routing and devices has prevented the implementation of multiple beam arrays. More importantly, the reliance on microwave phase shifters for beamforming leads to a bandwidth limitation that scales with the size of the array. Thus, the current technology is not compatible with the future needs for larger, more powerful and wider bandwidth. Because of these limitations, there have been a variety of efforts over the years to utilize photonic techniques in array applications with a particular emphasis on true time-delay (TTD) beamforming for wide instantaneous bandwidths.

One of the more promising techniques for TTD beamforming has been the use of optical dispersion as a variable delay line. The concept was first demonstrated in [1]. Variations have been proposed or demonstrated which use multiple wavelength sources and switching in different lengths of dispersive fiber [2] or by using a wavelength tunable laser and a single length of dispersive fiber [3].

Here at the Naval Research Laboratory (NRL), we have extended this concept by implementing a fiber-optic, "dispersive prism" [4]. In this technique, a single tunable laser is fed to the array elements or subarrays each of which has an amount of dispersion proportional to its position in the array. The resulting dispersion gradient is then translated to a time delay gradient by tuning the wavelength of the laser. The dispersion is implemented using highly dispersive optical fiber. This approach is efficient and simple.

The dispersive prism technique has been used to demonstrate both transmit and receive operation [4] which has shown squint-free, $\pm 60^\circ$ azimuthal steering over an instantaneous bandwidth of 2 to 18 GHz. Two-dimensional transmit array squint-free steering over the

full $\pm 45^\circ$ was also demonstrated over a 6 to 18 GHz instantaneous bandwidth [5]. Multiple, independent, simultaneous beams have also been shown in the receive mode [6] as has operation in the mm-wave regime [7] and wideband nulling [8].

In this paper, we will describe recent efforts at NRL aimed at improving the dispersive prism beamformer concept. The goal is to further develop the concept such that it may be transitioned beyond the simple field test and proof-of-concept stage to a truly viable wideband beamforming system for both military and commercial usage. The next section of the paper will discuss issues related to the use of chirped fiber gratings as opposed to dispersive fiber. The following section will treat the issues of the tunable laser source which is the critical to the overall system performance. Next, recent demonstrations of an architecture designed to greatly simplify the two-dimensional beamforming problem will be presented. This will be followed by conclusions.

II. CHIRPED FIBER GRATINGS

In order to make a system practical, real life issues such as long-term stability, affordability and reproducibility must be addressed. Many times, the critical parameters and issues necessary to effectively transition a system are not obvious in a laboratory setting. The dispersive prism beamformer was successfully field tested in a high-level Navy demonstration of a two-dimensional transmit array [9]. The beamformer employed highly dispersive fiber as the dispersive element.

Invaluable knowledge was gained from this exercise. Two key issues emerged from the demonstration, both of which involved the use of high dispersion fiber. The first was that in using commercially available dispersion compensating fiber ($D \sim 100$ ps/nm·km), the amount of fiber necessary resulted in a signal latency through the beamformer that was not acceptable for certain functions. The second issue involved the temperature stability of such long lengths of fiber. Due to the lengths involved (> 1 km), active temperature stabilization of the beamformer was employed. This is obviously not a desirable solution. The temperature stability issues may be mitigated by proper packaging such that all of the fibers experience the same environment. This can be accomplished through winding of all fibers on a single, insulated spool. Additional thermal testing of the system indicated that even this approach would require active temperature stabilization. Figure 1 shows a plot of the time-delay as a function of temperature for equal lengths (~ 270 m) of high dispersion and dispersion compensating fiber used

in [9]. It is readily apparent that the different fiber types exhibit different temperature coefficients due to changes in the waveguide dispersion of the fiber. Thus, for accurate operation over a large range of operating temperatures, some degree of thermal stabilization is still required.

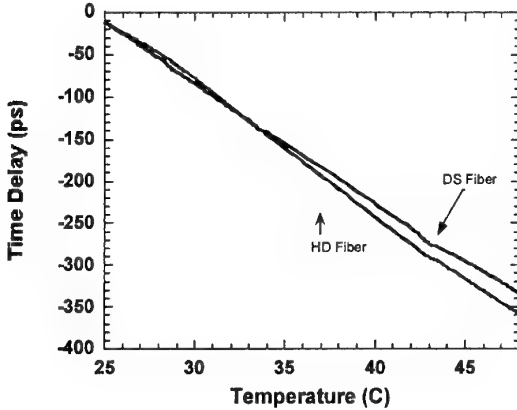


Figure 1. Time-delay variation with temperature for dispersion shifted and high dispersion fiber.

Both the latency and the need for thermal control of the beamformer prompted investigations into the use of chirped fiber gratings in place of the high dispersion fiber. Various researchers have investigated discrete or chirped fiber gratings as the time-delay elements in beamformers [10]. Preliminary investigations at NRL utilized identical gratings in a shared fashion between time-delay feeds [11]. Subsequent investigations verified the improved temperature stability which was expected due to the much shorter lengths of fiber necessary to achieve the necessary time-delays. Figure 2 shows temperature stability measurements of a chirped fiber grating compared to an equivalent length of high dispersion fiber. Additionally, fiber gratings may be housed in temperature insensitive packages. It appears that the use of fiber gratings will result in a robust system without need for temperature stabilization.

Current investigations of chirped fiber gratings center about the achievable time-delay resolution. Measurements on many identical gratings both with and without apodization indicate a minimum practical time-delay resolution of ~ 1 to 2 ps. This is more than sufficient for most array applications. One major difficulty in chirped grating-based approaches is the commercial unavailability of long gratings (> 15 cm). This limits the design and architecture of photonic beamforming. In efforts to avoid this problem, we have implemented and demonstrated a cascade grating approach which will be discussed further in section IV.

Another issue with the unavailability of long gratings is the resultant inability to properly apodize the gratings for minimum amplitude and phase ripple. In general, a beamformer will require a grating with good reflectivity ($> 90\%$) that does not vary appreciably over the useable

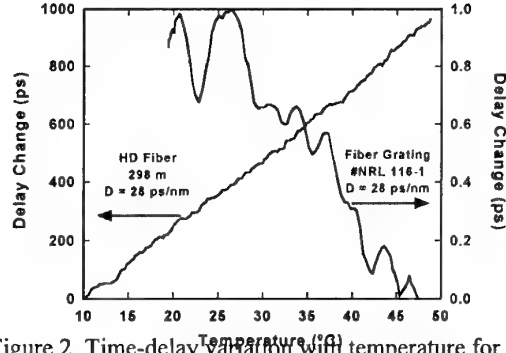


Figure 2. Time-delay variation with temperature for a chirped fiber grating and high dispersion fiber.

bandwidth which may be ~ 30 nm. Proper apodization (e.g. raised cosine, Gaussian) normally requires that a substantial portion of the bandwidth has a reflectivity less than that which is desired. Thus, to minimize the ripple, the phase mask and grating should be many times longer than the desired grating further reducing the available grating length. In practice, the most effective apodization profiles cannot be used. The impact of this is mostly evident in the fine ripple structure and not the more macroscopic time-delay errors mentioned earlier.

III. RAPIDLY TUNABLE LASERS

One of the key components which make dispersion-based beamforming practical is the ultra-fast tunable laser. Several forms of tunable lasers are available. For most beamforming applications, rapid beam-steering is a critical parameter. This places severe limits on the choice of tunable lasers.

For our systems we focus primarily on a commercial, tunable Super Structure Grating distributed Bragg reflector (SSG-DBR) laser [NTT ref]. Functionally, Altitun, Nortel and Lucent also produce similar devices. These lasers exhibit an inherent fast tuning ability (nanosecond speeds demonstrated) via three wavelength-control currents injected into the rear reflector, front

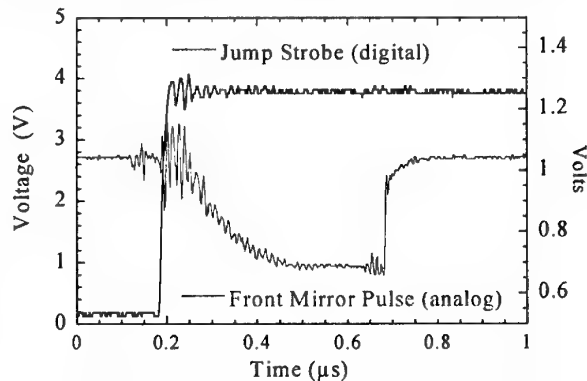
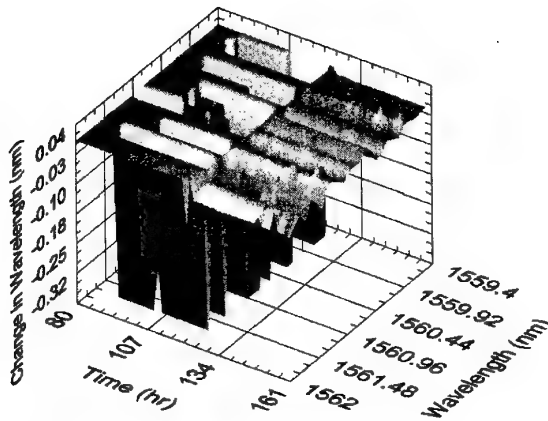


Figure 3. Measurement of the tuning speed of an SSG-DBR laser with a high-speed control circuit.

reflector, and phase control regions of the laser. Since there is currently no commercially available driver



boards

Figure 4. Measurement of the wavelength change of an SSG-DBR laser due to aging. Corrections to the control currents were applied at ~ 125 hours.

with fast switching times, a mixed analog/digital high-speed circuit board capable of driving the laser was developed and fabricated. The board allowed wavelength tuning of >20 nm with 0.1 nm resolution and 0.02 nm accuracy and demonstrated access times of < 500 ns. Figure 3 shows circuit board controlled laser wavelength switching speed to be ~ 450 ns.

To successfully implement the digital control of such a laser, an in-house developed software algorithm was necessary to determine the currents needed for each specific wavelength and to generate the look-up table containing the rear, front, and phase control currents [12]. Once this table or wavelength map is generated, the values are programmed into an electrically erasable/programmable read only memory (EEPROM). After programming, the board accepts differential TTL driving signals to load the desired wavelength and to initiate the wavelength switch, thus controlling the beam steering direction.

A major limitation of the SSG-DBR laser was a slight degradation or aging in the output wavelength over time. As aging occurs, the output wavelength changes by either mode hopping or drifting with no change in the input current values. A new wavelength correction algorithm was implemented to correct for this degradation. After an initial input current to output wavelength mapping, only a few wavelengths require monitoring. Measurements indicate that this only needs to be performed on a weekly or monthly basis and real-time monitoring is not required. These selected wavelengths are corrected by using a software feedback control loop controlling the injected currents and carefully monitoring the output wavelength. The algorithm computes a new vs. old injected current relationship to desired output wavelength to generate a linear relationship that is applied to correct ALL of the wavelengths simultaneously. This is possible since the initial mapping of the laser provides the general relationship of input current vs. output wavelength and this relationship is maintained over time.

Figure 4 shows the experimental results of the algorithm. Initially we tuned the laser in 0.1 nm steps over a bandwidth of 1540 to 1565 nm. Shortly after 80 hours, observations of corrupted wavelengths (mode-hops in this case) begin to appear. The correction

algorithm was applied at 125 hours to correct the corrupted wavelengths by monitoring a few selected wavelengths. The range 1559.4 to 1562 is shown in the figure for clarity. The equations could have been applied when there was 80 hours of use on the laser to preempt any mode hopping. It is important to note that only monitoring of a few drop out points can be used to correct all of the degenerate wavelengths. Also, all dropout wavelengths were corrected to within the ± 0.02 nm accuracy of the wavemeter used.

Component Level Diagram

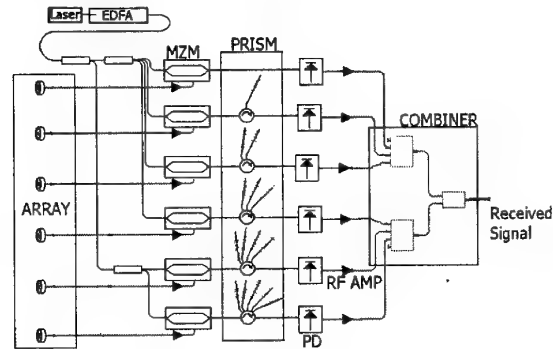


Figure 5. Schematic of a 1x6 grating-based receive beamformer.

Dynamic range and noise figure are still issues that require optimization if these fast tunable lasers are to find pervasive use in photonic beam forming systems. Insufficient line width (> 50 MHz) as well as insufficient optical power levels (~ -5 to 0 dBm) can yield increased RIN levels which lead to poor system performance from a microwave view. These issues are being actively investigated.

IV. RECENT SYSTEM RESULTS

As mentioned earlier, a cascade-grating approach has been proposed and demonstrated in order to circumvent the need for very long fiber gratings [13]. This technique makes use of the fact that gratings fabricated from the same phase mask are identical. Thus any grating imperfections or non-linearities in time-delay response are common to all channels and do not result in a time-delay error. The demonstrated architecture is shown in Figure 5.

The demonstrated system was a one-dimensional, six-element receiver with an element spacing of ~ 4 inches. This is believed to be the first continuously tunable, chirped grating, true time-delay ultra-wide bandwidth receive beamformer. This system exhibited squint-free, time-delay steering over azimuthal angles of $\pm 60^\circ$. Figure 6 shows typical data with the beamformer steered to 45° .

Another recent demonstration involves an approach to greatly simplify two-dimensional beamforming. This technique relies on the fact that the required time-delay gradient for any array steering vector is essentially one-dimensional in nature [14, 15]. Thus, if the required 1D

time-delay gradient is generated, a simple reconfiguration of the time-delay feeds will result in two-dimensional steering.

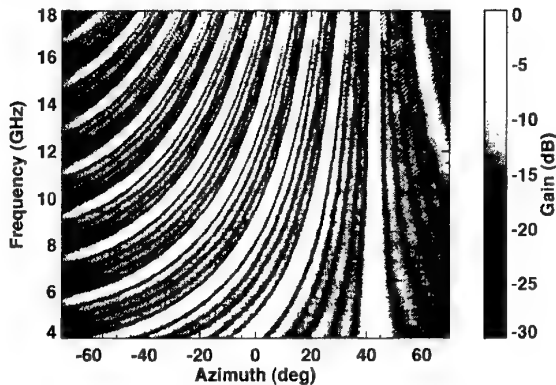


Figure 6. Anechoic chamber measurement of the receiver with the beam steered to 45°.

V. CONCLUSIONS

The use of dispersion-based techniques for beamforming applications has shown much potential. Investigations are now proceeding to address some of the more practical issues aimed at making the technique viable for "real-world" systems. These issues include the temperature stability and time-delay resolution of the beamformer. The use of chirped fiber gratings alleviates many of the issues with fiber-based dispersion techniques. Another critical issue is the performance and control of the tunable laser source. It was shown that by periodically monitoring a few wavelengths, the aging characteristics of all laser wavelengths may be compensated simultaneously. Other issues which were not discussed but will be presented include the phase and amplitude stability of the fiber-optic remoting cable, component wavelength flatness, RJN issues and modulator bias stability. Recent demonstrations of a fiber-grating receive beamformer and a simplified, reconfigurable array architecture indicate that many of the practical issues are being addressed.

ACKNOWLEDGMENTS

This work was supported by the Office of Naval Research.

REFERENCES

- [1]. R. Soref, "Optical dispersion technique for time-delay beam steering," *Appl. Opt.*, vol. 31, pp. 7395-7397, Dec. 1992.
- [2]. D.T.K. Tong and M.C. Wu, "A novel multi-wavelength optically controlled phased array antenna with a programmable dispersion matrix," *IEEE Photon. Tech. Lett.*, vol. 8, pp. 812-814, 1996.
- [3]. R. Soref, "Optical dispersion technique for time-delay beam steering," *Appl. Opt.*, vol. 31, pp. 7395-7397, Dec. 1992.
- [4]. M.Y. Frankel and R.D. Esman, "True time-delay fiber-optic control of an ultrawideband array transmitter/receiver with multibeam capability," *IEEE Trans. Microwave Theory Techn.*, vol. 43, no. 9, pp. 2387-2394, Sept. 1995.
- [5]. M.Y. Frankel, P.J. Matthews and R.D. Esman, "Two-Dimensional, Fiber-Optic Control of a True Time-Steered Array Transmitter," *IEEE Trans. on Microwave Theory and Techniques*, vol. 44 (12), pp. 2696-2702, Dec. 1996.
- [6]. P.J. Matthews, *et al.*, "A Wideband, Fiber-Optic, True Time-Steered Array Receiver Capable of Multiple, Independent, Simultaneous Beams," *IEEE Photon. Techn. Lett.*, vol. 10, no. 5, pp. 722-724, May, 1998.
- [7]. D.A. Tulchinsky, *et al.*, "Fiber-Optic Control of a Time-Steered Millimeter-Wave Transmit Array," *1999 Int. Topical Meeting on Microwave Photonics*, paper F-11.3, pp. 279-282, Melbourne, Australia, Nov. 17-19, 1999.
- [8]. P.J. Matthews, *et al.*, "Demonstration of a wideband, fiber-optic nulling system for array antennas," *IEEE Trans. on Microwave Theory and Techniques*, vol. 47 (7), pp. 1327-1331, July, 1999.
- [9]. J. Lawrence, *et al.*, "Advanced Electronic Countermeasures Transmitter For Ship Defense," *43rd Joint Electronic Warfare Conf.*, Colorado Springs, CO, April 27-30, 1998.
- [10]. See for instance, R.A. Minasian and K.E. Alameh, "Ultimate beam capacity limit of fibre grating based true-time-delay beam-formers for phased arrays," *1998 IEEE Int. Microwave Symp.*, paper TH2C-4, pp. 1375-1378, June, 1998 and refs. therein.
- [11]. J.E. Roman, M.Y. Frankel, P.J. Matthews, and R.D. Esman, "Time-steered array with a chirped grating beamformer," *Electron. Lett.*, vol. 33, pp. 652-653, Apr. 1997.
- [12]. P.D. Biernacki, M.Y. Frankel, M. Gingerich and P.J. Matthews, "A high-speed accurate tunable laser mixed digital/analog circuit board for fiber optic communications," *IEEE Journ. of Lightwave Technology*, vol. 17 (7), pp. 1222-1228, July, 1999.
- [13]. J.B. Medberry, P.D. Biernacki and P.J. Matthews, "Range Demonstration of an Ultra-Wideband, Continuous, Time Steered Array Using a Fiber-Optic, Cascaded Grating Prism," *2000 IEEE Int. Microwave Symp.*, Boston, MA, paper TUIF-52, June 11-16, 2000.
- [14]. M. Y. Frankel and R. D. Esman, "Reconfigurable time-steered array-antenna beam former," *Appl. Optics*, vol. 36, pp. 9261-9268, 1997.
- [15]. D.A. Tulchinsky and P.J. Matthews, "Demonstration of a Reconfigurable Beamformer for Simplified 2-D, Time-Steered Arrays," submitted to the 2000 Int. Topical Meeting on Microwave Photonics, Oxford, UK, Sept. 11-13, 2000.

BEAMTAP Beam Forming using a Traveling Fringes Detector

G. Kriehn, G.S. Pati, P.E.X. Silveira, F. Schlottau, K. Wagner
 Optoelectronic Computing Systems Center
 Department of Electrical and Computer Engineering
 University of Colorado, Boulder, CO 80309-0425
 1-(303) 492-4661 Fax: 1-(303) 492-5810, kelvin@colorado.edu

D. Dolfi, and J.P. Huignard
 Thomson CSF
 Laboratoire Central de Recherches
 Domaine de Corbeville
 91404 Orsay CEDEX, France

Abstract

Demonstration of traveling-fringes-detector operation for beam forming on simulated signals from a fiber-remoted phased array using a true-time-delay RF-photonic processor implementing the BEAMTAP (Broadband Efficient Adaptive Method for True-time-delay Array Processing) algorithm is presented.

1 Introduction

As future antenna array systems tend towards wider bandwidth and thousands or more elements, the communication and processing of these signals is becoming more complex and demanding. In this paper, we demonstrate an efficient RF photonic approach to performing these complex broadband beam-forming and adaptive jammer-nulling operations for very large phased-array antennas ($N > 1000$ elements) using the BEAMTAP algorithm and its optical implementation [1, 2]. BEAMTAP reduces the number of tapped-delay-lines required to process an N -element phased-array antenna from N to only 2, which can be seen in the algorithm diagram in Fig. 1. A tapped delay-line is used to update an adaptive weight matrix, which when read out and input into the shift-and-add delay-line, provides an adaptive algorithm with a single output $o(t)$ equivalent to the time-domain LMS adaptive beam former

$$o(t) = \sum_{n,m} s_n(t-m\tau) \int_{-\infty}^{t-M'\tau} s_n^*(t'-m\tau) [d(t')-o(t')] dt',$$

where the desired signal $d(t)$ is subtracted from the output signal $o(t)$ to produce the feedback signal $f(t)$ necessary for the weight adaptation.

The use of a single traveling-wave detector such as a photoconductive traveling-fringes detector [3, 4] (TFD) allows for the generation of the necessary shift-and-add time-delays in the electrical (rather than the optical) domain, while the tapped delay line can be implemented compactly using an acousto-optic device (AOD) for

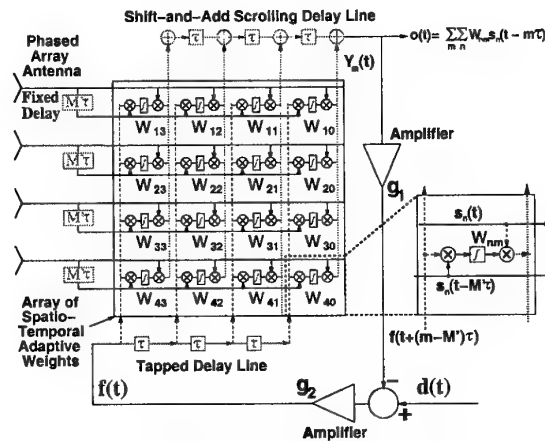


Figure 1: BEAMTAP algorithm for broadband squint-free true-time-delay beam forming using a single output shift-and-add scrolling delay line. For adaptive calculation of the weights within the array, the feedback and additional tapped delay-line is also required.

the input. A schematic diagram of the optical BEAMTAP architecture with the necessary TDLs is shown in Fig. 2. A single coherent laser is split using two beamsplitters to drive both the fiber-feed network and the BEAMTAP processor – the fiber-feed network from the phased array is shown on the left. Diffracted light from the AOD interferes with modulated signals from the array, which are imaged through lens system L_0 , to form gratings in the photorefractive crystal (PR crystal). Diffraction of the phased array signals off this grating are detected by a synchronous TFD which has a carrier velocity matched to the magnified acoustic velocity of the AOD by the lens systems L_1 and L_2 —producing a resonant charge carrier distribution $q(x_2, t)$. The output signal $o(t)$ is amplified by g_1 , subtracted from the desired signal $d(t)$, and fed back into the AOD as the feedback signal $f(t)$ amplified by g_2 , to close the adaptive feedback loop necessary for the system to cancel any jamming signals present in the signal environ-

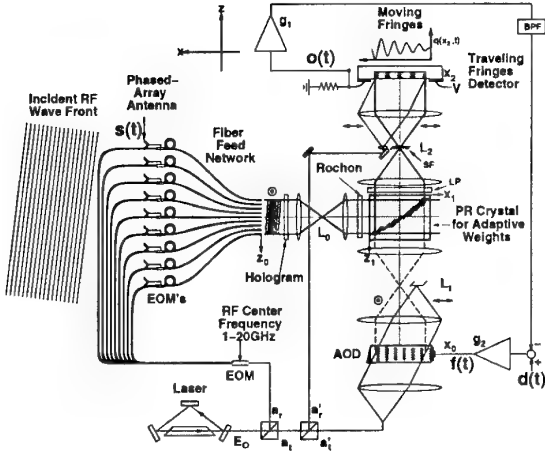


Figure 2: Optical BEAMTAP architecture.

ment. A Rochon prism, linear polarizer (LP), and spatial filter (SF) are used for the read-write isolation of the AOD beam from the diffracted phased array signals.

2 Traveling-Fringes Detector

A traveling-fringes detector for RF signals uses a photoconductive layer of GaAs which allows for detection of a 1 GHz signal at a center frequency up to 20 GHz. [4] The detector is based upon the synchronous drift of photo-generated carriers with a moving interference pattern generated by interfering two beams of coherent light tilted by θ with difference frequency f_d yielding a fringe velocity $v_f = f_d \lambda / \sin \theta$. Light which is incident on the photoconductive layer of the detector will generate photocarriers with a drift velocity v_d , and by varying the applied bias voltage in the layer, which in turn changes the carrier velocity, a resonance peak occurs when the fringe velocity v_f equals the photocarrier speed v_d . [3]

An optical implementation which allows the TFD to be used for broadband detection requires that an acousto-optic deflector (AOD) be used to simultaneously modulate and deflect an optical carrier with a broadband RF signal in which the deflection angle of the beam is linearly dependent upon the applied frequency. This is shown in Fig. 3. Each deflected beam experiences a Doppler shift with respect to the incident beam due to the interaction of the light with the acoustic wave such that the angular frequency of the diffracted wave is $\omega_d = \omega_o + \Omega$, where ω_o is the angular frequency of the incident laser beam and Ω is the angular frequency

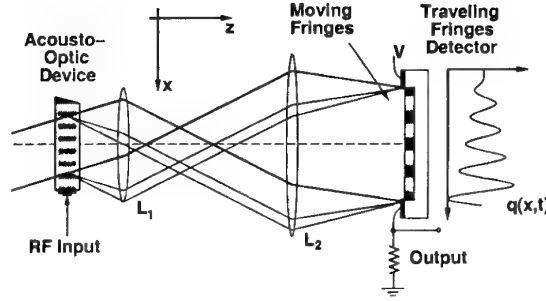


Figure 3: Generation and detection of a broadband RF signal using an acousto-optic device imaged onto a velocity matched traveling-fringes detector.

of the acoustic wave. Thus each frequency component diffracted by the AOD has a proportional frequency and angle that, with the appropriate magnification M , produces an image propagating with the detector's resonant velocity $v_f = Mv_A = v_d$ when interferometrically detected with the undiffracted reference beam from the AOD. The telecentric $4f$ lens system is used to scale the velocity of the moving interference pattern to match the photocarrier velocity of the TFD since the acoustic velocity of the AOD can be up to an order of magnitude slower than the carrier velocity of the detector, depending upon the type of carrier (electron or hole) being used for resonant detection.

3 Results

The time delay achievable with a $500\mu\text{m}$ width GaAs TFD using electron transport is limited to a few nanoseconds due to the high mobility of electrons in GaAs. By utilizing the 20 times lower mobility of holes for the resonant carriers in the TFD, we can increase the available time delay in the scrolling delay line to about 60ns, allowing for the squint free processing of arrays up to 20m in diameter. Previously we demonstrated broadband detection with the TFD using electron transport by detecting an $8\mu\text{s}$ 250 MHz BW chirp riding on a 750 MHz carrier. [5] Hole-resonant transport was achieved by reversing the bias across the device and by changing the magnification system between the AOD and TFD. Figure 4a shows an $8\mu\text{s}$ 250 MHz pulse-compressed chirp centered at a carrier frequency of 995 MHz which was input into the AOD, with the broadband detected output of the TFD shown in Fig. 4b. Notice that the full 250MHz bandwidth signal

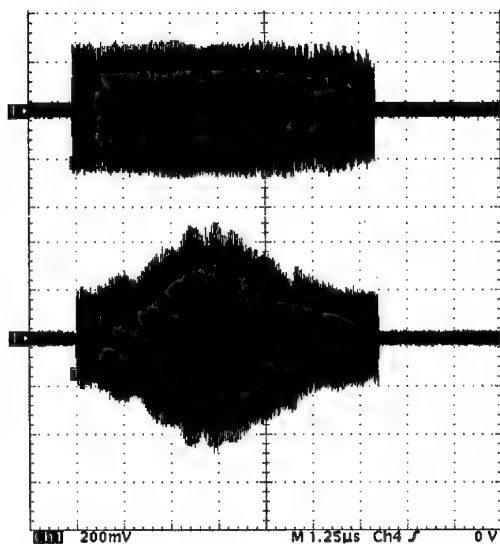


Figure 4: (a) $8 \mu\text{s}$ 250 MHz bandwidth chirp input into the AOD. (b) The detected output after amplification shows the reconstruction of the chirp signal using the TFD detector in a hole-resonant transport mode of operation.

has been faithfully reconstructed, with a slight amount of ringing present due to the frequency response of the amplifiers.

To verify the time-delay capability of the TFD in hole-transport mode, the detector was translated by $250 \mu\text{m}$ and the detected output signal was cross-correlated with the detected signal having no translation. The frequency spectrum of the pulse was digitally filtered to remove unwanted residual harmonics, and down converted back to baseband. Fig. 5 shows the auto-correlation in conjunction with the cross-correlation between the translated band untranslated signals demonstrating a delay of 60 ns demonstrating in addition to the faithful production of the time-delayed signal. Thus the TFD has the capabilities necessary for operation as a scrolling input delay-line for the optical implementation of BEAMTAP.

Figure 6 shows the experimental setup demonstrating the beam forming operation of the optical BEAMTAP processor. The AOD in the upper portion of the figure acts as a simulated array of inputs from an actual phased-array antenna, since the signal of interest $s(t)$ to be detected is delayed at each simulated antenna element as the acoustic waves traverse the illuminated laser spot within the aperture of the AOD.

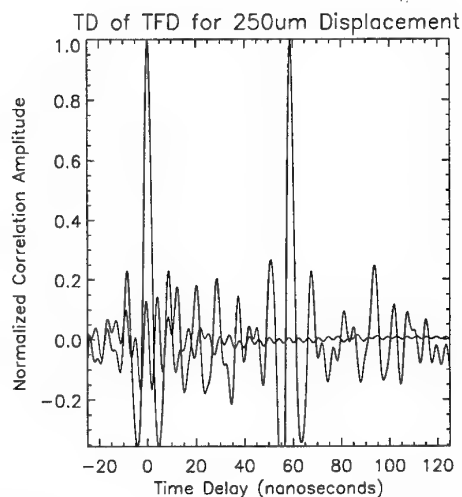


Figure 5: Autocorrelation of the TFD detected chirp waveform, superimposed with the cross correlation of the detected output after translating the detector $250 \mu\text{m}$, demonstrating 60 ns of time delay.

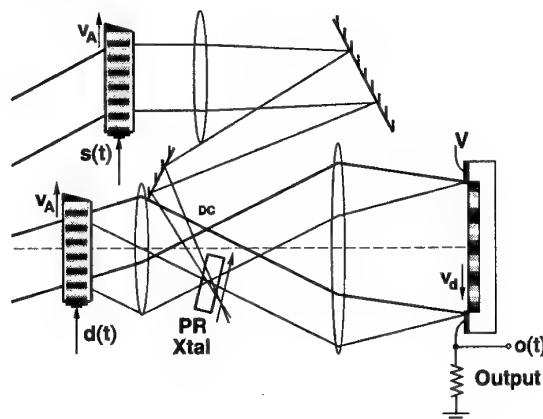


Figure 6: Experimental setup using an AOD to simulate the time-delays incident on the array to demonstrate the true-time-delay beam forming capabilities of optical BEAMTAP.

The diffracted light containing this signal of interest is focused into a photorefractive crystal, whereby diffracted light from the beam steering AOD containing the desired signal $d(t)$ creates a cross-correlation between the two signals. This cross-correlation builds up a holographic grating and produces a set of weights which allow for the beam forming operation and the coherent summation of the signal $s(t)$ once these weighted signals are fed into the TFD scrolling delay line. Diffracted light from the feedback arm of the

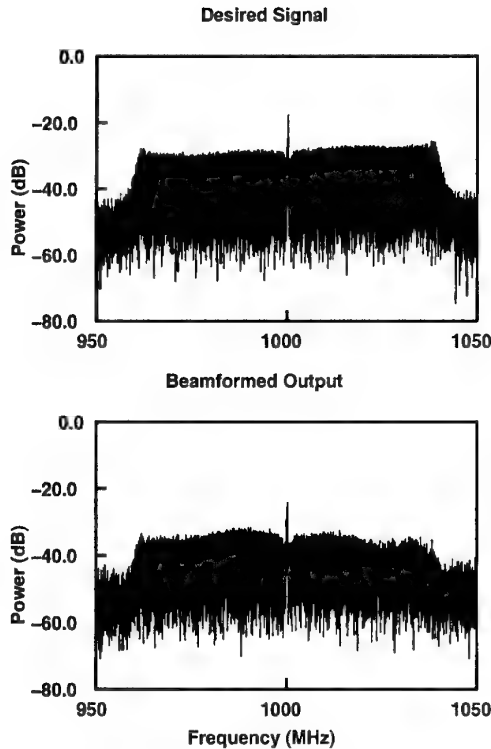


Figure 7: (a) Frequency spectrum of the desired signal $d(t)$. (b) Frequency spectrum of the beam formed output, showing that the signal spectrum of the signal of interest $s(t)$ has been reliably detected.

processor containing the desired signal $d(t)$ is then blocked so that the weight matrix can be read out using diffracted signals from the simulator, where they are imaged onto the TFD and interferometrically detected. Figure 7 show the detected output of the beam forming operation. Notice the faithful reconstruction of the signal across the full 80 MHz bandwidth, demonstrating the beam forming operation of the optical BEAMTAP processor.

4 Conclusion

We have shown how the time delay within a traveling-fringes detector can be increased using hole-resonant transport mode of operation to allow for the beam forming operation of the optical BEAMTAP processor. Experimental results have demonstrated 60 ns of time delay, and beam forming using an 80 MHz chirped pulse have been performed. A cross-correlation between the signal of interest and the desired signal create a weight matrix within a photorefrac-

tive crystal by the formation of a holographic grating. Diffraction of light containing the signal of interest off this grating and the subsequent interferometric resonant and coherent detection on the TFD, which acts as a scrolling-delay line, then allows for the beam forming operation of the BEAMTAP processor to be completed.

We wish to acknowledge the support by Dr. William Miceli of ONR and the Office of the Secretary of Defense DDR&E through the MURI program grant no N00014-97-1-1006. Useful discussions with Drs. S. Kraut, L. Griffiths, T. Sarto, S. Weaver, and T. Weverka are gratefully acknowledged.

References

- [1] K. Wagner, S. Kraut, L. Griffiths, S. Weaver, R. T. Weverka, and A. W. Sarto, "Efficient true-time-delay adaptive-array processing," in *Proc. SPIE*, vol. 2845, August 1996.
- [2] G. Kriehn, A. Kiruluta, P. E. X. Silveira, S. Weaver, S. Kraut, K. Wagner, R. T. Weverka, and L. Griffiths, "Optical BEAMTAP beam-forming and jammer-nulling system for broadband phased-array antennas," *Applied Optics* **39**, pp. 212–230, January 2000.
- [3] T. Merlet, D. Dolfi, and J.-P. Huignard, "A traveling fringes photodetector for microwave signals," *IEEE Journal of Quantum Electronics* **32**(5), pp. 778–783, 1996.
- [4] D. Dolfi, T. Merlet, A. Mestreau, and J.-P. Huignard, "Photodetector for microwave signals based on the synchronous drift of photogenerated carriers with a moving interference pattern," *Applied Physics Letters* **65**(23), pp. 2931–2933, 1994.
- [5] G. Kriehn, A. M. Kiruluta, K. H. Wagner, D. Dolphi, and J.-P. Huignard, "Detection of a broadband rf signal using a traveling fringes detector," in *Terahertz and Gigahertz Photonics*, vol. 3795, Proc. SPIE, 1999.

A BRIEF HISTORY OF PHOTONIC ANTENNA RECONFIGURATION

Michael L. VanBlaricum
Toyon Research Corporation

75 Aero Camino, Suite A • Goleta, CA 93117, USA
805-968-6787 x 157 • FAX 805-685-8089 • MikeVanB@Toyon.com

Abstract: The primary focus of photonics for antenna systems has, historically, been on the development of link and beam steering techniques. By using photonically controlled devices and materials it is possible to produce revolutionary changes in antenna elements and in the design and properties of arrays, opening the door for a new class of antennas. In this paper we survey the history and current status of photonically reconfigurable antennas. We look at photonic control of reactive devices and the optically variable capacitor (OVCTM) and the evolution of this device towards monolithic integration. Finally, we also will look at the state of photonically reconfigurable silicon and its application to antenna design.

1. Introduction

The use of photonic-based antenna feeds, links, and controls opens the possibility of unique, very high performance antenna systems. Historically, the primary application of photonic technology for antenna systems has been on the development of link and beam steering techniques. Over the last few years, however, work has begun to focus on using photonics to produce new approaches to the design of antenna elements themselves. By using photonically controlled devices and materials (switches, reactive devices, photoconductive materials) in the antenna aperture it is possible to produce revolutionary changes in antenna element and phased array design and properties.

Photonically controlled devices do not require conducting lines running to them in order to provide power or control signals but instead use fiber optical cables or direct optical illumination to control devices or to manifest changes in materials. Using these devices and materials it is possible to remotely change the effective characteristics (such as gain, tuning, bandwidth, and RCS) of an antenna aperture. Hence, photonics opened the door for a new class of antennas - Photonically Controlled Reconfigurable Antennas.

The idea of antenna reconfiguration is not a new one. Antenna designs using diodes or varactors to tune or switch the polarization states of an antenna have been around for some time. Patents by Schaubert [1] show that placing electronically controlled switching posts in patch antennas allows one to control the frequency, polarization, and directivity of this type of antenna. In a

patent by Bhartia [2] a pair of varactor diodes are used to replace the switching diodes as described by Schaubert. This approach allows the impedance of the "post" or "load" to be varied and hence more than two states can be obtained. Electronic reconfiguration using metallic control lines has always been limited in utility because of the interaction of the conducting control lines with the antenna element.

In 1985, Daryoush, Bontzos and Herczfled [3] introduced the concept of using an optically controlled PIN diode to tune a patch antenna. In their configuration, shining light directly on the device varied the PIN diode's impedance characteristics. This approach removed the wire connection and allowed the control device to be placed in the plane of the antenna itself. However, the use of direct optical illumination of a PIN diode has the problem that the quality factor (Q) of the device varies (degrades) as a function of the optical illumination. In other words, the resistance, as well as the capacitance vary and limit the use of this technique as a tuning device. Nevertheless, this appears to be the first use of optically controlled devices to reconfigure an antenna element.

In a 1988 patent, Dempsey [4] presented the concept of the Synaptic antenna in which a three-dimensional matrix of electrically conductive segments (wires) are configured with "photoresponsive devices" selectively placed between numerous adjacent segments. The "photoresponsive devices" are used as switches to control the path length of the conductive segments. This allows the reconfiguration of the conducting state of the system. Hence, the antenna can be changed by activating or deactivating the "photoresponsive devices." Figure 1 presents the conceptual drawing, taken from the patent [4], of this system.

In Dempsey's original patent there is no statement of how these "photoresponsive devices" are to be built. In 1989 Dempsey [5] presented a conference paper on the theory of the Synaptic antenna. In this paper the matrix of thin conductive line segments are joined or synapsed at nodes with photoconducting cells, called Photistors™, which can be turned on by optical energy alone. The Photistor™ was stated to have an equivalent circuit of a 10K ohm "dark" resistor in parallel with a 0.05 pf capacitor which essentially open-circuits the element. When the device is illuminated, the resistor assumes the "on" value of about 1-ohm, effectively shorting the segment.

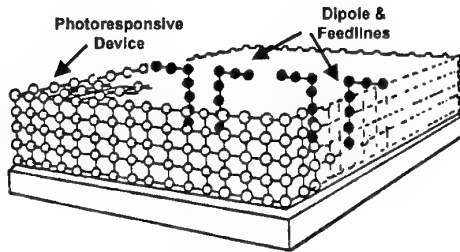


Figure 1 - A conceptual drawing of the generalized synaptic system [4] showing two dipoles and feedlines turned on via photoresponsive devices in a three dimensional matrix.

2. Photonic Switches

Photonic switches are the critical technology for most of the early photonic reconfigurable antenna concepts. Fortunately, optoelectronic switch technology has been studied for microwave circuits for some time. Microwave optoelectronic switches have several advantages over conventional PIN diodes or GaAs MESFETs besides the removal of a metal wire. Claims have been made that promise faster rise and fall times, broader bandwidth, ability to handle higher power, and simplicity of operation [6].

Two photoconductive materials commonly used to make photonic switches are GaAs and silicon. Both materials exhibit a high dark state DC resistance and a low illuminated state DC resistance. The Photistor™ discussed in the synaptic antenna has been reported to be a silicon photoconductor which can be switched from a $2000\ \Omega$ "off" impedance to a $6\ \Omega$ "on" impedance with $100\ \mu\text{W}$ of light [7] and a useful upper frequency of about 1 GHz. These devices were used by California Microwave, Inc [8] to build a digitally reconfigurable multi-band (100 MHz to 1000 MHz) antenna containing four synapses and twelve optical control fibers, which were used to operate the antenna in three different bands. The high-band and the mid-band synapses were configured as sleeved dipoles. The low band synapses were also sleeved dipoles but they were configured as a two-element array.

In the silicon photoconductor switch, the semiconductor switching material is illuminated directly. Another approach, that has been investigated, is to illuminate a photovoltaic (PV) cell, which then generates a voltage that activates a FET [9,10] or a PIN [11] switch. These devices are known as PV-FET and PV-PIN switches, respectively. In the PV-FET developed by Albares [10], a $3\ \Omega$ "on" resistance and a $>30\ \text{M}\Omega$ "off" resistance were reported using optical power less than 1 mW. The PV-PIN switch that was reported was designed to switch a VHF radio monopole antenna length from 90 to 180 cm, thus changing its resonant frequency.

The switches discussed so far were used to switch fairly basic dipole and monopole antennas into different lengths. A more complex and innovative, if not ambitious, reconfigurable antenna concept using photonic switch technology is the Structurally Embedded Reconfigurable Antenna Technology (SERAT) which has been reported by Gilbert [12] of Sanders. The basic SERAT concept is comprised of an array of dual-polarized dipole antenna elements whose dimensions can be altered with photonic activated RF switches. These elements are integrated into the top layer of a multilayered composite structure comprised of passive frequency selective surfaces (FSS) that form a broadband ground plane system. The reconfigurable aperture that was reported [12] was a 3×3 -array panel that was successfully operated from 500 MHz to 2 GHz.

3. Reconfiguration via Reactive Loading

Reactive loads can be used with great effect to control matching, radiation, and scattering characteristics of an antenna. The tuning, gain, or RCS of an antenna or array can be changed by varying the reactive impedance values of control loads placed either in the feed gap or in the arms of an antenna element. Pattern and RCS control is understood heuristically if one considers that the directivity and the RCS of an element are related to the distribution of current over the arms of an element (or over the aperture of the antenna). If this current distribution can be modified in phase and/or magnitude, then the directivity or RCS pattern will be changed.

Reconfigurable antennas may be constructed by embedding reactive loads such as varactor diodes within the radiating structure or the feed region. Optical control of varactor diode reactance for reconfigurable antennas offers all of the advantages normally associated with optical links—low-loss, lightweight, immunity to noise, isolation from RF circuit—but has the additional advantage of extremely low optical power requirements as compared with many other reconfigurable antenna technologies.

Varactor diodes may be controlled optically using two techniques: direct control, or indirect control. With direct control, the active region of the device is illuminated with the optical control signal. The same device thus performs both optical and microwave functions, which often involve contradictory design requirements. The maximum achievable capacitance tuning range is also limited for a given range of illumination intensities. Illumination of the varactor diode also leads to a reduction in the Q-factor of the diode. An alternative scheme is indirect control, where the optical control signal is first converted to a suitable electrical form by a dedicated detector. The electrical control signal governs the bias point of the varactor diode, which is part of the microwave network [13].

Optically Variable Capacitor (OVC™) circuits have been developed by Toyon [13] for indirect optical control. The OVC consists of a photovoltaic array that controls the reverse bias across a varactor diode. A change in the incident optical power leads to a change in the photovoltaic array output voltage. This varies the depletion width of the varactor diode and thereby its junction capacitance. Hence this arrangement makes it possible to control the capacitance using optical signals. There are several advantages to this method: 1) the optical signal is used for bias as well as control of the active device thus eliminating the need for external bias. 2) Since the photovoltaic array drives a reverse biased varactor diode (low leakage current) the optical power requirements are small. 3) The optical detection and variable capacitance functions are provided by separate components and hence it is possible to optimize them independently. The varactor diodes are designed to provide the desired capacitance swing with the lowest possible RF insertion loss while the photovoltaic arrays are designed to provide the desired bias swing across the varactors using as low optical power as possible.

Toyon [14] reported using the OVC™ for both tuning of electrical small loops and pattern control of spiral antennas. Figure 2 shows the tuning obtained for three different size electrically small loops. In this case, the Q was preserved over the entire tuning range of the loop.

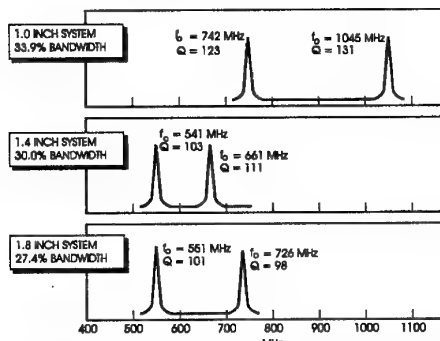


Figure 2 - Measured tuning range for three electrically small loop antennas tuned with Toyon's OVC™.

Nagra, et.al. [15] have reported a monolithic implementation of the OVC™ circuit in GaAs using a novel lateral oxidation technique for device isolation. A maximum capacitance swing from 1.1 pF to 0.47 pF was recorded. This device has been integrated in planar antenna and other microwave circuit structures. An optically tunable folded slot antenna incorporating the OVC as the tunable element is shown in Figure 3. The folded slot antenna was designed to be $\lambda/2$ long at 18 GHz. Due to capacitive loading of the antenna by the OVC, the resonance frequency was shifted down to 14.5 GHz. When optical power is incident on the OVC, the varactor capacitance decreases thus causing the resonance frequency to increase. The folded slot

antenna resonance frequency was tuned from 14.5 GHz to 16 GHz by using just 450 μ W of optical power.

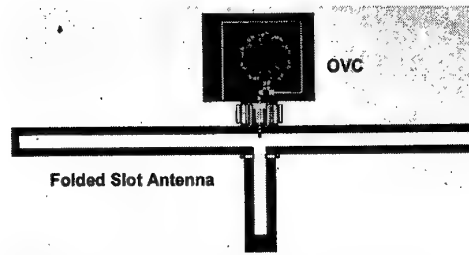


Figure 3 - Monolithic OVC controlling a folded slot antenna.

4. Photoconductive Reconfigurable Antennas

Photoconductive silicon based antennas activated by laser pulses have been investigated vigorously in recent years. A variety of novel technologies have been demonstrated in this area. A semiconductor element will become photoconductive when activated by CW laser illumination, and thus it can serve as a metal-like electromagnetic (EM) radiator [16,17]. When the laser source is off, the antenna element becomes essentially transparent to the EM wave, thus it will give no interference to nearby active elements and also is immune from EM detection. Many of the initial photoconductive reconfigurable antenna studies reported in the literature have used the basic bowtie antenna as the radiating element. Raytheon [16] has illuminated their antenna by shining laser light directly on the element. More recently, Sanders [18] has developed a light tank delivery system that uses optical fiber to feed the light on the element. This system is shown schematically in Figure 4.

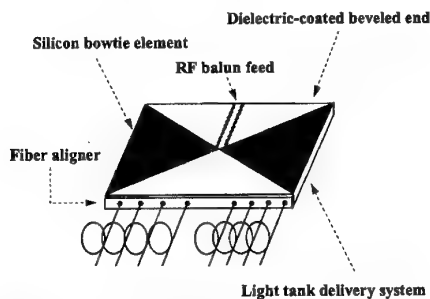


Figure 4 - The schematic of the Sanders [18] light tank delivery system.

5. Summary

We have briefly introduced the concept of photonically reconfigurable antennas and have shown examples of different reconfiguration technologies that are most commonly being studied presently. By using

photonically controlled devices and materials it is possible to produce revolutionary changes in antenna elements and in the design and properties of arrays. In this paper we surveyed the history and current status of photonically controlled switches for application in antennas. We also looked at photonic control of reactive devices and the optically variable capacitor (OVC™), the evolution of this device towards monolithic integration, and examples of how it is used. Finally, we briefly introduced photonically reconfigurable silicon and its application to antenna and array design.

6. REFERENCES

1. D. Schaubert, F. Farrar, S. Hayes, and A. Sindoris, "Frequency-Agile, Polarization Diverse Microstrip Antennas and Frequency Scanned Arrays," US Patent #4,367,474, Jan. 4, 1983.
2. P. Bhartia and I. Bahl, "Broadband Microstrip Antennas with Varactor Diodes," US Patent # 4,529,987, July 16, 1985.
3. A. Daryoush, K. Bontzos, and P. Herczfled, "Optically Tuned Patch Antenna for Phased Array Applications," *IEEE AP-S International Symposium Digest*, Philadelphia, PA, pp. 361-364, 1986.
4. R. Dempsey, "Synaptic Radio Frequency Interactive Systems with Photoresponsive Switching," US Patent #4,728,805, Mar. 1, 1988.
5. R. Dempsey and R. Bevensee, "The Synaptic Antenna for Reconfigurable Array Applications - Description," *IEEE AP-S International Symposium and URSI Radio Science Meeting*, June 26-30, 1989, San Jose, CA, pp. 760-763.
6. R. Simons, *Optical Control of Microwave Devices*, Artech House, Boston, 1990, pp. 157-164.
7. S. Wojtczuk, "Photistors: Bias-Free Optoelectronic Switches," *Proceedings of the Sixth Annual ARPA Symposium on Photonic Systems for Antenna Applications*, 5,6,7 March 1996. DTIC-ADB218390.
8. K. Turk, "Digitally Reconfigurable Antenna," *Proceedings of the 1996 Antenna Applications Symposium*, Allerton Park, Monticello, IL, Sept. 18-20, 1996.
9. J. Freeman, S. Ray, D. West, A. Thompson, "Optoelectronic Devices for Unbiased Microwave Switching," *IEEE International Microwave Symposium Digest*, June 1-5, 1992, Albuquerque, NM, pp. 673-676.
10. D. Albares, C. Sun, R. Nguyen, S. Hart, and C. Chang, "Photovoltaic-FET for Photonic Reconfiguration of Antennas," *Proceedings of the Sixth Annual ARPA Symposium on Photonic Systems for Antenna Applications*, 5,6,7 March 1996. DTIC-ADB218390.
11. C. Sun, R. Nguyen, D. Albares, C. Chang, and P. Cunningham, "Photovoltaic-PIN Switches for a Photonically Reconfigurable Monopole Antenna," *Proceedings of the Seventh Annual DARPA Symposium on Photonic Systems for Antenna Applications*, 14 - 16 January 1997, DTIC-ADB223415.
12. R. Gilbert and G. Pirrung, "Structurally Embedded Reconfigurable Antenna Technology," *Proceedings of the Sixth Annual ARPA Symposium on Photonic Systems for Antenna Applications*, 5,6,7 March 1996. DTIC-ADB218390.
13. C. Swann, M. VanBlaricum, and R. Mustacich, "Optical Tuning of an Electrically-Small HTS Antenna and Integration of Photonic Links to HTS Antennas," Toyon Research Corporation Final Technical Report #209C0200 on ONR Contract # N00014-94-C-0027, 22 March 1996.
14. T. Larry, C. Swann, M. VanBlaricum, "Photonic-Based Tuning and Control of Antenna Elements," *Proceedings of the 1995 Antenna Applications Symposium*, Allerton Park, Monticello, IL, Sept. 20-22, 1995.
15. A. S. Nagra, O. Jerphagnon, P. Chavarkar, M. VanBlaricum, and R. A. York, "Indirect optical control of microwave circuits using monolithic optically variable capacitors," *IEEE Transactions on Microwave Theory and Techniques*, vol. 47, pp. 1365-72, 1999.
16. JR. Liechty, P. Hein, R. N. Edwards, W. C. Nunnally, "Reconfigurable photonically excited antenna elements: RF measurements for receive and transmit applications," *Proceedings of the Sixth Annual ARPA Symposium on Photonic Systems for Antenna Applications*, 5,6,7 March 1996. DTIC-ADB218390.
17. D. Liu, D. Charette, M. Bergeron, H. Karwacki, S. Adams, and B. Lanning, "Structurally-embedded photoconductive silicon bowtie antenna," *IEEE Photonics Tech. Lett.*, Vol 9, No. 12 1997.
18. D. Liu, D. Charette, M. Bergeron, H. Karwacki, S. Adams, F. Kustas, "Structurally-Embedded, Photonically-Controlled Phased-Array Antenna (SEPCPAA)," *Proceedings of the Eighth Annual DARPA Symposium on Photonic Systems for Antenna Applications*, 13-15 Jan. 1998, Monterey, CA, DTIC-ADB233444.

Range Demonstration of a Reconfigurable Fiber-Optic Time-Steered 2D Transmit Beamformer

David A. Tulchinsky and Paul J. Matthews

Naval Research Laboratory
Code 5651, Optical Sciences Division
Washington, DC 20375-5338

Abstract

We present the first range demonstration of a 2-D, true-time delay, transmit beamformer based on the technique that produces 2-D steering by dynamically reassigning the output of a 1-D beamformer onto the input plane of a 2-D antenna array. Anechoic chamber testing of the reconfigurable beamformer, demonstrates squint-free steering to $\pm 45^\circ$ across the 6 to 18 GHz band in the azimuth and elevation directions and to ($\pm 30^\circ$ az, $\pm 30^\circ$ el) in the inter-cardinal $\pm 45^\circ$ directions.

I. Introduction

To steer wide bandwidth signals without beam squint, future multi-dimensional antenna arrays will most likely require the use of true time-delay (TTD) beamformers. Microwave based TTD beamformers suffer from severe drawbacks and are currently impractical [1]. As a result, several optical approaches have been proposed and built with various degrees of success [2-7]. These optical approaches tend to suffer from a number of difficulties including system complexity, optical power loss, component reproducibility, signal stability, and most notably system cost.

Here we present for the first time, a range demonstration of a 2-D TTD beamformer based on reconfigurable optical interconnections, as proposed by Frankel and Esman [8]. This architecture is based on the ability to dynamically reassign the connections between a 1-D beamformer's time-delay units (TDUs) and the individual elements of a 2-D antenna array. Reconfigurability enables mapping the linear time gradient of the 1-D beamformer onto a polar R, θ coordinate system. The amount of time delay, controls how far out in the radial direction the beam points, while the assignment of the connections between the TDUs and the

radiating elements of the antenna array, controls along which θ direction the beamformer steers. The assignment of the TDUs to the antenna elements is implemented using a reconfigurable optical switching matrix (OSM). This type of system enables 2-D array beam steering with reduced system complexity, cost, optical loss, and added design flexibility

II. System Design

The fiber-optic (FO) beamforming system, shown schematically in Fig. 1, is designed to actively drive a 3×3 antenna array in both azimuth and elevation directions. The TTD beamformer is based on the FO dispersive prism approach [9] and provides a 1-D wavelength-dependent time delay for three unique array elements. By tuning the wavelength of the laser, the optical-dispersion gradient in the beamformer is translated into a time delay, which is then routed to the appropriate array elements via the photonic OSM. This forms a 2-D time-steered far-field pattern.

An external cavity, wavelength-tunable semiconductor laser with a wavelength range of 1470-1590 nm serves as the optical source for the system. The 1.5 mW output of the laser is amplified to 200 mW by an erbium-doped fiber amplifier (EDFA) and is subsequently modulated by a 20 GHz Mach-Zehnder intensity modulator (MZM). A 4 to 18 GHz low noise preamplifier with a nominal gain of 40 dB is used at the RF input of the MZM to insure adequate dynamic range. The modulated optical carrier is further amplified by a second EDFA to overcome the optical insertion loss (~ 8 dB) of the MZM. The optical signal is then split into three unequal parts (to compensate for the unequal optical loss in the dispersive prism) and fed into a three-channel FO dispersive prism. The

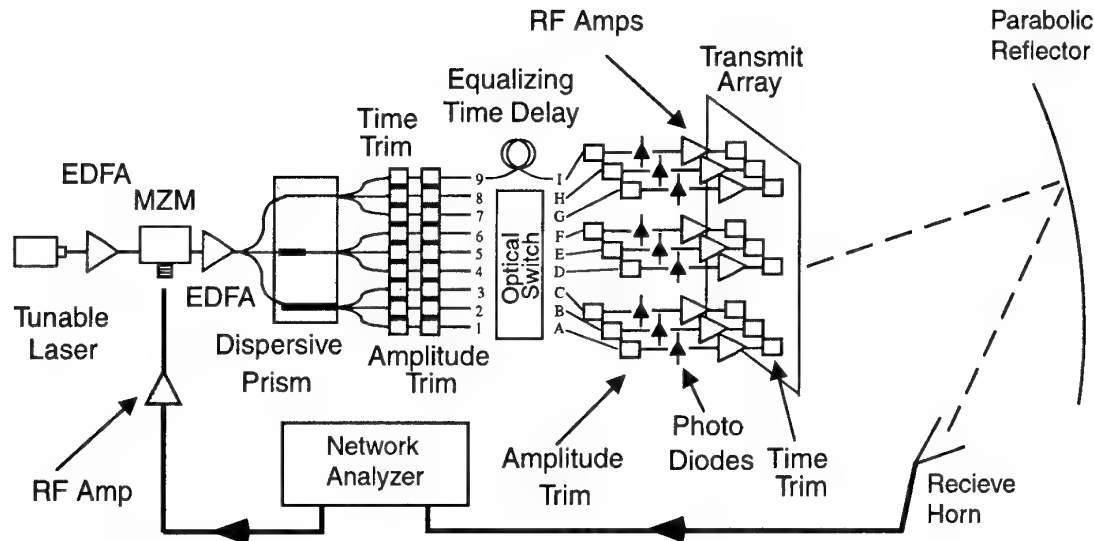


Fig. 1 Schematic diagram of the reconfigurable 2-D fiber optic TTD beamformer.

dispersion in the three arms of the FO prism are 0, -4.2, and -8.3 ps/nm, respectively.

Each link is then split into three equal parts for a total of nine optical paths. The links then continue through separate FO time shifters and FO attenuators, before being inserted into the OSM. The 8 x 8 OSM is a commercially available device [10] consisting of Mach-Zehnder interferometers and electronically controlled thermo-optic phase shifters. The device is strictly non-blocking resulting in any input port being able to be routed to any output port. The ninth optical link is routed through a 3.42 m length of fiber to compensate for the ~17 ps optical delay in the OSM. Since the ninth element is assigned to a fixed time delay, it acts as the pivot about which the polar steering axis of the beamformer rotates.

The optical signals then pass through a second set of attenuators, are demodulated by 20 GHz p-i-n photodiodes, and post-amplified by broadband (4 – 18 GHz) low-noise amplifiers, each having a nominal gain of ~40 dB. The outputs of the nine amplifiers are connected to microwave line stretchers and are then fed to every other input of an 8 x 32 flared-notch 2-D antenna. The antenna is designed such that the element spacing is $\lambda/2$ at 16 GHz [11]. Undriven elements are terminated into 50 Ω . The total radiated power of the current system is less than 5 mW.

The two sets of time delay shifters and

amplitude adjusters, both before and after the OSM, are used to compensate for path length and insertion loss differences in the input and output stages of the OSM. These adjustments enable a minimization of the overall system time and amplitude tracking amongst all of the optical paths possible through the OSM.

III. Results and Discussion

After assembly and packaging, the FO beamforming system was calibrated and tested in the laboratory. The antenna array and FO beamformer were then tested in a compact anechoic radar range. A network analyzer was used to drive the RF input of the system and detect the received signal. The radiation from the transmit antenna was focused onto the receive antenna by an off-axis parabolic microwave mirror. Mechanical 1-D scans in both azimuthal and elevation were taken across a $\pm 70^\circ$ range in 0.5° increments, at frequencies ranging from 4 to 18 GHz in 0.5 GHz increments.

Two examples of measured antenna patterns are shown in Fig. 2 which are intensity plots of the transmitted radiation as a function of mechanical 2(a) azimuth and 2(b) elevation angle and frequency. The images have been normalized for the frequency response of the system but not the element pattern of the antenna. Radial steering of the beam to an angle 30° off of broadside is

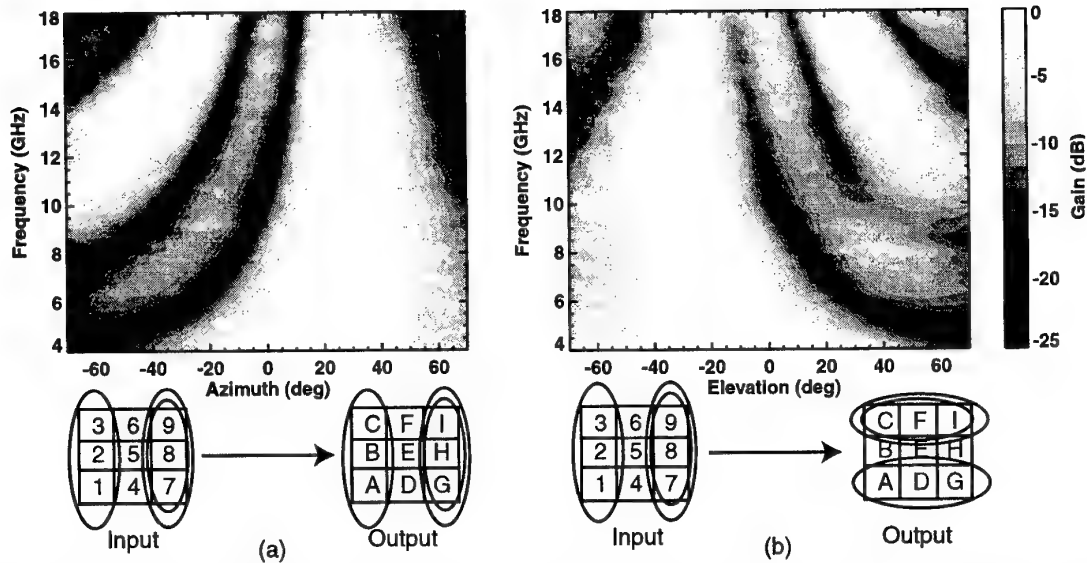


Fig 2. Array pattern intensity plots as a function of mechanical angle and frequency with the laser adjusted to steer 30° off of broadside ($\lambda = 1562.3$ nm) with the OSM configured for steering in (a) azimuth and (b) elevation. Inset: Diagram of the assignment of the input to the output ports of the OSM to steer the beam in the indicated direction.

achieved by detuning the laser 7.3 nm off of the broadside wavelength ($\lambda = 1555.0$ nm), introducing the appropriate amount of time delay between the antenna elements. Azimuthal steering is achieved by assigning, via the OSM, the (0)(1)(2) TDUs incident at the input channel sets (123)(456)(789), to the appropriate array elements sets (ABC)(DEF)(GHI). The resulting intensity pattern, shown in Fig 2(a), is steered to +30° in azimuth. By simply reassigning to which antenna elements the TDUs are assigned, (0)(1)(2) to (ADG)(BEH)(CFI), beam steering in elevation is achieved, as is shown in Fig. 2(b) with the beam steered to -30°. In both cases, the main beam is readily discernable at the expected steered angle (+ or -30°) and exhibits squint free operation over the full 4 to 18 GHz frequency range. The first grating lobe, calculated to be $\sim \pm 63.5^\circ$ away from the main beam at 18 GHz is clearly visible in both plots. A side lobe is also visible adjacent to the main beam. The degradation from ideal of the measured intensity patterns is due to problems with the performance of the antenna array elements and not the beamformer. At physical angles greater than $\pm 30^\circ$ off of broadside, element-to-element shadowing and mutual coupling between the array elements,

effectively limits the coherence of the radiation directed at these steering angles. This results in a degradation of the measured far-field intensity patterns. Amplitude tracking errors in the microwave components in the system and time delay errors in the OSM further degrade the patterns. The main beam was steered to several angles between $+45^\circ$ and -45° in both azimuth and elevation, yielding similar squint free results, across the RF band tested. In laboratory tests without the antenna elements, the beamformer was capable of squint free steering to $\pm 70^\circ$ [12].

Mechanical two-dimensional (azimuth and elevation) scans were also taken in 2.0° increments between $\pm 60^\circ$ in both elevation and azimuthal directions, and at frequencies between 6 and 18 GHz in 1 GHz steps. Two examples of these 2-D intensity scans are shown in Fig. 3. Assigning the TDUs to steer in elevation, Fig. 3(a) shows a 10 GHz beam steered to -30° . By assigning the sets of TDUs to diagonal elements, steering along the array's $\pm 45^\circ$ inter-cardinal planes is achieved. Figure 3(b) shows a 6 GHz beam steered 20° in azimuth and 20° in elevation. Similar beam patterns were observed across the RF band measured and with other steering configurations. The beams are well defined at the expected steered positions with side and

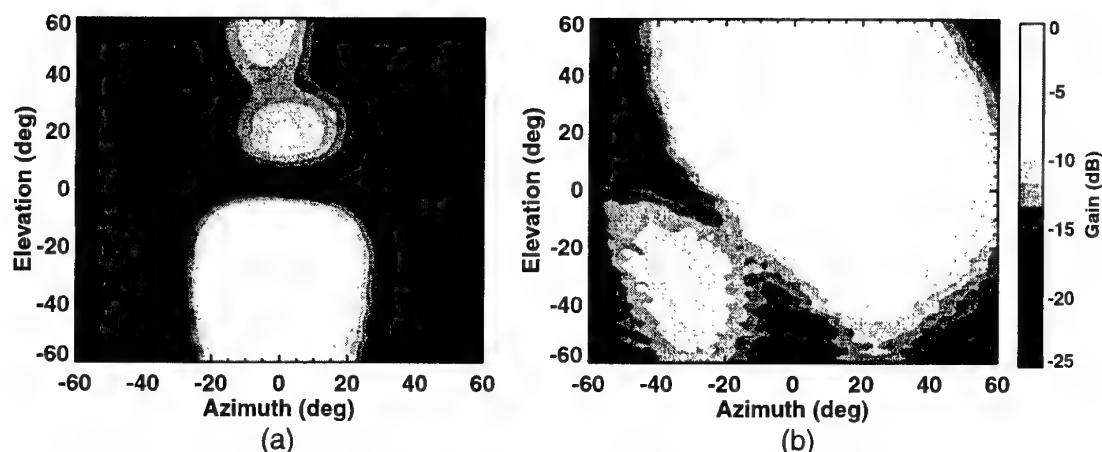


Fig. 3 Array pattern intensity plots as a function of azimuth and elevation angle (a) at a frequency of 10 GHz with the laser adjusted for 30° steering off of broadside with the OSM configured for -elevation steering (b) at a frequency of 6 GHz with the OSM configured for steering in the +45° inter-cardinal direction to (+20° azimuth, +20° in elevation).

grating lobes at the expected angular positions. The beam was successfully steered squint-free to several angles between -45° and $+45^\circ$ along the azimuth and elevation axis. Steering along the $\pm 45^\circ$ array inter-cardinal directions to ($\pm 30^\circ$ azimuth, $\pm 30^\circ$ elevation) was also demonstrated.

IV. Conclusions

We have developed a novel two-dimensional optical beamformer based on the ability to dynamically reassign the signal feed of a 1-D TTD beamformer to the physical elements of a 2-D antenna array. After characterization, the beamformer was used to drive a 3 x 3 antenna, whose antenna pattern was measured in an anechoic chamber. Measurements show squint free steering to $\pm 45^\circ$ in the horizontal and vertical directions and to ($\pm 30^\circ$ azimuth, $\pm 30^\circ$ elevation) in the $\pm 45^\circ$ inter-cardinal directions. Steering is achieved by simply changing the routing of the optical signal through the OSM in conjunction with changes in the optical carrier wavelength.

Acknowledgements

This work was supported by the Office of Naval Research.

References

- [1] R. C. Hansen, *Phased Array Antennas*, (New York: John Wiley & Sons, 1998).
- [2] *Selected Papers on Photonic Control Systems for Phased Array Antennas*, vol. MS 136. N. A. Riza and B. J. Thompson, Eds., (Bellingham, Washington: SPIE Optical Engineering Press, 1997).
- [3] N. A. Riza and N. Madamopoulos, "Phased-array antenna, maximum-compression, reversible photonic beam former with ternary designs and multiple wavelengths," *Appl. Optics*, vol. 36, pp. 983-996, 1997.
- [4] D. T. Tong and M. C. Wu, "Multiwavelength Optically Controlled Phased-Array Antennas," *IEEE Trans. on Microwave Theory and Tech.*, vol. 46, pp. 108-115, 1998.
- [5] X. S. Yao and L. Maleki, "A novel 2-D programmable photonic time-delay device for millimeter-wave signal processing applications," *IEEE Photon. Tech. Letters*, vol. 6, pp. 1463-1465, 1994.
- [6] D. Dolfi, P. Joffre, J. Antoine, J. P. Huignard, D. Philippet, and P. Granger, "Experimental demonstration of a phased-array antenna optically controlled with phase and time delays," *Appl. Optics*, vol. 35, pp. 5293-5300, 1996.
- [7] M. Y. Frankel, P. J. Matthews, and R. D. Esman, "Two-dimensional fiber-optic control of a true time-steered array transmitter," *IEEE Trans. on Microwave Theory and Tech.*, vol. 44, pp. 2696-2702, 1996.
- [8] M. Y. Frankel and R. D. Esman, "Reconfigurable time-steered array-antenna beam former," *Appl. Optics*, vol. 36, pp. 9261-9268, 1997.
- [9] R. D. Esman, M. Y. Frankel, J. L. Dexter, L. Goldberg, M. G. Parent, D. Stilwell, and D. G. Cooper, "Fiber-optic prism true time-delay antenna feed," *IEEE Photon. Technol. Lett.*, vol. 5, pp. 1347-1349, 1993.
- [10] NEL Electronics Corporation.
- [11] Hughes Ground Systems Group, El Segundo, CA.
- [12] D. A. Tulchinsky and P. J. Matthews, "Reconfigurable Fiber-Optic Control of a Time-Steered 2D Transmit Array," presented at IEEE MTT-S International Microwave Symposium Digest, Boston, MA, 2000.

BROADBAND NULLING FOR CONFORMAL PHASED ARRAY ANTENNAS USING PHOTONIC PROCESSING

Henry Zmuda, University of Florida
Graduate Engineering and Research Center
1350 North Poquito Road
Shalimar, FL 32579
phone: (850) 833-9350
fax: (850) 833-9366
email: zmuda@gerc.eng.ufl.edu

Edward N. Toughlian, ENSCO, Inc., and Paul M. Payson, AFRL/SNDR

Abstract— This paper presents a photonic architecture for independently steering the broadband nulls of linear and conformal phased array antennas. Analytic expressions quantifying bandwidth requirements are developed and simulation results demonstrating array performance are presented.

I. INTRODUCTION

This paper examines a tunable laser-based system for broadband null steering with conformal phased array antennas. The ability to place the array factor zeros at chosen angular coordinates is fundamentally different from broadband beamsteering [1], [2]. It is found that the array factor nulls of a broadband beamsteering system are *not* fixed in their spatial location as the RF frequency is varied, and consequently additional design constraints must be imposed to achieve broadband nulls. The problem becomes more challenging for the case of conformal arrays.

The nulling processor architecture described in this paper is entirely fiber-based and only a single length of high dispersion optical fiber is needed for the entire system. This single fiber feature is especially important since it provides a common processing element for all the optical signals and reduces the effects of errors by helping to maintain the extremely accurate element-to-element amplitude and phase tracking needed for deep nulls. With the photonic approach, the common optical path that exists as well as the ability to process the broadband RF information before down conversion more readily achieves this element-to-element gain and phase tracking. This

common optical path also makes the performance especially insensitive to temperature drift.

II. SYSTEM CONSIDERATIONS

It is well known that the directional characteristics (the array factor) of an N -element, linear, equally-spaced phased array antenna may be expressed as a polynomial of degree $(N - 1)$ and is given by

$$AF_N(\theta) = \prod_{n=1}^{N-1} (z(\theta) - z_n) = \sum_{n=0}^{N-1} a_{N-1-n} z(\theta)^n, \quad (1)$$

where $z(\theta) = \exp[-jkd \sin(\theta)]$, d is the antenna element spacing, $k = \omega/c$ is the free space wavenumber for radian frequency ω , and c is the speed of light in free space. The term $z_n = z(\theta_n) = \exp[-jkd \sin(\theta_n)]$ is a zero of the polynomial corresponding to a null at angular coordinate θ_n and is realized as a delay line with time delay $T_n = \frac{d}{c} \sin(\theta_n)$. Equation (1) gives the array polynomial coefficients explicitly as

$$\begin{aligned} a_0 &= 1, a_1 = -\sum_{i=1}^{N-1} z_i, a_2 = \sum_{i=1}^{N-1} \sum_{j=1}^{N-1} z_i z_j, a_3 = -\sum_{i=1}^{N-1} \sum_{j=1}^{N-1} \sum_{k=1}^{N-1} z_i z_j z_k, \\ &\dots, a_{N-1} = (-1)^{N-1} z_1 z_2 \dots z_{N-1} \end{aligned} \quad (2)$$

We see that a multiple delay line (transversal filter) implementation is needed to realize the a_n coefficients to support broadband nulling. Contrasted with the narrowband application, simple phase shifters can be used to generate in-phase and quadrature (I/Q) signals

and obtain a typical coefficient a_n in the array factor polynomial, *but only at a single frequency*.

The increased system complexity needed for broadband nulling can be justified by quantifying the null depth degradation of a *narrowband* null steering array over a nonzero RF bandwidth. For the narrowband case, the polynomial zero becomes $z_m = \exp[-jk_o d \sin(\theta_m)]$ which is a pure phase-shift and is independent of RF frequency since k_o is fixed. Consider then an array factor zero located at spatial coordinate θ_m , and with RF frequency $f_o + \Delta f$, where f_o is the center (carrier) frequency and Δf is the deviation from the carrier. Equation (1) may be bounded from below, assuming a half-wavelength array element spacing so that $k_o d = 2\pi f_o \frac{d}{c} = \pi$, and for a null at end-fire ($\theta_m = \pm 90$ degrees) as

$$|AF_N(\theta_m)| \leq 2^{N-1} \sqrt{B} \quad (3)$$

where B is the fractional bandwidth,

$$B = \frac{\Delta k}{k_o} = \frac{\Delta f}{f_o} \left(B \leq \frac{1}{2} \right).$$

Consider an application such as interference elimination for Global Positioning Systems (GPS), which operates (roughly) at $f_o = 1.2$ GHz with $\Delta f = 10$ MHz. From Equation (3) we see that for a two-element array ($N = 2$), the null depth at the band edge may be as large as -14.77 dB, a value generally considered as quite unacceptable in such applications. Requiring a more desirable interference suppression of -70 dB limits the worst-case usable bandwidth to 30 Hz, while relaxing the null depth to -60 dB results only in a 300 Hz usable bandwidth, values completely inconsistent with the GPS application. Hence, broadband null steering is clearly required for what would generally be regarded as a classical narrowband beamforming application.

III. APPLICATION TO CONFORMAL ARRAYS

For the conformal array, the general situation is shown in Fig. 1. For this case, a plane wave incident on the array at an angle θ measured with respect to some global x - y coordinate system, $\exp[-jk(\alpha x + \beta y)]$, with $\alpha = \cos\theta$, $\beta = \sin\theta$, is sampled by the array elements located at their spatial coordinates (x_i, y_i) , $i=0, \dots, N-1$. For the conformal array, the array function can be written:

$$f(\theta) = \sum_{i=0}^{N-1} a_i w_i \quad (4)$$

where w_i is the signal received by the i -th antenna element with $w_i = \exp[-jk(\alpha x_i + \beta y_i)]$. The coefficients a_i are determined to produce a null at $\theta = \theta_m$, namely

$f(\theta_m) = 0$. For the $N-1$ zeros we may write the array coefficients a_i , $i = 1, \dots, N-1$ as

$$[a_1 \ a_2 \ \dots \ a_{N-1}]^T = -a_0 \frac{\text{adj} W^T}{\Delta W} [w_0^{(1)} \ w_0^{(2)} \ \dots \ w_0^{(N-1)}]^T \quad (5)$$

where

$$w_j^{(m)} = \exp[-jk(\alpha_m x_j + \beta_m y_j)] \quad (6)$$

and where we have assumed an incident plane wave signal excitation as sampled by array element at spatial location (x_j, y_j) and evaluated at spatial frequency (α_m, β_m) , and where $\text{adj} W^T$ is the adjoint matrix of W^T , ΔW is its determinant, and $()^T$ denotes the transpose operation. For distinct nulls, the columns of W are independent and hence a nonzero ΔW is assured. If we then let $a_0 = -\Delta W$, each a_i may be realized as a simple transversal filter. Without loss of generality, we may take $(x_0, y_0) = (0, 0)$ so that $w_0^{(i)} = 1$ for all $i=1, \dots, N-1$.

We see that the additional complexity introduced by the conformal array results in the need for only $2N(N-1)$ independent time delays compared with the $2^{N-1}-1$ needed for the linear array using the classical Davies approach [2]. This suggests that the conformal array approach presented here would be preferred even for linear arrays when $2N(N-1) < 2^{N-1}-1$.

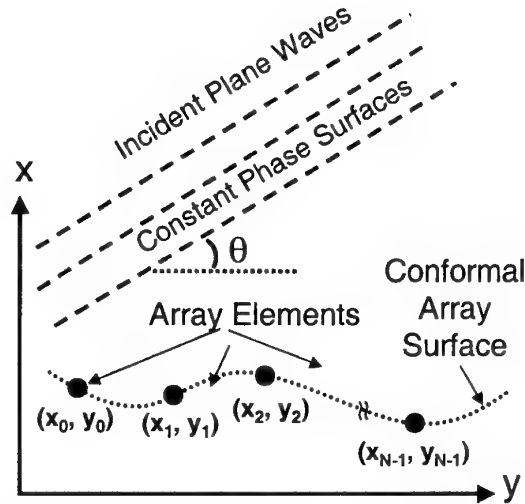


Fig. 1: Conformal antenna array geometry.

IV. PHOTONIC ARCHITECTURE

The generic photonic transversal filter structure required for each conformal array element as specified by Equation (5) is shown in Fig. 2. For tunable laser-based systems, continuously variable time delay is efficiently accomplished using a single High Dispersion Optical Fiber (HDOF) [1]. This HDOF is characterized as having a large negative chromatic dispersion term. A microwave signal used to modulate an optical carrier with wavelength $\lambda_o + \Delta\lambda$ will

undergo a *differential* time delay of $T(\Delta\lambda) = D \cdot \Delta\lambda \cdot L$ where D is the dispersion (in units of psec/nm-Km) and L is the length of the HDOF.

These $2N(N-1)$ delays are obtained using the bank of tunable lasers shown in Fig. 3, where each laser operates at a wavelength $\lambda(T_{ij})$ and has a tuning range $\Delta\lambda$; wide enough so that the necessary differential time delays specified above can be accessed via the HDOF. The laser outputs are optically summed as shown so that when delayed they form the appropriate polynomial coefficients a_0, a_1, a_2 , and so on. Negative coefficients are obtained by using a broadband electrical π -phase shifter at the appropriate electro-optic modulator (EOM) inputs. The EOM outputs are summed and coupled in a single length of HDOF that provides the desired wavelength dependent delay on each set of optical carriers. The HDOF output is coupled to a spectrally broad photodetector (PD) that recovers the properly delayed and summed microwave antenna signal and which constitutes the receiver's output. For an adaptive system, a portion of this output and possibly the output of each antenna element could be digitized, and an appropriate algorithm would then be used to adjust the laser operating wavelengths via the laser controller.

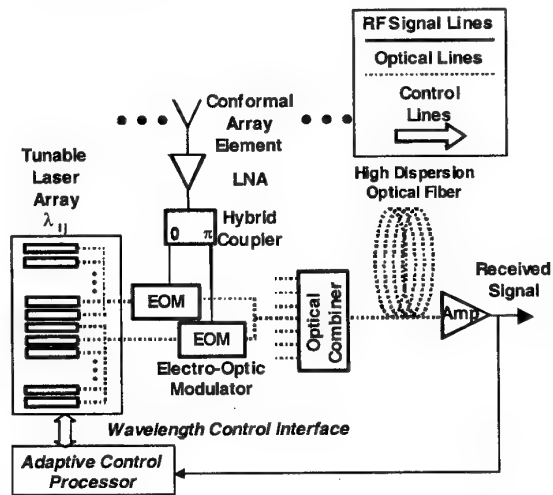


Fig. 2: Photonic beamformer for the conformal array processor. Details are shown for one antenna element.

V. SIMULATION RESULTS

Figs. 3a and 3b are plots of the simulated responses of a distorted four-element linear array and a conformal (nonlinear) array, respectively. The frequency and bandwidth of the interference are consistent with a scenario involving broadband jamming of a military GPS receiver. Note that the null is maintained across a wide spatial angle and that the peak gain is rather large. Such a broad spatial null would be useful in an environment containing many jammers scattered throughout a region. This scenario

“stresses” the array in the sense that the solution results in about 10 dB of (thermal) noise amplification, and the normalized gain is reduced by 10 dB. In Fig. 3a we place interferers at $-60, 0$, and 60 degrees. This is a more stressful scenario that results in 16 dB of (thermal) noise amplification and limits the maximum normalized gain to -10 dB. Finally, Fig. 3b illustrates null placement in a nonlinear array. The interferers are located at $0, 30$ and -70 degrees.

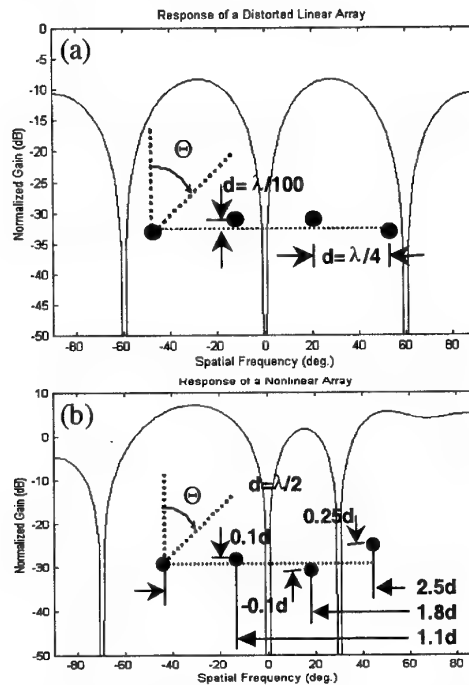


Fig. 3: Simulated response of a distorted four-element linear array ($f = 1.2$ GHz, $B = 10$ MHz) with (a) interferers at $-60, 0$, and 60 degrees and (b) interferers are located at $0, 30$ and -70 degrees.

ACKNOWLEDGEMENT

The authors wish to thank Dr. Mark Jones of Mission Research Corp. for his assistance in generating the simulated results.

REFERENCES

- [1] H. Zmuda, E. N. Toughlian, P. Payson, and H. Klumpe, III, "A photonic implementation of a wideband nulling system for phased arrays", *IEEE Photon. Technol. Lett.*, vol. 10, pp. 725-727, May 1998.
- [2] D.E. N. Davies, "Independent angular steering of each zero of the directional pattern for a linear array", *IEEE Transactions on Antennas and Propagation*, pp. 296-298, Mar. 1967.
- [3] J. Frank, "Bandwidth Criteria for Phased Array Antennas", in *Phased Array Antennas*, A.A. Oliner and G.H. Knittel, editors, Dedham, Massachusetts: Artech House, 1972.

PHOTONIC CHIP FOR STEERING A FOUR ELEMENT PHASED ARRAY ANTENNA

J. Stulemeijer¹, R. van Dijk², F.E. van Vliet², D.H.P. Maat³, M.K. Smit¹

¹Delft University of Technology, Department of Information Technology and Systems, TTT Laboratory, Photonic Integrated Circuits Group, POBox 5031, 2600 GA Delft, The Netherlands, Tel. +31-15-2781752, Fax +31-15-2784046, Email J.Stulemeijer@ITS.TUdelft.nl

²TNO-Physics and Electronics Laboratory, The Hague, The Netherlands

³Delft University of Technology, Department of Applied Physics, Delft, The Netherlands

Abstract

A polarization independent Photonic Integrated Circuit for phase steering of a four element Phased Array Antenna has been fabricated on InP. The chip is extremely small and suitable for packaging.

Introduction

Phased Array Antennas (PAAs) are becoming increasingly important and are under study for radar and wireless communication applications, see [1,2]. Optical processing of microwave signals is attractive because glass fiber has extremely low losses and a very high bandwidth. Photonic integration brings down the number of components in the optical beamformer. Previously we have realized a Photonic Integrated Circuit (PIC), for adjusting the phase and amplitude information for a 16 element PAA, see [3]. However this chip only worked for the TE polarization, it suffered from a high insertion loss and its output waveguides were not designed for coupling to a fibre array. The device we present here addresses those issues.

Chip Design

Basically this chip combines the signals of two lasers such that a microwave beat signal is formed in a photodiode behind the chip. Any optical phase shift will translate, by heterodyning, to a microwave phase shift behind the photodetector.

Two lasers with stable difference frequency, e.g. from an optical phase locked loop, are connected to inputs 1 and 2. 1x2 Multi-Mode Interference (MMI) splitters [4] are used, for splitting the signal into four equal parts. The waveguides are sorted in four pairs such that waveguides with signals from inputs 1 and 2 appear alternatively. In every waveguide a 2.57 mm long phase/amplitude modulator is included in the $[1\bar{1}0]$ direction (split in two parts, see Fig. 1) and a 1.13 mm long phase/amplitude modulator in the $[110]$ direction. In the $[1\bar{1}0]$ direction the phase shift experienced by the TE polarized light is slightly larger than for the TM polarized light. In the $[110]$ direction however the phase shift for the TM polarization is much larger than for the TE polarization. Therefore it is possible, with adjusting the voltage on both sections, to obtain a polarization independent phase shift. Before the light leaves the chip the signals in the waveguide pairs, coming from inputs 1 and 2, are combined in a 2x2 MMI 3dB coupler. The width of the in- and output waveguides is increased for optimal coupling to a lensed fiber. In this way the coupling loss can be reduced to around 5 dB.

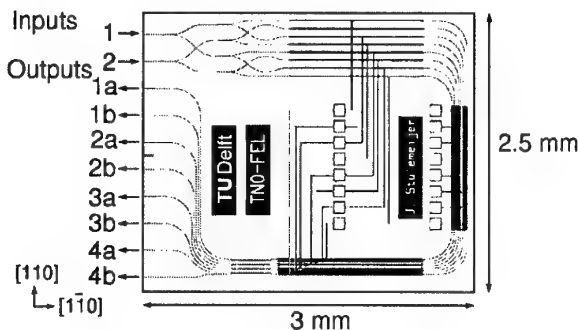


Figure 1: Design of phase controller chip.

Fabrication

This chip was fabricated on an N-doped InP substrate. Using an MOCVD a non doped 600 nm InGaAsP film layer with cut-off wavelength of 1.3 μm , a 1 μm p-doped cladding layer were and a 50 nm P-doped contact layer were deposited.

First the contact layer was removed by wet chemical etching everywhere outside the phase/amplitude modulators. Ridge waveguides were etched with a CH_4/H_2 plasma in a RIE machine using a SiN masking layer. The applied waveguide width was 2 μm and the etch depth was 150 nm into the film layer. For planarization and passivation a polyimide layer was spun on. The Ti/Au (20/180 nm) metallization was patterned using a lift-off process.

Measurements

The total excess loss of the device is 6.5 dB, total on chip losses including the splitting loss are 15.5 dB. All outputs are within ± 1.5 dB from this value. The propagation losses for a 2 μm waveguide losses are 1.5 and 1.8 dB/cm, for TE and TM polarization respectively. The total on chip waveguide length is about 1 cm. Each of the three phase/amplitude modulation sections gives around 1 dB insertion loss, because of discontinuities in the cladding layer which are used as electrical insulation. The input signal is distributed over eight output waveguides, therefore there is 9 dB splitting loss. The 2 dB that are left can be attributed to the excess loss of the MMI-couplers.

In figure 2 the phase shift of the phase/amplitude modulators, both parallel and perpendicular to the $[1\bar{1}0]$ direction, is plotted as a function of the applied voltage. The phase shifting along the $[1\bar{1}0]$ direction is more efficient because the electrode is 2.57 mm long vs. 1.13 mm in the perpendicular direction.

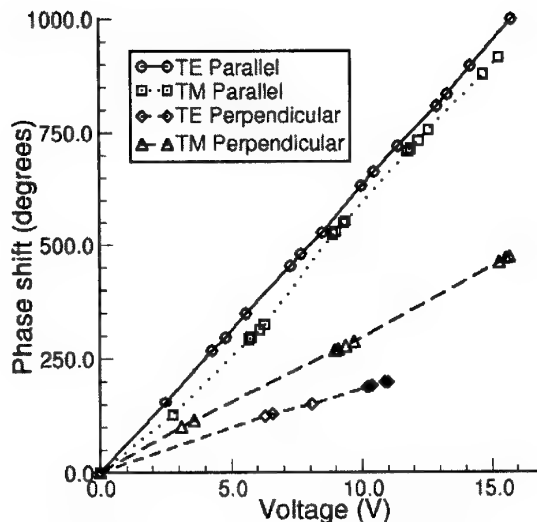


Figure 2: Phase shift as function of applied voltage.

A voltage on the phase/amplitude modulator does not only change the phase of the signal, it also introduces an extra attenuation. When a voltage of 15 V is put on the phase/amplitude modulator parallel to the $[1\bar{1}0]$ direction, an attenuation of 7.5 or 11 dB is incurred for the TE or TM polarization respectively. This effect is linear with electrode length and roughly independent of the waveguide orientation. The attenuation effect is not linear with applied voltage and will be larger at higher voltages.

To make sure that a polarization independent phase shift is applied, the ratio of the voltages applied to the phase/amplitude modulator in the parallel and the perpendicular to the $[1\bar{1}0]$ crystallographic direction must be fixed. A combined phase and amplitude state can be reached by first applying a certain phase shift, or in this case attenuation, to both input signals. Secondly a phase difference between the two input signals can be reached by changing these voltages slightly.

The operation of the chip was further tested by coupling two laser signals in the chip and looking at the signal that is generated in a photo diode. The measurement setup is shown in figure 3.

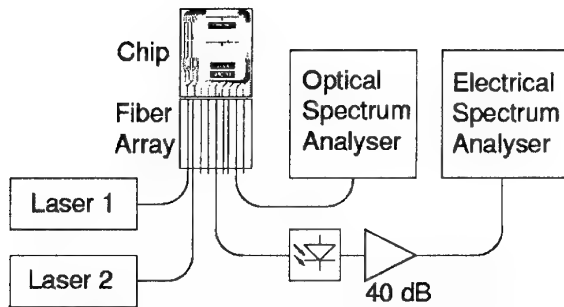


Figure 3: Measurement setup for heterodyning two lasers.

Two external cavity lasers were used as input lasers. Light was coupled into and out of the chip using an array of cleaved fibers. Which resulted in a coupling loss around 10 dB. An Optical Spectrum Analyser was used to monitor the signals coupled in and to position the input wavelengths closely together. The coupled signal from the two input lasers was mixed in a photodiode, amplified by 40dB and visualized on an Electrical Spectrum Analyzer (ESA).

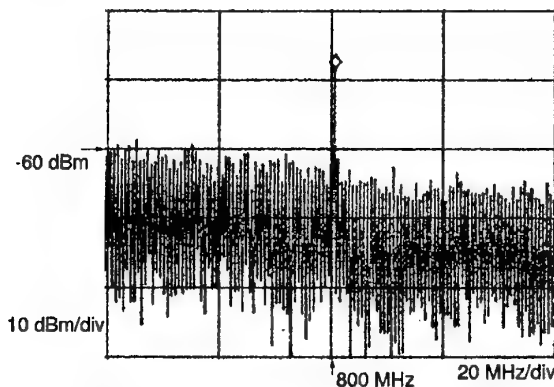


Figure 4: The beat signal of the two input lasers behind the chip.

In Figure 4 the resulting signal in the ESA is shown. The two input lasers were tuned at a frequency difference of 800 MHz. As a tuning range of 1 nm in wavelength corresponds to 120 GHz and lasers can be easily tuned over 5 nm, the tuning range of the output microwave frequency is almost unlimited, it is only restricted by the speed of the detector which can be larger than 50 GHz. The power of both input lasers is around 3 dBm. The chip gives a total insertion loss of 40 dB (16 dB on-chip loss, two times 12 dB coupling loss from the

chip without AR-coating to a cleaved fiber). So the signal at the photo diode is around -34 dBm. If the modes of the waveguides at the in and out coupling facets were adjusted to a cleaved fiber with a Spot-Size Converter, with 2 dB loss each, and if 20 dB of optical amplification could be included on the chip using Semiconductor Optical Amplifiers, than this chip would not produce any insertion loss.

Conclusion

We have realized a, small (2.5 x 3 mm), polarization independent photonic integrated circuit for controlling the phase of a 4 element phased-array antenna. The on chip losses are 15.5 ± 1.5 dB. All phase settings can be reached with a driving voltage below 4 V. The width of the in and output waveguides is optimized for coupling to a lensed fiber array with a coupling loss around 5 dB.

References

- [1] H. Zmuda and E.N. Toughlian, "Photonic Aspects of Modern Radar," Artech house, first edition, 1994.
- [2] Paul J. Matthews, "Practical photonic beamforming," in *Proc. of Microwave Photon. '99*, Melbourne, November 17-19, 1999, pp. 271-274.
- [3] J. Stulemeijer, F.E. van Vliet, K.W. Benoist, D.H.P. Maat and M.K. Smit, "Photonic Integrated Beamformer for Phased-Array Antennas," in *Proc. Microwave Photon. '98*, Princeton, October 12 - 14, 1999, pp. 131-134.
- [4] Lucas B Soldano and Erik C.M. Pennings, "Optical multi-mode interference devices based on self-imaging: Principles and applications," *J. Lightwave Technol.*, vol. 13, no. 4, pp. 615-627, Apr. 1995.
- [5] D.H.P. Maat, Y.C. Zhu, F.H. Groen, H. van Brug, H.J. Frankena, X.J.M. Leijtens, "Polarization independent dilated InP-based space switch with low crosstalk," *IEEE Photonic Technology Letters*, vol. 12, no. 3, March 2000

PHASED ARRAY ANTENNA BEAMFORMING USING A MICROMACHINED SILICON SPATIAL LIGHT MODULATOR

R A Wilson, P Sample, A Johnstone and M F Lewis

DERA, St Andrews Road, Malvern, Worcs, WR14 3PS, UK

Email: rwilson@dera.gov.uk Tel: +44 (0)1684 895342 Fax: +44 (0) 1684 896150

Abstract

We describe an rf/microwave/mm-wave free-space optical phased array antenna beamformer operating at 10GHz in transmission or reception with a reconfiguration speed of 30kHz through the use of a micromachined silicon phase Spatial Light Modulator (SLM).

Introduction

Phased array antennas have many advantages over their mechanically steered counterparts, which have long been recognised as being of particular importance in military systems. Nevertheless they have not been widely exploited to date because of the cost and technological difficulties of doing so. To overcome these difficulties a number of groups have sought to exploit the medium of photonics with its attractive properties for this application which include compactness, lightweight, and operation at rf, microwave or mm-wave frequencies, together with the use of optical fibre to provide a low-loss, flexible, and EMI-immune antenna-remoting capability [1,2,3]. At previous MWP conferences we have described the principles and performance of such a free-space photonic beamformer operating in a transmission mode at frequencies of 1.3 and 10GHz. This employs a single SLM as the means to control the phases of all the antenna elements of the array in parallel [4,5,6]. In this paper we describe a number of recent improvements to this earlier work, principally the introduction of a Dammann grating to optimise the utilisation of available light, and a micromachined silicon phase-only SLM which provides a reconfiguration speed of 30kHz, some 10,000 times faster than the linear nematic Liquid Crystal SLM used to demonstrate the principles of operation. In addition we describe the operating principle, construction, and performance of a corresponding receiving antenna array operating at 10GHz. We note that the transparency of photonic systems of this general kind to rf frequency makes them attractive candidates for use in future civilian fibre-wireless communications systems operating at mm-wave frequencies [7,8,9].

The basic beamformer

The basic beamformer for use in a transmission mode is shown schematically in figure 1, and its construction and operation are described succinctly below. It contains two stable lasers whose difference frequency

is maintained at the required rf frequency. We have used Lightwave Electronics diode-pumped YAG lasers operating at 1.3 μ m, whose frequency difference can be set anywhere from 0 to 100GHz. The laser outputs are combined in the beamsplitter, and the rf frequency is recovered by the mixing action of the photodetectors. As shown below, the phase of the rf output of each individual detector is set by means of the phase SLM through its effect on light from one of the lasers as it encounters each individual pixel. The combined laser outputs are conveyed to the detectors through single mode ribbon optical fibre which is EMI-immune and essentially lossless, allowing the antenna face to be remote from the beamformer itself. The rf signals from the detectors are amplified and transmitted by the individual elements of the phased array antenna. The antenna elements are spaced by one half of the rf wavelength, and the output rf beam is steered by imposing a linear phase shift across the array. Amplitude weighting to reduce sideline levels can be introduced, for example through a second SLM, but this has not been implemented to date.

Let the E-fields of the two lasers be of the same polarisation and given by:

$$E_1 = A \exp(j(\omega_1 t + \alpha)) + cc \quad \text{---(1)}$$

$$E_2 = B \exp(j(\omega_2 t + \beta)) + cc \quad \text{---(2)}$$

The detector current, i , varies as the optical intensity which is proportional to $|E_1 + E_2|^2$ and therefore contains the terms

$$i \sim AB \exp(j[(\omega_1 - \omega_2)t + (\alpha - \beta)]) + cc \quad \text{---(3)}$$

showing that the phase of the microwave beat frequency, $(\omega_1 - \omega_2)$, incorporates the phases, α and β , of the individual lasers, the SLM effectively acting as a compact array of electrically programmable phase shifters. Since the SLM construction is typically based on display technology, the number of phase shifters (pixels) available is very large and can easily satisfy the requirements of the largest phased array antennas contemplated to date with c.10,000 elements.

During the course of this work we have devised many variations on the schematic of figure 1, including that of reference [6], in which the two laser outputs are

combined prior to passage through the polarisation-sensitive linear nematic liquid crystal SLM. Such an arrangement has the advantage that any subsequent phase perturbations are largely cancelled by common-mode rejection. In reference [6] we also described a micromachined silicon phase SLM with a much faster response than the aforementioned liquid crystal device. In the present work we have incorporated such a micromachined SLM into a 10GHz transmitter and verified experimentally a reconfiguration speed of 30kHz, a rate adequate for most civil and military applications. We have also improved the utilisation of the available laser power by the use of a Dammann grating. Details of this demonstrator are described below.

The latest transmitter employing a Dammann grating and Micromachined silicon SLM

The Dammann grating is a form of optical diffraction grating in which the individual elements of the diffracting array are *phase* structures designed (a) to optimise light utilisation, and (b) to provide a chosen number of grating orders of nominally equal intensity in one or two dimensions [10]. When focussed these orders generate spots of identical (typically Gaussian) profile and are therefore ideal for the current application. We have used a grating designed by Dr M Taghizadeh of Heriot-Watt University to produce a linear array of 12 outputs to match our ribbon optical fibre, and which had a measured overall efficiency of 82%.

The micromachined silicon SLM comprised 8 modulators configured to provide 360° of analogue phase control, the details of which are the subject of a patent application by DERA. As shown in figure 2, this array also displayed good uniformity of its modulation characteristics, i.e. phase versus voltage. This SLM was incorporated in our most recent demonstrator which comprised the transmitting phased array antenna and three fixed 10GHz receivers. Under computer control the transmitter was steered towards the three receivers sequentially and their outputs recorded. This is shown in figure 3(a) on a slow timebase (20ms/div), while figure 3(b) shows on a faster timebase (20µs/div) the switch from receiver 3 to receiver 1. The transition occurs in ~25µs with no overshoot or ringing. This is consistent with the measured 30kHz frequency response of each individual element of the array, reference [6], figure 4. We believe that it is possible to design modulators with faster responses yet, as are required in the most demanding military applications.

The demonstration Receiving phased array antenna

Many applications require a steerable *receiving* antenna, and here we report the modification of our transmitting phased array antenna to demonstrate such functionality. As in the case of the transmitter the demonstrator used Commercial Off The Shelf (COTS) components wherever possible. The principle of our

chosen receiving array is to use the transmitter beamformer to generate an array of differentially phased rf signals, but to use them as local oscillator (l.o.) signals rather than signals to be transmitted. Thus the outputs of the photodetectors are now fed to the l.o. ports of conventional rf mixers, after amplification to a suitable level. In our demonstrator the rf signals to each mixer come directly from the patch antenna elements of the array, although in a real application they would normally be preamplified first using a Low Noise Amplifier (LNA). The i.f. outputs of the mixers are fed through short coaxial cables to a COTS combiner, as shown schematically in figure 4(a). The overall receiver is shown in figure 4(b), which includes the means to lock the rf frequency to a microwave synthesiser. The mathematics of the if signal formation from the l.o. and rf signals is the same as that of rf generation from the two laser beams (Eqs 1-3). In operation the l.o. signals are given a linear phase variation such that the i.f. signals (from the receiving direction of interest) are in phase and so add coherently in the combiner to form a peak output signal. The operation of our receiver has been verified experimentally and is shown in figure 5 when the receiver is steered in directions -30°, 0°, and +30° with respect to boresight.

In some applications the same antenna needs to be used for both transmission and reception. This is described as full-duplex operation when transmitting and receiving simultaneously, and as half-duplex when switchable between transmission and reception. Half-duplex functionality can be implemented in the present scheme in various ways, for example by adding components such as a circulator, and switches at each antenna element, as shown schematically in figure 6.

Conclusion

In this paper we have described progress in the development of free-space photonic beamforming techniques, principally in respect of efficiency and reconfiguration speed, but also the demonstration of a receiving array. The next phase of this work will involve the demonstration of high speed secure data transmission and reception at mm-wave frequencies.

Acknowledgements

The authors are grateful to various colleagues for useful discussions, and especially to John Bunyan and Dave King for the fabrication of the micromachined silicon SLM used in this work. This work was carried out as part of Technology Groups 7 and 9 of the UK MOD Corporate Research Programme.

© British Crown Copyright 2000/DERA. Published with permission of the Defence Evaluation and Research Agency on behalf of the Controller of Her Britannic Majesty's Stationery Office.

References

1. R Benjamin and A J Seeds, IEE Proceedings-H **139** (1992) pp526-534.
2. N Riza, Ed, SPIE Milestone series **MS 136** (1997).
3. P J Matthews, MWP'99 Digest, pp271-274.
4. Y Etem et al, MWP'96 Digest, pp209-212.
5. M F Lewis, MWP'97 Digest, pp23-26.
6. M F Lewis et al, MWP'98 Digest pp143-146.
7. L Noel et al, IEEE **MTT-45** (1997) pp1416-1423
8. A J Seeds, MWP'99 Digest pp1-4
9. T Kuri et al, MWP'99 Digest, pp123-126
10. H Dammann & K Gortler Opt Comm **3** (1971) pp312.

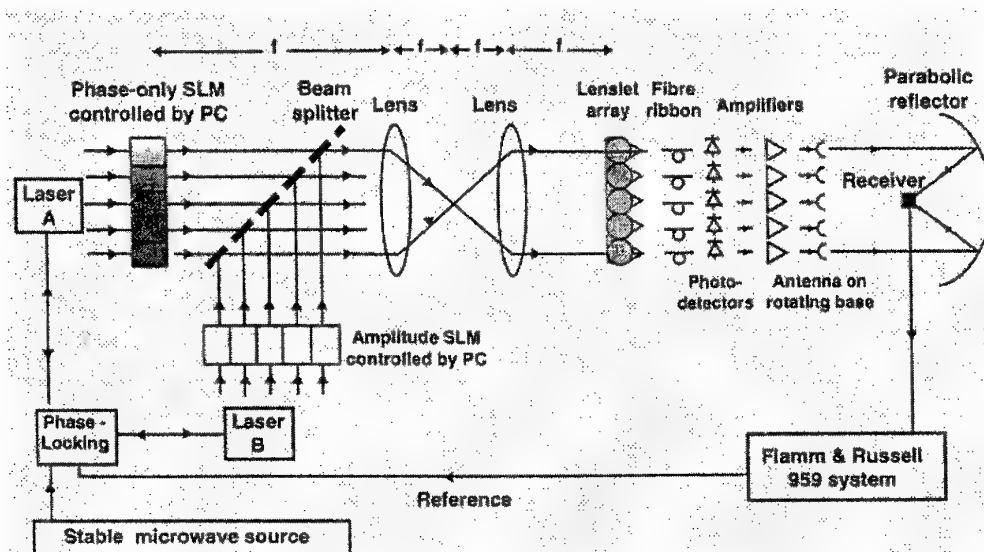


Figure 1. Schematic beamformer and test chamber components, [5]. (Not to scale)

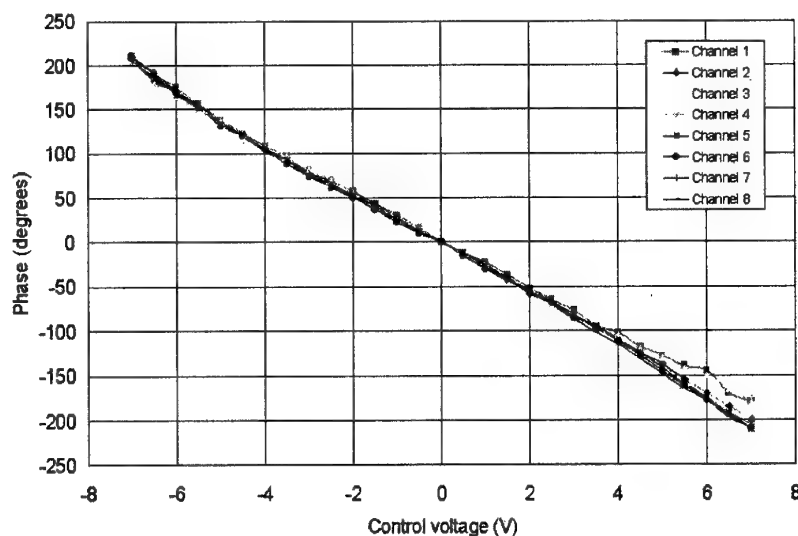
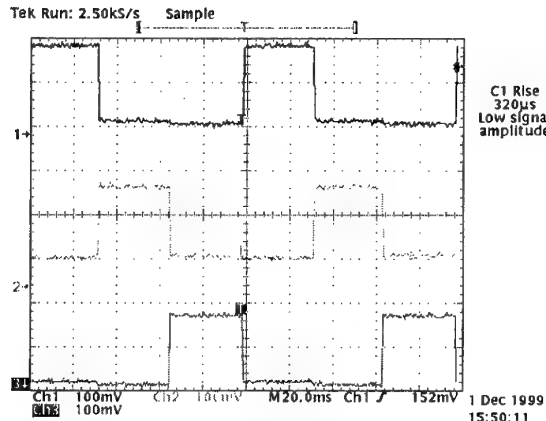
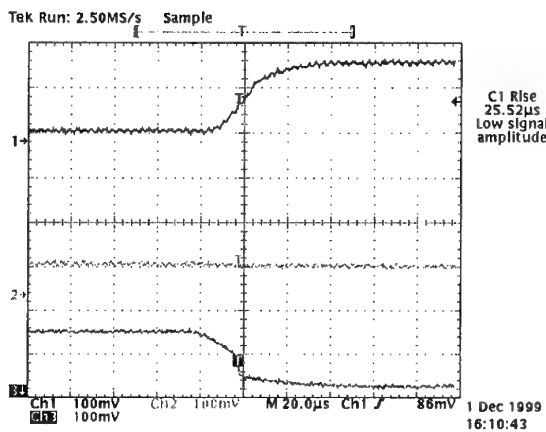


Figure 2. Phase modulation characteristics of 8 elements of micromachined silicon SLM.



(a)



(b)

Figure 3. (a) Detected outputs of three receivers illuminated sequentially by the 10 GHz phased array transmitter. Timebase: 20ms/div. (b) As figure 3(a) but showing the transition from receiver 3 to receiver 1 on a timebase of 20 µsec/div.

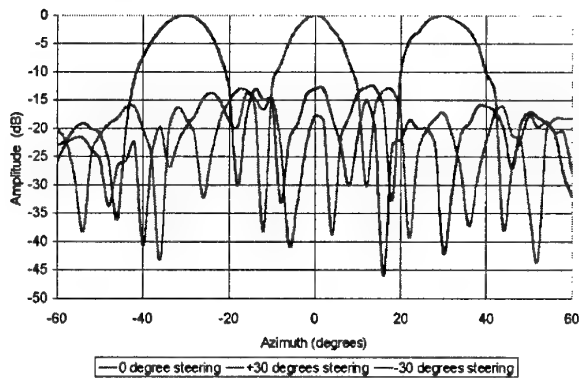
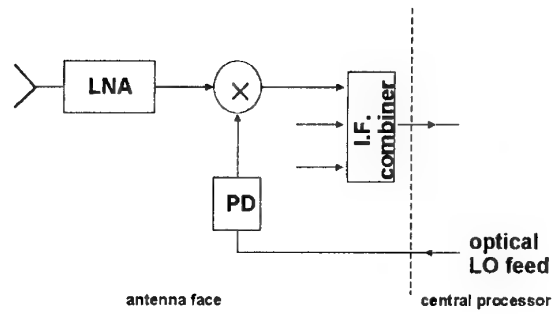
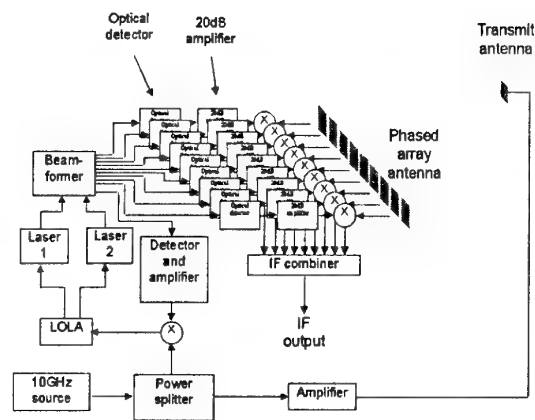


Figure 5. Measured response of the receiving array.



(a)



(b)

Figure 4. (a) One element of the receiving array. (b) the complete receiving array. In this test setup the i.o. frequency is 10.8 GHz and the LOLA input and i.f. output are at 800 MHz.

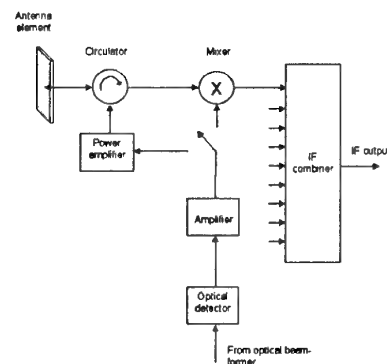


Figure 6. Schematic antenna element capable of half-duplex operation.

EFFICIENT OPTICAL CONTROL OF MICROWAVE CIRCUITS, ANTENNAS AND ARRAYS

James Vian and Zoya Popovic

University of Colorado, Boulder, CO 80309-0425, U.S.A.

Phone: (303) 492-0374, FAX: (303) 492-5323, zoya@colorado.edu

Abstract – We present an overview of work at the University of Colorado in the area of optical control of microwave circuits, antennas and active antenna arrays. In specific, we present X-band examples of two types of optically controlled microwave components: those where the optical device is used as a microwave component; and those where a standard optical component is combined with standard microwave components. The former is a slot antenna controlled with a PD in the feedline; and the latter example is that of a photodiode that controls the bias to a microwave SPDT switch. This switch is integrated with a transmit/receive (T/R) active antenna, which is then used as an element of a quasi-optical T/R array.

I. INTRODUCTION AND MOTIVATION

The goal of the work overviewed in this paper is to demonstrate the feasibility of efficient optical control of microwave circuits and antennas, as well as the advantages of optical over conventional techniques. The ultimate figure of merit for the efficiency of optical control is the required total optical power needed to perform a specific microwave function. Previously demonstrated optically controlled microwave circuits are either of analog type, where e.g. the bias of a varactor diode is varied optically [1], or of digital type in which the microwave switch is optically turned on and off [2]. In most switches demonstrated to date, optical power is used to generate carriers in microwave *pin* diodes [3,4,5]. A disadvantage of this technique is that, in general, photodiodes are lossy at microwave frequencies, and therefore reduce

the Q-factor of the circuit or antenna [5]. We have also observed this quality-factor reduction in a tunable second-resonant slot antenna [7]. The reduction in Q, however, enables a broad tuning bandwidth of 1.5 GHz around 10 GHz with at most 1 mW of optical power. This antenna is shown in Fig.1a, where a commercial photodiode (Fermionic FD300S3) is epoxied at the open end of a microstrip feed line, and a multimode fiber is epoxied to the active area of the photodetector. The measured tuning range, Fig.1b, shows that for optical powers between 0.06 μ W and 0.1mW, a continuous tuning of 1GHz is obtained. These results demonstrate the feasibility of relatively large analog tuning ranges (12% in the case of the antenna in Fig.1a) using optical control, with the expected associated tradeoff in antenna efficiency.

Another disadvantage of using optical power to generate carriers in microwave *pin* diodes is the fact that the insertion loss (IL) and isolation of the switch depend strongly on optical power, and as much as 40mW of optical power can be required to achieve an IL of 1.2dB and an isolation of 30dB [6]. The optically controlled digital microwave SPDT switch presented in this paper uses a small amount of optical power to control the bias of chip *pin* diodes. The advantage of this technique is that only the switching speed (rise and fall times) is a function of incident optical power, while the IL and isolation are independent of it and remain constant.

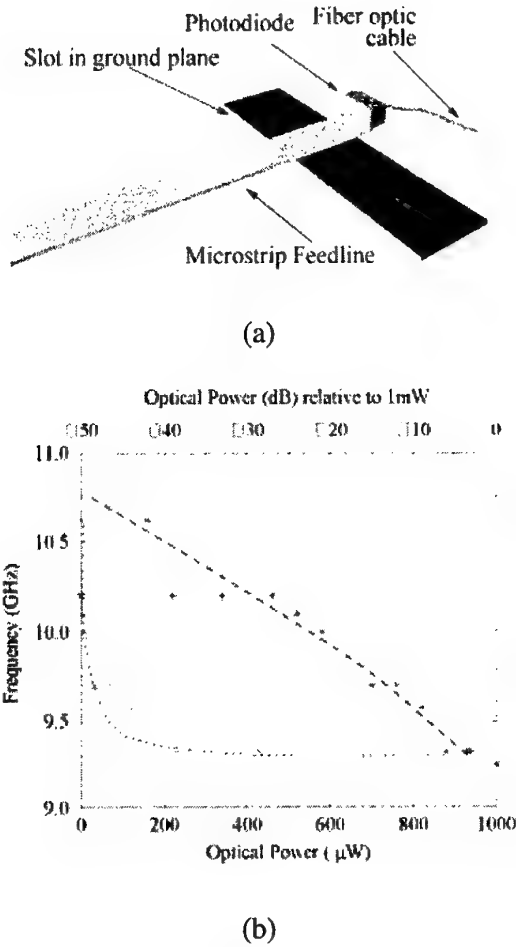


Fig.1. (a) Schematic of an optically-tuned slot antenna and (b) measured tuning range as a function of optical power (both linear and log scales in optical power are shown for clarity).

The SPDT switch is integrated with MMIC power amplifiers (PAs), low-noise amplifiers (LNAs) and patch antennas in a transmit/receive (T/R) active antenna in which the switching between T and R is accomplished optically in such a way that the switching speed is controlled by the amount of optical power. This active antenna is then used as the element of a half-duplex quasi-optical T/R lens antenna array. The switching speed of the array is independent of its size, and optical fibers that carry the switching control signals do not affect the microwave radiation.

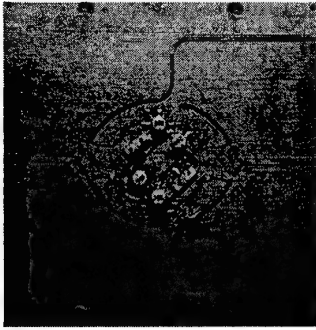
Compared to standard phased arrays, such active lens arrays have been demonstrated to have improved dynamic range in reception, higher effective radiated power in transmission, graceful degradation, and allow for phase-shifterless beamforming [8]. The active array presented in this paper is designed to be the front end of an adaptive system, in which the signal processing can be accomplished with either a nonlinear analog holographic optical processor [9], or with standard DSP algorithms. The advantage of the optical processing is in the design simplicity, large processing bandwidth, and possibly lower overall DC power consumption.

II. LOW-POWER OPTICALLY CONTROLLED MICROWAVE SPDT SWITCH

The optically controlled SPDT X-band switch is shown in Fig.2a. MA/Comm MA4GP032 *pin* diodes, with a 3Ω on-resistance at 3mA and 0.12pF capacitance in the off state are used for the microwave switch. Compact high-pass (HPF) and low-pass filters (LPF) are needed to separate the bias/control and RF signals. A second order HPF isolates the bias control for each side of the SPDT switch, with at least 20dB rejection below 1GHz and 0.1dB loss at 10GHz, and is implemented with a 2nH shunt bond wire and a 1pF chip capacitor at 10GHz. An additional bond wire is needed to connect the chip capacitor to the microstrip line and is designed to be resonant with the capacitor at 10GHz. A third order LPF biases the *pin* diodes with 27dB rejection (0.1dB reflection) of the 10GHz RF carrier. This LPF is implemented with 0.85nH bond wires and 3pF capacitors. The low impedance of this combination is transformed into a high impedance with a $\lambda_g/4$ long microstrip line causing a 0.1dB transmission loss at the bias line junction.

The optically-controlled bias to the *pin* diodes is implemented with a HP ATF26836 general purpose MESFET and Fermionics FD80S3 1300nm photo-diodes (PD) (with 0.95A/W

responsivity and an active area with a $80\mu\text{m}$ diameter). The MESFETs are used to sink and source the current of the *pin* diodes, allowing for small on/off response times. Push-pull PD's controls the gate bias point for the MESFETs. The MESFET gate capacitance and PD on-resistance dominate the rise and fall times of the bias control circuit. SPICE simulations indicate that the fastest expected rise (fall) time for the switch is 2.6ns at 7mW per PD, and is determined by the *RC* time constant resulting from the *pin* diode junction capacitance and the current-limiting resistor. For only $1\mu\text{W}$ of incident optical power, the switch rise time is approximately 2000ns.



(a)

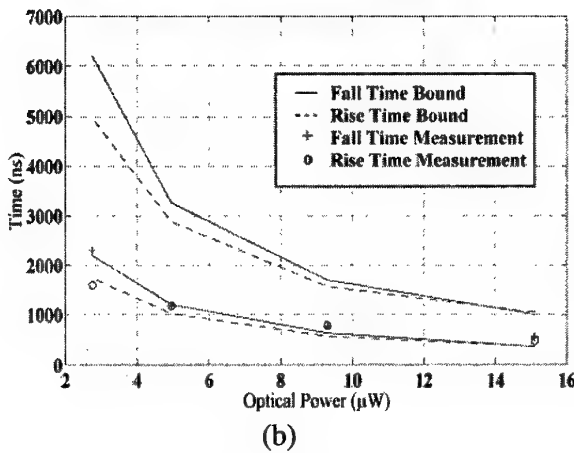


Fig.2. (a) Photograph of back-to-back optically controlled SPDT X-band switch. (b) Measured and predicted rise time as a function of optical power.

For testing the optical switching performance, variable length complimentary optical pulses with fast edges are needed. Two 3GHz Uni-Phase intensity electro-optic (EO) modulators

are used to generate the optical pulses. They are controlled by a function generator and inverting/non-inverting op-amps and two Veritect EO drivers. An Ortel 10mW 1300nm fiber-pigtailed laser diode is the optical source. The resulting optical pulse has a pulse width varying from 25ns to 7000ns with constant rise (fall) time of about 1ns. The optical pulses are incident on the PDs through free-space coupling from multimode fibers placed about 0.5mm above the PD chip. The loss resulting from free space coupling of the optical power limited the testing range of the switch (3 to $15\mu\text{W}$ were only available). The measured results agree with simulated values and fall within the simulated bounds, Fig.2b. The bounds result from uncertainty in optical power delivered to the PDs, which in our setup varied by +1.7dB and -2.7dB.

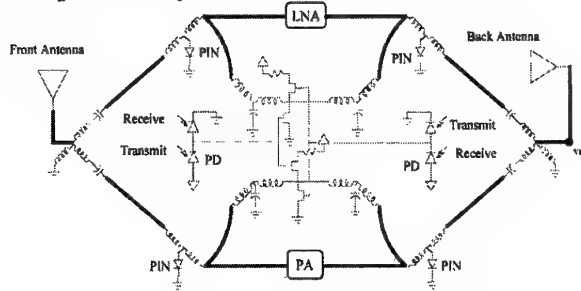


Fig.3. Schematic of an active transmit/receive antenna in which the switching between the T and R paths is accomplished optically using the SPDT switch from Fig.2a.

III. ACTIVE T/R ANTENNA ELEMENT WITH OPTICAL SWITCHING

Fig.3 shows the schematic of an active T/R antenna, which can be viewed as a bidirectional repeater [10]. 10-GHz patch antennas with a common ground plane and vias between feed and radiating sides of the array are used to improve isolation between in the input and output signals of the amplifiers. Off-the-shelf MMIC amplifiers are used for the PA (HP HMMC-5618) and LNA (United Monolithic Semiconductor CHA2063). An optical mount aligns the optical fibers to the PD with an accuracy of $200\mu\text{m}$, limited by the packaging of the commercial PD. The measured SPDT switch in the active antenna

element has an IL of 0.31dB and an isolation of 36dB over a 2.5GHz bandwidth.

Based on power and path loss measurements calibrated to an aperture the size of a unit cell ($0.75\lambda \times 1\lambda$), the gain contributed by the amplifiers is calculated to be 14dB from the PA and 16dB from the LNA, consistent with device specifications. An isolation of 30dB was measured for cases when: the active antenna was in receive mode while transmitting; the active antenna was in transmit mode while receiving; as well as when the active antenna was in the off state. These measurements are limited by edge diffraction and feed cross-polarization quality.

IV. DISCUSSION

The active antenna presented in the previous section is used as the element of a quasi-optical lens array, similar to the ones described in [8]. The optical control of such an array has multiple advantages over electronic control: the control signals do not couple to the RF signals and the fibers do not affect the radiation; and individual control of each unit cell of the array increases the switching speed making it the same as that of a single element. The array is designed using off-the-shelf components not optimized for speed or low power. The rise and fall times of the microwave switch are determined by the optical power, allowing the switch to be tailored to the application. Even though the 2.6-ns speed demonstrated in this paper requires relatively large optical power (about 10mW), the optical energy is low, equal to 21pJ, since the high power is only required during the rise time. For comparison, the fastest reported MEMS RF switch has a rise time of about 1 μ s and requires about 2nJ of control energy [11].

ACKNOWLEDGEMENTS

This work was funded by ONR and the Office of the Secretary of Defense through the MURI

program grant N00014-97-1-1006 and by Caltech through a ARO MURI in quasi-optical power combining grant DAAH04-98-1-0001.

V. REFERENCES

- [1] T. Larry, C. Swann, M. VanBlaricum, "Photonically-based Tuning and Control of Antenna Elements," *Proc. Of the 1995 Antenna Applications Symp.*, Alerton Park, Monticello, IL, Sept. 1995.
- [2] J.J.H. Wang, J.K. Tillery, G.T. Thompson, K.E. Bohannon, R.M. Najafabadi, M.A. Acree, "A Multiocitave-Band Photonically Controlled Low-Profile Structurally Embedded Phased Array with Integrated Frequency-Independent Phase Shifter," *1996 IEEE International Symposium on Phased Array Systems and Technology*, Boston, MA, October 1996.
- [3] P. J. Stabile, A. Rosen, P. R. Herczfeld, "Optically Controlled Lateral PIN Diodes and Microwave Control Circuits," *RCA Review*, No.47, pp.443-456, Dec. 1986.
- [4] J.L. Freeman, S. Ray, D.L. West, A. G. Thompson, M.J. LaGasse, "Microwave Control Using a High-gain Bias-free Optoelectronic Switch," *Optical Technology for Microwave Applications SPIE*, Vol.5, pp.320-325, 1991.
- [5] A. Daryoush, K. Bontzos, P. Hertzfeld, "Optically Tuned Patch Antenna for Phased Array Applications," *IEEE AP-S International Symposium Digest*, Philadelphia, PA, pp. 361-364, 1986.
- [6] S. S. Gevorgian, "Short-circuit Photocurrent-controlled Microwave PIN Diode Switch," *Microwave and Optical Technology Letters*, Vol.7, No.12, pp.553-555, Aug. 1994.
- [7] S. Stone, J. Vian, Z. Popovic, "Photonically Tuned Slot Antennas," *9-th Annual DARPA Symposium on Photonic Systems for Antenna Applications Proceedings, Session 10, PSAA-9*, Monterey, CA, Feb. 1999.
- [8] Z. Popovic, A. Mortazawi, "Quasi-optical transmit/receive front ends," *invited paper, IEEE Trans. on Microwave Theory and Techniques*, Vol. 48, No. 11, pp. 1964-1975, Nov. 1998.
- [9] D. Anderson *et al.*, "Optically Smart Active Antenna Arrays," *IEEE MTT 2000 International Microwave Symp. Digest*, Boston, MA, June 2000.
- [10] J. Vian, Z. Popovic, "A transmit/receive active antenna with fast low-power optical switching," *IEEE MTT 2000 International Microwave Symp. Digest*, Boston, MA, June 2000.
- [11] C. Goldsmith, *et al.* "Performance of low-loss RF MEMS capacitive switches," *IEEE Microwave and Guided Wave Lett.*, Vol.8, pp.269-271, Aug. 1998.

400 Mbit/s BPSK data transmission at 60 GHz-band mm-wave using a two-mode injection-locked Fabry-Perot slave laser

M. Ogusu, K. Inagaki, and Y. Mizuguchi
 ATR Adaptive Communications Research Laboratories
 2-2-2 Hikaridai Seika-cho Soraku-gun Kyoto 619-0288 Japan
 Phone:+81-774-95-1501 Fax:+81-774-95-1508

Abstract—400 Mbit/s BPSK data transmission at a carrier frequency of 60 GHz is demonstrated by two-mode injection-locking of a Fabry-Perot slave laser whose injection current is directly modulated by the data.

I. INTRODUCTION

Wireless communication links using fiber-based millimeter-wave (mm-wave) systems are expected to support high-capacity networks in the future. Optical generation of mm-wave carriers is necessary for such systems [1]–[7]. Methods based on the heterodyne detection of two waves in a photodetector (PD) and the optical injection-locking of semiconductor laser diodes can provide low phase-noise characteristics for the carriers [1]–[4][6]. Mm-wave generation based on two-mode injection locking of a Fabry-Perot (F-P) laser has the advantages of a tunable range for the generated carrier (59–64 GHz) and widely allowable detuning (8 GHz) between lasers [6]. The key to the wide tunability and stability is the low-Q characteristics of the F-P slave laser. The wide selectivity of the master laser's frequency [3][4][6] is also suitable feature for the design of optical networks. Signal modulation for the mm-wave sources based on optical injection-locking have been reported [1][2]. The configuration shown in reference [1] is based on wavelength multiplexing of an optical mm-wave source and an optical transmission signal for the purpose of long fiber transmission of the optical mm-wave source. In reference [2], the optical phase of one mode emitted from a slave DFB laser is modulated by injection current modulation. The injection current modulation of the locked F-P laser can also induce amplitude modulation (AM) of the locked modes [8]. Long transmission using AM of the locked modes by an external intensity modulator has been reported for fiber-radio systems [9]. By applying a digital base-band signal to the F-P slave laser directly, relatively high-speed data modulation to a 60 GHz carrier has been expected because of the wide locking range of the F-P slave laser [10]. As a result, we confirmed 1.2 Gbit/s ASK data transmission at a 60 GHz carrier

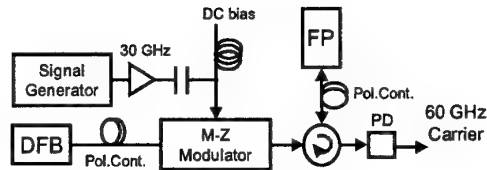


Fig. 1 Basic configuration

frequency.

In this paper, fiber transmission of BPSK data for 60 GHz fiber radio systems is demonstrated where the two modes of the F-P laser are injection-locked and the current is modulated by the data signal on an IF band whose central frequency is 2 GHz. The tunability of the mm-wave frequency and the reduction of the reference frequency for the master source were also examined.

II. OPTICAL GENERATION OF MM-WAVE BY TWO-MODE LOCKED F-P LASER

The basic configuration of two-mode locking for an F-P laser is shown in Fig. 1. The master source is subharmonics, which are obtained by an external optical modulator or direct modulation of the DFB laser [4]–[6]. Any two modes of the F-P slave laser are injection-locked to a pair of subharmonics through the three-port optical circulator when the frequency of the DFB laser is nearly the same as the central frequency of the two modes. A high-speed PD detects the two locked modes after the modes are transmitted to a conventional single-mode fiber. Figures 2a and 2b show the optical spectrum of the slave laser and the phase-noise characteristics of the carrier. Mode spacing of the F-P laser and the reference frequency of a signal generator (SG) were about 60 GHz and 30 GHz, respectively. Optical power of the subharmonics was -15 dBm, and the injection current of the F-P laser was 58 mA, which was 1.2 times larger than the threshold current [6]. The phase-noise was -93 dBc/Hz at 100 kHz offset from the 60 GHz carrier. The degradation of the phase-noise was only 3 dB compared to that of the signal generator with a mm-

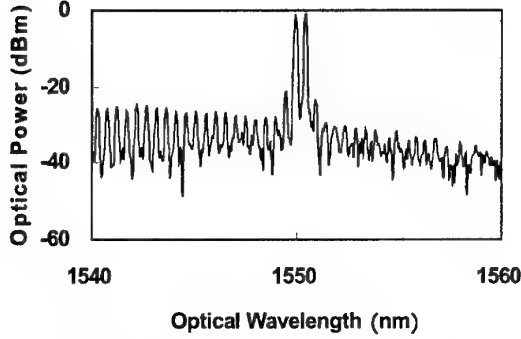


Fig. 2a Optical spectrum of slave laser

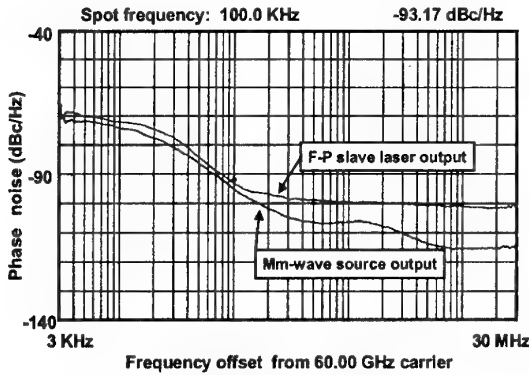


Fig. 2b Phase-noise of generated carrier

wave source module (HP83556A).

III. AMPLITUDE MODULATION FOR TWO LOCKED MODES

When the injection current of the two-mode locked slave laser is weakly modulated, the same phase modulation acts on the modes. Consequently, signal transmission based on the phase modulation could not be achieved because the phase change of locked modes was cancelled out by the heterodyne detection in the PD. However, the data can be detected if amplitudes of the locked modes are simultaneously modulated [10]. Ideal (no chirping) AM of the injection-locked slave laser using the current modulation can be performed when the locking bandwidth is wide enough to neglect the modulation frequency and the frequency deviation induced by the modulation [11]. Relatively high bit-rate modulation can be expected because of the widely allowable detuning between the lasers (8 GHz) [6]. Using current modulation of the F-P laser by NRZ base-band signals, 1.2 Gbit/s (PRBS 2⁷-1) ASK data with a 60 GHz carrier could be transmitted to a distance of 32 km [10]. A 60 GHz carrier with IF signal, which output from the two-mode locked and directly CW modulated F-P laser, could also be transmitted to a distance of 0-48km [8]. Then, we tried frequency chirp observation for a mode of the two-mode locked F-P laser whose injection current was directly modulated. We used

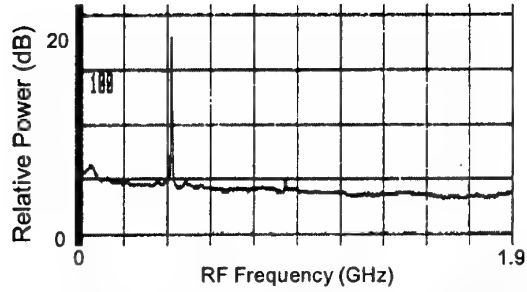


Fig. 3 Self-homodyne detection of a modulated mode (modulation frequency = 400 MHz)

the gated delayed self-homodyne technique for the mode, which was dropped by a fiber-Bragg-grating filter (0.4 nm bandwidth) from the slave laser output. Figure 3 shows a spectrum of O/E converted signal from a fiber interferometer by which an optical interference signal between the modulated and unmodulated mode was generated. The modulation frequency and the gate frequency of the modulation, which was decided by a length of the interferometer's delay line, were 400 MHz and 140 KHz, respectively. No frequency chirping was observed from the power spectrum of the interference signal (Fig. 3). Furthermore, no distortion component was found while the power of the modulation signal, which was applied to the F-P laser, was below 3 dBm. We also confirmed the chirp free performance in the modulation frequency range (< 600 MHz, 780 MHz- 2.5 GHz) where the locked F-P laser's response was flat [8]. This performance is desirable for long fiber transmission of the modulated modes.

IV. BPSK DATA TRANSMISSION

Figure 4 is an experimental setup for BPSK data transmission. The master source is subharmonics from a phase modulator driven by 30 GHz CW (+15 dBm). The BPSK signal is generated by a bi-phase modulator, 2 GHz local signal from a signal generator (SG2), and NRZ data from a pulse-pattern generator (PPG). The current of the F-P laser is modulated by this BPSK signal. The input power of the BPSK signal to the F-P laser was 3 dBm. The optical power of the two subharmonics used and the current of the F-P laser were -13 dBm and 55 mA, respectively. The modes whose amplitudes are modulated by the IF signal are amplified by an EDFA with 0.8 nm optical band-pass filter and are transmitted to a single-mode fiber. The optical power level at the PD is adjusted by an optically variable attenuator for measurement of bit-error-rate (BER) performance of the heterodyne-detected signal. The generated 60 GHz-band signal is down-converted to 2 GHz IF by an envelope detection circuit, which is composed of a power divider, mm-wave amplifiers, and a mixer.

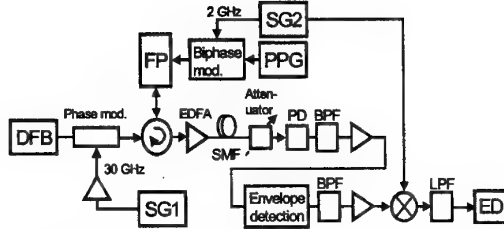


Fig. 4 Experimental setups for BPSK data transmission

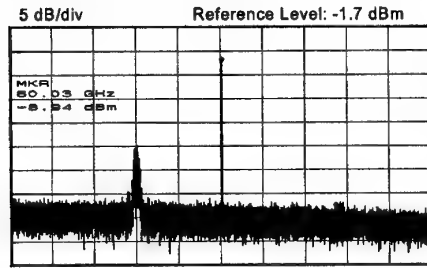


Fig. 5a Spectrum of modulated mm-wave carrier

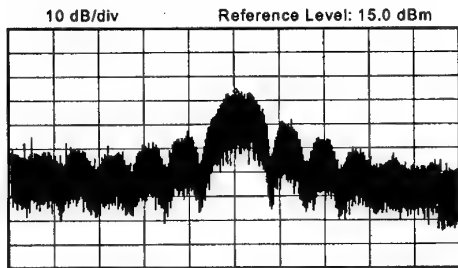


Fig. 5b Spectrum of down-converted BPSK signal

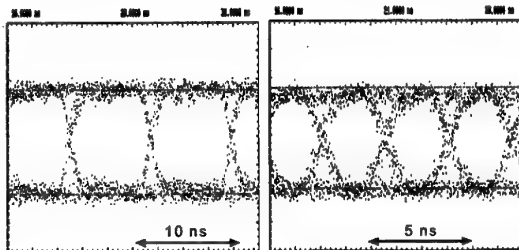


Fig. 5c Recovered eye-patterns of 156 Mbit/s (left) and 400 Mbit/s (right) signals

By multiplexing the BPSK signal and 2 GHz LO, the NRZ data is recovered. Figure 5a shows a spectrum of the mm-wave signal at the input port of the envelope detection circuit. The IF component around 62 GHz disappeared due to the gain bandwidth (30–60.5 GHz) of a front-end mm-wave amplifier. The down-converted BPSK signal and the recovered NRZ signal are shown in Fig. 5b and the left side of Fig. 5c when the data-rate and the fiber length were 156 Mbit/s (PRBS $2^{31}-1$) and 16 km, respectively. The BER performances are displayed in Fig. 6a when the

bit-rate is 400 Mbit/s (PRBS $2^{31}-1$) that corresponded to a bandwidth of the bi-phase modulator, and the eye-pattern is shown in the right side of Fig. 5c. The locked modes could be transmitted through 1, 4, 8 and 16 km fibers. A DFB laser's optical carrier and a pair of the 2nd subharmonics from the phase modulator were partly passed through the F-P laser. Then, two unwanted 60 GHz beat signals, which were induced from these three optical components, slightly interfered with the 60 GHz carrier generated by the locked modes. However, the received optical power's penalty was within 1.5 dB due to the fiber dispersion. Comparing the IF-band modulation with the base-band data modulation [10], the word-length of the pseudo-random patterns could be increased for the IF-band modulation. Stability for the injection-locking was degraded for the low frequency (< 100 KHz) modulation because the frequency deviation of the modulated laser becomes comparable to the locking bandwidth. This is the reason why it is possible to transmit the low frequency components that are up-converted to the IF-band.

Next, we examined the tunability of the generated mm-wave by evaluating the BER performance of the detected signal. The frequency of the mm-wave can be changed by adjusting the reference frequency output from the signal generator (SG1). The fiber length and the data-rate were 16 km and 156 Mbit/s, respectively. The BER performances for the cases of 55, 56, 57, 58, and 59 GHz are shown in Fig. 6b. In all cases, we confirmed that BER could be less than 10^{-9} . The power penalty was increased for the higher central frequencies of the mm-wave signals because the amplification coefficient of the front-end mm-wave amplifier was degraded as the frequency was increased and was extremely low over 60.5 GHz. Then the tunability of the mm-wave generated was confirmed for the data transmission. We believe that the tunability can be maintained in the range over 60 GHz [6] if the detection circuit is free from the bandwidth limitation.

Finally, reduction of the reference frequency for the master source was tested. Figures 7a and 7b show the optical spectrum and the received eye-pattern where the reference frequency, the power of the reference signal, the length of the fiber, and the data-rate were 15 GHz, +15 dBm, 16 km and 156 Mbit/s, respectively. Stable locking for data transmission was maintained by increasing the injection current into the F-P laser, namely the Q-value of the slave laser, although the optical power ratio of the 1st subharmonics to the 2nd subharmonics at the modulator output was about 7.0 dB (not shown). The injection current of the F-P laser was 62 mA, which corresponded to about 1.4 times the threshold current. In this condition, BER could be less than 10^{-9} . Due to the fiber

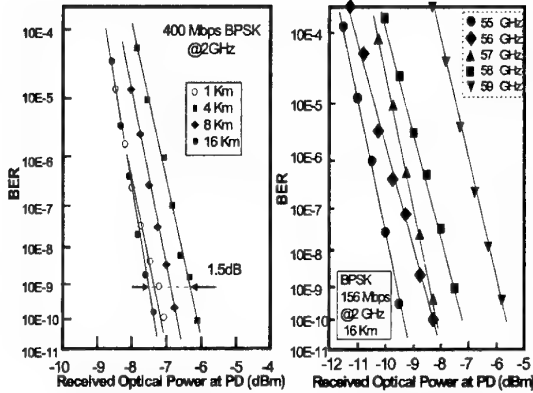
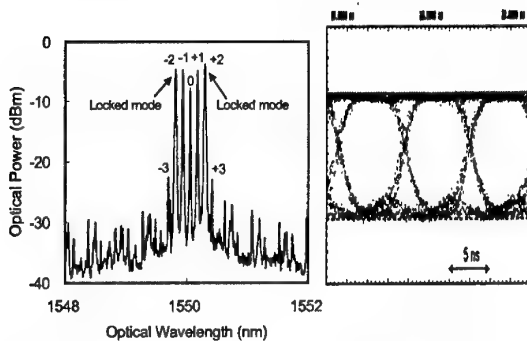


Fig. 6a BER performance 1

Fig. 6b BER performance 2

Fig. 7a Slave laser's spectrum
(reference frequency=15 GHz)Fig. 7b 156 Mbit/s
eye-pattern

chromatic dispersion, the 60 GHz signals emerging from the two pairs of the 1st and the 3rd subharmonics may affect the BER performance of the received signal which is generated by the locked modes. The optical power penalty caused by interference among the 60 GHz components was estimated about 1.8 dB from the optical spectrum of Fig. 7a. Accordingly, an optical narrow-band filter such as a fiber-Bragg-grating is needed at the optical circulator output for the rejection of the 1st or the 3rd subharmonics.

V. CONCLUSIONS

Ideal AM (no chirping) for the two locked modes have been achieved by the direct data modulation of the F-P slave laser with low Q cavity. Using this slave laser's modulation, we have successfully performed 1- 16 km transmission of 400 Mbit/s BPSK data signal at 2GHz IF-Band modulation. A tunable range of 55-60 GHz was confirmed by BER performance of BPSK data transmitted through a 16 km fiber.

ACKNOWLEDGEMENT

The authors would like to thank Dr. Komiyama, president of ATR Adaptive Communications Research Laboratories, for his continuous encouragement.

REFERENCES

- [1] L. Noel, D. Wake, D. G. Moodie, D. Marcenac, L. D. Westbrook, and D. Nasset, "Novel Techniques for High-Capacity 60-GHz Fiber-Radio Transmission Systems," IEEE Trans. Microwave Theory Tech., Vol. 45, pp. 1416-1423, 1997.
- [2] R. -P. Braun, G. Grosskopf, D. Rohde, and F. Schmidt, "Low-Phase-Noise Millimeter-Wave Generation at 64GHz and Data Transmission Using Optical Sideband Injection Locking," IEEE Photon. Technol. Lett., Vol. 10, pp. 728-730, 1998.
- [3] L. Goldberg, A. M. Yurek, H. F. Taylor, and J. F. Weller, "35GHz microwave signal generation with an injection-locked laser diode," Electron. Lett. Vol. 21, pp. 814-815, 1985.
- [4] Z. Ahmed, H. F. Liu, D. Novak, Y. Ogawa, M. D. Pelusi, and D. Y. Kim, "Locking Characteristics of a Passively Mode-Locked Monolithic DBR Laser Stabilized by Optical Injection," IEEE Photon. Technol. Lett., Vol. 8, pp. 37-39, 1996.
- [5] J. J. O'Reilly, P. M. Lane, R. Heidemann, and R. Hofstetter, "Optical generation of very narrow line-width millimeter wave signals," Electron. Lett., Vol. 28, pp. 2309-2311, 1992.
- [6] M. Ogusu, K. Inagaki, and Y. Mizuguchi, "Tunability for 60GHz-Band Millimeter-wave Generation Using Two-mode Injection Locking of a Fabry-Perot Slave Laser," ECOC'99 P3-5.
- [7] N. Mineo, K. Yamada, K. Nakamura, S. Sakai, and T. Ushikubo, "60-GHz band electroabsorption modulator module," OFC '98, Tech. Dig., Vol. 2, pp. 287-288, 1998.
- [8] M. Ogusu, K. Inagaki, and Y. Mizuguchi, "60 GHz Carrier and IF Signal Transmission Using Two-Mode Injection-Locking of a Fabry-Perot Slave Laser," submitted to IEEE Microwave and Guided wave Letter.
- [9] H. Schmuck and R. Heidemann, "High Capacity Hybride Fibre-Radio Field Experiments at 60 GHz," MWP'96 TU4-3.
- [10] M. Ogusu, K. Inagaki, and Y. Mizuguchi, "60 GHz-band Millimeter-wave Generation and ASK data Transmission Using 2-mode Injection-Locking of a Fabry-Perot Slave Laser," TSMMW 2000 P-12.
- [11] K. Kikuchi, T. Okoshi, and S. Tanikoshi, "Amplitude modulation of an injection-locked semiconductor laser for heterodyne-type optical communications," Optics Lett., Vol. 9, pp. 99-101, 1984.
- [12] J. M. Fuster, J. Marti, and J. L. Corral, "Chromatic dispersion effects in electro-optical upconverted millimetre-wave fibre optic links," Electron. Lett. Vol. 33, pp. 1969-1970, 1997.

Radio on Fiber System for Triple Band Transmission in Cellular Mobile Communication

Yasushi ITO Yoshio EBINE

Radio Network Development Department, NTT DoCoMo, Inc.

3-5 Hikari-no-oka, Yokosuka, Kanagawa, 239-8536 JAPAN

Tel +81-468-40-3165, Fax +81-468-40-3295, e-mail: yasushi@mlab.yrp.nttdocomo.co.jp

Abstract This paper proposes a compact and cost effective radio on fiber system in buildings for cellular mobile communication. The radio on fiber system supports triple bands, the 800MHz band and the 1.5GHz band for Personal Digital Cellular and the 2GHz band for IMT-2000. The system configuration and experimental results are introduced.

INTRODUCTION

The radio on fiber system with Sub-Carrier Multiplexing (SCM) simplifies the distribution of RF signals to provide Personal Digital Cellular (PDC) service in previously blind areas, such as buildings, underground malls and highway tunnels. In buildings, we can create a cost effective radio on fiber system by adopting a multi drop topology with Fabry-Perot Laser Diode (FP-LD); the RF signals lie within two bands (800MHz band and 1.5GHz band) [1][2]. In Japan, third generation mobile communication system (IMT-2000), which is assigned the 2GHz band, will be introduced in 2001. To utilize the optical fiber installed for PDC service, we have developed a radio on fiber system that can transmit in triple bands: 800MHz band, 1.5GHz band, and 2GHz band. The system construction, the required performance and measured performance are explained below.

SYSTEM CONSTRUCTION

The system construction of the radio on fiber system is shown in figure 1. The features of this system are as follows;

- (1) uses multi drop topology
- (2) uses cost effective FP-LD (convection cooled) without isolator
- (3) maximum number of access units is eighteen
- (4) triple band RF signals can be transmitted

Downlink optical signal is distributed to six access units to equalize the received optical power. The base unit can support three FP-LDs.

Each uplink uses three FP-LDs with different optical wavelengths, and the three wavelengths are detected by one PD in the base unit at the same time. To improve CNR, we adopt spectrum broadening with low RF frequency intensity modulation [3,4].

Three Single Mode Fibers (SMFs) must connect the Base unit to the six access units. If eighteen access units are used, nine SMFs are required.

We can utilize already installed optical fiber. Triple band RF signals can be transmitted by exchanging the base unit, access units, and antennas. Installation costs are low.

SYSTEM REQUIREMENTS

Table 1 shows the performance required of the radio on fiber system. RF performance in the 800MHz and 1.5GHz bands is shown in reference [1][2]. Required RF performance in the 2GHz band was set so as to provide the service radius of one hundred meters with one access unit. Twenty eight carriers are transmitted, including four carriers in the 2GHz band. The radio on fiber system can transmit triple band RF signals.

In IMT-2000 systems, the Adjacent Channel Leaking power Ratio (ACLR) depends on third order inter modulation distortion (IM3) performance. Increasing the number of carrier degrades Composite Triple Beat (CTB) and ACLR. The degradation in CTB and ACLR is estimated to be only 1.5dB.

The uplink noise figure of the radio on fiber system degrades the received sensitivity of the IMT-2000 system. The IMT-2000 uplink received sensitivity in the radio on fiber system is given by equation (1).

$$Pr' = Pr + NF_{opt} - NF_{bts} \quad (1)$$

Where Pr [dBm] is the uplink received sensitivity of the base station without radio on fiber system, Pr' [dBm] is the uplink received sensitivity of the base station in the radio on fiber system, NF_{bts} [dB] is the noise figure of the base station and NF_{opt} [dB] is the noise figure of the radio on fiber system. If the transmitted information data rate is 12.2kbps in IMT-2000, uplink received sensitivity is -122dBm/4MHz [3]. The uplink received sensitivity in the radio on fiber system is less than -84dBm/4MHz from equation (1).

On the uplink, the maximum input power of the access unit is about -27dBm due to a characteristic of the Japanese system. The channel adjacent to the IMT-2000 uplink band is used by the Personal Handy phone System (PHS) band. Even if the access unit receives a PHS

signal, the degradation in received sensitivity caused by IM3 is negligible. Required IM3 must satisfy equation (2)

$$G_{opt} + kT + NF_{opt} \gg IM3 \quad (2)$$

Where kT is thermal noise (-108dBm/4MHz) and G_{opt} is the link gain of the radio on fiber system.

Photographs 1 and 2 show the exterior of the radio on fiber system. Base unit size is W560-H450-T400mm, and access unit size is W250-H50-T200mm.

RF CHARACTERISTICS

Input power vs. output power and IM3 of fiber link was observed. Figure 2 shows downlink IM characteristic. Downlink CNR in the 2GHz band exceeds 45dB/4MHz and CTB is less than -50dBc.

Figure 3 shows uplink characteristics. Uplink CNR exceeds 45dB/4MHz. IM3 is less than -70dBc. When transmitting sixteen carriers within the 800MHz band, eight carriers in the 1.5GHz band, and four carriers within the 2GHz band, the Adjacent Channel Leaking power Ratio (ACLR) with 5MHz channel spacing in the 2GHz band is less than -45dBc. Figure 4 shows transmitted modulated 2GHz band spectrum of a downlink. Chip rate of modulated signal is 4.096Mcps.

CONCLUSION

We described a radio on fiber system that can transmit triple band RF signals to provide cellular service in buildings. Required specifications and measured performance were explained. Number of transmitted carriers is twenty eight, including four carriers within the 2GHz band (IMT-2000). Downlink CNR exceeds 45dB/4MHz and Composite Triple Beat (CTB) is less

than -50dBc and 2 GHz band Adjacent Channel Leaking power Ratio (ACLR) at 5MHz channel spacing is less than -45dBc.

REFERENCES

- [1] Y. Ebine., "Development of fiber-radio systems for cellular mobile communications," MWP '99, F-10.1
 [2] Y. Fuke et al., "RF sub-carrier optical transmissions using a bus type topology for personal digital cellular

systems," MWP '99, T-8.19

- [3] H.Sasai et al., "Optical access links suppressing optical beat interference with FP-LDs for microwave transmission," MWP'96, WE4-6
 [4] H.Sasai et al., "High performance long distance fiber-optic transmission unisolated Fabry-Perot Laser for mobile radio systems in the technical digest of OFC'97," Paper TuD3, pp.13-14, 1997

- [5] 3GPP, TS 25.104 v2.0.0, June, 1999

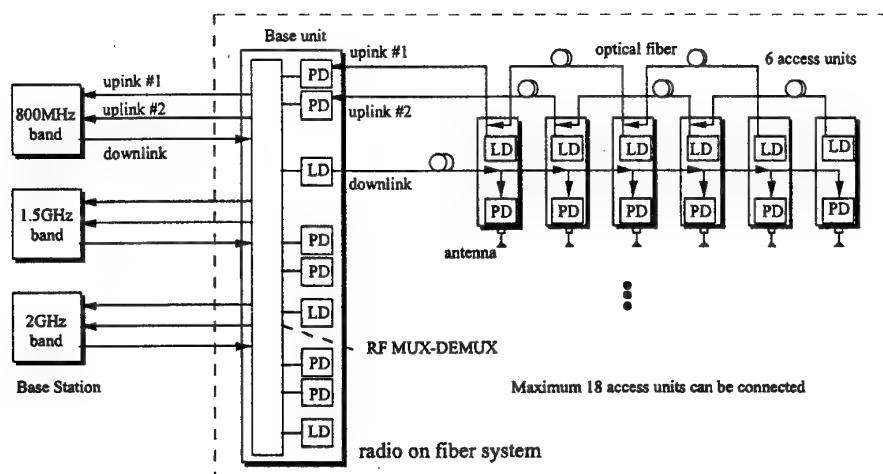
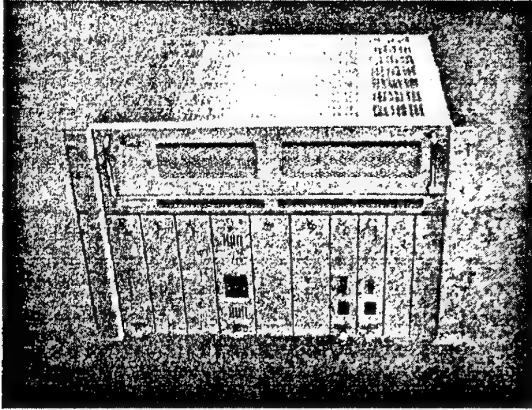


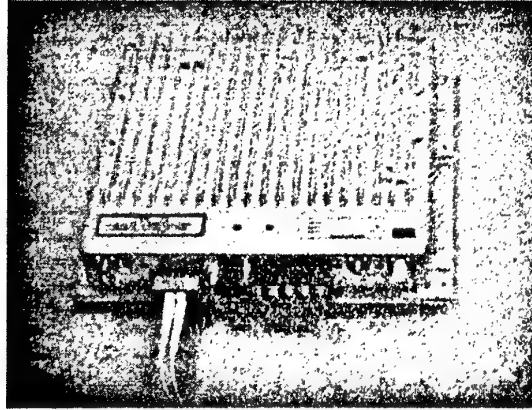
Figure 1. Construction of radio on fiber system for triple band RF transmission

Table 1. System requirement of radio on fiber system.

	downlink		uplink	
	PDC	IMT-2000	PDC	IMT-2000
Frequency bands	810-818 MHz 1.477-1.501 GHz	2.11-2.13 GHz	915-956 MHz 1.429-1.453 GHz	1.92-1.94 GHz
Maximum number of carrier	24 carriers	4 carriers	24 carriers	4 carriers
RF input power	-3dBm/carrier	-15dBm/carrier	-27dBm/carrier	-27dBm/carrier
RF output power	0dBm/carrier	0dBm/carrier	-27dBm/carrier	-27dBm/carrier
CNR	>45dB/21kHz	>45dB/4MHz	>55dB/21kHz	>40dB/4MHz
CTB	<-45dBc	<-45dBc		
IM3		-	<-56dBc	<-56dBc



Photograph 1. Base unit of radio on fiber system.



Photograph 2. Access unit of radio on fiber system.

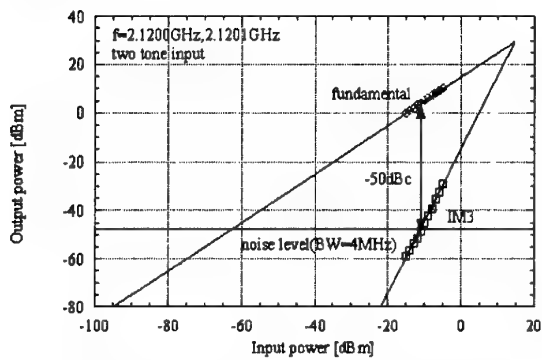


Figure 2. 2GHz band downlink IM characteristic of radio on fiber system.

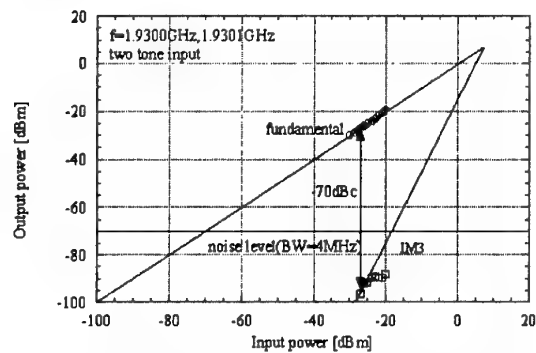
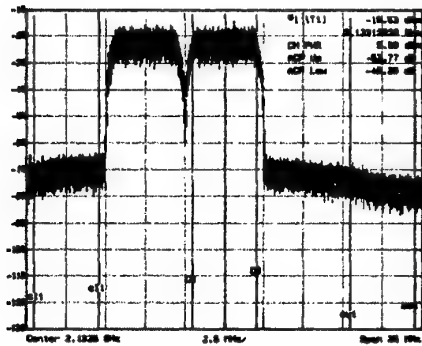


Figure 3. 2GHz band uplink IM characteristic of radio on fiber system.



H:2.5MHz/div,V:10dB/div

Figure 4. Transmitted downlink spectrum of IMT-2000 signal.

Penalty free W-CDMA radio signal transmission over fibre

Ralf E. Schuh¹, David Wake², Bertil Verri¹ and Erland Sundberg¹

(1) Telia Research AB, Hjälmaregatan 3, 201 20 Malmö, Sweden.

Tel: +46 40 105139, Fax: +46 40 307029

E-mail: Ralf.X.Schuh@telia.se

(2) BT Adastral Park, Martlesham Heath, Ipswich IP5 3RE, UK.

Abstract: This paper presents error vector magnitude and bit error rate measurements for the transmission of W-CDMA signals over optical fibre. A prototype W-CDMA test system in combination with a directly modulated optical link has been used to establish the maximum input power bounds for penalty free transmission.

Introduction

There is an increasing demand for indoor distributed antenna systems (DAS) for cellular communications networks in order to give indoor mobile subscribers higher quality of service and to provide increased capacity. Good indoor coverage will be even more important for the upcoming third generation radio systems, e.g. the universal mobile telecommunication system (UMTS) using wideband-code division multiple access (W-CDMA), which will enable subscribers to get higher data rates. The cell-size for these indoor systems will be small (picocells) and analogue optical feeders are an economical and flexible way to deliver the radio signal to these cells from a centralised location.

Previous work has shown that link distortion can be kept within acceptable limits, in terms of adjacent channel power leakage ratio (ACLR), as long as input power and fibre length are kept below certain values [1]. The purpose of this paper is to assess also the effects of link distortion on the baseband signal in terms of error vector magnitude (EVM), signal to noise ratio (SNR) and bit error ratio (BER). The input power and fibre length constraints imposed by these parameters can then be compared to those imposed by ACLR considerations to identify which is the main limiting factor. The maximum input power is of interest as it determines the dynamic range of the fibre

radio system (the lower power limit being given by the noise level of the system).

Experiment

Figure 1 shows the two experimental setups used for measuring ACLR, EVM and BER. A vector signal generator (SMIQ from Rohde & Schwarz) and a prototype W-CDMA test system were used to generate the W-CDMA signals at a carrier frequency of 2GHz with bandwidth of around 4MHz.

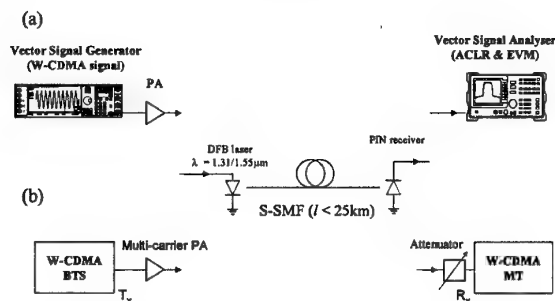


Figure 1: Experimental setups:

(a) ACLR and EVM

(b) BER

For both setups a single channel was used which gave a peak-to-average power ratio of about 6dB. This signal was fed into the optical links with various lengths of standard-single mode fibre (S-SMF). For the ACLR and EVM measurements, Figure 1 (a), the received signal was analysed using a vector signal analyser (FSIQ from Rohde & Schwarz). Recommended settings were used for the

SMIQ and FSIQ, which for back-to-back measurements gave an ACLR and EVM of less than -63dBc and 1.5%, respectively. For the BER measurement, Figure 1 (b), the signal was generated by the base station (BS) and fed into the mobile terminal (MT) of the W-CDMA test system via the optical link.

The broadband analogue optical links (0.1 to 4 GHz) used in these experiments were both from Ortel Corporation. The lasers used were (a) the model 10370A (1550nm DFB, output power = 7dBm) and (b) the model 10340A (1310nm DFB, output power = 3dBm). The 1dB power compression point and input third order intercept point of the two lasers used were very similar, according to the specifications. The optical receiver for both links was the Ortel model 10450.

Results and discussion

Figure 2 shows the measured signal spectrum for (a), short fibre length and low input power, and for (b), long fibre length and high input power.

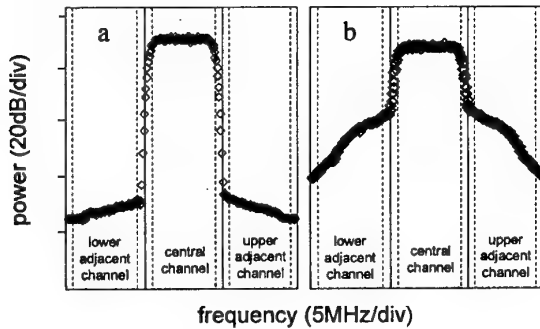


Figure 2: Signal spectrum traces:
(a) input power = 9dBm, fibre length = 2km
(b) input power = 17dBm, fibre length = 25km

The spectral regrowth can be clearly observed in figure 2 (b) as a result of the distortion. The distortion is caused by two main factors; laser nonlinearity and the interaction between laser chirp and fibre chromatic dispersion. ACLR and EVM were measured at a wavelength of $\lambda = 1.55\mu\text{m}$. The effect of these parameters on ACLR has been discussed previously [1].

From the ACLR measurements we could establish the following maximum bounds,

given in table 1 for the laser input power, in order to meet the UMTS downlink and uplink specifications [2, 3]. The values are given for the case of 32 channels.

Fibre span, km	Max. input power, dBm	
	DL	UL
0	12	14
2	12	14
12.5	11	13
25	9	12

Table 1: Maximum input power to meet ACLR specification for UMTS

Distortion also causes problems at baseband. The demodulated signal can be plotted in an IQ-constellation diagram. For QPSK modulation the decision points occur in four quadrants. Figure 3 shows the IQ diagram for (a), low input power and short fibre length, and (b), high input power and long fibre length. It can be seen in Figure 3 (a) that the spread around the ideal IQ points is uniformly distributed, indicating white noise as the main impairment. In Figure 3 (b) the spread around the ideal IQ points is skewed, indicating coloured noise which is caused by nonlinear distortion.

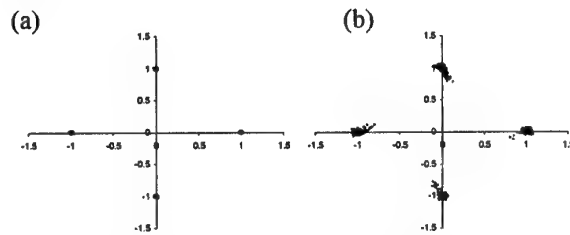


Figure 3: IQ-constellation diagram:
(a) input power = 9dBm, fibre length = 2km
(b) input power = 17dBm, fibre length = 25km

The most widely used modulation quality metric in digital RF communication systems is EVM. EVM provides a way to quantify the errors in digital demodulation and is sensitive to any signal impairment that affects the magnitude and phase trajectory of a demodulated signal. EVM is often more convenient to measure compared with BER

and can be calculated from the measured points in the IQ constellation diagram. Figure 4 shows how EVM varies with input power and fibre length. The following general observations can be made from this figure:

- EVM increases significantly for input power levels in excess of 15dBm and fibre lengths > 2km. The EVM increase is mainly due to the distortion caused by the interaction between laser chirp and fibre chromatic dispersion.
- for fibre lengths < 2km the EVM increase is mainly determined by the laser nonlinearity.

The same trends have been observed for the ACLR results [1].

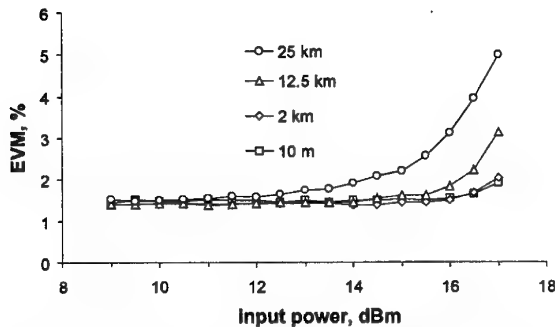


Figure 4: EVM rms value as a function of input power for several fibre lengths (for a single 32 kbps data channel).

EVM is related to BER through SNR. SNR is given as [4]

$$SNR = -20 \log \left(\frac{EVM}{100} \right) - \beta \quad (1)$$

where β is the peak-to-average power ratio (~ 6 dB for the single channel case). Figure 5 shows SNR calculated using equation 1 for the EVM data given in Figure 4.

For SNR values determined by additive white Gaussian noise (AWGN), which in our case is true for low fibre length and low input powers, the BER can be directly related to the SNR using standard tables given in many textbooks (for QPSK, a SNR > 15dBm gives a BER of $< 10^{-9}$). This also assumes ideal matched filtering. From Figure 5, even in the case of strong coloured noise (for high input powers and long fibre lengths), we would not

expect to have BER > 10^{-9} as the calculated SNR values are high.

Adding more channels to the system has the effect of increasing the peak-to-average power ratio of the input signal (CREST factor). For higher number of channels, e.g. 32 channels, the CREST factor can be up to 10dB [1]. This will further reduce the SNR by 4dB. Adding more than 32 channels will not increase the CREST factor significantly.

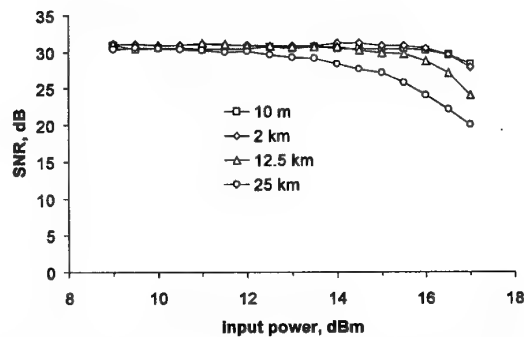


Figure 5: SNR as a function of input power for various fibre lengths (CREST factor is 6dB).

We have also performed BER measurements, see Figure 1 (b), using a prototype W-CDMA test system. RAKE reception and despreading of the W-CDMA signal are performed in this receiver.

The measurement was setup using 2km of S-SMF (as in most cases 2km of fibre will be sufficient for a DAS) and 1310nm lasers in the downlink and uplink between base station and mobile terminal. The raw BER in the downlink was measured on the pilot channel. A single data channel with a data rate of 128kbps was selected. The attenuator in front of the receiver was used to reduce and balance the received power.

Figure 6 shows the BER as a function of relative received power. The following can be noted:

- up to 6dBm input power virtually no BER penalty is observed, with respect to the back-to-back measurement using coax cable.
- for 12dBm input power the penalty is ~ 3 dB for BER of 10^{-3} .

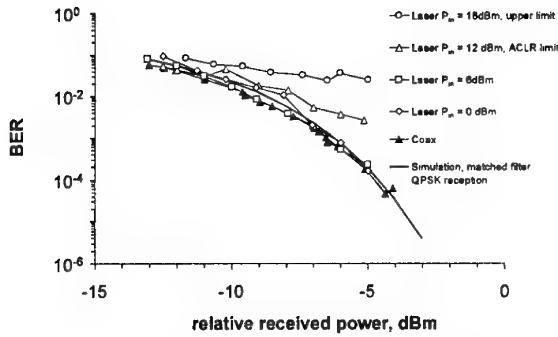


Figure 6: BER as a function of received power for 2km fibre length (for a single 128ksps data channel).

From the EVM measurement results we would not have expected to see any significant BER penalty due to the optical link even in the case of high input power to the laser. The following may explain the differences:

- for high input power the nonlinear distortion causes coloured noise
- the W-CDMA test system and vector analyser use different receivers which may be optimised for different operation conditions
- we also have observed instantaneous SNR values giving a difference of up to 15dB to the SNR_{rms} for high laser input powers
- although the lasers had similar specifications, the 1310nm laser is expected to have greater nonlinearity at high input power due to its lower bias current

However, if comparing BER with SNR the processing gain has to be considered too for the spread spectrum system, which would be ~15dB for the 128ksps channel (assuming white noise).

The main purpose of this work is to evaluate the input power and fibre span limits for penalty free W-CDMA transmission. We have been able to show penalty free W-CDMA signal transmission over 2km of standard single-mode fibre for laser input powers ≤ 6 dBm using a prototype base station and mobile terminal. The results have shown that

the complex W-CDMA receivers can be very sensitive to nonlinear distortion.

For the W-CDMA test system, the maximum input power to the laser is limited by the baseband distortion. However, for future W-CDMA systems (receivers) we would expect the maximum input power that can be applied to the optical link is determined by the UMTS specification for adjacent channel leakage power ratio, as predicted by the ACLR and EVM measurements.

Conclusions

To the author's knowledge, this paper has presented the first experimental results of penalty-free W-CDMA transmission over optical fibre. Further investigations are in progress in order to understand why W-CDMA receivers can be especially sensitive to interference from nonlinear distortion.

Acknowledgement

The authors wish to acknowledge Corning Optical Fibres UK for supplying the fibre, Nils Pickert of Rohde & Schwarz for the test equipment, Peter Almers and Christian Bergljung of Telia Research, Malmö for helpful discussions. This work was performed as part of EURESCOM Project P921 [6].

References

- [1] D. Wake and R. E. Schuh, "Measurement and simulation of W-CDMA signal transmission over optical fibre", IEE Electronics Letters, vol. 36, no. 10, pp. 901-902, 2000.
- [2] 3GPP TSG RAN WG4 document TS 25.104 v3.0.0 (1999-10), "UTRA (BS) FDD; Radio transmission and Reception"
- [3] 3GPP TSG RAN WG4 document TS 25.101 v3.0.0 (1999-10), "UE Radio transmission and Reception (FDD)"
- [4] HP Application Note 5968-3579E, "Testing and troubleshooting digital RF communications receiver designs", 1999.
- [5] P921 EURESCOM study group, "UMTS Radio Access", <http://www.eurescom.de/>

Error-Free Transmission of Radio QPSK Signals in an Optical Subcarrier Multiple Access System Suppressing Optical Beat Interference with Over-Modulation

Ichiro Seto, Tazuko Tomioka and Shigeru Ohshima

Corporate Research & Development Center, Toshiba Corporation

1, Komukai Toshiba-cho, Saiwai-ku, Kawasaki 212-8582, Japan

Tel: +81-44-549-2280, Fax: +81-44-520-1806, E-mail: ichiro.seto@toshiba.co.jp

Abstract Error-free transmission of radio QPSK signals was able to be achieved in an optical subcarrier multiple access system, suppressing optical beat interference with over-modulating Fabry-Perot lasers. Nine radio base stations with a data rate of 12.86 Mbit/s can be multiplexed.

1. Introduction

Fiber-radio techniques [1] offer many advantages for broadband wireless access networks such as the fixed wireless access (FWA) system [2]. These techniques will make it possible to process complicated operations in a center station (CS), such as (de)modulation of radio signals and channel control. Radio base stations (BSs) can be simply constructed of antennas, frequency up-/down-converters and an optical Tx/Rx. Among several fiber-optic networks, an subcarrier multiple access (SCMA) over a passive optical network (PON) is a promising architecture for a cost effective solution [3]. It is well known that optical beat interference (OBI) [4] causes serious damage in the upstream transmission of an optical SCMA system. At a receiver, OBI occurs when two or more lasers have closely spaced wavelengths and a large amount of noise is produced within the signal bandwidth. As a means of suppressing OBI, an over-modulation technique is useful [5]. This technique essentially consists of broadening optical spectra by over-modulating lasers. The signal modulation

scheme employed in Ref. [5] is frequency-shift keying, which has a constant envelope. In principle, this scheme causes no penalties due to clipping at over-modulating lasers. Quadrature phase-shift keying (QPSK) signals used for wireless access networks have a greatly varying envelope because the signal bandwidth is limited by a root roll-off filter (RROF). It is considered that nonlinear processing such as clipping causes penalties for envelope-varying signals due to odd-order distortion [6]. However, we found by computer simulations that clipping at over-modulating lasers does not induce critical penalties for radio QPSK signals.

In this paper, we demonstrate that radio QPSK signals can be transmitted in an optical SCMA system, suppressing OBI with the over-modulation technique. The optical dynamic range is experimentally examined and the multiple access capability of radio BSs is indicated.

2. OBI of over-modulated lasers

We utilized a cost-effective Fabry-Perot laser diode (FP-LD) as an upstream light source in an optical SCMA system. One useful parameter in characterizing OBI between two lasers is their relative optical beat interference noise (ROBIN) [7]. ROBIN is defined by $\text{ROBIN} = \langle i_n^2 \rangle / I_1 I_2$, where $\langle i_n^2 \rangle$ is the spectrum density of the noise current and I_1 and I_2 are the received photo-currents from each of the interfering lasers. This definition is analogous to

the definition of relative intensity noise (RIN). The measured ROBIN versus OMI (optical modulation index) is shown in Fig. 1. The ROBIN was generated by the two identical commercial FP-LDs with equal mode spacing. The two FP-LDs were modulated by sinusoidal signals having subcarrier frequencies of 400 MHz and 430 MHz, respectively. In the measurement, the ROBIN was maximized in a 200-MHz band by controlling the polarization and the wavelength of the two lasers. We can see that the ROBIN falls with the increasing OMI due to laser chirping. It can be seen that the ROBIN decreases more rapidly when the OMI exceeds 1.0. This is because the optical spectra of the two lasers are broadened due to the over-modulation.

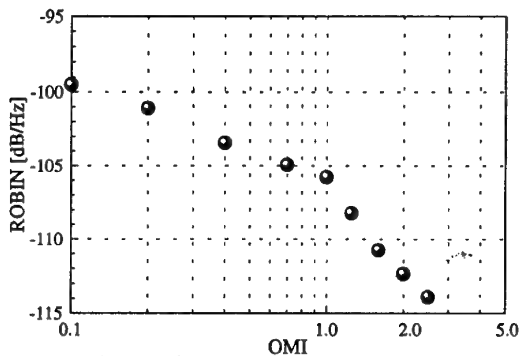


Fig. 1. ROBIN performance against OMI.

3. Simulation and experimental results

3.1 Computer Simulation

The penalty due to the over-modulation technique of radio QPSK signals was estimated by using computer simulation techniques. Fig. 2 shows the BER performance versus carrier-to-noise ratio (CNR) with $OMI < 1.0$ and $OMI = 2.0$. It was found that the power penalty due to over-modulation was 0.5 dB at $BER = 10^{-5}$. From Fig. 2, it is expected that nonlinear processing such as clipping at over-modulating lasers would induce no critical penalties for radio QPSK signals such as envelope-varying signals.

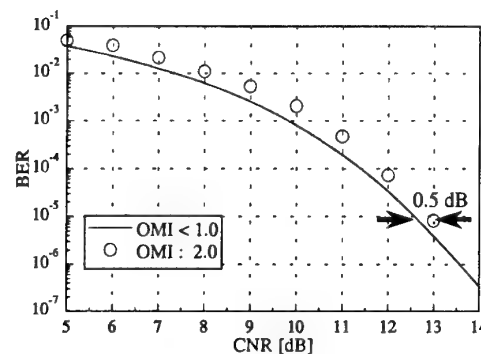


Fig. 2. Simulation results of BER performance.

3.2 Experimental setup

Fig. 3 shows our experimental setup for transmitting radio QPSK signals in an optical SCMA system. A 12.86 Mbit/s, $2^{23}-1$ pseudo-random-bit sequence from a bit error rate test set (BERTS) was sent to

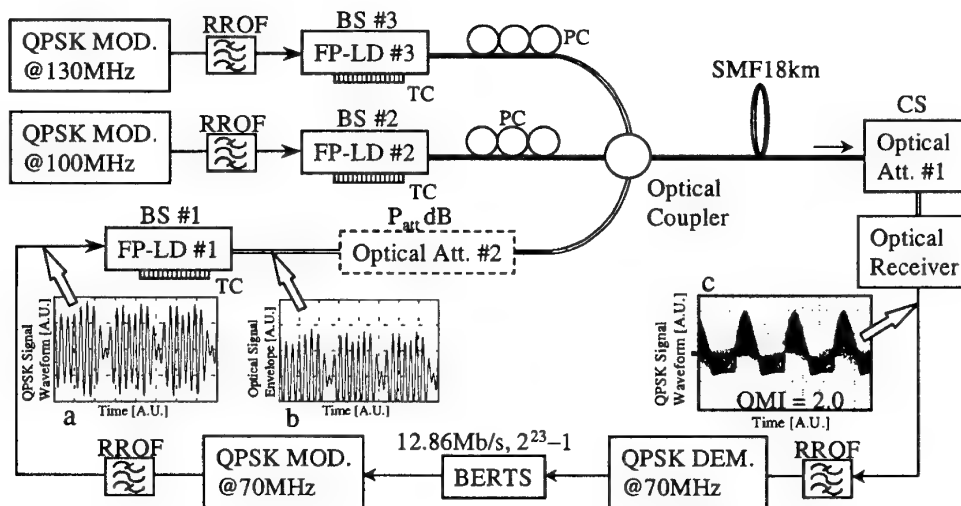


Fig.3. The experimental setup (a : QPSK signal waveform, b : optical signal envelope, c : QPSK signal waveform from LD#1).

each QPSK modulator to produce QPSK signals. The subcarrier frequencies for the BSs #1 – #3 were set at 70 MHz, 100 MHz and 130 MHz. The three QPSK signals were passed through RROFs having a roll-off factor, α , of 0.5 and were input to 1.3- μm Fabry-Perot laser diodes (LDs) #1 – #3, respectively. The LDs #1 – #3 were directly modulated with OMI of 0.8 or 2.0. The outputs from LDs with 0 dBm power were combined via an optical fiber coupler and were transmitted through 18 km of single-mode fiber (SMF). At the center station (CS), the combined outputs were detected by an optical receiver using a pin-PD. The three LDs were wavelength-tuned with temperature controllers (TCs) and polarization-aligned with polarization controllers (PCs) so that the maximum OBI at a subcarrier frequency of 70 MHz could be observed. After separating the desired signal from other signals by passing through an RROF, the data was recovered with coherent detection at a QPSK demodulator. The bit error rate (BER) performance was measured by the BERTS under several OBI conditions.

3.3 BER performance in the presence of OBI

Fig. 4 shows the BER performance versus the received optical power from LD #1 and the received subcarrier signal spectra in the presence of OBI among the three LDs with OMI = 0.8 or 2.0. The measuring conditions were: with OBI present among the three LDs; with OBI present between the two LDs (LD#2 and LD#3) with no OBI; and with no OBI at the Back-to-Back (B-T-B).

First, the receiver sensitivity was improved by 3.5 dB corresponding to the increased OMI. The laser bandwidth was sufficiently wider than the subcarrier signal spectra, so that the lower side of the signal waveform was deformed to the square form, as shown in Fig. 3c. At this deformation, no critical phase distortion was induced owing to the wide laser

bandwidth. Hence, radio QPSK signals were not sensitive to the over-modulation technique.

Second, we found that tolerance for OBI with OMI = 2.0 was much improved. With OMI = 0.8, BER floors were observed for the OBI between the two LDs, and for the OBI between the three LDs. On the other hand, no system impairment by OBI with OMI = 2.0 was observed. This was due to the suppressed OBI and the OMI gain, as shown in the received signal spectra of Fig. 4. In this case, the OBI level was decreased by 5 dB.

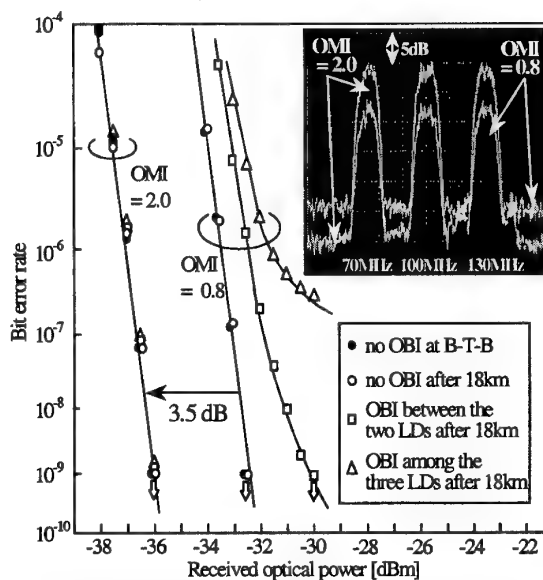


Fig. 4. The BER under several OBI conditions and the received signal spectra in the presence of OBI among the three LDs with OMI = 0.8 or 2.0.

3.4 Optical dynamic range

We now show the optical dynamic range of the SCMA system under the condition in which the OBI between LD #2 and #3 was maximized and the optical attenuation, P_{att} (the optical attenuator #2 shown in Fig. 3), was varied. The BER performance of the desired signal on the 70 MHz band is shown in Fig. 5. The optical power of LD #1 can be made 5 dB weaker than those of LD #2 and #3 when error-free transmission is achieved. The level of OBI is proportional to the square of the received optical power from the lasers generating the OBI. The

maximum number of OBI is equal to the number of the laser combinations. Hence, under the assumption that the received optical power from each LD is equal at the CS, five BSs with $\text{OMI} = 2.0$ can be multiplexed, compared to two BSs with $\text{OMI} = 0.8$.

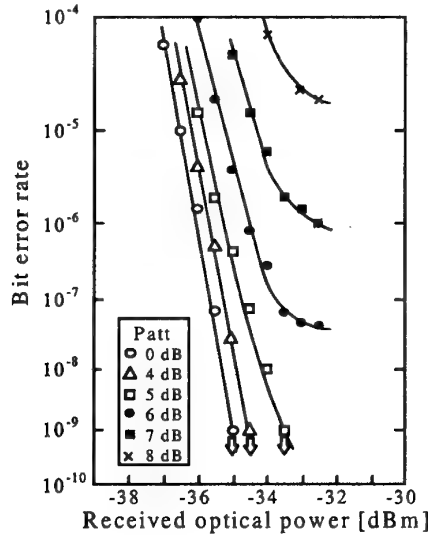


Fig. 5. The BER performance as a function of P_{att} .

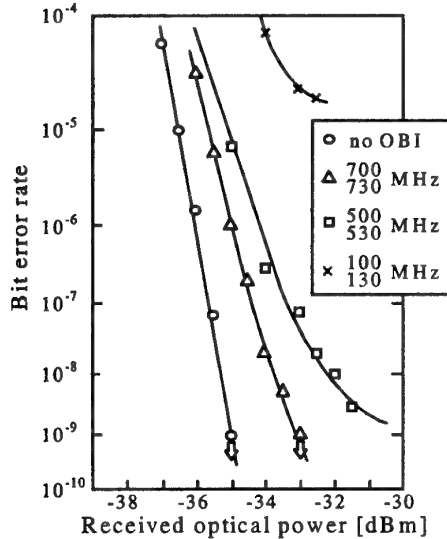


Fig. 6. The BER performance as a function of subcarrier frequencies at $P_{\text{att}} = 8$ dB.

3.5 Dependence of OBI on subcarrier frequencies

Fig. 6 shows the BER performance when replacing the subcarrier frequencies of 100/130 MHz at BS #2 and #3 by 500/530 MHz or 700/730 MHz, while keeping the condition of $P_{\text{att}} = 8$ dB, as shown in Fig. 5. It was found that the efficiency of suppressing OBI

was dependent on subcarrier frequencies where OMI was larger than 1.0. We think that the higher subcarrier frequencies, the more frequently the waveform goes under the threshold of the LDs. Consequently, the optical spectrum is broadened and the OBI level can be further decreased. Fig. 6 indicates that error-free transmission can be achieved at subcarrier frequencies of 700/730 MHz. This OBI level at $P_{\text{att}} = 8$ dB corresponds to the maximum OBI level among nine LDs. We assume that with higher subcarrier frequencies we can achieve an ever larger optical dynamic range.

4. Conclusions

We have shown that error-free transmission of radio QPSK (quadrature phase-shift keying) signals was able to be achieved in an optical SCMA (subcarrier multiple access) system, suppressing OBI (optical beat interference). In the case of over-modulating FP-LDs (Fabry-Perot laser diodes), by using subcarrier frequencies of a 700-MHz band with OMI (optical modulation index) = 2.0, nine radio BSs (base stations) with a data rate of 12.86 Mbit/s can be multiplexed. We believe that the fiber-radio architecture illustrated here provides a sufficient level of performance for broadband wireless access systems such as the FWA (fixed wireless access).

Reference

- [1] S. Y. Seidal et. al., IEEE Globecom'95, p.754-, 1995.
- [2] T. S. Chu and M. J. Gans, IEEE Trans. Veh. Technol. Vol. 40, No. 3, Aug. 1991.
- [3] T. H. Wood et. al., IEEE Photon. Technol. Lett. Vol. 6, No. 4, p. 575-, April 1994.
- [4] C. Desem, IEEE Photon. Technol. Lett. Vol., 3, p. 387-, 1991.
- [5] R. D. Feldman et. al., OFC'95, TuQ5, p. 90-, 1995.
- [6] Y. Akaiwa, "Introduction to digital mobile communication", Wiley-interscience, 1997.
- [7] S. L. Woodward et al., IEEE Photon. Technol. Lett., Vol. 10, No. 5, p.731-, May 1998.

Optical subcarrier multiplexing system using time sampling multiplexer to suppress optical beat interference

Yozo SHOJI and Hiroyo Ogawa

Communications Research Laboratory,

Ministry of Posts and Telecommunications,

3-4, Hikarino-oka, Yokosuka, Kanagawa 239-0847, Japan

TEL:+81-468-47-5075, FAX:+81-468-47-5079, E-mail: y-shoji@crl.go.jp

Abstract

We propose an optical subcarrier multiplexing system that uses optical sampling multiplexer to suppress optical beat interference in an up-link. This type of interference can be dramatically suppressed without distorting the signal by replacing the passive coupler-based multiplexer in a conventional sub-carrier multiplexing system with our proposed time sampling multiplexer. We discuss from theoretical viewpoints the effect of our proposed multiplexer on the BER, CNR and CIR performance.

1 Introduction

An optical sub-carrier multiplexing (SCM) system is one cost-effective solution to the demand that optical signals from/to several transceivers are multiplexed into one fiber link[1]. Some wireless service provider using radio-on-fiber technique seems fueling this demand because of their desire to reduce the number of leased optical fiber links used for their backbone networks connecting radio access points and base stations.

The up-link performance of an optical SCM system is severely deteriorated by optical beat interference (OBI)[3]. This interference is caused by the simultaneous photo-detection of several optical carriers having wavelengths that are very closely spaced. The wavelength of a laser has random characteristics in the manufacturing process, and furthermore they varies with changes of temperature. Thus, the OBI seriously damages the carried signals by falling into the signal band. Two kinds of scheme have already been proposed to avoid or suppress the OBI: wavelength control and OBI suppression by increasing an optical modulation index (OMI)[3]. The wavelength control method seems the most reliable because the frequency of the OBI can be controlled so as not to fall into the signal band. However, the control of a laser wavelength requires very expensive and complicated control systems such as an optical phase lock loop. In comparison with this method, the OBI suppression by increasing the OMI is a very cost-effective solution. Just increas-

ing the OMI causes the optical spectrum to spread and reduces the peak power of the OBI. However an OMI near or over 100% causes serious non-linear distortion to the amplitude of carried signals. Thus, this method cannot be applied to optical transmission systems carrying amplitude modulated signals, such as quadrature amplitude modulation (QAM) or multi-carrier signals.

To solve the above problems, we propose an optical sub-carrier multiplexing system that uses a sampling multiplexing technique. This system suppresses the OBI and can be applied to transfer any modulation format. The system can be created by a very simple modification of a conventional optical SCM system. You only need to replace the passive coupler-based multiplexer used at the multiplexing point with our proposed optical time-sampling multiplexer. No modification is needed at the remote access points and the base station. In the following sections, we discuss the effect of the sampling multiplexer on the BER, CNR and CIR performance from theoretical viewpoints.

2 System concept and configuration

Figure 1 shows the configuration of an optical SCM radio-on-fiber system using an optical sampling multiplexer in the up-link. The system is composed of remote access points (RAPs), the base station (BS), the sampling multiplexer, and fiber links to connect them.

We propose using the optical sampling multiplexer to multiplex signals from several RAPs. Note: if we use a passive coupler as a multiplexer, the system is the same as a conventional optical SCM system. The RAP has functions of frequency and E/O conversion. The laser diode (E/O) is directly modulated by a subcarrier signal, whose frequency is different for each RAP. The BS has functions of photodetecting (PD), band-pass filtering (BPF) for each subcarrier band, and demodulating (DEM). As shown in Fig. 1, the sampling multiplexer uses rotary-type optical switching, i.e. the continuous intensity modulated signals from the RAPs

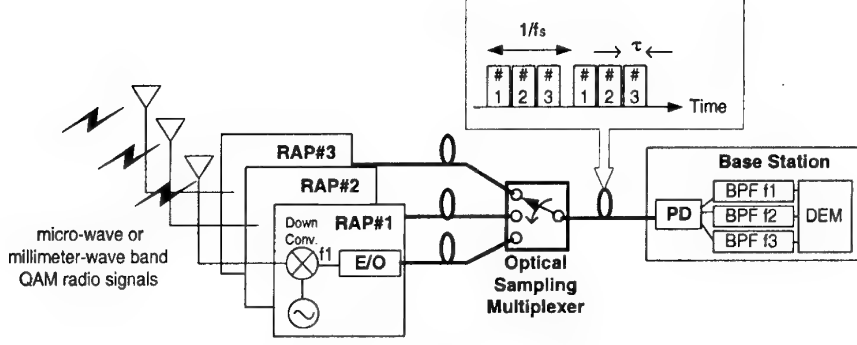


Figure 1: System configuration

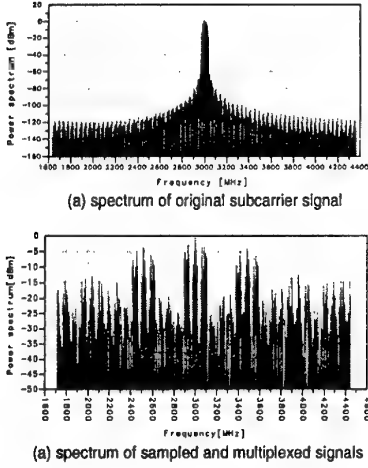


Figure 2: spectrum features of subcarriers before and after sampling multiplexing (3 channels)

are sampled, converted into pulses, and then relayed to the BS in different time slots. Because of this type of switching, the photodetector at the BS will not detect more than one signal at a time. Therefore, in principle an OBI is not generated if we can achieve ideal 100% switching isolation. The multiplexed signal format of the multiplexer output is similar to that of an optical time division multiplexing signal. However, very high switching isolation between channels is not required, and no time synchronization and demultiplexing in the time domain is not required because the demultiplexing is performed in the electrical subcarrier frequency domain.

Figure 2 shows the spectrum feature of the subcarriers before and after the sampling multiplexing, assuming that three channels are multiplexed. The sampling generates new periodic spectrum components in the upper and lower side bands. Their spacing is the same as the sampling frequency, f_s . Therefore, the sampling repetition frequency, f_s , has to be higher than the total occupied bandwidth of the subcarriers to avoid generation of the by-product frequency component that fall-

s into the signal band. We recommend using a pulse width per optical channel, τ , that is less than $1/(f_s M)$, where M is the number of channels. Actually, even if an overlap of pulses or a power leak between channels occurs, they do not create any serious interference between channels, but low channel isolation in time domain reduces the suppressive effect of the OBI.

3 Theoretical analysis of CIR and CNR performance

In this section, we analyze the CIR and CNR performance of the regenerated subcarrier signal at the BS. We assume here that one subcarrier signal modulates the laser with the same OMI for all RAPs.

The subcarrier signal is regenerated at the BS after the photodetection and bandpass filtering of the received sampled signals. The regenerated subcarrier signal power is characterized by the parameter $D(=f_s \tau)$ [5] and given by

$$P_{sig} = R^2 m^2 (P_o L_o D)^2 / 2, \quad (1)$$

where R , m , P_o , and L_o are respectively the photo-detector responsivity, the OMI, the average laser power, and the transmission loss. In the equation, L_o represents the fixed insertion loss of the sampling multiplexer and the fiber links. The signal power in a conventional optical SCM link can be obtained from Eq. (1) by substituting 1 for D and increasing the transmission loss, L_o , by $1/M$. The loss of the sampling multiplexer may be lower than that of a passive optical coupler. However, D should be inversely proportional to the number of optical channels. Thus, you can see that the proposed scheme suffers from a signal power penalty of $2 \times$ the insertion loss (dB) of the sampling multiplexer from a rough estimation.

To obtain the equation giving the OBI power, we assume the spectrum of the intensity modulated optical carrier. The optical spectral features under direct modulation are dominated by the optical frequency modulation (FM) with the intensity modulation (IM)

adding a small asymmetry[4]. Since the effect of IM on the spectral shape is so much smaller, we can neglect it. For two lasers i and j , the possible interference power, P_{int} , is given by [3]

$$P_{int} = \Gamma R^2 P_{oi} P_{oj} J_k^2(\beta_i) J_l^2(\beta_j); \quad \{k, l \in -\infty \dots -1, 0, 1 \dots +\infty\}, \quad (2)$$

where Γ is the fraction of beat power that falls into a subcarrier band, and β is the effective FM index. The FM index is related to linewidth enhancement factor, α , by

$$\beta \approx m\alpha/2. \quad (3)$$

In our proposed system, we have also to consider the affection of the time sampling and the switching isolation between the channels. Let $R_s (< 1.0)$ be the isolation of each switching path. the P_{int} resulting from the two lasers is given by

$$P_{int} = \Gamma R^2 D^2 R_s P_{oi} P_{oj} J_k^2(\beta_i) J_l^2(\beta_j); \quad \{k, l \in -\infty \dots -1, 0, 1 \dots +\infty\} \quad (4)$$

From equations (1) and (4), the CIR is given by

$$CIR = \frac{m^2}{2\Gamma R_s J_k^2(m\alpha/2) J_l^2(m\alpha/2)}. \quad (5)$$

Equation (5) indicates that the CIR improves in proportion to the isolation of the sampling multiplexer. If the sampling multiplexer works as an ideal optical switch ($R_s = 0$), no OBI is generated. In the case of $R_s = 1$, this corresponds to the representation of the CIR for a conventional system.

Regarding the CNR performance, the effect of time sampling on noise power has been studied in [5], and it reported that the power level of time-sampled-white noise is reduced by the factor of D . Considering that multiple channels are simultaneously photodetected in our proposed system, the CNR of the subcarrier after photodetection is given by

$$CNR_{sample} = \frac{R^2 m^2 (P_o L_o D)^2 / 2}{[RIN(RP_o L_o)^2 + 2eRP_o L_o]DMB_r + \frac{4k_b T B_r F}{R_{pd}}}, \quad (6)$$

where RIN , e , T , k_b , F , and R_{pd} are, respectively, the relative intensity noise, the electron charge, the noise temperature, the Boltzmann constant, the noise figure of the receiver, and the load resistance of the photodetector.

4 Numerical results for BER, CNR and minimum CIR performance

We first investigated the fundamental effect of the sampling multiplexer on a bit error rate (BER) characteristics by a simple simulation study assuming a

multiplexing of 4 subcarrier channels of 16QAM signal format. Figure 3 shows the BER vs. E_b/N_o where it is assumed that no noise is generated by an optical link and only the effect of the sampling is considered. E_b/N_o is defined as that just before the E/O conversion. The theoretical results and simulated results are shown in the figure for different switching isolation.

Figure 3 shows that the use of sampling multiplexer suffers 6 dB power penalty in the link design before E/O conversion, for example, wireless up-link design in the radio-on-fiber applications. The reasons of this result are that the sampling process reduces the white noise level only by $D = 1/M$, while a conventional method using a coupler reduces it by $(1/M)^2$. Therefore, in the condition that the noise power generated before E/O conversion dominates the total SCM system performance, our proposed system suffers a power penalty of $1/M$. However, as shown in the following results, the total link of a SCM system is dominated by a serious OBI and we have an idea that the suppression of the OBI is an important subject even if some degradation of CNR is sacrificed.

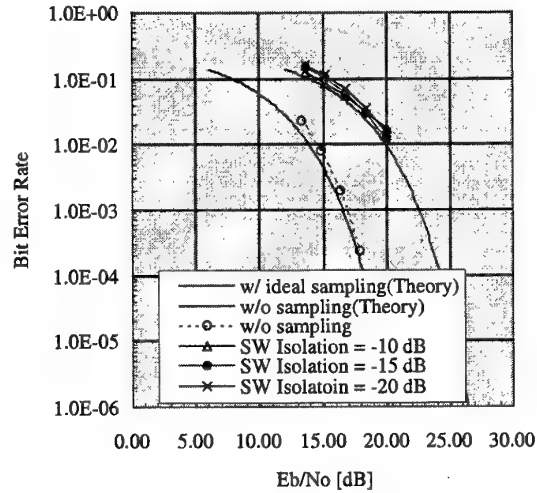


Figure 3: Effect of the sampling multiplexor on BER characteristics

Table 1 shows the parameters used to obtain the following numerical results. Figure 4 shows the received CNR performance versus the number of multiplexed optical channels for different OMIs (25% and 50%). The results of the conventional system is also shown in the figure. The proposed system has a CNR penalty of around 8 dB when there are more than ten channels due to the effect of the sampling multiplexer. However, the CNR performance is more than 20 dB for the proposed system even when 10 channels are multiplexed.

Table 1: Parameters used in calculations

Bandwidth of subcarrier B_r	58.5 MHz
Laser power P_o	10 mW
Optical transmission loss L_o (multiplexer insertion loss)	12 dB (5 dB)
E/O efficiency	0.24 W/A
PD efficiency	0.7 A/W
RIN	-150 dB/Hz
Linewidth enhancement factor	6
Noise figure of receiver	5 [dB]

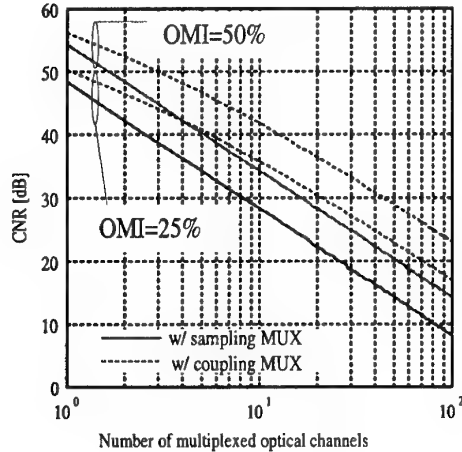


Figure 4: CNR performance versus the number of multiplexed optical channels

Figure 5 shows the CNR and the minimum CIR performance vs. the OMI. The multiplexing of ten channels is assumed in the calculation of the CNR, while the minimum CIR is given by the minimum value in Eq. (5), in all combinations of k and l .

You can see from the figure that the link performance is limited by the minimum CIR. The minimum CIR can be improved by increasing the OMI. However, you see from the figure that even if we used an OMI of 100%, the minimum CIR would be still less than 15 dB in a conventional system (w/ sampling MUX). For example, a 16QAM modulation signal requires a CNR and CIR of more than about 20 dB to obtain a BER performance of 10^{-4} . Because an amplitude modulation signal like QAM signal must be operated with some back-off from the saturation level, increasing the OMI is not effective for use in radio-on-fiber transmission of QAM modulation signals.

By using the proposed sampling multiplexer, the OBI can be suppressed by the same value as the isolation of the sampling multiplexer, as discussed in Sec. 3. Figure 5 shows that the minimum CIR is improved by 20 dB by using the sampling multiplexer at a switching isolation of 20 dB, and a minimum CIR of more

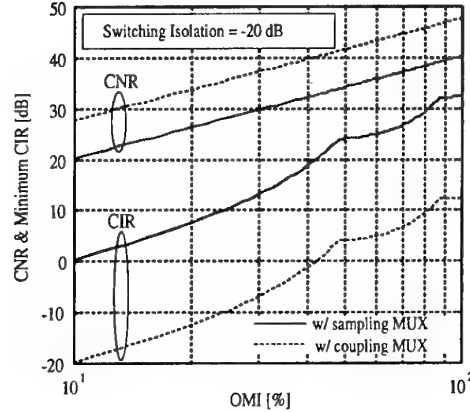


Figure 5: CNR and minimum CIR performance versus OMI

than 20 dB can be obtained even when we use an OMI of 50%.

5 Conclusion

The use of an optical sampling multiplexer was proposed as a method to couple signals in an optical subcarrier multiplexing system. With the proposed system, the minimum CIR can be suppressed by the same value as the switching isolation at the sacrifice of some CNR degradation.

References

- [1] T. E. Darcie, "Subcarrier multiplexing for multiple-access lightwave network," *J. Lightwave Technol.*, vol. 5, p.1103, 1987.
- [2] Y. Shoji, E. Okamoto, K. Hamaguchi, and H. Ogawa, "Optical SCMA Radio-on-Fiber Link using Optical Sampling Multiplexing Technique for Fixed Wireless Access," *IEICE General Conference*, B-5-312, pp.697, March 2000.
- [3] T. H. Wood and N. K. Shankaranarayanan, "Operation of a Passive Optical Network with Subcarrier Multiplexing in the Presence of Optical Beat Interference," *Journal of lightwave technology*, vol. 11, no. 10, pp.1632-1640, Oct. 1993.
- [4] G.P. Agrawal, "Power spectrum of directly modulated single-mode semiconductor lasers: Chirp-induced fine structure," *IEEE J. Quantum Electron.*, vol. 21, pp. 680-686, 1985.
- [5] H. Harada, S. Kajiya, K. Tsukamoto, S. Komaki, and N. Morinaga, "TDM Intercell Connection Fiber-optic Bus Link for Personal Radio Communication System," *IEICE Trans. Commun.*, Vol.E78-B, No.9, pp.1287-1294, Sept. 1995.

Impact of Optical Crosstalk in Fibre-Radio Systems Incorporating WDM

D. Castleford, A. Nirmalathas, and D. Novak

Australian Photonics Cooperative Research Centre, Photonics Research Laboratory
Department of Electrical and Electronic Engineering, The University of Melbourne, VIC 3010, Australia
Tel: + 61 3 8344 4650, Fax: + 61 3 8344 6678, Email: d.castleford@ee.mu.oz.au

ABSTRACT: We investigate analytically and experimentally optical crosstalk effects in fibre-radio systems incorporating wavelength-division multiplexing. Both in-band and out-of-band crosstalk are considered and the effect of the RF phase difference between the desired and crosstalk channels investigated. It is found that in-band incoherent crosstalk-induced power penalties are less severe than in conventional baseband transmission.

1 Introduction

The fibre-radio concept allows the distribution of broadband wireless signals between a large number of antenna base stations (BSs) and central office (CO) over optical fibre [1]. Typically in these networks radio signals are transported over the optical fibre as either intermediate frequency (IF) or radio frequency (RF). The application of optical networking concepts to fibre-radio systems has recently been proposed [2-5]. The use of wavelength division multiplexing (WDM) can simplify the network architecture using wavelengths to feed different antenna BSs, can support multiple interactive services on one fibre, and can greatly simplify network upgrades.

In any optical network incorporating WDM, optical crosstalk occurs due to imperfect optical components and leads to unwanted wavelengths interfering with the desired optical channel. The impact of optical crosstalk in the context of baseband optical transmission has been actively investigated [6-7]. These studies have shown that optical crosstalk can lead to severe system performance impairments such as power penalties and bit-error-rate (BER) floors. Previous investigations of fibre-radio systems incorporating WDM have considered possible network architectures and experimental implementations [2-5]. In addition, Griffin *et al.* [4] have examined the effect of crosstalk resulting from the modulator nonlinearity in a fibre-radio system operating at millimetre-wave frequencies. In this paper we present an analytical formulation for optical crosstalk effects in fibre-radio systems which can account for all potential sources of crosstalk. Both in-band and out-of-band crosstalk are considered and the model is confirmed by experiment.

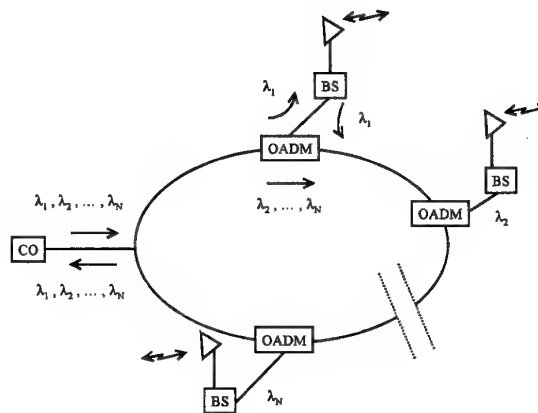


Fig. 1 Typical fibre-radio WDM ring network

2 Fibre-Radio Architecture

Fig. 1 shows an architecture for a typical fibre-radio system based on a WDM ring network. A CO distributes a number of wavelengths each carrying multiple modulated RF subcarriers. The ring topology allows the allocation of a single wavelength to a particular BS and the wavelength routing is enabled via optical add-drop multiplexers (OADMs). Upstream signal transmission is achieved by modulating upstream radio signals onto an optical carrier at the same BS wavelength, and adding it back into the ring via the OADM. As can be seen from the ring topology, two types of crosstalk can arise, namely in-band (homodyne) crosstalk and out-of-band (heterodyne) crosstalk. In-band crosstalk is at the same wavelength as the signal and occurs either when the 'add' wavelength or a reflected/delayed version of the dropped wavelength is present at the dropped channel. Meanwhile out-of-band crosstalk is by definition at a different wavelength and occurs when part of the 'through' wavelengths appear at the 'dropped' channel.

In the case of in-band crosstalk, the crosstalk can be both coherent or incoherent. Coherent crosstalk occurs when the crosstalk signal is a delayed version of the dropped channel, due to reflections or path delays in optical components, and the path length difference is less than the coherence length of the optical signal. If the path length difference is greater than the coherence length or the crosstalk signal arises from leakage of the 'add' wavelength (where the

optical source providing the 'add' wavelength is different to that supplying the 'drop' wavelength), then the in-band crosstalk is also incoherent. Meanwhile, out-of-band crosstalk resulting from unwanted WDM channels arising from different optical sources being present at the receiver, is inherently incoherent. In order to investigate crosstalk effects in fibre-radio systems which transport RF carriers, the electrical phase of the modulated RF signal must also be taken into account in addition to the optical phase of the desired channel and crosstalk signal.

3 In-band Crosstalk

In order to investigate the effect of optical crosstalk in fibre-radio systems, a simple analytical model was developed for both in-band and out-of-band crosstalk. The model includes the simple case of one wavelength channel and one interfering crosstalk signal. For an intensity modulation direct-detection system where a modulated subcarrier frequency ω_{RF} is applied to an external modulator, the desired and in-band crosstalk optical signals can be represented as:

$$\begin{aligned} E_1(t) &= E_1 \cos(\omega t + \theta_1) [1 + m_1 \cos(\omega_{RF} t + \phi_1)] \\ E_2(t) &= \sqrt{x} E_1 \cos(\omega t + \theta_2) [1 + m_2 \cos(\omega_{RF} t + \phi_2)] \end{aligned} \quad (1)$$

where E_1 , E_2 are the electric fields of the optical signals, ω is the optical frequency, m_1 and m_2 are modulation indices, x is the optical crosstalk power ratio, θ_1 and θ_2 represent the optical phase, and ϕ_1 , ϕ_2 are the electrical phases. If the in-band crosstalk is also coherent, then a fixed relationship exists between the two optical phase angles and the two electrical phase angles.

The effect of the optical crosstalk signal is to produce an additional unwanted RF signal component at ω_{RF} upon detection. The detected photocurrent I is proportional to the square of the electric field via:

$$I \propto (E^2) = (E_1 + E_2)^2 \quad (2)$$

The presence of two different signals at the same optical wavelength results in the following frequency components at ω_{RF} :

$$\begin{aligned} I(\omega_{RF}) &\propto m_1 \cos(\omega_{RF} t + \phi_1) \\ &+ x m_2 \cos(\omega_{RF} t + \phi_2) + \sqrt{x} \cos(\theta_1 - \theta_2) \\ &\times [m_1 \cos(\omega_{RF} t + \phi_1) + m_2 \cos(\omega_{RF} t + \phi_2)] \end{aligned} \quad (3)$$

The first two terms in Eqn. 3 represent the recovered ω_{RF} frequencies from the optical channel and the crosstalk signals themselves, respectively, while the last two terms are due to intermixing of the two optical carriers with the modulation sidebands of the other signal.

If the RF subcarrier at ω_{RF} is modulated with data in binary phase shift key (BPSK) format, a phase-locked loop (PLL) must be employed to recover the data. This PLL must be locked to the phase of the wanted channel, i.e. ϕ_1 . The signal waveform of the downconverted data channel (using a PLL) can then be represented by:

$$\begin{aligned} I_{down} &= I(\omega_{RF}) \cos(\omega_{RF} t + \phi_1) \\ &\propto m_1 (1 + \sqrt{x} \cos(\theta_1 - \theta_2)) \\ &+ m_2 \sqrt{x} \cos(\phi_1 - \phi_2) [\sqrt{x} + \cos(\theta_1 - \theta_2)] \\ &= m_1 [1 + \sqrt{x} \cos(\Delta\theta)] \\ &+ m_2 \sqrt{x} \cos(\Delta\phi) [\sqrt{x} + \cos(\Delta\theta)] \end{aligned} \quad (4)$$

where $\Delta\phi = \phi_1 - \phi_2$ is the RF phase difference between the desired channel and crosstalk signal, and $\Delta\theta = \theta_1 - \theta_2$ is the optical phase difference between the two optical carriers. Eqn. 4 shows that due to the multiplication effect of the PLL, the mixing products arising from the crosstalk signal itself and intermixing terms due to the signal carrier and crosstalk sidebands beating are multiplied by $\cos(\Delta\phi)$. This RF phase difference is clearly crucial since orthogonal RF carriers are rejected by the PLL.

We assume that $m_1 = m_2$ and the modulation format is BPSK. Assuming only Gaussian thermal receiver noise allows use of the complementary error function to calculate the BER [8]:

$$BER = \text{Erfc}(Q / \sqrt{2}\sigma) \quad (5)$$

where $Q = (I / \sigma)$ (decision threshold = 0) and σ is the standard deviation of the Gaussian thermal noise. When both the signal and crosstalk are present, I will vary depending on the four equiprobable logic bit combinations: 00, 01, 10 and 11. The average BER for a given crosstalk power ratio (x), optical phase difference ($\Delta\theta$) and RF phase difference ($\Delta\phi$) as well as signal power can then be calculated using Eqns. 4 and 5. In the case of coherent crosstalk, $\Delta\theta$ will be constant. Meanwhile incoherent crosstalk will lead to a stochastically varying $\Delta\theta$ (uniformly distributed between 0 and 2π) which therefore requires the averaging of BER over $\Delta\theta$. By varying the signal power and the crosstalk ratio, a set of BER curves can be obtained and optical power penalties for a BER = 10^{-9} calculated.

Fig. 2 shows the in-band incoherent crosstalk predicted using the analytical model, as a function of crosstalk level for $\Delta\phi = 0, \pi/4$, and $\pi/2$. In Fig. 2, the crosstalk ratio varies from -20 dB to 0 dB. In a single OADM, the 'add'-'drop' in-band crosstalk is in the order of -30 dB or better, while rejection of out-of-band WDM channels is typically -20 to -30 dB. However the crosstalk levels can rapidly increase in a cascaded system of OADMs. For comparison, Fig. 2 also plots the predicted power penalty for baseband data transmission. These results show that the power penalties arising from in-band crosstalk can vary depending on the RF phase difference between the crosstalk and desired signals. For example, at a crosstalk level of -12 dB, the power penalty is reduced by ~1.5 dB when $\Delta\phi$ is changed from 0 to $\pi/2$. This is to be expected as the full crosstalk signal amplitude is recovered by the PLL when $\Delta\phi = 0$. The difference in power penalties also increases with increasing x (e.g. ~4 dB at a crosstalk level of -4 dB). Fig. 2 also shows that

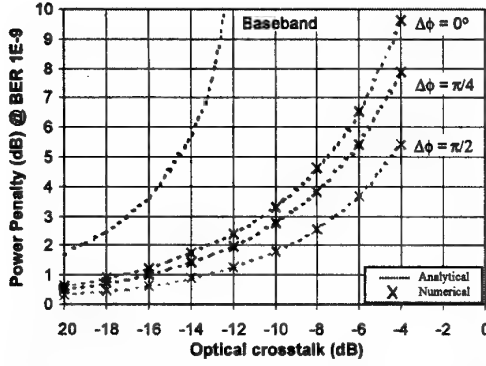


Fig. 2 Predicted optical power penalty versus optical crosstalk ratio due to in-band incoherent crosstalk

the crosstalk-induced optical power penalty is significantly worse in the case of baseband data transmission. This is due to the effect of the optical and electrical phase differences as well as the bipolar nature of the BPSK modulation format.

In order to confirm the analytical model, a commercially available optical link design simulation tool was used to analyse the effect of crosstalk. Fig. 2 also shows these numerical simulation results of power penalty indicating that very close agreement with the analytical model was obtained. It should be noted that the analytical model for in-band crosstalk assumes polarisation alignment of the desired channel and the crosstalk signal thereby giving predictions of optical power penalties which represents 'worst-case' scenarios in the network [9].

4 Out-of-band Crosstalk

4.1 Analytical Model

We now consider crosstalk arising from a signal that is at a different wavelength from the desired channel which can be represented as (following the previous analysis):

$$\begin{aligned} E_1(t) &= E_i \cos(\omega_i t + \theta_i) [1 + m_1 \cos(\omega_{RF} t + \phi_1)] \\ E_2(t) &= \sqrt{x} E_i \cos(\omega_i t + \theta_2) [1 + m_2 \cos(\omega_{RF} t + \phi_2)] \end{aligned} \quad (6)$$

where ω_i and ω_i represent the optical frequencies of the desired channel and the crosstalk signal, respectively. Ignoring all of the possible mixing terms at frequencies other than ω_{RF} , we get:

$$\begin{aligned} I(\omega_{RF}) &= I(\omega_{1RF}) + I(\omega_{2RF}) \\ &\propto m_1 \cos(\omega_{RF} t + \phi_1) \\ &\quad + \sqrt{x} m_2 \cos(\omega_{RF} t + \phi_2) \end{aligned} \quad (7)$$

As before, recovery of BPSK modulation using a PLL will result in the following downconverted signal:

$$\begin{aligned} I_{down} &= I(\omega_{RF}) \cos(\omega_{RF} t + \phi_1) \\ &= m_1 + \sqrt{x} m_2 \cos(\phi_1 - \phi_2) \\ &= m_1 + \sqrt{x} m_2 \cos(\Delta\phi) \end{aligned} \quad (8)$$

Comparing Eqn. 8 to Eqn. 4 shows that out-of-band crosstalk is only influenced by the RF phase difference, and therefore a potential reduction of crosstalk is possible when $\Delta\phi = \pi/2$.

Fig. 3 shows the predictions of the analytical model for out-of-band crosstalk for $\Delta\phi = 0, \pi/4$ and $\pi/2$, as a function of optical crosstalk ratio. Also shown in the figure is the predicted power penalty for baseband transmission. As for the case of in-band crosstalk, the optical power penalties for out-of-band optical crosstalk vary with $\Delta\phi$, with the largest power penalty occurring for $\Delta\phi = 0$. The actual power penalty for a particular crosstalk ratio however, is less for out-of-band crosstalk than for the in-band case. For example in Fig. 3, at -12 dB of crosstalk, the power penalty for all values of $\Delta\phi$ is less than 0.5 dB. In addition, the variation of power penalty with $\Delta\phi$ is reduced to less than 0.25 dB at the same crosstalk level. Fig. 3 shows that for an RF phase difference of $\Delta\phi = \pi/2$, when the crosstalk signal is at the same optical power as the desired channel (0 dB of optical crosstalk), the optical power penalty is 3 dB. This is as expected since the $\pi/2$ phase shift leads to a cancellation of the crosstalk contribution.

In contrast to the case for in-band crosstalk where the optical power penalty for baseband data transmission was significantly higher than for RF subcarrier transmission (at all crosstalk ratios), Fig. 3 shows that out-of-band crosstalk induced power penalties for baseband data transmission are very similar to those for RF subcarrier transmission.

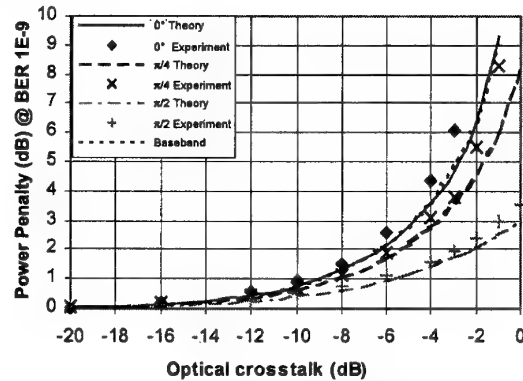


Fig. 3 Theoretical and experimental optical power penalties due to out-of-band incoherent crosstalk

4.2 Experiment

An experiment was carried out in order to confirm the theoretical predictions of out-of-band crosstalk. Fig. 4 shows the experimental setup. The desired channel and crosstalk signal are implemented by two separate optical paths, each comprising a distributed feedback laser ($\lambda_1 = 1549.4$ nm, $\lambda_2 = 1550$ nm) and an electro-optic modulator (EOM). Separate data channels at 155 Mb/s modulate an RF signal at 2 GHz in BPSK modulation format. An RF phase shifter was used to control the RF phase difference between the desired channel and crosstalk signal. The two signals are coupled together and amplified using

an erbium-doped fibre amplifier (EDFA) in order to compensate for losses in the optical link. An optical bandpass filter (BPF) with a bandwidth of 2 nm was included after the EDFA in order to filter out excess ASE. At the receiver, the optical signals are detected using a p-i-n photodetector (PD) and the same 2 GHz signal is used to downconvert the detected modulated RF signals and recover the data. A bit-error-rate testset (BERT) measures the BER of the recovered 155 Mb/s data as a function of optical crosstalk ratio (varied via the optical attenuator in the optical path of λ_2). By measuring a BER curve at a particular crosstalk ratio and carrying out a back-to-back system measurement, the crosstalk-induced optical power penalty could be determined. Fig. 3 shows the measured optical power penalty at a BER of 10^{-9} as a function of optical crosstalk ratio, for $\Delta\phi = 0, \pi/4$ and $\pi/2$, plotted alongside the theoretical predictions for out-of-band crosstalk. The measurements show very good agreement with theory, with a small discrepancy between the two sets of results appearing at higher crosstalk levels (> -4 dB). This is most likely due to experimental error and possible optical and electrical nonlinearities in the system.

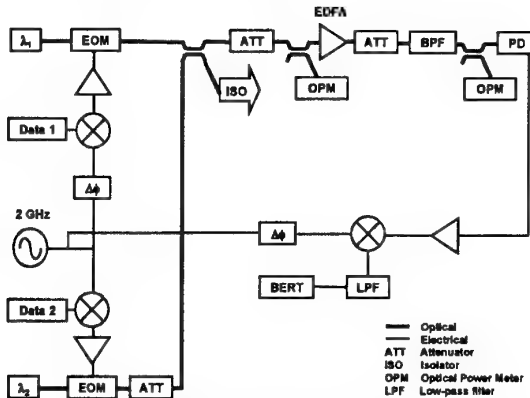


Fig. 4 Experimental setup for measurement of out-of-band crosstalk

5 Discussion and Conclusions

The predictions of in-band and out-of-band crosstalk induced power penalties clearly show that for fibre-radio systems which employ RF over fibre signal transmission, the effect of in-band crosstalk is much more significant. For example when $\Delta\phi = \pi/4$, at a crosstalk ratio of -8 dB, in-band incoherent crosstalk causes an optical power penalty of 4 dB, while that due to out-of-band incoherent crosstalk is only 1 dB. When comparing the in-band crosstalk-induced penalties for RF and baseband data transmission, a 1 dB penalty occurs at -17 dB of crosstalk for BPSK data transmission, however the same penalty arises at only -23 dB of crosstalk in baseband transmission. This shows the greater tolerance to the effect of optical crosstalk in RF over fibre

transmission employing BPSK modulation. In the case of out-of-band crosstalk, the crosstalk-induced power penalties in both the baseband and RF over fibre transmission schemes (for $\Delta\phi = 0$) are identical (-10 dB of crosstalk ratio giving a 1 dB optical power penalty) with the penalty reducing as $\Delta\phi$ goes to $\pi/2$. While the results presented in Figs. 2 and 3 apply to a single interfering crosstalk signal, the analytical model can be extended to accommodate an increased number of crosstalk signals.

We have presented a simple analytical model which can predict optical power penalties due to in-band and out-of-band optical crosstalk in fibre-radio systems employing WDM. The model considers the case of a single crosstalk interfering signal, a BPSK modulation format for RF over fibre transmission and also accounts for the RF phase difference between the desired channel and crosstalk signal. The model has been validated by measurement of out-of-band crosstalk, and future experimental work will investigate in-band crosstalk effects.

References

- [1] G.I. Zysman, R. Thorkildsen and D.Y. Lee, "Two-way wireless broadband access", *Bell Labs Technical J.*, pp. 115-129, 1996.
- [2] G.H. Smith, C. Lim, and D. Novak, "Millimeter-wave full duplex WDM/SCM fiber-radio access network", *Proc. OFC*, San Jose, CA, USA, pp. 18-19, 1998.
- [3] A. Stöhr, K. Kitayama, and D. Jäger, "Error-free full-duplex optical WDM-FDM transmission using an EA-transceiver", *Proc. MWP*, Princeton, NJ, USA, pp. 37-40, 1998.
- [4] R.A. Griffin, P.M. Lane, and J.J. O'Reilly, "Radio-over-fiber distribution using an optical millimeter-wave/DWDM overlay", *Proc. OFC*, San Diego, CA, USA, Paper WD6-1, 1999.
- [5] K. Kojucharow, M. Sauer, H. Kaluzni, D. Sommer, F. Poegel, W. Nowak, A. Finger, and D. Ferling, "Simultaneous electrooptical upconversion, remote oscillator generation, and air transmission of multiple optical WDM channels for a 60-GHz high-capacity indoor system", *IEEE Trans. Micro. Thy. Tech.*, Vol. 47, pp. 2249-2256, 1999.
- [6] E.L. Goldstein, L. Eskildsen, and A.F. Elrefaie, "Performance implications of component crosstalk in transparent lightwave networks", *IEEE Photon. Technol. Lett.*, Vol. 6, pp. 657-660, 1994.
- [7] P.J. Legg, M. Tur, and I. Andonovic, "Solution paths to limit interferometric noise induced performance degradation in ASK/direct detection lightwave networks", *J. Lightwave Technol.*, Vol. 14, pp. 1943-1954, 1996.
- [8] J.G. Proakis, *Digital Communications*, McGraw-Hill, 1983.
- [9] E.L. Goldstein, L. Eskildsen, C. Lin, and Y. Silberberg, "Polarization statistics of crosstalk-induced noise in transparent lightwave networks", *IEEE Photon. Technol. Lett.*, Vol. 7, pp. 1345-1347, 1995.

OPTICAL CONTROL OF MILLIMETRE-WAVE p-HEMTs WITH APPLICATIONS TO FIBRE RADIO

Stavros Iezekiel and Neil Bourhill
Institute of Microwaves and Photonics
School of Electronic and Electrical Engineering
The University of Leeds
Leeds, LS2 9JT, UK.

Tel.: +44 (0)113 233 2000; Fax.: +44 (0)113 233 2032; email: s.iezekiel@ieee.org

Abstract: The optical control of mm-wave p-HEMTs, and their application to self-oscillating optoelectronic mixers for fibre radio is reviewed.

I. INTRODUCTION

Millimetre-wave wireless systems are viewed as a future means of providing mobile users with the option of bit-rate hungry applications such as video conferencing, in addition to providing the "last mile" delivery of broadband data and HDTV in urban areas. Of particular interest is the band around 60 GHz which, by virtue of high atmospheric absorption, allows the formation of picocells with radii of the order of 100 m. These allow greater frequency reuse in addition to high bandwidths, which given the congested spectrum below 30 GHz, will become important.

In order to develop the low cost infrastructure required for mm-wave wireless systems, base stations will have to be mass produced. This entails a reduction in base station complexity, which in turn has spurred the development of fibre radio [1]. The basic principle of fibre radio is to confine the mm-wave radio equipment at a central office and then distribute optically both the mm-wave carrier and the modulation to the individual base stations, which then provide the interface to the wireless environment. Despite the conceptual simplicity of fibre radio, and a number of experimental demonstrations of it, consensus has yet to be reached on what the best implementation is. A number of architectures are available [2],[3],[4], and these can be implemented in many ways. There are two schools of thought on how to proceed (both containing variations on a theme), namely:

- (1) optical generation and transport of mm-wave signals at 60 GHz;
- (2) optical transport of the data signals with remote upconversion to 60 GHz at the base stations.

The former is advantageous in that it shifts complexity away from the base stations, (which in their simplest form contain mm-wave photodiodes, amplifiers and antennas) and to the central office. However, generation of mm-wave signals is problematic given the inability of laser diodes to be directly modulated much beyond 30

GHz. This has led to many different approaches, such as heterodyning [5], dual mode lasers [6] and the use of external [7] and electro-absorption modulators [2]. Moreover, chromatic dispersion can degrade performance, which requires more complicated schemes to overcome it such as single sideband modulation [8].

In contrast, the remote upconversion camp advocates transport of data over fibre at intermediate frequencies, with the upconversion to 60 GHz being carried out in the base stations. The advantage is that "off the shelf" optoelectronic components can be used in the fibre backbone and the chromatic dispersion penalty is mitigated. This is at the expense of having to perform two new operations in the base station: generation of a mm-wave local oscillator and mm-wave mixing (Fig.1). However, it is possible to accommodate these additional functions along with photodetection in a *single* device to produce an optoelectronic self-oscillating mixer (OESOM) [9],[10],[11],[12]. In this way, one recovers the simplicity and low cost that is required of the base stations whilst also retaining the simplicity of using the optical network for data transport alone.

The key to OESOMs is three terminal devices such as MESFETs, HBTs and HEMTs which have intrinsic gain and photoresponsivity. Using optical control techniques to provide a third port and with appropriate terminating circuits, they can photodetect an optical signal and simultaneously upconvert it by mixing with a self-generated oscillation.

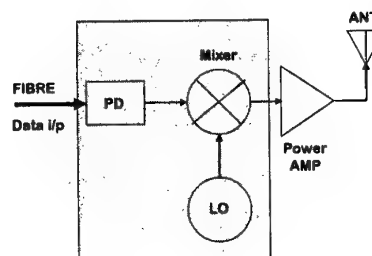


Fig.1 Remote upconverter. The components in the shaded box can be replaced with an OESOM.

II. OPTICAL CONTROL OF HEMTs

High electron mobility transistors (HEMTs) are good candidates for OESOMs. Firstly, they have low noise performance extending into the mm-wave region. Secondly, they are MMIC-compatible, which allows OESOMs to be produced in volume at low cost. Finally, they can be either GaAs- or InP-based, for optical control using short or long wavelengths respectively.

Three fundamental physical effects occur in an illuminated HEMT: the photoconductive, external and internal photovoltaic effect [13], [14]. In GaAs HEMTs, light of 850nm wavelength is only absorbed in the GaAs buffer layer. Under the influence of the electric field from the heterostructure, the resulting photogenerated electrons travel towards the 2-DEG layer as shown in Fig. 2. The transit time is of the order of tens of picoseconds [14]. The result is a change in conductivity in the GaAs layer.

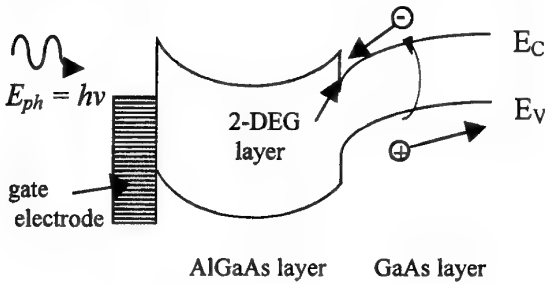


Fig. 2 Photoabsorption in a HEMT

Photogenerated holes drift towards the GaAs substrate layer, and this results in a positive charge build up in the substrate/source electrode contact. Charge neutrality is maintained by drawing in electrons from the source contact. The result is the internal photovoltaic effect, which has a high gain but a 3dB bandwidth of only around 25MHz. The positive charge build up induces an internal photovoltage, V_{ph} , which tends to forward bias the device. Optical effects can be modelled by including an optical current source between drain and source (I_{DSph}). In the absence of an external resistor at the gate, this optical current source dominates the photoresponse. Neglecting leakage currents between the HEMT terminals, I_{DSph} can be broken down into its component currents [15]:

$$I_{DSph} = I_{pc} + I_{pvi}$$

where I_{pc} is the photocurrent due to the photoconductive effect and I_{pvi} is the contribution from the internal photovoltaic effect. The internal photovoltaic current, I_{pvi} , is related to the photovoltage, V_{ph} , via the transconductance [15]:

$$I_{pvi} = g_m V_{ph}$$

The external current source (I_{DSph}) can be found by solving the transport properties of the device. Alternatively, the equivalent circuit approach absorbs the optical current sources into the model and accounts for their effects by modelling the changes to the equivalent circuit of the device. Since the optical coupling into commercially available HEMTs is estimated to be around 5%, the optical effects can be considered to be small-signal. In our work with an Agilent Technologies $6 \times 30 \mu\text{m}$ pHEMT that was illuminated by a 850nm VCSEL, on wafer characterisation was used to minimise errors and identify subtle effects. An increase in DC drain-source current of $I_{DSph} = 4.1\text{mA}$ occurred under illumination. The equivalent circuit elements that experienced significant changes due to illumination are highlighted in Fig. 3 by dashed boxes.

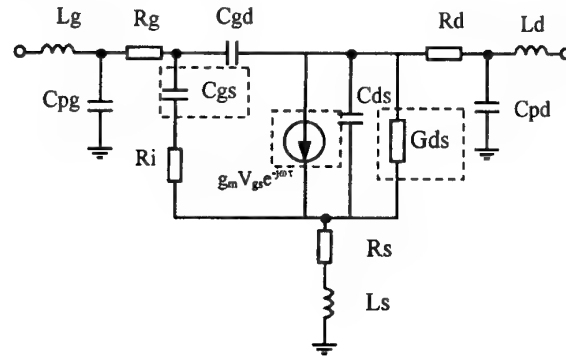


Fig. 3 Equivalent circuit modelling an optically controlled HEMT

The generation of an internal photovoltage, V_{ph} , and the change in the conductivity of the GaAs buffer layer lead to a change in the transconductance (g_m) and output conductance (G_{ds}) as well as gate-source capacitance (C_{gs}). The dominant RF effect is the change in the magnitude of S_{21} as shown in Fig. 4, whereas the phase of S_{21} is found to be insensitive to illumination.

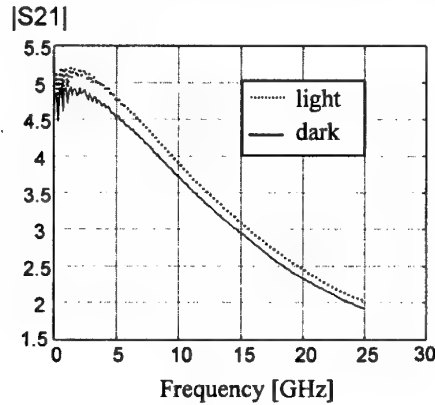


Fig.4 Change in the magnitude of S_{21} due to illumination

In the absence of external gate resistance, the change in gain was 1.21dB. Using an external gate resistor can increase the gain change to a suitable value for optical gain control of a microwave amplifier. However, the time constant associated with the gain control is large, making the circuit unsuitable for high-speed modulation of gain. A more practical approach would be to intensity modulate the optical source at an IF and use the internal photovoltaic effect. Although the internal photovoltaic effect has a 3dB bandwidth of around 20-30MHz, its useable response from a communications point of view extends up to around 1GHz. An improvement in optical coupling would further extend this useable bandwidth.

III. OPTOELECTRONIC SELF-OSCILLATING MIXERS

Examples of optical control include amplifier gain control, oscillator frequency tuning and direct and indirect optoelectronic mixing [16]. In these cases, the optical input is used to modify or control the performance of a single-function microwave subsystem. However, with proper circuit design, it is possible to configure HEMTs as self-oscillating mixers [17]. Under optical control, these will act as OESOMs that can be used in remote upconversion for fibre radio. Fig. 5 shows a MMIC-based pHEMT used as an OESOM.

4×15μm pHEMT

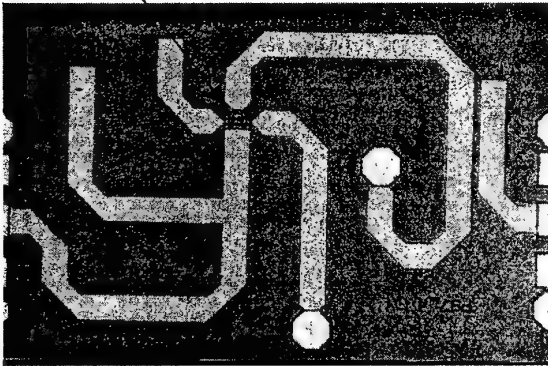


Fig. 5 MMIC OESOM (2mm × 1mm)

This circuit oscillated at 38.37GHz and experienced a 26MHz shift in oscillation frequency under 1mW of illumination from a VCSEL. The VCSEL was intensity modulated at an IF between 10MHz and 1GHz which was mixed within the device to generate a mm-wave double sideband AM signal (Fig. 6).

Central to the remote upconversion approach is the requirement of stabilising the oscillator so that jitter and phase noise do not significantly degrade the bit error rate performance. Conventional phase locked loop schemes may impose a penalty on the circuit complexity, reliability and power consumption, hence injection locking was investigated. With this approach,

an injection-locking signal could be optical distributed to remote transceivers.

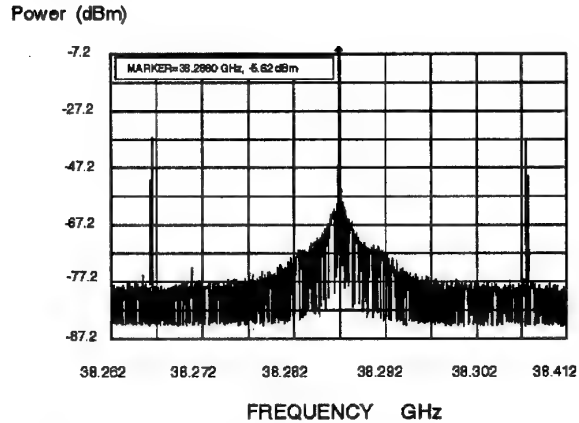


Fig. 6. Optoelectronic mixing within a mm-wave oscillator

In our experiments, a third subharmonic injection locking signal was applied to the oscillator through the gate terminal. The phase noise dropped by 14.1 dB to a level of -74.36 dBc/Hz at 100 kHz offset. An additional feature of remote upconversion is that the oscillators are placed in a remote environment and are thus subject to temperature variations. Therefore, the locking range of a remote upconversion system must be such that ambient temperature changes do not cause the oscillator to fall out of locking range. The temperature of the MMIC was varied from 40°C to 110°C causing a drop of 412 MHz in oscillation frequency. The locking range was found to be 636 MHz without the use of any temperature compensating circuitry.

The device also exhibits electrical conversion gain, G_C , defined as:

$$G_C = \frac{P_{RF}}{P_{IF}}$$

where P_{RF} and P_{IF} are defined as electrical RF and IF power, respectively. Thus, P_{IF} is measured as the photodetected signal power, hence conversion gain G_C is independent of optical coupling into the device. Positive feedback around the oscillation amplifies the RF signal if it is close to the LO frequency. Amplification can give a conversion gain of up to 30dB for a low IF of 10MHz. The unity conversion gain cut-off frequency was around 417MHz. Measured and modelled conversion performance as a function of LO proximity is shown in Fig. 7. Photodetected signal power varied by less than 1 dB as the device bias was varied over the entire bias plane (except for the ohmic region and knee area). The conversion gain is a strong function of device biasing conditions, varying by more than 10 dB, and with maximum conversion gain occurring at $V_{DS} = 1.6$ V and $V_{GS} = -0.6$ V.

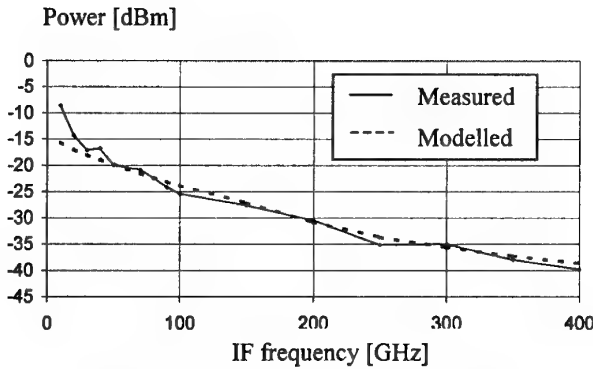


Fig. 7 Measured and modelled conversion performance as a function of IF

At this bias point the device was found to have maximum gain (S_{21}). Given that there is a linear relationship between RF power and the laser modulation signal power, this indicates that conversion gain is dependent on electrical gain but is largely independent of the device's photodetection characteristics.

CONCLUSIONS

The worldwide demand for mobile communications and broadband internet-type services is driving research into future generations of networks using mm-wave wireless-phonic interfaces. If fibre radio is to become reality, then base stations will have to be produced at low cost and decisions will have to be made in favour of either optical delivery of mm-waves or local generation of mm-waves. By making use of optoelectronic self-oscillating mixers, it is possible to achieve simplicity in the design of the fibre backbone with low cost at the base station. This will only be achieved if well established MMIC and HEMT technology is used to realise OESOMs. However, more mundane issues such as fibre alignment and packaging also need to be addressed.

ACKNOWLEDGEMENTS

The authors thank their colleagues for their input on this research programme, in particular: Dr Paul Steenson and Dr Mike Roberts.

REFERENCES

- [1] A.J. Cooper, "Fibre/radio for the provision of cordless/mobile telephony services in the access network", *Electron. Lett.*, Vol.26, pp2054-2056, 1990.
- [2] L. Noël *et al.*, "Novel techniques for high-capacity 60-GHz fiber-radio transmission systems", *IEEE Trans. Microwave Theory Tech.*, Vol. 45, pp 1416-1422, 1997.
- [3] J.J. O'Reilly *et al.*, "RACE R2005: Microwave optical duplex antenna", *IEE Proceedings-J*, Vol. 140, pp 385-391, 1993

- [4] H. Ogawa, D. Polifko and S. Banba, "Millimeter-wave fiber optics for personal radio communication," *IEEE Trans. Microwave Theory Tech.*, Vol. 40, pp. 2285-2293, 1992.
- [5] G. J. Simonis and K. G. Purchase, "Optical generation, distribution and control of microwaves using laser heterodyne," *IEEE Trans. Microwave Theory Tech.*, Vol. 38, pp 667-669, 1990,
- [6] D. Wake, C. R. Lima and P.A. Davies, "Optical generation of millimetre-wave signals for fibre-radio systems using a dual-mode DFB semiconductor laser," *IEEE Trans. Microwave Theory Tech.*, Vol. 43, pp 2270-2276, Sep 1995,.
- [7] J.J. O'Reilly and P.M. Lane, "Fibre-supported optical generation and delivery of 60GHz signals," *Electron. Lett.*, Vol. 30, pp 1329-1330, Aug 1994,
- [8] U. Gliese, S.N. Nielsen and T.N. Nielsen, "Limitations in distance and frequency due to chromatic dispersion in fibre-optic microwave and millimetre-wave links", *IEEE MTT-S International Symp. Dig.*, 1996
- [9] M.J. Roberts, N. Bourhill, S. Iezekiel, D.P. Steenson and C.M. Snowden, "Optoelectronic mixing in a MMIC W-Band self-oscillating mixer," *Electron. Lett.*, vol. 34, pp. 904-905, 1998.
- [10] N. Bourhill, S. Iezekiel, and D.P. Steenson, "Broadband mm-wave fiber radio upconverter using a self-oscillating optoelectronic mixer," *International Topical Meeting on Microwave Photonics*, 1999.
- [11] H. Sawada and N. Imai, "An experimental study on a self-oscillating optoelectronic up-converter that uses a heterojunction bipolar transistor", *IEEE Trans. on Microwave Theory Tech.*, pp 1515-1521, Vol. 47, 1999.
- [12] C. Rauscher and K.J. Williams, "Heterodyne reception of millimeterwave-modulated optical signals with an InP-based transistor," *IEEE Trans. on Microwave Theory Tech.*, Vol. 42, pp 2027-2034, 1994.
- [13] A.A.A. DeSalles and M.A. Romero, "Al_{0.3}Ga_{0.7}As /GaAs HEMT's under optical illumination," *IEEE Trans. on Microwave Theory Tech.*, Vol. 39, pp 2010-2017, 1991.
- [14] M.A. Romero, M.A.G. Martinez and P.R. Herczfeld, "An analytical model for the photodetection mechanisms in high-electron mobility transistors," *IEEE Trans. on Microwave Theory Tech.*, Vol. 44, pp 2279-2287, 1996.
- [15] A. Madjar, P.R. Herczfeld and A. Paoella, "Analytical model for optically generated currents in GaAs MESFETs," *IEEE Trans. on Microwave Theory Tech.*, Vol. 40, pp 1681-1691, 1992.
- [16] A.J. Seeds and A.A.A. de Salles, "Optical control of microwave semiconductor devices," *IEEE Trans. on Microwave Theory Tech.*, Vol. 38, pp 577-585, 1990.
- [17] M.J. Roberts, S. Iezekiel and C.M. Snowden, "A W-Band self-oscillating subharmonic MMIC mixer," *IEEE Trans. Microwave Theory and Tech.*, vol. 46, pp. 2104-2108, 1998.

SIGNAL TO NOISE RATIO ENHANCEMENT USING HETEROJUNCTION BIPOLAR PHOTOTRANSISTOR BY BASE CURRENT COMPENSATION

S. Dupont, M. Fendler, F. Jorge, S. Maricot, J-P. Vilcot, D. Decoster

*Institut d'Electronique et de Microelectronique du Nord - UMR CNRS 8520
 Departement Hyperfréquences et Semiconducteurs
 Université des Sciences et Technologies de Lille
 Avenue Poincaré, BP 69
 59652 Villeneuve d'Ascq, France*

Tel : +33 320 197 968 Fax : +33 320 197 966 E-mail : Samuel.DUPONT@iemn.univ-lille1.fr

Abstract: This paper presents experimental results on signal to noise ratio measurements performed on Hetero-junction PhotoTransistors. The comparison with PIN photodiode is also reported. Simulations have been done to determine the evolution of the SNR.

Introduction:

A high speed detection is required for radio over fibre systems. Several components have been designed and studied to achieve that purpose. Among those, we can refer to Metal-Semiconductor-Metal detectors (MSM), PIN and PIN-guide photodiodes, [1]-[4], and Heterojunction bipolar Photo-Transistors (HPT's), [5]-[10]. This paper deals with a special use of HPT's that leads to increase the power of the output signal keeping the mean DC current constant.

I. Device design and fabrication:

We use a HPT as optical to electrical converter. As for PIN diode, the device design is a trade off between electrical and optical properties: large quantum efficiency requires sufficient absorbing volume, (device area and collector layer thickness, (i.e.: absorbing layer)), on the other hand high speed operation require small capacitance (small area), and small transit time (thin collector layer). The device structure and epitaxy ensure optical wave-guiding properties with edge-illumination, referred as HPT-waveguide. The collector is 400 nm thick, the device area is $3 \times 15 \mu\text{m}^2$. The epitaxy is presented in Table 1. The electrical characterisation of device showed a unity gain cutoff frequency close to 60 GHz and a maximum frequency of oscillation around 42 GHz.

Layer	Material	Doping/Type (at./cm ³)	Thickness (nm)
Contact	Ga ₄₇ In ₅₃ As	$1.10^{19}/\text{n+}$	100
Emitter	InP	$5.10^{17}/\text{n+}$	150
Spacer	Ga ₄₇ In ₅₃ As	nid	50
Base	Ga ₄₇ In ₅₃ As	$2.10^{19}/\text{p++}$	100
Collector	Ga ₄₇ In ₅₃ As	nid	400
Spacer	Ga ₄₇ In ₅₃ As	$3.10^{18}/\text{n+}$	10
Sub-collector	Ga ₄₇ In ₅₃ As	$3.10^{18}/\text{n+}$	700
Buffer	InP	-	100
Substrate	InP	SI	400 μm

Table 1: Device epitaxy.

II. Experiment:

The transmission laser is a 1.3 μm Ortel DFB, it is polarised at 24.2 mA, and driven by a 0 dBm 7 GHz signal. Neither the polarisation nor the laser modulation conditions are changed during the experiment. A variable attenuation is used to modify the illumination conditions. A 10 dB coupler is inserted to monitor the optical incident power on the HPT during the measurements. A lensed fibre is used to launch the optical signal into the HPT-waveguide. Figure 1a&b is a schematic presentation of the experiment set-up.

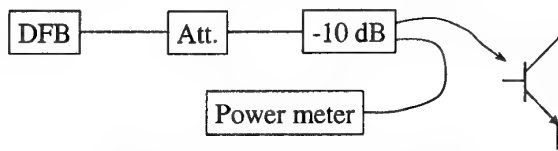


Fig. 1a: Optical experimental set-up.

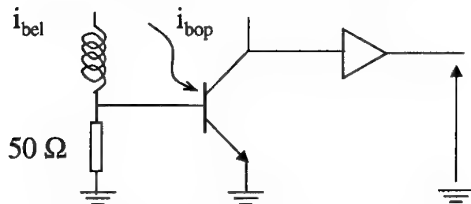


Fig. 1b: Electrical experimental set-up.

The HPT collector/emitter voltage, V_{CE} , is set to 1.2 Volts. The HPT can be polarised by a base electrical current and/or an optical illumination, electrical input and output are loaded on 50 Ω . Under an optical mean impinging power of 67 μW , the collector current is 4 mA. An output power of -39 dBm is measured at 7 GHz. The experiment consists in increasing the optical incident power, (which leads to an increase of the “optical” base current, i_{bop}), keeping the collector current, i_c , constant. A base negative compensation “electrical” current, i_{bel} , is so required to maintain the mean base current constant. The advantage of such a procedure is to operate the HPT under optical incident power that would be too important as regards to the collector DC current. As the output current is held constant, the output signal power increases, so the electrical modulation index is increased while the laser modulation conditions are kept constant. Figure 2 depicts

the output power increase versus the mean optical incident power increase. Optical power goes from 67 μW up to 400 μW , the output power has a 16 dB increase, raising up to -23 dBm, as shown on Figure 2. Under the same illumination conditions, the output power of a PIN diode whose structure is close to the HPT is -33 dBm, (device specifications: 0.4 A/W, $f_c > 40$ GHz).

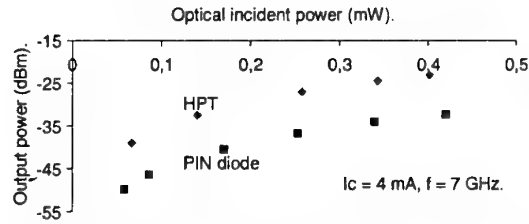


Fig. 2: Output power from HPT versus optical incident power, i_c is set to 4 mA.

III. Signal to noise ratio:

The measurements are made with a 300 kHz resolution bandwidth in a 20 MHz span. The noise floor determination is made under continuous optical illumination so that the laser RIN is included. A HP amplifier is inserted after the HPT, its gain at 7 GHz is 28 dB, and its noise figure is 7 dB. Figure 3 depicts the evolution of the SNR versus optical incident power. Without base current compensation the SNR is 77 dB, (≈ 6 dB better than the photodiode), the SNR is increased to 83 dB when the optical power is 400 μW . The increase of the SNR for the PIN diode is better but the absolute value of the SNR is still better for the HPT.

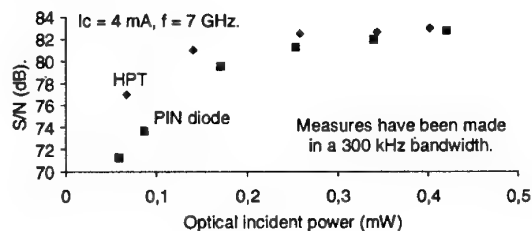


Fig. 3: SNR evolution with optical power increase.

The lower SNR increase for the HPT can be explained considering that the “optical” base

current and "electrical" base current are independent. Though their combined value is kept constant, their algebraic value increases with optical power and they act as two different noise sources which power increases in accordance to optical one.

IV. SNR evolution modelling:

An HPT electrical model has been developed to evaluate the different noise sources behaviours. The various noise sources are brought to the equivalent photogenerated current generator. Such an approach leads to the determination of the predominant noise sources for the HPT. It allows comparison with other kind of optical receivers, and the perception of the potential modifications to bring in priority to increase the device performances. Implementing the model with the experimental conditions, we have derived the evolution of the SNR with optical input power. Figure 4 presents the comparison of the results with experimental data. A good agreement is found: both approaches lead to a 6 dB SNR improvement with mean optical power being increased from 67 μ W to 400 μ W.

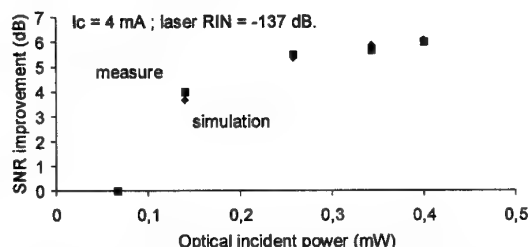


Fig. 4 : SNR improvement, simulated (◆) and measured (■) results.

Conclusion:

An original use of the HPT has been presented, it is based on optical base current compensation. It conveys the ability to increase optical incident power while maintaining the collector current constant. This leads to both output signal power and SNR improvement. A model of noise sources has been tested, results are in good agreement with measures.

References:

- [1] K.Kato, A. Kozen, Y. Muramoto, Y. Itaya, T. Nagatsuma, M. Yaita, "110 GHz 50%-efficiency mushroom mesa waveguide PIN photodiode for a 1.55 μ m wavelength", IEEE Photon. Tech. Lett., V. 6, N. 6, June 1994, pp 719-721.
- [2] I.S. Ashour, H. El Kadi, K. Sherif, J.P. Vilcot, D. Decoster, "Cutoff frequency and responsivity limitation of AlInAs/GaInAs MSM PD using a two dimensionnal physical model", IEEE Trans. on Electron Devices, Feb. 1995, V. 42, N. 2, pp 231-237.
- [3] E.H. Böttcher, E. Dröge, D. Bimberg, A. Umbach, H. Engel, "Ultra-wide-band (>40 GHz) submicron InGaAs Metal-Semiconductor-Metal photodetector", IEEE Photon. Tech. Lett., V. 8, N. 9, Sept. 1996, pp 1226-1228.
- [4] Yi Chen, S. Williamson, T. Brock, F.W. Smith, A.R. Callawa, "375 GHz bandwidth photoconductive detector", Appl. Phys. Lett., V. 59, N. 16, Oct. 1991, pp 1984-1986.
- [5] L.Y. Leu, J.T. Gardner, S.R. Forrest, "High gain, high bandwidth $\text{In}_{0.53}\text{Ga}_{0.47}\text{As}/\text{InP}$ heterojunction phototransistor for optical communications", J. of Appl. Phys., Jan. 1991, V. 69, N. 2, pp 1052-1062.
- [6] H. Shigematsu, T. Iwai, Y. Matsumiya, H. Ohnishi, O. Ueda, T. Fujii, "Ultra-high ft and fmax new self-alignment InP/InGaAs HBTs with a highly Be-doped base layer grown by ALE/MOCVD", IEEE Electron Device Letters, Vol. 16, No. 2, pp. 55-57, Feb. 1995.
- [7] C. Gonzalez, J. Thuret, J.L. Benchimol, M. Riet, "Optoelectronic up-converter to millimeter-wave bands using an heterojunction bipolar phototransistor", Sept. 98, ECOC'98.
- [8] D. Wake, D.J. Newson, M.J. Harlow, I.D. Henning, "Optically-biased, edge-coupled InP/InGaAs heterojunction phototransistors", Electron. Lett., V. 29, N. 25, Dec. 1993, pp 2217-2219.
- [9] V. Magnin, J. Van De Casteele, J.P. Vilcot, J. Harari, J.P. Gouy, D. Decoster, "A three terminal edge-coupled InGaAs/InP heterojunction phototransistor for multifunction operation", Mic.and Opt. Tech. Lett., V. 17, N. 6, Apr. 1998, pp 408-412.
- [10] R.A. Milano, P.D. Dapkus, G.E. Stillman, "An analysis of the performance of heterojunction phototransistors for fiber optic communications", Feb. 1982, IEEE Trans. on Electron Devices, V. 29, N. 2, pp 266-274.

A Two Heterojunction Bipolar Photo – Transistor Configuration for Millimeter Wave Generation and Modulation

J. Lasri, A. Bilenca, G. Eisenstein, D. Ritter, M. Orenstein, V. Sidorov, S. Cohen, P. Goldgeier

Electrical Engineering Dept., TECHNION, Haifa 32000, Israel

Tel. +972 4 8294 694

FAX +972 4 8323 041

E-mail gad@ee.technion.ac.il

Abstract

We describe an advanced millimeter wave source employing two InP/InGaAs heterojunction bipolar photo transistors. One, functioning as a 30 GHz self oscillator, was optically injection locked. The second acts as an optoelectronic mixer / modulator for analog and digital signals.

Introduction

The future mobile communication network will be integrated with massive fiber optics systems which will distribute data and optical control signals to remote base stations [1]. Since the low frequency portion of the spectrum is rather congested, much of the communication is likely to be at millimeter wave frequencies. A key missing component for the remote base stations is an efficient millimeter wave generator capable of being modulated by analog and digital data originating in distant central stations [2].

This paper describes an advanced millimeter wave source employing a two InP/InGaAs heterojunction bipolar photo - transistor (photo - HBT) configuration. One transistor is used as a 30 GHz self oscillator [3] which can be, if needed, injection locked by an optical signal to improve its spectral characteristics. The 30 GHz signal is coupled to a second photo - HBT serving as an optoelectronic mixer/modulator with the data being fed to its optical port at the base via an optical fiber [4],[5]. The two optical signals, one for injection locking and the second for modulation can be carried by different wavelengths and separated by a standard

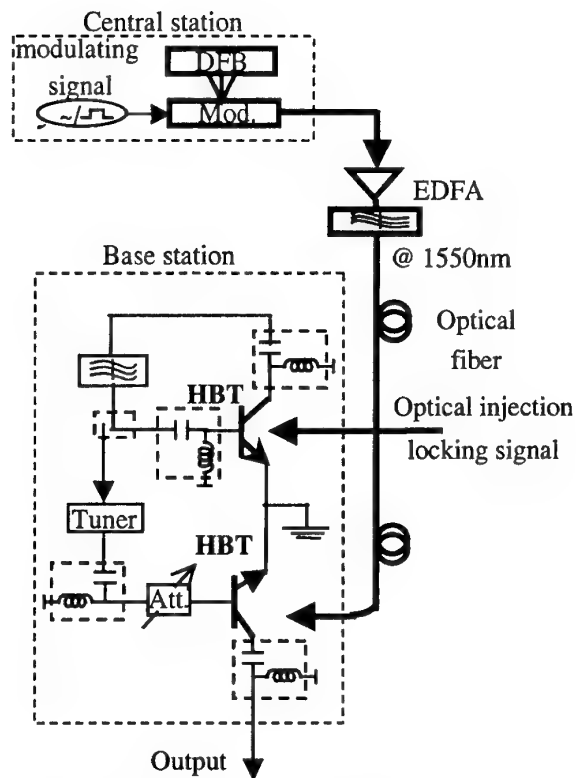


Fig. 1: Experimental arrangement

WDM demultiplexing scheme. The two transistor source ensures good isolation between the local oscillator (generated by the first HBT) and the data signal [6]. The experiments we report demonstrate optical injection locking as well as efficient analog modulation with low distortions and broad band digital modulation with error free capabilities.

Experiments

Fig. 1 describes the experimental arrangement. The self oscillator is constructed by connecting

the collector to the base via a 30 GHz narrow band pass filter, an attenuator and a tuner. In a free running mode, the 30 GHz output exhibits a phase noise of -68 dBc/Hz at 10KHz offset. A sinusoidally modulated optical input signal was used to injection-lock the oscillator and under optimum conditions, the phase noise was reduced to -80 dBc/Hz.

For analog modulation, the 30 GHz power at the input of the second photo-HBT was adjusted using the attenuator to a level of -10 dBm and an optical signal, modulated at 300 MHz was coupled to the optical port. A typical analog modulated spectrum is shown in Fig. 2. The analog modulation capabilities were characterized in terms of the dependence of the up-converted modulation component (at $30\text{ GHz} + 300\text{ MHz}$) on the input power of the 300 MHz spectral component measured by the modulating HBT operating as a photodetector, namely at zero bias to the base. The linearity of the analog modulation capabilities was tested by comparing the change with input modulating power of the fundamental modulation side band (at $30\text{ GHz} + 300\text{ MHz}$) with the second harmonic (at $30\text{ GHz} + 600\text{ MHz}$). The results are shown in Fig. 3. The use of the detected modulation signal as the input parameter ensures that this characterization is independent of the particular transmitter used in the central station.

Fig. 4 describes measurements of the linearity as a function of the average optical power. In this experiment we kept the RF power to the transmitter modulator constant at -10 dBm since the modulating input power scales with the average optical power. The linear dependence shown in the figure means that the HBT operates as a linear upconverter in the optical power range of up to ~ -2 dBm. Finally, we show in Fig. 5 the upconverted power as a function of the power of the 30 GHz carrier signal fed to the base of the modulating transistor. For low power levels, the up-conversion efficiency increases linearly with power, as expected, but eventually it saturates and starts to decrease as the HBT is driven out of its linear operating regime.

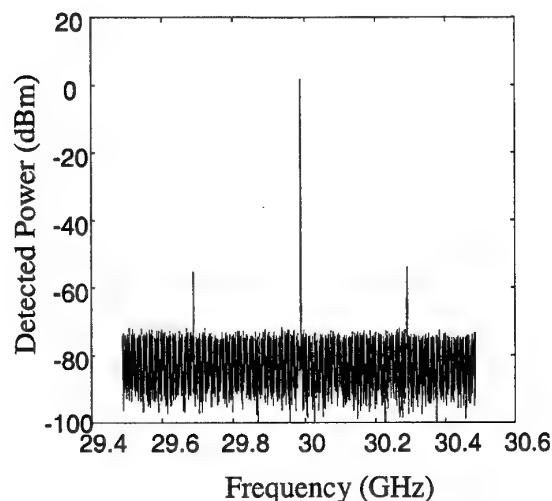


Fig. 2: 30 GHz source modulated by analog signal of 300MHz.

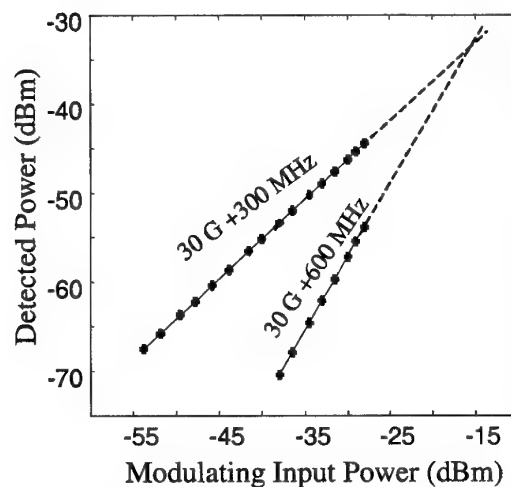


Fig. 3: Analog modulation as a function of the modulating signal (300 MHz) power with -10 dBm 30GHz source and -2 dBm optical input power.

The digital modulation capabilities were tested at a bit rate of 500 Mb/s. The collector output was detected using a coherent homodyne receiver and the resulting base band signal was characterized in both frequency and time domains. Figure 6 shows the base band spectrum with the typical sync envelope and no distortions. The insert of Fig. 7 shows the detected eye pattern which is very symmetric and wide open. The bit error rate (BER) curve

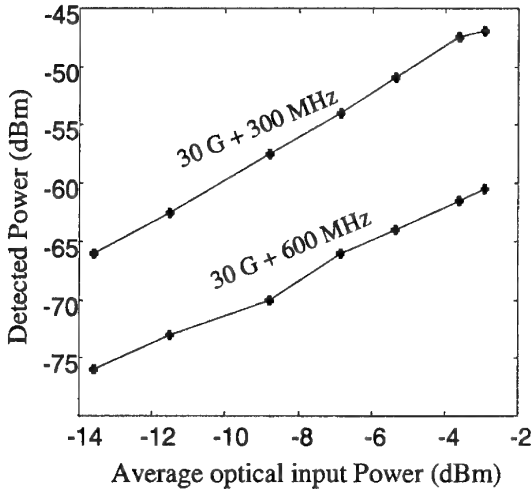


Fig. 4: Analog modulation as a function of the average optical power with -10dBm 30GHz source and -28dBm modulating (300MHz) input power.

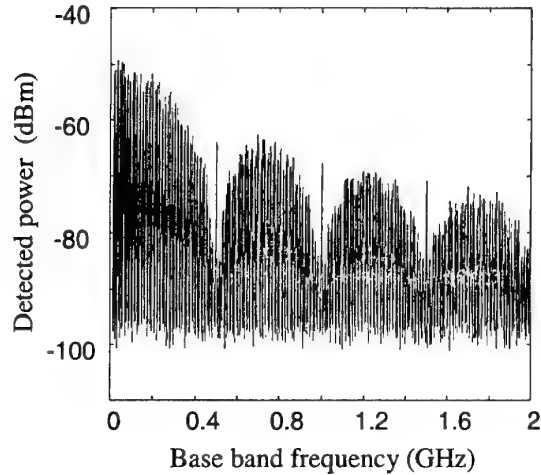


Fig. 6: Base band spectrum of 500 Mb/s digital modulation.

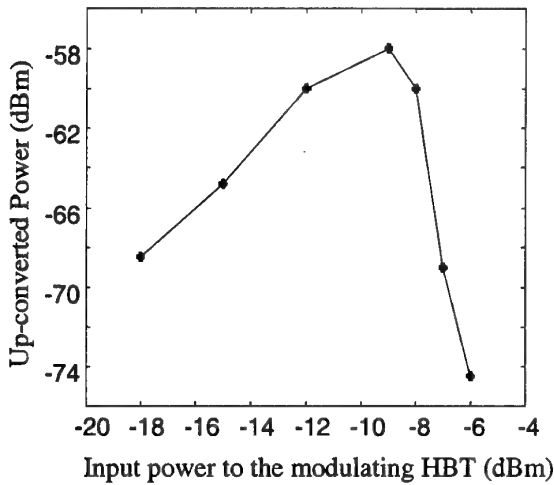


Fig. 5: Measured up-converted power as a function of the input power (from the 30GHz source) to the modulating HBT with -2dBm optical input power.

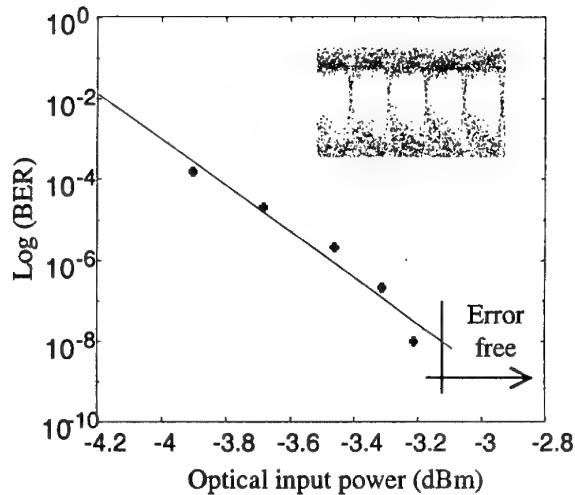


Fig. 7: Digital modulation at 500Mb/s of the 30GHz source.

exhibited in Fig. 7 was obtained by feeding the base band signal to the receiver of a BER test set and changing the optical power impinging on the HBT. The results show that the 30 GHz signal can be properly modulated with no errors.

Summary

We have demonstrated an advanced millimeter wave source employing a two InP/InGaAs

photo – HBT configuration. The 30 GHz signal generated in the first HBT was injection locked optically, exhibiting a phase noise as low as -80 dBc/Hz . It was also modulated efficiently with optically carried analog and digital data using the second HBT as an optoelectronic mixer / modulator.

Next we compare the time domain response of the HBT. In order to model the experiment in a reliable manner we took into account the optical amplifier spontaneous emission noise (ASE) which is added to the shot noise. Both the signal – spontaneous beat noise and spontaneous – spontaneous beat noise are considered.

For simplicity, we use the Gaussian approximation for the number of photoelectrons generated during detection. Figures 4 and 5 describe eye patterns for modulation rates of 300 Mb/s and 2.5 Gb/s, both modulating a 10 GHz carrier. The average optical power was 1 dBm and the data stream power was -28 dBm. The modeled results fit well to the experiments ($h_{\text{meas_300Mb/s}} / h_{\text{meas_2.5Gb/s}} = h_{\text{calc_300Mb/s}} / h_{\text{calc_2.5Gb/s}} \sim 2.13$). As expected, a higher bit rate lowers the eye opening, increases the zero-crossing distortion that produces jitter resulting in non optimum sampling times, lowers the noise margin, increases the sensitivity to the amplifier noise and results in an asymmetric or “squinted” eye. All these are mainly caused by ISI which results from some pulse distortion in the non linear mixing process and from the HBT’s frequency response.

Finally, we show in Fig. 6 and 7 measured bit error rate curves as a function of the optical power impinging on the HBT. Figure 6 shows the dependence on bit rate (in the range of 300 Mb/s to 2.5 GHz) for a 10 GHz carrier. The typical erfc curves are obtained. As the bit rate increases, the system requires a higher local oscillator signal (to maintain the error rate) thereby a higher optical power. Figure 7 shows similar bit error rate curves at 300 Mb/s for a 10 GHz and 45 GHz carrier frequency (the 45 GHz signal was generated by changing Δf to 22.5 GHz). Here the difference in sensitivity stems from the bandwidth limitation of the HBT which at 45 GHz requires a larger optical power, compared to the 10 GHz case, to achieve the same local oscillator power and hence the same error rate.

Conclusions

To conclude, we have demonstrated the use of a single InP / GaInAs photo HBT as an optoelectronic transducer operating at 10 GHz and 45 GHz. The carrier signal is generated by mixing two side bands of an optical signal and simultaneously applying a digital modulating signal to the base. A numerical model was presented together with experimental results which confirm it.

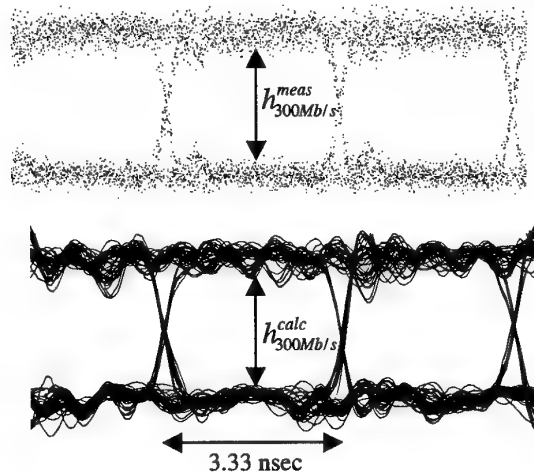


Fig. 4: Measured and calculated eye pattern for bit rate of 300 Mb/s at 10 GHz carrier

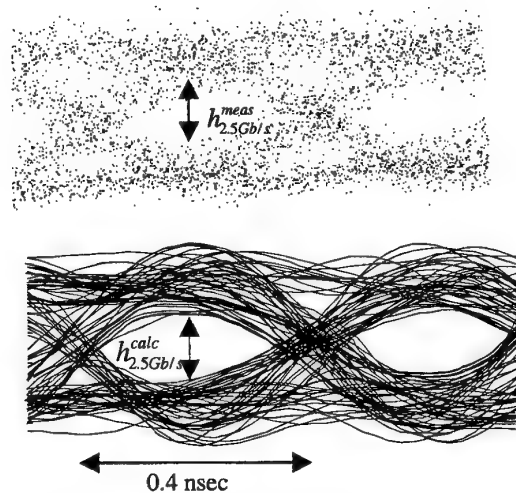


Fig. 5: Measured and calculated eye pattern for bit rate of 2.5 Gb/s at 10 GHz carrier

Multiple Quantum Well Asymmetric Fabry-Perot Modulators for RF-over-Fibre Applications

R. I. Killey¹, J. B. Song¹, C. P. Liu¹, A. J. Seeds¹, J. S. Chadha², M. Whitehead²,
P. Stavrinou², G. Parry², C. C. Button³

¹Optoelectronic and Optical Networks Group, Department of Electronic and Electrical Engineering,
University College London, Torrington Place, London, WC1E 7JE, UK,
Tel: +44 20 7679 3843, Fax: +44 20 7388 9325, Email: rkilley@ee.ucl.ac.uk

²Centre for Electronic Materials and Devices, Department of Physics, Imperial College, Prince Consort Road,
London SW7 2BZ, UK

³Department of Electrical and Electronic Engineering, EPSRC Central Facility for III-V Semiconductors,
University of Sheffield, Sheffield, S1 3JD, UK

Abstract We describe the development of InGaAsP multi-quantum well asymmetric Fabry-Perot modulators (AFPM) and present measurements of devices operating at 3 GHz. Advantages of the AFPM include low drive voltage and loss, high linearity and simple fibre alignment.

Introduction

Future broadband wireless networks will use optical fibre-based signal distribution within buildings and the urban environment. Optical modulators exhibiting high efficiency, linearity and long term stability will be required in such systems. These requirements can be met with the electro-absorption modulator (EAM). In addition to its low drive voltage and high linearity, it can be used as a modulator and detector simultaneously, significantly reducing the complexity of the base station. (Fig. 1). This has led to the development of concepts such as passive picocells, employing very simple radio base-units that are low-cost, small and unpowered [1].

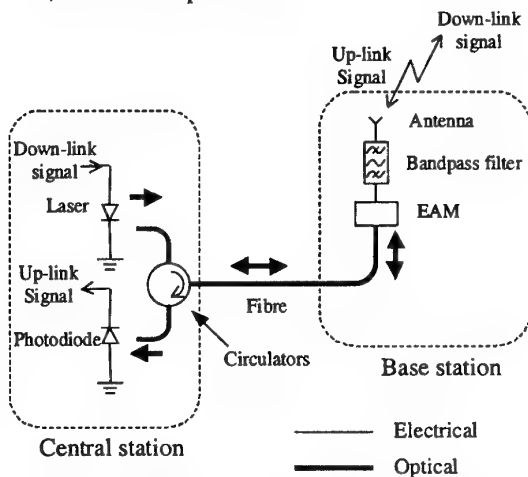


Fig. 1. EAM used as modulator and detector in a point-to-point connection between central and base stations

While fibre-radio systems have been successfully demonstrated using waveguide EAMs, cost and performance can be improved with the use of asymmetric Fabry-Perot modulators (AFPM). In Fabry-Perot modulators, the light propagates vertically through the wafer layers, and a Fabry-Perot cavity, formed from semiconductor distributed Bragg reflectors (DBR) and metal mirrors increases the modulation depth. In the AFPM, shown schematically in Fig. 2, the back mirror reflectivity is designed to be close to 100%, while a lower front mirror reflectivity is used. The output light is reflected from the device and can be separated from the input path using an optical circulator. The modulation sensitivity of the AFPM is made large by arranging the spacing between the mirrors to obtain destructive interference between the light reflected from the front mirror and back mirrors. A modulation depth of 20 dB for 5V drive voltage was achieved with the first GaAs/AlGaAs AFPMs [2], while InGaAsP/InP AFPMs operating at 1.55 μm with a modulation depth of 21 dB and modulation bandwidth of 20 GHz have been demonstrated [3].

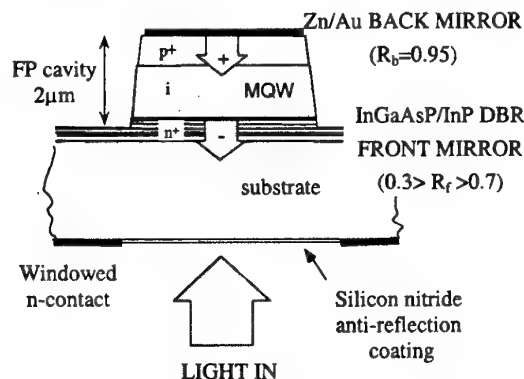


Fig. 2. Schematic of AFPM structure

The AFPM offers a number of advantages for microwave photonic applications. Low insertion loss is possible, as no waveguiding occurs within the device. The large area of the device allows simple

fibre alignment, reducing the packaging cost. An additional advantage is that, as the electric field oscillations of the light are always in the plane of the quantum wells, the device characteristics are independent of the input polarisation. Fig. 3 shows two AFPM configurations. In the top-addressed device, both mirrors are formed from semiconductor DBRs. However, this requires a large number of layers to achieve a high back mirror reflectivity. To avoid this, an alternative substrate-addressed design can be used, in which the p-contact metal doubles as the back mirror. InGaAs/InP substrate-addressed AFPMs have been demonstrated with 3 dB modulation depth and 1.8 dB insertion loss [4]. In this paper, the design and fabrication of AFPMs for microwave photonic applications is described.

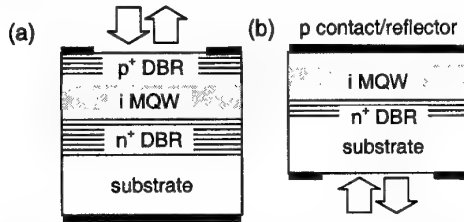


Fig. 3. (a) Top-addressed and (b) substrate-addressed AFPM configurations

Modulator design

The first step in the design process was the measurement of the electroabsorptive effect in the InGaAsP MQW active region, to obtain accurate material parameters for the modulator optimisation. This structure was grown by MOVPE and is shown in Fig. 4. Shallow quantum wells with quaternary well and barrier material were used to reduce the lifetimes of the photo-induced holes that saturate the absorption of deeper InGaAs/InP quantum wells at high optical intensity [4]. The 1 μm thick MQW structure was grown in a p-i-n diode structure, and individual devices isolated by wet-etching mesas through the p- and i- layers. The electric field across the MQW was applied by reverse-biasing the diode.

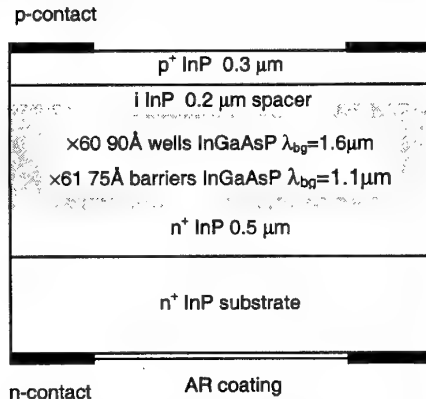


Fig. 4. p-i-n diode test structure to characterise the MQW electro-absorption

Tunable narrow linewidth light from a monochromator was transmitted through the biased MQW layers and detected, allowing measurements of the wavelength and voltage dependent absorption coefficient of the layers to be made (Fig. 5).

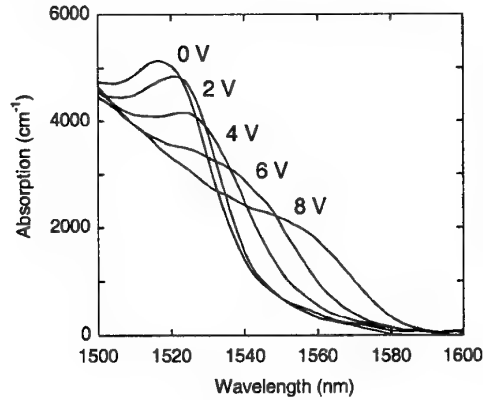


Fig. 5. Measured MQW absorption spectra

The measured MQW electroabsorption and calculated corresponding refractive index changes were used to model the modulation characteristics of the AFPMs. Reflection spectra of these multilayer devices were calculated using the transfer matrix method. An AFPM structure was designed to obtain a 3 dB modulation depth and an intrinsic loss of <3 dB (Fig. 6). A substrate-addressed configuration was chosen, consisting of the 60 period MQW active region tested previously and a 7.5 period front DBR, with $\lambda/4$ layers of InP and InGaAsP of bandgap $\lambda_{bg} = 1.4 \mu\text{m}$. The Au/Zn p-contact was not annealed, to maintain the high reflectivity at the metal-semiconductor interface. The calculated intensity modulation characteristics are shown in Fig. 7a.

Non-annealed Au-Zn contact/reflector

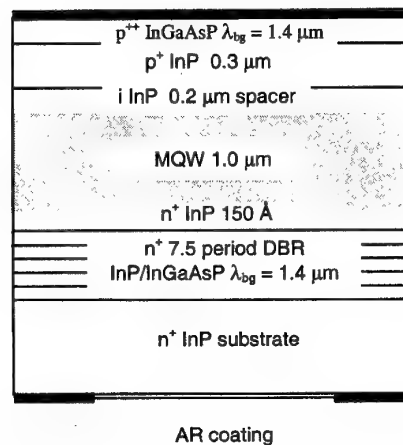


Fig. 6. Substrate-addressed AFPM structure, with 1 μm thick MQW active region and 7.5 period front distributed Bragg reflector.

The modulation characteristic at $\lambda = 1550$ nm was evaluated and a modulation sensitivity of $|dR/dV| = 0.08 \text{ V}^{-1}$ at 4.5 V DC operating point was obtained. From the spectral plots in Fig. 7a, it was found that dR/dV varies by less than 10% over the 1548–1552 nm wavelength range with the operating point maintained at 4.5 V.

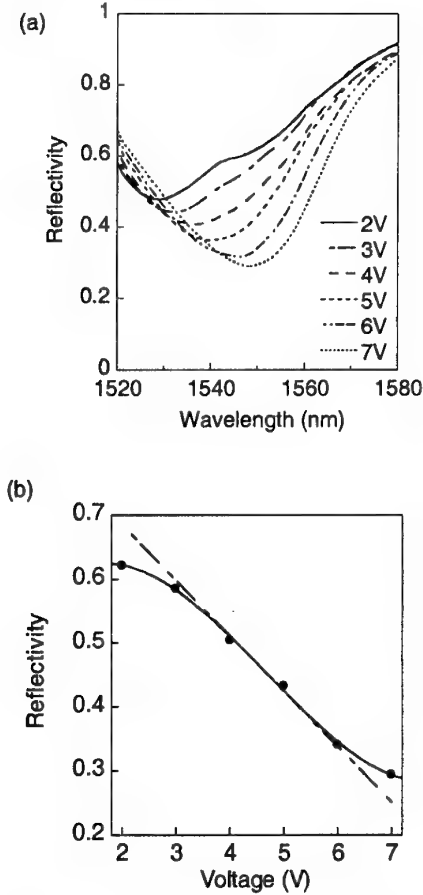


Fig. 7. (a) Calculated AFPM reflectivity spectra. (b) Modulation characteristic at $\lambda = 1550$ nm. Solid line: Third order polynomial fit. Dashed line: Ideal linear modulation

Linear modulation is desirable for multi-frequency RF systems, to avoid interference due to nonlinear intermodulation products. The linearity of the modulation characteristic was assessed by fitting a third order polynomial to the calculated reflectivity values at $\lambda = 1550$ nm (Fig. 7). This was used to calculate the third-order intermodulation product (IMD3) to signal ratio resulting from two RF signals with equal powers at a 4.5 V operating point (Fig. 8). It was found that with a 0.1 V peak-to-peak drive voltage from each signal, the expected ratio is -83 dB. To determine the effect of the Fabry-Perot resonator on the distortion, the IMD3 generated by a waveguide electro-absorption modulator was also calculated, using the simple equation for optical

transmission, $T = \exp(-\alpha(V)\Gamma L)$, where the same absorption values, $\alpha(V)$, as for the AFPM were assumed, and the product of the optical confinement and modulator length, ΓL , was chosen to obtain the same modulation sensitivity as the AFPM. A comparison of the plots in Fig. 8 shows less than 1 dB difference between the distortion generated by the two modulator configurations. Hence, the Fabry-Perot resonator is not expected to have a significant adverse effect on the modulation linearity.

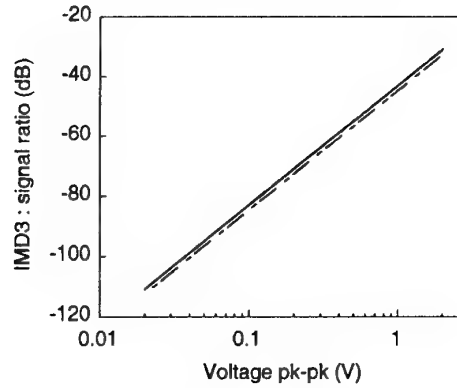


Fig. 8. Calculated IMD3 product to signal ratio for AFPM (solid line) and waveguide EAM (dashed line).

Experimental AFPM

Modulators with the design shown in Fig. 6 were fabricated, with the same growth and processing techniques as for the MQW test devices. Monochromator measurements of the voltage dependent reflectivity spectra are plotted in Fig. 9. The measurements confirm that a 3 dB modulation depth is possible with this design at the resonant wavelength of $1.55 \mu\text{m}$. The loss and drive voltage were higher than predicted and secondary ion mass spectroscopy measurements of the wafer showed that this is due to diffusion of the Zn dopant from the p^+ layer into the MQW layers.

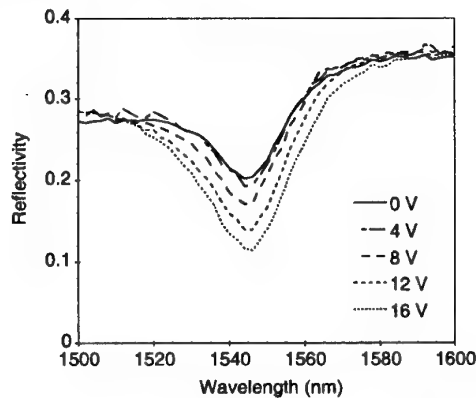


Fig. 9. Measured AFPM reflectivity spectra

The performance of the AFPM at microwave frequencies was then experimentally assessed. Modulators formed from 100 μm diameter circular mesas were used, with a capacitance of 0.85 pF, resulting in an expected 3.7 GHz 3 dB bandwidth. The experimental setup is shown in Fig. 10. The output of a tunable laser was reflected from the modulator via a 3 dB fibre coupler, and the modulated light detected using a high bandwidth photodetector. A network analyser was used to drive the AFPM and measure the output signal, and a variable attenuator at the output of the laser enabled the optical power to be adjusted.

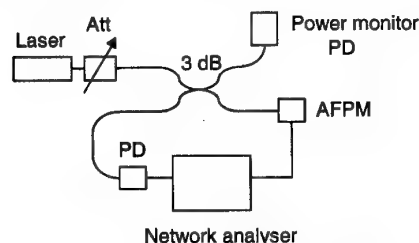


Fig. 10. Microwave modulation experiment

Fig. 11 shows the detected RF signal power for a range of optical powers, -8 to +4.5 dBm, input to the AFPM. Up to ~ 0 dBm, the detected RF power varied linearly with the optical power over the 0-3 GHz range. At higher powers, the build-up of photogenerated carriers in the MQW resulted in a reduction of the modulation sensitivity at high frequencies.

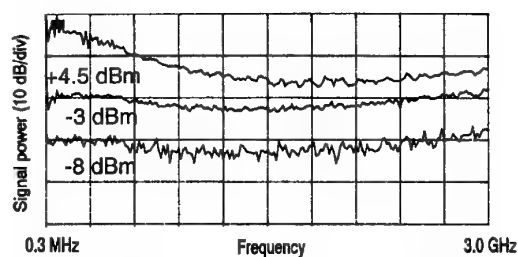


Fig. 11. Detected microwave power with -8 to +4.5 dBm optical input power.

Air-bridged modulators

In the experimental devices used to obtain the results described in the previous section, the p-contact bond-pad was located on top of the modulator mesa. Reducing the mesa diameter to $< 100 \mu\text{m}$ to allow > 3 GHz modulation bandwidth makes wire bonding to the p-contact pad in this position unfeasible. This problem is solved by moving the bond pad away from the mesa, and one technique currently under development is the air-bridged modulator, shown schematically in Fig. 12a. The air-bridge allows the bond-pad and p-contact to be connected, while remaining isolated from the n-InP layers. Fig. 12b

shows a photograph of a top-addressed air-bridge modulator fabricated at UCL. This technique will allow the next stage of microwave AFPM development.

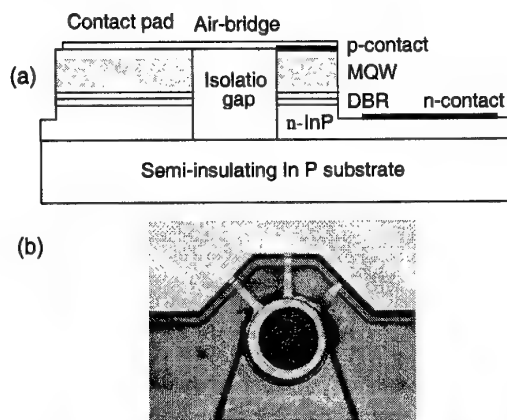


Fig. 12. (a) Schematic of an air-bridged AFPM. (b) Photograph of a top-addressed air-bridge modulator.

Conclusions The high efficiency, low loss and low cost of multi-quantum well asymmetric Fabry-Perot modulators make them attractive for radio-over-fibre applications. We have shown that it is possible to achieve a modulation efficiency $|dR/dV| > 0.08 \text{ V}^{-1}$ with < 3 dB intrinsic loss, and with a modulation linearity comparable to waveguide EAMs. Initial measurements of the high frequency operation of the modulators showed 3 GHz bandwidth with up to 0 dBm input optical power. Further refinement of the MQW design and growth and development of low-capacitance air-bridge structures will allow the AFPM operation to be extended to higher frequencies and optical powers.

Acknowledgements The authors would like to thank D. Wake and D. G. Moodie of BT for useful discussions and G. Hill, M. Pate and K. Dunwoody of the University of Sheffield for device processing. Aspects of this work were supported by the EPSRC Optoelectronic Systems Integration programme.

References

- /1/ D. Wake, D. Johansson and D. G. Moodie, *Electron. Lett.*, 33, pp. 404-406, 1997.
- /2/ M. Whitehead, A. Rivers, G. Parry, J.S. Roberts, C. Button, *Electron. Lett.*, 25, pp. 984-985, 1989.
- /3/ S. J. B. Yoo, J. Gamelin, R. Bhat, C. Caneau, M. A. Koza and T. P. Lee, in *Proc. Optical Fiber Comm. Conference 1996, (OFC'96), TuC1*.
- /4/ A. J. Moseley, J. Thompson, M. Q. Kearley, D. J. Robbins, M. J. Goodwin, *Electron. Lett.*, Vol. 26, pp. 913-915, 1990.

Performance of the Electroabsorption Modulator as an Integrated Optoelectronic Mixer for RF Frequency Conversion

D. S. Shin, G. L. Li, C. K. Sun*, S. A. Pappert*, W. S. C. Chang, and P. K. L. Yu

University of California, San Diego; Department of ECE; La Jolla, CA 92093-0407

* SPAWAR Systems Ctr.; San Diego, CA 92152-5001

Abstract: We present the performance of the multiple-quantum-well and Franz-Keldysh electroabsorption waveguides as an integrated photodetector/mixer for frequency conversion of RF signals. The InAsP/GaInP multiple-quantum-well waveguide exhibits a low phase noise and large SFDR conversion.

Summary

Microwave photonics is considered to be a viable alternative technology in some application areas where electronics has traditionally played a central role. Frequency converting photonic links for antenna remoting applications is an example of this where antenna front-end hardware complexity can be reduced and the deleterious effects of fiber dispersion may be avoided [1,2]. Many of the conversion schemes take advantage of the optical local oscillator (LO), which is less complex than the electronic LO at high frequency, and has shown lower phase noise [3]. There have been several proposals to achieve low conversion loss and large spur-free dynamic range (SFDR) for photonic frequency converting links [4-6]. One approach makes use of Mach-Zehnder modulators (MZM's) at very high optical LO power (350 mW) to achieve positive link conversion gain [5,6]. An alternative approach uses either a heterojunction phototransistor or heterojunction bipolar transistor (HBT) to convert the modulated optical radiation to the RF signal, by using the inherent nonlinearity of the device [7-9]. In [8], a 10.4-dB intrinsic conversion gain (-5.5 dB external conversion gain) was achieved using an electrical LO. In [9], two HBT's in a cascode configuration were used to achieve an intrinsic

conversion gain of 18.2 dB and an extrinsic conversion gain of 7.4 dB with a three-stub tuner.

In a prior work [10], we have proposed and demonstrated an alternate RF signal conversion approach using an electroabsorption (EA) waveguide as a photodetector/mixer. In this approach, frequency converted *electrical* RF signals from the EA waveguide, operating as an optoelectronic mixer (OEM), is generated and made available for subsequent signal processing. The down-converted RF signal can be sent through conventional electrical cable that has low attenuation at baseband/IF frequency. We have demonstrated a moderate conversion loss and high SFDR, RF signal mixing using moderate optical LO power and a simple system configuration [10].

In this work, we compare the performance of the multiple-quantum-well (MQW) and Franz-Keldysh effect (FKE) EA-OEM in this conversion scheme.

In EA waveguides, the electroabsorption process generates an electric-field dependent photocurrent, $I_{ph}(V, P_{opt}) = \eta_m(V)P_{opt}$, where P_{opt} is the optical power and $\eta_m(V)$ is the modulator's detection responsivity. η_m is dependent on the applied bias (therefore, the electric field), and is independent of optical power provided that the device is operated below saturation. When a DC optical power, P_0 , and modulation optical power, p at ω_{LO} , are incident on an EA waveguide driven by a DC bias voltage, V_b , along with a RF signal voltage, v at ω_s , the photocurrent generated at the device is given by:

$$I_{ph}(V, P_{opt}) = \eta_m(V_b + v \cos \omega_s t) \cdot (P_0 + p \cos \omega_{LO} t) \quad (1)$$

The up-and down-converted signals at $\omega_s \pm \omega_{LO}$ are obtained from a small signal analysis of $\eta_m(V_b + v \cos \omega_s t)$ as:

$$I_{ph}^{mix} = \frac{1}{2} \frac{d\eta_m}{dV} \bigg|_{V_b} v p \cos(\omega_s \pm \omega_{LO}) t \quad (2)$$

The higher order derivatives of η_m contribute to the harmonic and intermodulation distortions of this OEM. Note from $d\eta_m/dV|_{V_b}$ in (2) that the electroabsorption is crucial in generating the mixed signals. This distinguishes the electroabsorption mode of the EA-OEM from the usual *pin* photodetection where the responsivity is constant with voltage.

We first compare the current that gives the mixed signals detected by the remote detector, when the EAM is used as a modulator, to the integrated mixer photocurrent. The remote detector photocurrent can be expressed as $I_{trans} = \eta_d P_{opt} t_{ff} T(V)$ where η_d is the responsivity of the remote detector, t_{ff} is the transmission factor of the EAM, and $T(V)$ is the transfer function of the EAM normalized to the incident optical power. The corresponding photocurrent that gives the mixing of ω_s and ω_{LO} is:

$$I_{trans}^{mix} = \frac{1}{2} \eta_d t_{ff} \frac{dT}{dV} \bigg|_{V_b} v p \cos(\omega_s \pm \omega_{LO}) t \quad (3)$$

From I_{ph}^{mix} with I_{trans}^{mix} , the RF power of the converted signals can be obtained, assuming a 50- Ω load resistor. The ratio of powers of the frequency-converted signals in these two cases can be expressed in dB as:

$$Ratio = 20 \text{Log} \left(\frac{I_{ph}^{mix}}{I_{trans}^{mix}} \right) = 20 \text{Log} \left(\frac{dI_{ph}/dV}{dI_d/dV} \right) \quad (4)$$

Here I_{ph} and I_d are the photocurrent detected at the EA-OEM and the remote detector, respectively, and the derivatives are evaluated at the modulator bias, V_b .

In the experiment, AR coated strain-compensated InAsP/GaInP MQW EA waveguide that utilizes the quantum-confined Stark effect [11] and an InGaAsP/InP waveguide [12] that used the Franz-Keldysh effect were compared.

The MQW sample has 8 periods of 8.9-nm thick compressively-strained InAsP wells and 7.4-nm thick tensile-strained GaInP barriers, sandwiched by InGaAsP cladding layers. At $\lambda = 1.319 \mu\text{m}$, the transmission (as detected by a remote detector with 0.89-A/W responsivity) and photocurrent characteristics vs. DC bias of the two devices are shown in Fig. 1a and Fig 1b.

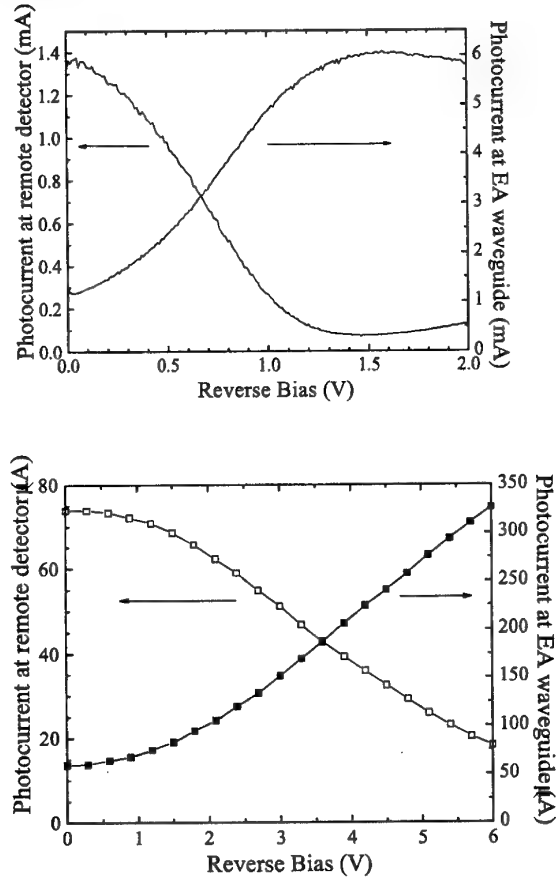


Fig. 1. Transmission and absorption characteristics of (a) the MQW (at 10 mW), (b) bulk InGaAsP waveguides (at 1 mW).

The normalized slope efficiencies are -1.1 V^{-1} and -0.18 V^{-1} , respectively, for these transmission curves. The fiber-to-fiber insertion loss of the waveguides are 8.0 dB and 11 dB, respectively.

The RF-frequency-mixing setup is shown in Fig. 2 [10] with two Nd:YAG lasers generating a beat tone at a 100-% modulation depth, which was used as an optical LO signal to the EA waveguide. Electrical voltage that contained the DC bias as well as the RF signal at ω_s was applied to the EA-OEM under test.

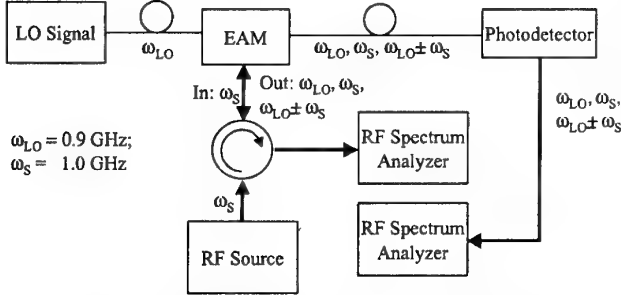


Fig. 2. Experimental set-up for the mixing experiment using the EA waveguide.

The DC bias was first set at the second order null point of the transmission curve, which corresponds to the highest slope efficiency of the photocurrent vs. DC bias curve. When the RF signal power was increased from -20 dBm to -10 dBm, the converted signal powers increased by 10 dB. They closely follow the behavior predicted by (2). The MQW EA waveguide became saturated around 10-mW of LO optical power.

Defining the conversion loss as the ratio of the input RF signal power to the output frequency converted signal power, the conversion loss for the case when the MQW EA-OEM was used as a photodetector/mixer is measured at 18.9 dB. This conversion loss is mainly limited by LO optical power (10 mW) and the saturation power of the MQW waveguide. When this MQW EA waveguide was used as a modulator/mixer and the converted signals were transmitted through the optical fiber as in [4-6], the conversion loss was increased to 27.8 dB. The increase in conversion loss is mainly due to the fact that the responsivity of the remote detector, η_d at the end of the fiber link combined with the EA waveguide insertion

loss, t_{ff} , was much smaller than that of the EA waveguide.

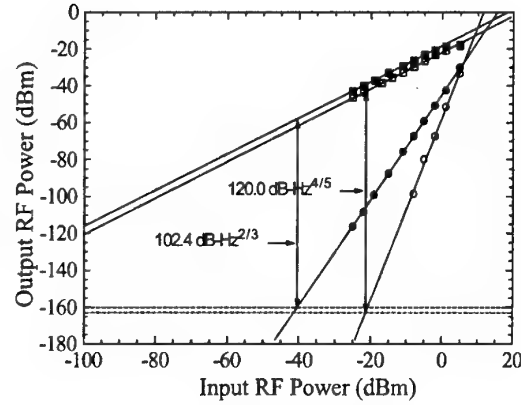


Fig. 3. Two-tone test of the MQW EA photodetector/RF mixer. Converted RF signals (■: for highest slope point, □: for third-order null point) and the IMD_3 's (●: for highest slope point, ○: third-order null point) are shown.

Two-tone SFDR measurement was carried out with the RF tones at 1.00 and 1.02 GHz and the optical LO tone at 0.90 GHz. The converted signals and the their third-order intermodulation distortions (IMD_3 's) were measured. (Due to the bandwidth limitation of the circulator, only the up-converted signals were measured.) When the MQW EA waveguide was biased at the highest slope point of the device photocurrent vs. DC bias curve (second-order null point), a SFDR of 102.4 dB-Hz^{2/3} was obtained at 10-mW optical LO power for the up-converted signal at 1.90 GHz. When the MQW EA-OEM was biased at the third-order null point of the device photocurrent vs. DC bias curve, the up-converted RF signal power was reduced by ~3 dB, but the sub-octave SFDR was measured at 120.0 dB-Hz^{4/5} with the fifth-order dependence on the input RF power. At the third-order null point, the IMD_3 due to the third-order input power dependence becomes null, making the IMD_3 depending on the next order, which is the fifth order. The results are shown in Fig. 3.

For the InGaAsP FKE EA-OEM, a larger RF conversion loss (29.2 dB) was measured at the same LO optical power of 10 mW, mainly due to the smaller slope efficiency of the FKE. However, the single-octave SFDR's of this photodetector/mixer are within 4 dB of those of the above MQW device, primarily due to the lower degree of saturation of the FKE device at 10 mW. These results are summarized in Table 1.

Device	Conversion loss (dB)	SFDR
InAsP/GaInP	18.9 (2 nd order null)	102 dB-Hz ^{2/3}
MQW	21.9 (3 rd order null)	120 dB-Hz ^{4/5}
Bulk	29.2 (2 nd order null)	98 dB-Hz ^{2/3}
InGaAsP	33.2 (3 rd order null)	117 dB-Hz ^{4/5}

Table 1. EA-OEMs at 10 mW optical LO power.

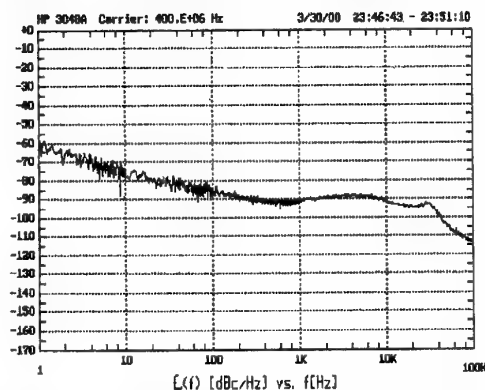
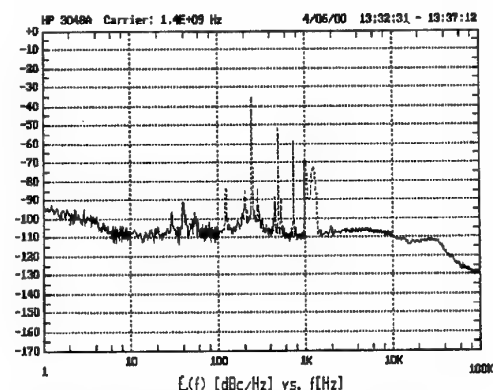


Fig. 4. Absolute phase noise of the RF source driving the MZM (optical LO generator).

Fig. 5. residual phase noise characteristic of the



EA-OEM up-converted signal at 1.4 GHz

We have also measured the phase noise characteristics of the converted signals. In the measurement, the optical LO (Fig. 4) is generated via external modulation of a high power laser using a lithium niobate MZM. Fig. 5 shows the residual phase noise spectrum of the up-converted using a 400 MHz optical LO signal.

In conclusion, we have demonstrated that the EA waveguide can be utilized as an OEM that possess low phase noise, large SFDR conversion properties. The conversion loss and SFDR are both dependent on the slope efficiency and saturation power level. At 10-mW LO power, a sub-octave SFDR of 120.0 dB-Hz^{4/5} was achieved with the MQW EA-OEM.

References

1. G. K. Gopalakrishnan, R. P. Moeller, M. M. Howerton, W. K. Burns, K. J. Williams, and R. D. Esman, *IEEE Trans. MTT*, **43**, pp. 2318-2323, 1995.
2. K.-I. Kitayama, and R. A. Griffin, *IEEE Photon. Technol. Lett.*, **11**, pp. 287-289, 1999.
3. X. S. Yao, and L. Maleki, *IEEE J. Quantum Electron.*, **32**, pp. 1141-1149, 1996.
4. C. K. Sun, R. J. Orazi, and S. A. Pappert, *IEEE Photon. Technol. Lett.*, **8**, pp. 154-156, 1996.
5. R. Helkey, J. C. Twinchell, and C. H. Cox, *J. Lightwave Technol.*, **15**, pp. 956-961, 1997.
6. H. Roussel, R. Helkey, *IEEE Microwave Guided Wave Lett.*, **8**, pp. 408-410, 1998.
7. C. P. Liu, A. J. Seeds, and D. Wake, *IEEE Microwave Guided Wave Lett.*, **7**, pp. 72-74, 1997.
8. Y. Betser, D. Ritter, C. P. Liu, A. J. Seeds, and A. Madjar, *J. Lightwave Technol.*, **16**, pp. 605-609, 1998.
9. Y. Betser, J. Lasri, V. Sidorov, S. Cohen, D. Ritter, M. Orenstein, G. Eisensein, A. J. Seeds, and A. Madjar, *IEEE Trans. MTT*, **47**, pp. 1358-1364, 1999.
10. D. S. Shin, G. L. Li, C. K. Sun, K. K. Loi, W. S. C. Chang, P. K. L. Yu, *IEEE Photon. Technol. Lett.*, **12**, pp. 193-195, 2000.
11. K. K. Loi, J. H. Hodiak, W. B. Mei, C. W. Tu, W. S. C. Chang, D. T. Nichols, L. J. Lembo, and J. C. Brock, *IEEE Photon. Technol. Lett.*, **10**, pp. 1572-1574, 1998.
12. G. L. Li, Y. Z. Liu, R. B. Welstand, C. K. Sun, W. X. Chen, J. T. Zhu, S. A. Pappert, and P. K. L. Yu, *IEEE Photon. Technol. Lett.*, vol. 11, pp. 659-61, 1999.

A 6 to 11 GHz All-Optical Image Rejection Microwave Downconverter

Shane J. Strutz and Keith J. Williams
 Naval Research Laboratory Code 5652, Building 215
 4555 Overlook Avenue, SW Washington, DC 20375
 Phone: (202) 404-1514; Fax: (202) 404-8645
 Strutz@ccs.nrl.navy.mil

Abstract

An all-optical image-rejection downconverter capable of downconverting 6-11 GHz RF signals into an IF band from 2 to 3 GHz is presented. RF signals received by the system are used to generate new optical wavelengths. These new wavelengths are filtered and used to downconvert the RF signals into the IF band through heterodyne detection. The system exhibited better than 20 dB of image rejection over its bandwidth and the spurious signals were more than 40 dB below the downconverted signal power.

I. Introduction

The use of analog photonic links has expanded from direct, transmitter-receiver pairs, to links with signal processing capability. The broadened capability of these links is due to the implementation of cascaded modulators, one to imprint a local oscillator (LO) upon the transmitted light and one to either mix this LO with a received RF signal [1-5], or to translate the optical frequency for direct heterodyne mixing [6].

Though upconverting and downconverting links work for narrow band

applications, they lack the image rejection capability required to instantaneously downconvert signals from ultra-wide-band antennas [7,8]. The image signals result from the mixing of two distinct RF signals, $\omega_{RF} = \omega_{LO} - \omega_{IF}$, with the LO signal, ω_{LO} , which produces two identical intermediate frequencies, ω_{IF} . The presence of images causes ambiguity in the determination of frequency [7].

In this paper, we present our preliminary work on an all-optical version of our previous image rejection downconverter system [8]. The system utilizes the sidebands generated by Mach-Zehnder modulators (MZM) and heterodyne detection to downconvert frequencies between 6 and 11 GHz into an intermediate frequency band between 2 and 3 GHz. The system offers more than 20 dB of image rejection and a conversion loss of 30-40 dB. Our system tests and a discussion of needed improvements are reported.

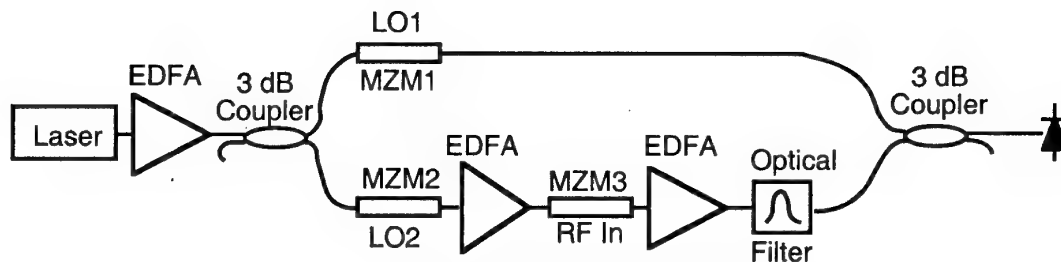


Figure 1. Experimental Configuration

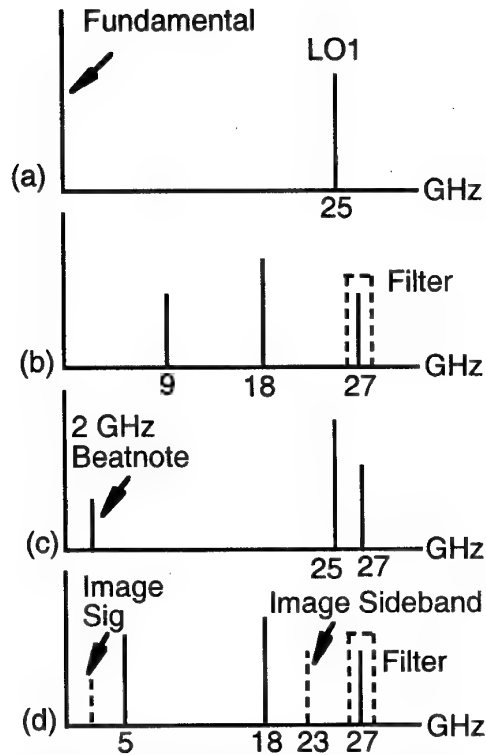


Figure 2. System Operation. (a) Optical sideband produced by LO1. (b) Optical sidebands produced by the interaction of LO2 and the RF input. (c) Heterodyne Downconversion. (d) Image rejection.

II. System Configuration and Operation

A diagram of an all-optical image-rejection microwave downconverter for remote applications is shown in Figure 1. Light from a fiber coupled laser (1550 nm) is divided into two paths by a 3dB polarization maintaining (PM) coupler. In one path, light is amplitude modulated by MZM1 which is driven with LO1 = 22-26 GHz. The amplitude modulation causes light to be shifted from the fundamental beam into the RF sidebands. The second path utilizes two cascaded MZMs. MZM2 modulates the light at 18 GHz (LO2) causing the generation of optical sidebands. The light is then amplified with an Erbium doped fiber amplifier (EDFA) before being modulated a second time by MZM3 (RF In). At this point, the path with the cascaded modulators contains wavelengths at the fundamental frequency (1550 nm), the fundamental \pm 18 GHz, the fundamental - RF Input, and the fundamental - 18 GHz-RF

Input. The light is amplified one more time before it is passed through a filter that selects one of the optical sidebands. When the two paths are recombined the beat signal produced by heterodyning the light at the filtered signal with the sideband produced by LO1 is detected. The RF powers of LO1 and LO2 were fixed to 30 dBm. PM fiber is required up to the final 3 dB coupler. Coherent instabilities in the fiber Mach-Zehnder are minimized, since the optical filter removes the original laser wavelength, such that only the appropriate LO2 - RF sidebands remain.

An example of how the system converts a received 9 GHz signal in to a 2 GHz IF is shown in Figure 2. First light is transferred into an optical sideband by MZM1 (LO1 = 25 GHz, Figure 2.a). At the same time, light in the second path is converted into 18 GHz sidebands by MZM2. The signal is amplified and additional 9 GHz sidebands are generated by the 9 GHz received signal that is present at MZM 3 (Figure 2.b). At this point, the optical spectrum in the second path consists of many optical wavelengths. Next, the light is passed through a narrow optical filter (tunable) which selects the 27 GHz sideband (Figure 2.b). Ideally, at this point the optical spectrum of the second path consists only of light at the frequency = fundamental + 27 GHz. Finally, the filtered sideband is heterodyned with the 25 GHz signal of path one, resulting in downconversion to 2 GHz (Figure 2.c).

The use of the narrow band filter allows the system to select a particular sideband for use in the heterodyne downconversion. As a result, image frequencies present at the RF input are rejected. For example, RF input at 5 GHz mixes with the 18 GHz (LO2) sideband to produce a 23 GHz sideband (Figure 2.d). Without the filter present, this would generate a duplicate 2 GHz signal at the output. Thus, the image rejection of the system is function filter extinction.

The system described above is ideal for remote applications, since both the LOs and the output may be remoted.

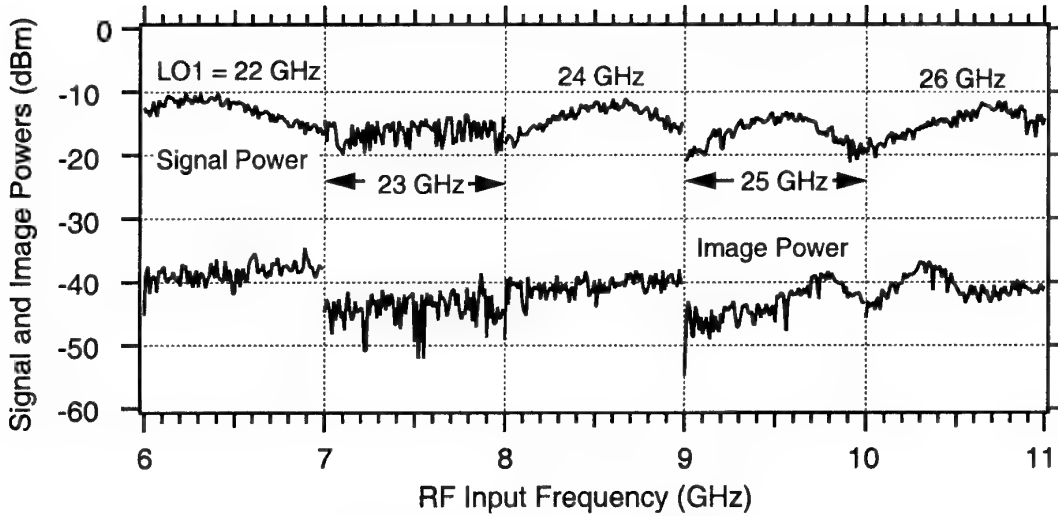


Figure 3. Conversion Loss and Image Rejection.

III. Results and Discussion

We first measured the conversion loss (CL) of the system versus the input RF frequency for various values of LO1 (22-25 GHz) and a fixed value of LO2 (18 GHz). Figure 3 shows the power of the converted signals versus the RF input frequency. The converted signal power was 30-40 dB below the RF input power. The variation in the conversion loss was due in part to the throughput of the optical filter, which was set to a fixed value for each LO2. Lower conversion losses resulted from frequency shifts near to the center wavelength of the optical filter. Due to the large conversion loss, this system required a preamplifier.

Next the image rejection properties of the system were measured. The RF frequencies in the image band of each LO1/LO2 frequency combination were injected directly into the RF input and the power of the converted signal was measured. As shown in Figure 3, the converted image signals were 20-30 dB below that of the desired signals. The image rejection performance of this system is typical of the performance reported using other optical mixing techniques [9-12].

The image rejection capability of our system was measured in order to demonstrate how this technique would work for extremely broad RF input ranges. It is important to note that if the RF input were band limited to 6-11

GHz there would be no images, since the image signals for the LO1=22-26GHz and LO2=18 GHz combination originate from RF inputs below 6 GHz.

Due to the large conversion loss, a preamplifier ($P_{IDB} = 27$ dBm, Gain 40 dB) was added to the system before measurement of the noise figure (NF). The NF of the link (Figure 4), including the preamp, varied between 16 and 24 dB. As with the conversion loss measurement, the NF mapped the throughput of the optical filter. In addition to enabling a noise figure measurement, adding the preamplifier to the system decreased the conversion loss to approximately zero.

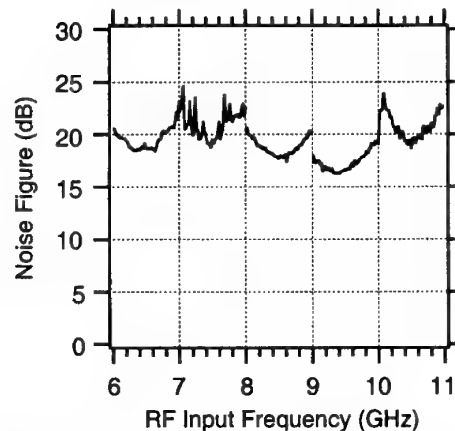


Figure 4. Noise Figure versus the Input Frequency.

Finally, experiments were performed to determine the spurious signal performance of

the system. This was done by sweeping the RF band for each LO1/LO2 combination and measuring the power level of any unintentional spurious signal which appeared at the IF output. Figure 5 shows that the spurious signals were more than 40 dB weaker than the desired IF signals. It may be possible to improve the spurious signal rejection by using a sharper filter.

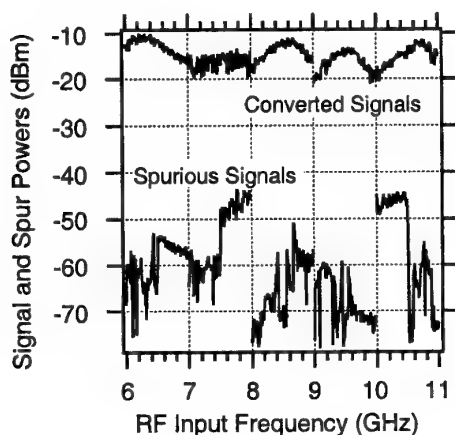


Figure 5. Spurious signal performance.

Even though significant image rejection was achieved, there are still areas, which must be addressed. First, the overall system noise figure of 16-24 dB is too high (> 60 dB without preamp). The noise figure is limited by the V_{π} (10 V) of our modulators. For example, utilizing 1 volt modulators [13] would decrease the NF of the system by 20 dB, allowing the use of a low-noise preamp (30 dB gain).

IV. Conclusions

An all-optical wide-band RF image rejection system with a net conversion loss of 30-40 dB and over 20 dB of image-rejection was presented. The NF of the system was below 24 dB when a 40 dB gain preamp was used. This image-rejecting downconverter system may be useful for frequency conversion in direction finding and other applications.

This research was supported by the Office of Naval Research.

- [1] R. Helkey, J. C. Twichell, and C. Cox III, "A Down-Conversion Optical Link with RF Gain," *J. Lightwave Technol.*, vol. 15, pg. 956-961, 1997.
- [2] C. K. Sun, R. J. Orazi, S. A. Pappert, and W. K. Burns, "A Photonic-Link Millimeter-Wave Mixer Using Cascaded Optical Modulators and Harmonic Carrier Generation," *IEEE Photon. Technol. Lett.*, vol. 8, pg. 1166-1168, 1996.
- [3] G. K. Gopalakrishnan, R. P. Moeller, M. M. Howerton, W. K. Burns, K. J. Williams, and R. D. Esman, "A Low-loss Downconverting Analog Fiber-Optic Link," *IEEE Trans. Microwave Theory Tech.*, vol. 43, pg. 2318-2323, 1995.
- [4] C. K. Sun, R. J. Orazi, and S. A. Pappert, "Efficient Microwave Frequency Conversion Using Photonic Link Signal Mixing," *IEEE Photon. Technol. Lett.*, vol. 8, pg. 154-156, 1996.
- [5] A. C. Lindsay, G. A. Knight, and S. T. Winnall, "Photonic Mixers for Wide Bandwidth RF Receiver Applications," *IEEE Trans. Microwave Theory Tech.*, vol. 43, pg. 2311-2317, 1995.
- [6] T. E. Darcie and B. Glance, "Optical Heterodyne Image-Rejection Mixer," *Electron. Lett.*, vol. 22, pg. 825-826, 1986.
- [7] A. Ward III, L. T. Nichols, P. D. Biernacki, and K. J. Williams, "An Ultra-Wideband Image Rejecting Microwave Downconverter Using WDM," *Microwave Photonics*, Melbourne, Australia, 1999.
- [8] S. J. Strutz and K. J. Williams, "Demonstration of a Wideband Image Rejection Microwave Downconverter," *IEEE Photon. Technol. Lett.*, June 2000.
- [9] H. Kamitsuna, and H. Ogawa, "Monolithic Image-Rejection Optoelectronic Up-Converters that Employ the MMIC Process," *IEEE Trans. Microwave Theory Tech.*, vol. 41, pg. 2323-2329, 1995.
- [10] R. J. S. Pedersen and F. Ebskamp, "New All-Optical RIN suppressing, Image Rejection Receiver with Efficient Use of LO- and Signal-Power," *IEEE Photon. Technol. Lett.*, vol. 5, pg. 1462-1464, 1993.
- [11] L. Chao, C. Wenyue, and J. F. Shiang, "Photonic Mixers and Image-Rejection Mixers for Optical SCM Systems," *IEEE Trans. on Microwave Theory Tech.*, vol. 45, pg. 1478-1480, 1997.
- [12] T. E. Darcie and B. Glance, "Optical Heterodyne Image-Rejection Mixer," *Electron. Lett.*, vol. 22, pg. 825-826, 1986.
- [13] Y. Shi, C. Zheng, H. Zhang, J. H. Bechtel, L. R. Dalton, B. H. Robinson, and W. h. Steier, "Low (Sub-1-Volt) halfwave voltage polymer electro-optic modulators achieved by controlling chromophore shape," *Science*, vol. 288, pg. 199-122.

Photonic True Time Delay Beamformer Demonstrator for a Radio Astronomical Array Antenna

Raymond van Dijk^{*}, Jaap D. Bregman[°], Anton Roodnat^{*}, Frank E. van Vliet^{*}

^{*}TNO Physics and Electronics Laboratory, PObox 96864, 2509 JG The Hague, The Netherlands

tel: +31 70 374 0417, fax: +31 70 374 0654, email: r.vandijk@fel.tno.nl

[°]ASTRON, PObox 2, 7990 AA Dwingeloo, The Netherlands

tel: +31 521 595 278, email: bregman@astron.nl

Abstract

The design and characterisation results of a prototype beamformer for receive application are presented. The four channel system uses switched fibre delay lines and signals are combined optically before addition on a single detector. An SFDR of 101 dB-Hz^{2/3} has been measured, which is good, given the use of a low power directly modulated laser diode.

Introduction

The Square Kilometre Array (SKA) is the next generation aperture synthesis radio telescope [1] planned for operation after 2010. It will use in the order of hundred telescope stations separated up to a few hundred kilometres. Each of the stations is larger than hundred metres in diameter to provide a total collecting area of a million square metres. An important class of station concepts uses array technology where signals of a few hundred up to ten thousand elements need to be combined to form multiple beams on the sky. In view of distance and bandwidth, fibre optics is the technology of choice, which supports both coherent [2] and incoherent signal processing.

At ASTRON a demonstrator program [3] addresses the application of wide band phased array technology with the goal of low cost solutions for RF frequencies. As second in this series a One Square Metre Array (OSMA) has been built for the 2 - 4 GHz band and is tested in an anechoic room for deterministic and adaptive nulling performance. The large bandwidth dictates the use of true time delay (TTD) steering as opposed to phase shifting. The 64 element array has a three level hierarchy, which starts with true time delay column beamformers for four elements, followed by true time delay row beamformers again using four inputs. The last stage is now formed by a photonic beamformer with four inputs and two bit resolution for the switched fibre delay covering the full ninety degree scanning range for the OSMA, that has been designed by TNO-FEL. It substitutes for a four-to-one power combiner that has

been used in previous tests of the OSMA. The advantage of the optical beamformer above an electrical implementation is the large bandwidth and the ease with which large delays are realised. These techniques are also applicable to phased array radar [4].

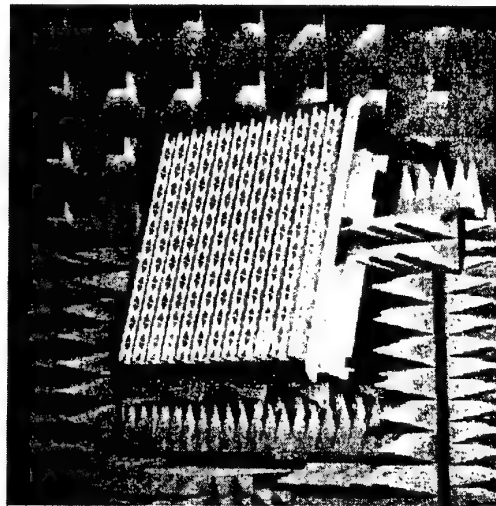


Fig. 1 OSMA demonstrator in anechoic room at Astron

The photonic beamformer uses incoherent optical signal combination on a single detector. A key advantage is effective nulling before detection, which limits the required dynamic range of the detector. Coherent adding requires control of the optical phase but has the advantage of additional circuit gain, which reduces the required dynamic range of the modulator. The latter is important for the Semiconductor Optical Amplifier modulators using a common light source, or for directly modulated lasers that are injection locked. The current prototype uses cheap DFB lasers, which allows us to address part of these aspects.

Analogue Optical Link

To perform the beamforming and signal addition in the optical domain, the RF signal has to be modulated onto an optical carrier. The most straightforward way to do this is by intensity modulating a laser diode with the RF signal. Laser diodes are not optimal for linearity nor for low RIN values but the measured performance was sufficient for this application. The signal is embedded in the noise for an astronomical radio receiver and the spurious free dynamic range (SFDR) is of importance only because of the high interference level of man-made interference.

Because of the high total optical loss in the beamformer plus combiner, the noise of the laser is below the shot noise and receiver thermal noise. For the same reason the upper linearity limit of the photodiode is not reached. The SFDR of the link could be enhanced by using components with matched noise and spurious levels. The optical power on the photodiode has to be higher for a better match.

The basic schematic of the photonic link is shown in figure 2. First the input RF signal (2...4 GHz) generated by a lower layer in the antenna hierarchy is amplified using a 24 dB low-noise amplifier (LNA) with 4.8 dB noise figure and 37 dBm output third-order intercept-point (OIP3). The LNA output signal is broadband matched to the laser diode using resistive matching. This signal directly modulates a DFB laser diode. The laser diode is Lucent's D572 1.5 μm uncooled laser diode which is relatively low-cost and originally intended for digital communication at 2.5 Gbit/s.

After optical processing in the optical beamformer the optical carriers are combined and detected using an MRV photodetector intended for analogue applications. The detected RF signal is amplified using a 35 dB LNA.

Link performance

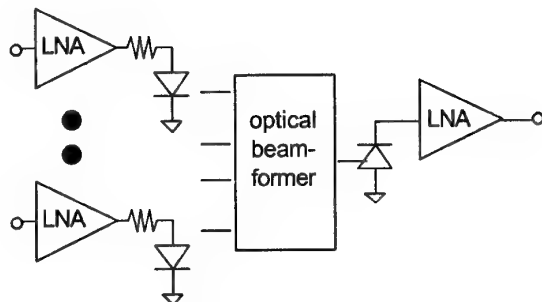


Fig. 2 Photonic link schematic, LNA before laser: +24 dB, after photodiode +35 dB.

The link performance is measured including the optical loss due to the beamformer. Results have been summarised in table 1.

Total gain is 10 dB in the band of interest. Loss due to the optical beamformer plus RF-optical interfaces is 49 dB. The laser has a slope efficiency of 0.1 W/A, the detector has a responsivity of 0.6 A/W. This accounts for 24.4 dB loss, the rest results from excess loss of the switches, fibre connector loss and 6 dB loss of the combiner.

Noise is dominated by noise generated by the photodetector LNA and photodetector shot-noise. Noise figure could be improved by more amplification, the reduction of the optical loss or the addition of optical amplification. The noise figure of the link is 30 dB.

The main source of suboctave distortion is the laser diode which results in a total output IP3 of 17 dBm.

This results in a total suboctave spurious-free dynamic range (SFDR) of 101 dB·Hz^{2/3}.

Because of high optical losses and high RF gain special care must be taken to appropriately reduce spurious EM coupling across the optical link. It was measured to be in the order of -85 dB which is 35 dB down with respect to the signal through the link.

Table 1 Summary of Photonic Link Performance

frequency range	2..4 GHz
gain	10 dB
noise figure	30 dB
output IP3	17 dBm
SFDR	101 dB·Hz ^{2/3}
channel-to-channel isolation	> 20dB

True Time Delay Beamforming

For beamsteering with a large frequency range, phase shifting will not suffice because of beamsquint [5]. Therefore true time delays have been used in the OSMA demonstrator. The first hierarchical layer consists of sixteen four channel RF beamforming modules. In each module four amplifiers, switchable attenuators and four bit microstrip line time delay is used. The signals of four channels are combined and fed to the output. These sixteen outputs are connected to the inputs of the modules in the next hierarchical level. These modules are identical however without the amplifiers. In the complete electronic set-up the four outputs are combined without beamsteering. This limits the scan range considerably but at this level true time delays in microstrip cannot be conveniently realised, due to the length required. The optical beamformer substitutes this last stage and adds, in the optical domain, the two largest bits to the beamformer.

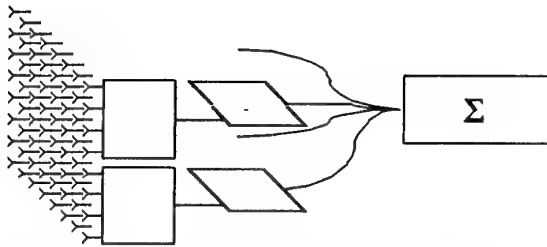


Fig. 3 Schematic of antenna frontend in OSMA with 64 antenna elements, 16 first level beamformers, 4 second level beamformers and the power combiner which has been replaced by a photonic beamformer.

The smallest delay is 31.25 ps and each subsequent line length is twice the former. This results in 16 settings which divide 360° at 2 GHz and allow a true time delay scan angle of 30° from bore sight for the all-electronic set-up. The addition of the optical beamformer with 0.5 and 1.0 ns delays extends the scan range in azimuth to 90° and in elevation to 39° from bore sight for the complete frequency range. Because multiple optical carriers are combined and detected at one photodetector heterodyning of adjacent optical wavelengths could occur. Sufficient optical carrier spacing is realised both by manufacturing variations and by different biasing currents of the laser diodes.

For the delay lines standard 9/125 μm fibre is used which is cut to the desired lengths with a precision of 1 mm which corresponds to 5 ps. FC-PC connectors are attached and polished. The switches from Photonic Integrated Research are SiO_2 thermo-optic 2x2 switches, which exhibit only 1 dB insertion loss fibre to fibre. The optical isolation between the two output channels is better than 25 dB if the switching current is individually tuned. When the switching current is set for all device together an isolation of 20 dB is attainable.

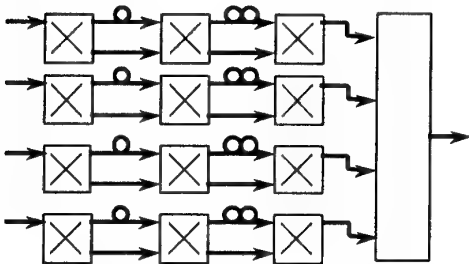


Fig. 4 Switched delay line configuration and fibre coupler

The delay lines were fabricated with lengths matching the required delay to better than 1 ps. The difference in delay between the channels has been eliminated by the addition of fibre before the 4:1 coupler.

Antenna measurements will be performed shortly and will be presented at the conference.

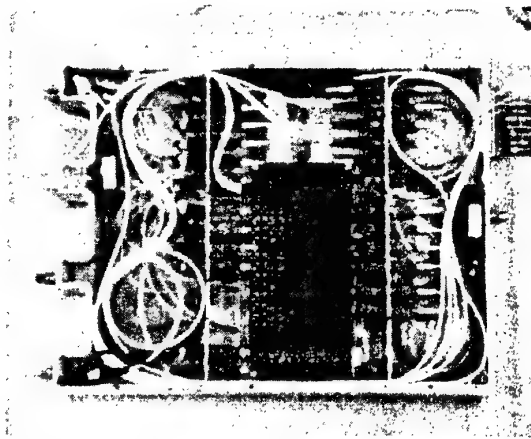


Fig. 5 Top view of the photonic demonstrator. The RF parts are situated below the metal covers on the left and right side. Dimensions: 340 x 265 x 43 mm.

Conclusions

A photonic true time delay beamformer has been realised with large time delays from potentially low cost components. An uncooled DFB laser for digital applications, a CATV photodiode and SiO_2 switches have been used. Signal addition is performed in the optical domain. The complete beamforming part of the system is frequency independent.

The optical link has a noise figure of 30 dB and an SFDR of $101 \text{ dB}\cdot\text{Hz}^{2/3}$.

References

1. Taylor et al., www.ras.ualgary.ca/SKA/science/science.html
2. K. Wagner et al., "Efficient True-Time-Delay Adaptive-Array Processing", SPIE vol. 2845, Aug 1996
3. A. Van Ardenne, F.M.A. Smits, "R&D for a Large Adaptive Radio Telescope", proc. Estec. workshop "Large antennas in Radio Astronomy" Feb. 1996
4. H. Zmuda, E.N. Toughlian, *Photonic aspects of modern radar*, 1994 Artech House
5. R.J. Mailloux, *Phased array antenna handbook*, 1994 Artech House

PHOTONIC DIFFERENTIAL DELAY BEAM FORMING NETWORK FOR PHASED-ARRAY ANTENNAS

Claude Bélisle, Caroline Delisle, John Oldham
Communication Research Centre

3701 Carling Avenue, Box 11490, Station H, Ottawa, Ontario K2H 8S2
Tel.:(613)998-2605, fax:(613)990-0316, claud.belisle@crc.ca

Abstract – A technique combining photonic and microwave technologies is proposed for phased-array beam steering. Performance results of a prototype implementation are given. The approach, based on a differential delay line network, significantly reduces the complexity of the phase weighting mechanism and the Tx/Rx modules by performing signal conditioning and phase weighting in the central processor.

1 Introduction

Phased array antennas, with electronic beam steering, have been the dream for both radar and communications applications for many years. Despite early promise, they have been slow in developing. Most array antennas still have fixed beams with POMS (Plain Old Mechanical Steering). The implementation difficulties arise from the practicality of implementing a low loss, lightweight signal distribution network, and of controlling a large number of phase shifters associated with the antenna elements. Photonics could provide the technology to alleviate the major drawbacks of a conventional microwave implementation. If fibre optics were used, instead of RF waveguides, then the distribution network could be made much smaller, lighter, more flexible, with reduced EMI problems. Photonics also offer the capability of remote control of the antenna sensors, thus reducing the complexity of the sensors.

In this paper, a photonic implementation of a phased array beamforming network is described. The technique presented, based on differential-delay network, simplifies considerably the phase weighting mechanism and allows a significant reduction in the complexity of the transmit and receive (T/R) modules.

In the following sections, the architecture is described, followed by a description of a scaled-down implementation of a 5.3 GHz phased array and performance results.

2 Architecture

In [1], a frequency scanning technique is proposed as a mean to adjust the phase of the microwave signal. By varying the frequency of the microwave signal propagating over a fixed path length the phase shift

required for beam steering can be obtained. The drawback is of course that the output frequency varies according to the desired phase shift. In [2], Seeds proposed the use of a differential delay network to obtain the desired phase shift and maintain the frequency of the transmitted signal. Two distribution networks are used, one with equal propagation distance to each antenna element and one with a length increment ΔL between the elements. Two signals of frequency f and $f-\Delta f$ are sent, one in each network. The signals are mixed at the antenna element and the sum frequency is kept. The phase of the resulting signal becomes a function of the frequency difference between the two signals as expressed by:

$$\Delta\phi = \frac{2\pi n \Delta L}{c} \Delta f \quad (1)$$

where n is the refractive index of the distribution network and c the speed of light. This approach however reduces the degree of freedom for the phase weights since the phase of each element is being set by the selection of the difference in frequencies.

In this paper, the differential delay network concept is further extended to the design of a two-dimensional phased-array antenna. The number of degrees of freedom is increased by combining two different phase weighting techniques. The receiving function of the antenna is also addressed and a schematic diagram of the Tx/Rx module is shown.

Figure 1 shows a functional block diagram of the transmit part of the beam forming network. The phase weighting mechanism is implemented using two separate processes for two orthogonal steering angles, one for the along track, one for the across track steering of the two-dimension antenna. This is possible since the required phase weight $\phi(x_n, y_m)$, which must be applied to element (n, m) to obtain a beam in the direction (α, β) , can be expressed as the sum of two phase weights, one along track, $\phi_{at}(x_n)$ and one across track, $\phi_{ac}(y_m)$ as shown in Equation 2.

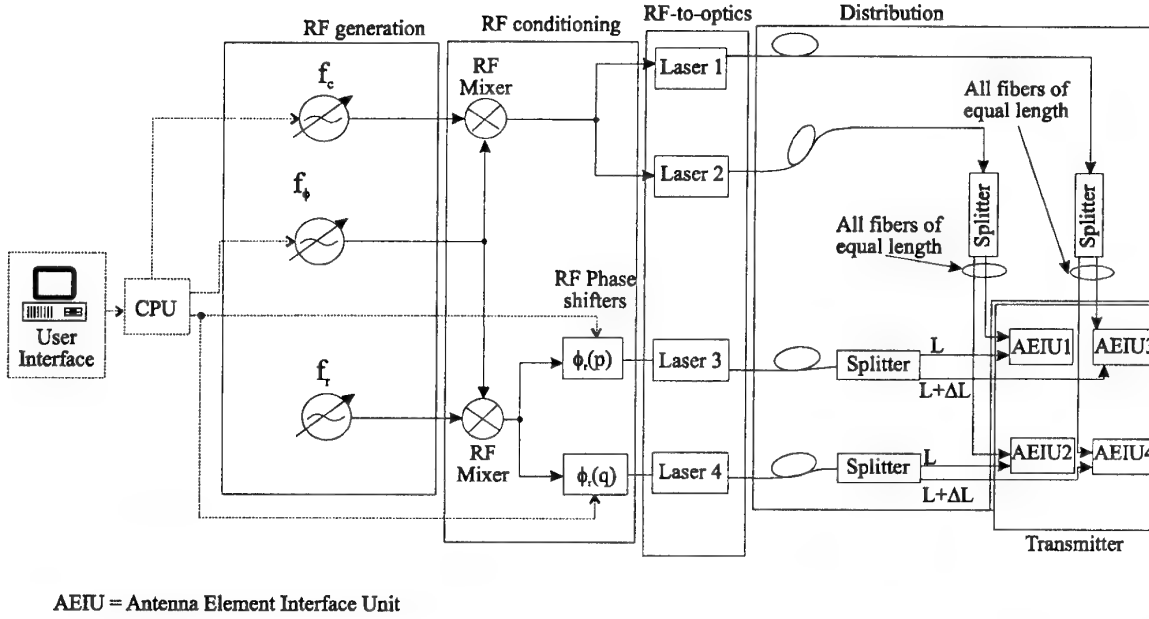


Figure 1 : Optoelectronic phased-array architecture for transmitting

$$\phi(x_n, y_m) = \frac{2\pi}{\lambda} \sin \beta (x_n \cos \alpha + y_n \sin \beta)$$

(2)

$$\phi(x_n, y_m) = \phi^{al}(x_n) + \phi^{ac}(y_m)$$

As shown in Figure 1, two signals are distributed to each antenna element interface unit (AEIU), one at frequency $f_{parallel} = f_c - f_\phi$ and one at frequency $f_{sequential} = f_r - f_\phi$. At the AEIU, the two signals are detected, and the resulting RF signals are amplified and mixed as shown in Figure 2. These two signals are the mixing products of a tone frequency and a variable frequency synthesiser.

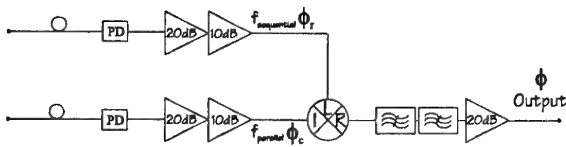


Figure 2 : Architecture of AEIU

In one arm, the sum frequency resulting from the mixing is kept, while the difference frequency is kept in the other branch. In Figure 1, the signal resulting from the mixing of f_ϕ and f_c is distributed to every antenna elements on an equal path distribution network. The signals detected at the different AEIUs are then all in phase. The distributed signal is an intensity modulated optical carrier. Multiple lasers are used to maintain a acceptable power level at the

antenna elements without using costly optical amplifiers.

Phase weighting is performed using the other mixing product ($f_r - f_\phi$). In this case, the mixing product is split into N branches, one per row of the antenna. To each of these signals, across track phase weights are applied using conventional RF phase shifters. These weights are provided to the system by the CPU, based on calculation requested by the user for the desired beam steering angle. Each across track phase weighted signals intensity modulates an optical carrier. Direct modulation is shown in Figure 1 but external modulation could be used for higher frequencies.

Along track phase weights are automatically created by the differential delay network approach. The modulated optical signals are distributed to the antenna elements sequentially fashion. Each element of a same row, receives the signal at a time Δt after its predecessor. Δt is equal to $n\Delta L/c$, where n is the refractive index of the optical fibre, c the speed of light in free space, and ΔL is the path length increment between two consecutive elements of a row. From Equation (1), the propagation delay imparts a phase shift between elements proportional to the frequency of the distributed signal. This frequency may be set by varying f_ϕ . From [3], the value of f_ϕ to provide along track phase shift can be computed from:

$$f_\phi = f_r \left(\frac{\Delta L}{\lambda k} \right) \sin \beta \sin \alpha \quad (3)$$

where, λ is the free space wavelength of the transmitted frequency.

The two intensity modulated optical input signals are detected and the resultant electrical signals are mixed. The sum frequency, $f_r + f_c$, is kept using a microwave filter. The mixed signal is now properly phased for beam steering as its phase equals the sum of the phase of the two modulation signals.

The same phase weighting mechanism can be used to steer the received beam. To accomplish this, the $f_r + f_c$ signal is used as the local oscillator for the down-conversion of the received signal. Out of the mixer IF port is a signal at the difference frequency between the LO and the received RF signal. The phase of the IF signals generated by every elements are automatically in phase and can be coherently added.

Figure 3 depicts another approach for the design of the AEIU.

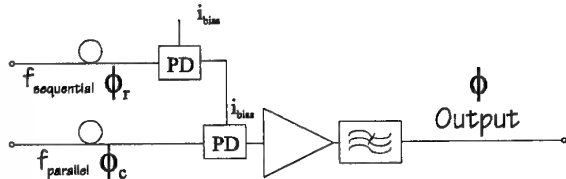


Figure 3 : Alternate design for antenna element

In this case, RF mixing is done by optical devices. Instead of using a conventional RF mixer, the output of a photodetector is fed into the bias port of the second detector [4]. The electrical signal out of this second detector contains the mixing product of the two signals modulating the input optical signals.

It can be seen, from equation 1, that only $M+N$ phase shifters (one per row and one per column) are actually required to address every element, instead of $M*N$. The consequence of this approach is that two distribution networks are needed, one to address the rows, one to address the columns. This would be too costly to realise with RF waveguides, but perfectly feasible with fibre optics.

3 System Implementation

The approach described above has been implemented at CRC in a two-by-two transmit only array. Table 1 gives the frequency plan for the three microwave signals used. The resulting RF signal was at 5.3 GHz.

Table 1 : Frequency plan

SYMBOL	VALUE
f_c	2.0 GHz \pm 50 MHz
f_r	3.35 GHz
f_ϕ	400 MHz \pm 50 MHz
$f_{\text{parallel}} = f_c - f_\phi$	1.6 GHz \pm 100 MHz
$f_{\text{sequential}} = f_r - f_\phi$	3.75 GHz \pm 50 MHz
$f_{\text{operation}} = f_{\text{parallel}} + f_{\text{sequential}}$	5.35 GHz \pm 50 MHz

Figure 4 shows the frequency spectrum of the antenna element output signal. It can be noted that the noise floor is around -67 dBc while some harmonics are at -50 dBc to -40 dBc. The digital synthesiser feeding f_c was found to be the source of the spurious harmonics.

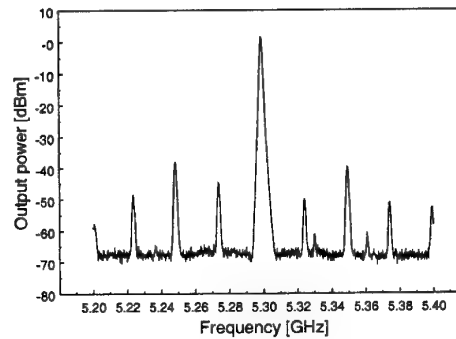


Figure 4 : Output of antenna element

Figure 5 illustrated the across track phase steering capability. As shown in equation 1, the phase shift between two elements on the same row varies linearly with the frequency of the signal f_ϕ . A frequency shift of ± 40 MHz on f_ϕ imparts a phase shift of 180° on the output signal at 5.3 GHz.

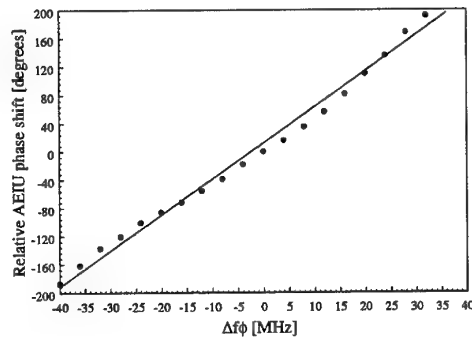


Figure 5 : Across track steering

A linear relationship also applies between the phase difference between two elements in the same column and the phase applied to the phase shifters of those elements. Figure 6 illustrates the along track phase steering capability. The phase shift between two antenna elements on the same column varies linearly with when the phase applied to the phase shifter of one of the elements.

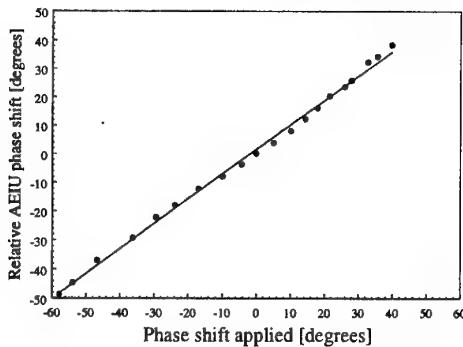


Figure 6 : Along track steering

Total antenna steering is achieved by combining the effects of the along and across track phase weight. Figure 7 illustrates the total antenna steering capabilities. The phase applied on the phase shifter of one element is varied for two different values of the frequency of signal f_0 . The output phase varies linearly with the phase applied on the phase shifter as illustrated in Figure 6, and a 30° phase shift is imparted by a 5 MHz frequency shift as illustrated in Figure 5.

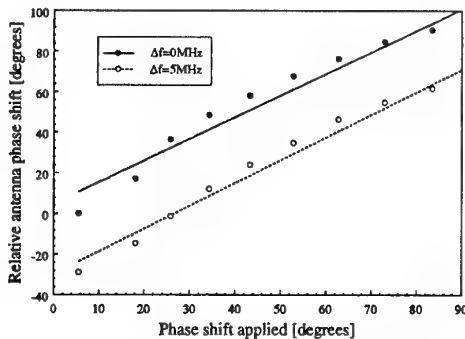


Figure 7 : Total steering

4 Conclusion

A novel architecture for phased array beam steering has been proposed and performance results of a scaled-down implementation have been given. The architecture combines photonic and microwave technologies. The approach is based on the separation of the phase weights into two orthogonal directions, one along track and one across track. The across track steering is done using an optical differential delay line network, while the along track steering is done using conventional microwave phase shifters. This enables a reduction of the number of RF phase shifters to $M+N$ compared to $M*N$ for conventional designs. Offsetting the reduction of the number of phase shifters is the addition of two frequency synthesizers. A signal-to-spurious ratio of 53 dB at the output of the AEIU was obtained. Linear properties of the along and across track phase steering relative to phase shifting and differential delay was demonstrated in the laboratory.

References

- [1] Matthews P.J., "Practical Photonic Beamforming", Microwave Photonics 99 Digest, p.271-274, MWP99, November 1999.
- [2] A.Seeds, "Optical Beamforming Techniques for Phased-Array Antennas", Microwave journal, July 1992, pp. 74-83.
- [3] C.Bélisle, "Design of an Opto-Electronic Beam Forming Network for an Advanced Synthetic Aperture Radar", CRC technical note 96-003, Nov. 1996, 55 p.
- [4] V.E.Behrens-Zaror, "Design of an Optoelectronic Mixer Using a Metal-Semiconductor-Metal Photodetector for a 5.3 GHz to 3.3 GHz Application", M.Eng. thesis Carleton University, Ottawa, Ontario, Canada, May 1996, 152p.

BROADBAND BEAMFORMING NETWORK USING INTEGRATED OPTIC RF PHASE SHIFTERS

A. Mitchell and R. B. Waterhouse
 Australian Photonics Cooperative Research Centre
 Department of Communication and Electronic Engineering
 RMIT University
 Melbourne, VIC 3000
 Australia
 Telephone: +613 9925 2896
 Fax: +613 9662 1060
 Email: rwaterhou@rmit.edu.au

ABSTRACT

The performance of an integrated optical RF phase shifter is analysed in the context of a phased array antenna. The device consists of a variable optical directional coupler and an integrated feedback loop. A basic model of a linear array utilising these devices indicates its suitability for broadband phased array applications.

I. INTRODUCTION

Phased array technology over the years has developed from relatively diverse military applications and is finding use in a growing list of commercial possibilities. Optical beamforming networks have several well-known advantages over their electrical counterparts including their broadband nature, reduced weight and size and immunity to EMI [1], [2]. It is these factors that have seen the recent proposal and development of optical beamformers time steered systems (for example, [3]). Unfortunately associated with the implementation of most optical beamforming networks are the high component/installation costs. For this reason, as was pointed out in [2], there are only few examples of real-world systems taking advantage of this technology (one such example is in [4]).

Recently we introduced an integrated photonic device that can provide a broadband, tunable RF phase shift [5], [6]. The device comprises of a variable optical directional coupler and an optical feedback loop, either integrated within the device (as in [6]) or external to the coupler using an optical fibre [5]. The device can yield true-time delay over multiple octaves, with the upper frequency limit set by the size of the feedback loop and its associated resonance. Importantly, an optical beamforming network utilising this photonic device does not require a tunable optical source to provide the necessary time delay thereby reducing the overall cost of the beamformer. Also the photonic proposed RF phase shifter can provide variable phase shifts, so unlike typical switched path delay lines networks (for example [4]), it does not suffer the associated resolution problems [3].

In this paper, we investigate the previously developed integrated optic RF phase shifter [5], [6], in a beamform-

ing network. In particular we propose a suitable architecture that optimises the performance of the devices in concert. Models of this system performance are presented.

II. REVIEW OF DEVICE AND CHARACTERISTICS

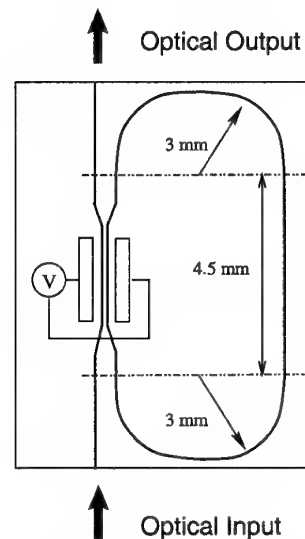


Fig. 1. Schematic of the phase shifter device indicating integrated directional coupler and delay line.

As mentioned before, the integrated optic RF phase shifter consists of a variable optical directional coupler with an output port fed back to one of its input ports via a delay line [5] as depicted in Figure 1. The delay line causes a phase shift in the optical signal proportional to its length. By varying the applied DC bias to the coupler, the amount of optical power in the feedback loop can be adjusted resulting in a variable phase shift of the output signal of the device. The magnitude and phase trends of the device as a function of the applied DC voltage have recently been verified for several configurations utilising the proposed photonic device [5], [6].

Figure 2 shows the theoretical phase response of an in-

egrated optic RF phase shifter with $\alpha = 0.04\text{cm}^{-1}$, at an optical wavelength of $1.3\text{ }\mu\text{m}$ and a loop length of 2.8 cm , similar to the integrated device presented in [6] over the frequency span of $0\text{--}1.8\text{ GHz}$. From this diagram it is evident that there is a reasonable range of phase shifts that scale approximately linearly with frequency. For the phase shifter in Figure 2 there is however, a sharp resonance towards 2.2 GHz where the delay along the feedback loop equals 180° , causing the phase response to become strongly non-linear and therefore must be avoided for true time delay operation. The device in Figure 2 (and [6]), has a phase tuning range of $35\text{--}95^\circ$ (for a phase error of less than 6°) at 1.2 GHz , corresponding to coupling ratios, x , between $0.65\text{--}1$. Of course $x = 0$ can also be used to provide zero phase shift. An in depth evaluation of the dependence of the length and associated losses is given in [5], [6].

Figure 3 shows the corresponding plot of the resulting amplitude of the integrated optic RF phase shifter over the same frequency span. As can be seen from Figure 3, the attenuation of the device varies as a function the applied bias and in some circumstances as a function of frequency as well. When the device is completely off ($x = 0$), the loss due to the loop is zero, when the device is completely on ($x = 1$), the resonator contributes loss equal to one complete circuit of the loop. At intermediate points, due to the recirculating nature of the resonator, optical losses in excess of a complete loop circuit could be expected. Further as the frequency varies and the RF phase delay caused by the loop approaches 180° , the RF signal modulated onto the optical carrier will begin to cancel, further contributing to the signal loss through the device.

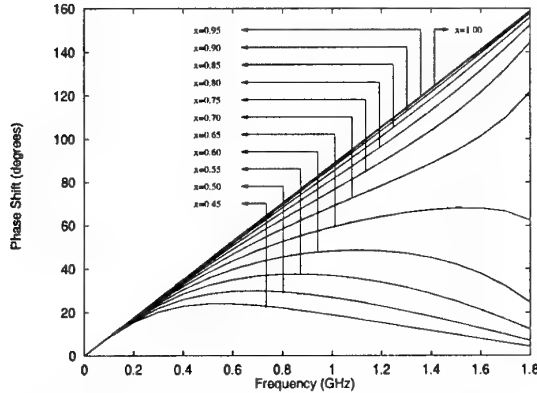


Fig. 2. The frequency dependent phase shift produced by the integrated photonic-RF phase shifter for several coupling ratios (x).

The cancellation approaching resonance can be avoided by operating the device well below the resonant frequency. As discussed in [5] and pointed out earlier, to maintain linearity of phase with frequency, the device must be operated below this frequency in any case. The signal attenuation due to optical losses within the loop is of more significance. Although it is possible to fabricate very low attenuation bends with very small radii, the

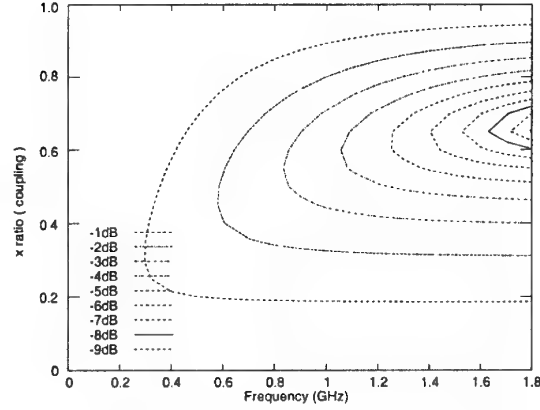


Fig. 3. The frequency dependent amplitude variation produced by the integrated photonic-RF phase shifter for several coupling ratios (x).

tunability of the device depends upon a certain amount of loss within the recirculating loop to dampen the resonance as discussed in [5].

III. PROPOSED BEAMFORMING ARCHITECTURES

Typically, the broadband phase shifter is to be used in a fairly large array environment such as for radio astronomy telescopes [7]. The performance of the device in [5], [6] should therefore be analyzed with reference to its impact on the predicted performance of such an array. Having verified in [5], [6] that the realized integrated device does indeed behave as predicted by Equation 1 in [5], this equation can be used to model the device in the development and analysis of a phased array antenna system model.

The simple one dimensional linear antenna array to be modeled consisted of 32 identical isotropic radiating elements. Each of these elements was spaced 7.5 cm apart ensuring no grating lobes occur in visible space when scanning to 60° at 1.8 GHz . Using the expression for the phase required for each element (Equation 6-18 in [8]) and the previously given array specifications, the largest phase shift required for an antenna element will be about 4500° for scanning to 60° at 1.8 GHz . From Figure 2, the maximum phase shift available for a single device is about 160° and thus around 28 nominally identical phase shifters would need to be cascaded for each antenna element to ensure 60° coverage. Examination of Figure 3 indicates that attenuation of several dB per device could be expected. If 28-cascaded devices were required the cumulative attenuation would be intolerable. It is thus clear that the attenuation of the device is an issue that must be addressed. The following sections present two proposed beamformer configurations and comment on how device attenuation may be countered with each.

A. Phase system architecture A

A simple model where each active phase shifter contributes an equal amount of phase shift to the overall phase shift per antenna element is depicted in Figure 4.

The number of active phase shifters is the desired phase shift divided by the maximum phase shift for a single device plus one. All remaining phase shifters can be switched off $x = 0$. The desired phase shift is then divided equally amongst the active phase shifters, whose x value, and corresponding bias voltage, can be found by numerically solving Equation 1 in [5]. In this approach the active phase shifters have x close to 1, which, as can be seen from Figures 2 and 3, provides the most linear phase and also minimal frequency dependent attenuation.

The array performance was analyzed by calculating the array factor and then determining the beam angle and side-lobe level from this value. The beam squint is defined as $(\theta_{desired} - \theta_{actual})/\theta_{desired}$ and side-lobe level for the system depicted in Figure 4 are presented in Figures 5 and 6. The calculation of x values for each active phase shifter was conducted at 1.4GHz, in anticipation of the bowing of phase response evident in Figure 2. This explains why the beam squint and side lobe levels have nulls at this frequency. Although the choice of this frequency was arbitrary, a more sophisticated means of choosing the frequency at which the phases should be calculated could be devised to optimally balance the errors at both low and high frequencies.

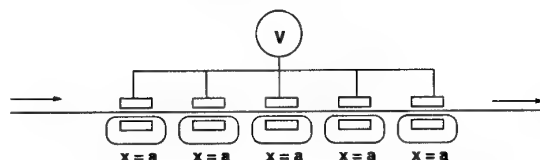


Fig. 4. Schematic diagram of phasing system A. Phase shift is divided equally among active phase shifters.

The beam squint in Figure 5 is at a maximum at low scan angles due to the nature of its definition. For all angles, the beam squint is above 1most of the band. The side-lobe level remains around -13dB in the ideal case while the cumulative phase errors of this system causes the side-lobe level in Figure 6 to rise at large beam angles and higher frequencies. For 60°, the side-lobe level begins to rise towards higher frequencies but remains tolerable at below -10dB.

It would seem that the device could operate reasonably well across the whole band from 200MHz to 1.8GHz with a scan angle of up to 60°. This is due mostly to the fact that the cascaded architecture allows most of the shifters to be operated near $x = 1$ where the frequency dependent phase error is lowest. Note also that near $x = 1$ the frequency dependent attenuation is also a minimum, and so an amplification scheme based on the number of active phase shifters and the x used by each could be devised to compensate for the excess losses.

B. Phase system architecture B

In light of the fact that keeping the phase shifters near $x = 1$ is desirable, an improvement can be made to system architecture A. This improved system is depicted in Figure 7. The number of phase shifters required is chosen

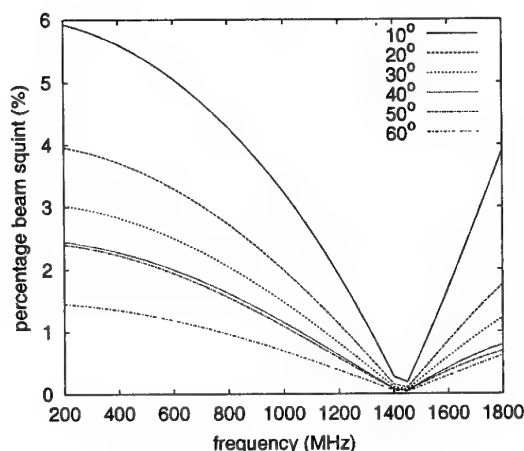


Fig. 5. The simulated beam squint as a function of frequency for a range of beam angles using phasing system A.

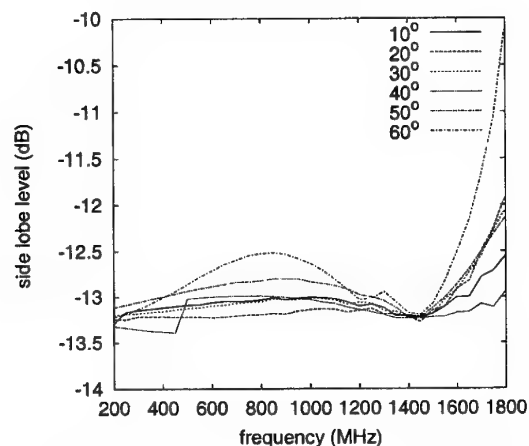


Fig. 6. The simulated side lobe level as a function of frequency for a range of beam angles using phasing system A.

exactly as for system A. The difference between system A and system B is in how the phase shift is distributed across the active phase shifters. The desired phase shift is divided by the maximum phase shift available for a single device to give an integer number and a remainder. The integer number is the number of phase shifters that are set completely on, while the remainder is fine-tuning performed by a single phase shifter device. The remainder phase shift could be a very small value, requiring a low value of x . As is evident from Figures 2 and 2, it is at low values of x that the frequency dependent phase non-linearity and attenuation are most severe and should thus be avoided. These low x values can be avoided by reducing the number of on shifters by one and then dividing the total of the remainder phase shift plus the maximum single device phase shift between the two devices. This scheme has been adopted for System B whenever the remainder phase shift was less than half the maximum available phase shift.

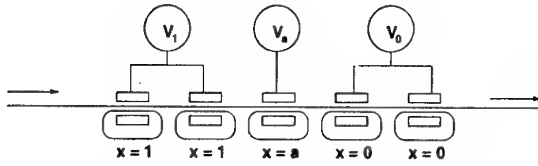


Fig. 7. Schematic diagram of phasing system B.

Figures 8 and 9 present the beam squint and side-lobe level predicted for a phased array based on system B. Notably, the beam squint is an order of magnitude less than System A. The side-lobe level is also improved. Aside from the improved performance offered by this architecture, one of its main advantages is its significant reduction of frequency dependent variations in both phase and magnitude. A device with either $x = 0$ or $x = 1$ has no frequency dependent phase discrepancy or attenuation. Thus regardless of phase shift required, a maximum of two phase shifters will be responsible for limiting the bandwidth of this system. Further if the attenuation of a device in its on state and its off state can be minimized, then the excessive attenuation due to many cascaded devices could be avoided. One possible method to achieve this would be to design the feedback loop with the minimum possible loss, but incorporate an adjustable loss mechanism such as an integrated absorption or leakage modulator. The loss of the loop could then be added only when needed for the active modulators performing the fine-tuning.

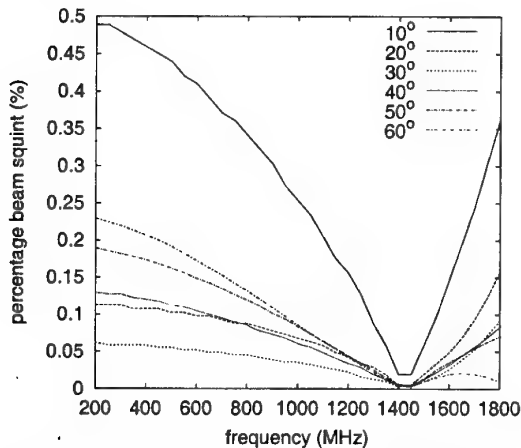


Fig. 8. The simulated beam squint as a function of frequency for a range of beam angles using phasing system B.

IV. CONCLUSIONS

The performance of the integrated photonic RF phase shifter of [6] in a 32 element antenna array has been investigated and it has been found that the device showed great promise for beam steering in large broad band antenna arrays.

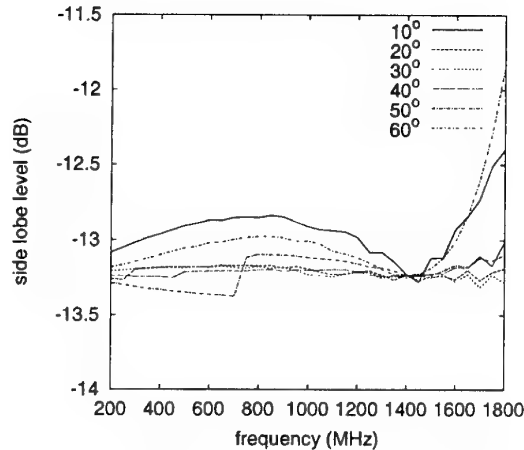


Fig. 9. The simulated side lobe level as a function of frequency for a range of beam angles using phasing system B.

ACKNOWLEDGEMENTS

This work was supported in part by the Australian Research Council.

REFERENCES

- [1] I. Frigyes and A. J. Seeds, "Optically generated true-time delay in phased-array antennas," *IEEE Trans. Microwave Theory Tech.*, vol. 43, no. 8, pp. 2378–2386, Sept. 1995.
- [2] P. J. Matthews, "Practical photonic beamforming," in *IEEE International Topical Meeting on Microwave Photonics (MWP99)*, Melbourne Australia, Nov. 1999, pp. 271–274.
- [3] M. Y. Frankel, P. J. Matthews, and R. D. Esman, "Fiber-optic true time steering in an ultrawide-band receive array," *IEEE Trans. Microwave Theory Tech.*, vol. 45, no. 7, pp. 1522–1526, Aug. 1997.
- [4] W. Ng, A. A. Walston, G. L. Tangonan, J. J. Lee, I. L. Newberg, and N. Bernstein, "The first demonstration of an optically steered microwave phased array antenna using true-time-delay," *J. Lightwave Technol.*, vol. 9, no. 9, pp. 1124–1131, Sept. 1991.
- [5] K. Ghorbani, A. Mitchell, R. B. Waterhouse, and M. W. Austin, "A novel tunable rf phase shifter using variable optical directional couplers," *IEEE Trans. Microwave Theory Tech.*, vol. 47, no. 5, pp. 645–647, May 1999.
- [6] A. Mitchell, K. Ghorbani, M. W. Austin, and R. B. Waterhouse, "Integrated optic RF phase shifter for continuous beam steering at 1–1200 MHz," in *2000 IEEE MTT-Symposium, Boston USA, June 2000*, p. to be presented.
- [7] "'Square Kilometer Array' online documentation," <http://www.atnf.csiro.au/SKA>.
- [8] C. A. Balanis, *Antenna Theory: Analysis and Design*, 2nd Edition, Wiley, New York, 1997.

Beam-Steering of Receiving Array Antenna Using Local Signal Beamformer by Optical Signal Processing

Tomohiro Akiyama, Keizo Inagaki, and Yoshihiko Mizuguchi

ATR Adaptive Communications Research Laboratories

2-2 Hikaridai Seika-cho, Soraku-gun, Kyoto 619-0288, JAPAN

Tel: +81-774-95-1566, Fax: +81-774-95-1508, e-mail: aki@acr.atr.co.jp

Abstract— Beam-steering of receiving array antenna using local signal beamformer by optical signal processing is demonstrated in the X-band. The arriving direction of RF beam is recognized from the location of the light in optical signal processor.

I. INTRODUCTION

Array antennas are expected to be effective for use in advanced wireless communications, such as mobile radio communications, wireless LANs and satellite communications [1]. Recently, the application of photonics technology to microwave array antennas has been studied [2]. An optically controlled phased array antenna is suitable for fiber-optic microwave or millimeter wave links. In particular, coherent optical techniques generate the high-quality microwave carrier signals directly from the frequency offset between the lights by a heterodyne technique [3-8]. The relative phase shifts between adjacent antenna element are introduced in the optical domain where wavelength is considerably short, thus reducing beamformer size requirements. Optical components such as a lens and optical fibers can be combined to make a beamformer using the spatial optical signal processing method. The use of a Fourier transform (FT) lens enable beam forming to be carried out by simply arranging the light source in the front focal plane of the FT lens. However, in coherent optical techniques, most papers have discussed only the transmission mode, very few have discussed the receiving mode. This is because of the difficulty of achieving optical phase stability, i.e. maintaining optical path lengths. Shibata *et al.* proposed the use of optical integrated circuits in order to remove disturbance [7]. However, there is a problem that high power RF input is required, because an efficiency of

optical modulator array is low. Ji *et al.* proposed a local signal beamformer by optical signal processing. In this beamformer, because the reception signal is processed in microwave domain, it is not influenced disturbance of optical domain [8]. However, they confirmed the fundamental principle with only microwave components. They did not prove this method using optical signal processor (OSP).

We constructed a receiving mode of an array antenna using local signal beamformer by optical signal processing, and demonstrated beam-steering of receiving operation in the X-band.

II. RECEIVING OPERATION OF OPTICAL PROCESSING ARRAY ANTENNA [8]

In a reception microwave antenna, usually, LO pumping to the mixer stage of all the receivers is introduced for the frequency conversion, and the beam formation is performed in the RF or IF region. Usually, the LO signal is a pure unmodulated sinusoid wave. Here, we describe a configuration for beam reception by using an LO signal generated by the OSP as used in the transmission mode of antennas [4-6]. Therefore, a large number of variable phase distributions of LO signals can be produced by the tunable lasers in the OSP. Such a large number of LO signals is quite difficult to generate simultaneously by using RF techniques.

The configuration of the receiving mode of the antenna is shown in Fig. 1. As shown in [4-6], the transmitted microwave signals are generated by the frequency-offsets between signal lasers and a reference laser. In the receiving mode of the antenna, the microwaves generated by lights are used as LO signals, and a mixer array is introduced between the output of OSP

and array antenna elements. Their received RF signals are downconverted to IF signals, and only the IF signals whose phase gradient matches that of the LO signals can be maximally summed by the IF combiner before entering the receiver. The basic principle can be proved as follows.

The RF signals received by an arbitrary equispaced linear antenna element n are given by

$$E_{RF_n} = A e^{-j\omega_{RF}t - jn\beta} \quad (1)$$

and the LO signals generated by the OSP feed are given by

$$E_{LO_n} = B e^{-j\omega_{LO}t - jn\alpha} \quad (2)$$

Therefore, the IF signals generated by a microwave mixer can be written as

$$E_{IF_n} = A B e^{-j(\omega_{RF} - \omega_{LO})t + jn(\alpha - \beta)} \quad (3)$$

where A and B are applied elemental amplitude weights, ω_{RF} and ω_{LO} are the frequencies of RF signals received by the antenna and LO signals generated by the OSP, and α and β are phase-steps of RF and LO signals with the same phase fronts, respectively.

Considering only the first-order difference frequency output of mixer and the case of constant A and B , the summation of these IF signals in Eq. (3) will be combined by an IF power combiner as

$$\begin{aligned} E_{IF} &= A B e^{-j\omega_{IF}t} \sum_{n=0}^{N-1} e^{jn(\alpha - \beta)} \\ &= A B e^{-j\omega_{IF}t + j(N-1)\sigma/2} \frac{\sin N\sigma/2}{\sin \sigma/2} \end{aligned} \quad (4)$$

where $\omega_{IF} = \omega_{RF} - \omega_{LO}$ is IF band frequency, and $\sigma = \alpha - \beta$ is the phase-step of IF signals.

We note that the maximum value of the fractional part in Eq. (4) is N , when $\sigma = l \cdot 2\pi$, where $l = 0, 1, 2, \dots$. Therefore, the maximum value of the IF signal power sum only appears when the phases of the RF and LO signals are equal. Consequently, the same frequency IF output from all mixers should be in phase for a signal received at the array antenna from a particular direction, and will produce a maximum output from the IF combiner at a particular RF frequency. Signals arriving from other directions have a variety of phases and suffer partial cancellation. The LO signal beamformer using OSP functions as a matched filter.

When multiple beams of the same frequency are received from different directions, they can be discriminated in the IF frequency domain by using different-frequency and different-phase distributions of LO signals which are created by OSP, and the beam directions

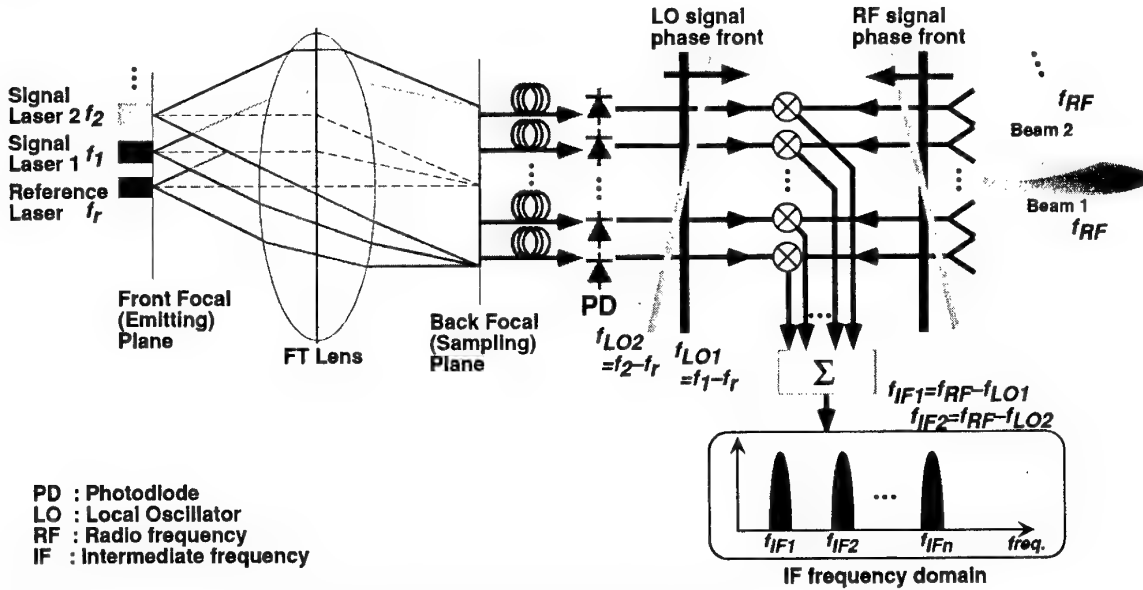


Fig. 1. Configuration of the receiving mode of optical signal processing array antenna.

summed by the IF combiner, and measured by the spectrum analyzer.

In this experiment, the frequencies of LO and RF signals were in the X-band, and the IF signal frequency f_{IF} was 1.0 GHz. The receiving array antenna was a 0.6-wavelength-spaced four-element linear array antenna, and each element was a circular patch antenna. The reference laser was connected to the port #0 of the emitting waveguide and the signal laser to the ports from #1 to #5. When the signal laser was connected to the port #3, the main beam was steered in the front direction. We changed the connection port with the signal lasers using the optical channel selector. Fig. 3 shows the measured received IF power level of the optical signal processing array antenna, that is the RF antenna pattern. Each line represents a port number of the waveguide. Changing the port transformed the radiation pattern of the optical beam in the OSP and tilted the phase distribution of the LO signal. The direction of the received beam was steered by changing the port of the waveguide, and the expected directions were achieved.

IV. CONCLUSIONS

We constructed a receiving mode of an array antenna system using local signal beamformer by optical signal processing, and demonstrated beam-steering of the received RF signal in the X-band. The availability of the receiving mode was confirmed. Furthermore, a multibeam reception array antenna can be possible by using different frequency of LO signals same as the multibeam transmitting antenna [6], and by discriminating arriving direction in downconverted IF domain [8].

ACKNOWLEDGMENTS

The authors would like to thank Dr. B. Komiya, president of ATR Adaptive Communications Research Laboratories, and Dr. T. Ohira, head of Department 3, for their continuous encouragement, and Dr. I. Chiba of Mitsubishi Electric Corporation for his helpful discussions.

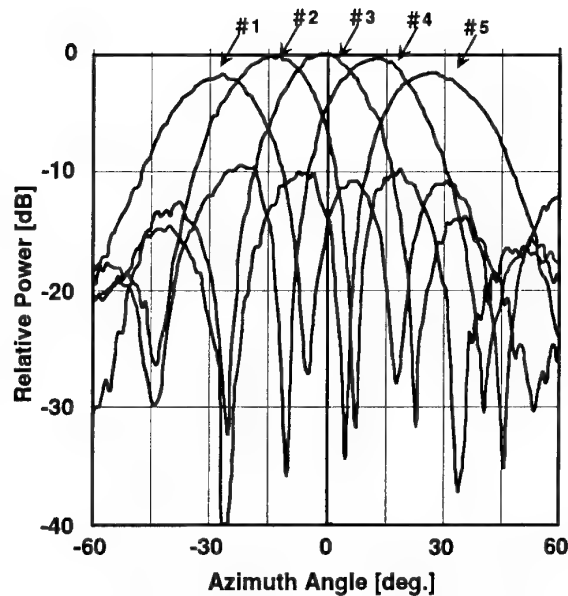


Fig. 3. Measured IF power level of the receiving mode of the optical signal processing array antenna.

REFERENCES

- [1] K. Inagaki, "Wideband personal communication system using optical signal processing array antenna," *MWE'97 Microwave Workshop Digest*, pp. 135-140, 1997.
- [2] P. J. Matthews, "Practical photonic beamforming," *International Topical Meeting on Microwave Photonics, MWP'99*, pp. 271-274, 1999.
- [3] G. A. Koepf, "Optical processor for phased-array antenna beamformation," *Optical Technology for Microwave Applications, SPIE*, vol. 477, pp. 75-81, 1984.
- [4] K. Inagaki, Y. Ji, O. Shibata and Y. Karasawa, "Optical signal processing array antenna studies in ATR for advanced wireless communication system," *International Topical Meeting on Microwave Photonics, MWP'97*, pp. 27-30, 1997.
- [5] T. Akiyama, K. Inagaki and Y. Mizuguchi, "Beam-steering and multibeam formation of Ku-band phased array antenna using optical signal processing beamforming network," *International Topical Meeting on Microwave Photonics, MWP'99*, pp. 173 - 176, 1999.
- [6] T. Akiyama, K. Inagaki and Y. Mizuguchi, "Multibeam optical signal processing array antenna using optical waveguide arrays and lens," *Proceeding of the 2000 International Symposium on Antenna and Propagation, ISAP'2000*, 2000, to be published.
- [7] O. Shibata, K. Inagaki, and Y. Karasawa, "Beam-forming network characteristics of spatial optical signal processing array antenna for multibeam reception," *IEEE MTT-S International Microwave Symposium, TH2C-3*, pp. 1371 - 1374, 1998.
- [8] Y. Ji, K. Inagaki, O. Shibata, and Y. Karasawa, "Receive mode of optical signal processing multibeam array antennas," *IEEE Microwave and Guided Wave Letters*, vol. 8, No. 7, pp. 251 - 253, 1998.

A Novel Two-Element Active Antenna for varying the Direction of Microwave Radiation by Optical Illumination

Youhei Ueno, Motohira Katsuragi and Yukio Yamamoto, Member IEEE

Department of Electrical Engineering and Electronics,

Faculty of Engineering, Osaka Sangyo University

3-1-1 Nakagaito, Daito, Osaka, 574-8530, JAPAN

Phone:+81-72-875-3001, Fax:+81-72-870-8189, E-mail:yamamoto@elec.osaka-sandai.ac.jp

Abstract:

This paper proposes a novel two-element active antenna for optical scanning beam in X-band. A MESFET in the element antenna works both as a negative resistance and an optically controllable reactance. Laser illumination to the MESFET in one of the antenna elements causes a shift of its free-running frequency and creates a phase difference between the oscillations of the two antenna elements, therefore, the radiation beam can be scanned. In experimental results, the beam direction has been scanned by 26 degrees optically.

1. Introduction

Typical studies in microwave photonics include basic optical-microwave interactions, photonic devices operating at microwave frequencies, photonic control of microwave devices, high-frequency transmission links, and the use of photonics to implement various functions in microwave systems[1][2].

In telecommunication systems, another recent key technology is quasi optical power combining through the free space. Usually, the beam scanning is accomplished by giving a constant phase progression in the array elements, using as many phase shifters as array elements.

York and Liao developed loosely-coupled quasi-optical oscillator arrays in which the constant phase progression can be established by slightly detuning the peripheral array

elements, while maintaining mutual synchronization[3][4].

Shimasaki and Tsutsumi reported that laser illumination to a FET caused the shift of 36 MHz in the free running frequency of the single oscillator and the radiation beam was scanned due to a phase difference of arrayed circular patch antennas. As the result, however, the beam direction was changed by only 3 degrees[5].

The authors reported that S_{22} -parameters for a MESFET can be widely changed and its input reactance looking into the drain of the MESFET is also remarkably changed by laser illumination. Therefore, an optically tunable oscillator can be constructed using this reactance of the MESFET, which also works as a negative resistance[6]. In the case of negative resistance circuit included in a bandpass filter, an optical shift of 123 MHz in the oscillation frequency was observed[6].

In this paper, as an application of the optically controlled negative resistance circuit to active antennas, a novel two-element active antenna will be proposed and its scanning area will be remarkably improved in comparison to the previously reported results[5].

2. Principle and design method

In the special case of the use of only two element arrays, following York[4], the synchronized frequency (ω_0) can be written as

$$\omega_A = \omega_0(1 + \varepsilon \sin \Delta\theta) \dots (1)$$

$$\omega_B = \omega_0(1 - \varepsilon \sin \Delta\theta) \dots (2)$$

$$\varepsilon = E / (2Q) \dots (3)$$

where ω_A and ω_B are free-running frequencies of the two elements A and B, E is a coupling coefficient, Q is the Q-factor of the oscillator, and $\Delta\theta$ is a constant phase progression between the elements. The equations show that the radiation pattern can be scanned by adjusting the two free-running frequencies.

Using the above mentioned MESFET oscillator, we can change the direction of the microwave beam by varying the power of the optical laser illumination on one of the MESFETs in a two-element active antenna.

The single-element antenna can be composed of a rectangular patch antenna and the MESFET negative resistance circuit used in the bandpass filter[6].

3. Experimental setup

The schematic of a single active antenna element is shown in Fig. 1. The length and the width of the rectangular patch are 9.07 mm and 9.40 mm, respectively. The resonance frequency is actually 10.082 GHz.

The circuit is fabricated on a woven-glass-reinforced Teflon substrate with a thickness of 0.762 mm and a dielectric constant of 2.55. The MESFET used was NE72084B (NEC Co.) with its cover removed. The gate of the MESFET is connected to the termination (82Ω) through a low-pass filter whose cutoff frequency is 8.8 GHz. The source of the MESFET is grounded through a reactance.

Figure 2 shows the arrangement of the two-element active antenna. The two elements A and B are arranged symmetrically at a distance of d and coupled to each other through the radiation.

The coupling angle is adjustable by varying the distance (d), therefore, it is possible to

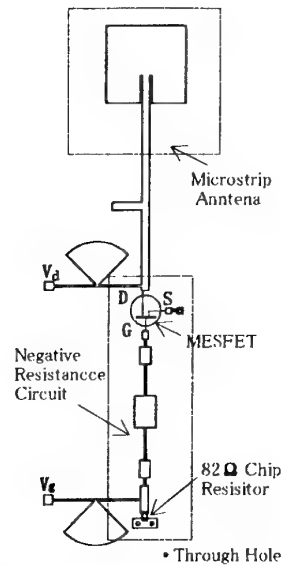


Fig. 1, A single active antenna element.

select the suitable mode between an anti-phase and an in-phase oscillations. The shortest distance (d) is 19.4 mm for the in-phase mode in this experiment, therefore, 19.4 mm has been adopted as the distance (d) in this report. It corresponds to the condition that $d = 0.6\lambda_0$,

where λ_0 is the free space wavelength of the synchronized frequency. The oscillation condition of each element is different in spite of using the same type MESFETs. Therefore, the synchronization has been accomplished by varying the DC bias voltage to set their intrinsic free-running frequencies close to each other.

In the case for element B, a hole of 2.3 mm in diameter is bored at the position of the MESFET on the substrate and the MESFET is mounted so as to illuminate the gate area from the back side through the hole.

The radiation pattern is scanned by merely changing the free-running frequency of the element B with the optical illumination.

The light source is a semiconductor laser LT015MDO (Sharp Co.) whose wave length is 830 nm. Using a small lens, the light is focused on the gate area. The radiated

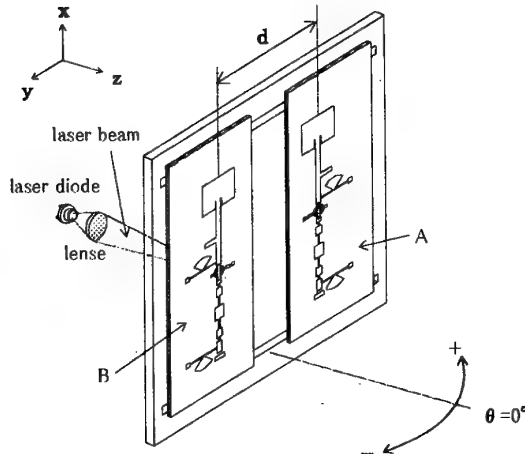


Fig. 2. Arrangement of the two element active antenna.

microwave is detected by a pyramidal horn antenna 100 cm apart from the active antenna, and the frequency and the power are measured with a spectrum analyzer.

4. Experimental results

4-1 Single-element antenna

Figure 3 shows the dependences of the oscillation characteristic of the single element on illuminated optical power. The MESFET conditions are following: the gate voltage is -1.15 V, the drain voltage is 2.44 V, the drain current is 22.31 mA. As the illumination power is increased from 0 to 19.8 mW, the oscillation frequency shifts from 9.974 to 9.953 GHz, and the relative output power is increased from -21.4 to -18.8 dB.

Figure 4 shows the measured radiation pattern in H-plane for the single element antenna. The solid line and the dashed line represent the co-polarization and the cross-polarization characteristics, respectively. The cross-polarization level is more than 10 dB smaller than the co-polarization level within ± 35 degrees from the center direction. The pattern is not symmetrical, and the reason for this is possibly due to the fact that the fabricated element antenna has an asymmetric

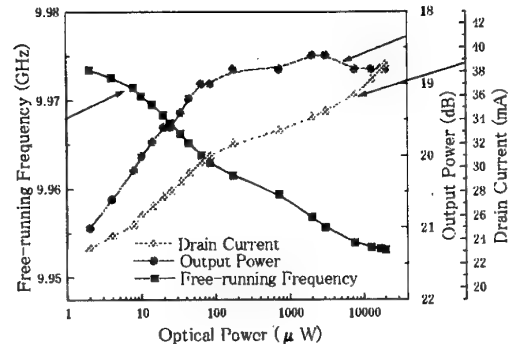


Fig. 3. Frequency shift, relative output power and drain current as a function of the illuminating optical power.

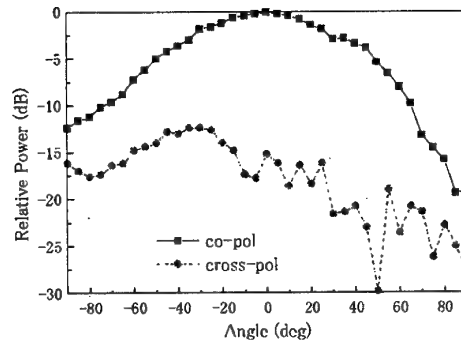


Fig. 4. H-plane pattern of a single active antenna element

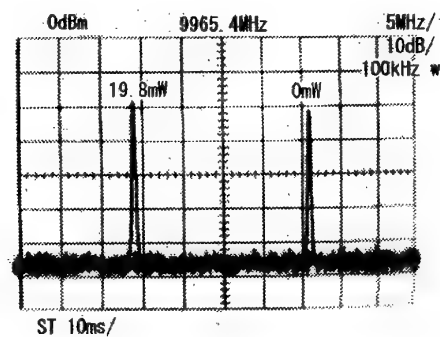


Fig. 5. Oscillation spectrums of a single active antenna element when the illuminating laser powers are 0 and 19.8 mW.

pattern.

Figure 5 shows an example of the oscillation spectrum and its shift due to laser illumination. The drain and gate voltages are 2.47 V and -1.15 V, respectively.

The observed frequency shift is 22.1 MHz from 9.9758 GHz to 9.9537 GHz, when the illuminating laser power is increased from 0 to 19.8 mW.

4-2 Two-element antenna

Figure 6 shows the radiation patterns in H-plane for a two-element antenna when the element B is illuminated with the laser power 0, 20.5 μ W and 3.06 mW. The drain and the gate voltages for the element A are 1.90 V and -0.57 V, respectively. For the element B, the gate voltage is kept at -1.15 V, however, laser

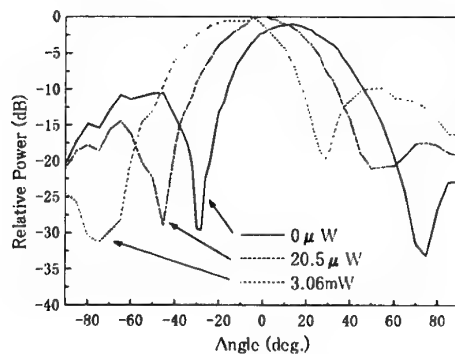


Fig. 6. Radiation pattern shift for illuminating optical power.

illumination causes the increase in the drain current from 22.2 mA to 34.8 mA when the laser power increases from 0 to 3.06 mW. Concurrently, the free-running frequency of the element B is shifted by 17.9 MHz from 9.9733 to 9.9554 GHz. As the result, the beam direction is scanned by 26 degrees from 13 to -13 degrees due to the laser power increasing from 0 to 3.06 mW.

5. Conclusions

The experimental considerations on the two-element active antenna for optical scanning beam in X-band have been presented. A MESFET in the element antenna works both as a negative resistance and an optically controllable reactance. First, it was confirmed that laser illumination to the MESFET in one of the element antenna causes a shift of its free-running frequency. Second, creation of a phase difference between their oscillations was also confirmed, because the radiation beam was scanned.

Third, the beam direction has been scanned by 26 degrees optically. This scanning angle is remarkably large.

References

- [1] "Special Issue on Microwave and Millimeter Wave Photonics," IEEE Trans. Microwave Theory Tech., MTT-43, no.9 part 2, pp.2181-2441, Sep. 1995.
- [2] "Special Issue on Microwave and Millimeter-Wave Photonics," IEEE Trans. Microwave Theory Tech., MTT-47, no.7 part 2, pp.1149-1397, July 1999.
- [3] P. Liao and R. A. York, "A New Phase-Shifterless Beam-Scanning Technique Using Arrays of Coupled Oscillators," IEEE Trans. Microwave Theory Tech., MTT-41, no.10, pp.1810-1815, Oct. 1993.
- [4] R. A. York, "Nonlinear Analysis of Phase Relationships in Quasi-Optical Oscillator Arrays," IEEE Trans. Microwave Theory Tech., MTT-41, no.10, pp.1799-1809, Oct.1993.
- [5] H. Shimasaki and M. Tsutsumi, "Optical Control of Radiation Characteristics of Coupled Active Antennas," 1998 Asia-Pacific Microwave Conference Proceedings, pp.1059-1062, Dec. 1998.
- [6] Y. Yamamoto, Y. Imon, S. Mikumo and M. Katsuragi, "Tuning a Bandpass Filter by Optical Control of a Negative-Resistance Circuit," IEEE Trans. Microwave Theory Tech., MTT-46, no.12, pp.2006-2010, July 1999.

Novel Photonically Controlled Antenna for MMW Communications*

George W. Webb, Susan Angello, Wayne Vernon, Mario S. Sanchez¹, and Stephen C. Rose²

Innova Laboratories, Inc.

6370 Lusk Blvd., F111

San Diego, CA 92121 USA

Tel: (858) 452-8760 Fax: (858) 452-0478 e-mail: gwwebb@innova-labs.com

Abstract - We describe a new optically-controlled, narrow beam antenna for point to point communications. A computer controlled light source photo-injects a spatially varying plasma into a photo-conducting wafer for MMW beam control. Antennas based on this approach will be inexpensive and offer many advantages.

Introduction

Scanning antennas with narrow beams are required for many point to point communications applications. Mechanically scanned antennas are often slower than desired while electronically scanned antennas, which employ thousands of phase shifters, are too expensive. For these reasons, alternative scanning methods have been of recent interest [1-9, also see 10,11].

We have developed a non-mechanical MMW scanning technique which employs a light-modulated photoconducting antenna [3-4, 7, 8]. The technique has been demonstrated at 35 GHz [7] and 94 GHz [7,8]. Here we describe its application to a compact communications antenna at 20 GHz. Communications antennas based on this approach promise to be fast, inexpensive, and easily controlled.

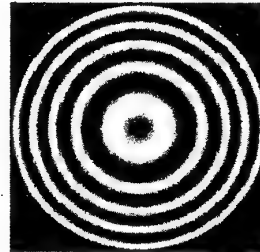
Transient Plasma-Based Fresnel Zone Plates

It is well known that Fresnel zone plates work by blocking out of phase radiation [12]. Our scanning technique is based upon a *transient* Fresnel zone plate. In this approach a spatially varying density of charge carriers is created by optical injection of plasma into a semiconductor or photoconductor wafer which blocks MMW radiation.

Figure 1a) shows the relative phase of a ray emitted from a source *S*, which passes through an aperture, and arrives at a detection point *P*. The phase of rays is plotted with a gray scale on the plane of the aperture at the point where the ray passed through the aperture. Here *S* and *P* have been chosen to be *collinear* with the aperture. Those rays with phase represented from white to gray are taken to be in-phase. Conversely, those rays with phase from gray to black are out-of-phase. If the out-of-phase rays are blocked, then the only rays arriving at *P* would be in-phase and a large increase in intensity at *P* would result. Our approach employs a photo-injected plasma to block the out-of-phase rays.

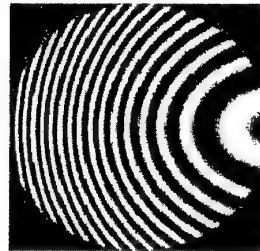
PHASE PLOTTED ACROSS
13.5" DIAMETER APERTURE

20 GHz Beam, 0 deg. Off-Axis



a

20 GHz Beam, 45 deg. Off-Axis



b

Figure 1. Gray scale plot of ray phase at detection point plotted on plane of aperture where ray went through aperture; source at 17.8 cm from 35 cm diameter aperture, distant detector, 20 GHz radiation. a) Detector 0° off axis, b) Detector 45° off axis.

The relative phase distribution displays the relative symmetry of the source, detection point and the aperture. In particular, the relative phase depends on the angle that *P* makes with the axis of the aperture. If the relative position of the detection point *P* is moved off-axis, then the distribution of relative phase at *P* is changed. Figure 1b shows the phase distribution when *P* is moved to 45° off-axis, all other parameters remaining

* Research supported under DARPA contract no. DAAH-98-C-R060

the same. Evidently, to send a beam to the direction 45° off axis requires that a different ray distribution must be blocked; accordingly it is necessary to change the light pattern and thus the spatial distribution of the plasma. Therefore, we wish to integrate a light source which has a high degree of controllability with a photoconducting material in which a plasma can be photo-injected.

Composite Wafer

We have investigated a variety of materials for the photoconductor. Experimental results are given for Si wafers with dark resistivity in the range $1000\ \Omega\text{-cm}$, diameter of 150 mm, and thickness of 1.1 mm. An approximate antenna diameter of 35 cm was chosen for the frequency and beam diameter desired. Since the largest wafer available with the necessary properties is 15 cm, a composite wafer was fabricated, as shown in Figure 2.

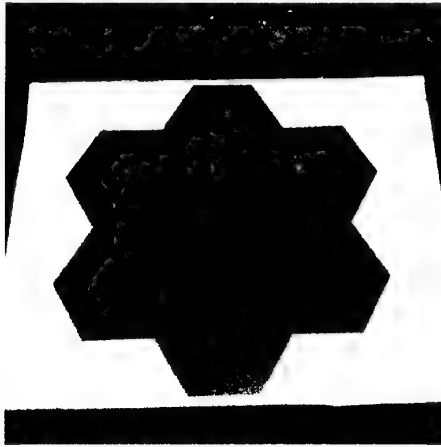


Figure 2. Composite wafer assembled from seven Si hexagons cut from 15 cm circular wafers.

Light source

For photo-injection, light of wavelength below the band gap is used. As described earlier [7], a programmable light array (PLA) projects a light pattern onto the back of the wafer. A front feed transmits MMW through the wafer which are reflected at the back of the wafer by a MMW reflector that is transparent to the light array [7]. In this way the MMW make a double pass through the wafer.

Figure 3 displays a PLA consisting of 3046 LEDs having a peak LED output at $0.88\ \mu$. The light array electronics is controlled by a PC through a fiber optic interface which can switch the lights on/off at the maximum rate of 240 MHz (240M lights/sec.) The maximum rate is thus 80K frames per second; however the overall scan rate is limited by the properties of the photoconducting material to a few kHz. An advantage of the fiber optic interface is that it allows the LED electronics package to be made more compact. The overall thickness of the LED array and electronics, neglecting ancillary components, is 6 cm.

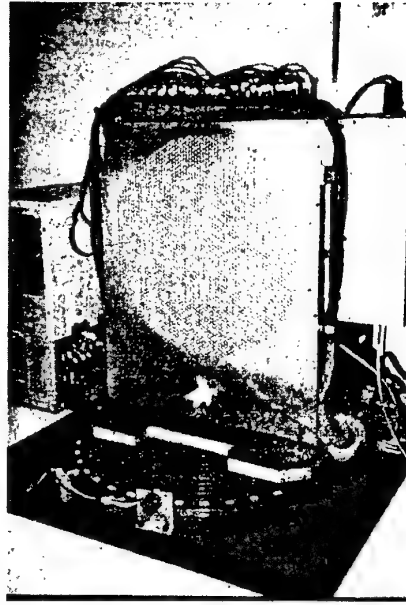


Figure 3. Programmable light array 35 cm diameter with 3046 infrared emitting LEDs.

Assembled Antenna and Feeds

The assembled antenna with wafer assembly and feed is shown in Figure 4. A personal computer (PC), used for antenna control, is at the left of the antenna. Fiber optic control lines connect the antenna with a custom fiber optic interface board in the PC. A standard pyramidal feed horn is positioned in front of the composite wafer and directed at the wafer. A 20 GHz receiver is connected to the feed.

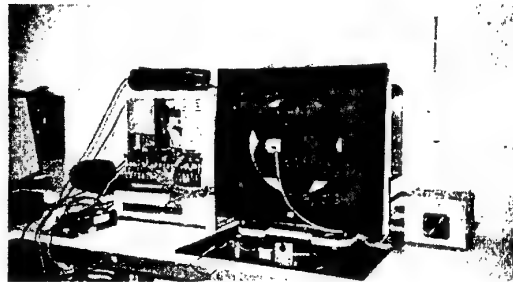


Figure 4. Assembled antenna with control PC and standard feed horn.

As configured in Figure 4, the overall thickness of the light array and feed horn is 28 cm. The feed horn comprises 22 cm of the overall thickness. For some applications it is desired to minimize overall thickness. Accordingly, a Cassegrain feed assembly was fabricated in place of the standard feed. A side view of the antenna with the Cassegrain feed and sub-reflector is shown in Figure 5. With the Cassegrain feed, overall antenna thickness is reduced to 20 cm.



Figure 5. Side view of antenna with Cassegrain feed assembly. A 7.6 cm diameter planar sub-reflector and its feed horn can be seen.

Results

A series of measurements were made with the antenna configured as a receiver. It is known [7, 8] that the technique obeys reciprocity, functioning equally well as a transmitter. Both the Cassegrain feed and standard feed were used. The two feeds behaved similarly, with the Cassegrain having an approximate 2 dB penalty in power. Figure 6 shows a typical two-dimensional scan, in this case with the Cassegrain feed.

2D Scan, 1deg grid, Cassegrain Feed, 19.33 GHz



Figure 6. 19.33 GHz receive beam scanned on $30^\circ \times 30^\circ$ square grid with 1° grid spacing at 1000 Hz. Transmitter 20 m at $(0^\circ, 0^\circ)$.

In Figure 6, the transmitter is co-linear with the antenna axis and 20 m away. The beam was hopped on a $30^\circ \times 30^\circ$ square grid with a 1° grid spacing at a rate of 1000 hops/second. The main lobe is clearly evident

when the receive beam is directed at the transmitter, as are the side lobes and nulls when the light pattern is changed to direct the beam off-axis.

Beam width and maximum scan angle were measured. E-plane beam profile data are shown in Figure 7. The beam is raster scanned by changing the light pattern in software. There are five separate beam scans with the transmitter moved off-axis to 0° , 15° , 30° , 45° , and 60° and the beam scanned from -10° to $+60^\circ$. Peak to side lobe ratio is about 15 dB and beam width is as narrow as 3.5° . Main lobe power decreases by 3 dB at 45° and by 5 dB at 60° .

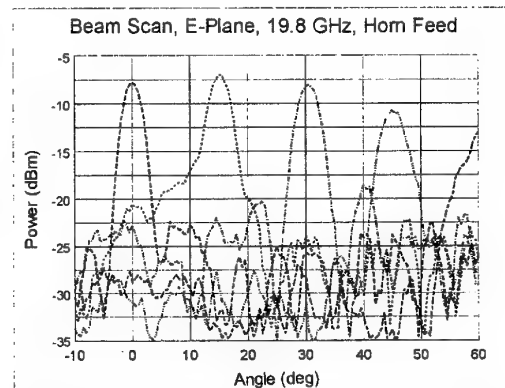


Figure 7. E-plane beam scans from -10° to 60° with the relative angle varied between antenna and remote transmitter. A feed horn is 18 cm from the antenna. The beam is scanned at 1000 Hz by changing the light pattern with software.

Figure 8 shows the received power when the beam is fixed at five different angles and the antenna rotated (antenna scan) with respect to the transmitter. This procedure maps out the true sidelobe structure for a given fixed beam. Once again beam width is about 3.5° with modest broadening of off axis beams. In general, it is seen that beam scan and antenna scan data are similar.

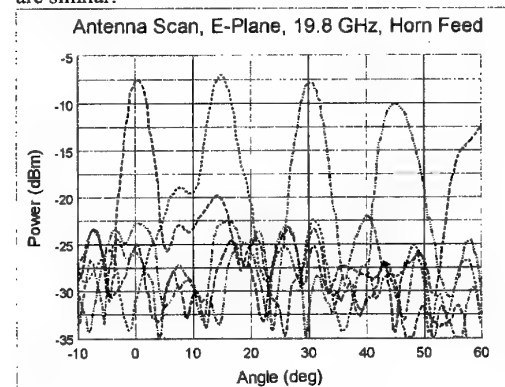


Figure 8. E-plane antenna scans from -10° to 60° with five different fixed beams. The relative angle is varied between antenna and transmitter. A feed horn is 18 cm from the antenna.

Discussion and Conclusions

In this work, results were reported for a new antenna for MMW communications based on our photo-injected plasma technique for beam control. This antenna operates at a lower frequency, is larger in diameter, relatively more compact, and has a greater scan angle than previous antennas built with this technique.

The antenna was operated in a receiving mode over the range from 18.5 to 21 GHz. This frequency range was limited by the particular receiver attached to the antenna. The receive frequency of 18.5 GHz is the lowest frequency used with the technique so far. In other experiments reciprocity has been demonstrated for the technique showing that it works equally well as receiver or transmitter [7].

The new programmable light array contains more LEDs (3000), and is larger in diameter (35 cm) than previous ones we have built. A composite technique for producing new larger 35 cm diameter wafers was developed. This larger overall diameter of the antenna allowed a narrow beam width of 3.5° to be maintained at the lower frequencies near 20 GHz.

Even though the array is larger in diameter, a new fiber optic antenna-computer interface allowed the antenna to be made more compact than previously; the thickness of the light array with drive electronics is only 6 cm. With a Cassegrain feed, the overall antenna thickness is 20 cm and 28 cm with a standard horn feed.

One- and two-dimensional scanning data were presented. In these measurements the beam was hopped at up to 2000 Hz or hops per second. It was found that *beam scan* and *antenna scan* patterns were quite similar. Maximum scan angle was determined to be $\pm 45^\circ$ using a 3dB criterion. However, useful scanning was observed out to $\pm 60^\circ$.

Approximately 50% of the rays are blocked compared to a full aperture. In addition, the remaining in-phase rays have a distribution of phases over 180° compared to a fixed parabolic reflector or a phased array with perfect control over phase. We estimate that the maximum efficiency is approximately -10 dB as presently configured.

The antenna uses relatively inexpensive components. Therefore, it is inferred that when antennas are produced in quantity, they will be relatively inexpensive. Scanning communication antennas based on this approach promise to be fast, inexpensive, and easily controlled. Their advantages are the ability to rapidly steer the beam over a fixed reflector, and at much lower cost than a phased array.

1 Now at Sony Corp

2 Now at Stanford University

Acknowledgements

We thank Phil Datte for valuable guidance and assistance with the fiber optic interface. It is a pleasure to thank Joe Mancini for valuable discussions and advice on applications, and for constant encouragement.

References

- [1] M. Matsumoto, M. Tsutsumi, and N. Kumagai, "Radiation of millimeter waves from a leaky dielectric waveguide with a light-induced grating layer," *IEEE Trans. Microwave Theory Tech.* vol. MTT-35, no. 11, pp 1033-1042, 1987.
- [2] P.J. Stabile, A. Rosen, D. Gilbert, R.E. Marx, M.T. Duffy, G. Looney, G. Evans, J.C. Connolly, W. Janton, N. Hughes, and J.K. Butler, "Optically controlled millimeter-wave dielectric waveguides using silicon-on-sapphire technology," *CLEO 92*, pp.336-338.
- [3] G.W. Webb and L.H. Pinck, "Light-Controlled MMW Beam Scanner", *Proc. 1993 SBMO International Microwave Conference*, Vol. II, Sao Paulo, Brazil, IEEE Cat. No. 93TH0555-3, p. 417.
- [4] G.W. Webb and L.H. Pinck, "MMW Beam Scanner Controlled by Light", *Proc. Workshop on Millimeter-Wave Power Generation and Beam Control*, Huntsville, AL, Special Report RD-AS-94-4, U.S. Army Missile Command, p. 333.
- [5] A.R. Rosen, P.J. Stabile, R. Amantea, W.J. Janton, D.B. Gilbert, and J.K. Butler, "Active Millimeter Wave Antenna Array Steered by Optically Induced Gratings," *Proc. Workshop on Millimeter-Wave Power Generation and Beam Control*, Huntsville, AL, Special Report RD-AS-94-4, U.S. Army Missile Command, p. 341.
- [6] V.A. Manasson, L.S. Sadovnik, V.A. Yepishin, and D. Marker, "An Optically Controlled MMW Beam-Steering Antenna Based on a Novel Architecture," *IEEE Trans. On Microwave Theory and Techniques*, 45 1497 (1997).
- [7] G.W. Webb, S.C. Rose, M.S. Sanchez, J.M. Osterwalder, "Experiments on an Optically Controlled 2-D Scanning Antenna," 1998 Antenna Applications Symposium, Allerton Park, Monticello, IL, September 16-18, 1998, p. 99.
- [8] G.W. Webb, W. Vernon, M.S. Sanchez, S.C. Rose, and S. Angello, "Optically Controlled Millimeter Wave Antenna," *Proceedings International Topical Meeting on Microwave Photonics*, Melbourne, Australia, November 17-19, 1999, p.275.
- [9] R.A. Sparks, N. Slasby, J. Prince, and J. Munro, "Eight Beam Prototype Fiber Optic Rotman Lens," *ibid.*, p.283.
- [10] D.S. Lockyer, J.C. Vardaxoglou, and M.J. Kearney, "Plane Wave Transmission Response of Selectively Doped and Micromachined Silicon Wafer Under Optical Illumination," *ibid.*, p.169.
- [11] G. Delgado, J. Johansson, A. Larsson, and T. Andersson, "Optically Controlled Spatial Modulation of (Sub-) Millimeter Waves Using *nipi*-Doped Semiconductors," *IEEE Microwave and Guided Wave Lett.* 5, 1051 (1995).
- [12] G.R. Fowles, *Introduction to Modern Optics*, 2nd Ed. Dover Publ. New York, 1975.

FAST MODULATION PERFORMANCE OF UNCOOLED SEMICONDUCTOR LASERS

R.V. Penty, A. B. Massara, M. Webster, K. A. Williams and I. H. White

Centre for Communications Research, University of Bristol, Merchant Venturers Building,

Woodland Road, Bristol, BS8 1UB, United Kingdom

Tel: (+44) 117 954 5187 Fax: (+44) 117 954 5206

e-mail: Richard.Penty@bristol.ac.uk

Abstract: This paper reviews the current state of the art of uncooled, high bandwidth lasers. It explains why high bandwidth is difficult at high temperatures and presents some possible routes to improve on current technology.

Introduction

The explosion in the internet has placed great demands on the physical infrastructure tasked with transporting the data from router to router and from router to user. Whilst router to router traffic is generally handled by the upper layers of the telecommunications network, usually over WDM with well-understood technology, the ever-increasing demand for bandwidth by the user has meant that optical communications is penetrating ever closer to the desktop and the home, such access technology traditionally being over copper based links.

This has led to datacommunications standards, such as Gigabit Ethernet [1], being set where the predominant physical layer transport is over fibre for the first time. Indeed it is expected that 10 Gigabit Ethernet will be standardised in 2001 to meet the growing network demand.

The requirements placed on optical sources in datacommunications networks are very different from those in telecommunications systems. The fact that the cost of an optical source will be met by a single user in a datacommunications network, rather than shared between many as in a telecommunications scenario, results in severe pressure to drive down the cost. This results in much activity in low cost packaging, such as designing a laser for high efficiency and tolerance for coupling to optical fibre to allow pick and place positioning rather than the more expensive active alignment techniques employed for telecoms lasers. However, probably the requirement with most bearing on the high bandwidth operation of lasers for e.g. 10 Gigabit Ethernet is the need for uncooled operation to enable the removal of the thermo-electric cooler employed in telecoms laser packages. The standards require either 0-70 °C or -40-85 °C operation and this may have severe consequences for datacommunications lasers unless careful design is employed.

Datacommunications standards specify two wavelength regimes for operation. The short wavelength regime employs lasers operating around 850nm over multimode fibre and here VCSELs are generally employed. For improved transmission distance over multimode fibre and for extended reach over single mode fibre, lasers operating around 1300nm are used. Currently edge emitting lasers are employed but there is a great deal of activity towards the commercialisation of 1300nm VCSELs.

1300nm Uncooled Lasers

Ideally lasers would not have any temperature dependent characteristics. However, lasers exhibit both temperature dependent threshold currents and bandwidths. The severity of these effects depends on the material systems employed in the laser. Current 1300nm lasers employ the InGaAsP materials system.

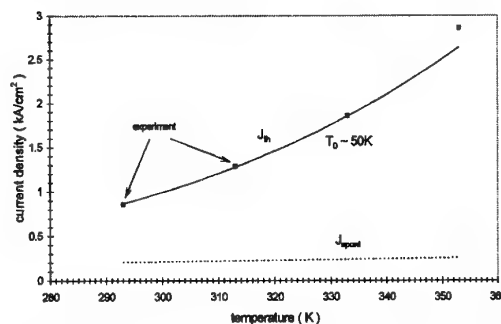


Figure 1: Dependence of threshold current density on temperature (points – experimental, line – first principles theoretical)

Figure 1 shows the temperature dependence of the threshold current density of a typical 1300nm InGaAsP laser. As can be seen the threshold rises by nearly a factor of three over a 20-85°C temperature range. The solid line shows the results of drift diffusion modelling of the laser. The simulations show a significant (up to 80-90 %) Auger component of the threshold current. Such a high proportion of the Auger recombination is partly due to the charge neutrality violation found in the quantum wells. The effect on the bandwidth is shown in figure 2 over a similar temperature range. A small signal 3dB bandwidth of 5.5GHz is measured at room temperature dropping to 3.6GHz at 85°C.

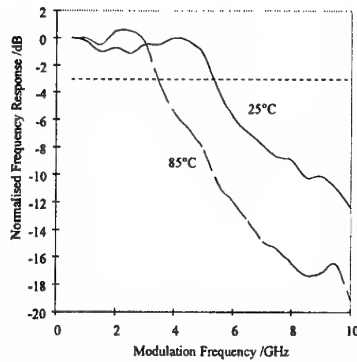


Figure 2: Small signal response as a function of temperature with laser bias 15mA above threshold

Limitations of InGaAsP Based Lasers

1300nm InGaAsP lasers exhibit quite severe temperature effects. The quantum wells employed in these lasers have to have relatively low barrier heights to achieve emission at 1300nm. As the temperature rises, this results in a reduction in the material gain. The consequence of this and other temperature dependent effects (such as Auger) is an increase in threshold current and (because of reduced differential gain) a reduction in bandwidth [2]

Uncooled Operation of InGaAsP Device Bandwidth

Having understood the bandwidth limitation mechanisms, it is clear that one route to maximising the bandwidth is to minimise the threshold carrier density in the quantum well. This will have the threefold effect of reducing the Auger recombination rate, the thermionic emission leakage rate and of obtaining a relatively high value of differential gain. In InGaAsP devices, the obvious route to achieving this is to increase the number of quantum wells.

An InGaAsP-InP ridge-waveguide laser was supplied from Agilent Technologies. Its active region contained seven 0.8% compressively strained quantum wells – a greater number was not possible at the time because of morphology problems associated with accumulated strain in the growth process. The 280μm long Fabry-Perot laser had one facet HR coated to 88% (to further reduce the operating carrier density) and the output facet was cleaved. The laser emitted with a centre wavelength of 1.3μm. Its threshold current was 18mA at a temperature of 25°C, increasing to 36mA at 70°C, resulting in a characteristic temperature of 74K. The device is bonded junction side up on a temperature-controlled submount, with wideband 50Ω matched electrical connection.

The small signal frequency bandwidths of the laser are shown in Figure 3. At room temperature, the laser achieves a small signal bandwidth in excess of 10GHz though this degrades to about 6GHz at a temperature of 85°C. This performance is nevertheless sufficient to allow NRZ modulation of the laser at a data rate of 10Gb/s for temperatures up to 70°C [3].

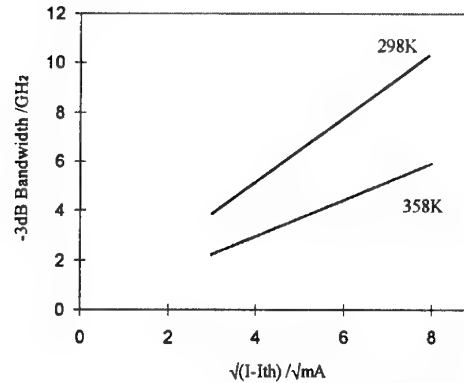


Figure 3: Small signal bandwidth of InGaAsP laser as a function of temperature

Bandwidth Extension via Multicontact Lasers

An attractive way of increasing the bandwidth of a given laser diode is to use the “gain lever” effect. Here a laser cavity has its contacts segmented so that there is typically a long contact and a short contact. The long contact may be driven at a high bias current and the short section driven with a low current and the RF signal. The low bias to the short section results in a high value of differential gain, and therefore high speed, though in a low value of absolute gain. The long section allows a high value of gain to overcome the low gain of the short section.

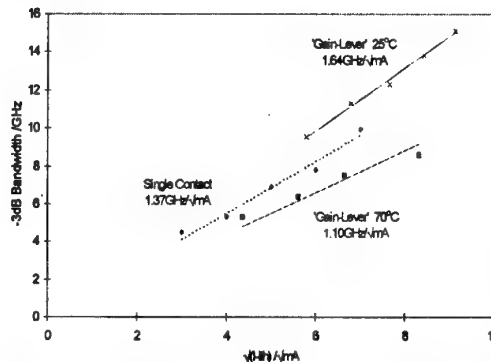


Figure 4: Comparison of single contact and gain lever device small signal bandwidths

A similar laser to that in the previous section had a 7:1 length ratio contact split introduced by focussed ion beam etching. Small signal bandwidth measurements carried out with the RF drive to the

short section yielded the results shown in figure 4. As can be seen, the twin contact device exhibits a room temperature bandwidth in excess of 15GHz in comparison to the 10GHz bandwidth of the single contact device. The modulation efficiency increases from 1.37 to 1.64GHz/ $\sqrt{\text{mA}}$. A bandwidth in excess of 8.6GHz is measured at a temperature of 70°C.

Impact of Material on Bandwidth

As was shown earlier, the low barrier height for InGaAsP based QW lasers operating at 1300nm leads inevitably to poor temperature performance. In order to improve upon this, different material systems are necessary which offer the ability to achieve higher barrier heights. InGaAsN [4] and quantum dot lasers [5] have been extensively researched over the last few years with this goal in mind. Both materials may be grown on GaAs substrates and thus allow very high barriers. Initial temperature performance results have been encouraging with room temperature T_0 in excess of 100K being achieved. However, currently in both cases values of T_0 drop with increasing temperature. In addition, no high speed modulation results have to date been demonstrated.

Of more immediate commercial interest is the use of AlInGaAs [6]. The inclusion of Al in place of P allows the use of higher barriers in a material system that is well developed. Figure 5 shows the result of simulations of the small signal bandwidth of a laser based on this material system at a temperature of 85°C. The device clearly shows a bandwidth in excess of 10GHz under these conditions, indicating the potential of this material system.

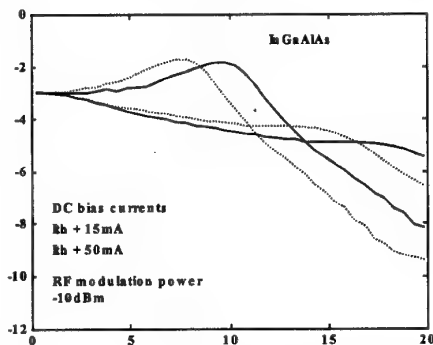


Figure 5: Simulated small signal frequency response of AlInGaAs Laser

Uncooled 850nm VCSELs

The other main laser type which is being considered for uncooled operation within datacommunications networks is the VCSEL. Intense research over the last few years has led to the development of GaAs/AlGaAs VCSELs which are extensively used

in short haul (up to ~500m) multimode fibre links such as within the Gigabit Ethernet standard. The inherent low cost of these device, along with the ease of fibre coupling associated with their circular mode profile, make them extremely attractive for this application.

The GaAs/AlGaAs material system has high QW barriers as well as a low Auger coefficient when compared with InGaAsP and so temperature dependent material gain is not a significant problem for uncooled applications. However, VCSELs suffer from other thermally associated problems. The Bragg stack cavity wavelength and the gain peak tune at different rates with temperature and it is important to take this into account during the design. In addition, the current injection is through the Bragg stacks which have high impedances (of the order of tens of ohms) which can lead to the active region temperature being higher than the module temperature. In addition the large area of VCSELs can result in high capacitance, limiting the bandwidth of the devices. However, the development of the oxide confined VCSEL structure has largely solved this problem.

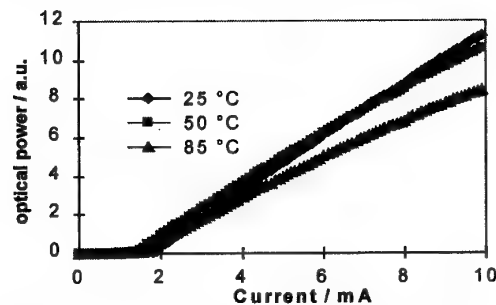


Figure 6: Light current characteristics of oxide confined VCSEL as a function of temperature

Figure 6 shows the light current characteristic of a 7 μm diameter oxide confined GaAs/AlGaAs VCSEL. As can be seen, the device operates with little change in threshold current over the temperature range 25-85°C. The gain-cavity detuning effect has been designed out by detuning the cavity at room temperature. The effect of this can be seen by observing that the threshold current first falls and then rises with temperature. Figure 7 shows the small signal bandwidth performance of the VCSEL as a function of drive current. The laser has a small signal bandwidth in excess of 8GHz at a current of 8mA, indicating its suitability for 10Gb/s operation [7].

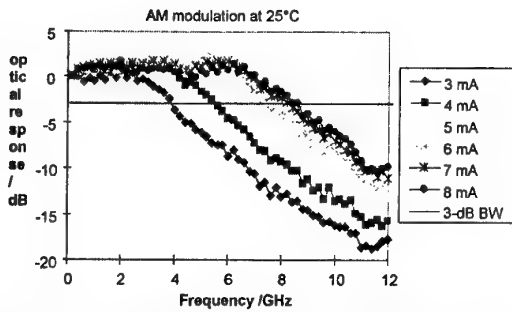


Figure 7: Small signal frequency response of oxide confine GaAs/AlGaAs VCSEL

System Performance Over Multimode Fibre

The forward impedance of the laser was measured to be $\sim 45\Omega$ and so the laser was bonded onto a high speed submount (bandwidth $>15\text{GHz}$) without any matching circuitry. The device was driven with a dc bias and 10Gb/s pattern (using a 1V swing from a pattern generator) via a bias T. Figure 8 show the 10Gb/s eye diagrams at both 25 and 85°C . As can be seen the eyes are clearly open at both temperatures though there is evidence of additional patterning, notably an increased overshoot, at 85°C .

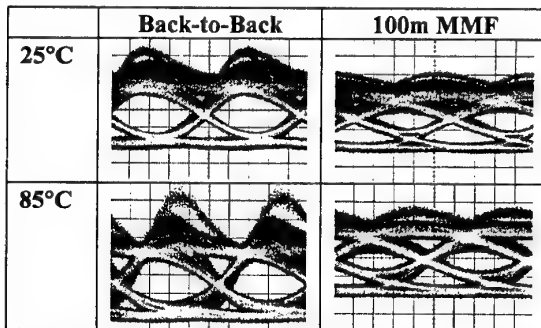


Figure 8: Transmission performance of 10Gb/s VCSEL signal over MMF as a function of temperature

The signals were then transmitted over 100m of standard $50\mu\text{m}$ core multimode fibre. After transmission, the eyes are open at both temperatures though there is significant eye closure. This is a result of the low bandwidth of the fibre which is rated at a bandwidth.length product of 400MHz.km at this wavelength. New multimode fibres are however under development with much lower differential mode dispersion which should allow transmission over at least 300m at an operating wavelength of 850nm .

Conclusions

This paper has described some of the problems associated in obtaining high bandwidth for 1300nm datacommunications lasers at high operating temperature. Routes to improving upon the temperature performance, via device design and the

use of new materials, were discussed. It was shown it was possible to obtain $\sim 10\text{GHz}$ operation at temperatures up to 70°C though alternative material systems such as AlInGaAs show enhanced bandwidth at higher temperatures. AlGaAs VCSEL structures, another important datacommunications laser class, achieve $\sim 10\text{GHz}$ operation even at 85°C .

Acknowledgements

The authors would like to acknowledge the support received from the UK Engineering and Physical Sciences Research Council (EPSRC) under the PHOTON project. A. B. Massara and M Webster acknowledge personal support from EPSRC (in conjunction with Agilent Technologies, under the CASE award scheme for ABM). K. A. Williams acknowledges support from the Royal Society. The edge emitting lasers in this work were supplied by Chris Park at Agilent Technologies in Ipswich and the VCSELs by Mike Tan at Agilent Laboratories in Palo Alto.

References

1. <http://www.gigabit-ethernet.org>
2. J. O'Gorman *et al.*, "Temperature dependence of long wavelength semiconductor lasers", *Appl. Phys. Lett.*, **60**, pp. 1058-1060, 1992.
3. AB Massara *et al.*, "Ridge waveguide InGaAsP lasers with uncooled 10Gbit/s operation at 70°C ", *Electron. Lett.*, **35**, pp.1646-1647, 1999
4. MR Gokhale *et al.*, "Low-threshold current, high-efficiency $1.3\mu\text{m}$ wavelength aluminum-free InGaAsN-based quantum-well lasers", *IEEE Photon. Tech. Lett.*, **12**, pp.131-133, 2000
5. G Park *et al.*, "Low-threshold oxide-confined $1.3\mu\text{m}$ quantum-dot laser:", *IEEE Photon. Tech. Lett.*, **12**, pp. 230-232, 2000
6. T Ishikawa *et al.*, *Proceedings of 10th Intern. Conf. On Indium Phosphide and Related Materials (IPRM'98)*, pp. 729-732, 1998
7. M Webster *et al.*, "Performance of 10 Gb/s VCSELs operating at 85°C ", Paper CTuF2, CLEO'2000, San Francisco, 2000

Enhanced Direct Modulation Efficiency by FM to IM Conversion

H. L. T. Lee*, R. J. Ram

Research Laboratory of Electronics, Massachusetts Institute of Technology, 26-459, Cambridge MA, 02139

phone: (617)258-0273, fax: (617)258-7864, email: harrylee@mit.edu

O. Kjebon, R. Schatz

Laboratory of Photonics and Microwave Engineering, Royal Institute of Technology, Electrum 229,S-116 40 Kista, Sweden

phone: +46-08-7521281, email: olle@ele.kth.se

Abstract — Enhanced modulation efficiency of a directly modulated, high speed DBR laser of up to 400% has been demonstrated using FM to IM conversion in optical fiber. Link noise figure is improved by 8dB and dynamic range by 3dB at 10GHz.

I. Introduction

The use of optical links to transmit electrical signals by small signal modulation relies on the conversion of electrons to photons at the transmitter and photons to electrons at the receiver. For single element semiconductor lasers, the efficiency of this process is fundamentally limited to 100%, whereby each injected modulation electron is converted into a photon, which is converted to a received electron. This limit can be overcome by recognizing that: 1) For lasers where the index of refraction is coupled to the material gain, each injected modulation electron also serves to change the optical frequency of the background photons. 2) A dispersive element can be used to convert the optical frequency modulation into an intensity modulation.

FM to IM conversion occurs when, for the case of anomalous group velocity dispersion, lower optical frequency photons travel faster than higher optical frequency photons and a frequency modulation is converted into an intensity modulation when faster photons meet slower photons. Because each injected modulation electron changes the optical frequency of a large number of background photons, the resulting intensity modulation, after dispersive conversion, corresponds to a single modulation electron producing a multitude of received electrons. Thus, the received electrical signal can be stronger than the transmitted electrical signal with no FM to IM conversion.

Recently, researchers have gone to great lengths to enhance the modulation efficiency of optical links to improve link gain by series coupling active regions or by using external modulation.

Series coupling active regions improves direct modulation efficiency by causing each injected electron to emit more than one photon. Ideally, each electron emits the same number of photons as series coupled active regions. The series coupling has been accomplished using a number of methods. One method is series coupling through external circuitry in which 189%[1] and 117%[2] modulation efficiency was achieved. However, the bandwidth is limited by high parasitics and is complicated to implement as it requires combining the power of multiple lasers into a single fiber. Another method is epitaxial coupling through tunnel junctions in which 99%[3] modulation efficiency was achieved. This eliminates the problems with parasitics but suffers from increased device heating since the DC voltage is increased by the number of junctions and power dissipation is increased.

Very high modulation efficiency and positive link gain can be achieved with external modulation by using very high DC laser power and low V- π modulators. Using resonant impedance matching to the photodetector and modulator, +31dB of link gain at 150MHz was achieved using 225mW of optical power through a Mach-Zender external modulator[4]. The operating principle is similar to FM to IM conversion in that the electrons that operate the external modulator are able to modulate a multitude of photons passing through the modulator if the DC laser power is high enough. This technique suffers, however, from the expense of the external modulator, and the need for large, high power laser source.

The primary advantage of using FM to IM conversion over existing methods is simplicity. The aforementioned coupling between the index of refraction and gain, which allows direct modulation of a large number of photons, is present in all semiconductor lasers, and dispersion is present in all optical fibers. This technique requires only a single laser element and uses direct modulation of the semiconductor laser. While the use of FM to IM conversion as a method for improving the direct

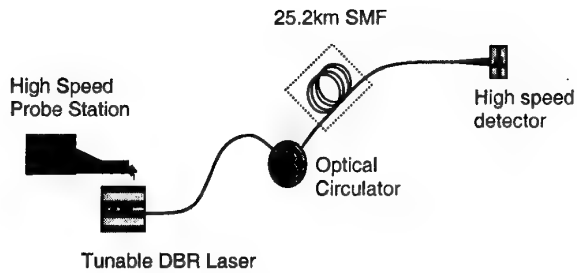


Figure 1. Experimental setup for FM-IM conversion link measurements.

modulation characteristics of semiconductor lasers has been studied theoretically[5], along with the effects of dispersion on noise and distortion in optical links[6,7], very little experimental work has been done in this area. The changes in the system response due to dispersive fiber gratings and various lengths of optical fiber were reported in [8], showing enhancements up to 7dB, however, distortions and system performance were not investigated. Here we present experimental results demonstrating up to 400% modulation efficiency with improved noise figure and dynamic range in optical links using FM to IM conversion composed of directly modulated high speed DBR lasers and 25.2km of single mode fiber.

II. Experiment

FM enhanced modulation efficiency can be implemented with a semiconductor laser with a high FM response, a low loss dispersive element, such as a length of optical fiber or chirped fiber bragg grating, and a detector. In a semiconductor laser, changes in the index of refraction are coupled to changes in the gain through the linewidth enhancement factor, or alpha factor[9], which can be enhanced with frequency dependent feedback which, for example, occurs in a distributed bragg reflector laser through an effect called detuned loading[10]. Key features for maximizing the strength of the received signal are high fiber coupling efficiency and high photodetector quantum efficiency.

Experiments were carried out, in the setup shown in Fig. 1, with a high speed DBR laser[11], fabricated at the Semiconductor Laboratory at KTH in Stockholm. The laser is probed with a high-speed coplanar probe and coupled to single mode fiber. The optical circulator provides a stage of isolation and 25.2km of fiber is used as the dispersive element. S_{21} measurements are obtained with a calibrated vector network analyzer and distortion and noise measurements were performed with two-tone modulation and detection with a spectrum analyzer

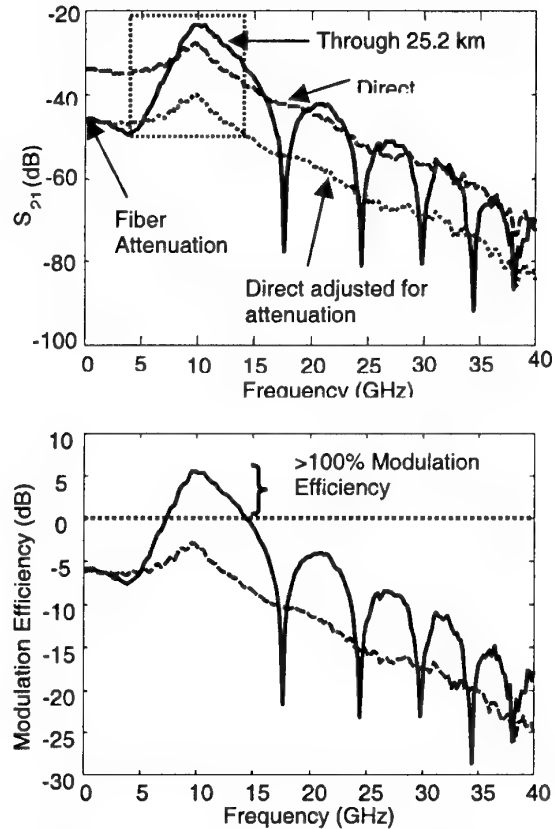


Figure 2. a) S_{21} measurement for link with and without optical fiber. Solid line is with 25.2km SMF-28, dashed line is back to back transmission, and the dotted line is the back to back case adjusted for fiber attenuation. b) Extracted modulation efficiency of the laser. >100% efficiency occurs for frequencies between 7.4 and 14GHz.

with a low noise preamplifier for link noise measurement. Comparisons between three link conditions are described. Back to back transmission without dispersion (dashed lines), the link with 25.2km of fiber (solid lines), and the link with an equivalent amount of optical attenuation (dotted lines) obtained by misaligning a connector that occurs after the optical isolation provided by the circulator.

Fig. 2a) shows measured S_{21} for a high speed DBR laser for the three cases described above. Even after 25.2km of fiber, FM to IM conversion results in a signal that is approximately 6dB higher than with no fiber, indicating that a 16dB signal enhancement is achieved to compensate the ~10dB loss due to fiber attenuation, which is shown in the low frequency portion of the trace where dispersion does not effect

the signal much. Because the modulation response at frequencies well below the relaxation oscillation

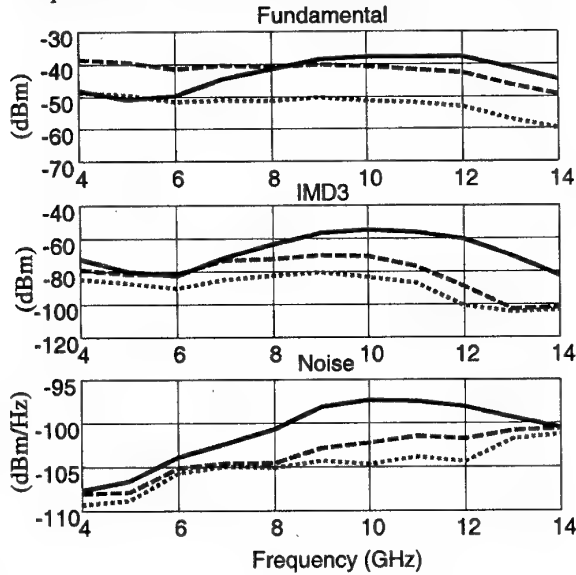


Figure 3. Fundamental, 3rd order intermodulation distortion, and noise spectral density for link with 25.2km SMF-28 (solid), back to back (dashed) and back to back with optical attenuation equivalent to the fiber (dotted).

frequency corresponds to the DC slope efficiency, the contribution to the link gain by the laser modulation efficiency can be extracted. The measured -34.4dB link gain in the back to back case was combined with the measured 0.24 W/A slope efficiency to calculate a -22dB contribution from the coupling and link losses, impedance mismatches, and detector responsivity. This was in agreement with independently measured parameters. This external contribution was removed to extract the effective laser modulation efficiency which is shown in Fig. 2b), where the frequency range between 5GHz and 17GHz shows improvement over the back to back case and the frequency range between 7.4GHz and 14GHz show greater than 100% modulation efficiency with a peak of 400% at 10GHz.

While the link gain is improved by using FM to IM conversion, because frequency modulation is inherently non-linear, the intermodulation distortions are increased and the overall noise is higher due to conversion of phase noise into intensity noise. The degree that these impairments limit system performance is dictated by the noise and nonlinear distortion of the receiver. For our measurement setup, the noise is primarily limited by the receiver (spectrum analyzer with preamplifier) noise floor and distortion is dominated by the laser. This is evident

in Fig. 3 where the fundamental, intermodulation distortion and noise are shown. The noise floor for

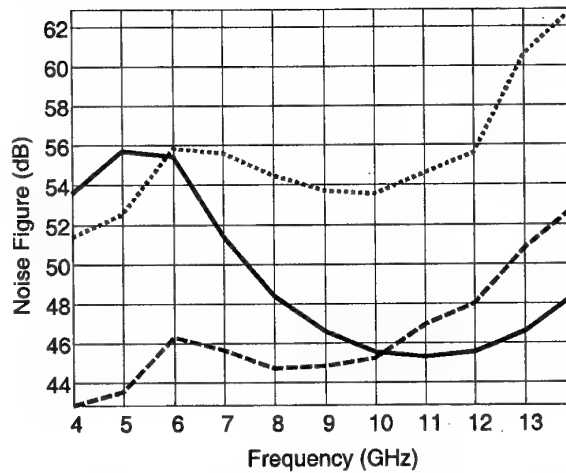


Figure 4. Noise figure for link with 25.2km SMF-28 (solid), back to back (dashed) and back to back with optical attenuation equivalent to the fiber (dotted).

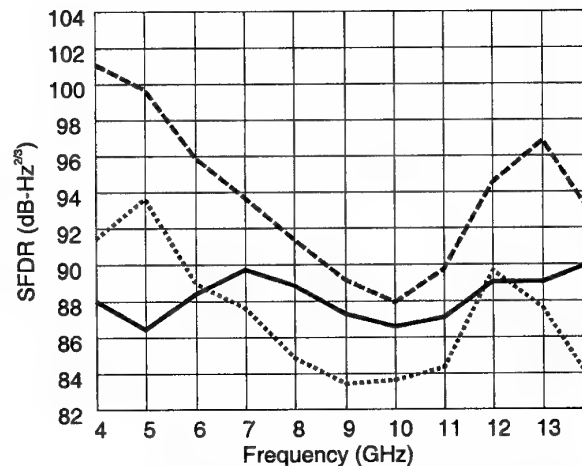


Figure 5. Third order spur free dynamic range for link with 25.2km SMF-28 (solid), back to back (dashed) and back to back with optical attenuation equivalent to the fiber (dotted).

the optically attenuated case essentially follows the noise floor of the spectrum analyzer. Fig. 3 also clearly shows the increase in intermodulation distortion from FM to IM conversion which is as much as 28dB higher (at 12GHz) than the back to back case.

The measurements in Fig. 3 can be combined into link performance measures such as noise figure and third order free dynamic range shown in Figs. 4 and 5. The noise figure for the FM-IM link is improved by as much as 4.5dB at 14GHz and overall

improvement with respect to the back to back case occurs for frequencies above 10GHz indicating the signal gain increases more than the noise. With respect to the optically attenuated case, for frequencies above 6GHz the noise figure is improved by as much as 10dB because the noise is receiver limited and the signal is reduced more than the noise. The improvement in noise figure comes with the penalty of reduced dynamic range with respect to the back to back case by approximately 1.5dB at 10GHz and 8dB at 13GHz, which is due to increased intermodulation distortion. With respect to the optically attenuated case, however, the dynamic range is improved for frequencies between 6GHz and 12GHz by approximately 3.5dB, indicating that for lossless dispersive elements, overall link performance can be improved since the rise in 3rd order distortion is less than three times the signal enhancement.

III. Conclusions

In summary, when adjusted for fiber attenuation, FM-IM conversion can yield up to 16dB enhancement in link gain, corresponding to an effective modulation efficiency of 400%, or four photons per modulating electron. This essentially compensates for the gain reduction and increased noise figure due to fiber attenuation. While FM modulation is inherently nonlinear, the increase in distortion is less than three times the increase in signal, meaning link performance will be improved over a link that uses a preamplifier to boost the modulation current to compensate for fiber attenuation. This effect has been employed to enhance the noise figure and spur free dynamic range.

IV. References

- [1] C. Cox, H. Roussel, R. J. Ram, R.J. Helkey, "Broadband, directly modulated analog fiber link with positive intrinsic gain and reduced noise figure," *International Topical Meeting on Microwave Photonics*, Princeton, NJ, October 1998, pp. 157-160.
- [2] S. G. Ayling, D. R. Wight, and M. B. Allenson, K.P. Hilton, G.W. Smith, "Novel integrated laser devices with greatly enhanced quantum efficiency and intrinsic RF matching for low loss, broad band opto-microwave applications," *Microwave Photonics '98*, October 1998, pp. 161-164.
- [3] S. G. Patterson, G. S. Petrich, R. J. Ram, and L. A. Kolodziejski, "Continuous-wave room temperature operation of bipolar cascade laser," *Electron. Lett.*, vol. 35, no. 5, pp. 395-396, 1999.
- [4] C. Cox, E. Ackerman, and G. Betts, "Relationship between gain and noise figure of an optical analog link," in *IEEE Microwave Theory Tech. Symp. Dig.*, San Francisco, CA, June 1996, pp. 1551-1154.
- [5] G. Yabre and J. Le Bihan, "Intensity Modulation Technique Using a Directly Frequency-Modulated Semiconductor Laser and an Interferometer," *J. Lightwave Technol.*, vol. 13, no. 10, pp. 2093-2098, 1995.
- [6] G. J. Meslener, "Chromatic Dispersion Induced Distortion of Modulated Monochromatic Light," *IEEE J. Quantum Electron.*, vol. QE-20, no. 10, pp. 1208-1216, 1984.
- [7] J. Wang and K. Petermann, "Small Signal Analysis for Dispersive Optical Fiber Communication Systems," *J. Lightwave Technol.*, vol. 10, no. 1, pp. 96-100, 1992.
- [8] M. McAdams, E. Peral, D. Provenzano, W. K. Marshall, and A. Yariv, "Improved laser modulation response by frequency modulation to amplitude modulation conversion in transmission through a fiber grating," *Appl. Phys. Lett.*, vol. 71, no. 7, pp. 879-881, 1997.
- [9] C. H. Henry, "Theory of Linewidth of Semiconductor Lasers," *IEEE J. Quantum Electron.*, vol. QE-18, pp. 259-264, 1982.
- [10] R. F. Kazarinov and C. H. Henry, "The Relation of Line Narrowing and Chirp Reduction Resulting from the Coupling of a Semiconductor Laser to a Passive Resonator," *IEEE J. Quantum Electron.*, vol. QE-23, pp. 1401-1409, 1987.
- [11] O. Kjebon, R. Schatz, S. Lourdudoss, S. Nilsson, B. Stalnacke and L. Backbom, "30GHz direct modulation bandwidth in detuned loaded InGaAsP DBR lasers at 1.55 μ m wavelength," *Electron. Lett.*, vol. 33, pp. 488-489, 1997.

INTEGRATED TANDEM ELECTROABSORPTION MODULATORS FOR HIGH-SPEED OTDM APPLICATIONS

Volkan Kaman, Yi-Jen Chiu, Thomas Liljeberg and John E. Bowers

Department of Electrical and Computer Engineering
University of California, Santa Barbara, CA 93106, USA
Tel: 1-805-893-4883 Fax: 1-805-893-3262 (kaman@opto.ucsb.edu)

Sheng Z. Zhang

Agilent Technologies
370 West Trimble Rd., San Jose, CA 95131

Abstract: An integrated tandem traveling-wave electroabsorption modulators is demonstrated as an optical short pulse generator and demultiplexer for >100 Gbit/s optical time-division-multiplexed systems. Optical pulses of 4.2 ps width at 30 GHz with an extinction ratio in excess of 30 dB are achieved.

Introduction:

Optical fiber transmission based on single channel optical time division multiplexing (OTDM) has recently surpassed 100 Gbit/s [1-3]. These experiments make it likely that future TDM systems will employ optical means of increasing the transmission capacity of a single channel. Sinusoidally driven electroabsorption (EA) modulators have become key devices as optical short pulse generators and optical demultiplexers for high-speed OTDM experiments. An 80 Gbit/s OTDM data stream was realized by short pulses generated from EA modulators without using any non-linear pulse compression, which is the highest aggregate data rate achieved using this technique to date [4]. On the other hand, a 160 Gbit/s optically multiplexed data stream was demultiplexed down to 10 Gbit/s using only EA modulators [1]. Due to the advances in high-speed electrical TDM, it is inevitable that the next generation of OTDM systems will operate at a base rate of 40 Gbit/s with optical multiplexing to 160 Gbit/s or more [5].

High-speed OTDM systems, unlike electrical TDM systems, require very high extinction ratios and short pulsewidths for both the optical transmitter and the demultiplexer [2]. Single EA modulators are usually limited to ~20 dB dynamic extinction ratio, which is sufficient for demultiplexing purposes, but can lead to incoherent interference between multiplexed adjacent pulses at the transmitter. Therefore, a fiber-coupled pair of separate modulators was used for pulse generation in [4] and for demultiplexing in [1]. The use of tandem EA modulators has its advantage of not only increasing the dynamic extinction ratio, but also in reducing the switching window. However, it is

desirable to integrate these modulators on a single chip to eliminate the optical amplifier, which compensates for coupling losses between the modulators [6-7]. This will not only result in a compact and cost-effective transmitter (or receiver), but also the configuration will be more robust to environmentally induced timing asynchronization.

In this paper, we investigate the optical short pulse generation and optical demultiplexing capability of an integrated tandem traveling-wave EA modulators at repetition frequencies of 30 and 40 GHz for > 100 Gbit/s OTDM systems. This is also the first demonstration of optical pulse generation using traveling-wave EA modulators, which were previously demonstrated in a 30 Gbit/s data modulation experiment [8].

Device Characteristics:

The 2- μm wide, 300 and 400- μm long traveling-wave EA modulators were fabricated with MOVCD grown ten periods of strain-compensated InGaAsP quantum wells on semi-insulated InP substrate [9]. The 20- μm long optical waveguide between the two modulators was defined by H^+ ion implantation to render the region semi-insulating. The measured impedance was about 10 k Ω . The ion implantation also extended 50 μm into each modulator in order to reduce capacitance and microwave crosstalk; however, the absorption region for each modulator was shortened by 100 μm . Both modulators were terminated in a thin-film resistor and a dielectric capacitor, which reduced heating effects in the modulators and the terminations. This allowed for long-term operation of the tandem without any external temperature cooling. Figure 1 shows a photograph of the integrated tandem EA modulators.

Static Characteristics:

Figure 2 shows the attenuation characteristics of the tandem as a function of reverse bias. An optical input power of 6.5 dBm was applied at 1555 nm. The insertion loss of the device was 15 dB, which

will be improved by AR-coating the facets. Each device was individually characterized by keeping the other modulator at zero bias. The 400- μm device achieved a maximum extinction of 38.8 dB at -6 V while 26.2 dB of extinction was observed for the 300- μm device. The difference in the maximum extinction ratio is due to the shorter absorption region of the 300- μm device. It should also be noted that for higher reverse biases, a saturation of absorption is observed for both devices. Even though it is desirable to apply a high reverse bias for very short pulse generation using sinusoidal modulation, the absorption saturation at high reverse biases will deteriorate the extinction ratio. On the other hand, the tandem configuration shows an improved extinction ratio with a maximum of 55.3 dB at -6V. The absorption saturation is well suppressed in comparison to single device operation.

Dynamic Characteristics:

The optical switching capability of the tandem EA modulators was first characterized at 30 GHz. Both modulators were driven with 7 V_{pp} sinusoidal RF signals, which were synchronized by an electrical delay line. The width of the obtained pulses were measured using an autocorrelator and deconvolved assuming a gaussian pulse shape as inferred from the optical spectrum measurements. Figure 3 shows the obtained pulse widths as a function of reverse bias to the modulators. It is very important to mention that the following criteria were used for these measurements: (1) the average optical output power of the tandem was higher than -24 dBm in order to ensure that the signal-to-noise ratio of the pulses would not be deteriorated after subsequent amplification for system experiments, and (2) the dynamic extinction ratio was estimated to be > 30 dB. The minimum pulse width satisfying these criteria was 4.9 ps at reverse biases of -4.5 V and -4 V for the 300- μm and 400- μm devices, which is shown in Figure 4. This optical switching window is well suited for > 100 Gbit/s optical demultiplexing applications [2]. The pulse widths obtained from the individual 300- μm and 400- μm devices at a reverse bias of -4.5 V were 6.9 ps and 6 ps, respectively. Figure 5 shows the optical spectrum of the modulated tandem EA modulators, which has a gaussian shape of 0.75 nm bandwidth. The time-bandwidth product of 0.46 for the 4.9 ps pulses suggests that the pulses were slightly chirped. When the tandem was followed by dispersion compensating fiber (DCF) with a dispersion of about -6 ps/nm, the pulses were linearly compressed to a transform-limited pulse width of 4.2 ps (Figure 4). This pulse width suggests that the tandem is suitable as an optical pulse source for simultaneous polarization and time division multiplexed systems in excess of 100 Gbit/s.

The optical switching response of the tandem EA modulators was also performed at 40 GHz. The RF drive was limited to 4 V_{pp}, which resulted in a compromise between minimum pulse width, dynamic extinction ratio and average optical output power. A minimum optical pulse width of 5.9 ps with a bandwidth of 0.58 nm was achieved. The extinction ratio was estimated to be ~20 dB. These results should improve when the tandem is driven with higher power RF amplifiers at 40 GHz and enable low-penalty optical demultiplexing of a 160 Gbit/s OTDM data stream [1].

Conclusion:

An integrated tandem traveling-wave EA modulators was demonstrated as a viable high-speed optical source and demultiplexer. Optical pulses with high extinction ratios and less than 5 ps width were achieved for repetition frequencies of > 20 GHz.

Acknowledgements:

The authors would like to acknowledge Gerry Robinson for providing technical support, Stephanus Spammer from Corning, Inc. for donating the dispersion compensating fiber, and Carlton Creamer from Sanders Co. for donating the 30 GHz MMIC power amplifiers. This work was supported by DARPA under the MOST program.

References:

- [1] B. Mikkelsen, G. Raybon, R. -J. Essiambre, K. Dreyer, Y. Su, L. E. Nelson, J. E. Johnson, G. Shtengel, A. Bond, D. G. Moodie and A. D. Ellis, "160 Gbit/s single-channel transmission over 300 km nonzero-dispersion fiber with semiconductor based transmitter and demultiplexer", *ECOC '99*, PD2-3, 1999.
- [2] A. D. Ellis, J. K. Lucek, D. Pitcher, D. G. Moodie and D. Cotter, "Full 10 x 10 Gbit/s OTDM data generation and demultiplexing using electroabsorption modulators", *Elec. Lett.*, vol. 34, pp. 1766-1767, 1998.
- [3] S. Kawanishi, Y. Miyamoto, H. Takara, M. Yoneyama, K. Uchiyama, I. Shake and Y. Yamabayashi, "120 Gbit/s OTDM system prototype", *ECOC '98*, pp. 43-45, 1998.
- [4] D. D. Marcenac, A. D. Ellis and D. G. Moodie, "80 Gbit/s OTDM using electroabsorption modulators", *Elec. Lett.*, vol.34, pp.101-103, 1998.
- [5] A. D. Ellis, R. J. Manning, I. D. Phillips and D. Nasset, "1.6 ps pulse generation at 40 GHz in phaselocked ring laser incorporating highly nonlinear fibre for application to 160 Gbit/s OTDM networks", *Elec. Lett.*, vol. 35, pp. 645-646, 1999.

- [6] H. Tanaka, S. Takagi, M. Suzuki and Y. Matsushima, "Optical short pulse generation by double optical gate operation of tandem connected electroabsorption modulators driven by sinusoidal voltages", *Elec. Lett.*, vol. 29, pp. 1449-1451, 1993.
- [7] F. Devaux, D. Jahan, F. Alexandre, A. Ougazzaden, E. Vergnol and M. Carre, "Tandem of modulators for high on/off pulse generation (-55 dB)", *Elec. Lett.*, vol. 33, pp. 1491-1492, 1997.
- [8] V. Kaman, S. Z. Zhang, A. J. Keating and J. E. Bowers, "High-speed operation of travelling-wave electroabsorption modulator", *Elec. Lett.*, vol. 35, pp. 993-995, 1999.
- [9] S. Z. Zhang, Y. J. Chiu, P. Abraham, J. E. Bowers, "25 GHz polarization-insensitive electroabsorption modulators with traveling-wave electrodes", *IEEE Photon. Tech. Lett.*, vol. 11, p.191-193, 1999.

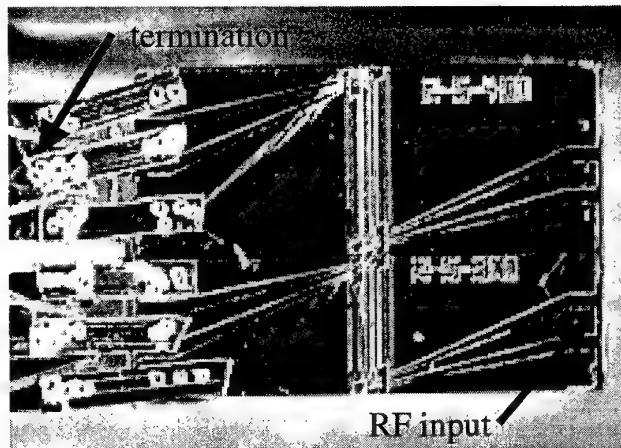


Figure 1 – Photograph of the integrated tandem EA modulators

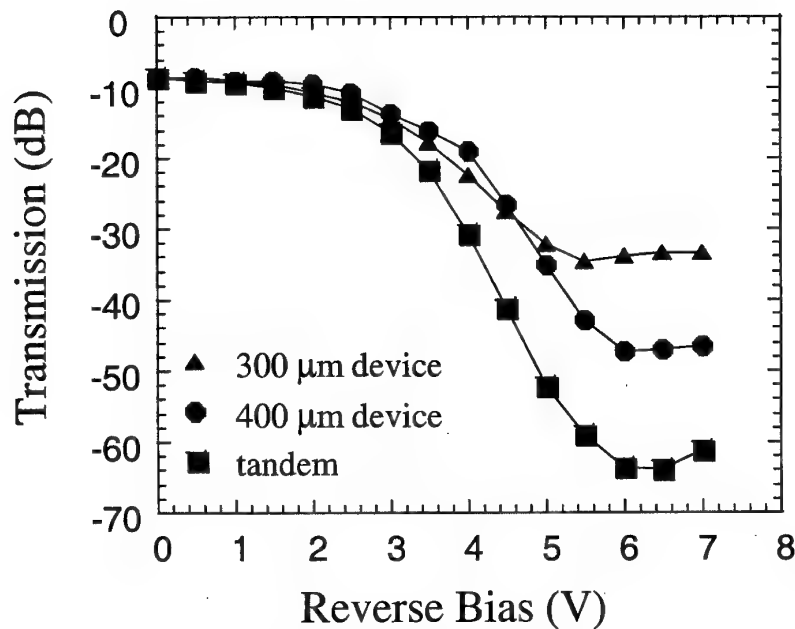


Figure 2 – Attenuation vs. reverse bias characteristics

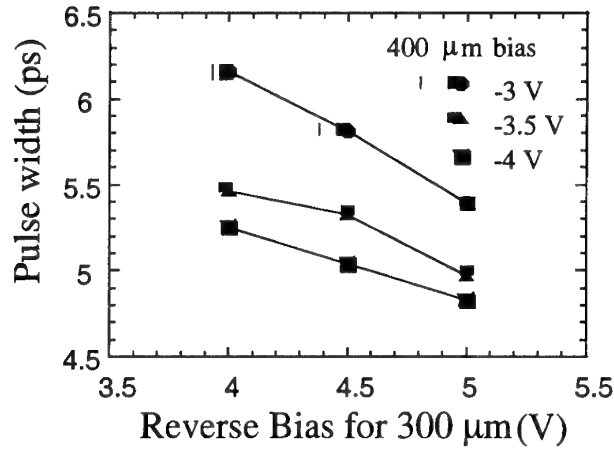


Figure 3 – Pulse widths vs. reverse biases of 300- μm (x-axis) and 400- μm (symbols) devices

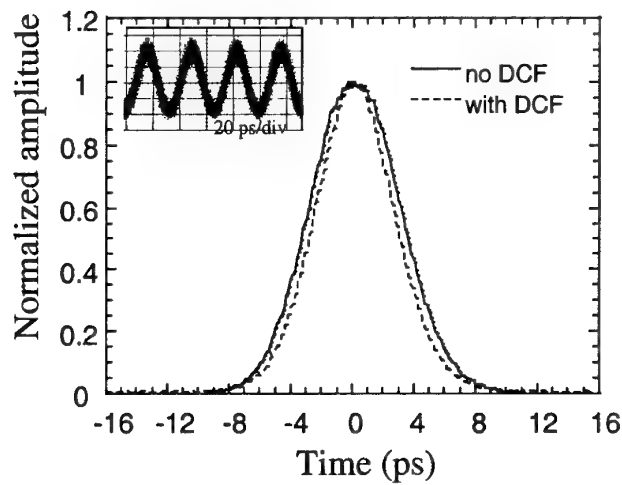


Figure 4 – Autocorrelation trace of 30 GHz pulses (inset: oscilloscope trace)

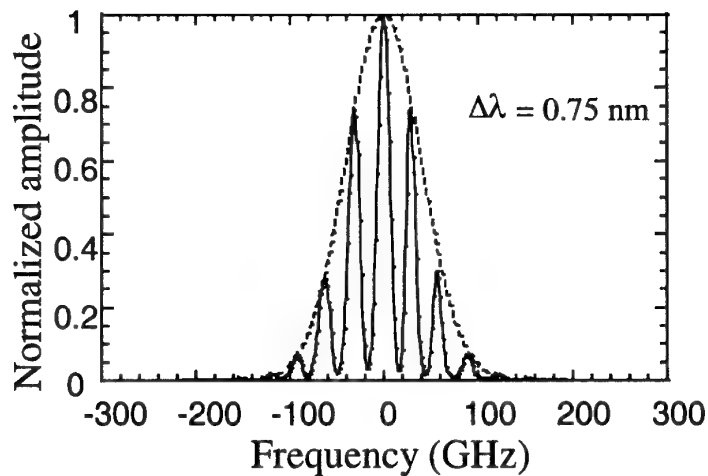


Figure 5 – Optical spectrum of 30 GHz pulses

A FOLDED-PATH GaAs TRAVELLING-WAVE MODULATOR FOR PHASED-ARRAY RECEIVERS

R. G. Walker and C. Edge

Marconi Technology, Caswell, Towcester, U.K. NN12 8EQ

Introduction

There are significant benefits in the use of optics in phased array antenna systems. These are particularly compelling for complex multi-beam antenna systems and include improved weight and power distribution between the antenna panel and central systems and the potential for frequency-independent and wideband beamforming elements.

The receive link in such a system requires a linear optical transmitter driven by the output of the antenna LNA. This subsystem is demanding in terms of noise figure and dynamic range, requiring high modulation efficiency, high optical power and highly linear modulation. Direct modulation of a laser would be marginal with respect to linearity, particularly at frequencies above a few GHz, and would require a substantial DC power feed to each R/T module for the laser drive and cooling. Heat management would also be an issue. An external optical modulator is preferred, in spite of its larger physical size and higher RF drive level, since it can provide wideband linear modulation and allows the optical source to be remote from the R/T module.

Physical packing constraints of the many elements in a microwave phased-array antenna panel encourage a narrow profile for each R/T module with both optical ports at one end of the modulator and the RF input at the other. There is no space for a 180° fibre-loop within such a module; thus we consider the possibility of a retro-reflective or folded-path electro-optic modulator. Such a modulator configuration is the subject of this paper. It involves a radical departure from the usual port conventions: i.e. optical ports at opposite ends with RF access from the side.

Travelling Wave GaAs Modulators

The folded-path modulator is based on a well-characterised GaAs/AlGaAs travelling-wave design that we have previously used for microwave photonic systems. This device has a 3dB

bandwidth of 23GHz and provides a very flat response over the 2-18GHz band (Figure 1). V_{π} (on-off Voltage swing) is 9V at 1540nm.

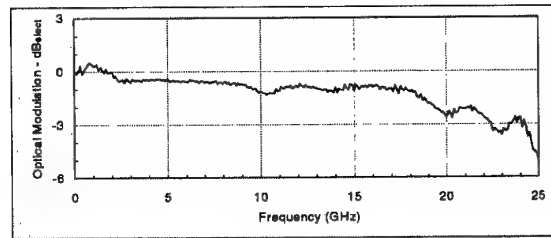


Figure 1 Non-folded GaAs travelling-wave modulator response.

The modulator is based on the well-known Mach-Zehnder interferometer, which has a differential phase-modulation region of rib-waveguides furnished with self-aligned electrodes. Optical split and recombination functions utilise Multimode Interference (MMI) elements [1] (Figure 2). These provide much improved manufacturing tolerance compared with directional-coupler or Y-branch alternatives, and are of low-loss.

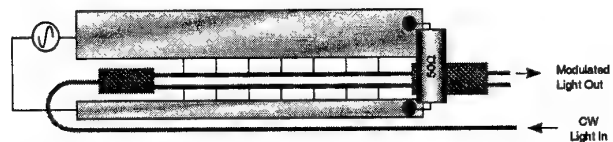


Figure 2: Schematic loaded-line modulator with a folded optical path using an on-chip hairpin bend.

The optical waveguides consist of ribs etched into the surface of a GaAs/AlGaAs slab-waveguide whose in-grown n-type doping profile is designed to confine the applied back-bias field from a self-aligned electrode to the immediate vicinity of the guided-optical mode. Electrically induced phase-shifts in the waveguides are due (in order of diminishing importance) to a combination of electro-optic, majority carrier depletion, and electro-refractive effects.

Several etches are applied to provide varying functionality. The lightest etch defines the waveguides while deeper etches, which inhibit outer slab-guiding, define MMI and spatial-filter structures. The deepest etch removes the epitaxial material entirely to provide electrical isolation and air-bridges in the electrode metallisation.

The travelling-wave modulator has segmented electrodes connected by air-bridges to the coplanar RF transmission-line (Figure 2). This configuration constitutes a capacitively loaded line with a low-pass filter, slow-wave characteristic that achieves the required RF/Optical velocity-matching [2].

Optical Path Folding

Figure 2 illustrates one possible arrangement using an on-chip hairpin bend to achieve the necessary optical path-folding. Some waveguide bends will be employed within any configuration; however, a full 180° bend requires a lot of space due to lower limits on the radius of curvature.

The chosen configuration uses a 2×2 MMI in combination with a High Reflection (HR) coated facet (Figure 3). The MMI element (in tandem with its mirror-image) provides a full-cross one-to-one re-imaging between its ports.

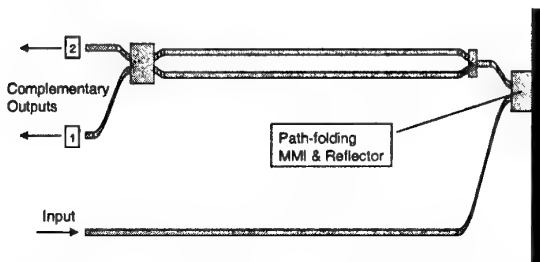


Figure 3: Illustration of the retro-reflective folded-path configuration

An alternative design based on the HR facet approach is to also fold the Mach-Zehnder modulator at the reflector. This was rejected as being incompatible with the travelling-wave design (half the route would be counter-propagating). Also, because the complementary modulated output light is returned to the optical source, risking instability in the laser due to optical feedback.

MMI Path-Folder Design

A major issue with any re-imaging reflector scheme is that light lost due to imperfect imaging is mostly returned towards the input thereby

degrading the optical S_{11} . The chosen MMI approach was checked for sensitivity to etching, width facet position, and facet orientation (tilt). MMIs of different widths were also compared with a near equivalent 2×2 directional coupler. The latter offers the narrowest available image-profile at the facet and therefore possibly the best tolerance to tilt. Simulation used a modal decomposition and propagation method and took account of directional coupling between MMI I/O waveguides.

Sensitivity to Waveguide Etch

Figure 4 compares the sensitivity of through-loss and return-loss of such a reflector to waveguide etching for a directional coupler and an MMI design.

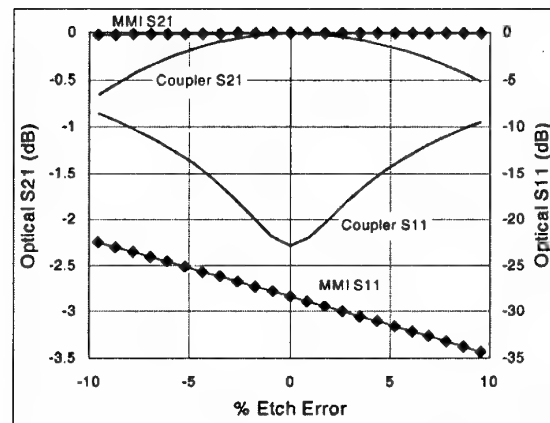


Figure 4: Tolerance to etch depth in MMI and directional-coupler based reflectors

The results illustrate the main benefit of using an MMI rather than a directional coupler design: namely that it is very much more tolerant to waveguide fabrication variations. It was found that the greater the pitch width and length of the MMI the better the S_{11} . Also, as Figure 4 shows, deeper etching generally improves S_{11} even when this degrades the S_{21} .

Sensitivity to Facet Tilt

An MMI path-folder can be made tolerant to the HR-facet position simply by defining its length in the layout, adding waveguide 'stubs' to convey the twin-image to the facet. Slight accidental facet-tilt is not so easily eliminated. In practice this is minimised during fabrication by aligning to a pre-cleaved reference-flat rather than relying on the ground-flat provided by the wafer-supplier, which has can be up to $\pm 0.5^\circ$ in error in some cases.

It would be expected that the through-loss and return-loss due to facet-tilt would increase with profile-width at the facet, as this increases the differential phase-shift due to the tilt. Figure 5 shows this to be true; however, overall, the performance is improved by increased spacing unless the tilt is large due to the better imaging properties of wider MMIs.

Clearly, the angular alignment needs to be accurate to within $\pm 0.05^\circ$.

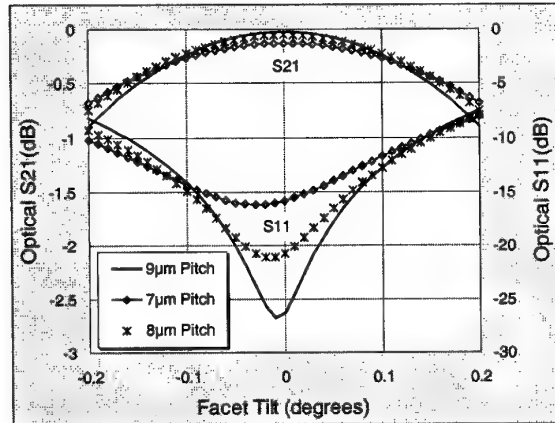


Figure 5: Tolerance to facet-tilt in MMI reflectors of different widths.

Device Assessment

Folded path optical modulator devices designed for operation up to 18 GHz have been fabricated and assessed for optical and electro-optic parameters. A common I/O lens-system was used, with a pellicle beam-splitter to separate the incident and output light. Residual transmitted light through the HR-coating was used to assist initial alignment using standard through-path, optical-bench techniques.

A number of waveguide test-structures were included with the device to facilitate diagnosis. These included retro-reflective straight waveguides and isolated path-folding MMIs.

Optical Losses

HR Facet Reflectance was determined to be 95% by comparing the signal returned from the HR-facet with that from a silver surface mirror of previously determined reflectance.

Waveguide Loss was estimated to be 0.5-0.7 dB/cm using the absolute signal returned from the HR facet via a length of straight waveguide.

Path-Folding MMI Loss average value was 1.2 dB (lowest 0.6 dB).

Other Loss Contributions are due to scattering at connections to electrodes, crossovers and electrode segmentation. An estimated 1.3dB is due to the large number of such disturbances.

Overall, the relative device loss is 3.4dB and the absolute chip-loss (including HR facet and waveguide loss but not I/O coupling) is just below 6dB. The figures for the modulator alone are 1.5dB (relative) and 2.8dB (absolute), showing the overhead due to the path-folding arrangements to be about a factor of two.

Optical Return Loss

The presence of the HR-facet means that there is the possibility of optical feedback to the source laser if the path-folding MMI is ill-tuned or the facet misaligned. The optical return-loss was assessed by comparing the returned signal with that from a silver surface-mirror. A background figure of -23dB, measured on regions of the facet remote from any waveguides, is due to the single-layer AR coating which can be improved by the use of a more elaborate multi-layer coating. The optical S_{11} from the input waveguide was only 0.2dB above this background, showing that the contribution from the path-folding structures is much less than -23dB.

RF Assessment

The RF modulation bandwidth was assessed initially using a modified linear-path test-fixture in order to keep the HR-facet clear for optical alignment purposes. The results (Figure 6) indicate that the compromises to the RF launch in this fixture have introduced a response notch around 17GHz. However, elsewhere, the response is similar to that of the equivalent linear device (Figure 1). Purpose-designed packages (work in progress) with RF end-launch are not expected to reproduce this feature.

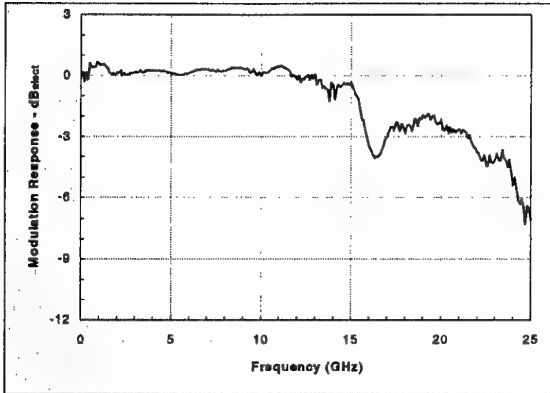


Figure 6: Measured Modulation Response in test-fixture

Conclusions

We have designed and demonstrated a d.c.-18GHz GaAs travelling-wave modulator suitable for a complex multi-beam phased-array antenna receive system. The defining feature of the design is on-chip optical path-folding to enable the needed dense packing of the Rx modules with RF input at one end and optical interrogation from the other. Chip loss is below 6 dB. The optical S_{11} is low and dominated by the AR-coating of the optical facet.

Results for fully packaged modules should be available at the meeting.

Acknowledgements

This work has been partly supported by US Army CECOM under agreement DAAB07-98-3-D004.

References

- 1 L.B. Soldano & E.C.M. Pennings: Optical Multimode Interference devices based on self-imaging: principles and applications, *J. LtWave Tech.* 13 (4), pp. 615-627, 1995.
- 2 R G Walker: 'High-speed III-V semiconductor intensity modulators' (Invited Paper), *IEEE J. of Quantum Electronics*, 27(3), March 1991, pp. 654-667

Novel Optical Single-Sideband Suppressed-Carrier Modulator Using a Bidirectionally-Driven Electro-optic Modulator

A. Loayssa, J. M. Salvade, D. Benito and M. J. Garde

Departamento de Ingeniería Eléctrica y Electrónica, Universidad Pública de Navarra,

Campus de Arrosadia, 31006 Pamplona, Spain

Tel.: +34 948 169840, Fax: +34 948169720

Email: alayn.loayssa@unavarra.es

Abstract. We introduce a novel optical single-sideband suppressed-carrier modulator design using a standard Mach-Zehnder electro-optic modulator and passive components that is bias and chirp-parameter insensitive. Up to 25 dB sideband suppression and 19 dB carrier attenuation are experimental demonstrated.

I. INTRODUCTION

In recent years, much effort has been devoted to the compensation of dispersion impairments in microwave/millimeter-wave fiber optic links. Among the different methods proposed to allow dispersion tolerant transmission, the optical single-sideband (OSSB) modulation offers a very simple system to completely avoid the electrical carrier suppression effect [1]. Additionally, OSSB has another important application to the characterization of the transfer function of optical devices such as fiber Bragg gratings [2].

Various implementations of this modulation format can be found in the literature. Sideband filtering [3], the analogous of vestigial-sideband modulation in the electrical domain, is a simple technique but it requires the filter frequency to be critically tuned to the optical source. More interesting are the OSSB electro-optic modulator structures either based on the Hartley or compatible single-sideband concepts. In the former method, the electrical signal and its Hilbert transform are applied to the two electrodes of a dual-drive Mach-Zehnder biased in quadrature [4]. The hybrid or compatible single-sideband method uses a cascade combination of Mach-Zehnder (MZ) amplitude modulator and phase modulator also driven by the electrical signal and its Hilbert transform [5]. Therefore, both techniques rely on the use of non-standard electro-

optic modulators: one uses a specific, patented type of dual-electrode electro-optic modulator (EOM) and the other requires integration of MZ modulator and phase modulator on the same substrate.

In this paper we propose and experimentally demonstrate a novel OSSB electro-optic modulator structure based on the use of a standard single-electrode MZ-EOM and passive fiber optic components. Unlike previous OSSB EOM designs, this modulator has the benefit of being independent of the MZ-EOM bias phase shift and thus allows implementation of optical carrier suppression biasing the MZ-EOM for minimum transmission [6]. Therefore, avoidance of chromatic dispersion effects and reduction of the RF link insertion loss are simultaneously achieved.

II. MODULATOR DESIGN.

Fig. 1 a) shows the new modulator scheme. It uses an MZ-EOM inside a Sagnac interferometer that is biased at quadrature by a nonreciprocal element inside the structure. This design is similar to the Sagnac interferometer amplitude modulator (SIAM) [7] but using an amplitude modulator instead of a phase modulator inside the interferometer.

The modulator operation is described as follows. The polarized light from a CW optical source enters the modulator and is split in a polarization maintaining coupler (PMC). The resulting optical signals counter-propagate in the interferometer passing bidirectionally through the biasing element and MZ-EOM and finally recombine at the output. Polarization maintaining fiber (PMF) is used to achieve a stable polarization of the light within the structure.

The MZ-EOM is of the standard single travelling-wave electrode type with residual chirp parameter of α_{MZ} . The

electrode electrical termination ($\sim 50 \Omega$) is removed so that access is given to both input and output ports. In order to achieve OSSB the light passing bidirectionally through the MZ-EOM has to be modulated with the desired electrical signal in one direction and its Hilbert transform in the opposite direction. At high modulation frequencies, the electrical signal in a travelling-wave electrode only modulates efficiently the optical signal that copropagates with it. Therefore, the MZ-EOM can be used to modulate the two counter-propagating optical signals if electrical signals are introduced through both ports of the electrode [8]. This concept is illustrated in the modulator design of Fig. 1 a), where the electrical signal and its Hilbert transform enter the two MZ-EOM electrode ports and each electrical wave modulates the light that co-propagates with it.

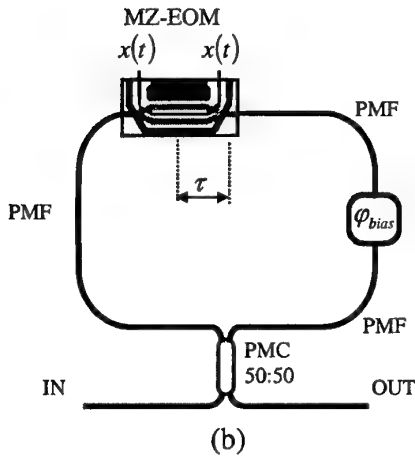
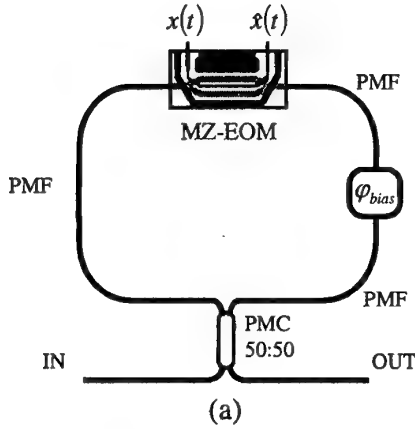


Figure 1. Schematic diagram of the OSSB modulator for (a) wideband and (b) narrowband operation.

The 90° Hybrid coupler needed to obtain the Hilbert transformed electrical signal is not necessary if the OSSB modulator is to be used for a narrow-band application, i.e. transmission of bandpass millimeter-wave signal over fiber optic links. As it is illustrated in Fig. 1 b), in this case the same signal is applied to both ports of the electrical electrode and the MZ-EOM is located asymmetrically in the interferometer so that at the output the modulating electrical signals have a relative delay τ . This delay is adjusted to provide an approximated 90° phase difference at the frequency band of interest.

The optical field at the output of the proposed modulator when it is driven with an electrical carrier of frequency f_e is given by

$$e_{OUT}(t) = \frac{E_0}{2 \cdot L} \cdot \left[\begin{aligned} & j \cdot \cos\left(\frac{m}{2} \cdot \sin(2\pi f_e t) + \frac{\phi_{Bias}}{2}\right) \cdot \exp\left(-j \cdot \frac{\alpha_{MZ} \cdot m}{2} \cdot \sin(2\pi f_e t)\right) \\ & + \cos\left(\frac{m}{2} \cdot \cos(2\pi f_e t) + \frac{\phi_{Bias}}{2}\right) \cdot \exp\left(-j \cdot \frac{\alpha_{MZ} \cdot m}{2} \cdot \cos(2\pi f_e t)\right) \end{aligned} \right] \cdot \exp(j \cdot 2 \cdot \pi \cdot \nu_0 t) \quad (1)$$

where E_0 is the optical field amplitude at the modulator input, ν_0 is the optical carrier frequency, m is the optical modulation depth and ϕ_{Bias} and L are the MZ-EOM bias phase shift and insertion loss. This expression can be expanded in terms of Bessel functions to give

$$e_{OUT}(t) = \frac{E_0}{4 \cdot L} \sum_{n=-\infty}^{+\infty} \left[\begin{aligned} & (j + (-j)^n) \cdot J_n\left(\frac{m}{2}(1 + \alpha_{MZ})\right) \cdot \exp\left(j \cdot \frac{\phi_{Bias}}{2}\right) \\ & + J_n\left(\frac{m}{2}(1 - \alpha_{MZ})\right) \cdot \exp\left(-j \cdot \frac{\phi_{Bias}}{2}\right) \end{aligned} \right] \cdot \exp(j \cdot 2 \cdot \pi \cdot n \cdot f_e t) \cdot \exp(j \cdot 2 \cdot \pi \cdot \nu_0 t) \quad (2)$$

where J_n is the n th-order Bessel function. As it can be seen the n th sideband is null whenever $(j + (-j)^n) = 0$ this occurs for $n = \dots, -7, -3, +1, +5, \dots$, and independently of the MZ-EOM chirp parameter and bias phase shift. In

contrast, previous OSSB EOM designs required the bias phase shift to be set at quadrature.

The optical power at the modulator output for arbitrary electrical signals is given by

$$P_{OUT}(t) = \frac{P_0}{4 \cdot L} \cdot \left[1 + \frac{1}{2} \cdot \left(\cos(m \cdot x(t) + \phi_{Bias}) + \cos(m \cdot x(t) + \phi_{Bias}) \right) \right] \quad (3)$$

where the residual modulator chirp has been neglected ($\alpha=0$) and $x(t)$ is the normalized applied RF signal.

III. EXPERIMENTS.

The experimental setup used to demonstrate the new OSSB modulator design is shown in Fig. 2. Due to the unavailability of a wide bandwidth EOM the feasibility of the system is demonstrated at low frequencies using a lumped element electrode MZ-EOM that equally modulates the light passing bidirectionally through it. This MZ-EOM is asymmetrically located in the interferometer with a delay τ adjusted to provide 90° phase shift at selected frequencies. The MZ-EOM has 19 dB of extinction ratio, 1 GHz bandwidth and $V_\pi = 6V$.

A 1550-nm DFB laser followed by an isolator is used as the optical source and the modulator output is connected to a heterodyne optical spectrum analysis arrangement. The nonreciprocal biasing element (ϕ_{Bias}) is implemented as in [7] with a quarter-wave plate between oppositely oriented 45° Faraday rotators. The insertion loss of the OSSB modulator was measured to be 11 dB. This is the addition of the insertion loss of the MZ-EOM (4 dB), biasing element (1.2 dB) and PMC

(6.8 dB).

To test the performance of the OSSB modulator it was driven with a 434-MHz 0-dBm RF signal. At this frequency the phase difference between the bidirectional modulating electrical signals is 90°. The modulator output optical spectrum for different MZ-EOM bias phase shift is depicted in Fig. 3. These are the optical spectra translated to the electrical domain by heterodyne mixing with a tunable laser (TL). In Fig. 3 a) the MZ-MEO bias phase shift is set at quadrature ($\phi_{Bias} = \pi/2$) and in b) at minimum transmission ($\phi_{Bias} = \pi$). The results are consistent with the theoretical prediction of sideband cancellation independent of the MZ-MEO bias. About 25 dB of sideband cancellation is obtained and this value is only limited by the uniformity of the PMC. If this modulator were used in a fiber link, the dispersion-induced electrical power ripple would be reduced to less than 1 dB.

Comparing the optical spectra of Fig. 3 b) (minimum transmission) and c) (maximum transmission, $\phi_{Bias} = 0$) we can see that the optical carrier is suppressed 19 dB. As expected this value equals the extinction ratio of the MZ-EOM used. Suppression of the optical carrier increases the effective optical modulation depth. This can lead to a reduction of the RF insertion loss of a link equal to the carrier suppression if the average optical power level is increased to compensate the attenuation of the carrier [9]. Furthermore, if the OSSB modulator is used for characterization of the transfer function of optical devices, the measurement dynamic range is increased suppressing the optical carrier.

Another design of OSSB suppressed-carrier modulator was presented in [10]. However, it requires a dual-drive OSSB modulator that is introduced inside a Sagnac interferometer for optical carrier suppression. The design presented in this article has a different operating principle: the Sagnac interferometer is used for sideband suppression and the optical carrier is attenuated setting the MZ-EOM bias phase shift.

In conclusion, we have presented a novel OSSB modulator design, which main advantages are that it uses a standard off-the-shelf externally terminated MZ-EOM and that it provides bias and chirp-parameter independent sideband cancellation. In this modulator the MZ-EOM bias phase shift can be set to suppress the optical carrier and reduce the RF link insertion loss or increase the dynamic range in optical transfer function

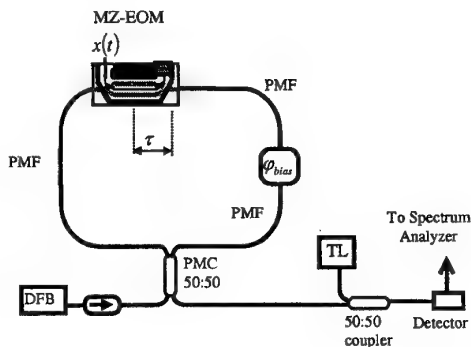


Figure 2. Experimental Setup.

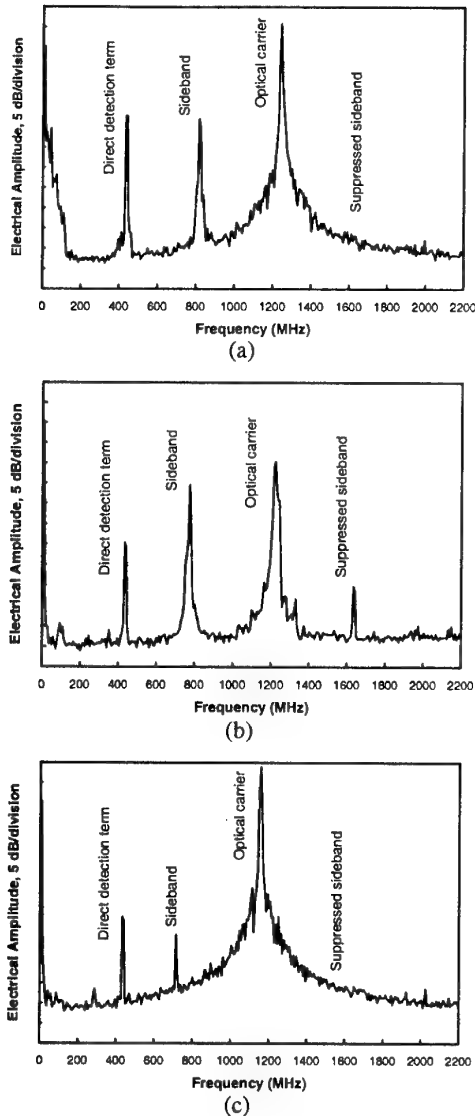


Figure 3. Heterodyned optical spectrum for (a) $\phi_{Bias} = \pi/2$, (b) $\phi_{Bias} = \pi$ and (c) $\phi_{Bias} = 0$.

measurement applications. The feasibility of the design has been experimentally demonstrated at low frequencies and operation at higher frequencies will be reported elsewhere.

This research was partially supported by Spanish Comisión Interministerial de Ciencia y Tecnología within project TIC98-1073-C02-02 and by a research project of the Gobierno de Navarra.

References

1. G. H. Smith, D. Novak, and Z. Ahmed, "Overcoming chromatic-dispersion effects in fiber-wireless systems incorporating external

modulators," *IEEE Trans. Microwave Theory Tech.*, vol. 45, pp. 1410-1415, 1997.

2. J. E. Román, M. Y. Frankel, and R. D. Esman, "Spectral characterization of fiber gratings with high resolution," *Opt. Lett.*, vol. 23, pp. 939-941, 1998.
3. J. Park, W. V. Sorin, and K. Y. Lau, "Elimination of the fibre chromatic dispersion penalty on 1550 nm millimetre-wave optical transmission," *Electron. Lett.*, vol. 33, pp. 512-513, 1997.
4. G. H. Smith, D. Novak and Z. Ahmed, "Technique for optical SSB generation to overcome dispersion penalties in fiber-radio systems," *Electron. Lett.*, vol. 33, pp. 74-75, 1997.
5. B. Davies, and Jan Conradi, "Hybrid Modulator Structures for Subcarrier and Harmonic Subcarrier Optical Single Sideband," *IEEE Photon. Technol. Lett.*, vol. 10, pp. 600-602, 1998.
6. R. Montgomery, and R. DeSalvo, "A Novel Technique for Double Sideband Suppressed Carrier Modulation of Optical fields," *IEEE Photon. Technol. Lett.*, vol. 7, pp. 434-436, 1995.
7. M. L. Dennis, I. N. Duling III, and W. K. Burns, "Inherently bias drift free amplitude modulator," *Electron. Lett.*, vol. 32, pp. 547-548, 1996.
8. R. D. Esman, and M. J. Marrone, "Passive Elimination of Polarization Sensitivity of Fiber-Optic Microwave Modulators," *IEEE Trans. Microwave Theory Tech.*, vol. 43, pp. 2208-2213, 1995.
9. R. D. Esman, and K. J. Williams, "Wideband Efficiency Improvement of Fiber Optic Systems by Carrier Subtraction," *IEEE Photon. Technol. Lett.*, vol. 7, pp. 218-220, 1995.
10. M. Y. Frankel, and R. D. Esman, "Optical Single-Sideband Suppressed-Carrier Modulator for Wide-Band Signal Processing," *J. Lightwave Technol.*, vol. 16, pp. 859-863, 1998.

EFFECT OF PILOT TONE-BASED MODULATOR BIAS CONTROL ON EXTERNAL MODULATION LINK PERFORMANCE

Edward I. Ackerman and Charles H. Cox III

Photonic Systems, Inc.

100 Wildwood Dr., Carlisle, Massachusetts 01741

Phone: (978) 369-0729, FAX: (978) 318-0556, email: eackerman@photonicssinc.com

ABSTRACT

The dynamic range of an external modulation link in which a pilot tone maintains a Mach-Zehnder modulator at quadrature bias is limited to $64/(\pi m_{PT})^4$, where m_{PT} is the modulation depth of the pilot tone.

INTRODUCTION

In an analog external modulation link that uses an external modulator, the third-order intermodulation distortion products generated by the modulator's nonlinear transfer function set the upper limit on the RF signal powers that can be relayed by the link with high signal fidelity. If the laser that provides unmodulated light to the modulator has sufficiently low relative intensity noise (RIN), then shot noise sets the lower limit on the RF signal power.

Analytical models [1] and experimental measurements [2] have both shown that, for an external modulation link that uses a Mach-Zehnder interferometric modulator (MZM) at its quadrature bias and a detector operating at a DC photocurrent of 2.5 mA, the range of RF signal powers between these two limits, which is the intermodulation-free dynamic range ($IMFDR_3$), is approximately $110 \text{ dB} \cdot \text{Hz}^{2/3}$. In this paper we show that the conventional method of maintaining the MZM bias at quadrature, involving the injection of a pilot tone with a typical modulation depth of 2.5%, reduces this $IMFDR_3$ to roughly 62 dB.

ANALYSIS

The bold curve in Figure 1 shows the transfer function of an MZM, which dictates how the link's output RF signal power and second-order distortion products vary with modulator bias. Maintaining the MZM bias at quadrature is especially important in links operating in systems with bandwidths wider than one octave, because only at the quadrature bias point are second-order distortion products minimized.

Figure 2 shows the method that is used most frequently for maintaining MZM bias voltage at quadrature point. This consists of a local oscillator that generates a pilot tone, usually at around 1 kHz or so, and a photodetector that taps a small percentage of the MZM's optical output power. The photodetector feeds a circuit that filters out all but the second harmonic of the pilot tone frequency, and a feedback loop continuously adjusts the MZM's DC bias voltage to minimize the detected second harmonic.

Injecting a pilot tone to control the MZM's bias point lowers the link's $IMFDR_3$ because the third-order nonlinearity of the modulator's transfer function results in intermodulation distortion products at two *in-band* frequencies equal to the desired RF signal frequency plus and minus twice the pilot tone frequency. These distortion products appear at the link output and cannot be filtered out unless one limits the link's operational bandwidth to less than twice the pilot tone frequency.

For the external modulation link in Figure 2, in which a quadrature-biased MZM is modulated by two-tone signal $v_{RF}(\cos \omega_{RF1}t + \cos \omega_{RF2}t)$ and pilot tone $v_{PT} \cos \omega_{PT}t$, the optical power illuminating the detector, P_D , can be represented as:

$$P_D = P_{D,\max} \left[\frac{1}{2} + \frac{\pi}{2} [m_{RF}(\cos \omega_{RF1}t + \cos \omega_{RF2}t) + m_{PT} \cos \omega_{PT}t] + \frac{\pi^3}{12} [m_{RF}(\cos \omega_{RF1}t + \cos \omega_{RF2}t) + m_{PT} \cos \omega_{PT}t]^3 + \dots \right], \quad (1)$$

where $P_{D,\max}$ is the optical power illuminating the photodetector at the output of the link when the MZM is biased for maximum transmission, and where the modulation depth m is defined as v/V_π . Expressing P_D as a function of m allows for the possibility that the RF and pilot tones are applied to separate electrodes of the MZM, which may have different V_π 's.

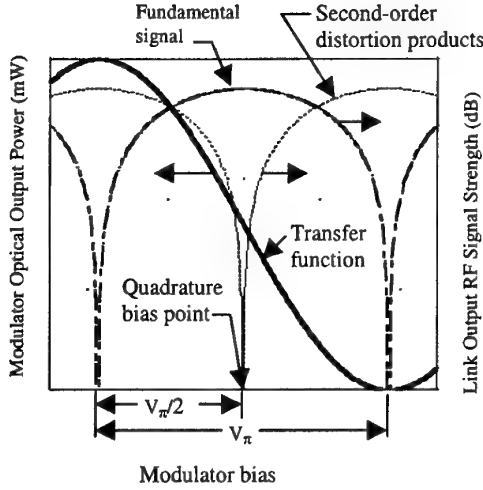


Fig. 1 Transfer function of an MZM, plus the link output power at the fundamental RF and second-order distortion frequencies.

To determine the effect of the pilot tone on the link's dynamic range requires using equation (1) to calculate the magnitude of P_D at three frequencies: 1) RF signal frequency ω_{RF1} (or equivalently, ω_{RF2}), 2) in-band intermodulation distortion product frequency $2\omega_{RF1} - \omega_{RF2}$ (or equivalently, $2\omega_{RF2} - \omega_{RF1}$), and 3) in-band intermodulation frequency $\omega_{RF1} \pm 2\omega_{PT}$ (or equivalently, $\omega_{RF2} \pm 2\omega_{PT}$):

$$|P_D(\omega_{RF1})| = P_{D,max} \frac{\pi}{2} m_{RF}; \quad (2)$$

$$|P_D(2\omega_{RF1} - \omega_{RF2})| = P_{D,max} \frac{\pi^3}{16} m_{RF}^3; \quad (3)$$

$$|P_D(\omega_{RF1} \pm 2\omega_{PT})| = P_{D,max} \frac{\pi^3}{16} m_{RF} m_{PT}^2. \quad (4)$$

The photodetector at the link output generates electrical power at each of these frequencies according to the relation:

$$P_{out} = \frac{1}{2} |I_D|^2 R_{out}, \quad (5)$$

where I_D is related to P_D through the detector responsivity, and where R_{out} is the link output impedance. The detector also generates shot noise power at the link output as follows:

$$\begin{aligned} N_{out} &= 2q \langle I_D \rangle R_{out} B \\ &= q I_{D,max} R_{out} B \text{ at quadrature bias,} \end{aligned} \quad (6)$$

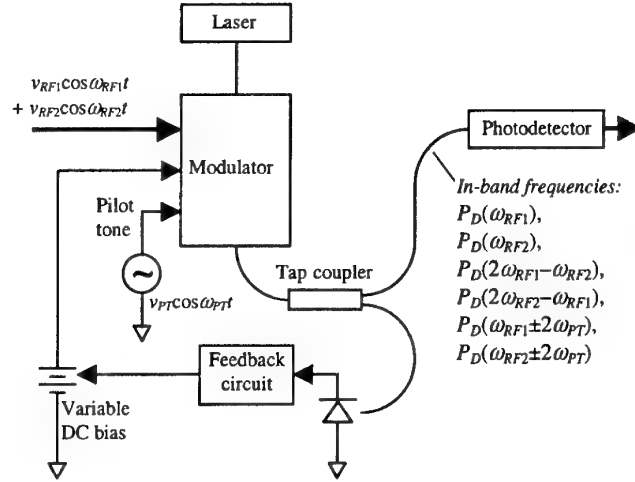


Fig. 2 Method of controlling external modulator bias by injecting a pilot tone and using feedback correction to maintain quadrature bias.

where q is the electronic charge and B is the instantaneous receiver bandwidth.

For a link that sees two equal-power input RF signal tones, Figure 3 shows how the link output powers at the three frequencies in equations (2)-(4) vary with input power. Also plotted in Figure 3 is the link output noise power, which is independent of the RF input power and which is assumed to be dominated by the shot noise. In the absence of a pilot tone, shot noise limits $IMFDR_3$ of an MZM-based external modulation link to a value of:

$$IMFDR_3 = \left(\frac{I_{D,max}}{qB} \right)^{2/3}, \quad (7)$$

which corresponds to about $110 \text{ dB} \cdot \text{Hz}^{2/3}$ for $\langle I_D \rangle = I_{D,max} / 2 = 2.5 \text{ mA}$. In addition Figure 3 shows that, when a pilot tone is present, $IMFDR_3$ can be limited by the mixing of an RF tone and the pilot tone rather than by the mixing of two RF tones. Thus the actual link dynamic range is whichever is smaller of what was calculated using equation (7) or

$$IMFDR_3 = \frac{64}{(\pi m_{PT})^4}. \quad (8)$$

Note that Equation (8), which is simply the square of the ratio of equations (2) and (4), depends only on the pilot tone strength and not on B .

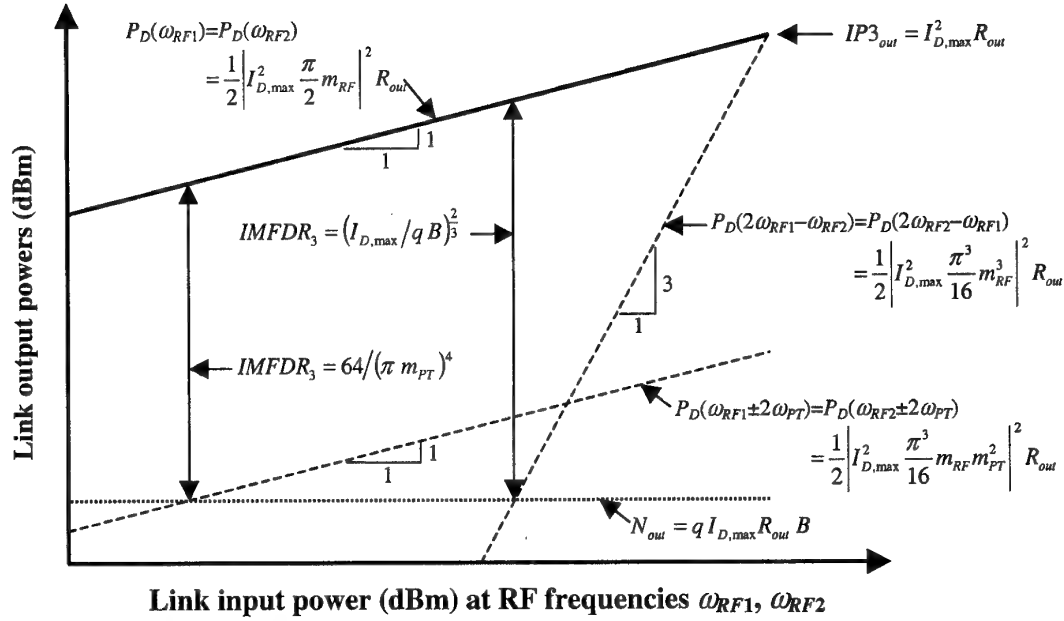


Fig. 3 Relationship between MZM-based external modulation link's two-tone input signal power and output powers at the tone frequencies and at the frequencies where in-band distortion products are generated. Like the output power at the signal frequencies ω_{RF1} and ω_{RF2} , the output powers at the in-band intermodulation distortion frequencies $\omega_{RF2} \pm 2\omega_{PT}$ and $\omega_{RF1} \pm 2\omega_{PT}$ increase linearly (i.e., with a slope of 1) with respect to link input power at ω_{RF1} and ω_{RF2} . Thus, as the figure shows, the degree of IMFDR₃ degradation caused by the use of the pilot tone depends on the receiver instantaneous bandwidth B .

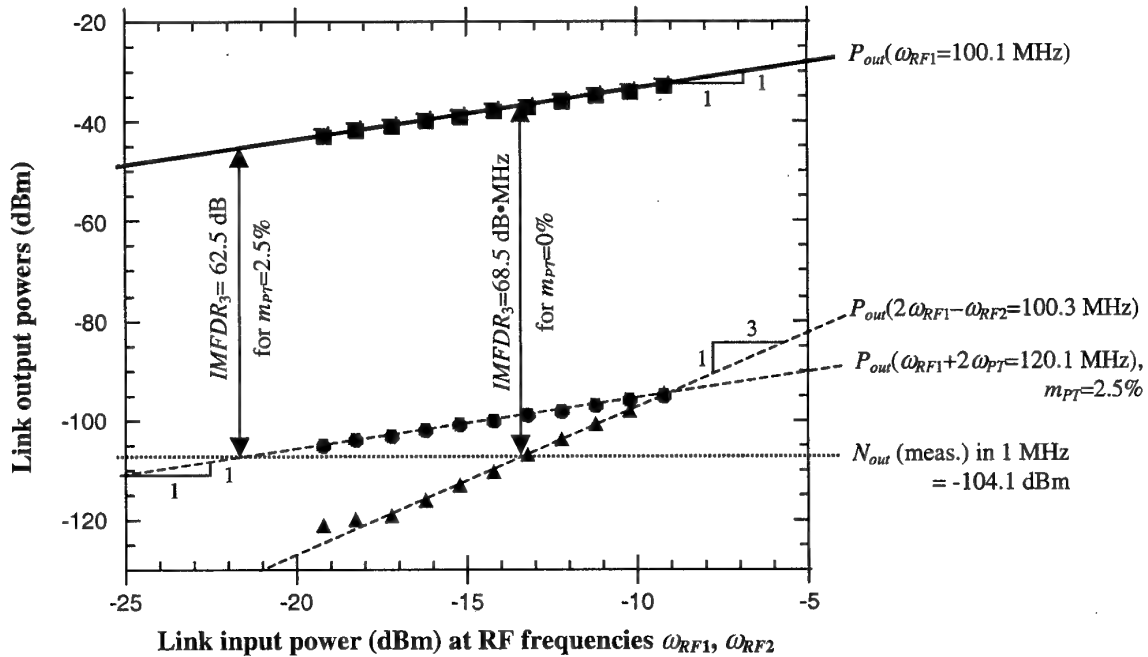


Fig. 4 Results of two-tone intermodulation distortion measurement on an MZM-based external modulation link with and without pilot-tone based modulator bias control (i.e., with pilot tone modulation depth $m_{PT} = 2.5\%$ and 0% , respectively). Measured data and extrapolated curves are shown.

EXPERIMENT

To verify that Figure 3 and the equations from which it is derived are valid, we performed measurements on the type of link diagrammed in Figure 2. We used an InGaAsP diode laser with a PM fiber pigtail to provide 30 mW of low-RIN optical power at $\lambda=1.55\ \mu\text{m}$ to the modulator. For the modulator we used a standard lithium-niobate MZM with an input PM fiber and output SM fiber pigtail and with separate RF and DC bias electrodes. The DC electrode exhibited a V_π of about 4.8 V. For the signal photodetector we used an InGaAs PIN photodiode with a responsivity of 0.9 A/W. The laser bias current was adjusted such that when the MZM was at quadrature bias we measured 2.5 mA of DC photocurrent.

For the experiment we used two signal generators to provide the modulator's RF input port with tones at 99.9 MHz and 100.1 MHz, and used an RF spectrum analyzer with the resolution bandwidth set to $B=1\ \text{MHz}$ to measure link output signal and noise powers at all frequencies of interest. We performed two-tone intermodulation distortion measurements with the MZM bias controlled manually, and subsequently with a 10 MHz pilot tone of amplitude $v_{PT}=120\ \text{mV}$ ($\approx 2.5\%$ of 4.8 V) applied to the DC electrode of the MZM. The individual data points on the plot in Figure 4 show how our measurements confirmed that, for these values of B and m_{PT} , $IMFDR_3$ is degraded by about 6 dB due to the use of a pilot tone-based MZM bias controller. Note that for smaller values of B , the output noise would be proportionally smaller, and therefore the $IMFDR_3$ degradation due to the pilot tone would be even more pronounced.

CONCLUSIONS

We have shown that using a pilot tone-based control circuit to maintain a modulator's optimum bias point can have a detrimental effect on an external modulation link's dynamic range. The specific extent of the performance degradation depends on the instantaneous bandwidth of the receiver in the system, and on the strength of the pilot tone.

To counteract this effect, a bias control circuit of this type may need to use a weaker pilot tone in conjunction with an optical coupler that has a higher tap percentage. For instance, reducing the

typical pilot tone modulation depth from 2.5% to 0.5% implies that the typical 1% optical tap coupler should be replaced by a 5% coupler in order to maintain the same detection sensitivity.

The findings we have reported and experimentally verified using an MZM also carry implications for other types of external modulators—including "linearized" modulators, in which the third-order distortion is cancelled using one of a variety of methods [3]. That is, if the linearized bias point is maintained using a pilot tone-based feedback circuit, the modulator may generate stronger in-band intermodulation distortion products by mixing the pilot tone with an input RF tone than by mixing two input RF tones, resulting in smaller link dynamic range than what the linearized modulator would otherwise enable.

REFERENCES

- [1] E. Ackerman and C. Cox, "Trade-offs between the noise figure and dynamic range of an analog optical link," *Proc. Photonic Systems for Antenna Applications Conf.*, February 2000.
- [2] G. Betts, C. Cox, and K. Ray, "20-GHz optical analog link using an external modulator," *IEEE Photon. Technol. Lett.*, vol. 2, pp. 923-925, December 1990.
- [3] U. Cummings and W. Bridges, "Bandwidth of linearized electro-optic modulators," *J. Lightwave Technol.*, vol. 16, pp. 1482-1490, August 1998.

MILLIMETRE-WAVE BANDWIDTH ELECTRO-ABSORPTION MODULATORS AND TRANSCEIVERS

Andreas Stöhr, Robert Heinzelmann, and Dieter Jäger

Gerhard-Mercator-Universität, ZHO - Optoelektronik, Lotharstr. 55, 47057 Duisburg, Germany
Phone: +49 203 379 - 2825, Fax: +49 203 379 - 2409, E.mail: stoehr@uni-duisburg.de

This paper reports on high-speed electroabsorption modulators (EAMs) tailored for analogue fibre-optic microwave and millimetre-wave (mm-wave) transmission. Important device issues of broadband lumped and travelling-wave (TW) EAMs are discussed. Additionally, the concept of a lumped EAM with an impedance tuning circuitry is presented for mm-wave narrow-band wireless applications. Further focus is laid upon a multifunctional millimetre-wave electroabsorption transceiver (EAT) that not only acts as a conventional modulator but can simultaneously be employed as a photodetector and an optoelectronic mixer (EATX).

Introduction

Electroabsorption modulators (EAMs) are a very attractive alternative among the various types of optical modulators because they offer a number of excellent features. Its high bandwidth-to-drive voltage ratio and low chirp together with its integrability with lasers and electronic drive circuitry are just some of the important attributes of EAM that have made these components almost indispensable to high-bit rate fibre-optic communication systems. Recently, 10-Gbit/s and 20-Gbit/s systems employing packaged EAM modules have been reported and 40-Gbit/s experiments are well underway [1-3]. Besides these digital applications, EAM are also very attractive for analogue radio frequency (RF) fibre-optic transmission systems because they offer the potential for high RF link gain and exhibit low distortion and high dynamic range [4-6]. Its small size and compactness are additional features altogether indicating that external EAM may provide a cost-effective solution for the fibre-optic transmission of micro- and millimetre-waves [7].

Another feature of electroabsorption waveguide structures is that they can be utilized not only for modulation but also for photodetection thus offering the potential for analogue RF fibre-optic transceiver applications [8-10]. Such EA modulator-/photodetector components, which we call electroabsorption transceiver (EAT), comprise dual-functionality in a single chip. EATs allow full-duplex fibre-optic data transmission at microwave

and mm-wave carrier frequencies and, obviously, high-speed EAT are very attractive components for wireless picocellular systems and interactive remote sensing applications. Recently, experimental set-ups for fibre based sub-carrier multiplexed (SCM) wireless picocellular networks employing EAT have been realized and "error-free" full-duplex broadband data transmission at microwave and 60-GHz mm-wave carrier frequency has been achieved [10,11].

This paper reports on electroabsorption modulators tailored for analogue fibre-optic applications in the microwave and millimetre-wave regime. Important device issues of lumped EAM and TW-EAM for analogue applications including the potential for high RF link gain are addressed. A lumped EAM terminated by an impedance tuning circuit is presented to exhibit an improved link gain within a narrow frequency band in the mm-wave regime. Further focus is laid upon multifunctional millimetre-wave electroabsorption transceivers that not only act as conventional modulators but can simultaneously be employed as photodetectors (EAT) and also as optoelectronic mixers (EATX).

Millimetre-wave EAM

Lumped EAM - The high-frequency response of a lumped EAM is mainly limited by the device capacitance. Providing that the devices are small and microwave losses are negligible, the 3-dB cut-off frequency of the RF link gain of lumped EAMs with a *p-i-n*-diode optical waveguide structure and

an open termination port is given by the well-known RC time constant:

$$f_{3dB} = (2 \cdot \pi \cdot Z_S \cdot C'_M \cdot L)^{-1}. \quad (1)$$

Here Z_S is defined as the characteristic impedance of the source transmission line, C'_M represents the total modulator capacitance per unit length and L denotes the device length. Obviously, for high-frequency operation the total device capacitance $C'_M L$ should be small, but reducing the waveguide length or increasing the thickness of the intrinsic region results in a smaller modulation efficiency. Recently, short lumped EAMs (63 to 100- μm) with a p - i - n -diode waveguide structure have been investigated by various authors exhibiting large bandwidths in excess of 40-GHz [12,13]. In [14] we demonstrated a 65- μm short non-terminated lumped EAM with a record bandwidth of about 70-GHz using a *Schottky-i-n*-diode structure. However, as mentioned above, lumped EAMs with short lengths have lower modulation efficiencies and require relatively higher driving voltages.

Travelling-wave EAM - To overcome this length limitation the travelling-wave (TW) concept has been applied to EAMs. Because the electrode capacitance of the electrical transmission line is distributed, TW-EAMs are not limited by the RC time constant. Thus they allow for longer devices with the potential for improved bandwidth-to-drive-voltages [15,16]. Recently, a 200- μm long TW-EAM with a 54-GHz bandwidth and a driving voltage of only 1.5-V (for 10-dB extinction) was reported [17]. An essential requirement for broadband TW-EAMs is the realisation of a low-loss electrical transmission line that is terminated by an impedance, matched to the characteristic impedance of the transmission line. Furthermore, it is required that the microwave phase velocity is matched to the optical group velocity. Another important design issue one has to consider is the quite large optical propagation loss per unit length that is typically in the order of 15 to 20-dB/mm [1,18] for EAMs based on a multiple quantum well (MQW) structure. Because of the high optical and electrical losses, the maximum length for optimum modulation efficiency of a TW-EAM currently appears to be around 200- μm [19].

EAM with impedance tuning circuit - All the above mentioned requirements and design issues for TW-EAM are often conflicting and difficult to fulfil. Additionally, many analogue applications, such as wireless communication do not require full-band operation from DC but devices tailored to have a peak response in the frequency band of interest. For those applications, it appears to be of advantage to enhance the modulation efficiency of the EAM only within the narrow frequency band of interest. This can be achieved by employing an electrical impedance tuning circuit [20]. Since an EAM is driven by the electric field in its active capacitance C_M , a high voltage is required in order to increase the modulation efficiency. Consequently, for narrow band applications, an impedance tuning circuit as termination of a lumped EAM should be used to increase the input impedance of the EAM within the frequency band of interest. This way, a larger RF link gain is achieved because a larger voltage is applied to the EAM. For comparison, we simulated the RF link gain versus frequency for a non-terminated lumped EAM, a travelling-wave EAM with impedance and velocity matching and an EAM with a lossy open stub as termination optimised for maximum link gain at 60-GHz. To allow for a fair comparison, all simulated devices have a 200- μm long and 4- μm wide waveguide with a 300-nm thick intrinsic region. Frequency dependent microwave propagation losses as well as intrinsic losses have been considered. As can be seen from Fig. 1, the link gain of the impedance tuned EAM at 60-GHz is improved by 7.2-dB to the non-terminated lumped EAM and by 5-dB to the TW-EAM. Additionally, it should be noted, that due to the tuning circuit the input reflection coefficient is shifted from values close to -1 to much smaller values. Thus s_{11} of the impedance tuned EAM is much smaller as compared to the lumped and TW-EAM (Fig. 2), and therefore back-reflection into the EAM driver circuitry is avoided by a certain amount.

Millimetre-wave EAT

Another feature of EA waveguides is that they can simultaneously be used not only for optical modulation but also for optical detection. Such modulator/detector components exhibit a large potential for simplified full-duplex bi-directional

millimetre-wave transmission, when used as an electroabsorption transceiver (EAT). Previously, we employed EATs in wireless picocellular systems and demonstrated full-duplex mm-wave fibre-wireless transmission of broadband data employing a dual-wavelength approach to separate the optical up- and downlink carrier [10,11]. Here, we propose another 60-GHz mm-wave transceiver element that is distinct as it provides additionally mixer functionality (EATX). The EATX simultaneously acts as a mm-wave photodetector, an IF-band external modulator, and a IF-to-RF upconverter. To experimentally investigate its mixing performance a set-up for optical heterodyning (Fig. 3) was used. Two laser diodes (λ_1 and λ_2) whose beat frequency is equal to the desired mm-wave RF carrier frequency (57-GHz) are combined. Furthermore, one of the laser diodes is directly modulated by an IF signal (2.6-GHz). In this configuration, the EATX generates the mm-wave RF carrier and simultaneously upconverts the IF signal to the mm-wave region thus avoiding the

necessity for a mm-wave EAM. The electrical output signal of the EATX is shown in Fig. 4, demonstrating efficient mm-wave upconversion with a carrier power of -30-dBm and a carrier-to-upconverted-sideband ratio of 15-dBc.

Conclusion

Broadband lumped EAMs and travelling-wave EAMs are discussed. An impedance tuned EAM design is presented that provides improved RF link gain at mm-wave frequencies. This device is especially dedicated to narrow-band wireless applications in the mm-wave regime. Additionally, multifunctional EATs and EATXs are discussed and efficient IF-to-mm-wave frequency upconversion is experimentally demonstrated.

Acknowledgement

The authors thank Prof. K. Kitayama, Osaka University, and Dr. T. Kuri, CRL Tokyo, for their cooperation regarding the transceiver work.

References

- [1] T. Ido et al., *J. of Lightwave Technol.*, vol. 14, no. 9, pp. 2026-2034, 1996.
- [2] K. Yamada et al., *OFC-95*, Technical Digest, pp. 24-25, 1995.
- [3] F. Devaux et al., *IEEE Photon. Technol. Lett.*, vol. 5, no. 11, pp. 1288-1290, 1993.
- [4] K. Yoshino et al., *ECOC-96*, Proceedings, pp. 203-206, 1996.
- [5] S. Kaneko et al., *J. of Lightwave Technol.*, vol. 14, no. 4, pp. 669-676, 1999.
- [6] K.K. Loi et al., *IEEE Photon. Technol. Lett.*, vol. 10, no. 11, pp. 1572-1574, 1998.
- [7] K. Kitayama, *Fiber and Integrated Optics*, vol. 19, no. 2, pp. 167-186, 2000.
- [8] L. Noel et al., *IEEE Trans. on Microwave Theory and Techniques*, vol. 45, no. 8, part 2, pp. 1416-1423, 1997.
- [9] R.B. Welstand et al., *IEEE Photon. Technol. Lett.*, vol. 8, no. 11, pp. 1540-1542, 1996.
- [10] A. Stöhr et al., *IEEE Trans. on Microwave Theory and Techniques*, vol. 47, no. 7, part 2, pp. 1338-1341, 1999.
- [11] A. Stöhr et al., *Electron. Lett.*, vol. 35, no. 19, pp. 1653-1655, 1999.
- [12] K. Yoshino et al., *J. of Lightwave Technol.*, vol. 17, no. 9, pp. 1700-1707, 1999.
- [13] K. Satzke et al., *Electron Lett.*, vol. 31, no. 23, pp. 2030-2031, 1995.
- [14] A. Stöhr et al., *Appl. of Photonic Technology 2*, Plenum Press, eds. Lampropoulos, Lessard, pp. 871-876, 1997.
- [15] N. Dagli, *IEEE Trans. on Microwave Theory and Techniques*, vol. 47, no. 7, pp. 1151-1171, 1999.
- [16] V. Kaman et al., *Electron. Lett.*, vol. 35, no. 12, pp. 993-935, 1999.
- [17] K. Kawano et al., *Electron. Lett.*, vol. 33, no. 18, pp. 1580-1581, 1997.
- [18] K. Yamada et al., *Electron. Lett.*, vol. 31, no. 3, pp. 237-238, 1995.
- [19] G.L. Li et al., *IEEE Trans. on Microwave Theory and Techniques*, vol. 47, no. 7, part 2, pp. 1177-1183, 1999.
- [20] N. Mineo et al., *OFC-98*, Technical Digest, vol. 2, pp. 287-288, 1998.

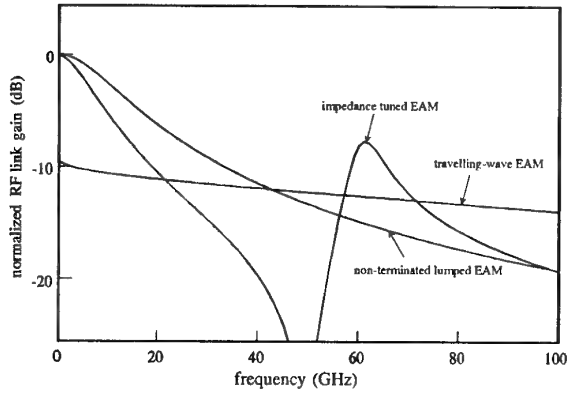


Fig. 1: Comparison of normalised RF link gain at mm-wave frequencies employing non-terminated lumped EAM, TW-EAM or impedance tuned EAM.

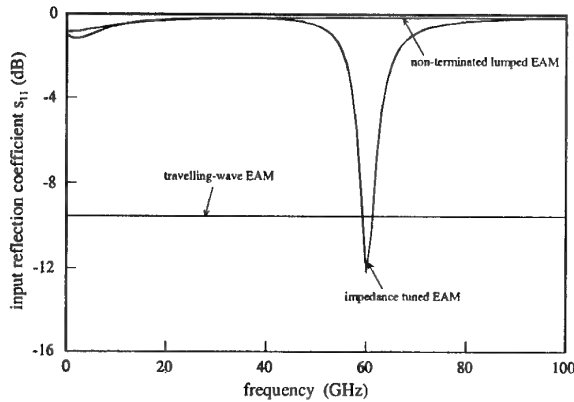


Fig. 2: Comparison of the input reflection coefficients at mm-wave frequencies of non-terminated lumped EAM, TW-EAM and impedance tuned EAM.

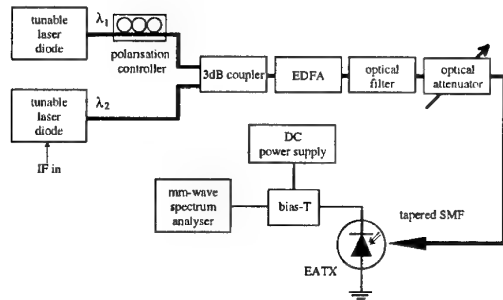


Fig. 3: Experimental set-up for photonic IF-to-mm-wave upconversion employing an mm-wave EATX

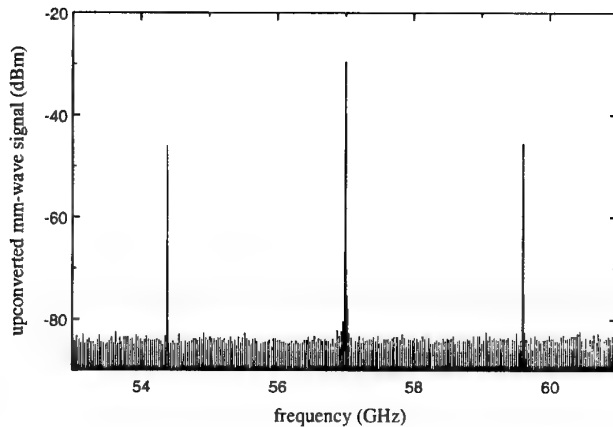


Fig. 4: Measured signal spectrum of an IF signal (2.6GHz) upconverted to mm-wave frequency (57GHz) by using an EATX.

MILLIMETRE-WAVE RADIO-OVER-FIBRE TRANSMISSION USING AN OPTICAL INJECTION PHASE-LOCK LOOP SOURCE

L.A. Johansson and A.J. Seeds

Department of Electronic and Electrical Engineering, University College London,
Torrington Place, London WC1E 7JE, United Kingdom.

Tel: +44 20 7679 7928, Fax: +44 20 7387 4350, E-mail: a.seeds@ee.ucl.ac.uk

ABSTRACT

A broadband millimetre-wave radio-over-fibre demonstration experiment is presented, using an optical injection phase-lock loop as the optical source. 140 Mbit/s ASK data is transmitted with a 36 GHz carrier using fibre-pigtailed commercial off-the-shelf components

INTRODUCTION

Millimetre-wave radio-over-fibre presents an attractive method for delivery of broadband wireless services. A key requirement for such systems is an efficient technique for the optical generation of the millimetre-wave carrier. Laser diodes can generally not be directly modulated at millimetre-wave frequencies and chromatic dispersion limits the transmission distance to a few hundred metres in standard single-mode fibre [1]. Alternative generation methods include the use of external optical modulators [2,3] and optical heterodyning with optical phase lock loops (OPLL) [4] or optical injection locking (OIL) [5].

External optical modulators can be modulated at millimetre-wave frequencies. However, optical insertion losses are large, particularly for schemes which generate dispersion tolerant modulated optical signals. Kitayama [2] used a chirped fibre grating to compensate for the fibre dispersion, thus being able to use double sideband modulation to transmit 155 Mbit/s DPSK data but this approach requires custom compensation of the fibre length used. Another approach has been demonstrated by Smith et al [3], where a Mach-Zehnder optical modulator, with the electrodes driven out of phase by $\pm \pi/2$, was used to generate optical

and electrical single sideband modulation to transmit 155 Mbit/s BPSK data.

Optical heterodyning, i.e. the beating of two closely spaced optical frequency components spaced by the required millimetre-wave frequency on a photodetector offers high dispersion tolerance. High power is available, as all optical power contributes to the generated signal, high frequencies are attainable, limited only by the photodetector bandwidth and data can easily be placed on only one optical component. One method that has been demonstrated by Gliese et al, is the optical phase lock loop [4]. It was used to transmit 100 Mbit/s PSK data on a 9 GHz carrier. The limitation of this approach is the requirement for very low group delay components and micro-optic construction to limit the loop delay time or alternatively the need for specialised narrow linewidth lasers. However, wide locking range can be obtained with active feedback. Optical injection locking has been demonstrated by Braun et al [5] with transmission of 140 Mbit/s CPFSK data on a 60 GHz carrier. OIL can use standard DFB lasers to generate millimetre-wave signals with high purity but with limited locking range due to the finite injection ratio. Common to both of these heterodyne demonstrations is that no optical amplifier was needed in contrast to the modulator-based demonstrations.

This paper describes a novel method for the optical generation of a millimetre-wave carrier by optical heterodyning, without the limitations of the OIL and the OPLL. Transmission of 140 Mbit/s ASK data, applied to one of the optical lines in a dispersion resistant format is demonstrated.

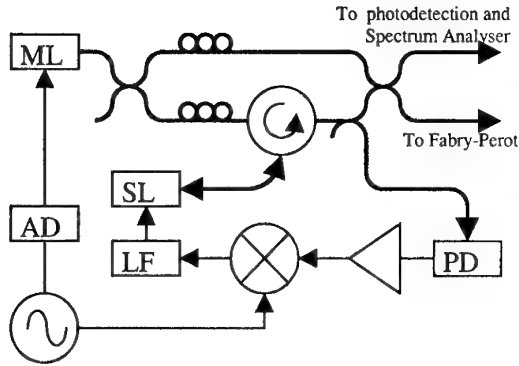


Fig. 1. Experimental arrangement for the fibre based OIPLL system. ML: master laser, SL: slave laser, PD: photodetector, LF: loop filter, AD: adjustable delay line. Thick line indicates the optical path.

THE OIPLL

In [6], an all-fibre millimetre-wave optical injection phase lock loop (OIPLL) system was demonstrated for the first time. Fig. 1 shows the experimental layout of the OIPLL system. A millimetre-wave carrier was optically generated by a fibre integrated optical injection phase lock loop, Fig. 2. Single sideband noise spectral density of -92 dBc/Hz at 10 kHz offset and phase error variance lower than 0.005 rad² in 100 MHz bandwidth were measured. The locking bandwidth exceeded 30 GHz. The requirements for short loop propagation delay or low combined laser linewidth that apply to an OPLL system are much less stringent for an OIPLL system, allowing lasers with linewidths about 100 MHz to be used in a fibre based system with 20 ns loop propagation delay, retaining the excellent locking bandwidth and the long term stability found in an OPLL system. The wider locking range of the OIPLL relative to OIL illustrated by Fig. 3, also ensures much improved long-term stability and prevents loss of lock due to fluctuations in the external environment. Fig. 4 shows the total phase error variance of the OIPLL as a function of noise bandwidth. The performance of the OIPLL is limited by the noise floor due to the finite injection ratio in the injection locking process for carrier offsets greater than a few

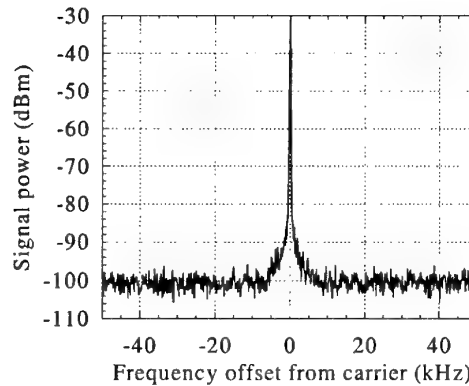


Fig. 2. Spectrum of generated 36 GHz beat signal. Span: 100 kHz, Res. b/w: 100 Hz.

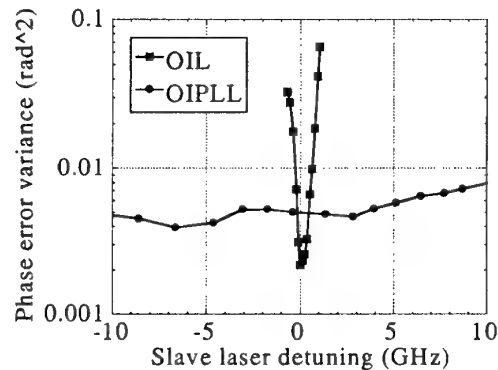


Fig. 3. Phase error variance in a 100 MHz noise bandwidth as a function of slave laser detuning for the OIPLL and corresponding OIL system.

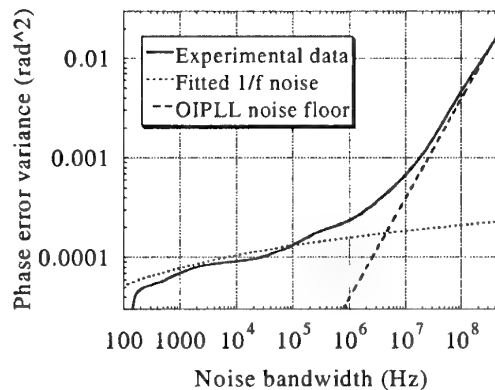


Fig. 4. Phase error variance of the OIPLL as a function of noise bandwidth.

megahertz. At lower frequencies, the noise is limited by the phase noise of the reference, with $1/f$ characteristics. An implication of this is that for higher data rates (~ 100 Mbit/s) there would be little penalty for applying multilevel modulation formats for fixed data rates.

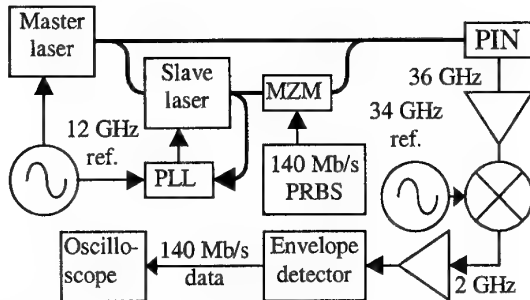


Fig. 5. Experimental layout for data transmission experiment. Thick line indicates optical path.

TRANSMISSION EXPERIMENT

Fig. 5 shows the experimental layout of the data transmission experiment. A 140 Mbit/s PRBS feeds an optical Mach-Zehnder optical modulator imposing ASK data onto one of the optical lines of the heterodyne system. The received 36 GHz signal was down-converted to 2 GHz in a triple balanced mixer. The ASK modulated carrier was then demodulated in a simple envelope detector and the recovered signal was observed on a digital oscilloscope. The resulting eye diagram is shown in Fig. 6, showing good eye opening characteristics. In this simple transmission experiment, the performance of the radio-over-fibre system would be limited by the characteristics of the radio path, rather than by the spectral purity of the optically generated carrier.

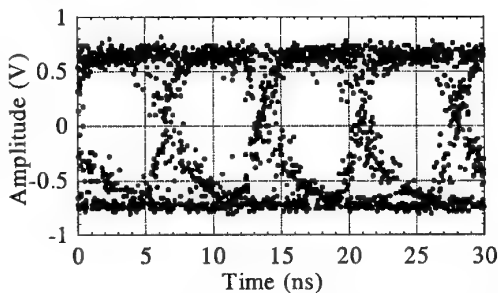


Fig. 6. Recovered eye diagrams for 140 Mbit/s ASK data.

CONCLUSION

In this paper the use of an optical injection phase lock loop as a source for millimetre-wave radio-over-fibre transmission systems has been demonstrated for the first time. 140 Mbit/s ASK data has been transmitted at 36 GHz carrier frequency. This demonstration shares the common advantages of using millimetre-wave generation by optical heterodyning; high efficiency eliminating the need for optical amplifier and ease of applying data to only one optical line to give a dispersion resistant system. The OIPLL compares favourably to alternative methods of optical heterodyning, OPLL and OIL in that it can be realised with commercial off-the-shelf technology and offers high environmental stability. Good phase noise suppression together with a wide locking range has been demonstrated together with dispersion resistant modulation using only a baseband optical modulator. Further work will concentrate on detailed evaluation of transmission characteristics over practical radio-over-fibre networks.

ACKNOWLEDGMENTS

This work was supported by the UK Engineering and Physical Sciences Research Council under the Optical Systems Integration Programme in collaboration with Nortel Networks and BT Advanced Communication Technology Centre. The authors would like to acknowledge BT Advanced Communication Technology Centre (Dr. D. Wake) for the supply of lasers.

REFERENCES

1. U. Gliese, S. Norskov and T.N. Nielsen, "Chromatic dispersion in fibre-optic microwave and millimeter-wave links," *IEEE Trans. Microwave Theory Tech.*, vol. 45, pp. 1716-1724, 1997.
2. K. Kitayama, "Fading-free transport of 60 GHz-optical DSB signal in non-

- dispersion shifted fiber using chirped fiber grating," *International Topical Meeting on Microwave Photonics, Technical Digest*; Princeton, New Jersey, pp. 223-226, 1998.
3. G.H. Smith and D. Novak, "Broad-band millimeter-wave (38 GHz) fiber-wireless transmission system using electrical and optical SSB modulation to overcome dispersion effects," *IEEE Photon. Technol. Lett.*, vol. 10, pp. 141-143, 1998.
 4. U. Gliese, T.N. Nielsen, S. Norskov and K.E. Stubkjaer, "Multifunctional fiber-optic microwave links based on remote heterodyne detection," *IEEE Trans. Microwave Theory Tech.*, vol. 46, pp. 458-468, 1998.
 5. R.-P. Braun, G. Grosskopf, D. Rodhe and F. Schmidt, "Optical millimeter-wave generation and transmission experiments for mobile 60 GHz band communications," *Electron. Lett.*, vol 32, pp. 626-628, 1996.
 6. L.A. Johansson and A.J. Seeds, "Millimetre-Wave Modulated Optical Signal Generation with High Spectral Purity and Wide Locking Bandwidth using a Fibre-Integrated Optical Injection Phase-Lock Loop," *IEEE Photon. Tech. Lett.*, vol. 11, June 2000.

Dispersion Effects of Optical Filter in DWDM Millimeter-Wave Fiber-Radio Systems

K. Kitayama, T. Kamisaka, K. Onohara

Department of Electronics and Information Systems, Osaka University

2-1 Yamadaoka, Suita, Osaka 565-0871, JAPAN

Phone: +81 6-6879-7692/ Fax: +81 6-6879-7688/ E-mail: kitayama@comm.eng.osaka-u.ac.jp

and

W. Chujo

Communications Research Laboratory, MPT

4-2-1 Nukui-Kitamachi, Koganei, Tokyo 184-8795, JAPAN

Phone: +81-42-327-5552 / Fax: +81-42-327-7035 / E-mail: chujo@crl.go.jp

Abstract-

Theoretical analysis of the dispersion effect of Fiber Bragg grating (FBG) in DWDM fiber-radio systems is presented. The experiments verify that signal fading occurs to 60GHz-band optical DSB signal near the band edge of FBG.

I. Introduction

To accommodate a large number of antenna bas stations (BSs) in millimeter (mm)-wave fiber-radio access systems, dense wavelength division multiplexing (DWDM) will be a powerful approach[1]. A wide bandwidth extending over 25THz of doped-fiber amplifiers has recently become available from 1450nm to 1650nm, including S+, S, C, L, and L+ bands, in the low-loss transmission window of optical fibers. The highest spectrum efficiency[2] and optical add/drop multiplexing (OADM) using fiber Bragg gratings (FBGs)[3] have been demonstrated in DWDM mm-wave fiber-radio systems. Recently, it has been pointed out that the dispersion effect of optical filters could be detrimental in DWDM IM-DD optical communication systems[4]. This might be the case with DWDM fiber-radio systems.

In this paper, we will present the theoretical analysis of dispersion effect of FBG on mm-wave optical signals. The experiment verifies that the fading occurs to 60GHz-band optical DSB signal near the band edge of FBG. This will suggest that the dispersion effects has

to be considered in the DWDM channel allocation for mm-wave fiber-radio access systems.

II. Theoretical analysis

A. System model

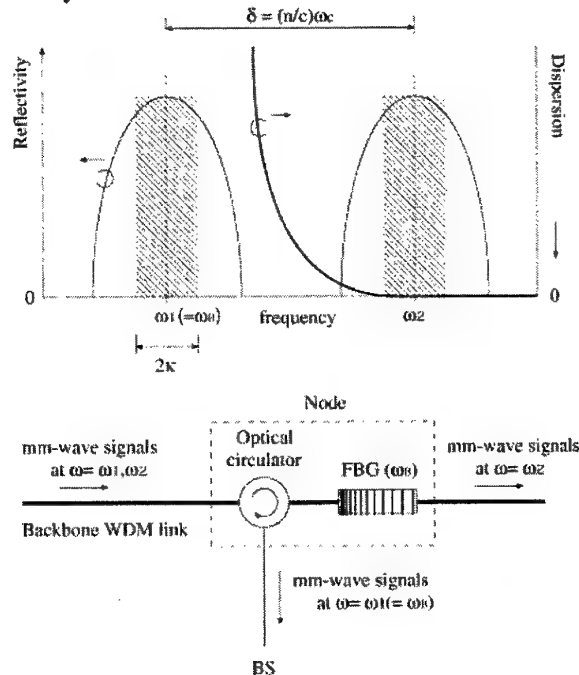


Fig.1 DWDM fiber-radio system employing the OADM using a FBG and the wavelength channel allocation.

Let us consider DWDM fiber-radio system employing the OADM as shown in Fig.1. A FBG in reflection along with an optical

circulator serves as the OADM. At each node the downlink optical radio signals are dropped from the backbone WDM link and delivered to BSs. From BSs the uplink optical signals are added to the backbone and transmitted to the CS. A few optical radio signals may be multiplexed on a single wavelength. The wavelength channel allocation is also depicted in Fig.1. There is the ITU-T standard for WDM grids of $193.100\text{THz} \pm 50\text{GHz} \times N$, ($N=1,2,\dots$) in 1550nm region. However, the mm-wave fiber-radio systems may require the different wavelength allocation, otherwise the channels may traverse the neighboring grid. This will be an issue to be addressed.

B. Dispersion of FBG

The FBG is a versatile optical filter widely used for WDM applications. Suppose that for simplicity there are two mm-wave radio signals on a mm-wave subcarrier frequency ω_m on the optical carrier frequency ω_i ($i=1,2$); one is reflected by the FBG and dropped, and the other passes through the FBG. Assume that the optical carrier ω_1 is set to be equal to the Bragg frequency ω_B of the FBG, so that it is reflected by the FBG, while the optical carrier ω_2 is set apart from ω_B .

Let us look at the dispersion effect of the FBG on the pass-through channel which will be allocated on the next to the dropped channel. The propagation constant β_g and the quadratic dispersion β_g'' of FBG are given by[5]

$$\beta_g(\delta) = \frac{n_{\text{eff}}}{c} \pm \delta \left\{ 1 - \left(\frac{\kappa}{\delta} \right)^2 \right\}^{1/2}$$

$$\beta_g''(\delta) = \pm \left(\frac{n_{\text{eff}}}{c} \right)^2 \frac{1}{\delta} \left(\frac{\kappa}{\delta} \right)^2 \left\{ 1 - \left(\frac{\kappa}{\delta} \right)^2 \right\}^{-3/2} \quad (1)$$

and the detuning parameter δ is

$$\delta = \frac{n_{\text{eff}}}{c} (\omega - \omega_B) \quad (2)$$

where n_{eff} is the effective refractive index of the FBG, and κ is the coupling coefficient characterizing the strength of grating. Here, the material dispersion is neglected. As is schematically illustrated in Fig.1, the dispersion goes infinity for $\kappa/\delta=1$. This occurs at the edge of amplitude reflection band of 2κ .

Obviously, the dispersion effect on the pass-through channel could be detrimental when the wavelength is allocated near the band edge.

C. Dispersion effect on mm-wave optical signal

The optical field of intensity-modulated optical carrier ω_i at the input of optical fiber is expressed by

$$E_i(0,t) \equiv \sqrt{I_0} e^{j\omega_i t} \left[1 + \frac{m}{2} (1 + j\alpha) \cos \omega_m t \right], \quad (i=1,2) \quad (3)$$

where I_0 is the signal intensity, α the chirp parameter of the light modulator, and m the modulation depth. Here, the laser phase is ignored because the phase noise effect can be negligible in the practical systems using DFB laser diodes[6]. After passing through the FBG, the optical field of output signal is expressed by

$$E(L,t) = \sqrt{I_0} \exp j\{\omega_0 t - \beta_f(\omega_0)L_f - \beta_g(\omega_0)L_g\}$$

$$+ \frac{m}{2} \sqrt{(1+\alpha^2)} I_0 \exp j\{(\omega_0 + \omega_m)t - \beta_f(\omega_0 + \omega_m)L_f$$

$$- \beta_g(\omega_0 + \omega_m)L_g + \tan^{-1} \alpha\}$$

$$+ \frac{m}{2} \sqrt{(1+\alpha^2)} I_0 \exp j\{(\omega_0 - \omega_m)t - \beta_f(\omega_0 - \omega_m)L_f$$

$$- \beta_g(\omega_0 - \omega_m)L_g + \tan^{-1} \alpha\} \quad (4)$$

where β_f represents the propagation constant of optical fiber, L_f and L_g the lengths of optical fiber and FBG, respectively. Hereafter, the fiber dispersion is omitted for the sake of demonstration simplicity. It should be noted that the dispersion effect of optical fibers on the mm-wave optical DSB signal can be compensated either by using FBG[7] or optical phase conjugator[8]. After detecting the signal using a photodetector, the output photocurrent i_p is obtained as

$$i_p \propto 2mI_0 \sqrt{1+\alpha^2} \cos \frac{1}{2} \{-\omega_m^2 \beta_g''(\omega_0)L_g + 2 \tan^{-1} \alpha\}$$

$$\bullet \cos\{\omega_m t - \tau(\omega_0)L_g\} \quad (5)$$

where τ denotes the group delay of FBG. It is seen from Eq.(5) that the signal intensity changes depending on the dispersion of FBG, and the signal completely fades for the worst scenario that the condition,

$\omega_m^2 \beta_g''(\omega_0) L_g + 2 \tan^{-1} \alpha = n\pi$ ($n=1, 2, \dots$) is satisfied.

III. Experiment

A. Experimental setup

The experimental setup of the OADM for 60GHz-band optical signal is shown in Fig.2. Two DFB laser diodes are used; the wavelength of LD1 is set at $\lambda_1=1549.2\text{nm}$ which is equal to the Bragg wavelength, λ_B of FBG, and the wavelength of LD2, λ_2 is tunable. A 60GHz-band InGaAsP electroabsorption modulator (EAM) is used as the EO converter[9]. A pin photodiode having 3dB bandwidth of 50GHz is used as the OE converter. A FBG along with an optical circulator is placed between the laser sources and the detector.

The two optical carriers are intensity-modulated with the EAM by applying the mm-wave signal, thus generating two optical DSB signals. The data signal is 156Mbit/s NRZ $2^{23}-1$ PRBS in a DPSK format with the intermediate frequency (IF) of 2.6GHz and the local oscillator (LO) of 57.0GHz. The optical DSB signal is detected by the photodetector, and the output electrical signal is demodulated and directed to the BERT.

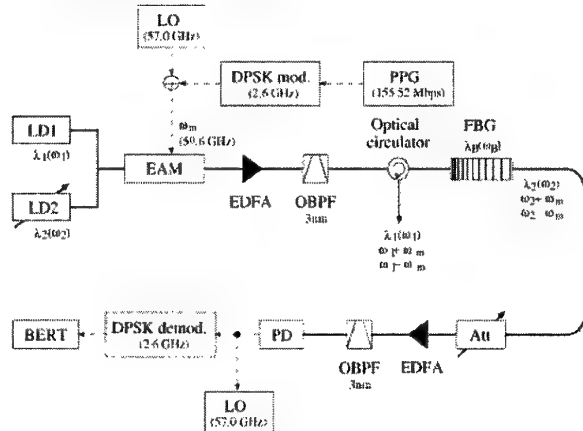


Fig.2 Experimental setup of the OADM for 60GHz-band optical signal.

B. Experimental results

The measured optical spectrum of optical signal after the FBG is shown in Fig.3. The measured power reflectivity of FBG is also shown in the inset. It maintains roughly 90% reflectivity is over 2nm wide spectral range. It

shows that the other optical signal at $\lambda_1=1549.2\text{nm}$ is completely dropped by the FBG. The detected 59.6GHz signal power and its theoretical prediction of Eq.(5) are plotted as a function of wavelength λ_2 in Fig.4. The transmitted power and the dispersion of the FBG are also shown. The signal fading is clearly observed. As increasing the dispersion value in the shorter wavelength region, the fading becomes more frequent. This tendency is supported by the theory. The bit error rate measurements for the 156Mbit/s PRBS data also confirmed the signal fading.

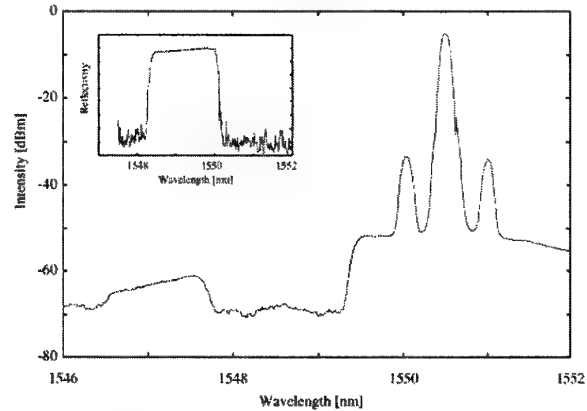


Fig.3 Measured optical spectrum of optical signal after the FBG and the measured power reflectivity of FBG.

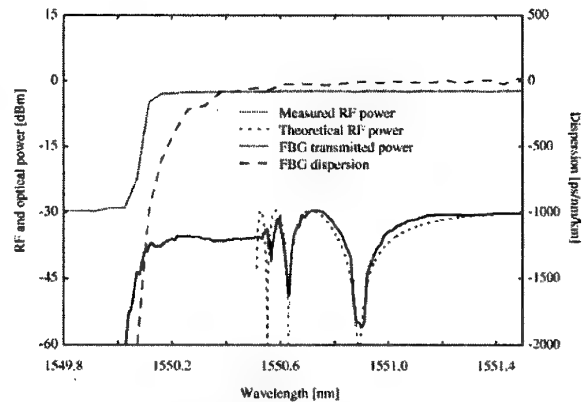


Fig.4 Detected 59.6GHz signal power and its theoretical prediction of Eq.(5) as a function of wavelength λ_2 . The transmitted power and the dispersion of the FBG are also shown.

IV. Conclusion

Theoretical analysis of the dispersion effect of FBG in DWDM fiber-radio systems has been presented. The experiments have verified

that signal fading occurs to 60GHz-band optical DSB signal near the band edge of FBG. This suggests that the dispersion effects has to be considered in the DWDM channel allocation for mm-wave fiber-radio access systems.

Acknowledgement

The authors would like to thank Y. Tomiyama of Communication Research Laboratories (CRL) for assisting in experiment. K. Kitayama would like to thank for the support by the Center of Excellence (COE), Japan. T. Kamisaka and K. Onohara wish to thank for the Trainee Program of CRL.

References

- [1] K. Kitayama, T. Kuri, H. Yokoyama, and M. Okuno, "60GHz millimeter-wave generation and transport using stabilized mode-locked laser diode with optical frequency DEMUX switch," *IEEE 1996 Global Telecommunications Conference (GLOBECOM'96)*, pp. 2162-2169 (London, 1996).
- [2] K. Kitayama, "Highly spectrum efficient OFDM/PDM wireless networks by using optical SSB modulation," *J. Lightwave Technol.*, vol.16, pp. 969-976, 1998.
- [3] R. Heinzlmann, T. Kuri, K. Kitayama, A. Stöhr, and D. Jager, "OADM of 60GHz-millimeter-wave signal in WDM radio-on-fiber ring," *2000 Optical Fiber Conference(OFC2000)*, FH4 (Baltimore, 2000).
- [4] B. J. Eggleton, G. Lenz, N. Litchiniser, D. B. Patterson, and R. E. Slusher, "Implications of fiber grating dispersion for WDM communication systems," *IEEE Photonic Technol. Lett.*, vol.9, pp.1403-1405, 1997.
- [5] R. Kashap : *Fiber Bragg gratings* (Academic Press, 1999).
- [6] K. Kitayama, "Ultimate performance of optical DSB signal based mm-wave fiber-radio system: Effect of laser phase noise," *J. Lightwave Technol.*, vol.17, pp.1774-1781, 1999.
- [7] K. Kitayama, "Fading-free transport of 60GHz-optical DSB signal in non dispersion shifted fiber using chirped fiber grating," *International Topical Meeting on Microwave Photonics(MWP'98)*, WB4 (Princeton 1998).
- [8] H. Sotobayashi and K. Kitayama, "Cancellation of signal fading for 60GHz subcarrier multiplexed optical DSB signal transmission in non-dispersion-shifted fiber using midway optical phase conjugation," *J. Lightwave Technol.*, vol.17, pp.2488-2497, 1999.
- [9] T. Kuri, K. Kitayama, A. Stohr, and , Y. Ogawa, "Fiber-optic millimeter-wave downlink system using 60GHz-band external modulation," *J. Lightwave Technol.*, vol.17, pp.799-806, 1999.

156 Mb/s DPSK Optical MM-Wave Transmission Employing a 60 GHz Optoelectronic Image Rejection Mixer

Y. Ozeki, K. Nishikawa*, M. Kishi and M. Tsuchiya

Department of Electronic Engineering, University of Tokyo

7-3-1 Hongo, Tokyo 113-8656, Japan

Tel: +81-3-5841-6779, Fax: +81-3-5841-6779, E-mail: ozeki@ktl.t.u-tokyo.ac.jp

**Presently with Fujitsu Laboratories Ltd.*

Abstract— This paper reports on the demonstration (BER < 10^{-9}) of 156 Mb/s DPSK optical mm-wave signal transmission over a 20 km standard single-mode fiber with an 18 dB optoelectronic image rejection mixer employed.

I. INTRODUCTION

In future broadband wireless access systems employing the schemes of fiber-optic millimeter-wave (mm-wave) links [1], it is attractive to centralize the signal processing functionalities to a central office (CO) and to make antenna base stations (BSs) ultimately simple [2]. It is because such BS simplification provides not only reduction in their construction and maintenance costs but also highly flexible capability to keep up with renewal in modulation format or frequencies.

On the other hand, it is important to generate an RF signal with suppressed LO or image components when those are unnecessary from the viewpoint of efficient use of frequency resource. Such an essential functionality can be realized in a CO with fiber-optic mm-wave links employed by either of the followings: (a) the electrical mm-wave filtering method or (b) the electrical mm-wave phase control as usually used in an electrical image rejection mixer (IRM). However, it is not possible in the former to deal with modification of RF frequencies, leading to increase in inflexibility of the links. As for the latter, on the other hand, related monolithic integrated circuit technologies are still premature.

We proposed, as a possible alternative to surpass those conventional methods, the optoelectronic IRM (OE-IRM) scheme [3] which

offers not only suitability to fiber-optic mm-wave links but also fairly high image rejection (IR) ratios at mm-wave frequencies or higher without either (a) or (b) employed. Indeed, we have shown its basic concept and confirmed its operational principle by a preliminary experiment with an acoustooptic modulator [3]. It was followed by the successful demonstration of 156 Mb/s ASK optical mm-wave signal transmission [4] employing an OE-IRM with a finite bandwidth.

However, the ASK format is not an ultimate solution from the IRM operation point of view in spite of its merit that the transmission characteristics are not heavily affected by the carrier phase noise. In this paper, we report on the demonstration of 156 Mb/s OE-IRM-based optical mm-wave signal transmission over a 20 km-long standard single-mode fiber (SMF) with the differential phase shift keying (DPSK) format. As well known, the DPSK format is more frequently utilized in the wireless access systems than the ASK format.

II. CONFIGURATION OF THE OE-IRM

Figure 1 shows the OE-IRM configuration which we used in the present work [4][5]. The polarization mode dispersion (PMD) filtering method [3] is chosen for the elimination of unnecessary sideband signals. Its operational principle is as follows. The input to OE-IRM is a dual-mode optical LO signal, which is first divided by a fiber Bragg grating (FBG) and an optical circulator: one (OLO1) is reflected by the FBG and the other (OLO2) is transmitted. The former is led into a Mach-Zehnder Modulator (MZM), in which an optical IF

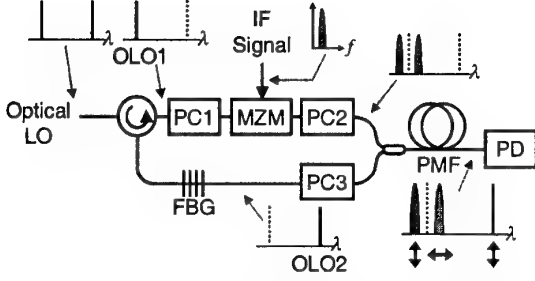


Fig. 1. The OE-IRM configuration employing the PMD filtering method; PC, polarization controller.

signal is generated by double sideband modulation with the suppressed carrier (DSB-SC) method. After the optical IF signal and OLO2 are combined, they are led into a polarization maintaining fiber (PMF). Its length is around $L_\pi = (2\Delta\tau\Delta f)^{-1}$ [6] so that the polarization states of two sidebands of optical IF signal are orthogonal to each other at its output (see in Fig. 1). Here, $\Delta\tau$ is a PMD value and $\Delta f (= 2f_{IF})$ is the optical frequency separation. By adjusting the polarization state of OLO2, the heterodyne-detection of these spectra provides a mm-wave upper sideband (USB) signal at $f_{LO} + f_{IF}$ with suppressed signals at f_{LO} and $f_{LO} - f_{IF}$ (lower sideband, LSB).

Similarly to our previous result [3], the expected output optical spectra are those of optical-single-sideband modulation, providing the robustness to the chromatic dispersion penalty [7]. In addition, this configuration is advantageous compared with that in our original work [3]: dual-mode optical LO signals generated in various ways [8]–[11] are acceptable, in some of which required electric circuits can be simplified.

In comparison with other optical filtering techniques such as a Fabry-Perot filter, a Mach-Zehnder filter and so on, the PMD filtering method is attractive since the filtering characteristics are dependent only on Δf and are independent of the lightwave frequency. One should note here that the polarization retardation depends on the IF signal frequency. This gives a limiting factor of bandwidth; the USB to LSB ratio (IR ratio) is expressed by $10 \log [\tan^2(\pi f_{offset}/4f_{IF})]$ dB when the IF signal frequency is set off by f_{offset} from f_{IF} . It was confirmed experimentally that the measured IR ratio coincided with such estimation and that a 20 dB IR

ratio bandwidth of more than 400 MHz was derived at $f_{IF} = 2$ GHz [4]. Moreover, one can expect that the bandwidth will be even broadened if a higher IF frequency is used.

Higher performance can be expected with a similar configuration if one uses a broadband optical frequency shifter (OFS) [4][12][13]. However, it is not commercially available at present. Therefore, we have reserved the study on the ultimate performance of OFS-based OE-IRM for the future works and will place our emphasis on the investigation of the performance of the PMD filtering-based configuration hereafter in order to examine the potential of OE-IRM.

III. FIBER-OPTIC TRANSMISSION EXPERIMENT

We demonstrated the optical mm-wave DPSK signal transmission using the OE-IRM. Figure 2 shows the experimental setup. A LiNbO₃ MZM (LO-MZM) was driven by a 28.5 GHz signal to generate a 57 GHz dual-mode optical LO signal through the DSB-SC method [8]. A 2 GHz DPSK IF signal was generated from a 155.52 Mb/s PRBS 2²³-1 NRZ signal in the CO, amplified, and injected into the OE-IRM. We should note that the propagation lengths of OLO1 and OLO2 along the fibers should be similar to each other. Otherwise, the phase noise in the laser light causes an RF phase noise generated by the heterodyne-detection and affects the DPSK signal demodulation. The length of PMF ($\Delta\tau = 1.59$ ns/km) L was 78 m while L_π is 78.6 m. The difference between L and L_π leads to negligible influence on the filtering characteristics and the output RF power. A 1.0 nm optical band-pass filter was set at the output of OE-IRM to remove the ASE noise of EDFAs.

The output light of the OE-IRM was transmitted over a 20 km-long standard SMF to a BS. A 59 GHz DPSK signal was generated in a pin-photodiode at BS and amplified. Figure 3 shows the RF spectra of the BS output. The corresponding RF powers are shown in Table I, which indicate that IR ratio and USB to LO ratio are 18 dB and 8 dB, respectively, even after 20 km SMF transmission. These values are, however, lower than those expected from the results of single tone measurement [4]. The reason is not clear at

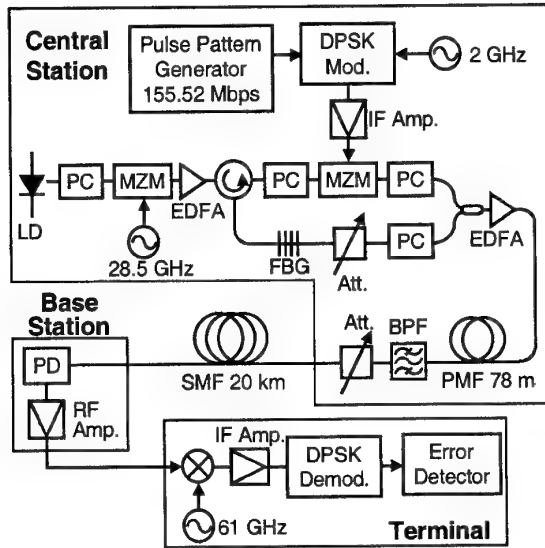


Fig. 2. Experimental setup for 156 Mb/s optical mm-wave signal transmission over a 20 km SMF.

present and, therefore, detailed investigation is needed to improve it. Since there exists a slight amount of PMD in the standard SMF, it would be worried that the initial polarization states are distorted to some extent through the whole transmission, resulting in possible degradation in the IR ratio. However, it was found out to be only 1 dB in the present experiment.

The BS and a wireless terminal were connected by a coaxial cable and free-space transmission between them was omitted this time, which should be done in the future. The mm-wave signal thus generated was down-converted to 2 GHz therein and the baseband signal was regenerated by the DPSK demodulator. Figure 4 shows measured bit error rate (BER) characteristics with an obtained eye diagram (inset). The latter shows clear eye opening, while a BER of $< 10^{-9}$ was achieved at the received optical power P_{opt} of -14.5 dBm. These results suggest that the OE-IRM utilized here possesses potentially what was expected concerning the DPSK optical mm-wave transmission. One exception is the rather poor IR ratio.

We used an external cavity laser diode as an optical source and, therefore, the phase noise included in it was low enough to prevent the signal degradation. However, one should be careful and clarify the effect when one uses a laser diode of low coherence. Furthermore, temporal fluctuation in the fiber length

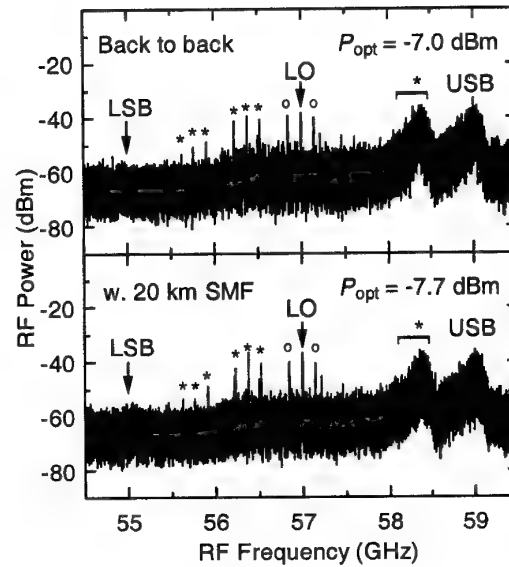


Fig. 3. The RF spectra generated in the BS. Note that the LSB component is suppressed. The peaks marked with asterisks are spurious response due to harmonic mixer used for the measurement and are not real signals. The ones with circles are upconverted 156 MHz signals which were included in the IF signal.

TABLE I
MEASURED RF POWER

	LSB	LO	USB
Back to back	-47 dBm	-38 dBm	-28 dBm
20 km SMF	-47 dBm	-37 dBm	-29 dBm

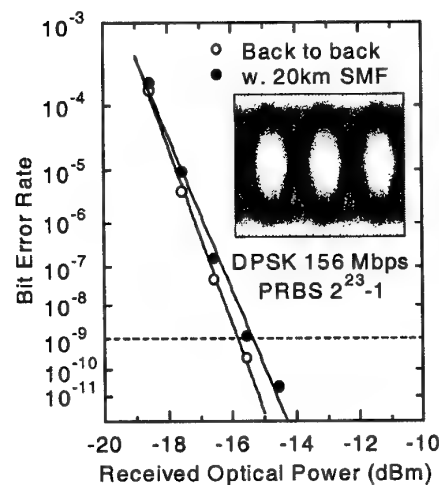


Fig. 4. Measured BER plotted as functions of received optical power P_{opt} and eye diagram.

causes the phase variation in the photo-detected mm-wave signal. Probably a phase-lock loop circuit is required in a mobile terminal in order to utilize the BPSK format.

IV. CONCLUSION

By using an OE-IRM configuration with the PMD filtering scheme, 156 Mb/s DPSK optical mm-wave transmission was performed and BER of 10^{-9} was achieved. The obtained image rejection ratio is 18 dB which could be improved. It is thus confirmed that an OE-IRM can be applicable to the fiber-optic wireless links with the DPSK format although more detailed investigation on the suppression ratios is needed

ACKNOWLEDGMENTS

The authors would like to thank S. Shiraishi and H. Hasebe of Sumitomo Electric Industries for providing the FBG. They would also like to thank T. Kamiya for his continuous encouragement.

REFERENCES

- [1] H. Ogawa, D. Polifko, and S. Banda, "Millimeter-Wave Fiber Optics Systems for Personal Radio Communication," *IEEE Trans. Microwave Theory Tech.*, vol. 40, pp. 2285-2293, 1992.
- [2] T. Ohno, S. Fukushima, Y. Doi, Y. Muramoto, and Y. Matsuoka, "Application of Uni-Traveling-Carrier Waveguide Photodiodes in Base Stations of a Millimeter-Wave Fiber-Radio System," in *Tech. Dig. MWP'99*, pp. 253-256, paper F-10.2.
- [3] K. Nishikawa and M. Tsuchiya, "60 GHz Optoelectronic Mixing with High Image Rejection Ratio ($> 36\text{dB}$)," in *Tech. Dig. MWP'99*, pp. 235-238, paper F-9.5.
- [4] Y. Ozeki, K. Nishikawa, M. Kishi and M. Tsuchiya, to be submitted.
- [5] Similar configurations have been reported for different purposes from ours; for instance, J. O'Reilly and P. Lane, "Remote Delivery of Video Services Using mm-Waves and Optics," *J. Lightwave Technology*, vol. 12, pp. 369-375, 1994;
- M. Ogura, T. Arakawa, S. Kojima, M. Kobayashi and M. Izutsu, "A Study of a Mm-wave Transmission System by Optical Fiber," in *Proc. the 2000 IEICE General Conference, Hiroshima*, p. 698, paper B-5-313. (in Japanese);
- [6] H. Schmuck, "Effect of polarisation-mode-dispersion in fibre-optic millimetre-wave systems," *Electron. Lett.*, vol. 30, pp. 1503-1504, 1994.
- [7] U. Gliese, S. Nørskov, and T. N. Nielsen, "Chromatic Dispersion in Fiber-Optic Microwave and Millimeter-Wave Links," *IEEE Trans. Microwave Theory Tech.*, vol. 44, pp. 1716-1724, 1996.
- [8] J. J. O'Reilly, P. M. Lane, R. Heidemann, and R. Hofstetter, "Optical generation of very narrow linewidth millimetre wave signals," *Electron. Lett.*, vol. 28, pp. 2309-2311, 1992.
- [9] K. Sato, A. Hirano, M. Asobe and H. Ishii, "Chirp-compensated 40 GHz semiconductor modelocked lasers integrated with chirped gratings," *Electron. Lett.*, vol. 34, pp. 1944-1946, 1998.
- [10] D. Wake, C. R. Lima, and P. A. Davies, "Transmission of 60-GHz Signals Over 100km of Optical Fiber Using a Dual-Mode Semiconductor Laser Source," *IEEE Photon. Technol. Lett.*, vol. 8, pp. 578-580, 1996.
- [11] L. Noël, D. Wake, D. G. Moodie, D. D. Marcenac, L. D. Westbrook, and D. Nasset, "Novel Techniques for High-Capacity 60-GHz Fiber-Radio Transmission Systems," *IEEE Trans. Microwave Theory Tech.*, vol. 45, pp. 1416-1423, 1997.
- [12] M. Izutsu, S. Shikama, and T. Sueta, "Integrated Optical SSB Modulator/ Frequency Shifter," *IEEE J. Quantum Electron.*, vol. QE-17, pp. 2225-2227, 1981.
- [13] S. Shimotsu, S. Oikawa, T. Saitou, N. Mitsugi, K. Kubodera, T. Kawanishi, and M. Izutsu, "LiNbO₃ Optical Single-Sideband Modulator," in *Proc. OFC 2000*, Feb.2000, paper PD16.

Laser Phase Noise Free Optical Heterodyne Detection Technique for 60-GHz-Band Radio-on-Fiber Systems

Toshiaki Kuri and Ken-ichi Kitayama[†]

Communications Research Laboratory, MPT,

4-2-1, Nukui-Kitamachi, Koganei, Tokyo 184-8795, JAPAN

Phone: +81-42-327-6331 / Facsimile: +81-42-327-7035 / E-mail: kuri@crl.go.jp

[†] Department of Electronics and Information Systems, Osaka University,

2-1, Yamadaoka, Suita, Osaka 565-0871, JAPAN

Abstract— Optical heterodyne detection technique of millimeter-wave-band fiber-radio signal with phase noise cancellation is proposed. Error-free detection of a 59.6-GHz, 156-Mb/s-DPSK signal transmitted over a radio-on-fiber system is experimentally confirmed without any serious phase noise effect.

I. INTRODUCTION

In radio-on-fiber systems, the external modulation provides a simple base station (BS) configuration, leading to accelerating an initial commercial deployment [1]. We have already reported the fiber-optic millimeter-wave (mm-wave) down- and up-link systems using a 60-GHz-band electroabsorption modulator (EAM) [2]–[3]. To receive large optical power enough to get error-free transmission quality, the system cannot help using optical amplifiers. In analog optical systems such as radio-on-fiber applications, however, accumulated amplified spontaneous emission (ASE) noise from optical amplifiers cannot be removed any longer. The noise is fatal for the photodetected signal. It is generally well-known that optical coherent detection has higher-sensitivity for received optical signal than direct detection [4]. So, we expect that the coherent detection can avoid using optical amplifiers

In this paper, laser phase noise free optical heterodyne detection technique of mm-wave fiber-radio signals with phase noise cancellation is proposed. In proposed technique, a

free-running dual-mode local light source is used to detect a 60-GHz-band fiber-radio signal. Because only two components of the optical signal are selected out by the local light and used to demodulate, this technique is theoretically immune from the fiber dispersion which causes the signal fading, even if the optical signal is double sideband (DSB) format. When two photodetected signals in the first intermediate-frequency (IF) range are multiplied each other, the differential component appears in the second IF range without any laser phase noise. This means that this detection technique is in principle free from the laser phase noise. To confirm the principle, the error-free detection of 60-GHz-band, 156-Mb/s-DPSK fiber-radio signal is experimentally demonstrated.

II. PRINCIPLE

Figure 1 (a) shows the principle of optical heterodyne detection technique of mm-wave fiber-radio signal with phase noise cancelling circuit (PNC). The system basically consists of a single-mode light source, an optical external modulator, a dual-mode local light source, an optical power combiner, photodetector (PD), and a PNC. There are two possible configurations of the PNC: (A) square law and (B) multiplier [5].

Optical carrier from the single-mode light source, f_1 , with the phase noise of $\phi_1(t)$ is modulated with a mm-wave radio-frequency

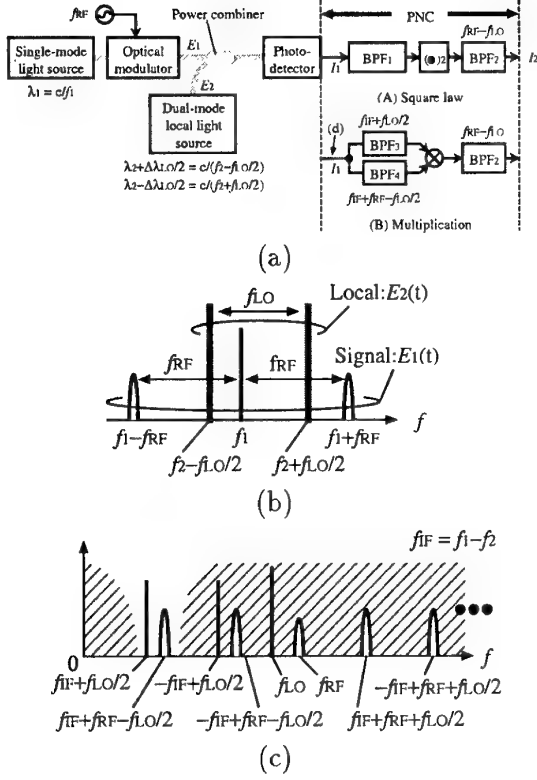


Fig. 1. (a) Block diagram of the proposed technique. (b) Optical signal spectra: $E_1(t)$ and $E_2(t)$. (c) Photodetected signal spectra: $I_1(t)$.

(RF) signal, f_{RF} . The normalized electric field, $E_1(t)$, can be written generally as the following Fourier Series.

$$E_1(t) = \sum_{n=-\infty}^{\infty} a_n e^{j\{2\pi(f_1 + n f_{RF})t + n\theta(t) + \phi_1(t)\}}, \quad (1)$$

where $\theta(t)$ is the payload data on the RF signal. On the other hand, normalized electric field of the optical local tone which put into the PD, $E_2(t)$, was also written by

$$E_2(t) = e^{j\{2\pi(f_2 - \frac{f_{LO}}{2})t + \phi_2(t)\}} + e^{j\{2\pi(f_2 + \frac{f_{LO}}{2})t + \phi_2(t)\}}, \quad (2)$$

where $f_2 \neq f_1$, $\phi_2(t)$, and f_{LO} are the center frequency, the phase noise, and the frequency interval of the dual-mode local light source, respectively. The single-mode and dual-mode local light sources are independently being driven. Figure 1 (b) shows the

combined optical spectra. When $E_1(t)$ and $E_2(t)$ are optically heterodyne-detected with the PD having square-law profile, the output electric signal, $I_1(t)$, appears at the output of the PD.

$$\begin{aligned} I_1(t) &= \mathcal{R} E_1(t) \cdot E_2^*(t) = \\ &\mathcal{R} \sum_{n=-\infty}^{\infty} e^{j\{2\pi(f_{IF} + n f_{RF} + \frac{f_{LO}}{2})t + n\theta(t) + \phi_{IF}(t)\}} \\ &+ \mathcal{R} \sum_{n=-\infty}^{\infty} e^{j\{2\pi(f_{IF} + n f_{RF} - \frac{f_{LO}}{2})t + n\theta(t) + \phi_{IF}(t)\}} \\ &= \mathcal{R} a_0 e^{j\{2\pi(f_{IF} + \frac{f_{LO}}{2})t + \phi_{IF}(t)\}} \\ &+ \mathcal{R} a_1 e^{j\{2\pi(f_{IF} + f_{RF} - \frac{f_{LO}}{2})t + \theta(t) + \phi_{IF}(t)\}} \\ &+ (\text{the other components}) \end{aligned} \quad (3)$$

Here, \mathcal{R} represents the responsivity of the PD, $f_{IF} \equiv f_1 - f_2$, and $\phi_{IF}(t) \equiv \phi_1(t) - \phi_2(t)$. Figure 1 (c) shows the spectra of $I_1(t)$. If only the first and second terms in Eq. (3), $f_{IF} + f_{LO}/2$ and $f_{IF} + f_{RF} - f_{LO}/2$, are multiplied, the second IF signal, $I_2(t)$, can be given after passing through BPF_2 .

$$I_2(t) = a_0 a_1 \mathcal{R}^2 e^{j\{2\pi(f_{RF} - f_{LO})t + \theta(t)\}} \quad (4)$$

Here, the bandwidth of bandpass filters, BPF_1 including both $f_{IF} + f_{LO}/2$ and $f_{IF} + f_{RF} - f_{LO}/2$, BPF_2 at $f_{RF} - f_{LO}$, BPF_3 at $f_{IF} + f_{LO}/2$, and BPF_4 at $f_{IF} + f_{RF} - f_{LO}/2$ must be optimized enough to pass through only the desired signals. From Eq. (4), no laser phase noise term remains. This means that this detection technique is in principle free from the laser phase noise. In addition, the fiber dispersion effect, which causes the fading of the photodetected signal, does not seriously affect to the transmission quality because only 2 components of optical signal, i.e. carrier and one sideband, are detected.

III. EXPERIMENT

A. Experimental Setup

Figure 2 shows a experimental setup to confirm the principle. An optical system in the setup consists of a distributed feedback laser diode (LD₁), a 60-GHz-band EAM [2],

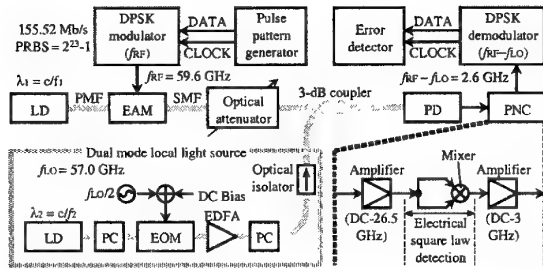


Fig. 2. Experimental setup.

a 3-dB optical coupler, a tunable laser diode (LD_2), two polarization controllers (PCs), an LN modulator (EOM), an erbium-doped fiber amplifier (EDFA), an optical isolator, and a PD. The PNC based on the square law scheme consists of two electric amplifiers, and an electric mixer (the bandwidth of RF, LO, and IF ports are 5–18 GHz, 5–18 GHz, and DC–3 GHz, respectively).

An optical carrier (λ_1) is intensity-modulated with a 59.6-GHz [$=f_{RF}$], 155.52-Mb/s-DPSK signal (PRBS = $2^{23}-1$) by the EAM. An optical local tone (λ_2), which is modulated with a 28.5-GHz [$=f_{LO}/2$] sinusoidal wave at the carrier-suppressed bias of the EOM, and the optical signal are combined via the 3-dB coupler, and then optically heterodyne-detected by the PD. The EDFA was used to amplify the optical local tone. The isolator was used to avoid the reflection at the 3-dB coupler. In the PNC, the heterodyne-detected signal is amplified by the first electric amplifier with the limited bandwidth (DC–26.5 GHz), power-divided, mixed in the electric mixer, and then amplified again by the next amplifier (2–4 GHz). The 2.6-GHz [$=f_{RF} - f_{LO}$] IF signal after the mixer is demodulated by a DPSK demodulator to extract the data and the clock.

B. Experimental Results

The measured optical spectrum is shown in Figs. 3. The thick and thin lines represent the optical signal and local tone in front of the PD, respectively. The wavelengths of LD_1 and LD_2 were around 1550.27 nm [$=\lambda_1$] and 1550.17 nm [$=\lambda_2$], respectively. The insertion optical losses of the EAM at the bias

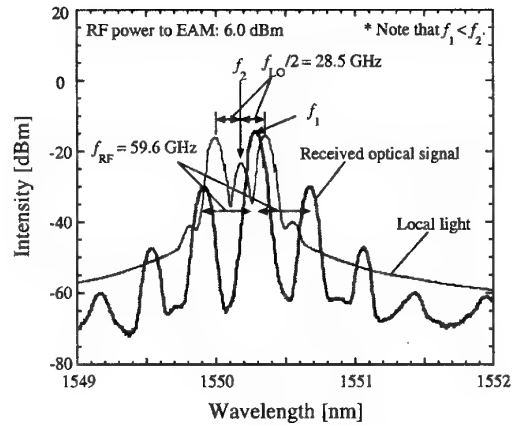


Fig. 3. Measured optical spectrum.

of -1.5 V and the EOM at the bias of 1.5 V were about 11 and 25 dBm, respectively. The reason why the EOM insertion loss was large is that it was driven at the bias of V_π in order to perform carrier-suppressed DSB modulation. The power of f_{RF} put into the EAM was 6 dBm at the same bias, corresponding to the modulation depth of about 44 %. In the optical local tone, the carrier still remained. This may also remain after mixing, but it is easily removed if λ_1 and λ_2 is adequately allocated as mentioned below.

The photodetected signals before and after the mixer were also measured. Figure 4 shows their results. The photodetected signals appear at around 12.4 GHz [$=f_{IF} + f_{LO}/2$], 15.0 GHz [$=f_{IF} + f_{RF} - f_{LO}/2$], and 16.2 GHz [$=-f_{IF}$]. Note that $f_1 < f_2$. These show large phase noises due to LD_1 and LD_2 . As shown in Fig. 4(b), however, 2.6-GHz IF signal was generated. The linewidth was less than 30 Hz and the single sideband phase noise was less than -73 dBc/Hz at 10 kHz apart from the carrier, in spite that the linewidth of the LD_1 and LD_2 was 5 MHz and 100 kHz, respectively. Hence, the phase noise cancellation was successfully demonstrated. Although the undesired signal, $-f_{IF}$, was remained, it never affected to the 2.6-GHz IF signal because we never made $-f_{IF}$ and $f_{IF} + f_{LO}/2$ symmetrical for $f_{IF} + f_{RF} - f_{LO}/2$.

We also measured the BERs as a function of optical signal power put into the PD.

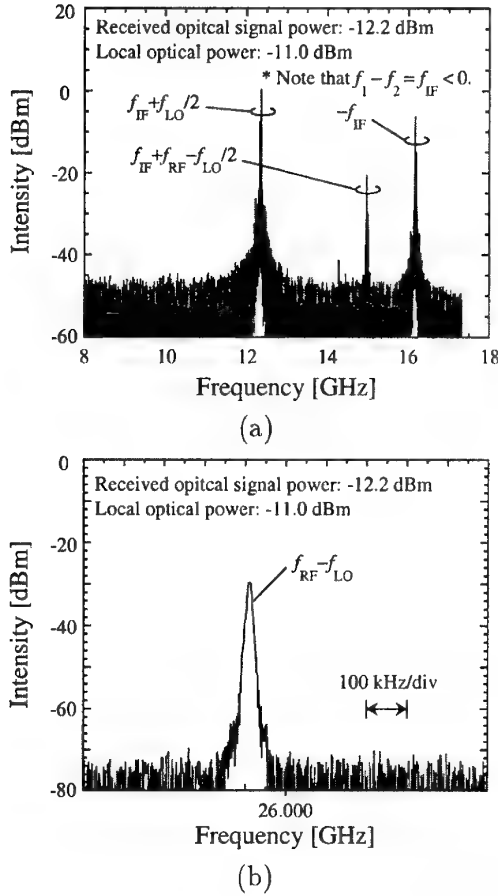


Fig. 4. Photodetected signals (a) before the mixer and (b) after the mixer.

Optical local power put into the PD was -11 dBm. RF input power put into EAM of f_{RF} was 6 dBm. No BER floor was observed within the measured range. The minimum received optical signal power to get the BER of 10^{-9} was -12.5 dBm. When the RF power was lower than 5.5 dBm, it was actually hard to achieve the BER of less than 10^{-9} even if the higher optical signal power up to -9.2 dBm was put into the PD. This is due to the ASE noise from the EDFA which is unwillingly used to give the high power of the optical local tone, causing a BER floor. But it is never an essential problem because some high-power dual-mode local light sources with no additive optical noise have been proposed, for example, 2-mode DBR-MLLD [6] or 2-mode injection-locked FP-LD [7].

As mentioned the above, it was experimentally confirmed that the proposed technique is free from the laser phase noise.

IV. CONCLUSION

We have proposed optical heterodyne detection technique of mm-wave fiber-radio signal with phase noise cancellation. The error-free detection of 59.6-GHz, 156-Mb/s-DPSK fiber-radio signal has been experimentally confirmed without any phase noise. In addition, this technique has been also theoretically immune from the fiber dispersion effect.

We expect that this technique leads to the realization of radio-on-fiber systems without additive optical noise.

ACKNOWLEDGMENTS

Their thanks are due to W. Chujo, T. Itabe, and T. Iida of the CRL, MPT for their encouragement.

REFERENCES

- [1] K. Kitayama, "Architectural considerations of radio-on-fiber millimeter-wave wireless access systems," in *Proc. ISSSE'98*, Pisa, Italy, pp. 378-383, Sep. 1998.
- [2] T. Kuri, K. Kitayama, A. Stöhr, and Y. Ogawa, "Fiber-optic millimeter-wave downlink system using 60GHz-band external modulation," *J. Light-wave Technol.*, vol. 17, no. 5, pp. 799-806, May 1999.
- [3] T. Kuri, K. Kitayama, and Y. Ogawa, "Fiber-optic millimeter-wave uplink system incorporating remotely fed 60-GHz-band optical pilot tone," *IEEE Trans. Microwave Theory Technol.*, vol. 47, no. 7, pp. 1332-1337, July 1999.
- [4] T. Okoshi, K. Emura, K. Kikuchi, and R. Th. Kersten, "Computation of bit-error-rate of various heterodyne and coherent-type optical communications schemes," *J. Opt. Commun.*, vol. 2, no. 3, pp. 89-96, Sep. 1981.
- [5] R. Gross, R. Olshansky, and M. Shumidt, "Coherent FM-SMC system using DFB lasers and a phase noise cancelling circuit," *IEEE Photon. Technol. Lett.*, vol. 2, no. 1, pp. 66-68, Jan. 1988.
- [6] T. Ohno, S. Fukushima, Y. Doi, Y. Muramoto, and Y. Matsuoka, "Application of uni-travelling-carrier waveguide photodiodes in base stations of a millimeter-wave fiber-radio system," in *Technical Dig. MWP'99*, Melbourne, Australia, F-10.2, pp. 253-256, Nov. 1999.
- [7] M. Ogusu, K. Inagaki, and Y. Mizuguchi, "60 GHz-band millimeter-wave generation and ASK data transmission using 2-mode injection-locking of a Fabry-Perot slave laser," in *Technical Dig. TSMW2000*, Yokosuka, Japan, P-12, pp. 181-184, Mar. 2000.

Electronic Linearization and Bias Control for Externally Modulated Fiber Optic Link

Vikram Magoon* and Bahram Jalali
Optoelectronic Circuits and Systems Laboratory,
University of California, Los Angeles,
Los Angeles, CA 90095-1594.

ph: 310-825-9655, fax: 310-206-2239, email: jalali@ucla.edu.

* Presently with Conexant Systems, Newport Beach, CA

Abstract- We present the design and fabrication of a monolithic predistortion linearization circuit with application to externally modulated analog fiber optic links. Results indicate 24dB suppression of 3rd order distortion at 1.3 GHz. We also present experimental results on the first fully-digital bias compensation loop. The circuit exhibits 25dB suppression of 2nd order distortion.

I. Introduction

Analog fiber-optic links find applications ranging from antenna remoting and Hybrid Fiber Coax (HFC) systems. For applications requiring wide dynamic range, Mach-Zehnder interferometers are commonly used for external modulation of the laser. Biased at the quadrature point, even-order distortion is eliminated and only odd-order nonlinearities remain. In such links, the maximum modulation depth is limited by the nonlinear transfer function of the modulator. A well-known problematic feature of a Mach-Zehnder modulator is slow drifts in the bias point resulting in generation of even-order harmonics.

Predistortion of the RF signal has proven to be an effective method for enhancing the dynamic range of links employing Mach-Zehnder external modulators [1]. The predictable sinusoidal light vs. voltage (L-V) characteristic of the modulator allows the design of preconditioning electronic circuits to compensate for the modulator non-linearity. Previous work in this area relies mostly on discrete diode-pair based circuits [2]. Recently, we demonstrated the first monolithic CMOS predistortion linearization circuit [3]. The circuit achieved 17dB suppression of third order intermodulation products from DC to 1.3 GHz. The experiments used an external Variable Gain Amplifier (VGA) to match the circuit's full-scale range to the V_{π} of the modulator.

In this work, we report a fully integrated linearizer which, in addition to the predistortion circuit, hosts an on-chip VGA. The circuit exhibits 24dB of 3rd order intermodulation distortion up to 1.3GHz. In addition, we demonstrate the first fully-digital control loop for eliminating the drift in the dc bias point. The fully-

digital design uses a high resolution oversampling Σ - Δ Analog-to-Digital Converter (ADC) and Digital Signal Processing (DSP) and represents a high-performance, low-cost and robust solution for eliminating the bias drift in Mach-Zehnder modulators.

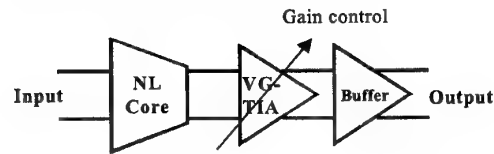


Fig. 1 Block diagram for the monolithic CMOS linearizer. NL: non linear; VG-TIA: variable gain transimpedance amplifier.

II. Predistortion Linearizer

We first describe the approach for synthesizing an \arcsin (odd) function using square law CMOS devices. Taylor series expansions of the functions $y = \sin(x)$ and $y = \arcsin(x)$ are given by,

$$\sin(x) = x - \frac{x^3}{6} + \frac{x^5}{120} + \dots \quad (1)$$

$$\arcsin(x) = x + \frac{x^3}{6} + \frac{3x^5}{40} + \dots \quad (2)$$

The design starts with a current-biased differential transconductance CMOS amplifier exhibiting the following transfer characteristic,

$$I = \beta V \sqrt{1 - \frac{V^2}{\alpha}} \quad (3)$$

where $\beta = \mu_n C_{ox} \frac{W}{L}$ and $\alpha = 4(V_{GS} - V_T)^2$. Here,

μ_n is the electron mobility, C_{ox} is the oxide capacitance, V_T is the threshold voltage, and W and L are the gate width and length, respectively.

Equation (3) can be expressed in a series of the form:

$$y = x - \frac{x^3}{2\alpha} - \frac{x^5}{8\alpha^2} + \dots \quad (4)$$

Comparing with (2), an inversion in the sign of the cubic term is needed to obtain the correct functional shape. This can be realized by subtracting the output of this amplifier from that of a linear amplifier with gain k ($y = kx$). Resulting in,

$$y = (k-1)x + \frac{x^3}{2\alpha} + \frac{x^5}{8\alpha^2} + \dots \quad (5)$$

Comparing to (5), this function can be mapped to the \arcsin function to the fifth order term if $\alpha = \frac{5}{9}$ and

$k = \frac{32}{5}$. These parameters can readily be set by appropriate choice of transistor dimensions and bias.

The circuit described above is the Non-Linear (NL) core of the linearizer and is the first stage in the overall monolithic circuit shown in Figure 1. The NL core is followed by a Variable Gain Trans-Impedance Amplifier (VG-TIA) which provides the degree of freedom required for matching the full-scale of the NL core to that of the modulator. The buffer stage prevents bandwidth reduction due to capacitive loading of the output.

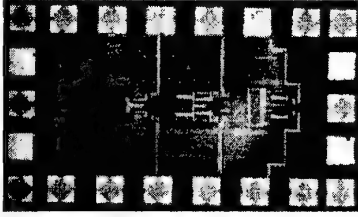


Fig 2 Chip photo for the linearizer described in Fig. 1.

The circuit, shown in Figure 2, was fabricated in a 0.35 μm CMOS process. The die measures 1.8 x 0.8 mm². An optical link was set up with a 1500nm external cavity laser driving the LiNbO₃ modulator. A single

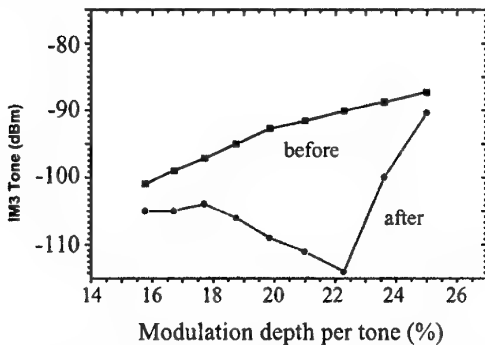


Fig. 3 Measured 2-ton IMP3 vs. modulation depth per tone, at 1.3 GHz.

tone test was performed at 60MHz and 2-tone tests were performed at 1.3GHz and 1.7GHz to verify

linearization performance. Figure 3 shows the measured 2-tone performance at 1.3 GHz. The circuit demonstrated a maximum of 24dB suppression of third order distortion. At 1.7 GHz, the suppression is reduced to 15dB. Table 1 summarizes the linearizer performance.

Supply Voltage	3.3 V
Supply Current	130 mA
Area	1.8 x 0.8 mm ²
Bandwidth	2GHz
Performance @60MHz	24dB suppression
@1.3GHz	24dB suppression
@1.7GHz	15dB suppression

Table 1. Performance summary.

The reduction in the performance at high frequency is due to the finite circuit bandwidth. The circuit must produce 3rd order distortion terms, with correct amplitude and phase to cancel those produced by the modulator. At frequencies close to the -3dB frequency (~ 2 GHz) distortion tones produced by the circuit suffer a phase shift resulting in non-ideal distortion cancellation. In general, the magnitude and phase of the out-of-band distortion terms produced by the modulator are important. The nonlinearity of the modulator mixes these tones down into the signal band where they contribute to distortion cancellation. From this point of view, a fixed \arcsin predistorter is not ideal at high RF signal frequencies. In such cases, a multitone circuit where the amplitude and phase of harmonics can be individually controlled may be preferable [1].

III. Digital Bias Control

To detect the drift in the bias point of the modulator, a low frequency pilot tone with small amplitude can be added to the RF signal [4]. Bias drift in the modulator gives rise to even order harmonics of the pilot tone, which can be detected and used to apply a correction signal to the modulator bias. Consider the L-V characteristic of a Mach Zehnder modulator biased approximately about the quadrature point,

$$P = P_0 \sin\left(\frac{\pi A_p}{V_\pi} \sin(\omega_p t) + \phi\right) = P_0 \sin(m \sin(\omega_p t) + \phi) \quad (6)$$

where $V_{in} = A_p \sin(\omega_p t)$ is the low frequency pilot tone, ϕ bias offset from quadrature, and m is the modulation index.

The 2nd harmonic term harmonic component, P_2 , is given by,

$$P_2 = P_0 \frac{m^2}{4} \phi \cos(2\omega_p t) \quad (7)$$

Thus the amplitude and phase of the 2nd harmonic is determined by the bias offset term ϕ . This tone can be demodulated and used to generate a signal to correct for the bias. In previous implementations, the demodulation, consisting of filtering, down conversion and integration, were performed in the analog domain. In our implementation, the entire processing is performed in the digital domain resulting in a high performance, robust, flexible and low cost solution.

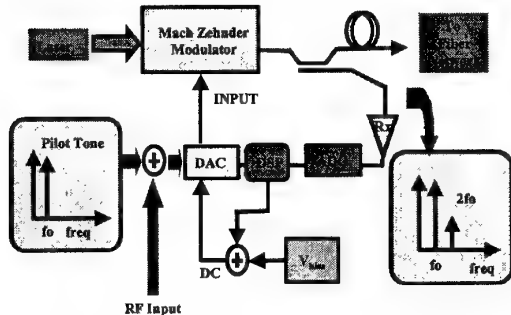


Fig. 4 Block diagram of the fully-digital bias compensation loop. The loop employs a Σ-Δ ADC and performs filtering, down conversion and integration of the pilot tone distortion in the digital domain.

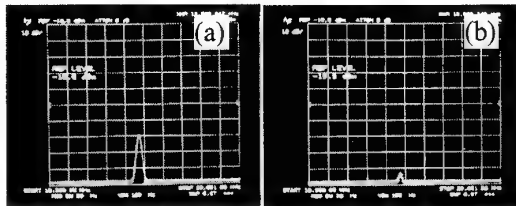


Fig. 5 Second harmonic distortion before (a) and after (b) application of the bias control loop. Over 25dB suppression achieved.

The fully-digital DSP based control loop is shown in Figure 4. At the core of the loop is a DSP processor. A 2kHz pilot tone was applied to the modulator along with the RF input. The second harmonic distortion product was sensed using a photodiode and a high-resolution Σ-Δ A/D converter. The digitized data is processed by the DSP. We developed a demodulation algorithm based on digital Finite Impulse Response (FIR) filter. The DSP generates a correction signal, which is converted back to analog using an 8-bit Digital-to-Analog Converter (DAC). This output drives the DC bias port of the modulator.

To test the performance of the bias compensator, a bias offset was intentionally introduced. Figure 5 shows the

2nd harmonic of the pilot tone before (a) and after (b) the compensation. By correcting for the bias point offset, the loop suppresses the 2nd harmonic tone by 25dB. The locking time of the loop depends on the initial bias offset and ranges from 10 sec for an offset of 150mV to 20 sec for 400mV offset. Because of the high-resolution Σ-Δ ADC used, the loop is capable of very high degree of cancellation. In our experiments, the observed distortion suppression was limited by the spectral purity of the pilot tone used.

IV. Conclusion

We have presented a fully monolithic linearization circuit realized in the CMOS process. The circuit achieves 24dB of IMP3 suppression at frequencies as high as 1.3GHz. In addition, we demonstrated the first fully-digital bias compensation loop. The loop exhibits 25dB suppression of 2nd order distortion.

REFERENCES

- [1] Wilson, G. Predistortion techniques for linearization of external modulators, 1999 Digest of the LEOS Summer Topical Meetings: RF Photonics for CATV and HFC Systems (Cat. No.99TH8455).
- [2] M. Nazarathy, J. Berger, A.J. Ley, I.M. Levi, Y. Kagan, "Progress in Externally Modulated AM CATV Transmission Systems," *Journal of Lightwave Technology*, vol. 11, pp. 82-105, Jan. 1993.
- [3] Y. Chiu, "1 GHz Predistortion Linearization Circuits for Broadband Analog Fiber Optic Links," M.S. thesis, EE department, UCLA, 1997.
- [4] Nazarathy et al., US Patent Number 5,161,044, 1992

IMPACT OF ASE ON PHASE NOISE IN LMDS INCORPORATING OPTICAL FIBRE BACKBONES

Christina Lim¹, Ampalavanapillai Nirmalathas¹, Dalma Novak¹, and Rod Waterhouse²

¹Australian Photonics Cooperative Research Centre, Photonics Research Laboratory
Department of Electrical and Electronic Engineering, The University of Melbourne, VIC 3010, Australia
Tel: +61 3 8344 6800 Fax: +61 3 8344 6678 E-mail: c.lim@ee.mu.oz.au

²Australian Photonics Cooperative Research Centre
Department of Communication and Electronic Engineering, RMIT University, Melbourne VIC 3000, Australia

ABSTRACT

We investigate the impact of ASE on the phase noise in LMDS incorporating optically amplified transport links. ASE noise is found to dominate and significantly increase the phase noise of the received rf signal after transmission over > 70 km of optical fibre. This effect is also demonstrated in a transmission experiment with 4 MHz 16 QAM data at 28 GHz.

I INTRODUCTION

Millimetre-wave (mm-wave) fibre-radio access networks are being considered for the future distribution of broadband interactive services [1,2]. One particular example is the local multipoint distribution service (LMDS) which operates at ~28 GHz [2]. Optical fibre with its inherent advantages such as low loss, large bandwidth, and immunity to electromagnetic interference, serves as an ideal medium for the distribution of the LMDS radio signals to the remote antenna sites. In such systems, signal distribution as rf over fibre offers the advantage of simpler antenna base station hardware, requiring only electronic amplification and opto-electronic conversion. However fibre chromatic dispersion can have a severe effect on the achievable signal-to-noise ratio (SNR) of the recovered radio signal [3]. Optical single-sideband with carrier modulation can reduce the SNR penalty [4,5] however fibre chromatic dispersion will continue to introduce a phase decorrelation between the optical carrier and single-sideband, leading to an increase in the phase noise of the recovered mm-wave signal [6,7].

In a fibre-radio system incorporating optical feed networks, optical amplification will often be required in order to overcome losses associated with fibre attenuation, coupling and splitting losses. Such optical amplifiers will then introduce amplified spontaneous emission (ASE) noise into the optical link. Previously, the effect of ASE noise from the optical amplifier on the system noise figure has been investigated [8]. However, the impact of ASE noise on the phase noise of the recovered rf signal in a fibre-radio system has yet to be quantified.

In this paper, we present the first investigation of the effect of optical amplifier ASE noise on the phase noise of the recovered rf signal in LMDS incorporating an optical feed network. Our experimental and theoretical investigation shows that ASE noise can cause a significant increase in the phase noise of the received rf signal for long fibre link lengths. We also demonstrate the impact of the phase noise on the transmission of 16 QAM modulation format data at 28 GHz over optical fibre.

II EXPERIMENTAL SETUP

Fig. 1 shows the experimental setup for the optical feeder link in a LMDS and fixed wireless access system for the transportation of rf signals at both 28 GHz and 38 GHz (also allocated for fixed wireless access). A 1550.1 nm distributed feedback (DFB) laser with a linewidth of 10 MHz is used to drive a dual-electrode Mach-Zehnder modulator (MZM). The MZM is biased at quadrature and the mm-wave signal is applied to each electrode with a phase shift of 90° present in one arm. This configuration produces optical single-sideband with carrier modulation [4]. Although higher order harmonics are also present,

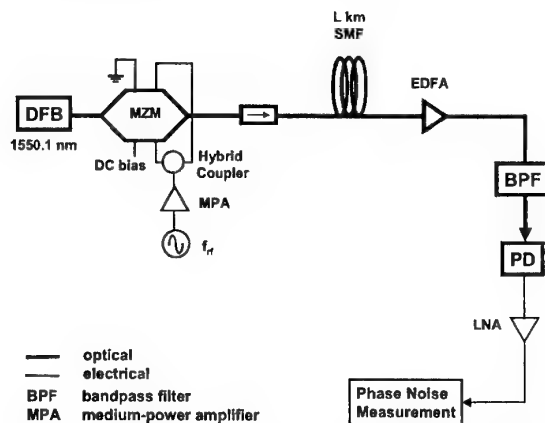


Fig. 1 Experimental setup for phase noise measurements with $f_r = 28$ GHz and 38 GHz

these components are negligible relative to the first order modulation sideband.

The optical signal is then transported over L km of single-mode fibre (SMF) before it is detected using a high-speed photodetector (PD). An erbium-doped fibre amplifier (EDFA) was incorporated in the link in order to compensate for coupling losses and fibre attenuation to maintain a constant received average optical power at the PD. After the fibre link, the detected mm-wave signal was amplified using a low-noise amplifier (LNA) and the phase noise measured using the phase noise utility of a 40 GHz rf spectrum analyser (HP9564E). The resulting rms phase jitter of the mm-wave signal was then obtained for a 1 MHz integration bandwidth.

Fig. 2 shows the measured rms phase noise of the detected signal at 28 GHz. Also shown in Fig. 2 is the measured rms phase noise for a frequency of 38 GHz. The measurements show that the phase error first increases gradually with fibre length until a certain distance ($L \approx 70$ km) whereupon the phase error increases much more rapidly. The higher rms phase error obtained for the transmission of 38 GHz over fibre can be attributed to the higher phase noise of the rf drive electronics at 38 GHz and also the different optical link gain required to maintain a constant received average optical power.

III PHASE NOISE MODEL DEVELOPMENT

In order to explain the phase noise measurements of Fig. 2, an analytical model of the system was developed. The optical single-sideband signal from the MZM can be represented mathematically by:

$$E_{out}(t) = A_0 e^{j[2\pi f_0 t + \theta(t)]} + A_1 e^{j[2\pi(f_0 + f_{rf})t + \theta(t)]} \quad (1)$$

where A_0 and A_1 are the amplitudes of the optical carrier and the first order sideband, f_0 is the optical frequency, f_{rf} is the modulating rf frequency and $\theta(t)$ represents the phase fluctuations of the optical source. As the optical signal propagates along a dispersive fibre link, the carrier and the sideband experience a differential propagation delay, τ , as a result of fibre chromatic dispersion where [6,7]:

$$\tau = DL \frac{\lambda^2}{c} f_{rf} \quad (2)$$

In Eqn. 2, D is the fibre dispersion parameter, L is the fibre transmission length, c is the speed of light in a vacuum, and λ is the wavelength. The differential delay results in a phase decorrelation between the two optical signals which leads to an increase in the phase noise of the recovered mm-wave signal at the receiver [6,7].

The phase noise of the recovered mm-wave signal has the following phase fluctuation spectrum

assuming the optical source has a Lorentzian power spectral lineshape [9]:

$$S_{\Delta\theta}(f) = \frac{2\Delta\nu}{\pi f^2} \sin^2(\pi f \tau) \quad (3)$$

where $\Delta\nu$ is the linewidth of the optical source. The amount of propagation delay-induced phase noise can be quantified using a root-mean-square (rms) phase error, $\sigma_{\Delta\theta}$, as expressed by [6]:

$$\sigma_{\Delta\theta} = \sqrt{\int_0^{B_e} S_{\Delta\theta}(f) df} \quad \text{for } B_e \ll \frac{1}{\tau} \quad (4)$$

$$\approx \sqrt{2\pi\Delta\nu\tau^2 B_e}$$

where B_e is the electrical noise bandwidth. Assuming the noise contributions within the link are independent, the total contributions to the rms phase noise of the detected mm-wave signal, σ_{link} , can be expressed as:

$$\sigma_{link} = \sqrt{\sigma_{\Delta\theta}^2 + \sigma_{other}^2} \quad (5)$$

where σ_{other} is the rms phase error arising from other noise contributions. σ_{other} can be measured at $L = 0$ km and it is assumed to be constant for all fibre lengths. Using (4) and (5) with $D = 17$ ps/km.nm, $c = 3 \times 10^8$ m/s, $\lambda = 1550.1$ nm, $B_e = 1$ MHz, and $\Delta\nu = 10$ MHz, the predicted σ_{link} is plotted in Fig. 2 for rf frequencies of both 28 and 38 GHz. It can be seen that while the theory matches the measured values of phase error for smaller fibre lengths, the predicted σ_{link} does not agree with experiment as L increases. The measurements show that the rms phase noise increase rapidly for $L > 70$ km while σ_{link} increases only very gradually with fibre length. This suggests that delay-induced phase noise is not the dominant noise contribution in the link which leads us to investigate the effect of the EDFA ASE noise contribution.

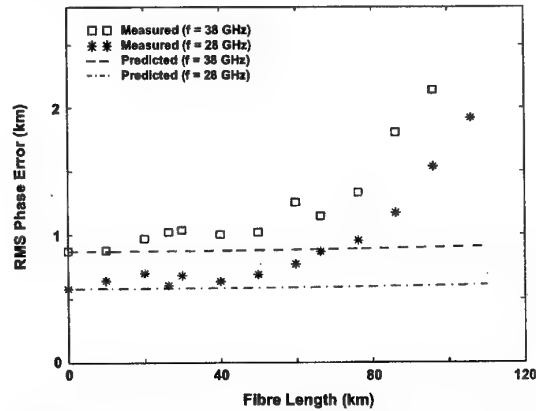


Fig. 2 Measured and predicted rms phase error of the recovered mm-wave signal for $f_{rf} = 28$ GHz and 38 GHz

When the gain of the EDFA is increased to compensate for losses in the fibre link, the ASE noise increases in a similar manner. The ASE noise contribution from the optical amplifier is converted to signal-spontaneous and spontaneous-spontaneous beat noise in the rf domain. The overall ASE noise can therefore be approximated from the measured phase noise of the received rf signal. It is assumed that the phase noise at offset frequencies from the carrier of more than 1 MHz is dominated by ASE. The ASE rms phase noise contribution, σ_{ASE} , can then be approximated from the following expression [10] using the measured phase noise at 1 MHz offset from the carrier, $\phi_{1\text{MHz}}$ in dBc/Hz:

$$\sigma_{ASE} = \sqrt{2 \cdot 10^{\frac{\phi_{1\text{MHz}}}{10}} \cdot df} \quad (6)$$

Using Eqn. 6, the predicted rms phase noise for the detected mm-wave signal is now given by:

$$\sigma_{link} = \sqrt{\sigma_{\Delta\theta}^2 + \sigma_{other}^2 + \sigma_{ASE}^2} \quad (7)$$

Fig. 3 shows the measured and predicted rms phase noise (obtained from Eqn. 7) for both 28 and 38 GHz. The predicted phase jitter shows good agreement with the measured results which indicates that ASE noise from the EDFA in the link is the dominant contribution to the phase noise of the detected mm-wave signal. When the length of the fibre link is increased, the EDFA gain must also be increased which leads to an increase in the ASE noise within the optical link. This explains the rapid increase in the rms phase noise of the received mm-wave signal as the fibre transmission length increases. Similar results were obtained when a different EDFA was incorporated into the link.

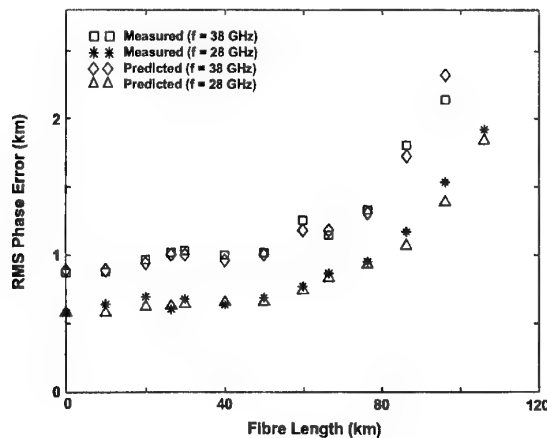


Fig. 3 Measured and predicted rms phase error including EDFA ASE noise for $f_{rf} = 28$ GHz and 38 GHz

IV TRANSMISSION EXPERIMENT

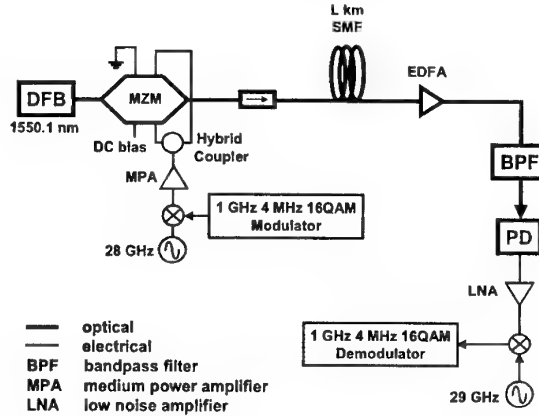


Fig. 4 Experimental setup for the transmission of 4 MHz 16 QAM at 28 GHz over L km of SMF

The phase noise of the detected rf signal has been shown to have a significant impact on system performance when transmitting data in higher order modulation formats [6]. To investigate the effect of ASE on system performance when transmitting higher order modulation format data at mm-wave frequencies in an optically amplified link, we demonstrate the transmission of 4 MHz 16 QAM data at 28 GHz over various fibre lengths. Fig. 4 shows the experimental setup. 4 MHz 16 QAM data at an intermediate frequency of 1 GHz is upconverted to 28 GHz using a mm-wave balanced mixer in conjunction with a 28 GHz oscillator. The modulated 28 GHz signal is applied to a dual-electrode MZM generating optical single-sideband modulation. The optically modulated signal is then transported over 0, 50 and 96 km of SMF before the 16 QAM data is recovered using appropriate carrier and data recovery circuits.

The impact of the increased phase noise on the recovered data is evident in Fig. 5 which shows the recovered constellation of the 16 QAM data for transmission over 0 km, 50 km and 96 km of fibre. Also plotted in Fig. 5 is the measured rms phase error of the detected 28 GHz signal. The constellation of the received data after transmission over 96 km of SMF is significantly dispersed which indicates an increase in the system noise and degraded system performance. This is as expected and correlates with the measured rms phase noise which is higher for longer fibre lengths due to EDFA ASE.

V CONCLUSIONS

We have investigated experimentally contributions to the phase noise of the recovered rf signal in LMDS incorporating an optically amplified feed network. We have established experimentally and

analytically that ASE noise from the optical amplifier within the optical link dominates the phase noise of the received rf signal for transmission over > 70 km of fibre and leads to a significant increase in the rms phase error. This in turn leads to degraded system performance when transmitting higher order modulation formats. These results have great significance for the design of fibre-fed mm-wave fibre-radio systems where it is essential that the link gain is carefully tailored in order to minimise the impact of ASE noise on the recovery of the wireless data.

ACKNOWLEDGMENT

This work was supported by the Australian Research Council.

REFERENCES

- [1] R. Heidemann and G. Veith, "mm-wave photonics technologies for Gbit/s-wireless-local-loop", *Proc. OECC'98*, Chiba, Japan, 1998.
- [2] J. Park, A.F. Elrefaie, and K.Y. Lau, "1550-nm transmission of digitally modulated 28-GHz subcarriers over 77 km of nondispersion shifted fiber", *IEEE Photon. Technol. Lett.*, vol. 9, no. 2, pp. 256-258, 1997.
- [3] H. Schmuck, "Comparison of optical millimeter-wave system concepts with regard to chromatic dispersion", *Electron. Lett.*, vol. 31, pp. 1848-1849, 1995.
- [4] G.H. Smith, D. Novak, and Z. Ahmed, "Technique for optical SSB generation to overcome dispersion penalties in fibre-radio systems", *Electron. Lett.*, vol. 33, no. 1, pp. 74-75, 1997.
- [5] J. Park, W.V. Sorin, and K.Y. Lau, "Elimination of the fibre chromatic dispersion penalty on 1550 nm millimetre-wave optical transmission", *Electron. Lett.*, vol. 33, no. 6, pp. 512-513, 1997.
- [6] U. Gliese, S. Norskov, and T.N. Nielsen, "Chromatic dispersion in fiber-optic microwave and millimeter-wave links", *IEEE Trans. Micro. Thy. Tech.*, vol. 44, no. 10, pp. 1716-1724, 1996.
- [7] H. Schmuck, "Carrier-to-noise limitations in optical mm-wave links due to phase-induced-intensity-noise", *Electron. Lett.*, vol. 33, no. 14, pp. 1236-1237, 1997.
- [8] R.A. Griffin, P.M. Lane, and J.J. O'Reilly, "Optical amplifier noise figure reduction for optical single-sideband signals", *J. Lightwave Technol.*, vol. 17, no. 10, pp. 1793-1796, 1999.
- [9] H.E. Rowe, *Signals and Noise in Communication Systems*. New York: Van Nostrand, 1965, pp. 113-116.
- [10] W.P. Robin, *Phase Noise in Signal Sources*. London: Peter Peregrinus Ltd., 1982.

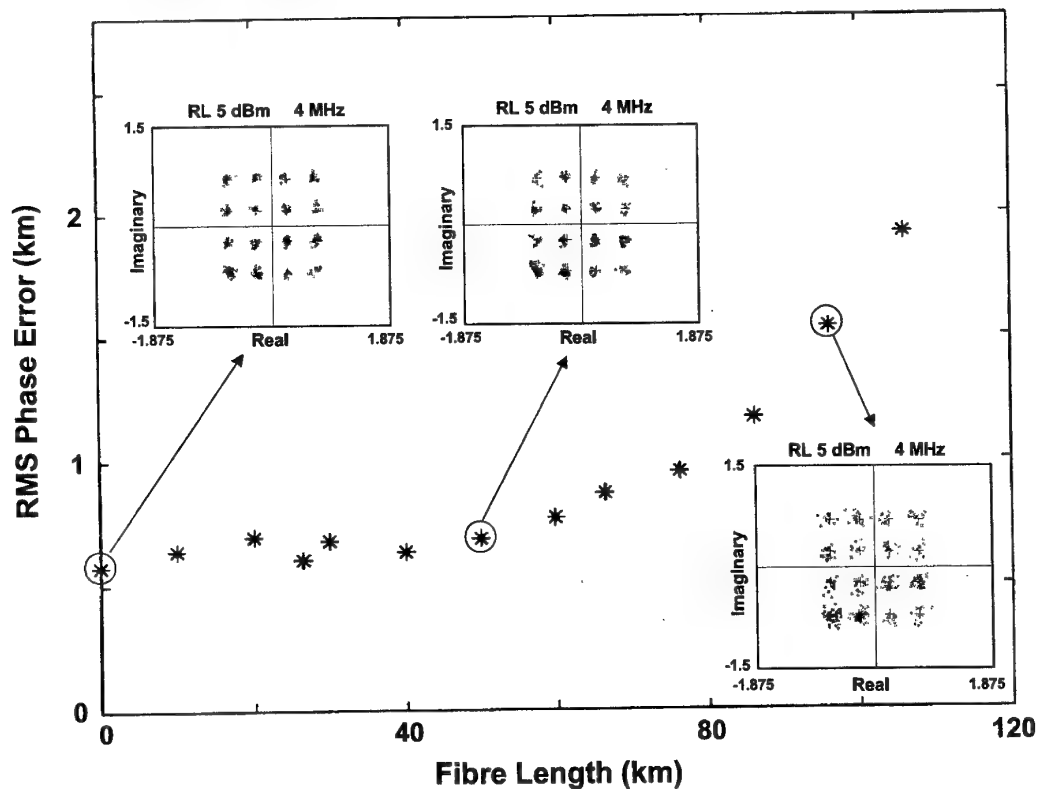


Fig. 5 Measured recovered 4 MHz 16 QAM constellation (at $f_c = 28$ GHz) for transmission over 0, 50 and 96 km

A STUDY OF DOPED PATCH AND DIPOLE ANTENNA ARRAYS WITH PHOTONIC INTERACTIONS

D S Lockyer¹, J C Vardaxoglou¹ and G J Ensell²

(1) Department of Electronic and Electrical Engineering
Loughborough University
Loughborough
Leicestershire
LE11 3TU
UK

Tel: +44 (1509) 222815
Fax: +44 (1509) 222830
Email: j.c.vardaxoglou@lboro.ac.uk

(2) Microelectronics Centre
Department of Electronics and Computer Science
University of Southampton
Highfield, Southampton, SO17 1BJ, UK

Abstract

A technique to control the transmission properties of arrays doped in silicon is described. Photonic excitation creates plasma, which alters array performance. This can be controlled using optical masks and the resonant frequency can be tuned.

Introduction

We have developed a technique whereby we fabricate millimetre wave antenna arrays within a high resistivity ($\rho > 6 \text{ k}\Omega\text{cm}$) semiconductor (silicon) substrate by means of depositing the resonant elements as heavily doped regions within the base structure. Depending on the dopant concentration, these areas then behave essentially as conducting regions and the entire array behaves in a similar fashion to a conventional frequency selective surface (FSS) [1].

When the substrate is illuminated by an optical source of a suitable wavelength, the photoconductive nature of the silicon [2,3] enables the array performance to be manipulated and/or controlled. In this paper

we present results that demonstrate changes in the performance of arrays of conducting patch and dipole elements. When these arrays are illuminated by a microwave plane wave, in the range 16-40 GHz, they exhibit resonances which are dependent on the dimensions of the elements involved and on the lattices on which they are arranged. When they are photonicallly excited, however, we are able to remove the resonant effect and also, by the use of a mask, to change the resonant frequency.

Doping of arrays

The doping of a high resistivity wafer enables an array pattern to be created within it. The dopant is generally boron or phosphorous, depending on the particular type of doping (n or p) that is required for the application being considered. Whilst virtually any pattern may be printed there is a limit to the depth into the silicon that the dopant will penetrate, although the very high free carrier concentrations that are obtained mean that this does not pose a significant problem at our microwave

frequencies. The process employed in this case, to dope only certain parts of a wafer, involves the implantation of Boron atoms into the silicon. The dopant is implanted using a high temperature, solid source technique. This creates areas of (near metallic) low resistivity, which contrast with the surrounding high resistivity (undoped) regions. The doped regions then behave similarly to the conducting portions of a conventional FSS when a plane wave is incident upon the array. In order to achieve the doping, a mask firstly needs to be made in the form of an image of the pattern to be implanted. The mask is made of a ceramic material to enable it to withstand the high temperatures involved in the process. The mask is then fused with the dopant, which is transferred to the silicon by a solid source contact technique in a furnace operating at a temperature of up to 1000°C. The dopant atoms gradually diffuse into the silicon and have a maximum penetration of about 10 μm . At the surface of the silicon the solid solubility (free carrier concentration) of the dopant is in the region of $10^{19} - 10^{21} \text{ cm}^{-3}$. (However, this is at the surface only and decreases as the dopant penetrates further into the silicon). This concentration is sufficient to enable the doped array to act as a conventional FSS, albeit with a relatively thick (300 μm) dielectric.

Measurement set up

Plane wave transmission measurements have been performed in the range 16-40 GHz. The system uses a swept signal generator in conjunction with a scalar network analyser and a pulsed Xenon source which emits primarily in the near IR (800-1000 nm). The entire system is synchronised so that a measurement is taken for every frequency of the sweep range (dependent on the resolution), and ensures that each measurement is sampled when the output of the source (duration ≈ 5 ms) is at its maximum intensity. This enables us to measure the silicon samples when the photoconductivity is a maximum also.

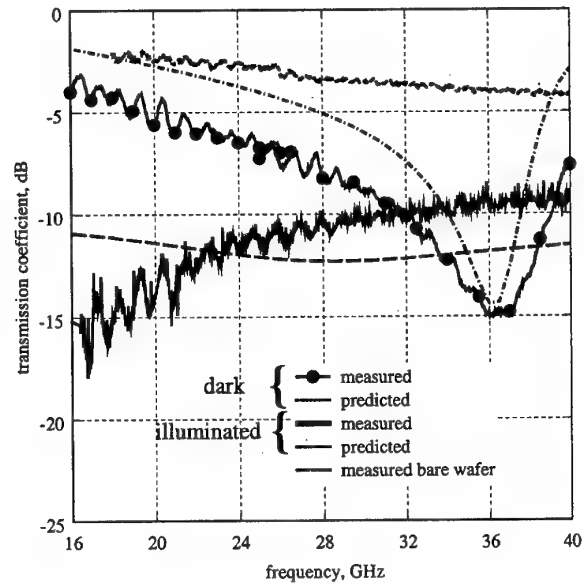


Fig. 1. Performance of a doped dipole array under photonic excitation

Doped dipole array

Fig. 1 shows the transmission response of a doped array of dipole elements having a length of 1.8 mm, width 0.2 mm and on a square lattice of periodicity 2.5 mm. The elements are modelled by means of a plasma density of $2 \times 10^{18} \text{ cm}^{-3}$ to a depth of 10 μm . The cases illustrated are both dark and illuminated, and the response of a bare wafer is included for reference. In the dark state the array resonates close to 36 GHz and it can be seen that the measured and predicted results are in good agreement showing that the doped array behaves as expected. When the optical source is activated, however, the plasma layer that is formed by the photonic activity has a marked effect on the transmission response. The resonance that was at 36 GHz has disappeared and there is essentially a "switching off" of the response across the range. A predicted curve for the "off" state is also included on the graph and was produced by modelling the elements, as previously described, together with a layer of "dark" silicon ($\epsilon_r = 11.8$) of 100 μm and a further layer of induced plasma (concentration $1.8 \times 10^{15} \text{ cm}^{-3}$) of 200 μm . The overall results tie in quite well and it is noticeable that, at low frequencies, the measured silicon demonstrates

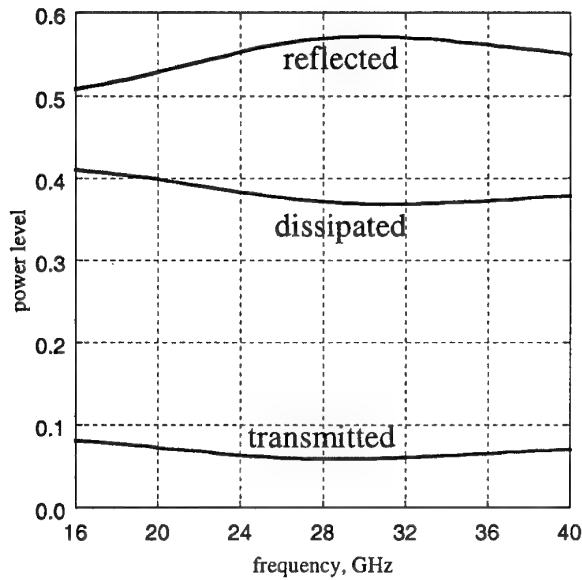


Fig. 2. Distribution of incident power by a phonically excited doped dipole array

a significant increase in the attenuation which is attributable to dissipation within the silicon [4]. The level of dissipated power is shown in Fig. 2. This clearly shows the effect of the plasma on the transmission through the array, and demonstrates that although the microwaves are largely prevented from penetrating right through the device, about 40% of the incident energy is actually dissipated within the silicon. In fact, using the configuration described above we need to increase the concentration level of the plasma region to over 10^{19} cm^{-3} in order to reduce the dissipation below 10% across the range. This arises due to the inherently lossy nature of the plasma itself, and can also be seen from the modelling of it as a complex permittivity [5].

Doped patch array

A separate study was carried out using an array consisting of doped patch elements. The square dimensions of the patches are 3mm and they are arranged on a 5mm square lattice. Once again they are modelled as a plasma of concentration $2 \times 10^{18} \text{ cm}^{-3}$ and a depth of $10 \mu\text{m}$. The performance of this array in the dark state and under illumination is shown in Fig. 3. In the dark state there is a strong resonance at 32 GHz, which is associated with the element dimensions and further periodic

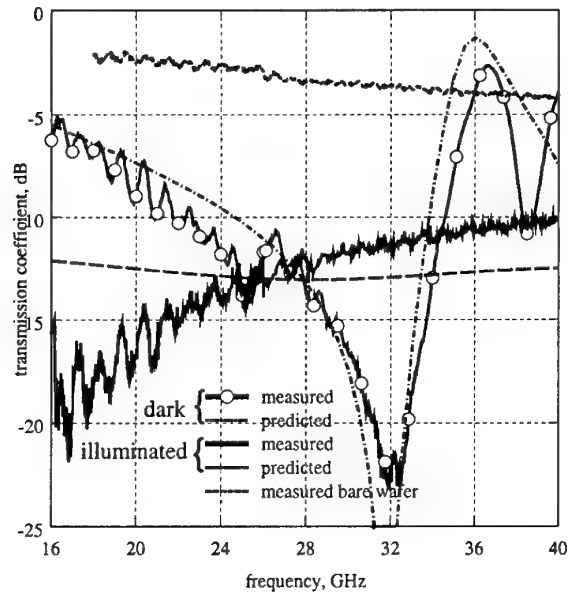


Fig. 3. Performance of a doped patch array under photonic excitation

effects above 36 GHz, and these have been accurately predicted by our model. Under illumination, however, there is a similar transformation to that of the dipole case insofar as the resonance and periodic effects are removed due to the layer of plasma that has been induced by the photonic activity. This indicates that we are able to turn on and off the resonance of the doped array, but by placing a negative image mask of the array, (Fig. 4), in front of the patches we are able to move the resonance from its initial position at 32 GHz.

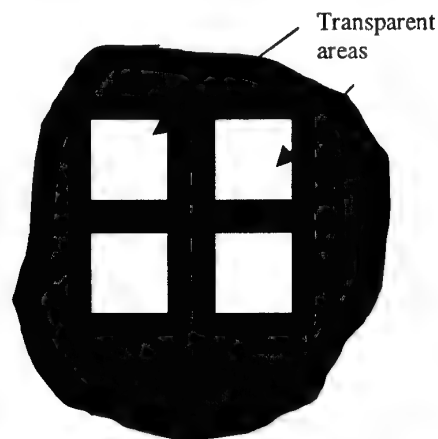


Fig. 4. Negative image mask of a patch array

The action of the negative image mask is to expose the doped patches themselves to the incident radiation. The effect of this is that the photons diffract around the edges of the clear regions of the mask, and around the edges of the plasma to form a "pool" of plasma around the doped areas. Effectively this increases the size of the patch elements and consequently reduces the resonant frequency of the array.

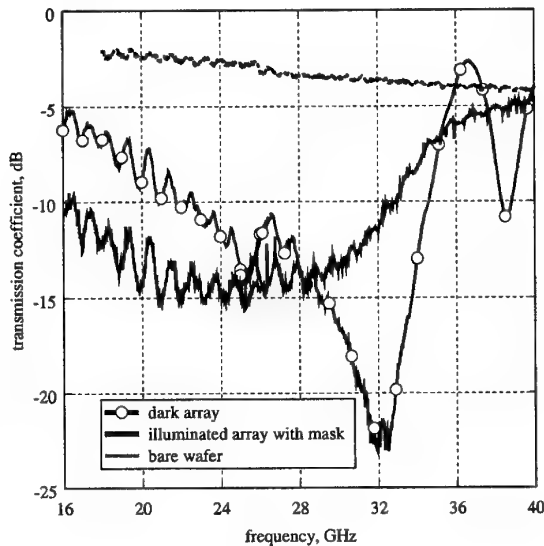


Fig. 5. Altering the resonance of a doped patch array using a negative image mask

This is evident from Fig. 5, which demonstrates that the resonant frequency has been shifted down from 32 GHz to near 25 GHz. We have also used the mask on the far side of the array i.e. away from the doped areas but have found that without the presence of the dopant, the plasma diffuses too far and obscures the resonance rather than shifting it. Using a positive mask, where the dark areas cover the array elements allows plasma to form all around the elements and thereby produces a similar effect as that observed in Fig. 3, where the effect of the plasma layer is to dampen the periodic effect of the array.

Conclusions

In this paper we have demonstrated that it is possible to control and/or tune the

performance of a pre-formed doped array by means of photonic excitation. We have used a Xenon lamp and a synchronised measurement system to turn off the resonant effects of doped arrays of dipole and patch elements and have also been able to move the resonance of the patch array. The formation of the plasma has enabled us to control the plane wave microwave transmission responses of such structures when they are set into a high resistivity silicon wafer.

Acknowledgements

This work is supported by a grant from the Engineering and Physical Sciences Research Council.

References

1. Vardaxoglou, J. C.: "Frequency Selective Surfaces: Analysis and Design". Research Studies Press, 1997.
2. Lee, C.H, Mak, P.S, and DePhonzo, A.P.: 'Optical control of millimeter-wave propagation in dielectric waveguides', IEEE J. Quantum Electron., QE-16, pp. 277-288
3. Platte, W.: 'Periodic-structure photoexcitation of a silicon coplanar waveguide for selective optoelectronic microwave control'. 'IEEE Trans. Microwave Theory and Tech., MTT-38, No. 5, 1990, pp 638-646.
4. D.S Lockyer, J.C. Vardaxoglou and M.J. Kearney: "Transmission through optically generated inductive grid arrays". IEE Trans. Microwave Theory Tech., Special Issue on Microwave and Millimetre-wave Photonics, MTT-47, No. 7, 1999, pp. 1391-1397.
5. J. C. Vardaxoglou, "Optical switching and generation of periodic arrays and FSS", Invited paper, Proc. IEEE International Conference on Electromagnetics in Aerospace Applications, ICEAA, Torino, Italy, pp. 51-56, 1997.

INVESTIGATIONS IN MICROWAVE OPTICAL LINKS – ACCENT ON QAM

I. Frigyes, A. Hilt, S. Csernyin

Budapest Technical University, H-1111 Budapest, Goldmann Gy. tér 3; t-frigyes@nov.mht.bme.hu

Abstract Various-depth field descriptions and their use are summarized. Effects in optical links are investigated being of particular importance if QAM microwave signals are transmitted. In this framework modulator-induced nonlinear distortion, IBPD (In Band Power Difference) and fiber nonlinear refraction effects are discussed.

1. Introduction

One of the most spectacular trends in present day telecommunications is the development of wireless networks. The required increase of overall capacity and need of the individual users requires the application of smaller cells¹, of new frequency bands² (such 60 GHz) as well as of more sophisticated modulation systems³. (QAM or TCM.) Analog optical links transmitting modulated microwaves/millimeter waves (MW/MMW) are well known to be suited to solve problems related to the first two of these: their loss is rather low, their bandwidth is high and so they are well applicable as access links connecting the CS (Central Station) to the BSs (Base Stations). Many problems emerging in these links are discussed in detail and several operating experimental systems are reported. These problems include – among others – link insertion loss and noise figure⁴, effects of fiber dispersion⁵ and fiber birefringence⁶. Different depth of approach is needed in dealing with these, based on investigation of optical intensity, of optical field and of optical field vectors, respectively. One purpose of the present paper is to summarize, various models of these links. On the other hand not too much attention is paid to particular problems arising if QAM rather than PSK or MSK modulation schemes are applied in the RF transmission. QAM transmission and its coded version TCM is much more sensitive to linear and nonlinear distortion and to carrier phase noise as PSK or MSK – see e.g. ⁷; as far as known by the authors there are only a few papers reporting on QAM transmission (e.g.⁸) but even these do not analyze the link from this point of view. The second and main purpose of this paper is to investigate some of these problems.

The organization of the paper is, as follows: in section 2 models of the microwave/fiber optic links are discussed applicable for the determination of various link characteristics. Section 3 deals with the effect of modulator nonlinearities; penalty in signal energy is determined. In section 4 linear distortion is investigated and its effect on QAM is determined. Section 5 deals with one of the nonlinear effects of an optical fiber i.e. nonlinear refraction. Conclusions are drawn in section 6.

2. Models of microwave fiber-optical links

Several models are available to describe MW/MMW optical links. In the simplest model *incoherent* optical working regime is assumed. The E/O converter (either a direct modulated laser diode or an external modulator)

transforms the electrical signal into the optical domain. In this way modulating MW signal is converted into optical intensity. L km of fiber, optical connectors, couplers and splices introduce attenuation. Finally, the photodetector reconverts the optical intensity into electrical power. Although this *incoherent model* of IM/DD links is well discussed in the literature it presents some fundamental limits since in this model the phase states of the optical carrier and the sidebands are not taken into account.

Exact explanation of chromatic and polarization mode dispersion (PMD) problems requires a more detailed model where the calculation is based on the optical field and not on intensity. Since phase state of the optical field has a role in the model we can refer this as *coherent model* of an IM/DD optical link. Fig.1 shows the detected power level after optical transmission as calculated by such a coherent model. The incoherent model would not account for the transmission zeros.

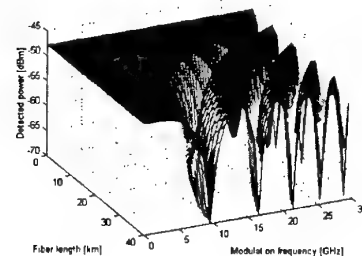


Fig. 1. Detected level of the optically transmitted fundamental MW signal vs. modulation frequency f_{RF} and fiber length L . The *coherent model* is also suitable to estimate harmonic levels of the MW modulation signal generated in the optical path. Considering an MW fiber-optic link besides of the optical transmitter and the receiver, the optical fiber itself induces harmonics; this is due to dispersion. As shown in Fig.2 exact modeling of harmonic generation requires a calculation based on the optical field instead of on a purely intensity basis.

The *coherent model* can further be extended to deal with polarization effects based e.g. on the *Jones-calculus*. Polarization coupling and PMD problems can be discussed as well if the optical field is written in vectorial form composed of orthogonal polarization components and optical transfer functions are replaced by transfer matrices. Lastly, without entering into details it is mentioned that in some cases (especially for long haul links) the above described field-vector based *deterministic* model should be accomplished with a *statistical model* when such effects as phase noise, aging, temperature dependence mechanical stress cannot be neglected.

In what follows the second of these i.e. the deterministic, scalar, coherent model will be used.

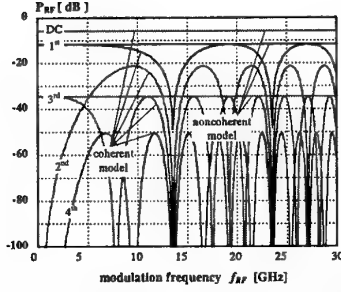


Fig. 2 Levels after 20 km fiber: coherent & incoherent results

3. Effect of the distortion caused by a Mach-Zehnder modulator

To investigate the effect of this distortion on QAM transmission the complex envelope representation of the signal will be applied (this would not be appropriate e.g. in determining carrier harmonics). Assume a situation in which an M-QAM-modulated RF carrier modulates light intensity. It is well known⁹ that the output optical field-strength of the modulator is a distorted replica of the modulating voltage. Operating in the quasi-linear regime of the modulator (i.e. applying a bias of $V_{\pi}/2$ with V_{π} the voltage causing a phase shift of π) and applying a photodetector at the output of the modulator, complex envelope of the output signal (i.e. of the detected photocurrent) can be written as

$$\frac{I_{out}(t)}{I_0} = \left\{ 1 - \sin \left[m \sum_{(k)} b(t - kT) (a_k \cos \omega_c t - q_k \sin \omega_c t) \right] \right\} \\ = \left\{ 1 - \sin \left[m \operatorname{Re} \sum_{(k)} b(t - kT) A_k e^{j\varphi_k} e^{j\omega_c t} \right] \right\} \quad (1)$$

with I_0 the average photo-current;

$m = u_0 \pi / V_{\pi}$ and u_0 the rms amplitude of the modulating voltage;

$a_k, q_k = \pm \frac{2l-1}{\sqrt{M-1}}$; $l = 1, 2, \dots, \sqrt{M}/2$, the in-phase and quadrature components of symbol # k , respectively;
 A_k and φ_k the corresponding amplitude and phase,
 $b(t)$ the pulse waveform.

As seen only for very low m is this a detected linear modulation; however, if $m \ll 1$ must be kept, dynamic range of the link is very low; on the other hand the signal will be distorted if m is increased. In order to get a dynamic range as high as possible it is of high importance to determine: what is the maximum of m resulting in a tolerable increase of error probability.

Fortunately the sinusoidal nonlinearity is a rather tractable one. Its describing function $T(u_0)$ (i.e.: ratio of the output signal fundamental harmonic to the input sinusoid) can be given as

$$T(u_0) = \frac{2J_1(\sqrt{2}\pi u_0/V_{\pi})}{\sqrt{2}\pi u_0/V_{\pi}} \quad (2)$$

with $J_1(\cdot)$ the first-order Bessel function.

Further MQAM symbol error probability (if additive white gaussian noise is the only disturbing effect) is given as⁷

$$P_E = 2 \left(1 - 1/\sqrt{M} \right) \operatorname{erfc} \frac{d}{\sqrt{N_0}}; d = \frac{\sqrt{E_{peak}}}{\sqrt{2}(\sqrt{M}-1)} \quad (3)$$

with d the distance of signal vectors from the closest decision boundary in the signal space;

N_0 the additive noise spectral density;

E_{peak} the peak energy of the signal constellation.

As an effect of the nonlinearity the peak energy will be decreased by a factor $T(u_0)^2$; as a consequence, distance d will be decreased too but – except in the case of QPSK – much more than the energy (see Fig. 1). Thus a (rather tight) bound of the penalty in signal energy due to the nonlinearity of the optical modulator is

$$L_{\sin, QAM} < 20 \lg(d/d') = \\ = -20 \lg \left[(\sqrt{M}-1) T(u_0) - (\sqrt{M}-2) \right] \quad (4)$$

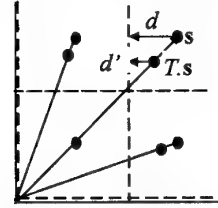


Fig. 1 Constellation diagram showing distortion effect on the highest amplitude signal vector
 In Fig. 2 computed magnitudes of this loss are shown.

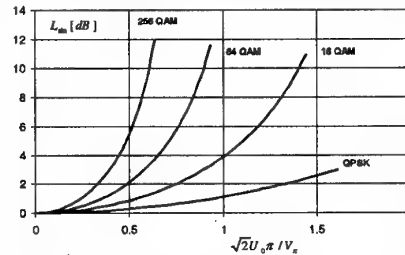


Fig. 2

Computed loss due to modulator nonlinearity in 4-, 16-, 64- and 256QAM

4. Linear distortion induced by fiber dispersion

A secondary effect of loss due to fiber dispersion is IBPD: loss is not constant in the frequency band of the signal. This may cause a much higher increase in error probability than dictated by the decrease of E/N_0 .

To go into details: complex envelope of the optical field strength at point $z=0$ of a fiber can be written as

$$s(0, t) = \sqrt{P_0} \left[1 + j e^{jm(t) \cos \omega_c t} \right]; m(t) = \frac{u_0 \pi}{V_{\pi}} \sum_{(k)} A_k e^{j\varphi_k} b(t - kT)$$

Fundamental harmonic and the constant term is only of interest; so we can write:

$$s(0, t) = \sqrt{P_0} \left[1 + j J_0(m(t)) - 2J_1(m(t)) \cos \omega_c t + HH \right] \approx \\ \approx \sqrt{P_0} \left[1 + j - m(t) \cos \omega_c t \right] \quad (5)$$

with HH : higher order harmonics of ω_c .

The approximation is justified as – as shown in section 3 – in order to keep the loss due to distortion low, m must be kept rather low. But then the distortion of the waveform can be neglected.

The phase constant of the (standard) fiber is given as

$$\beta = \beta_0 + \beta_1(\omega - \omega_0) + \frac{\beta_2}{2}(\omega - \omega_0)^2 \quad (6)$$

with $\beta_i = d^i \beta / d\omega^i$; $i=1, 2$; $\beta_2 \neq 0$

ω_0 the optical angular frequency.

Thus the field-strength at point z of the fiber can be written as¹⁰

$$s(z, t) = \sqrt{P_0} e^{-\alpha z} u(z, \tau); \tau = t - \frac{z}{v_g} \quad (7)$$

with $v_g = 1/\beta_1$ the group velocity and α the attenuation constant.

Then it is $u(z, \tau)$ what characterizes the signal distortion while propagating along the fiber:

$$u(z, \tau) = \mathbf{F}^{-1} \left\{ U(0, \omega) \exp \left[j \frac{\beta_2 z}{2} \omega^2 \right] \right\} \quad (8)$$

(\mathbf{F}^{-1} : inverse Fourier-transform; $U = \mathbf{F}\{u\}$)

The detected photo-current is proportional to $|u|^2$. Assume first that $u(z=0, \tau)$ is the unmodulated carrier (or any other sinusoid with $\omega \approx \omega_c$); then

$$|u(z, \tau)|^2 = \frac{4u_0}{V_\pi} \cos \omega_c \tau \cos \left(\frac{\beta_2 z}{2} \omega^2 - \frac{\pi}{4} \right) + DC + 2nd \text{ harm} \quad (9)$$

So a "modulation transfer function" can be defined:

$$K(z, \omega) = \sqrt{2} \cos \left(\frac{\beta_2 z}{2} \omega^2 - \frac{\pi}{4} \right); a \triangleq \frac{1}{K(z, \omega)^2} \quad (10)$$

and with that the detected photo-current is:

$$\frac{i_{RF}(L_f, \tau)}{I_0} = \sqrt{2} m(L_f, \tau) \cos \omega_c \tau \cos \left(\frac{\beta_2 L_f}{2} \omega^2 - \frac{\pi}{4} \right); \quad (11)$$

$$m(L_f, \tau) = \mathbf{F}^{-1} \{ K(L_f, \omega) \cdot M(0, \omega) \}$$

with L_f the length of the fiber

$M(0, \omega)$ the Fourier-transform of $m(0, \tau)$ and

a the loss at (z, ω) .

In Fig. 5 simulated error probability vs. E/N_0 is shown with a selected ω_c and L_f . Note the increase of the error probability due to the linear distortion.

Analyzing (11) an approximate formula can be derived for IBPD:

$$IBPD \approx 20 \lg \left[1 + \beta_2 L_f (a, \omega_r) \omega_r^2 \sqrt{a(\omega = \omega_c) - 1} B / f_c \right] \quad (11a)$$

with ω_r any appropriate reference angular frequency,

$L_f(a, \omega_r)$ the fiber length corresponding to a at ω_r

B the signal bandwidth.

Note: IBPD is significant if relative bandwidth is high and a is also rather high.

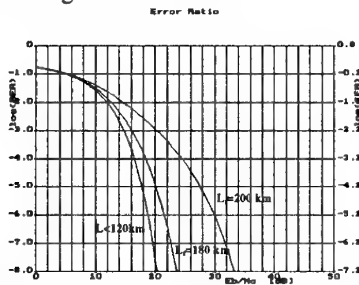


Fig. 3 Effect of fiber dispersion on the error probability of 64 QAM; $f_c = 5$ GHz, $B = 200$ MHz

As it is known one countermeasure to fiber-dispersion induced loss and linear distortion is the application of single-sideband modulation⁶. In this case – by an analysis similar to the above – it can be shown that

$$K(z, \omega) = \exp \left[\frac{j \beta_2 z}{2} \omega^2 \right] \quad (12)$$

thus there is no loss due to dispersion but (in principle) there is a frequency-linear group delay distortion. Magnitude of this is in most cases negligible.

5. Effect of fiber nonlinear refraction

Optical field-dependent character of the refraction index results in nonlinear phase shift as the signal propagates along the fiber¹⁰ – called SPM, Self Phase Modulation. This phenomenon is widely discussed in the literature (see¹⁰ and the references therein), taking mainly optical pulse propagation into account. As far as known by the authors effects on optical fields modulated by microwave signals carrying digital modulation was not yet discussed. In what follows, nonlinearity only is taken into account, i.e. the joint effects of that and dispersion are not touched. So the results can be regarded as valid in the 1,3 μm band or at 1,55 μm in dispersion-shifted fibers. I.e. close to the zero-dispersion point of the fiber.

Nonlinear effects can be of interest and need to be investigated, as there is an attempt to increase the optical power. The first reason for increasing optical power is that the gain of the optical microwave link is proportional to the optical power if an external modulator is applied⁴ (this is not the case in direct modulation of the laser), the second is the availability of high power lasers. Ref. 11 for example reports on the application of 225 mW, although at a rather low RF.

As it is discussed e.g. in¹⁰, nonlinear phase shift due to SPM at point z of the fiber is

$$\Phi_{NL} = |u(0, \tau)|^2 \cdot \frac{z_{eff}}{L_{NL}}; L_{NL} = \frac{1}{\gamma P_0}; z_{eff} = \frac{1 - e^{-\alpha z}}{\alpha} \quad (13)$$

and consequently

$$u(z, \tau) = u(0, \tau) \cdot \exp[j \Phi_{NL}(z, \tau)] \quad (14)$$

here γ is the power-dependent part of the phase constant of the fiber; it can be taken as $3 \text{ W}^{-1} \text{ km}^{-1}$;

L_{NL} is the nonlinear length characteristic to the fiber length above which nonlinear phenomena can be of significance;

P_0 is the peak optical power at $z=0$;

α is the attenuation constant of the fiber; 0,25 dB/km = 0,0575 Np/km can be taken for 1300 nm;

z_{eff} is the effective length; note that $z_{eff} \leq 1/\alpha$.

As seen in (14), i. optical carrier will be chirped due to SPM but ii. this will have no effect on link performance if light is modulated by the (modulated) RF carrier, as $|u(z, \tau)|^2 = |u(0, \tau)|^2$.

The situation is completely different in remote heterodyned links. Various concepts of this type of transmission are listed e.g. in⁵. Basic operating principle of each of them is more or less the same: there are two, phase locked optical carriers, frequency difference of which corresponds to the RF local oscillator frequency; one of these is modulated by an IF carrying (in our case in QAM or TCM form) the information bearing signal; and at the base station this is up-converted to the RF carrier – in the photodetector or in a separate microwave mixer.

The signals present at the input of the fiber are then (described by their complex envelopes)

$$u_1(0, \tau) = 1 + j \cdot e^{j m(\tau) \cos \omega_{IF} \tau} \approx 1 + j - m(\tau) \cos \omega_{IF} \tau \quad (15)$$

$$u_2(0, \tau) = B_2 e^{j \omega_{LO} \tau}; B_2 \triangleq \sqrt{P_{02}/P_{01}}$$

Note that in this case there are two signals co-propagating along the fiber. Then XPM (cross-phase-modulation) has to be taken into account besides of SPM. Phase shift in channel #1 and #2 can be given then¹⁰ (SPM and XPM respectively)

$$\Phi_{NL1} = \Phi_{NL}; \Phi_{NL2} = 2\Phi_{NL} \quad (16)$$

At cross-section z of the fiber u_i will be multiplied by $e^{j\Phi_{NLi}}$; $i=1,2$ according to (13)-(14). If there is a photodetector at $z=L_f$ the photo-current contains several combination-frequency terms of inputs u_1 and u_2 – among these the modulated upper and lower sidebands of ω_{LO} . One of these is chosen as RF carrier (the upper, in what follows) and so the RF current can be written as

$$\frac{i_{RF}(L_f, \tau)}{I_0} = A_2 m(\tau) \cos(\omega_{LO} \tau + \omega_{IF} \tau + \Phi_{NLk}) \quad (17)$$

With subscript k it is explicitly stated that Φ_{NL} depends on symbol # k . That is, XPM and SPM causes AM-to-PM conversion, what increases error probability.

Note, that the phase recovered by the carrier synchronizing system coincides with the average phase. Taken this into account, an elementary calculation, similar to that resulting in (4) we get an upper bound of the loss due to the AM/PM conversion

$$L_{AM/PM} < 20 \lg(d/d') = -20 \lg[(\sqrt{M} - 1)\sqrt{2} \cos(\pi/4 + b\Phi_{NL}) - (\sqrt{M} - 2)] \quad (18)$$

with a a function of M : $b = 0,57$ in 64QAM, $b = 0,44$ in 16QAM, and, of course, $b = 0$ in QPSK.

In Fig. 4 computed penalty due to SPM/XPM induced AM-PM conversion is shown for 16QAM and 64QAM.

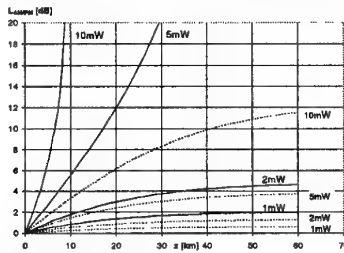


Fig. 4 AM-to-PM loss in remote heterodyning transmission $B_2=1$; solid lines: 64QAM; dotted lines: 16QAM

6. Conclusions

Three distortion phenomena in microwave fiber optic links were discussed, mainly from the point of view of QAM transmission. This, somewhat refined characterization will absolutely be needed in future applications in mobile and other wireless networks operating with QAM. As, high-level modulation schemes are very sensitive both to linear and to nonlinear distortion. The application of the simplest, i.e. single-electrode-pair Mach-Zehnder modulator was throughout assumed; some of the results should be modified in the case of different modulators, however with similar results.

An explicit formula was derived for the apparent power loss due to the modulator nonlinearity. Dynamic range of

the link can be determined based on this. On the other hand from formula (4) it can be seen that this distortion can easily be compensated for by the application of a so-called *compromise-predistorter*. This could increase the dynamic range by several dB-s. This point, however, needs further elaboration.

Fiber dispersion caused linear distortion was discussed next. It was shown that dispersion, besides of causing RF loss, causes also linear distortion. This can increase the dispersion-induced penalty (possibly up to infinity by closing the eye pattern), decreasing thus the maximal length of fiber sections. This phenomenon is known from the techniques of high capacity digital radio⁷; like in that technique, equalizers – adaptive or not – can counteract to this impairment; this possibility can and should be kept in mind in network design. A more effective countermeasure would be to apply single sideband modulation; in this case i. dispersion causes no loss; ii. there is, a group-delay distortion, its magnitude, however, is very low, depending only on the bandwidth and not on the RF carrier; in this way length of the fiber can significantly be increased.

As a third point SPM and XPM effect was investigated. It is shown that this has no effect on intensity modulated links, can cause, however, a significant AM-to-PM conversion in remote heterodyned links even if optical power is a moderate 10 mW or so. Note that it is not only this effect what limits the optical power and excludes the use of very high power but also stimulated Brillouin-scattering¹⁰; therefore investigating power levels much higher than say 10 mW has not too much sense.

Acknowledgment

This work was sponsored by OTKA the Hungarian Foundation for Scientific research (Project T-026277).

References

- ^{1,3} Broadband wireless communications, Workshop at IEEE PIMRC99, Sept. 12-15, 1999, Osaka, Japan
- ² Opperman & al. edit.: Spread spectrum for global communications IEEE JSAC, Vol. 18 No. 1, Jan. 2000
- ⁴ Frigyes, I.: "Basic microwave properties" in H. Al Raweshdi & S. Komaki ed.: Radio over fiber..., Boston, London, Aertech House, 2000
- ⁵ Gliese, U. & al.: Chromatic dispersion in fiber-optic microwave ..., IEEE Trans MTT, Vol. 44, No 10, pp. 1716-1723, Oct. 1996
- ⁶ Hofstetter & al.: Dispersion effects in optical..., IEEE Trans. MTT Vol. 43, No. 9, pp. 2263-2269, Sept. 1995
- ⁷ Frigyes, I. & al.: Digital microwave transmission, Amsterdam, Elsevier, 1989
- ⁸ Vergnol, E. & al.: New modulation scheme...OFC 2000 Digest, Baltimore, USA, March 2000
- ⁹ Alfemess, R. Waveguide electrooptic modulators, IEEE Trans Vol. MTT-30, No. 8, pp. 1121-1137, Aug. 1982
- ¹⁰ Agrawal, G. P.: Nonlinear fiber optics, San Diego etc., Academic, 1995
- ¹¹ Cox, C & al.: Relationship between gain and noise figure, 1996 IEEE MTT-S Digest pp. 1551-1554

Theoretical consideration on transferring transparency for RF signal bandwidth on Direct Optical Switching CDMA Radio-on-Fiber Networks

Kazuo Kumamoto Katsutoshi Tsukamoto Shozo Komaki

Dept. of Communications Engineering, Fac. of Engineering, Osaka Univ., Japan

Yamada-oka 2-1, Suita-shi, Osaka, Japan

Tel. +81-06-6879-7717, Fax. +81-06-6879-7715

E-mail : kumamoto@roms.comm.eng.osaka-u.ac.jp

I. Introduction

Recently, Fiber-Optic-Radio-Highway has been studied to solve many problems in the microcell/picocell technologies[1]. Figure 1 illustrates the concept of radio highways, which can realize the universal capability and flexibility for various types of air interfaces. A radio base station(RBS) is only equipped with an E/O(electric-to-optic) and O/E(optic-to-electric) converters, and all of complicated functions such as RF modulation, demodulation and so on, are performed at a control station(CS).

As a multiple access method in radio highways, CDMA will be a strong candidate, because CDMA is superior to TDMA[2] in its asynchronous access property, and to SCMA[3] in its flexibility and transparency for radio air interfaces.

To realize the radio highway with CDMA scheme, we have proposed direct optical switching(DOS)-CDMA systems[4][5], which can easily encode and decode an optical signal by using optical switch(OSW). Since any types of radio signals can be converted into the intensity of optical CDMA signals, the optical direct detection can be employed. When transferring RF signal in the DOS-CDMA system, the code period is required to be shortened less than the bandpass sampling period[6] in order to generate no distortion. However, DOS-CDMA system has to transfer various RF signals with various bandwidths. In addition, a longer code period can improve the received carrier-to-interference-power-ratio(CIR). Therefore the fixed code period determined independently of RF bandwidth is preferable to improve both transparency for various RF signal formats and the received CIR. This is from the fact that since the received CIR of DOS-CDMA is proportion to the length of spreading codes with any chip rate, the received CIR can be improved by using longer code period when chip rate is fixed[4][5].

In this case, however, since the code period is longer than the bandpass sampling period, the spectral aliasing distorts the regenerated RF signals. In this paper, therefore, we theoretically analyze the spectral aliasing distortions on the regenerated RF signal.

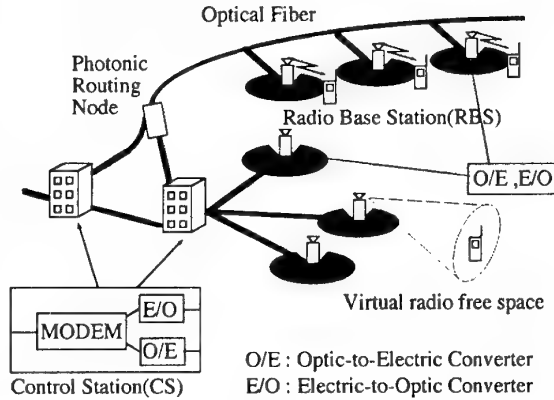


Fig.1 : Concept of the radio highway

II. Spectral aliasing in DOS-CDMA system

A. Principle of DOS-CDMA system

Figure 2 illustrates the configuration of the DOS-CDMA system[4][5]. At the transmitter of k -th RBS, an optical carrier is intensity-modulated(IM) by the RF signal received at the RBS, and on-off-encoded at the OSW driven with the k -th biased bipolar code, $c_k(t)$. After that, many DOS-CDMA signals from M transmitters are multiplexed, and transferred to the CS. At the CS, DOS-CDMA signals are power-split to each receiver, and correlated at the optical polarity reversing correlator (OPRC)[4] driven with the biased bipolar code identical to a desired transmitter. At the OPRC, the DOS-CDMA signal is divided into two branches by 3dB coupler. The OSW of the upper branch is driven with "1" of the biased bipolar code and the OSW of the lower branch is driven with "0" of the biased bipolar code.

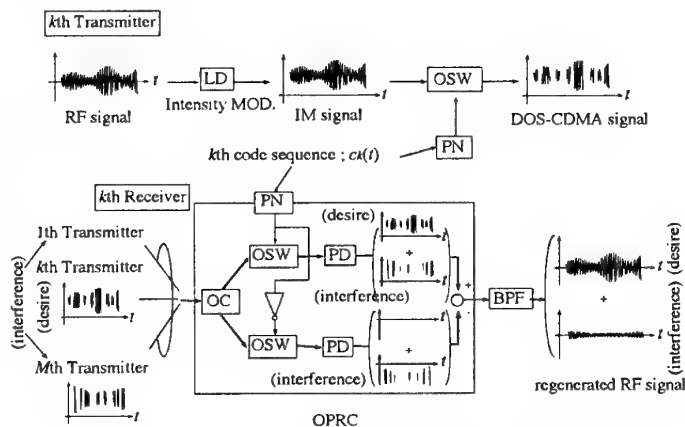


Fig.2 : Configuration of DOS-CDMA system

As a result, the PD output of the upper branch is the sum of the desired signal and the interference signals, and the PD output of the other branch includes only the interference signals. The power of the interference signals from both branches can be reduced by the subtraction after photodetections. Thus, as the output of OPRC, we obtain the desired signal contaminated with some reduced-power interference signals. At this stage, however, the desired signal is still the on-off pulsed signal, so in order to obtain the original RF signal, we finally interpolate it by using a bandpass filter(BPF).

B. Spectral aliasing distortions on DOS-CDMA signal

In the DOS-CDMA system, the received RF signals have various bandwidths, that is, various required bandpass sampling periods. However, to keep a transparency in DOS-CDMA system, code spreading period of RF signals should be fixed for every RF signals. Thus, bandpass sampling period and code period are mutually independent, and when code period is longer than bandpass sampling period, RF signal does not meet the bandpass sampling theorem and the spectral aliasing distortions occur to the regenerated RF signals.

Figure 3 illustrates the spectral aliasing of sampled RF signal which has f_0 of carrier frequency and B_f of bandwidth, in the case of code period, T_L , is longer than required bandpass sampling period, T_s . From the Fig.3, if RF signal is bandpass filtered by BPF of bandwidth of B_f , spectral aliasings(black area) cause the regenerated RF signal distortion. However, if $T_L \leq T_s$, RF signal satisfies bandpass sampling theorem and no spectral aliasing distortions are occurred. In addition, T_L becomes long compared with T_s , number of aliasing spectrums are increase, and influence of spectral aliasing distortion becomes serious.

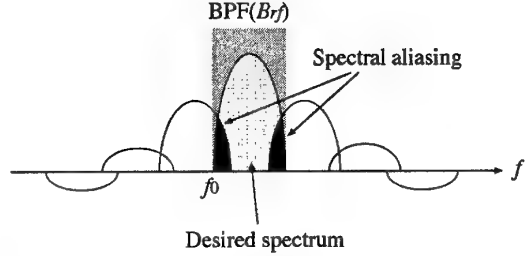


Fig.3 : Spectrum aliasing of sampled signal

III. Theoretical analysis of spectrum aliasing distortion

The code spreading of DOS-CDMA system, when spectrum aliasing distortions occurs, is corresponded to the higher-order bandpass sampling of the RF signal. Figure 4 illustrates the N th order bandpass natural sampling process of the RF signal. In this case, the sampling pulses of a spreading code are randomly positioned in a period, T_L , and each pulse has spectral aliasings illustrated in Fig.3, because T_L is longer than the required bandpass sampling period, T_s .

A sampled signal, $f^*(t)$, is expressed as

$$f^*(t) = \sum_{i=1}^N f_i(t) = \sum_{i=1}^N \{f(t) \times \sum_{n=-\infty}^{+\infty} [p(t - nT_L - \tau_i)]\} \quad (i=1,2,3, \dots, N) \quad (1)$$

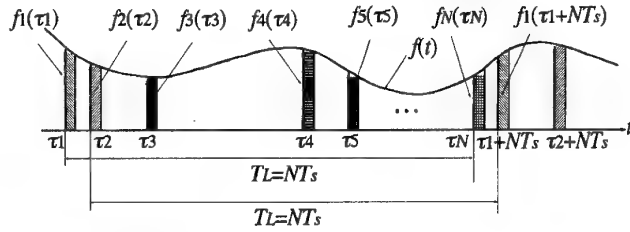


Fig.4 : Nth order sampling of RF signal

where $f(t)$, $f_i(t)$, $p(t)$ and τ_i are the received RF signal which intensity modulates LD, the i -th sampled sequence, the rectangular pulse with its width of chip rate, T_c , and its amplitude of 1, and the time position of the i -th pulse, respectively. The spectrum of the N th order bandpass sampled signal, $F(f)$, is given by

$$F(f) = \sum_{i=1}^N F_i(f) \quad (i=1,2,3, \dots, N) \quad (2)$$

and

$$F_i(f) = \sum_{n=-\infty}^{+\infty} \frac{T_c}{T_L} \frac{\sin \pi \frac{T_c}{T_L} (f - \frac{n}{T_L})}{\pi \frac{T_c}{T_L} (f - \frac{n}{T_L})} F(f - \frac{n}{T_L}) e^{-j2\pi \tau_i / T_L} \quad (i=1,2,3, \dots, N) \quad (3)$$

Thus, the RF output, P_d , is given by

signal power of desired spectrum at the BPF

$$P_d = C = N \int_{f_0}^{f_0+B_f} |F(f)|^2 df \quad (4)$$

and aliasing spectrum power, P_a , is given by

$$P_a = \sum_{n=1}^{T_L/B_f} \left\{ \int_{f_0+n/T_L}^{f_0+B_f} \left| \sum_{i=1}^N F_i(f) \right|^2 df + \int_{f_0}^{f_0+B_f-n/T_L} \left| \sum_{i=1}^N F_i(f) \right|^2 df \right\} \\ + \sum_{n=2f_0/T_L}^{2f_0/T_L+T_L/B_f} \left\{ \int_{f_0}^{f_0+n/T_L} \left| \sum_{i=1}^N F_i(f) \right|^2 df + \int_{f_0-B_f+n/T_L}^{f_0+B_f} \left| \sum_{i=1}^N F_i(f) \right|^2 df \right\} \quad (5)$$

On the other hand, the received CIR without spectral aliasing distortions is given as[4][5][7]

$$CIR = \frac{C}{I} = \begin{cases} \frac{T_c}{0.29(M-1)T_c} & \text{For Prime Codes} \\ \frac{T_c}{(M-1)T_c} & \text{For M Sequences} \end{cases} \quad (6)$$

where M is number of the connected RBSs. From Eqs.(4)(5)(6), the received CIR with spectral aliasing distortions is given by

$$CIR = \frac{C}{I + P_a} \quad (7)$$

IV. Numerical results

This section shows some numerical results about the influence that spectral aliasing distortions give to the received CIR. As parameters used for a calculation, number of connected RBSs, M , is 10 and carrier frequency of RF signal, f_0 , is 1.9GHz, and switching speed of OSW, that is, chip rate, $1/T_c$, is 10MHz.

Figure 5 shows a relationship between CIR of the regenerated RF signals and the code length, TL/T_c , for M sequences. In this figure, the RF signal with its upper limit line is obtained the ideal condition that spectral aliasing is ignored. It is found from this figure, if we require the received CIR of more than 40dB, we should use code length of more than 100000 words and bandwidth of less than 1.5MHz. It is also found, in the case of M sequences, the spectral aliasing distortions hardly deteriorate the CIR even if using BPF to interpolate the RF signal. However, when broadband RF signal with its bandwidth of more than 1.5MHz, is transferred, its CIR reaches the saturated value determined by aliasing spectrum power, P_a . Thus, to transfer RF signal whose bandwidth is more than 1.5MHz in high quality, we must reduce P_a by using high chip rate code more than 10MHz to shorten TL in Eq.(5).

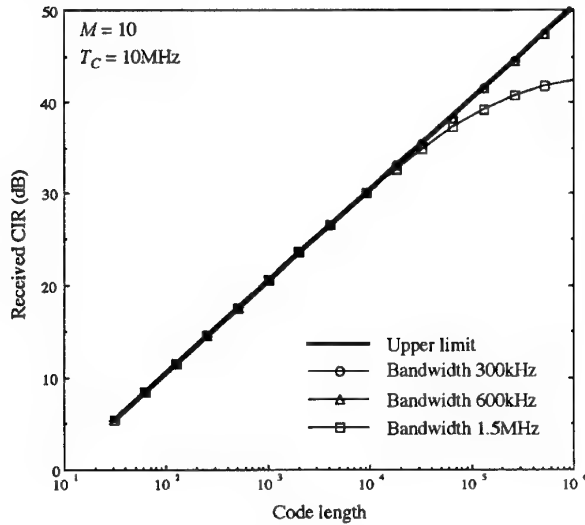


Figure 5 : CIR versus code length(M sequences)

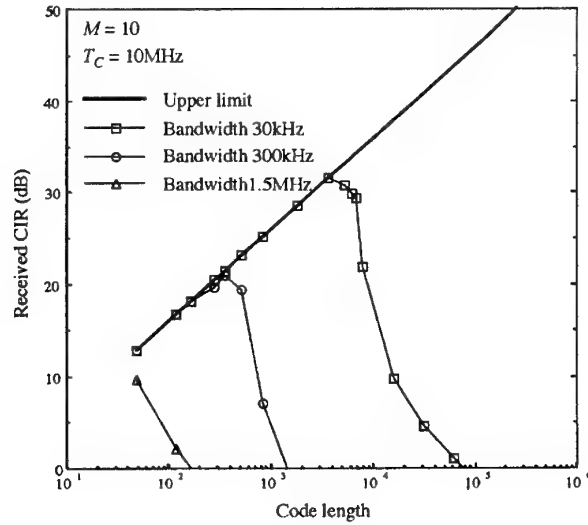


Figure 6 : CIR versus code length(prime codes)

Figure 6 shows a relationship between CIR of the regenerated RF signals and code length for prime codes. In the case of prime codes, influence of spectral aliasing distortions is conspicuous, and the received CIR is more deteriorated compared with M sequences, because pulse duty of prime code is lower than that of M sequences and RF signal power C is smaller than that of M sequences. Thus, C/P_a is lower than that of M sequences. It is found from Fig.6 that if we require more than 30dB of received CIR, we should use the code length about 5000 words and bandwidth of only less than 30kHz. However, by using prime code, we can configure the receiver simpler with single OSW and single PD, moreover, the chip synchronization can be established easily because of its low pulse duty. In the prime code, RF signal whose bandwidth is more than 30kHz can be also transferred by using more high chip rate code than the case of M sequence.

In this way, broadband RF signal can be transferred by using high chip rate code, but it is difficult to realize because of limitation of OSW speed and difficulty of chip synchronization. To transferring broadband RF signals without high chip rate code, we have proposed a method of using a proposed aliasing canceler[7] which can remove the spectral aliasing distortions. In the case of using an aliasing canceler, received CIR of these figures can be closed to upper limits.

V. Conclusions

In this paper, we have analyzed theoretically about the CIR of the regenerated RF signal considering the spectral aliasing distortions when code period is longer than bandpass sampling period. As the results, following are obtained.

In the M sequences, if we require the received CIR of more than 40dB, we should use code length of more than 100000 words and bandwidth of less than 1.5MHz. And in the prime code, if we require more than 30dB of received CIR, we should use the code length about 5000 words and bandwidth of only less than 30kHz. To transfer broadband RF signals in DOS-CDMA, we should use high chip rate code.

References

- [1] S.Komaki, K.Tsukamoto, M.Okada, and H.Harada, "Proposal of Radio Highway Networks for Future Multimedia-personal Wireless Communications", *ICPWC'94*, Bangalore India, pp.204-208, Aug.1994.
- [2] H.Harada, S.Kajiya, K.Tsukamoto, S.Komaki, and N.Morinaga, "TDM Intercell Connection Fiber-optic Bus Link for Personal Radio Communication Systems", *IEICE TRANS. COMMUN.*, vol.E78-B, pp.1287-1294, Sep.1995.
- [3] M.M.Banet and M.Kavehrad, "Reduction of optical beat interference in SCM/WDM networks using pseudorandom phase modulation", *IEEE J. of Lightwave Tech.*, vol.LT-12, No.10, pp.1863-1868, Oct. 1994.
- [4] S.Park, K.Tsukamoto, and S.Komaki, "Polarity-Reversing Type Photonic Receiving Scheme for Optical CDMA Signal in Radio Highway", *IEICE Trans. on Electron.*, Vol.E81-C, No.3, 462-467, Mar.1998.
- [5] S.Park, K.Tsukamoto and S.Komaki, "Proposal of Direct Switching CDMA for Cable-To-The-Air System and Its Performance Analysis", *IEICE TRANS. COMMUN.*, vol.E81-B, No.6, pp.1188-1196, June.1998.
- [6] A.Kohlenberg, "Exact Interpolation of Band - Limited Functions", *J.Appl.Phys*, vol.24, pp.1432-1436, Dec.1953.
- [7] K.Kumamoto, S.Park, K.Tsukamoto and S.Komaki, "Application of Aliasing Cancelling Scheme for Direct Optical Switching CDMA System with Higher-Order Bandpass Sampling", *Proc. of PIMRC'99*, No.A4-5, Sep.1999.

INCREASING THE CHANNEL NUMBER IN WDM MM-WAVE SYSTEMS BY SPECTRAL OVERLAP

C. G. Schäffer, M. Sauer, K. Kojucharow, H. Kaluzni

University of Technology, Communications Laboratory, D-01062 Dresden, Germany

Phone: +49 351 463 3941, Fax: +49 351 463 7163, Email: schae@ifn.et.tu-dresden.de

Abstract: *The demux filter requirements in WDM mm-wave transmission systems are theoretically and experimentally investigated. Optical channel spacings of less than the mm-wave frequency are feasible, which was confirmed by data transmission at 60 GHz.*

INTRODUCTION

Optical mm-wave transmission systems offer the potential for flexible and low-loss distribution of signals at mm-wave range to remote antenna units. Especially if numerous base stations in mobile broadband communication systems are to be connected to a central control station, an optical backbone for mm-wave signal transport is required [1]. In order to feed remote base stations at distances of some kilometers, mm-wave signal generation techniques leading to dispersion-tolerant signal transmission are preferable [2,3]. Further significant cost reduction can be achieved, if a wavelength division multiplex (WDM) system is applied, since optical amplifiers can be used by all channels.

We proposed and demonstrated an optical mm-wave transport system applying simultaneous upconversion of the individual data signals at IF range in each WDM channel by a single high-speed electro-optical modulator (EOM) to mm-wave range [4]. Initial experiments at 60 GHz were carried out at a channel spacing of 200 GHz, however, we also demonstrated a 7 channel experiment with a spacing of 100 GHz [5]. In [6], we presented initial results on further reduction of channel spacing. In general, a channel spacing according to the ITU grid is preferable, since optical components such as multiplexers developed for telco systems can be used (cost aspect!).

Further reduction of channel spacing would increase the number of channels in the Erbium band and is investigated in this paper. Evaluation of the spectral requirements for demux filters in WDM mm-wave

systems is presented. The application of special tailored fiber Bragg grating filters seems to be an ideal solution, especially if distributed demultiplexing (dropping of a single WDM channel at each base station site, see Fig. 1) using add/drop-multiplexers (ADM) is applied. It is theoretically and experimentally (at 60 GHz) demonstrated that an overlap of the modulation sidebands is feasible, leading to channel spacings of less than the mm-wave transmission frequency and hence a new demultiplexing scheme.

SYSTEM DESCRIPTION

The general system setup for simultaneous upconversion is shown in Fig. 1. Wavelength-selected laser diodes are directly modulated via the injection current with the data signal at IF range. The optical output signals are wavelength multiplexed using a single multiplexer and subsequently the combined optical signal is fed into a high-speed external modulator driven by a LO tone at high frequency. After optical amplification, the signal is transmitted over standard fiber and dropped off the fiber bus at each base station site by add/drop-multiplexers.

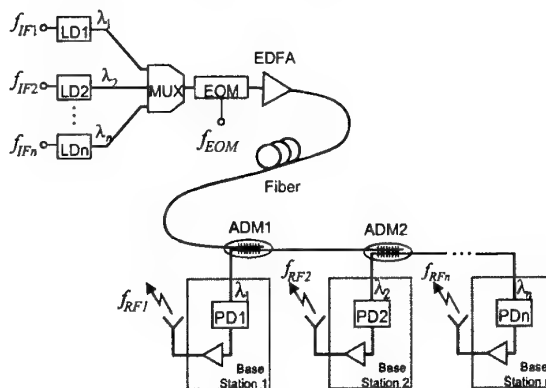


Fig. 1: General setup for simultaneous upconversion.

We have demonstrated that mm-wave transmission over approx. 50 km is feasible using this direct IF modulation/external upconversion scheme at 60 GHz [7,8]. There is no synchronization required between the data signals of different channels, the IF can be varied for obtaining different mm-wave transmission frequencies in adjacent picocells and in uplink mode the mm-wave LO signal can be used for downconversion of the received signal to IF range for easy transport back to the central control station.

WDM CHANNEL SPACING

In Fig. 2, the optical spectrum for two WDM channels of a direct IF modulation/simultaneous upconversion system with the external Mach-Zehnder modulator biased at minimum transmission point is shown schematically. In this case, the mm-wave transmission frequency of channel (i), $f_{RF}^{(i)}$, is obtained from $f_{RF}^{(i)} = 2f_{EOM} + f_{IF}^{(i)}$ with f_{EOM} denoting the EOM modulation frequency and $f_{IF}^{(i)}$ being the center IF of channel (i). It is obvious from Fig. 2 that higher EOM modulation sidebands from adjacent channels ($i-1$) and ($i+1$) affect the signal at $f_{RF}^{(i)}$. However, their power is typically very low and only the $\pm 3^{rd}$ EOM sidebands lead to critical distortions in case of a channel spacing of $\Delta f_{WDM} \approx 4f_{EOM} + f_{IF}^{(i)}$ [9].

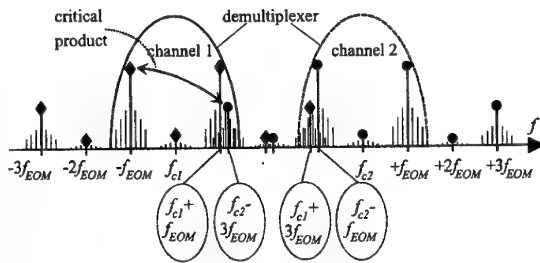


Fig. 2: General optical spectrum for two channels.

If the channel spacing is further reduced, there is no distortion of the signal at $f_{RF}^{(i)}$. Even an overlap of the 1st order EOM sidebands of adjacent channels can result in a distortion-less signal at $f_{RF}^{(i)}$ in channel (i) and is proposed and demonstrated in this paper. In this case, however, the WDM sources have to be wavelength-stabilized to high extend and the demux filter need to have steep edges.

If the 1st order EOM sidebands overlap, there are multiple modulated optical carriers in the same optical channel and the beat notes produced by the mixing of different optical carriers at a photodetector may interfere with the microwave subcarriers, hence reducing the carrier-to-interference ratio (CIR). A general model of optical beat interference (OBI) is given in [10]. In our system (Fig. 1), the drop function is realized with a demux filter having a transfer function $H_{Bragg}(f)$. Considering the independent single-mode laser fields with the same polarization state, the power spectral density of the photocurrent is given by [10]

$$S_i(f) = R^2 |H_{Bragg}(f)|^2 \times \left\{ \sum_{k=1}^N S_{I_k}(f) + \sum_{i=1}^{N-1} \sum_{j=i+1}^N 4S_{E_i} \otimes S_{E_j}(f) \right\} \quad (1)$$

where R is the responsivity of the detector, S_{I_i} are the power spectral densities (PSD) of the intensities $I_k(t)$ and $S_{E_i}(f)$ are the PSD of the optical fields. The second term contains the optical beat notes. The OBI terms are described by a two-sided Lorentzian PSD of a signal centered at a frequency f_0 , which corresponds to a possible difference of two optical components (for small-signal modulation). The FWHM of a spectrum is given by the laser linewidth and chirp. In the experiments, the quotient of FM index and IM index is approx. $M/m \approx 4.1$.

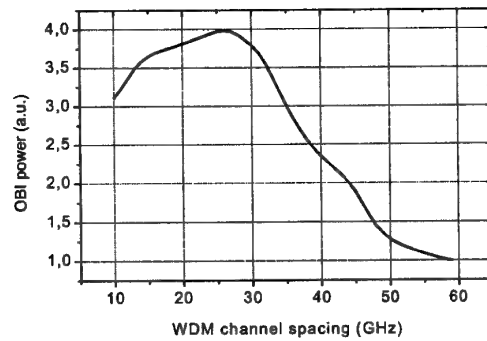


Fig. 3: OBI power versus WDM channel spacing for a 3 laser system.

When computing the OBI power, $\Delta f_{WDM} \gg B_T$ is assumed for simplicity (B_T total bandwidth of baseband), so that the integral of the PSD's of the laser can be approximated as $2B_T S_{E_j}(0)$. Fig. 3 shows the total interference power in a three channel system

($N = 3$) as a function of the channel spacing Δf_{WDM} . The maximum of interference power is generated, when the spectra of the three $S_{E_i}(f)$ have a center frequency of 30 GHz and the BER increases. As optical demux filter, a symmetrical filter with a flat top of 66 GHz, a FWHM width of 70 GHz and a width of 108 GHz @ -20 dB is assumed.

In systems using such small channel spacings as discussed here, beat interference always occurs. A sharp slope of the demux filter is necessary to reduce the influence of the higher spectral part of the laser PSD yielding to lower total interference power. Outside the pass band >-25 dB are required to avoid crosstalk of other spectral components [9].

Since the spectral components overlap, a new demux scheme has to be applied. First, the total optical signal has to be power divided by a factor depending on the signal overlap. Then the demux function is applied in such a way that in each optical branch some channels are lost, however, altogether all channels are demultiplexed.

EXPERIMENTAL RESULTS

Using the setup of Fig. 1 with three laser diodes, experimental data transmission (50 MBit/s 512-carrier OFDM with DQPSK subcarrier modulation) at 60 GHz has been carried out.

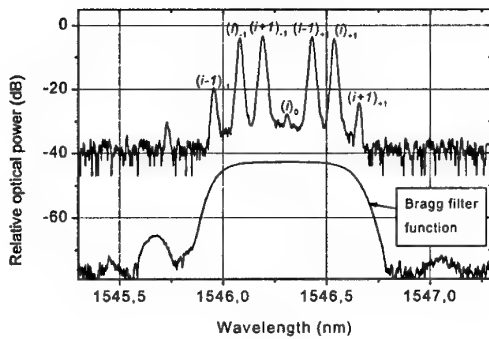


Fig 4: Measured optical spectrum before detection.

Laser 2 as center channel (i) was directly modulated with an individual signal centered at $f_{IF} = 2.3$ GHz. Laser 1 and laser 3 served as adjacent channels ($i-1$) and ($i+1$) and were modulated with a different (independent) signal of the same format and at the same IF. The channel spacing was varied and the bit error rate

(BER) measured. A specially designed fiber Bragg grating in conjunction with an optical circulator served as demux filter.

Fig. 4 depicts the optical spectrum with channel (i) selected by the Bragg grating at a channel spacing of $\Delta f_{WDM} \approx 15$ GHz. The EOM modulation sidebands are denoted. The IF modulation sidebands cannot be resolved. Furthermore, the Bragg filter function is shown.

In Fig. 5, the BER versus channel spacing is shown for the center channel (i) (laser 2) at SNR = 17 dB with different distortions by adjacent channels. First, there is the case of distortion by just one adjacent channel (laser 1 or laser 3) and second, there is distortion from both sides (laser 1 and laser 3). As can be seen in Fig. 5, in case of distortion from laser 3 no degradation of BER is observed until the channel spacing approaches ~35 GHz. By further reduction of channel spacing, a rapid increase of BER is obtained due a spectral overlap of the IF modulation sidebands. If the distortion is only from laser 1, almost the same behavior is obtained. However, around 50 GHz a small degradation of BER is observed, indicating that the SNR is decreased. This is due to the fact that there is a significant side-lobe on the short wavelength side of the fiber Bragg grating filter, see Fig. 4.

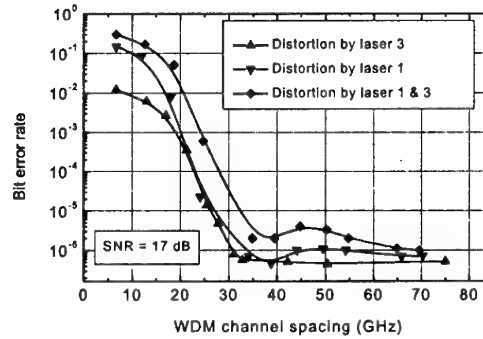


Fig. 5: BER versus channel spacing for channel 2.

At a channel spacing of approx. $\Delta f_{WDM} \approx 60$ GHz, heterodyning of the upper sideband of laser 1 and the lower sideband of laser 2 occurs and no BER is measurable.

CONCLUSIONS

It has been shown that a significant reduction of channel spacing below the frequency of $\Delta f_{WDM} \approx 4f_{EOM} + f_{IF}^{(i)}$ is feasible, if the optical demux filter has steep edges and very low side-lobes. Even a channel spacing of less than the mm-wave transmission frequency can be realized, resulting in an overlap of the 1st order EOM sidebands of adjacent channels and hence leading to a significant increase in channel number. This setup requires a new demultiplexing scheme for channel separation. A theoretical analysis on filter requirements has been carried out. Transmission experiments at 60 GHz resulted in low BER for $\Delta f_{WDM} < f_{RF}$ and demonstrated the feasibility of the proposed system.

ACKNOWLEDGMENT

The project was supported by German Research Council (DFG) under contract INK 13.

References

- [1] K. Kojucharow, M. Sauer, H. Kaluzni, D. Sommer, F. Poegel, W. Nowak, A. Finger, D. Ferling: "Simultaneous electro-optical upconversion, remote oscillator generation and air transmission of multiple optical WDM channels for a 60 GHz high capacity indoor system.", IEEE Transactions on Microwave Techniques and Theory, vol. 47, no. 12, pp. 2249-2256, 1999
- [2] R. A. Griffin, P. M. Lane, J. J. O'Reilly: "Dispersion-tolerant subcarrier data modulation of optical millimetre-wave signals.", Electronics Letters, vol. 32, no. 24, pp. 2258-2260, 1996
- [3] J. M. Fuster, J. Marti, V. Polo, F. Ramos, J. L. Corral: "Mitigation of dispersion-induced power penalty in millimetre-wave fibre optic links.", Electronics Letters, vol. 34, no. 19, pp. 1869-1870, 1998
- [4] M. Sauer, K. Kojucharow, H. Kaluzni, D. Sommer, W. Nowak: "Simultaneous electro-optical upconversion to 60 GHz of uncoded OFDM signals.", International Topical Meeting on Microwave Photonics (MWP'98), WB3, pp. 219-222, Princeton, USA, 1998
- [5] K. Kojucharow, H. Kaluzni, M. Sauer, C. Schäffer, A. Finger: "Millimeter-wave wireless LAN based on simultaneous upconversion technique of optical WDM channels.", European Microwave Week - European Gallium Arsenide and Related III-V Compounds Application Symposium (GAAS'99), G-TuF2, pp. 369-374, Munich, Germany, 1999
- [6] K. Kojucharow, M. Sauer, H. Kaluzni, D. Sommer, C. Schäffer: "Experimental Investigation of WDM Channel Spacing in Simultaneous Upconversion Millimeter-Wave Fiber Transmission System at 60 GHz-Band.", IEEE MTT-S International Microwave Symposium (MTT'00), WE4C-7, Boston, 2000
- [7] M. Sauer, K. Kojucharow, H. Kaluzni, M. Otto: "Impact of laser chirp on carrier and IMD power in electro-optical upconverted millimetre-wave fibre optic links.", Electronics Letters, vol. 35, No. 10, pp. 834-836, 1999
- [8] M. Sauer, K. Kojucharow, H. Kaluzni, M. Otto, C. Schäffer: "Comparison of different IF band modulation techniques for electro-optical upconversion and fiber transmission at 60 GHz.", International Topical Meeting on Microwave Photonics (MWP'99), T-8.3, pp. 145-148, Melbourne, Australia, 1999
- [9] R. A. Griffin, P. M. Lane, J. J. O'Reilly: "Crosstalk reduction in an optical mm-wave/DWDM overlay for radio-over-fibre distribution.", International Topical Meeting on Microwave Photonics (MWP'99), T-7.5, pp. 131-134, Melbourne, Australia, 1999
- [10] N. K. Shankaranarayanan, S. D. Elby, K. Y. Lau: "WDMA/Subcarrier-FDMA lightwave networks: "limitations due to optical beat interference.", IEEE Journal of Lightwave Technology, vol. 9, no. 7, pp. 931-943, 1991

SIMULTANEOUS BASEBAND AND RF MODULATIONS SCHEME IN GBIT/S MILLIMETRE-WAVE WIRELESS-FIBRE NETWORKS

V. Polo, A. Martinez, J. Marti, F. Ramos, A. Griol, R. Llorente

ITACA Research Institute, ETSI Telecomunicacion

Universidad Politecnica de Valencia

Camino de Vera s/n, 46022 Valencia (SPAIN)

Tel. ++3496-387 7307 / Fax ++3496-387 7199

Email: jmarti@dcom.upv.es

Abstract

A novel modulation scheme to simultaneously transmit broadband signal at both baseband and millimetre-wave RF carriers over optical fibre links is proposed and demonstrated. The key parameters of this technique are optimised for achieving best performance in Gbit/s wireless millimetre-wave fibre networks.

I. INTRODUCTION

Gbit/s millimetre-wave wireless-fibre networks are envisaged to provide broadband services in the local-loop [1]. Different approaches to transmit broadband signals between control stations and base station in mm-wave radio over fibre networks have been proposed. In principal, these approaches consists of : (i) transmitting the signals on RF carriers or (ii) on IF carriers, or otherwise at (iii) baseband (BB) to be further upconverted at the remote site [2]. To increase the fibre-radio network flexibility a combination of the above stated feeding techniques is desired. Likewise, for instance, some network nodes (base stations) may be fed using a RF technique and others using a baseband technique. To our knowledge, no simultaneous transmission in RF and baseband signals has been demonstrated yet. In the paper a novel scheme to simultaneously transmit baseband and RF broadband signals in fibre-radio links is proposed and demonstrated for Gbit/s data rates. The key parameters of the technique are optimised to enable simultaneous transmission.

II. SIMULTANEOUS BB AND RF MODULATION SCHEME

The experimental arrangement to demonstrate the novel modulation scheme to simultaneously transmit RF and BB signals is depicted in figure 1. A laser source is externally modulated using a dual-electrode Mach-Zehnder electrooptical modulator (DE-MZM). One of the DE-MZM RF ports is driven by the 90° phase-shifted local oscillator (f_{LO}) tone obtained at the hybrid coupler output. The digital PRBS baseband signal is combined with the local oscillator signal and further applied at the other RF port of the DE-MZM. The DE-MZM bias is adjusted using a power supply. The optical modulated signal is launched into the standard optical fibre, and is further photodetected and amplified at the receiving end. No optical filter at the output of the DE-MZM to eliminate f_{LO} harmonics was used, as in [2], due to their levels were low enough in relation to the f_{LO} signal.

The proposed modulation scheme has been also modelled as follows. The electric field at the output of the DE-MZM when it is biased at quadrature may be expressed as:

$$E_{out} = \frac{E_{in}}{2} \cdot (-J_0(\alpha) \cdot (1 + \sin \gamma \cdot p(t)) \cdot \sin \omega_0 t + \cos \gamma \cdot J_0(\alpha) \cdot \cos \omega_0 t - J_1(\alpha) \cdot (1 + \cos \gamma) \cdot \cos(\omega_0 - \omega_{LO})t + J_1(\alpha) \cdot (1 - \cos \gamma) \cdot \cos(\omega_0 + \omega_{LO})t - J_1(\alpha) \cdot p(t) \cdot \sin \gamma \cdot (\sin(\omega_0 + \omega_{LO})t - \sin(\omega_0 - \omega_{LO})t)) \quad (1)$$

where E_{in} is the input electric field, $p(t)$ represents the [-1,+1] PRBS signal, and $J_0(.)$ and $J_1(.)$ stand for the zero and first order first-kind Bessel functions, respectively, and their arguments are

$$\alpha = \frac{\pi \cdot V_{LO}}{V_{\pi}} \quad (2a)$$

$$\gamma = \frac{\pi \cdot V_{BB}}{V_{\pi}} \quad (2b)$$

V_{π} is the half-wave voltage of the DE-MZM and V_{LO} and V_{BB} are the local oscillator and baseband data voltages, respectively. At the output of the photoreceiver the three significant terms of the current are at baseband:

$$I_{BB} \propto 2 \cdot J_0^2(\alpha) \cdot (1 + p(t) \cdot \sin \gamma) + 4 \cdot J_1^2(\alpha) \quad (3)$$

at f_{LO} ,

$$\begin{aligned} I_{f_{LO}} \propto & \cos(\beta f_{LO}^2) \cdot \cos \gamma \cdot \cos(\omega_{LO} t + \pi/4) + \\ & + \sin(\beta f_{LO}^2) \cdot \cos(\omega_{LO} t - \pi/4) + \\ & + \sin(\beta f_{LO}^2) \cdot \sin \gamma \cdot p(t) \cdot \cos(\omega_{LO} t - \pi/4) \end{aligned} \quad (4)$$

and at $2f_{LO}$,

$$I_{2f_{LO}} \propto 4 \cdot J_1^2(\alpha) \cdot \sin \gamma \cdot p(t) \cdot \sin(2\omega_{LO} t) \quad (5)$$

where : $\beta = \frac{\pi \cdot L \cdot D \cdot \lambda^2}{c}$, and L is the fibre length, D is the fibre dispersion parameter (ps nm/km) and λ and c the wavelength and vacuum velocity of light.

From (5) it is noticed that the data signal is upconverted to $2f_{LO}$ when $\sin \gamma = 1$ and thus for $V_{BB} = V_{\pi}/2$. In addition, a dispersion-tolerant transmission is achieved at this frequency. From (4), it may be deduced that a dispersion-tolerant tone is obtained at f_{LO} , even though also data is modulated on this tone depending on β .

III. EXPERIMENTAL RESULTS

In order to evaluate the influence of the DE-MZM bias voltage, the electrical spectrum at the photoreceiver output for a 1.25 Gbit/s PRBS signal and a f_{LO} of 5 GHz when transmitting over 50 km fibre span was obtained, shown in figure 2. In this figure it can be seen that depending on the DE-MZM bias voltage the data spectrum moves from f_{LO} (see fig. 2 (a),(b) and(d)) to BB and $2f_{LO}$ (in quadrature case, see fig.2(c)), which is the optimum case. In addition, a high level LO is also achieved, which might be used at the base station to modulate the upstream signal, as shown in figure 1.

Moreover, the performance of the received signal at base band and at $2f_{LO}$ is measured. Due to laboratory equipment limitations the Q-parameter was only measured at 622 Mbit/s for the BB signal as a function of the received optical power and bias voltage, depicted in figure 3, and at 52 Mbit/s for the $2f_{LO}$ signal as a function of the bias voltage, as shown in figure 4.

In figure 3, it may be observed that good performance are obtained for the BB broadband data in quadrature. A Q of 6 (BER= 10^{-9}) may be achieved for a received optical power around -12 dBm (if an EDFA was included or high optical power was used). Also in this figure it can be seen that the best performance is obtained in quadrature and the system performance sensitivity to the DE-MZM bias voltage is moderate.

In figure 4, it may be observed that a Q ~8 (BER < 10^{-11}) is achieved at the quadrature points. It should be noticed that the quadrature points for BB and $2f_{LO}$ are different due to the frequency variation of the DE-MZM V_{π} parameter.

IV. CONCLUSION

In conclusion, a simultaneous base band and RF modulation scheme for Gbit/s millimetre-wave fibre radio systems is proposed and demonstrated. The novel modulation scheme enables the transmission of broadband signals at base band and at double frequency of a local oscillator. The influence of the voltage bias of the DE-MZM on the system performance has been evaluated, as well as, a modulation scheme model is provided.

References

- [1] R. Heidemann, G. Veith "mm-wave photonic technologies for Gbit/s wireless-local-loop". Proc.OECC'98, paper 15A1-3, pp.310-311, Chiba, Japan, 1998.
- [2] C. Lim, A.Nirmalathas, D. Novak, R.Waterhouse, "Optimisation of baseband modulation scheme for millimetre-wave fibre-radio systems", Electron.Lett., vol.36.n.5, pp.442-443, 2000.

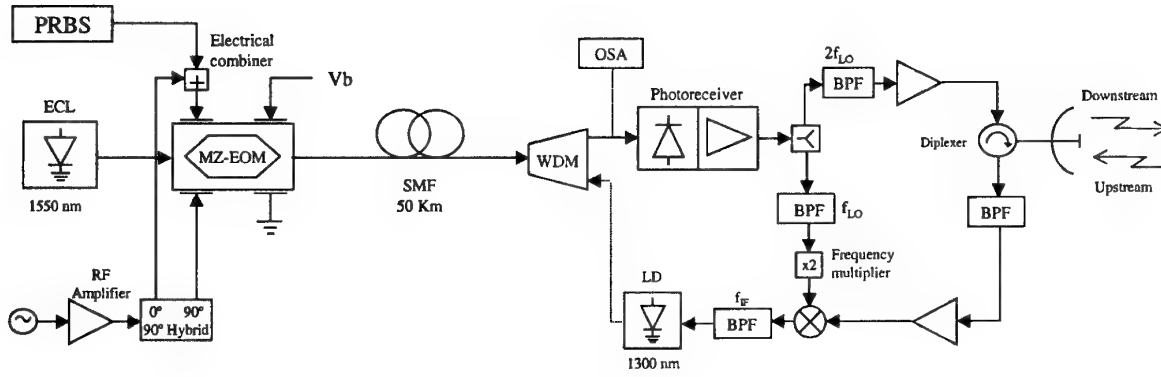


Figure 1. Experimental arrangement of the simultaneous BB and RF modulation scheme

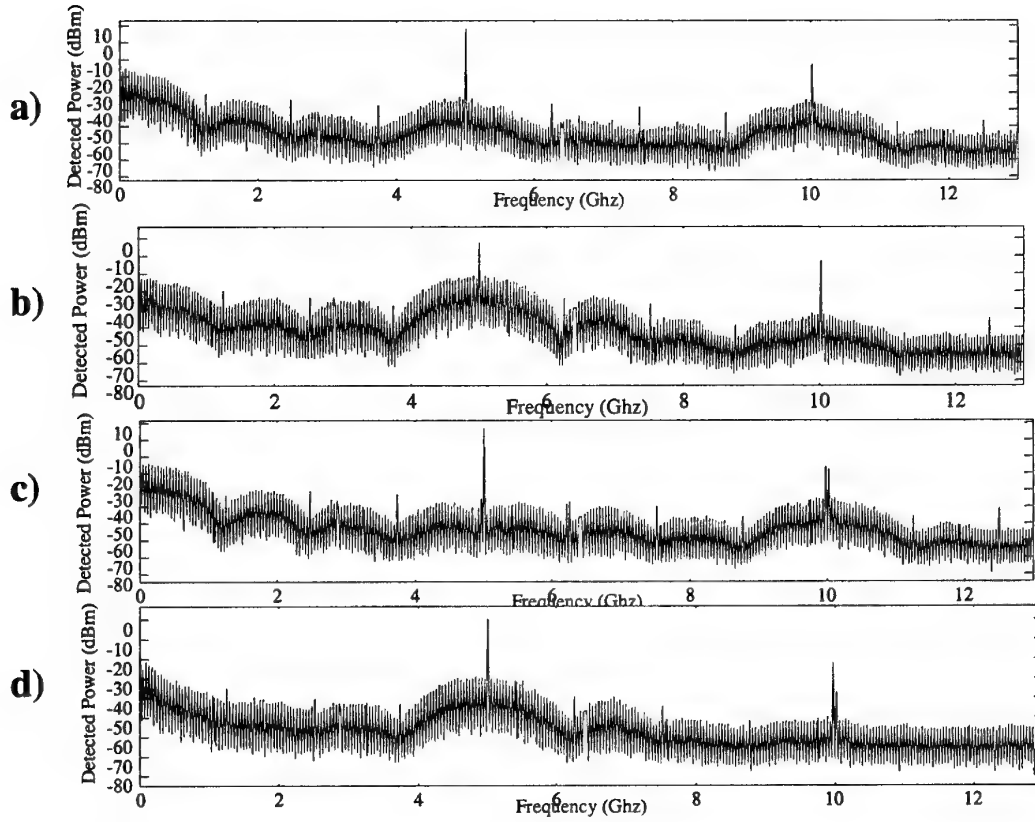


Figure 2. Electrical spectra at the photoreceiver output for different DE-MZM bias voltage. (a) 3 V, (b) 6 V, (c) 9 V-quadrature, (d) 12 V.

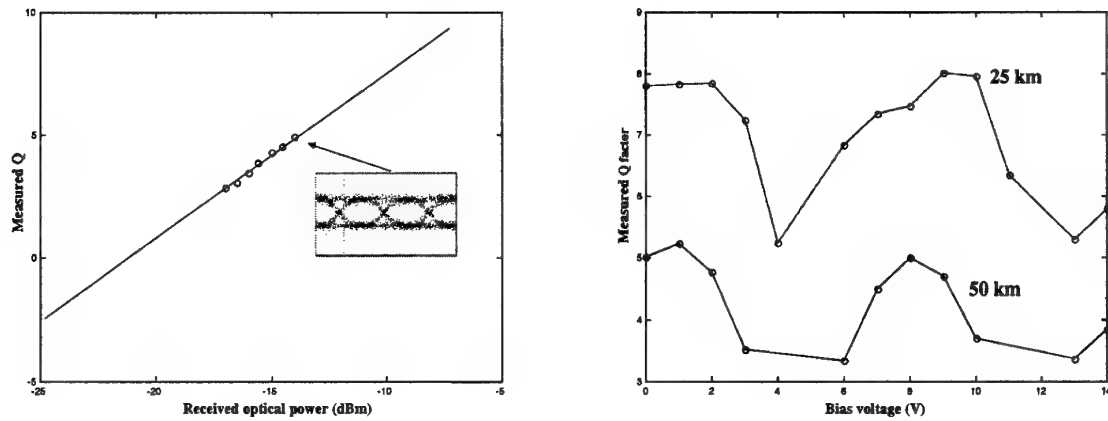


Figure 3. Q-parameter for BB 622 Mbit/s transmission as a function of the received optical power (left, DE-MZM in quadrature) and DE-MZM bias voltage (right)

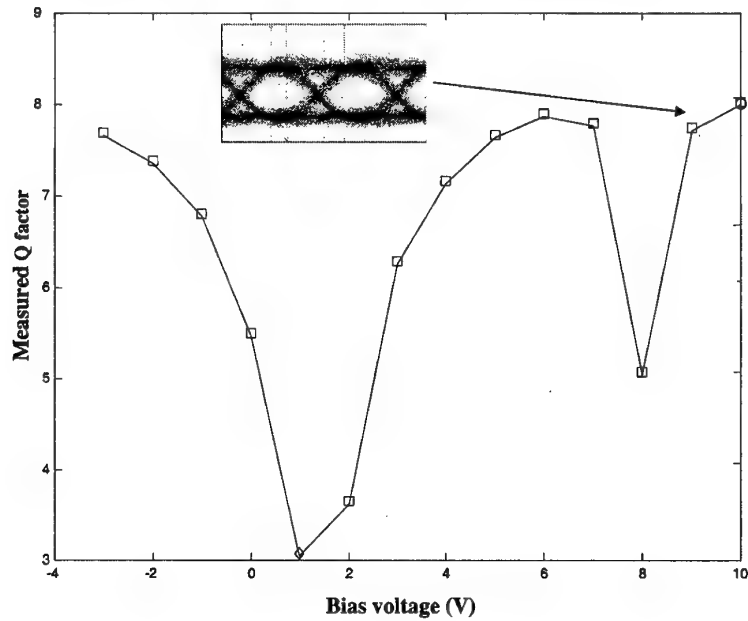


Figure 4. Q-parameter against the DE-MZM bias voltage for a 52 Mbit/s transmission over 50 km fibre span at $2f_{LO}$ of 10.24 GHz.

AN INTEGRATED FIBER OPTICS / BROADBAND WIRELESS ACCESS DEMONSTRATOR FOR THE NEXT GENERATION INTERNET (NGI) NETWORK EXTENSION

H. Izadpanah, D. J. Gregoire, F. A. Dolezal, W. Ng, D. Yap and G. Tangonan
HRL Laboratories, LLC

3011 Malibu Canyon Rd., Malibu, CA 90265

Tel: (310) 317-5563, Fax: (310) 317-5485, Email: hizad@hrl.com

Abstract

We report on the implementation and integration of gigabit fiber networks and a multi-Mbit wireless access NGI network demonstrator. The focus is to merge photonic technology and networking with the broadband wireless access system.

Summary

As illustrated schematically in Figure 1, the Broadband Wireless Access (BWA) system architecture [1,2] consists of four distinct network segments:

- A short range (< 500 m) micro-cell Access Point (AP) for PMP distribution topology to places such as inner city buildings with concentrated high bandwidth users.
- A single RF platform with multi-band modular IF stages utilizing Hybrid Fiber Radio (HFR) interconnection technology. The HFR technique is used to integrate multi-band wireless services (NII, mm-wave, and LaserCom) to the backbone network.
- A centralized Network Operation Center (NOC) to integrate the radio/network switching, routing, and service mixing functions
- Apply innovative techniques to merge microwave photonic and digital fiber-optic technologies with the fixed BWA for flexible, heterogeneous, and unified network operation

In the demonstrator, special emphasis is given to Wireless Local Loop (WLL) applications, versatile service access, rapid system deployment, and network reconfiguration. We will present test results for a single-Hub/three-user testbed including the performance of a field operated portable node.

To evaluate the access operation and link performance, multi-band links are adapted at 28 and 38 GHz for direct performance comparison in various environmental conditions (e.g. multi-path,

rain fade, and availability). For mixed-service delivery, links are implemented, on a single analogue RF platform, with broadcast TV channels (80 digital channels in 500 MHz bandwidth) and multiple high-speed data streams. We have designed, developed, and demonstrated the AP IF/RF sub-system and implemented a "beta" version of AP/user modems for data rates up to 155 Mbps.

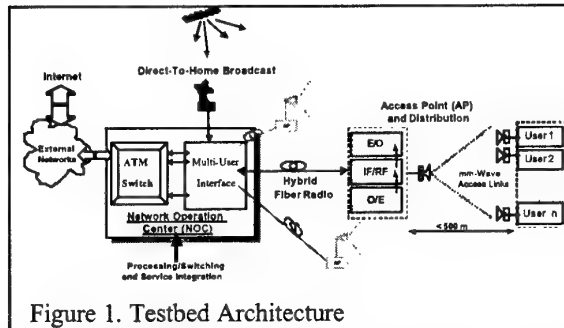


Figure 1. Testbed Architecture

The advantage of microwave RF Photonics [3,4] is that it expands, and merges not only the distribution and access of channels, but it also incorporates "networked" functionality and control into the wireless links. Figure 2 illustrates the role of RF photonics in a wireless/fiber network interface as demonstrated in the program. The otherwise traditional "antenna remoting" scenario has been replaced by a networked integrated service link.

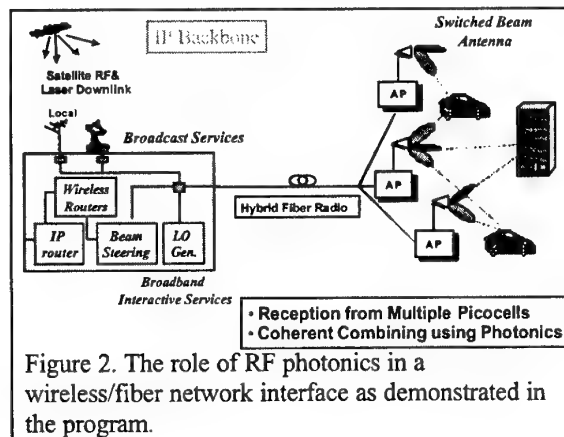


Figure 2. The role of RF photonics in a wireless/fiber network interface as demonstrated in the program.

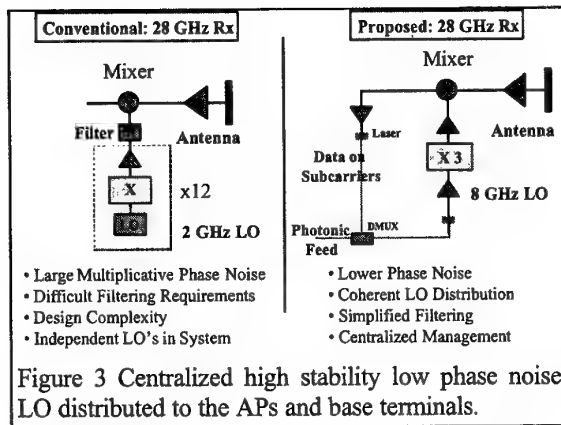


Figure 3 depicts the centralized high stability low phase noise LO distributed to the APs and base terminals. A two channel (12 and 16 GHz) photonic unit was demonstrated for evaluating the performance of a switched photonic link in distributing LO signals [5] shown in Figure 4.

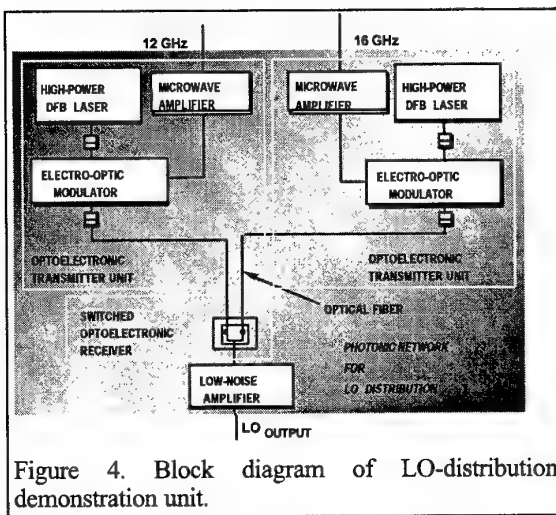


Figure 4. Block diagram of LO-distribution demonstration unit.

The measured residual phase noise is as low as -145 dBc/Hz at frequency offsets greater than 100 kHz (compared to typical isolated LO manufacturer's specification of -95 dBc/Hz) shown in Fig. 5. The scheme provides the flexibility of frequency tuning, channel selection, and dynamic bandwidth allocations. The advantages of an experimentally deployed LO distribution will be presented to illustrate the added tuning functionality and phase quality in the system as well as lowering the

electrical IF/RF terminal complexity and cost compared to a pure all electrical solutions.

To investigate mm-wave propagation issues, we have used a high resolution channel sounder at the 38 GHz LMDS band to model the channel based on the measurements and simulation results. The models will address the performance limits for broadband wireless access, in terms of data transport capability under realistic commercial deployment conditions. Based on the model, a broadband channel-adaptive radio modem is examined for dynamic bandwidth allocations.

We also will present the concept of a portable wireless access node for a bi-directional ATM-based connection to a fixed broadband fiber network. The goal of this effort is to demonstrate the feasibility of a rapidly deployed access node with application in specialized scenarios, e.g. emergency response. The portable node could also serve as a backbone connection in an area with no installed fiber infrastructure.

In conclusion, many new RF-phonic techniques are proposed and tested for a mm-wave BWA system integrated with the existing fiber networks. The schemes provide reduced system complexity, operation cost, and component counts.

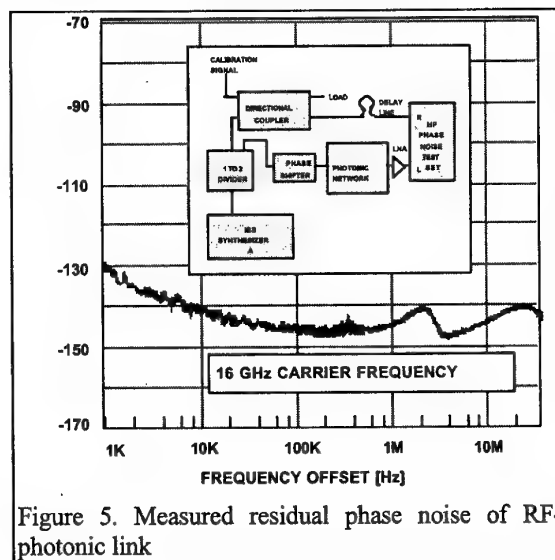


Figure 5. Measured residual phase noise of RF-phonic link

References

1. H. Izadpanah, D. Gregoire, J. Schaffner, and HP Hsu, "mm-Wave Wireless Access Technology For The Wideband Wireless Local Loop Applications", 1998 IEEE Radio and Wireless Conference (RAWCON'98) Colorado Springs, CO, Aug., 1998
2. J. Schaffner, H. Izadpanah, and HP Hsu, "Millimeter Wave Wireless Technology and Testbed Development for Wideband Infrastructure Access", WCC'98, San Diego, CA, Nov. 1998
3. G. Tangonan, W. Ng, and H. Izadpanah, "Photonics Manifolds for Wireless Communications", *Invited Talk, OFC Conference Proc. # FH2, March 2000.*
4. G. Tangonan, W. Ng, and H. Izadpanah, "Photonic Manifolds for Broadband Wireless Communications", *OIDA Workshop on Microwave Photonics, Santa Monica, CA, March 29-30, 2000*
5. D. Yap, H. T. Wang, J. Pikulski, Y. M. So, "Photonic Distribution of RF Local-Oscillator Signals", Presented at the 9th DARPA Symposium on Photonic Systems for Antenna Applications, Monterey, CA, Feb. 1999

An Optically Amplified Four-channel WDM Downconverter for

Wideband Microwave Receiver Applications

ST Winnall*, KL Mahady, DB Hunter and AC Lindsay

Defence Science and Technology Organisation, PO Box 1500, Salisbury SA 5108 Australia.

Phone 61 8 8259 6558, fax 61 8 8259 5938, email stephen.winnall@dsto.defence.gov.au

**Also with Dept. Communication and Electronic Engineering, RMIT University, Australia.*

Abstract – A wideband (1-18 GHz) four channel microwave downconverter employing wavelength division multiplexing and optical amplification is demonstrated. Theoretical analysis and experimental results are included. A compressive dynamic range of 97 dBHz was obtained and performance improvements are outlined.

Introduction

Modern Electronic Warfare (EW) receivers can benefit from the advantages that photonic processing technologies offer. Microwave downconverting photonic receivers have advantages of lightweight, wide bandwidth operation, reduced intermodulation products and high isolation between signal ports. Previously, single channel microwave photonic downconverters have been demonstrated [1-4] which exhibit infinite isolation between local oscillator (LO) and radio frequency (RF) ports, as well as significantly reduced intermodulation products between LO and RF signals at the intermediate frequency (IF) output. The mixing process occurs by cascading the non-linear transfer function of each of the Mach-Zehnder optical modulators. In this work, a four-channel microwave downconverter is demonstrated which exploits commercially available wavelength division multiplexed (WDM) components. Signals from four physically separated antennas are simultaneously downconverted with a single phase coherent local oscillator source. The system performance is enhanced by the use of optical amplification employing an erbium-doped fibre amplifier (EDFA) [5] and balanced IF photodetection to reduce relative intensity noise (RIN) [6]. An IF processing circuit was designed in order to achieve balanced detection, narrowband matching, IF amplification and video detection. Theoretical analysis and experimental results are presented and improvements discussed.

Theoretical Analysis and Experiment

The architecture is illustrated in Figure 1. The RF to IF conversion loss consists of the loss due to the fibre optic link (LL) and an excess due to downconversion process (CL). The total loss is given by:

$$\rho = CL \cdot LL \quad (1)$$

The conversion loss term is given by

$$CL = J_1^2(X_{LO}) \quad (2)$$

where $J_1(X_{LO})$ is the Bessel function of the first kind in which

$$X_{LO} = \frac{\pi V_{LO}}{V_{\pi LO}} = \frac{\pi \sqrt{k_{LO} R_{LO} P_{LO}}}{V_{\pi LO}} \quad (3)$$

where V_{LO} is the voltage incident on the LO modulator, $V_{\pi LO}$ is the halfwave voltage of the LO modulator, P_{LO} is the power applied to the LO modulator, R_{LO} is the termination resistor on the local oscillator modulator and k_{LO} is the LO port matching coefficient. The link loss is determined by:

$$LL = \left(\frac{\pi R_L}{V_{\pi RF}} \right)^2 k_{out} k_{RF} \quad (4)$$

i is the total photocurrent at the photodetector when the modulators are biased at quadrature, R_L is the load resistance, $V_{\pi RF}$ is the halfwave voltage of the RF modulator, and k_{RF} is the RF port matching coefficient. Narrowband impedance matching is employed at the IF stage to improve sensitivity. An IF transformer is used which requires the following expression for the output matching coefficient:

$$k_{out} = \left(\frac{n R_o}{n^2 R_L + R_o} \right)^2 \left(1 - \left(\frac{R_L - R_o}{R_L + R_o} \right)^2 \right) \quad (5)$$

where n is the turns ratio of the IF transformer and R_o is the transimpedance resistor at the photodetector. In the case where there is no matching transformer and $R_L = R_o$, the expression for the link loss reduces to the form derived in [1],[2].

The incorporation of several WDM wavelengths in this work for parallel downconversion does not have a degrading effect the system performance with respect to the modulator bias point variation with wavelength. Specifically, the interferometric nature of the LO modulator's transfer function means that perfect quadrature bias can only be achieved for one wavelength. The equivalent shift from quadrature $\Delta\phi$ experienced by a shift in wavelength $\Delta\lambda$ can be given by

$$\Delta\phi = \frac{\pi \Delta\lambda}{2\lambda} \quad (6)$$

where λ is the laser wavelength. For the case of four wavelengths separated on the ITU grid by 200 GHz, the deviation from quadrature is significantly less than 0.1° . Conversely, amplifying several WDM laser channels with an EDFA results in lower equivalent saturation power for each channel [7]. The EDFA in this system is

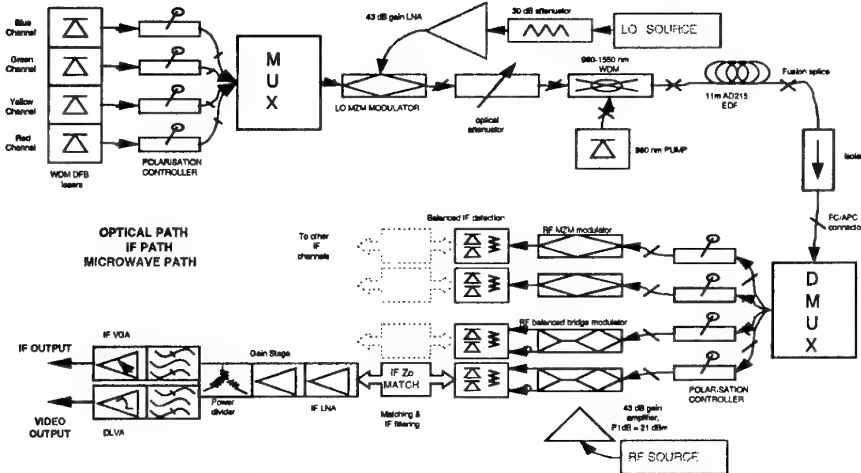


Figure (1) – Experimental layout

operated as a power amplifier. Thus, the reduction in the saturated power should be included as an equivalent loss for N WDM channels as [7]

$$SL = 10 \log(1/N) \quad (7)$$

This equivalent loss has a detrimental effect on performance inasmuch as increasing the number of channels in this architecture results in a reduction of photocurrent at the photodetector and hence a reduction in the dynamic range of the link. This tradeoff can be offset by the use of an EDFA with higher saturated output power.

Link performance parameters such as sensitivity and dynamic range require calculation of the output noise power spectral density N_{out} given by:

$$N_{out} = 4kT + 2qR_L i + RIN(f)R_L i^2 \quad (8)$$

where k is Boltzmann's constant, T is the system temperature (the same temperature is assumed for RF and IF ports), $RIN(f)$ is the relative intensity noise, q is the electronic charge. The factor of 4 in the first term of (8) represents the high input impedance of the detector log video amplifier (DLVA) rather than the usual 50Ω matched load. In this case, the thermal noise contribution would be kT [2]. The second term represents the shot noise produced by the photodetection process and the third term is the relative intensity noise contributions of both the laser source and the amplified spontaneous emission (ASE) noise from the EDFA [8]. The noise sources described in (8) dominate over any referred input noise due to the relatively high insertion loss of the link and conversion loss process.

Figure 2 shows the experimental and theoretical detector log video amplifier (DLVA) output noise voltage as a function of photocurrent for balanced and unbalanced detection. The theoretical curves are calculated using (8). The calculated power spectral density is then referred to a voltage at the output of the system via the DLVA transfer function and the IF filter bandwidth. This graph illustrates that the system is RIN limited above a photocurrent of approximately 1 mA even with balanced detection. Experimentally, balanced detection affords a reduction in noise of >9 dB at a total

photocurrent of $i=3\text{mA}$. Increased noise reduction may be achieved if it were possible to increase the photocurrent. However this corresponds to a RIN of -163 dB/Hz , which is comparable to state-of-the-art diode-pumped solid state lasers [9]. Also shown for comparison in Figure 2 is the shot noise limit. The difference between measured and theoretical curves is $<1.4\text{dB}$ for low photocurrents. This discrepancy is possibly due to the difference between designed and actual IF bandwidths.

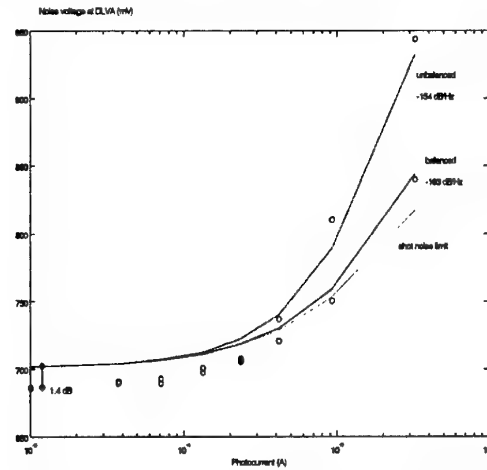


Figure (2) - Output noise of link at DLVA (circles – measured, lines –theory)

For EW receivers, another useful parameter describing system performance is the minimum detectable signal (MDS) referred to the input of the system. This sets the theoretical lower limit on sensitivity and corresponds to the case of unity signal to noise ratio. This can be determined by:

$$MDS(\text{dB}) = 10 \log(B) + EIN(\text{dBm/Hz}) \quad (9)$$

$$EIN(\text{dBm/Hz}) = Nout(\text{dBm/Hz}) + CL(\text{dB}) + LL(\text{dB}) + 4.7 \quad (10)$$

where B is the IF bandwidth and EIN is the equivalent input noise density. The extra 4.7 dB is due to folding of uncorrelated noise sidebands into the IF receiver

bandwidth [1]. The experimental MDS in the case of no RF amplification as a function of photocurrent is depicted in Figure 3, along with the theoretical values calculated from (9). Note that this is not a fit to the data but an *a priori* calculation based on measured device data and the equations outlined in the theoretical analysis. As expected, there is little improvement in MDS with increasing photocurrent in the shot noise limit.

Typically a wideband receiver will have improved sensitivity through the use of a low noise RF amplifier at the input to the system. At the output of the link, IF amplification can be used to increase the signal level to be compatible with the DLVA and analog to digital (A/D) converters. In this case the noise figure is given by [10]

$$F_T = F_1 + \frac{F_L - 1}{G_1} + \frac{F_3 - 1}{G_1 \rho} \quad (11)$$

where ρ is defined in equation (1), F_T is the total system noise figure, F_1 and G_1 are the noise figure and gain of the microwave RF LNA, F_3 is the noise figure of the IF stage, and F_L is the noise figure of a photonic downconverter without RF amplification [1]

$$F_L = \text{EIN}(\text{dBm/Hz}) + 174(\text{dBm/Hz}) \quad (12)$$

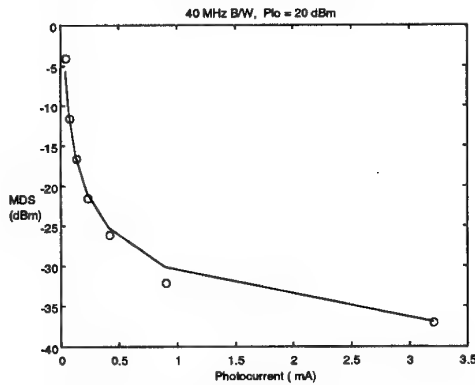


Figure (3) - MDS as a function of photocurrent

Another useful measure of the system performance in EW is the tangential signal sensitivity (TSS). In this case the finite bandwidth of the video detection process as well as the IF bandwidth must be taken into account. The TSS corresponds to a receiver output signal to noise ratio of approximately 8 dB [12].

In order to determine the system dynamic range, both the compressive and spur-free dynamic ranges need to be calculated. These are determined by:

$$\text{CDR}(\text{dB}) = P_{1\text{dB}}(\text{dBm}) - \text{MDS}(\text{dB}) \quad (13)$$

$$\text{SFDR}(\text{dBm.Hz}^{2/3}) = \frac{2}{3}(\text{TOI}(\text{dBm}) - \text{EIN}(\text{dBm/Hz})) \quad (14)$$

TOI is the input third order intercept point and P1dB is the input 1dB compression point to the system. For the case of the link without any amplification, the parameters TOI and P1dB are referred to the input of the link and are given by:

$$\text{TOI} = \frac{4}{R_L} \left(\frac{V_{\pi\text{RF}}}{\pi} \right)^2 (R_o = R_L = 50\Omega) \quad (15)$$

$$P_{1\text{dB}} = \frac{1}{2R_L} \left(\frac{0.951V_{\pi\text{RF}}}{\pi} \right)^2 \quad (16)$$

In the case of high gain RF preamplification, the cascaded system values for P1dB and TOI can be determined from [13]

$$\frac{1}{\text{TOI}_{\text{system}}} = \frac{1}{\text{TOI}_{\text{RFLNA}}} + \frac{G_1}{\text{TOI}} + \frac{G_1 \text{LLCL}}{\text{TOI}_{\text{IF}}} \quad (17)$$

$$\sqrt{\frac{1}{P_{1\text{dBsystem}}}} = \sqrt{\frac{1}{P_{1\text{dB RFLNA}}}} + \sqrt{\frac{G_1}{P_{1\text{dB}}}} + \sqrt{\frac{G_1 \text{LLCL}}{P_{1\text{dBIF}}}} \quad (18)$$

where $\text{TOI}_{\text{RFLNA}}$ and TOI_{IF} are the input third-order intercept points of the RF low noise amplifier (LNA) and the IF amplification stages respectively. $P_{1\text{dB RFLNA}}$ and $P_{1\text{dB IF}}$ are the input 1dB compression points of the RF LNA and the IF stages. The conversion loss as a function of LO power was measured for each channel. The results for the 'blue' channel are depicted in Figure 4, along with a fit to equation (2).

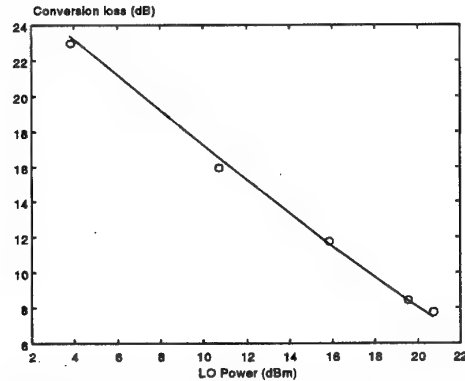


Figure 4 Conversion loss as a function of LO power

Once the photonic section had been characterised, a microwave LNA was included as a preamplifier in order to increase system sensitivity. Measurements were taken on two of the balanced channels for 10 GHz and 16 GHz LO frequencies for the channels nominally denoted 'blue' and 'yellow'. Figure 5 illustrates several required parameters for the system:

MDS and Noise figure (F_T), P1dB and CDR, the ability to parallel process spatially separated RF signals and the reduction in efficiency of the downconverter with increasing frequency. This is modelled as an increase in with frequency. This results in both increased conversion loss due to the LO modulator, and also increased link insertion loss due to the RF modulator's response. This loss can be compensated with the use of an amplifier with a frequency dependent positive gain slope. MDS here is defined as the 'knee' or intersection between linear fits to the noise floor and the signal gradient with input RF power. The nonlinearity for small RF powers is an artefact of the DLVA detection method [14]. There is

little difference between the yellow and blue channel conversion efficiencies of these two channels. The other channels had typically ~1 dB of variation due to variable optical loss in the optical multiplexer and optical components, as well as the EDFA gain spectrum. Table 1 lists measured (in bold) and calculated system parameters for the amplified and unamplified links. For comparison, the values for a link with no EDFA are included, illustrating the EDFA as a means of improving system performance. The optical power that would be required to achieve the same dynamic range is also calculated in the case of no optical amplification. This illustrates the beneficial employment of the EDFA to provide sufficient optical power.

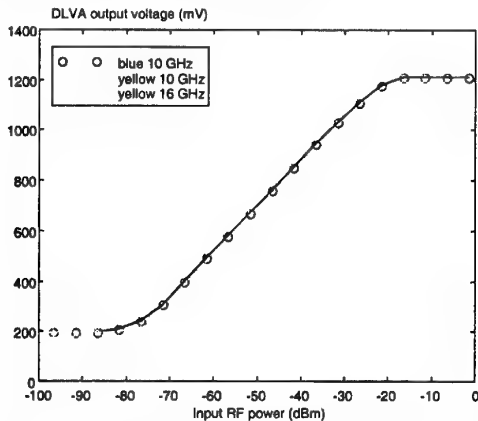


Figure 5 - Conversion efficiency for varying channels and frequency

	LINK NO EDFA	LINK WITH EDFA & RF LNA
MDS	-29 dBm	-80 dBm - 80 dBm
TSS	-21 dBm	-71 dBm - 71 dBm
CDR	55 dB	56 dB 57 dB
SFDR	94 dBHz ^{2/3}	94 dBHz ^{2/3}
NF	70 dB	18 dB 18 dB
B/W	76 dBHz	76 dBHz
Optical Power	195 mW	--

Table 1 - System parameters
(measured results in bold)

While the system has very competitive sensitivity to existing receiver systems and provides parallel processing functionality, there is room for improvement. Namely:

- Reducing the RF modulators' halfwave voltages for fixed microwave amplifier P1dB will improve sensitivity up to the point where the amplifier nonlinearity is no longer the dominant source of compression in the system. For this architecture the compression points of the link and LNA will be equal for a $V_{\pi} = 10V$, but the NF is reduced by 8 dB.
- Increasing the EDFA saturated output power by improving the design. Commercial EDFAs are

available with a saturated output power of +30 dBm.

- Increasing the LO power to ~ 27 dBm for a fixed LO halfwave voltage of 8V will result in lower conversion loss up to the theoretical limit. This will reduce the noise figure of the system, and
- Improved balancing between the arms of each balanced receiver at the IF frequency will result in shot-noise limited performance.

Conclusions

A four-channel WDM optically amplified superheterodyne receiver operating over 1-18 GHz per channel has been demonstrated. The system exhibits a compressive dynamic range of 57 dB in a 40 MHz detection bandwidth, and a spur-free dynamic range of 94 dBHz^{2/3}. A noise figure of 18 dB has been demonstrated with a TSS of -71 dBm referred to a 40 MHz effective detection bandwidth. Four channel parallel processing of spatially separate microwave RF signals has been performed with a single LO source.

References

- [1] A. C. Lindsay, GA Knight and ST Winnall, "Photonic Mixers for Wide Bandwidth RF receiver applications", *IEEE T-MTT-43 Special Issue on Microwave and Millimetre-Wave Optoelectronics*, pp 2311-2317, 1995
- [2] G. K. Gopalakrishnan, RP Moeller, MM Howerton, WK Burns, KJ Williams, and RD Esman, "A Low-Loss Downconverting Analog Fibre-Optic Link" *IEEE T-MTT-43 Special Issue on Microwave and Millimetre-Wave Optoelectronics*, pp 2318-2323, 1995
- [3] K. J. Williams and RD Esman, "Optically Amplified Downconverting Link with Shot-Noise Limited Performance", *IEEE Photon. Technol. Lett.*, Vol. 8, No. 1, January 1996, pp 148-150.
- [4] JM Fuster and J Marti, "Optimisation of the Dynamic Range in Optically aAmplified Harmonic Downconverting Fiber-Optic Links" *IEEE Phot. Tech. Lett.*, Vol 11, No. 7, July 1999 pp 877-879.
- [5] D Mongardien, C Moronvalle and F Deborgies, "Microwave Signal Distribution Using an Optical Amplifier", *IEEE MTT-S Digest*, 1993, pp731-734.
- [6] E Ackerman, S Wanuga, J MacDonald and J Prince, "Balanced Receiver External Modulation Fiber-Optic Link Architecture with Reduced Noise Figure", *IEEE-MTT-S Digest*, 1993, pp723-726.
- [7] E Desurvire, *Erbium-Doped Fiber Amplifiers - Principles and Applications*, New York, John Wiley & Sons, 1994, p 340.
- [8] A Cavaciuti and B Sordo, "Noise Measurements in EDFAs" *OFC Tech Digest*, 1994, paper WM9.
- [9] Lightwave Electronics 125 Series specification sheet
- [10] J B Tsui, *Microwave Receivers with Electronic Warfare Applications*, John Wiley & Sons, 1986, p 14.
- [11] J. Tsui, "Tangential Sensitivity of EW receivers", *Microwave J.*, Oct 1981, pp 99-102.
- [12] DD Vaccaro, *Electronic Warfare Receiving Systems*, Boston, Artech House, 1993.
- [13] Analog Devices AD8307 Spec. sheet Rev. A, 1999.

OPTICAL UPCONVERSION OF 100 Mb/s BPSK MICROWAVE SUBCARRIER SIGNALS USING AN UNBALANCED MACH-ZEHNDER INTERFEROMETER

G. Maury¹, B. Cabon¹, A. Hilt^{1,2}, J-F Le Bigot¹

¹LEMO, UMR CNRS 5530, ENSERG, BP 257, 38016 Grenoble Cedex 1, France

²BME-MHT, Technical University of Budapest, H-1111 Budapest, Goldmann György tér 3. V2 épület, Hungary
email : maury@enserg.fr, fax : +33 4 76 85 60 80

Abstract : A new technique for remote upconversion of a 100 Mb/s BPSK microwave subcarrier signal is proposed and demonstrated. It is based on the insertion of an unbalanced Mach-Zehnder interferometer in a microwave fiber-optic link.

1. Introduction

Due to the requirement of broadband services and radio interfaces, many communication systems, such as wireless local loops, mobile broadband systems or wireless local area networks, are proposing to use the mm-wave radio technology. In this context, the main transmission medium is the optical fiber offering a lot of advantages, like low attenuation and enormous bandwidth [1]. Therefore, various techniques for generating optical signals at mm-wave frequencies, that are often beyond the bandwidth of available optical sources or modulators, have been studied. Some of these techniques include laser and external modulator nonlinearities, cascaded linear modulations, nonlinear photodetection or optical heterodyning [2-4]. We have already presented a new technique for optical-MW mixing by inserting a passive all-optical device in a MW fiber-optic link. Using a DFB laser diode (LD) directly modulated by two MW signals and an UMZ to convert optical FM into IM, mixing and consequently upconversion is achieved after quadratic photodetection [5]. This approach allows the use of LD that do not have to operate at high frequencies and requires a simple UMZ which can be used to realize mixing simultaneously at different optical carriers. Therefore, it leads to considerable cost savings and could be advantageously

inserted in the fiber-radio systems that also incorporate WDM in order to simplify their network architecture ([6-7]).

In this paper, we describe the UMZ and explain the principle of optical-MW mixing. Then, simulations as well as experimental results concerning the upconversion of a 100 Mb/s binary phase shift keying (BPSK) MW subcarrier are presented to demonstrate the interest of this technique.

2. UMZ integrated on glass-substrate for optical-MW mixing

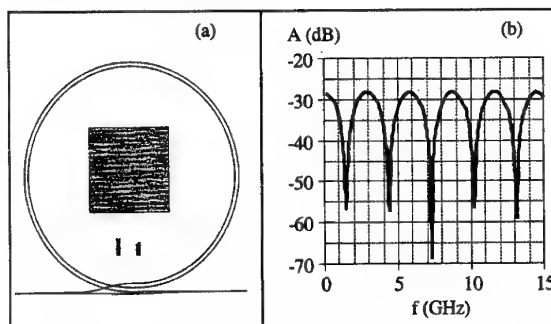


Figure 1 : Layout of the integrated UMZ interferometer circuit (a) and the corresponding frequency response (b).

One advantage of our technique is that it relies on a passive optical component that can be compact, low-cost and of easy fabrication. For example, an UMZ integrated in commercial glass-substrate by Ti^+/Na^+ ion exchange has been fabricated. This exchange process has been chosen because it provides high index increase and low curvature loss. Therefore, spiral waveguides with bend radius of about 5 mm could be used as delay lines. The path length difference has been designed to be 6.3 cm and a compact device ($1 \times 1.5 \text{ cm}^2$) has

finally been obtained (figure 1.a). In this way, the integrated UMZ has a free spectral range (FSR) of 3 GHz. This can be proved by measuring its frequency response with a MW network analyzer HP8510 and a lightwave component analyzer HP84320A used for E/O and O/E signal conversions (figure 1.b).

According to the theoretical analysis, mixing is issued from the coherent beating of the spectral components of the optical field filtered by the UMZ. Some components can be suppressed depending on their value related to the FSR. Therefore, it has been shown that best mixing performance (maximum power of the mixing products together with total rejection of the fundamentals) appears for particular input frequency values of the form $(2k+1)FSR/2$, $k \in \mathbb{N}$, and that the bandwidth in which the variation of the mixing products power is lower than 3 dB is equal to $FSR/2$ [5]. Here, optimal frequency bandwidths of input signals are therefore centered around 1.5 GHz, 4.5 GHz, 7.5 GHz...

As the principle of optical-MW mixing is based on the optical FM/IM conversion, it directly depends on the interference regime at the UMZ output : mixing is optimal when the conversion is the most non-linear, that means at maximum or minimum of transmission. So, the control of the interference regime is very important. A thermoelectric cooler and a thermistor are used to control the temperature of the glass-substrate and thus to fix the path length difference at a determined value. In addition, by controlling the temperature of the LD, the emitted wavelength can be fixed, and the interference regime can be stabilized consequently. The control of the interference regime is realized either by varying the substrate temperature or the emitted wavelength by tuning the bias or the temperature of the LD.

3. Upconversion of a 100 Mb/s BPSK MW subcarrier : simulations

Applications of our method can be found in fiber-optic transmission systems to upconvert MW subcarriers modulated by digital signals.

Testing was initially carried out through simulations with the COMSIS software. The system is shown on figure 2. The FSR of the UMZ is equal to 3 GHz. A 100-Mb/s NRZ $2^{23}-1$ pseudorandom bit sequence modulates the phase of the signal at a frequency $f_{RF} = 4.45$ GHz with a BPSK format. The power of the modulated signal is $P_{RF} = 2$ dBm. A CW signal at a frequency $f_{LO} = 1.55$ GHz and a power $P_{LO} = -2.5$ dBm is then added and the total signal is applied to the LD. The LD is a conventional DFB one, emitting 2 mW at $1.3 \mu\text{m}$ and with a linewidth enhancement factor $\alpha = 6.5$. The input MW frequencies have been chosen close to the optimal values but not exactly equal to 1.5 GHz and 4.5 GHz in order that their harmonics are different from their intermodulation products. The goal is to upconvert the MW subcarrier around the mixing frequency $f_{mix} = f_{RF} + f_{LO} = 6$ GHz. After detection by a PIN PD with a responsivity of 0.7 A/W and a dark current of 0.7 nA , a bandpass filter selects this frequency. Then, the 6 GHz-signal is directed to an ideal synchronous BPSK demodulator to recover the transmitted data.

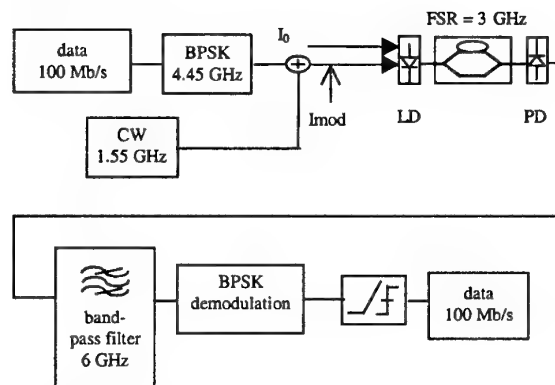


Figure 2 : Setup for upconverting optically transmitted subcarriers of digital signals.

In these initial simulations, the propagation in the optical fiber or the addition of noise by optical amplifiers eventually included in the link or at the reception were not considered since we were first interested by the effect of the UMZ inserted in the optical link.

As it can be seen on figure 3, the optical link including the UMZ realizes the upconversion

of the MW subcarrier. The spectrum of the LD modulation current only contains the digital signal around 4.45 GHz and the CW signal at 1.55 GHz. But, the spectrum of the PD current contains the digital signal upconverted around 6 GHz. By choosing correctly the interference regime, the power at this frequency is maximal. A strong rejection of the input signal at 4.45 GHz, greater than 15 dB, is obtained in the detected output signal. The eye diagram after demodulation shown in the inset is well-opened and the digital signal is recovered with no errors, confirming the fact that upconversion is realized with minimal distortions by the insertion of the UMZ.

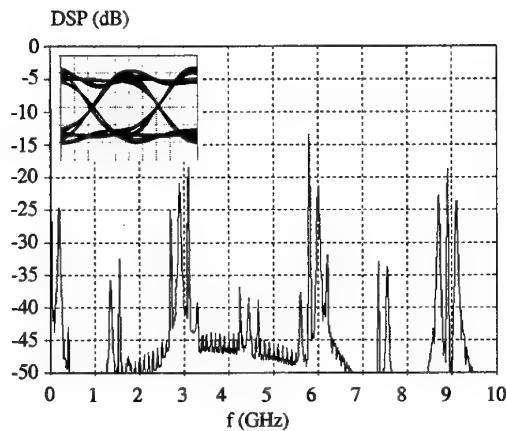


Figure 3 : Normalized power spectrum of the current detected at the output of the PD. The inset shows the recovered eye without noise added in the transmission link.

4 Experimental results

The optical link described above, with the same modulation conditions, has been implemented to demonstrate the upconversion of the 4.45 GHz subcarrier. A pattern generator of a bit-error-rate test-set generates the 100-Mb/s NRZ $2^{23}-1$ pseudorandom bit sequence. The PD is directly followed by a broadband amplifier with a gain of 30 dB. As shown in figure 4.a, the spectrum of the LD modulation current only contains the digital signal around 4.45 GHz and the CW one at 1.55 GHz. The insertion of the UMZ in the optical link induces the upconversion of the signal at 6 GHz (figure 4.b). As expected, the

input signal at 4.45 GHz is well rejected : in the output spectrum, the rejection is higher than 15 dB. By comparing the spectra of the PD current when the PD is placed at the output of the LD or at the output of the UMZ, we measured a conversion loss of -21 dB. This can be easily improved with a better coupling between the input fibers and the UMZ, for example by designing tapers on the input and output waveguides.

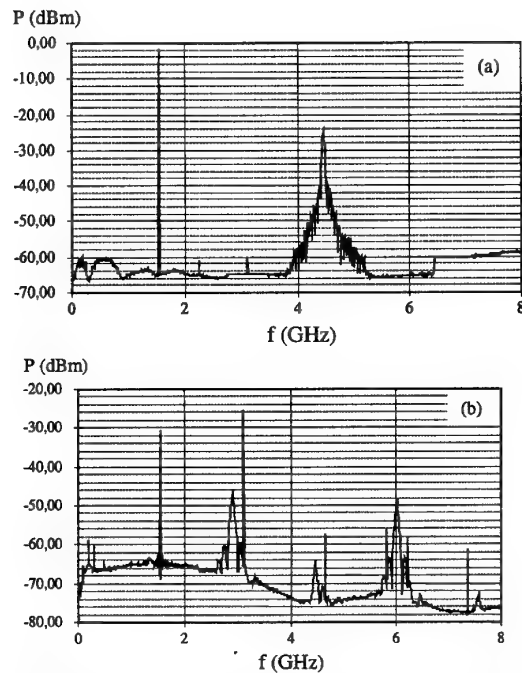


Figure 4 : Measured power spectra of LD modulation current (a) and at PD output (b).

Finally, all the performance expected are experimentally verified. Further experiments incorporating demodulation of the 100 Mb/s signal at 6 GHz will be realized to quantify the BER characteristics of this optical upconversion scheme.

5. Conclusion

The upconversion of a 100 Mb/s BPSK subcarrier transmitted on a fiber-optic link has been successfully demonstrated by using a compact UMZ integrated on glass-substrate. Temperature control of the device allows optimized performance and stable response and the experimental results are in good agreement with models. This method can be

applied any time the modulation is frequency limited by the bandwidth of laser diodes or external modulators thus limiting the frequency of the subcarrier transporting the digital signal. Thanks to the passive nature of the UMZ used here, it generates low conversion loss : in our case, a gain could even be achieved by optimizing the coupling between the optical device and the input and output fibers. It can also be easily implemented in WDM systems. Finally, this concept is efficient, cost effective and may be applied to modern hybrid radio-fiber wireless systems.

References

- [1] T. Kuri, K. Kitayama, A. Stöhr, Y. Ogawa, "Fiber-Optic Millimeter-Wave Downlink System Using 60 GHz-Band External Modulation", *Journal of Lightwave Technology*, vol. 17, no. 5, May 1999, pp 799-806.
- [2] T. Young, J. Conradi, W. R. Tinga, "BER Characteristics of $\pi/4$ DQPSK Microwave Subcarrier Signals on Optical Fiber Using Mach-Zehnder Modulator Nonlinear Upconversion", *IEEE Photonics Technology Letters*, vol. 8, no. 11, Nov. 1996, pp 1552-1554.
- [3] C. K. Sun, R. J. Orazi, S. A. Pappert, W. K. Burns, "A Photonic-Link Millimeter-Wave Mixer Using Cascaded Optical Modulators and Harmonic Carrier Generation", *IEEE Photonics Technology Letters*, vol. 8, no. 9, Sept. 1996, pp 1166-11168.
- [4] H. Ogawa, Y. Kamiya, "Fiber-Optic Microwave Transmission Using Harmonic Laser Mixing, Optoelectronic Mixing, and Optically Pumped Mixing", *IEEE Transactions on Microwave Theory and Techniques*, vol. 39, no. 12, Dec. 1991, pp 2045-2051.
- [5] G. Maury, A. Hilt, B. Cabon, V. Girod, L. Degoud, "Remote Upconversion in Microwave Fiber-Optic Links Employing an Unbalanced Mach-Zehnder Interferometer", *SPIE 44th Annual Meeting, International Symposium on Optical Science, Engineering, and Instrumentation*, Denver, USA, July 1999, paper 3795-71.
- [6] K. Kojucharow, M. Sauer, H. Kaluzni, D. Sommer, F. Poegel, W. Nowak, A. Finger, D. Ferling, "Simultaneous Electrooptical Upconversion, Remote Oscillator Generation, and Air Transmission of Multiple Optical WDM Channels for a 60-GHz High-Capacity Indoor System", *IEEE Transactions on Microwave Theory and Techniques*, vol. 47, no.12, Dec.1999, pp 2249-2256.
- [7] G. H. Smith, D. Novak, C. Lim, "A Millimeter-Wave Full-Duplex Fiber-Radio Star-Tree Architecture Incorporating WDM and SCM", *IEEE Photonics Technology Letters*, vol. 10, no. 11, Nov 1998, pp 1650-1652.

Colliding Pulse Mode-Locked Lasers on Semi-Insulating Substrate at 1.5 μm

H.K. Lee, M.W. Street, S.D. McDougall, E.A. Avrutin, A.C. Bryce, J.H. Marsh

Department of Electronics and Electrical Engineering, University of Glasgow, Glasgow G12 8LT, Scotland, UK

H.Lee@elec.gla.ac.uk

Tel: +44-141-330 6024

Fax: +44-0141-330 4907

Abstract

Colliding pulse mode-locked lasers operating at 1.5 μm were fabricated on a semi-insulating substrate, which should allow direct modulation of the saturable absorber at a sub-harmonic frequency using an electrical signal more efficiently.

I. Introduction

The colliding pulse mode-locking technique is a very effective method for generating optical pulses in the picosecond range. With the saturable absorber section placed at the centre of the laser cavity, two pulses are generated simultaneously in the laser and collide in the saturable absorber, resulting in twice as much energy saturating the absorber than the gain medium and leading to sharper, more stable pulses [1-4]. However, in mode-locked lasers, spontaneous emission causes noise in the gain, refractive index and photon density, which, in turn, produces variations in the timing of each mode-locked pulse. It degrades the timing resolution that is essential for many applications. In order to linewidth-narrow these devices, injection locking to an electrical signal at a sub-harmonic frequency could be used. However, so far, 1.5 μm CPM lasers have been fabricated on doped substrates and so high speed direct modulation of these devices is problematic due to parasitic capacitance which increases the RC time constant.

Here, we applied the CPM technique to produce pulses at a repetition rate of 135 GHz. For the first time to the best of our knowledge, 1.5 μm CPM lasers were fabricated on a semi-insulating substrate in order to reduce the parasitic capacitance. The reduced capacitance will allow direct modulation of the saturable absorber at a sub-harmonic frequency using an electrical signal

more efficiently. With stabilised pulse trains, these devices could be also used as sources to linewidth narrow sub-THz or THz devices by injection locking.

II. Device Material, Design and Fabrication

The material used was grown by the metal organic vapour phase epitaxy technique on a semi-insulating InP substrate. It has a 1.2 μm thick InP upper cladding layer and an InGaAs contact layer. 0.2 μm of the upper cladding is an undoped spacer layer and the remaining 1 μm is doped with Zn to a concentration of $1 \times 10^{18} \text{ cm}^{-3}$. The lower cladding layer is a 1 μm thick InP doped with Si to a concentration of $2 \times 10^{18} \text{ cm}^{-3}$. The waveguide core contains five 55 Å InGaAs quantum wells with 120 Å InGaAsP ($\lambda_g = 1.26 \mu\text{m}$, where λ_g corresponds to the bandgap) barriers and is completed by 500 Å of InGaAsP ($\lambda_g = 1.18 \mu\text{m}$) and 800 Å of InGaAsP ($\lambda_g = 1.1 \mu\text{m}$) on either side of the well region.

Figure 1 and 2 show the schematics of the structure of the CPM laser. It is a ridge waveguide based structure with 2 mesas and a 3 μm wide waveguide. The first mesa is to make the contact with the n^{++} layer. The second mesa is to reduce the overlap of the contact metal with the n^{++} layer, thus minimising capacitance. The gain section is 610 μm long, the saturable absorber section is 20 μm long and the gap between the gain and the absorber sections on the waveguide is 10 μm , giving a total cavity length of 650 μm . To obtain good electrical isolation between the gain and the saturable absorber sections, the highly doped InGaAs cap layer was removed from the gap regions between the sections using a selective wet-etching technique. The measured dc electrical isolation was 2 k Ω .

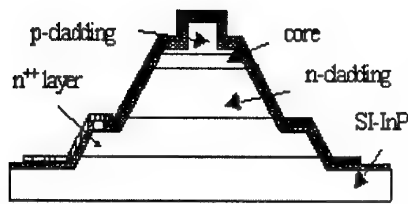


Figure 1 : Cross-section schematic of a CPM laser on Si-substrate.

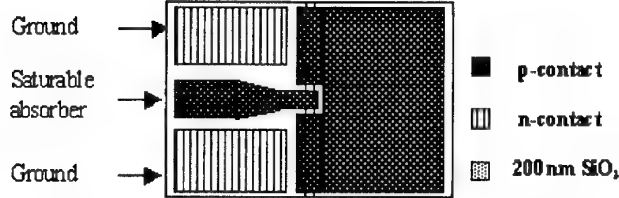


Figure 2 : Plan schematic of a CPM laser on Si-substrate.

III. Experimental Results

The device reported here has a threshold current of 60 mA. It can be seen in figure 3 that the cavity mode separation from the lasing spectrum when both the gain and the saturable absorber sections are forward biased with 70 mA is 0.55 nm. On application of a reverse bias level of -0.5 V to the saturable absorber section and a forward bias of 90 mA to the gain section, alternate modes were suppressed and the mode-spacing was doubled to 1.10 nm as shown in figure 4. Numerical simulations using a distributed time domain model suggest that this is sufficient evidence to indicate CPM at 135 GHz. CPM spectra were observed from this device at reverse bias level ranging from -0.5 V to -0.9 V. As can be observed in figure 4, the optical spectrum suffers a shift of 4 nm to the longer wavelengths when the absorber is reverse biased and become very asymmetric when the laser is mode-locked. These effects may be explained by self phase modulation (SPM) mainly in the gain section.

Longer CPM lasers of similar structure using similar material have also been fabricated. The longer cavity length is 2.2 mm and the saturable absorber is 60 μm long. These long devices have threshold current of 180 mA with the saturable absorber floating. On application of a reverse bias level of -0.8 V to the saturable absorber section and a forward bias of 230 mA to the gain section the mode spacing doubles from 0.16 nm, for the saturable absorber floating, to 0.32 nm, indicating CPM at a frequency of 39 GHz.

III. Further Work and Conclusion

We have achieved the fabrication and operation of colliding pulse mode-locked semiconductor lasers on a semi-insulating substrate. Measurements of linewidth narrowing using an electrical signal at sub-harmonic frequencies will be reported. Electrical measurements will be carried out to obtain the value of the reduced parasitic capacitance and will be presented.

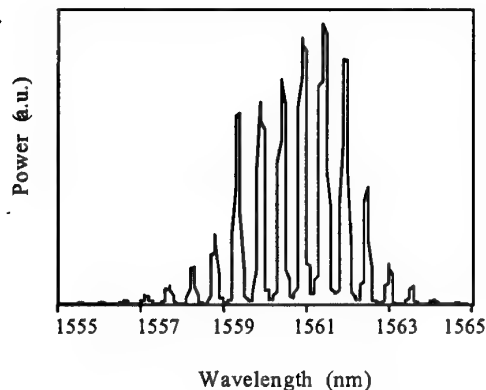


Figure 3 : Spectrum of device fully forward biased with 75 mA.

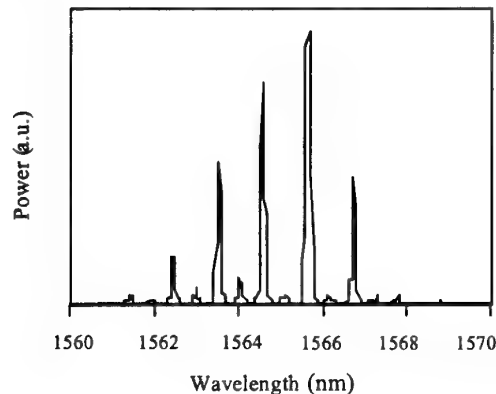


Figure 4 : CPM spectrum of laser operated at 90 mA with -0.5 V absorber bias.

IV. References

- [1] P. Vasil'ev, V.N. Morozov, Y.M. Popov and A.B. Sergeev, "Subpicosecond pulse generation by a tandem-type AlGaAs DH laser with colliding pulse mode-locking", *IEEE. J. Quantum. Electronics*, Vol.22, pp.149-151, 1986
- [2] M.C. Wu, Y.K. Chen, T.Tanbun-Ek, R.A. Logan, M.A. Chin and G. Raybon, "Transform-limited 1.4 ps optical pulses from a monolithic colliding pulse mode-locked quantum well laser", *Appl. Phys. Letters*, Vol.57, pp.759-761, 1990
- [3] J.R. Karin, R.J. Helkey, D.J. Derickson, R. Nagarajan, D.S. Allin, J.E. Bowers and R.L. Thorton, "Ultrafast Dynamics in Field-Enhanced Saturable absorbers", *Appl. Phys. Letters*, Vol.64, No.6, pp.676-678, 1994
- [4] J.F. Martins-Filho, E.A. Avrutin, C.N. Ironside and J.S. Roberts, "Monolithic multiple colliding pulse mode-locked quantum well lasers : Experiment and Theory", *IEEE Journal of selected topics in Quantum Electronics*, Vol.1, pp.539-551, 1995
- [5] S. Gee, R. Coffie, P.J. Delfyett, G. Alponse and J. Connelly, "Intracavity Gain and Absorption Dynamics of Hybrid Mode-locked Semiconductor Lasers Using Multi-Quantum Well Saturable Absorbers", *Appl. Phys. Letters*, Vol.71, pp.2569-2571, 1997

Dependence of Semiconductor Laser Intermodulation Distortions on Fiber Length and its Reduction by Optical Injection Locking

H.-K. Sung, Y.-K. Seo, and W.-Y. Choi

Dept. of Electrical & Computer Eng., Yonsei University

134 Shinchon-dong, Sudaemun-ku, Seoul, Korea.

Tel : +82-361-2874 ; Fax : +82-312-4584 ; E-mail : wchoi@yonsei.ac.kr

Abstract

We experimentally investigate the dependence of semiconductor laser intermodulation distortions (IMDs) on fiber transmission length. IMDs in fiber optic link are degraded over transmission through dispersive fiber. We show that IMDs can be reduced and made less dependent on fiber transmission length by using injection-locked DFB and Fabry-Perot (FP) semiconductor lasers.

1. Introduction

Subcarrier multiplexed (SCM) fiber optic systems with direct laser intensity modulation have many applications such as wireless local loop, cable television distributions and fiber-radio systems. The direct modulation of semiconductor laser is a simple, low-cost approach for transmitting RF-range subcarriers. However, the nonlinear distortions due to semiconductor laser nonlinearities and fiber dispersion can severely degrade overall system performance [1].

Hence, it is needed to suppress semiconductor laser nonlinearities and also to reduce IMD dependence on fiber length. As one method for suppressing nonlinearities of semiconductor lasers, optical injection locking of semiconductor lasers has been widely investigated and found very effective [2, 3]. The optical injection locking scheme requires two light sources - master laser (ML) and slave laser (SL). The light from ML is injected into SL and SL's output is locked to ML. Two major parameters for the injection locking are frequency detuning - frequency difference between ML and SL - and injection power ratio. If the injection

locking conditions are satisfied, improvements in laser dynamics such as relaxation oscillation frequency increase and frequency chirp reduction can be achieved [4, 5].

When optical signals produced by a directly-modulated semiconductor laser are sent over fiber, their third-order intermodulation distortions (IMD3) can be degraded because of the fiber dispersion. There has been not much investigation on this issue and we report results of our experimental investigation on the dependence IMD3 degradation on fiber length. In addition, we demonstrate that IMD3 dependence on fiber length can be much reduced by using injection-locked semiconductor lasers.

2. Experimental setup

Fig. 1 shows the experimental setup for measuring IMD3 dependence on fiber length for free-running and injection-locked semiconductor lasers. For injection-

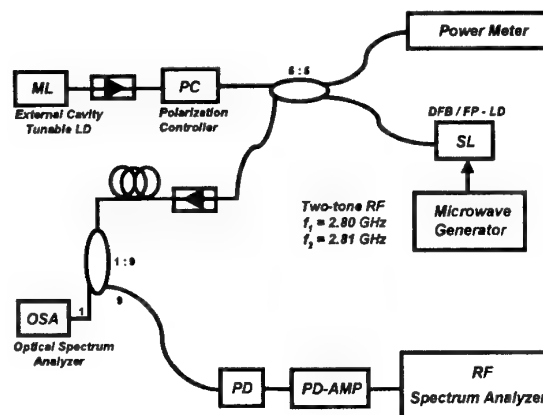


Fig. 1. Experimental Setup

locking, the external-cavity tunable light source is used for ML. For SL, a commercially available, fiber-coupled, isolator-free DFB (Samsung SDL-24) and FP (Samsung SFL-24, $\Delta\lambda = \sim 0.84\text{nm}$) lasers are used. Optical isolators with $>50\text{dB}$ isolation are used to prevent light coupling from SL to ML and protect the SL against backreflected light as shown in the figure. For generating subcarriers, SL is directly modulated by two-tone RF signals ($f_1 = 2.80\text{GHz}$, $f_2 = 2.81\text{GHz}$) and, consequently, third-order intermodulation products (IMP3) at $2f_1 - f_2 (= 2.79\text{GHz})$ and $2f_2 - f_1 (= 2.82\text{GHz})$ are generated. Standard single-mode fiber with different length from 5 to 40 km is used in the experiment.

3. Results

I. DFB-LD

For both free-running and injection-locked states, SL (DFB-LD) is biased at 15mA ($\approx 1.9I_{th}$) and directly modulated by two-tone RF signals. The power level of both RF signals before Bias-T is kept at -0.8dBm . To achieve the stable injection-locked state, the frequency offset between ML and SL was set at 4.1GHz , where stable locking range about 5GHz , and the injection ratio at about -6dB . Received RF powers at the fundamental ($f_2 = 2.81\text{GHz}$) and IMP3 ($2f_2 - f_1 = 2.82\text{GHz}$) frequencies are measured while the fiber length is varied in the increment of 5 km up to 40km . In this condition, the IMD3 dependence on fiber length for both free-running and injection-locked states is investigated.

Fig. 2 shows an example of the measured RF spectrum at the fundamental and IMP3 frequencies in the free-running and injection-locked state after 30km transmission. IMD3 for the free-running state is -9.83dBc (Fig. 2(a)) and IMD3 for the injection-locked state (Fig. 2(b)) is -19.08dBc where IMD3 is defined as the ratio of the power at IMP3 frequency to the power at the fundamental frequency. About 9.25dB reduction in IMD3 is achieved by optical injection locking.

In Fig. 3(a), the received RF powers at the fundamental and IMP3 frequencies are plotted for the free-running and injection-locked state at various fiber

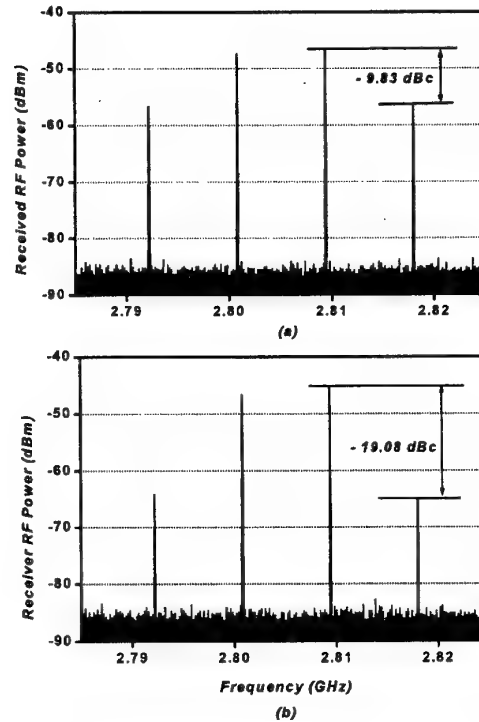


Fig. 2. Measured power spectra of the DFB-LD directly modulated by two-tone RF signals after 30km transmission for (a) free-running and (b) injection-locked state.

lengths. Overall, the received RF powers at both fundamental and IMP3 frequencies decrease with increasing fiber length and this is due to the fiber loss and dispersion. However, this reduction is smaller for the injection-locked state. IMD3 dependence on fiber length is shown in Fig. 3(b). In the free-running state, IMD3 is -20.1dBc back-to-back and -6.58dBc at 40km transmission, which shows IMD3 degradation of 13.52dB after 40km transmission. In the injection-locked state, IMD3 is -23.97dBc back-to-back and -18.81dBc at 40km transmission. The IMD3 degradation is only 5.16dB in the injection-locked state and its variation is maintained within about 5dB for the entire transmission length. Compared to the free-running state, the injection-locked state has 12.23dB reduction in IMD3 for 40km fiber transmission.

II. FP-LD

FP-LD is used as SL instead of DFB-LD in order

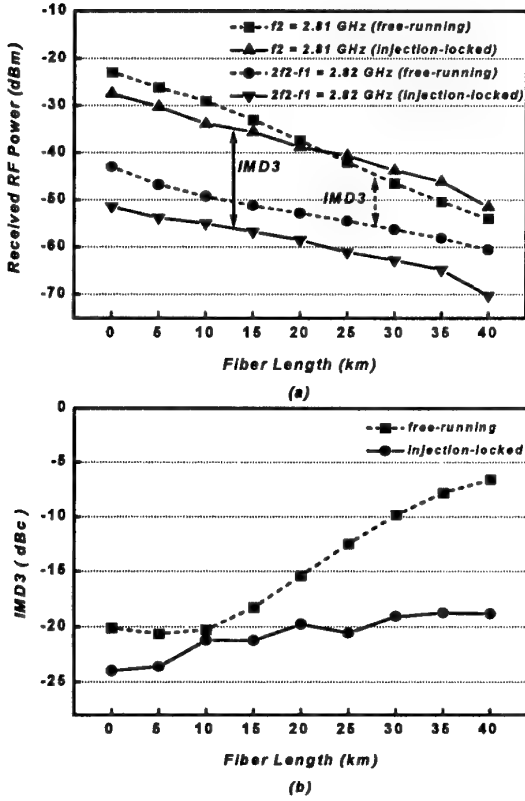


Fig. 3. (a) Received RF power at f_2 and $2f_2 - f_1$
(b) IMD3 when DFB-LD is used as SL.

to investigate the IMD3 dependence of FP-LD on fiber length. SL is again biased at 15mA ($\approx 3.3I_{th}$) and directly modulated by two-tone RF signals at $f_1 = 2.81$ GHz and $f_2 = 2.82$ GHz. The power level of both RF signals before Bias-T are kept at -0.8 dBm. In order to achieve injection locking, one injection target mode among FP-LD's multi-modes is chosen and ML is tuned within the locking bandwidth. In this experiment, we chose a side-mode located at the shorter wavelength side from the peak mode so that the larger injection locking bandwidth can be utilized [6]. Since the optical power of the injection-locked FP mode is much smaller compared to that of DFB-LD's fundamental mode, the injection locking bandwidth is much larger for FP-LD than DFB-LD. Hence, injection locking of FP-LD can be achieved more easily than DFB-LD. The injection ratio between ML and FP-LD target mode is about -0.45 dB and the stable locking range is about 30GHz.

Fig. 4 shows an example of the measured RF spectra at the fundamental and IMP3 frequencies for the free-running and injection-locked states after 20km transmission. Fig. 4(a) shows IMD3 of -5.7 dBc in the free-running state. The RF spectrum of the injection-locked state in Fig. 4(b) shows IMD3 of -24.21 dBc. 18.51 dB reduction in IMD3 is achieved with injection-locked FP-LD. In Fig. 5(a), the received RF powers at the fundamental and IMP3 frequencies are plotted for the free-running and injection-locked states. In the free-running state, the received RF powers at the fundamental and IMP3 frequencies show a significant fluctuation, while the received RF powers of free-running DFB-LD decrease monotonously. The fluctuation shown by the free-running state is related to the modal dispersion of FP-LD [7]. Fig. 5(b) shows that IMD3 variation for injection-locked FP-LD is bounded within about 5dB for the entire transmission

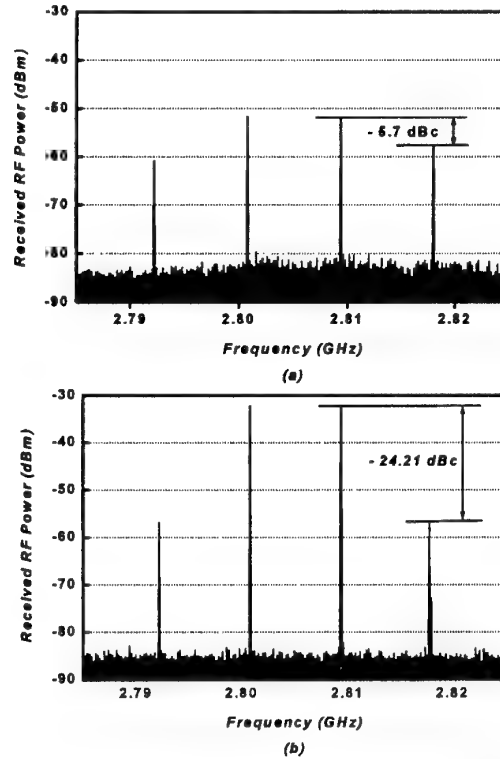


Fig 4. Measured power spectra of the FP-LD directly modulated by two-tone RF signals after 20km transmission for
(a) free-running and (b) injection-locked state.

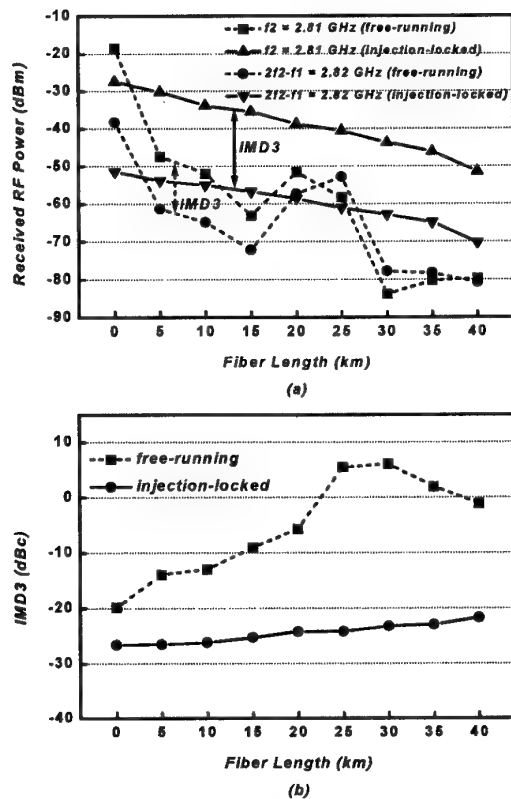


Fig. 5. (a) Received RF power at f_2 and $2f_2-f_1$ range, which is quite comparable with that of the injection-locked DFB-LD.

(b) IMD3 when FP-LD is used as SL.

4. Conclusions

We have experimentally shown the dependence of IMD3 of directly modulated DFB- and FP-LD on fiber length and that IMD3 can be reduced by optical injection locking of both DFB- and FP-LD. IMD3s for free-running semiconductor lasers are degraded due to the combined effect of the semiconductor laser nonlinearities and fiber dispersion. But, in the injection-locked case, semiconductor laser nonlinearities are suppressed, and the influence of fiber dispersion is much reduced. In our experiments, 12.23 dB reduction in IMD3 for DFB-LD and 20.55 dB reduction for FP-LD can be achieved with injection locking, and IMD3 variation was bounded within ~5dB for up to 40km transmission. In addition, the injection-locked FP-LD shows almost the same IMD characteristics as the injection-locked DFB-LD.

References

- [1] E. Peral and A. Y. Yariv, "Large-signal theory of the effect of dispersive propagation on the intensity modulation response of semiconductor lasers," *J. Lightwave Technol.*, vol.18, no. 18, pp. 84-89, Jan. 2000.
- [2] G. Y. Yabre and J. L. Bihan, "Reduction of nonlinear distortion in directly modulated semiconductor lasers by coherent light injection," *IEEE J. Quantum Electron.*, vol. 33, no 7, pp. 1132-1140, July 1997.
- [3] X. J. Meng, T. Chau, and M. C. Wu, "Improved intrinsic dynamic distortions in directly modulated semiconductor lasers by optical injection locking," *IEEE Trans. Microwave Theory Techniques*, vol.47, no7, pp. 1172-1176, July 1999.
- [4] R. Lang, "Injection locking properties of a semiconductor laser with external light injection," *IEEE J. Quantum Electron.*, vol. 18, no 6, pp. 976-983, June 1982.
- [5] G. Yabre, "Effect of relatively strong light injection on the chirp-to-power ratio and the 3dB bandwidth of directly modulated semiconductor lasers," *J. Lightwave Technol.*, vol.14, no. 10, pp. 2367-2373, Oct. 1996.
- [6] Y. Hong and K. A. Shore, "Locking characteristics of a side-mode injected semiconductor laser," *IEEE J. Quantum Electron.*, vol. 35, pp. 1713-1717, Nov. 1999.
- [7] S. Hunziker and W. Baechtold, "Fiber dispersion induced nonlinearity in fiber-optic links with multimode laser diodes," *J. Lightwave Technol.*, vol. 9, no. 3, pp. 371-373, Mar. 1997.

Nonlinear Distortion Suppression in dual parallel analog modulation of DFB-LD

Hyun-Do Jung and Sang-Kook Han

Department of Electrical and Computer Engineering, Yonsei University,
Shinchon-Dong, Seodaemoon-Ku, Seoul 120-749, Korea

Tel: 82-2-361-4016, Fax: 82-2-361-3565

E-mail: skhan@yonsei.ac.kr

Abstracts

A novel linearization method of DFB-LD using dual-parallel scheme is proposed. This scheme consists of two different wavelengths DFB-LD and an optical combiner. By controlling only the bias current of LDs, the intermodulation distortion can be suppressed. IMD3 suppression of more than 15dB was experimentally obtained.

Due to the increase of mobile communication subscriber and the demand on a good quality service, it is needed to unify the wire and wireless communication networks. A RF signal transmission through the fiber optical links have been received an increasing attention related to these issues. The fiber optical links are optimal for the transmission of high-fidelity signals for sub-octave analog applications, such as antenna remoting of cellular/PCS signals and beam forming for phased array antennas. It is necessary for these systems to have a high linearity in order to satisfy the signal-to-noise ratio at receiver. Nonlinear distortions introduced by the directly modulated laser diode can limit the performance of the system considerably. In a low RF frequency range, a

static distortion which is caused by the nonlinear light-versus-current characteristic of LD is dominant. However, a dynamic distortion due to nonlinear interaction of electrons and photons in the active layer of laser diode is dominant in high frequency range and depends on the modulation frequency.

This dynamic distortion limits a high frequency operation of DFB-LD near the resonance peak. Several methods are proposed to reduce the dynamic distortion levels. One scheme uses the injection-locking technique which uses a mode-pulling mechanism provided by the external injection[1]. Another scheme is the tailoring of the current-pulse shape[2]. A small current step in the leading edge of the current pulse is applied to reduce

the amplitude of relaxation oscillation, thus reducing the distortion significantly. However, these techniques are rather complicated to implement in the system.

In this paper, we propose a novel linearization technique to suppress the nonlinear distortion of DFB-LD. This scheme is a simple and can be implement easily. The validity of the proposed scheme is confirmed through the experiments.

Figure 1 shows the proposed scheme. This scheme consists of two DFB-LDs and an optical coupler. Originally, a dual-parallel scheme have been used in the electro-absorption modulator[3]. In the case of EA modulator, a static nonlinearity of transfer curve causes RF signal distortion. The phase of third order intermodulation distortion(IMD3) varies with a DC bias voltage. By controlling the bias position of each EA modulator, the phase difference of the IMD3 can be made out-of-phase. These out-of-phase IMD3 signals are combined to photodetector and the suppression is realized. Because the system parameter needed to be controlled is only the bias position, this scheme is very simple.

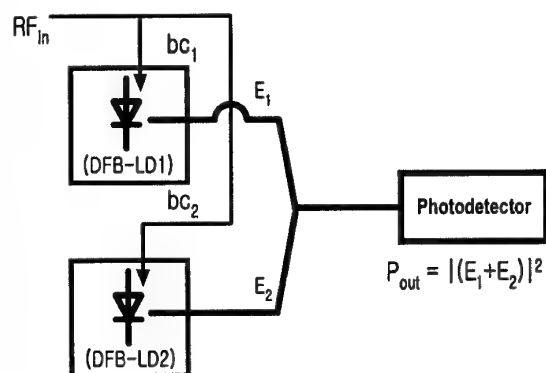


Fig. 1 Proposed dual-parallel DFB-LD modulation scheme

We have examined the capability of applying the dual-parallel scheme to direct modulation of DFB-LD. The experimental setup to suppress the intermodulation distortion is illustrated in Figure 2. We used two DFB-LDs with the wavelength difference of 1nm. The two RF signals with the input power of +0dBm were applied to each DFB-LD. The output from two DFB-LDs were combined to 3-dB optical coupler and connected to a high-speed photodetector. The RF amplifier was used to increase detected RF signals. These amplified signals were analyzed by a RF spectrum analyzer.

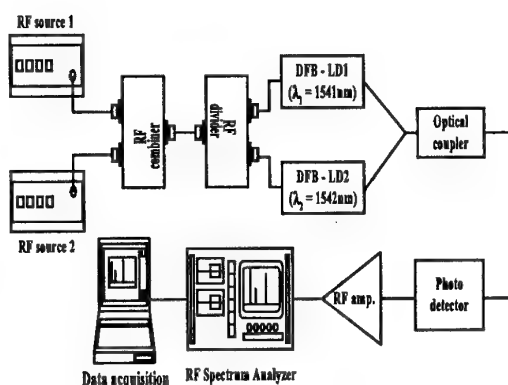
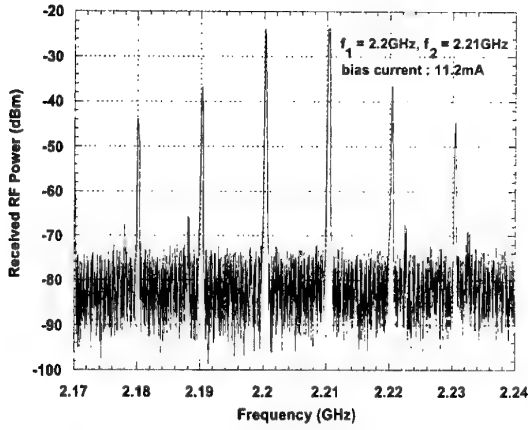


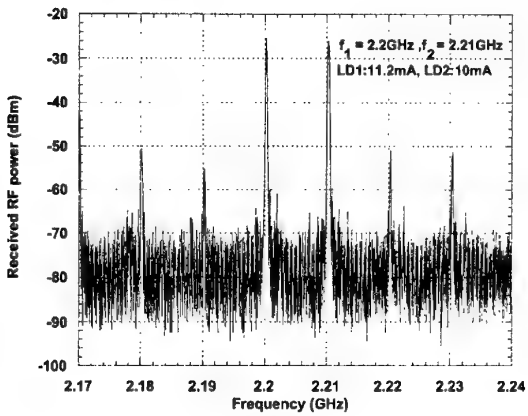
Fig. 2 Experimental setup

For low RF frequency region, the static distortion due to the sub-linearity of light-verses-current (L-I) characteristic becomes dominant. However, the proposed method hardly affected the distortion signal level in this frequency range. It is thought that L-I curve of DFB-LD is very linear that we expected in low frequency region. In high frequency range, the intermodulation distortion due to the nonlinear dynamics of electron and photon was large. The bias current of one DFB-LD was fixed at this IMD3 level and that of the other LD was

swept for wide bias current range. Then, the IMD3 level was suppressed at certain bias position. Figure 3 shows these results.



(a) Single LD



(b) Dual-Parallel scheme

Fig.3 Measured nonlinear frequencies

For two-tone RF signals of 2.2GHz and 2.21GHz, the difference between fundamental signal and IMD3 was 12dB for single LD. In the case of dual-parallel scheme, the difference was about 27dB. Consequently, the IMD3 suppression of 15dB was achieved.

These results can be explained as follows. When LD is amplitude modulated, the frequency modulation is accompanied. This chirping by frequency modulation acts as a dominant nonlinear component at high

frequency range. The AM and FM modulated optical wave is represented as

$$E = E_0 [1 + M \cos(2\pi f_m t)] \cdot \exp[j(2\pi f_0 t + \beta \sin(2\pi f_m t))] \\ \beta = \Delta F / f_m \quad (1)$$

where M is the amplitude modulation index, β , is the frequency modulation index, and ΔF is the maximum frequency deviation.

The exponential function in Eq. (1) represents the effect of FM. It can be expanded by Bessel function as follows[4]

$$E = J_0(\beta) E_0 \sin(2\pi f_0 t) \\ + J_1(\beta) E_0 \sin[2\pi(f_0 + f_m)t] \\ - J_1(\beta) E_0 \sin[2\pi(f_0 - f_m)t] + \dots \\ + J_k(\beta) E_0 \sin[2\pi(f_0 + k f_m)t] \\ + (-1)^k J_k(\beta) E_0 \sin[2\pi(f_0 - k f_m)t] \quad (2)$$

In eq. (2) the magnitude of coefficient of each term correspond to the distortion amplitude. The modulation index, β , varies with the bias current. The suppression of IMD3 in experiments is thought that the phase difference of IMD3 between two LD becomes out-of-phase as β varies with bias current.

In summary, we have proposed a novel dual-parallel scheme for IMD reduction of directly modulated DFB-LD. This method is very simple compared to the previously reported schemes and only a DC bias current controlling was used to reduce the nonlinearity of DFB-LD. A 15dB of IMD3 reduction was obtained experimentally.

Acknowledgement

This work is financially supported by Korean Ministry of Information and Communication

Reference

- [1] H. -K. Sung, Y. -K. Seo, and W. -Y. Choi, *Tech. Digest of the 1st Japan-Korea Joint Workshop on Microwave Photonics*, Th1-1, p.77, 2000.
- [2] R. Olshansky and D. Fye, *Electron Lett.*, Vol. 20, No. 22, p.928, 1984.
- [3] H. -D. Jung, G. -W. Lee, and S. -K. Han, *J. Lightwave Technol.*, (submitted)
- [4] Soichi Kobayashi et al., *IEEE J. Quantum El.*, Vol. QE-18, No. 4, 1982.

EFFICIENT PHOTORECEIVERS FOR MILLIMETRE-WAVE CELLULAR SYSTEM BASE STATIONS

L.Gomez-Rojas, X.Wang, N.J.Gomes and P.A.Davies

Photonics Group, Electronic Engineering Laboratory, University of Kent at Canterbury, UK
Tel +44 (0) 1227 827993, Fax +44(0) 1227 456084, email leg@ukc.ac.uk

Abstract: Hybrid integrated photoreceiver modules exhibiting high performance at millimetre-wave frequencies are demonstrated. Novel PIN photodiode plus amplifier resonant modules and injection-locked oscillators are presented and their potential performance in cellular system base stations discussed.

I. Introduction

Broadband networks combining optics and millimetre-wave electronics have been attracting research interest for use as backbones in future mobile/wireless communications systems [1-2]. Due to the interest in picocellular systems, and the large number of remote base stations (RBS) required for coverage in such systems, much research has been devoted to simplifying the base stations. For example, transporting a millimetre-wave reference over optical fibre and performing only the up- and down-conversion of IF/baseband data in the RBS, will avoid the need for millimetre-wave sources and modulators. High-speed photoreceivers, however, still form an essential part of the base station.

Microwave and millimetre-wave photoreceivers using PIN photodiodes and amplifiers have been widely investigated in the past [3-7], including the use of hybrid and fully monolithic technology [5-7]. In most cases, it has been assumed that reactive matching only is necessary as the photodiode behaves as a current source. At lower frequencies, higher input impedance amplifiers can be used to maximise signal levels. At high frequencies this is no longer the case as generally the current has to be delivered into a 50-ohm modular amplifier. Resonant matching including real part transformers can improve receiver performance. We have recently demonstrated this principle for a photodiode plus amplifier configuration in which a 2.9 dB improvement in output power, compared to an idealised configuration of the same photodiode and amplifier without real-part matching, was obtained at 27 GHz over a bandwidth >1GHz [8]. An alternative approach for photoreceivers is the use of optically injection locked oscillators. This type of photoreceiver is characterised by high output power but limited bandwidth. Wider locking bandwidths have been achieved at low frequencies [9]. At high

frequencies this becomes very challenging, as transistors do not provide as much gain as at lower frequencies and simulations used in the design become less accurate. Also, the locking bandwidth is dependent on the level of the locking signal, and photodetectors delivering large output signals, such as the phototransistor used in [9], do not have the necessary bandwidth to operate at millimetre-wave frequencies. In this paper we demonstrate high performance modules based on both technologies and analyse their potential for use in cellular system RBSs working in the millimetre-wave region.

The millimetre-wave modulated optical signal is intended as reference signal and will be used to provide local-oscillator (LO) drive to the up- and down-converter mixers in the system. For minimum conversion loss, an optimum LO drive level of -2 dBm is recommended. Considering that the reference signal will drive the up- and down-converters simultaneously, a 1 dBm output power signal is desired. However, the requirement for LO input power is flexible. A margin of around 4 dB is available to allow linear operation in the mixer at the expense of some minor degradation in conversion efficiency ~0.5 dB. Of course, amplification of the LO signal after reception using the designed modules would provide the required drive level, but at the cost of additional components and complexity. With regard to the LO operation frequency, broadband operation will allow flexibility in radio frequency allocation to the RBSs. This, however, is not entirely necessary as the radio frequency can be defined by varying the IF.

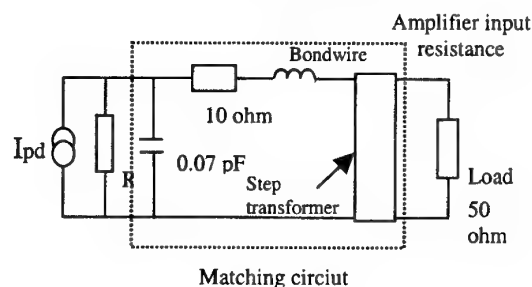


Figure 1. Schematic diagram of the photodiode - amplifier receiver modules

II. Photodiode plus amplifier modules

The basic design of these modules is based on a step transformer and a lumped reactive element [8]. A schematic diagram of our photodiode-amplifier modules is shown in Figure 1.

To achieve broader operating bandwidth, the design must take account of the effect on the resonant frequency of the matching of the real and reactive parts of the system together. The frequency response of the resonant circuit is directly dependent on the dimensions of the step transformer and/or the length and shape of the bondwire, the latter being more critical as it involves the reactive part of the circuit

When both the real and reactive parts of the matching network are tuned at the same frequency a broad and flat passband characteristic can be obtained. This is shown in Figure 2, where for comparison a passband characteristic when a mismatch between the real and reactive parts is present is also shown.

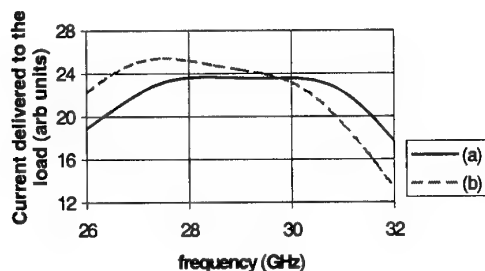


Figure 2. Simulated output current vs frequency for a) real and reactive matched and b) mismatch between real and reactive parts

III. Optically Injection Locked Oscillator

The design of the injection locked oscillator OILO is based on a negative impedance technique with a common source configuration chosen to achieve an output power sufficient for our system's requirements [10]. A schematic diagram of the oscillator is shown in Figure 3.

For the resonator, an open circuit transmission line was chosen. The end of the microstrip line resonator was chosen as the injection point since the value of the output power is smallest at this point. This maximises the locking bandwidth, which is inversely proportional to the square root of the oscillator's free running output power at the injection point [11]. Also, direct connection of the photodiode to the resonator would stop the oscillation, as the resonator is terminated by the photodiode. A mismatched circuit was then

designed to maintain the open-end property of the resonator while allowing most of the 30 GHz signal to go through.

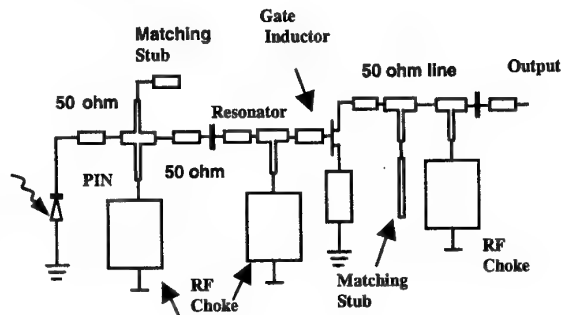


Figure 3. Circuit schematic of the millimetre-wave optically injection locked oscillator

IV. Measurement Results

The performance of the photodiode-amplifier modules and optically injection-locked oscillators was measured using a master/slave laser sideband injection locking system [12]. Two photodiode-amplifier modules were fabricated. Both were designed for 30 GHz operation. The step transformers should operate at this frequency with a high level of accuracy. Much more difficult to control is the resonance of the reactive matching as this depends on bondwire length. Module (a) was found to have a peak operating frequency of 27 GHz and a 1 GHz 3-dB bandwidth see Figure 4. Module (b) has a shorter bondwire length, about 0.55 mm rather than 0.7 mm, and it was found to operate at 29 GHz, much closer to the design frequency. As expected from the discussion in Section II, this also leads to a much broader and flatter passband characteristic.

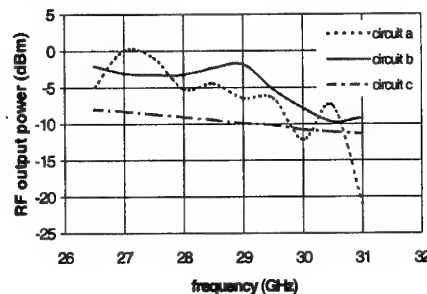


Figure 4. Output power response of fabricated photodiode-amplifier modules a) Module with a 0.7 mm long bondwire, b) Module with a 0.55 mm long bondwire and c) Ideal response for a commercial PD directly connected to a 50 ohm modular amplifier

As can be seen in Fig.4, module (b) has a 3-dB bandwidth of >3 GHz, with a cut-off frequency of 29.5GHz. Also, shown in Fig.4 for comparison is the ideal response that could be obtained with a New Focus photodiode module (with similar responsivity and bandwidth) directly connected to a 50-ohm modular amplifier similar to that used in our photoreceiver modules. In terms of output power, our matched photodiode-amplifier modules show an improvement of 2.9 and 2.0 dB respectively for modules (a) and (b) on top of the 6 dB improvement that would be expected by removing the 50-ohm termination resistor in the New Focus module.

For the OILO, several circuits were fabricated; their free running frequencies were in the range from 28 to 32 GHz depending on circuit fabrication variation and the devices used. The maximum output power of the free running oscillator was around 5 dBm (controlled by the bias condition). The locking bandwidth was measured by varying the millimetre-wave modulation frequency of the injected signal. The maximum locking bandwidth of 2.6 MHz was achieved with lower oscillation power of -12 dBm. Considering the application of this approach to photoreceivers for the antenna unit, a trade-off between power and locking bandwidth is unavoidable. However according to calculations, a theoretical locking bandwidth between 70 and 350 MHz should be achievable.

When comparing both technologies as alternative photoreceivers modules for remote base stations the advantages and disadvantages of either approach are clear. The photodiode plus amplifier modules have sufficient bandwidth for many millimetre-wave communication applications. However, the maximum output power (with optimum optical coupling and near 100% modulation) from our modules is only -2 dBm, 3 dB below the optimum power necessary to drive the mixers on our base station. In addition, the RF output power changes with optical signal power, giving less tolerance to fibre distribution system variations as compared to the OILO, as clearly seen in Figure 5. With regard to the injection locked oscillator presented here, the main advantage lies in terms of output power (mainly dependent on the bias condition), as seen in Fig.5. However, OILOs operate only over a very restricted locking bandwidth – the potential bandwidth of our oscillators is only a few hundred megahertz - with their being a trade-off between locking bandwidth and output power.

The plots shown in Figure 5 have been obtained as follows: Curve (a) shows the insensitivity of the OILO output power to variations in locking signal level – the latter has been plotted in terms of the incident optical power level

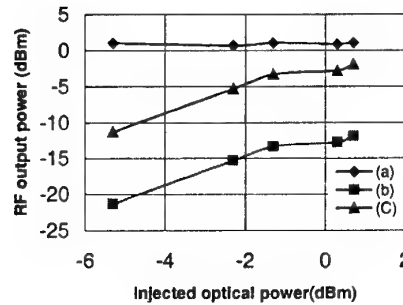


Figure 5 Comparison of RF output power dependence on incident average optical power for a) the optically injection locked oscillator, b) PD + amplifier module at 0V and c) PD + amplifier module at -1V and maximum modulations index

These results were obtained with a millimetre-wave modulation depth of 83.7% and an optical coupling arrangement giving 280 μ A photocurrent. The output power of the matched photodiode-amplifier module for the same optical signal conditions and with the photodiode unbiased is shown as curve (c). Curve (b) shows the output power of the photodiode-amplifier module when the millimetre-wave modulation depth is increased to 87%, the optical coupling is optimised and a -1 V bias is applied to the photodiode. As yet, we have not reproduced similar conditions for measurement of the OILO, but we would again expect little change in output power.

Conclusions

In summary we have demonstrated high performance broadband and narrowband hybrid photoreceivers in the millimetre-wave region. Highly efficient broadband photodiode plus amplifier modules and high output power injection locked oscillators in the millimetre-wave region have been accurately designed and tested. Their use in remote antenna units for pico-cellular mobile communications has also been discussed. A system demonstrator using the photodiode plus amplifier approach is currently under construction.

Acknowledgments

This work was funded by the Optoelectronic Systems Programme of the UK Engineering and Physical Sciences Research Council. We acknowledge useful discussions with our collaborators in this project at UCL, BT and Nortel Networks. The photodiodes were supplied by David Wake, BT. Luis Gomez-Rojas is partly supported by the EU's ERDF.

References

- [1] D. Wake, L.D. Westbrook, N.G. Walker, and L.C. Smith, 'Microwave and millimetre-wave radio fibre', *BT Technol. J.*, vol.11, pp.76-88, April 1993
- [2] N. Imai, H. Kawamura, K. Inagaki, Y. Karasawa, "Wide-band Millimeter-wave/optical-network applications in Japan," *IEEE Trans. Microwave Theory Tech.*, vol. 45, pp. 2197-2207, Dec. 1997
- [3] M. Marin, D.F. Hewitt, P.K. Lee, and R.S. Tuckee, 'Low noise tuned optical receivers using commercial 50ohm modular microwave amplifiers', *Electron Lett.* Vol. 27, No 15, July 1991, pp.1378-1379.
- [4] T. Darcie, L.B. Kasper, J.R. Talman, and C. Jr Burrus, 'Resonant p-i-n-FET receivers for lightwave subcarrier systems', *J. Lightwave Technol.*, Vol.6, No. 4, April 1988, pp 582 - 589
- [5] J.Y. Liang, and C.S. Aitchison, 'The noise performance of 20 GHz optical receivers using a distributed amplifier and P-I-N photodiode combination with matched and unmatched input terminations wire bonding and flip chip', 1996 *IEEE MTT-S Intl. Microwave Symposium*, San Francisco Ca, vol. 2, June 1996 pp. 903-906.
- [6] A. Iqbal, and I.Z. Darwazeh, 'Transimpedance gain modelling of optical receivers employing a PIN photodiode and HBT distributed amplifier combination' *IEE Colloquium on Opto-electronic interfacing at microwave frequencies*. 1999, London, p 3/1-3/9.
- [7] Y. Baeyens, A. Leven, W. Bronner, V. Hurm, R. Reuter, K. Kohler, J. Rosenzweig, and M. Schlechtweg, 'Millimetre-wave long-wavelength integrated optical receivers grown on GaAs', *IEEE Photonics Tech. Lett.*, July 1999, Vol. 11, No 7, pp 868-870.
- [8] L. Gomez-Rojas, N.J. Gomes, X. Wang, P.A. Davies and D. Wake, 'High performance optical receiver using a PIN photodiode and amplifier for operation in the millimetre-wave region' submitted to the 30th European Microwave Conference EUMW2000, Paris, 2-6 October 2000
- [9] D. Sommer and N. J. Gomes, "Wide-locking bandwidth optically injection-locked oscillators: S-parameter design and modulation effects," *IEEE Trans. Microwave Theory Tech.*, Vol. 43, pp. 1424-1434, July 1995
- [10] X. Wang, N.J. Gomes, L. Gomez-Rojas, P.A. Davies, and D. Wake '30GHz Microstrip HEMT oscillator using indirect optical injection locking', Accepted for presentation at the *IEEE Microwave Theory and Techniques, Intl. Microwave Symposium 2000*, Boston, MA, 11-16 June 2000
- [11] R. Adler, "A study of locking phenomena in oscillators," *Proceedings of the I.R.E. Waves and Electronics*, pp. 351-357, Aug. 1946
- [12] D. S. George, N. J. Gomes, P. A. Davies and D. Wake, 'Further observation on the Optical generation of Millimeter-wave signals by Master/Slave laser sideband injection locking,' *International Topical Meeting on Microwave Photonics.*, Digest, Post-deadline papers, pp5-7, Duisburg/Essen, Germany, Sep. 1997.

An X-Band Balanced Optical Hybrid Mixer for μ -Wave Optical interconnect in Active Phased Array Radar and Communication Systems.

S. K. Banerjee, U. Goebel, P. Nüchter
DaimlerChrysler Aerospace, Ulm, Germany

Abstract

In the following contribution an X Band Hybrid Electro Optical Mixer for a Photonic Microwave Receiver is described. The application of balanced hybrid mixer in the in the Phased Array Radar, Communication system and ESM receiver will reduce overall loss and hence the cumulative noise figure of the system and thus enhance the spurious free dynamic range of the receiver.

Introduction

The requirements in wide bandwidth, immunity to EMI and conformity will soon reach the limits of conventional microwave distribution techniques. The microwave photonic distribution technologies will provide the need of the next generation of shared, conformal aperture, active phased array antennas for communication, ECM, ESM and Radar systems. The adaptation of photonic technique in the microwave environment will only be possible if the photonic technologies overcome the following hurdles: The industrialisation of microwave/optical component, reduction of high production cost, an easy optical snap in interconnection technique and increased Spurious Free Dynamic Range (SFDR) of the photonic microwave receiver.

At present the stringent requirement of SFDR can only be achieved by using sophisticated optical components (i.e. Very low Relative Intensity Noise Laser with very high Third Order Intercept point and low loss optical true time delay unit). The use of optical hybrid mixer promises to reduce significantly some of problems associated with conventional link.

Photonic Distribution Network (In the Receiver Configuration)

The schematic below shows a conventional receive path, which may consist of a single T/R module or a sub-array followed by a low noise amplifier. The received RF signal is then converted to Optical signal directly (Laser intensity modulation) or externally (Mach Zehnder Modulator). Since the array requires thousand or more such converters, cost becomes the major issue and enforces the use of direct Laser modulation, although the Mach Zehnder Modulator is superior in respect to Dynamic Range, Modulation Bandwidth, Link gain and Noise Figure. The modulated optical signal is then feed to an optical network

(i.e. True Time Delay Unit) and then reconverted in to RF signal by a PIN photo diode, followed by a low noise RF amplifier. The RF signal is then down converted to an IF signal by a microwave mixer for further signal processing.

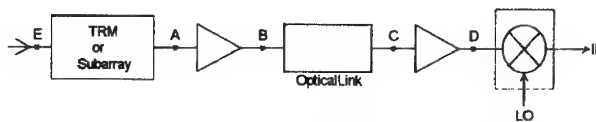


Figure 1: Schematic View of a Conventional Receive Path

Typical System Parameter of a Conventional Receive Path

Set Parameter: Laser RIN -140 dB/Hz, Coupled modulated optical power 3mW, TTD loss 5 dB Optical,

100 Hz Bandwidth, Mixer Conversion Loss 7 dB and 50 Ω broad band optical links with -30 dB loss.

Designed System Parameter that can be obtained: Cumulative Gain of 25dB, Cumulative Noise Figure of 16 dB and the Resulting Noise Floor of -113 dBm in 100 Hz bandwidth.

The above Parameter can only be improved if one of the following set parameter is changed:

Reduce Laser RIN -140 dB/Hz to -160 dB/Hz, which will improve Cumulative Noise Figure by 7dB, the Resulting Noise Floor by -122 dBm and Cumulative Gain remain at 25dB.

Or reduce Optical Link Loss to -20dB, which will improve Cumulative Noise Figure by 7dB, the Resulting Noise Floor by -122 dBm and increase Cumulative Gain to 35dB.

This paper describes the method for reducing Optical link loss as Laser with low RIN value and a high TOI Point is not a practicable or economical solution for the receiver application.

The link loss can be reduced by reducing R_{in} and increasing R_{out} of the optical link. For broad band applications

this can be achieved by using low output impedance HEMT impedance converting amplifier as Laser driving circuit and high input impedance coplanar amplifier or transimpedance stage as detection circuit. Such amplifier for detector circuits in X band are in development stage and will be available in few years for commercial uses.

Proposed Balanced Mixer configuration

In Figure 2. Proposed mixer configuration is shown. The mixer consist of a low output impedance (ca 12,5 ohm) μ /mm wave amplifiers which feeds the LO signal to the junction of cathode of PD1 and anode of PD2, the two PIN or MSM photo diodes as shown below. Advantage of this configuration is that only a few components are required. The physical size of photo diodes can be relative large (easy coupling) as frequency response associated with the charging and discharging of the junction capacitance plus parasitic capacitance has only to be considered for the IF band. The optical signal, which is intensity modulated with received μ /mm wave signals is splitted via an optical power divider and feed to the photo diodes. The intermediate frequency is amplified by a transimpedance amplifier(receiver output impedance does not have to be 50 Ω , gain and bandwidth can be selected as required). The band stop filter symbolized by Z_{low} and Z_{high} ensure proper LO matching(Z_{high} may be used to compensate PD's Capacitance). The Isolation between LO and RF is ideal. Lastly this configuration increases the relative gain by 3dB as the Laser intensity can be doubled without increasing any side effect.

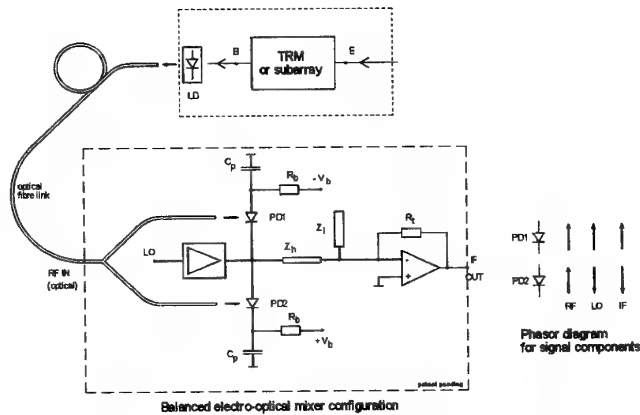


Figure 2: Schematic view of a Balanced Optical μ /mm-wave mixer

Experimental Setup and Results

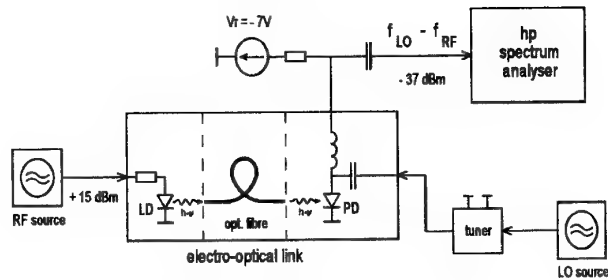


Figure 3: Measurement Setup

An experimental microwave down-converting electro optical link with InGaAs PIN photodiode (Epitaxx 25 B) was realised as shown in Figure 3. The mixing process was established by modulating the carrier drift velocity by LO signal.

To evaluate the characteristic of the PIN diode a sets of measurements were made. From the measured data a non linear equivalent circuit was developed. The circuit model will assist to develop and optimise the proposed balanced optical μ -wave mixer.

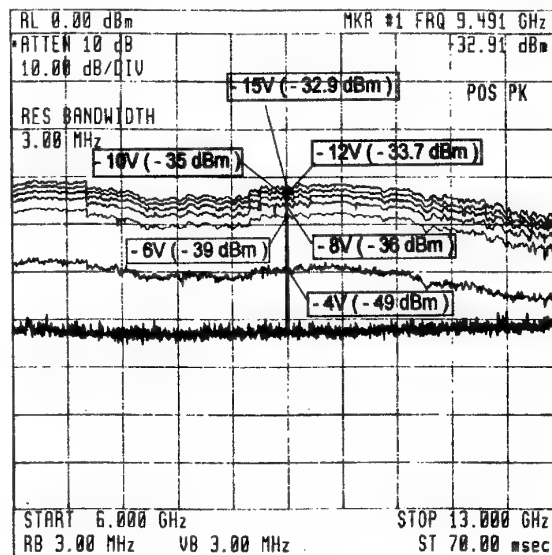


Figure 4: Measured Optical Link ResponseParameter is Reverse Bias of the Photodiode

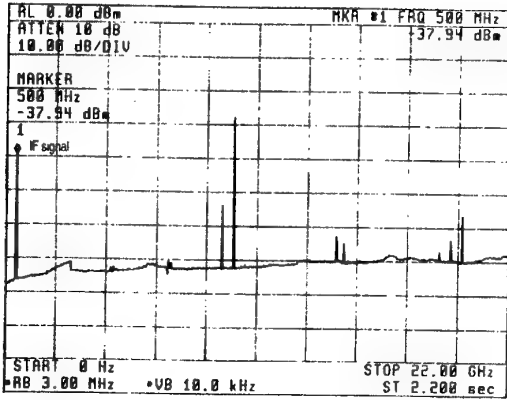


Figure 5: Down Converted Optical Link signal with External Mixer
(Conversion Loss = 5dB)

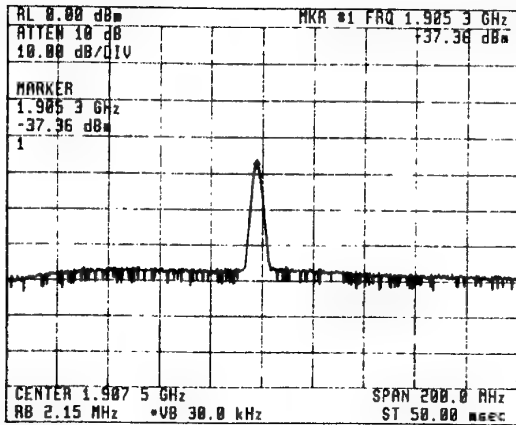


Figure 6: μ Wave / Optical Down Converted Signal- Relative Conversion Loss 4.4dB
FLO = 9.21GHz, +27dBm; FRF = 7.31GHz (-33dBm)

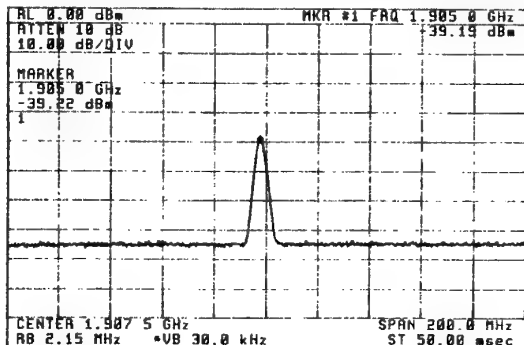


Figure 7: μ Wave / Optical Down Converted Signal Relative Conversion Loss 6.2dB
FLO = 9.21GHz, +25dBm; FRF = 7.31GHz (-33dBm)

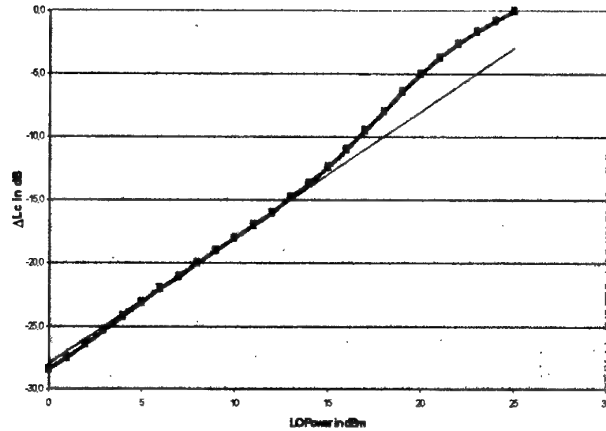


Figure 8: Relative Conversion Loss vs. LO Power
FRF = 9.21 GHz and FLO = 7.31 GHz

The figure 4 shows the direct RF detection response of the link in respect to the diode reverse bias voltage. For reference the optical link output signal was feed to an external mixer which exhibits a conversion loss of 5 dB and was recorded in the figure 5. The figure 6 shows the saturated down converted signal of the electro-optical mixer, the increase noise floor with respect to the figure 7 is due to an external power amplifier, which was used to increase LO signal level by 2dB. The figure 8 shows the relative conversion loss vs. LO power, the conversion loss value of figure 7 was taken as the reference level. The black line is the theoretical prediction from simple model without considering saturation velocity or clipping due to transition in to photovoltaic mode.

A Brief Model Description

Photo conductive Mixing

The following theory assumes that the PIN-Diode i-zone is completely illuminated and illumination is parallel to the junction [7], §13 Fig. 13c/.

The homogeneous carrier density along the slab due to the perpendicular illumination, is given by

$$(1) \quad \left. \begin{aligned} \frac{dn}{dt} &= -\frac{n}{\tau} + G \\ G &= \eta \cdot \frac{P_{opt}}{h\nu} \cdot \frac{1}{WLD} \end{aligned} \right\} \frac{dn}{dt} + \frac{n}{\tau} = \eta \cdot \frac{P_{opt}}{h\nu} \cdot \frac{1}{WLD},$$

and the associated photo current is

$$(2) \quad I_p = q\mu nE \cdot WD = \frac{q\mu WD}{L} \cdot n \cdot V.$$

Introducing the normalised carrier density

$$(3) \quad v = \frac{q\mu WD}{L} \cdot n,$$

the photo current and the normalised carrier density can be written as

$$(4) \quad I_p = v \cdot V$$

$$(5) \quad \tau \frac{dv}{dt} + v = \frac{q\eta}{h\nu} \cdot P_{opt} \cdot \frac{\mu\tau}{L^2} = K \cdot P_{opt},$$

where the parameter K incorporates physical, geometric and material parameters of the PIN-diode and the illuminating light.

For simplicity it is assumed that the carrier lifetime is much smaller than the time scale of optical power variation, i.e., a steady state approximation $\frac{dv}{dt} = 0$ is made.

This leads to the quasi-static solution

$$(6) \quad \begin{aligned} v(t) &= K \cdot P_{opt}(t), \\ I_p(t) &= K \cdot P_{opt}(t) \cdot V(t). \end{aligned}$$

With this approximation the intrinsic photo current I_p can be implemented easily as a simple multiplier in a non-linear circuit simulator like ADS [8].

The limit of validity can be estimated from (5), which can be rewritten as

$$(7) \quad (1 + s\tau) \cdot v(s) = K \cdot P_{opt}(s)$$

in the Laplace domain and leads immediately to the limit $\omega\tau \ll 1$ for the quasi-static formulation (6).

Saturation Velocity

For high electric fields the linear relation μE in (2) will be clipped by the saturation velocity of carriers. This can be considered by means of a "clipping" voltage in (4) and (6), respectively, such that

$$(8) \quad V' = V_c + (V - V_c) \cdot H(V - V_c).$$

As usual, the Heaviside step function should be implemented as some "soft" function like

$$(9) \quad H(x) \approx \frac{1}{2} [1 + \tanh(hx)],$$

where h models the gradient of the step function.

A first implementation of (8) and (9) however indicates, that the transition into the photovoltaic mode, i.e. $V \geq 0$ must be taken into account as well, for example, in order to model effects like saturation of conversion loss.

Conclusion

We have demonstrate conversion loss of 4.4 dB of an X-band optro-electric hybrid mixer. The measured value is better than a conventional mixer. The relative conversion loss was improved by another 6 dB with transimpedance output stage (at 100 MHz IF), which corresponds to total improvement of nearly 7 dB of link loss relative to direct detecting conventional link. The theoretical model of the photo conductive mixing process was developed and the experimental values are in agreement with theoretical simulation. It can be concluded that by reducing the link loss in a photonic-microwave receiver by using electro-optical hybrid mixer will fulfil the specification in respect to its noise figure, resulting noise floor and spurious free dynamic range. A balanced electro-optical mixer, which will be realised soon with currently available commercial components

Glossary

E	electric field inside i-slab
G	generation rate of electron-hole pairs
H	Heaviside step function
L	length of uniformly illuminated i-slab
n	density of electrons
P_{opt}	instantaneous optical power incident on photoconductor
q	elementary charge
V	voltage across i-slab
V_c	clipping voltage
s	Laplace variable
WD	cross section of uniformly illuminated i-slab
η	quantum efficiency
$h\nu$	energy of incident light
ω	angular frequency of light intensity modulation
μ	electron mobility
v	normalised carrier density
τ	carrier lifetime

References

- [1] S. Banerjee, G. Zimmer, H.P. Feldle, P. Marten, and L.P. Schmidt, 'An X-band phased array microwave/ photonic beamforming network', IEEE MTT-S 1993, N-4
- [2] Photonik I: 'Optische Verbindungstechniken in aktiven phasengesteuerten Antennen', DASA final report, 1993
- [3] C. P. Liu, A.J.Seeds 'Noise Performance of a Two-Terminal InP/InGaAs Hetrojunction Phototransistor Optoelectronic Mixer', IEEE MWP 97 TH 4-6 University Duisburg Germany
- [4] M. Djebbari, G. Kompa 'Measurement and Physics Table-Based Nonlinear CAD MSM Photodiode Model', International IEEE Workshop 97 University Kassel Germany
- [5] G. Ja'ro', T.Berceli, A. Zo'lomy ' New Optomixer Surpassing Photodetection at Microwaves', IEEE MWP 97 TH 5-5 University Duisburg Germany
- [6] S. Banerjee, U.Gobel, P. Nüchter, M. Wagner and B. Abele, 'A Balanced Electro Optical Mixer for increasing Spurious Free Dynamic range of a μ -Wave Optical Link', IEE-Colloquium on Opto-electronic Interfacing at Microwave Frequencies ,April 99
- [7] S. M. Sze, *Physics of Semiconductor Devices*, 2nd ed., Wiley1981
- [8] ADS, Advanced Design System, Hewlett-Packard, 1999

Experimental Demonstration and Modelling of Optoelectronic Mixing and Digital Modulation in a Single InP Photo Heterojunction Bipolar Transistor

A. Bilenca, J. Lasri, G. Eisenstein, D. Ritter, M. Orenstein, V. Sidorov, S. Cohen, P. Goldgeier

Electrical Engineering Dept., TECHNION, Haifa 32000, Israel

Tel. +972 4 8294 694

FAX +972 4 8323 041

E-mail gad@ee.technion.ac.il

Abstract

We describe microwave signal generation and digital modulation by optoelectronic mixing in a single InGaAs / InP heterojunction bipolar phototransistor. Modeling and experimental verification are demonstrated for 10 and 45 GHz signals modulated at rates up to 2.5 Gb/s.

Introduction

Heterojunction bipolar photo-transistors (photo-HBT's) can serve simultaneously as optically controlled microwave signal generators and as modulators. The optoelectronic mixing process in photo-HBT's has been previously characterized [1-3] and used in various configurations for applications related to analog radio on fiber communication [4], phased arrays [5] and laser locking in WDM systems [3].

This paper describes an advanced microwave source based on mixing of two optical signals in a photo-HBT and simultaneously applying a digital modulating signal to the base. The proposed configuration may act as part of a transceiver system in which the base-band digital information is imprinted on a microwave carrier which is generated by an optical signal transmitted from a distant control station. The experimental configuration is shown in Fig. 1. A 1.55 μm DFB laser is externally modulated at a frequency $\Delta f / 2$ with the modulator biased at V_π in order to suppress the optical carrier [6]. The optical signal coupled to the HBT consists then of two side bands separated by Δf which

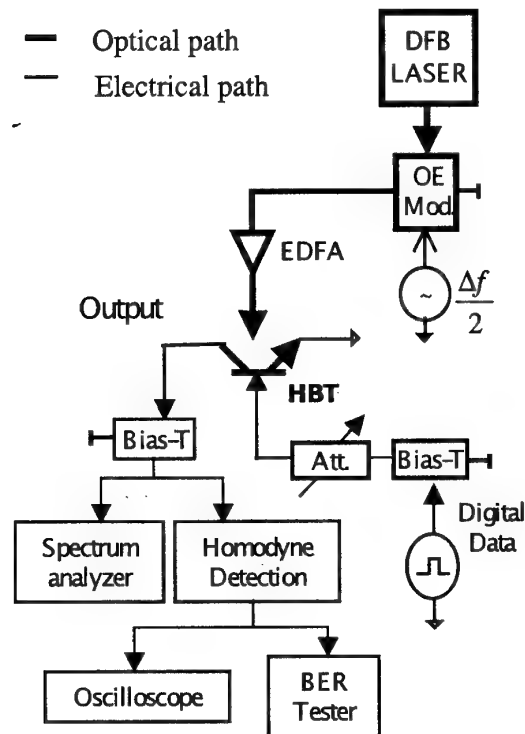


Fig. 1: Experimental setup

is the generated carrier frequency. Simultaneously, a pulse pattern generator drives the base so that the collector current comprises a digitally modulated microwave signal. The photo-HBT is biased so as to keep it in the active mode ensuring the most efficient photo mixing performance and distortionless modulation. The output signal is characterized by a spectrum analyzer and for time domain measurements, it is down converted to base-band using homodyne detection.

Model

The dual role of the photo-HBT as an optoelectronic mixer and digital modulator requires a device model which considers all inherent nonlinear mechanisms. It is based on the large signal π -model (shown in Fig. 2) to describe the emitter-current dependence of the dynamic emitter resistance. It is similar to the conventional charge control large-signal model in the linear operating regime. The main components are: 1) a nonlinear input capacitance $C_{\pi} = C_{be_depletion} + C_{be_diffusion} = C_{be} + (\tau_f / N_f / V_T) \cdot I_s \cdot \exp(V_{be}(t) / N_f V_T)$, where τ_f is the forward delay time, N_f the base-emitter diode ideality factor and V_T the thermal voltage (the base-collector and base emitter depletion capacitance, C_{be} and C_{bc} , are assumed to be constant), 2) a current gain β_0 , 3) an additional current source between the collector and the base representing the induced photo-current and shot noise produced during the detection process. The HBT model is described as a two port network characterized by two differential equations. The HBT model is then embedded into the experimental setup, which is also represented by differential equations stemming from basic Kirchoff laws. The equations are solved numerically using the MATLAB / SIMULINK software package. The parameters used in the simulations were extracted from DC and S-parameter measurements.

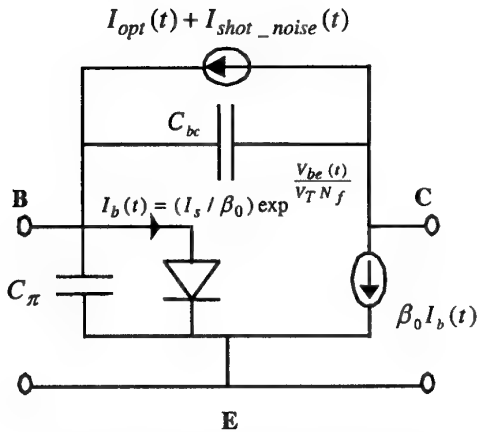


Fig. 2: HBT large signal Π -model

Results

The first experimental results we show is the spectrum of a 10 GHz carrier modulated by a pseudo random bit pattern at 300 Mb/s with a word length of $2^{23}-1$ at $V_{be}=0.73V$ and $V_{ce}=1.5V$. The average optical power was -2 dBm and the modulating signal (data stream) power was -28 dBm. In Fig. 3 we compare a measurement of the averaged power spectrum (shown in a bold line) to a calculated spectrum. The predicted shape $\text{sinc}^2(f/B)$, B being the bit rate, is clearly seen in both cases. We also observe that both measurements and simulations show different gain levels of the high and low frequency side lobes. This is due to different effects of the input network on the amplitudes and phases of the high and low frequency components of $V_{be}(t)$. We have observed experimentally and verified numerically that this asymmetric behavior increases with the modulation rate.

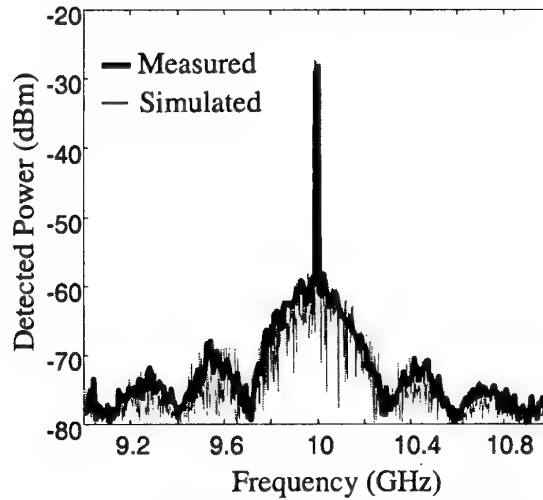


Fig. 3: Measured and calculated 300 Mb/s modulated spectrum at 10 GHz carrier

References

- [1] A. J. Cooper, "Fibre/radio for the provision of cordless/mobile telephony services in the access network", *Electron. Lett.*, vol. 26, no. 24, pp. 2054-2056, Nov. 1990.
- [2] G. H. Smith and D. Novak, "Broadband millimeter-wave fiber-radio network incorporating remote up/down conversion", *IEEE MTT-S International Symp. Dig.*, pp. 1509-1512, 1998.
- [3] H. Sawada and N. Imai, "An experimental study on a self oscillating optoelectronic up-converter that uses a heterojunction bipolar transistor", *IEEE Tran. On Microwave Theory and Tech.*, vol. 47, no. 8, pp. 1515-1521, August 1999.
- [4] Y. Betser, D. Ritter, C.P. Liu, A.J. Seeds, A. Madjar, "A single-stage three-terminal heterojunction bipolar transistor optoelectronic mixer", *IEEE Journal of Lightwave Technol.*, vol. 16, no. 4, pp. 605-609, 1998.
- [5] J. Lasri, Y. Betser, V. Sidorov, S. Cohen, D. Ritter, M. Orenstein, G. Eisenstein, "HBT optoelectronic mixer at microwave frequencies: modeling and experimental characterization", *IEEE Journal of Lightwave Technol.*, vol. 17, no. 8, pp. 1423-1428, 1999.
- [6] Y. Betser, J. Lasri, V. Sidorov, S. Cohen, D. Ritter, M. Orenstein, G. Eisenstein, A.J. Seeds, and A. Madjar, "An integrated heterojunction bipolar transistor cascode optoelectronic mixer", *IEEE Tran. On Microwave Theory and Tech.*, vol. 47, no. 7, pp. 1358-1364, July 1999.

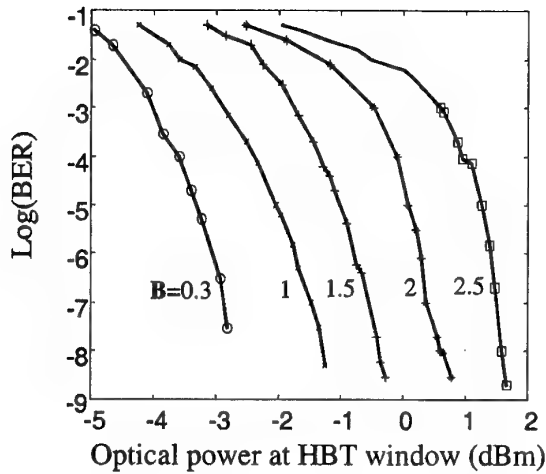


Fig. 6: BER measurement at different bit rates, B , (in GHz) at 10 GHz carrier

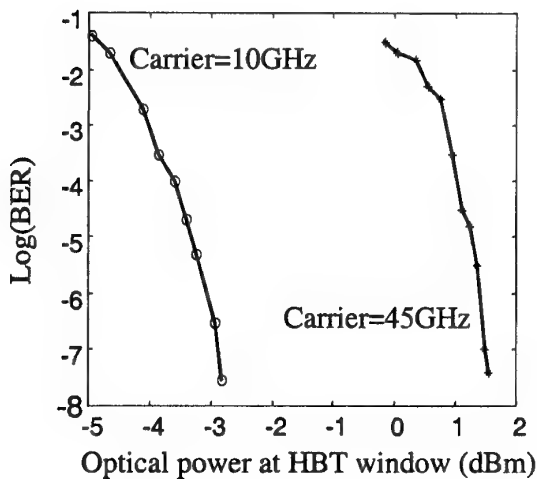


Fig. 7: BER measurement at different carrier frequency

optoelectronic mixer, *Journal of Lightwave Technol.*, 16, pp.605-609, 1998.

[3] J. Lasri, P. Goldgeier, V. Sidrov, D. Ritter, M. Orenstein, G. Eisenstein, Y. Betset, Y. Satubi, Frequency Locking at 50 GHz Spacings Using Optoelectronic Mixing in Photo-Heterojunction BipolTransistors, *IEEE Photonic technolog. Lett.*, 11, pp.1298-1300, 1999.

[4] C. Gonzales, J. Thuret, J.L. Bechimol and M. Riet, InP/InGaAs bipolar phototransistors as front-end photoreceivers for HFR distribution networks, *Technical Digest of Microeave Photonics 1999*, pp.35-38.

[5] D. C. Scott, D. V. Plant, and R. Fetterman, 60 GHz sources using optically driven heterojunction bipolar transistors, *Appl. Phys. Lett.* Vol. 61, no. 1, July 1992.

[6] J.J. O'Reilly, P.M. Lame, R. Heidemann, R. Hofstetter, Optical generation of very narrow linewidth millimeter wave signals, *Electron. Lett.*, 28, pp.2309-2311, 1992.

References

- [1] J. Lasri, Y. Betser, V. Sidrov, S. Cohen, D. Ritter, M. Orenstein, G. Eisenstein, HBT Optoelectronic Mixer at Microwave Frequencies: Modeling and Experimental Characterization, *Journal of Lightwave Technol.*, 17, pp.1423-1428, 1999.
- [2] Y. Betser and D. Ritter, C.P. Liu and A.J. Seeds, A. Madjar, A single stage three terminal heterojunction bipolar transistor

High Frequency and Broadband Signal Measurements by Ultrafast Opto-Microwave Intermixing and Sampling

Wei-lou Cao, Min Du, and Chi H. Lee

University of Maryland, Department of Electrical and Computer Engineering, College Park, MD 20742, USA
Tel: (301)405-3729, Fax: (301)314-9281, Email: wlcao@eng.umd.edu

Nicholas G. Paulter

NIST, Gaithersburg, MD, USA

Abstract

Low frequency replication (600 kHz to 18 MHz) of a high frequency waveform (1 GHz to 30 GHz) was achieved using a photoconductive-based optical-microwave (OM) sampler. This OM sampler performs better than a 20 GHz digitizing sampling oscilloscope and is also superior to the standard pump and probe systems with orders of magnitude improvement in data acquisition rate.

1. Introduction

As electronic signals move to higher frequencies and wider bandwidths, there is need for new methods of measuring these high-frequency/high-speed (tens of GHz) and/or high bit rate (tens of GBs/s) signals[1-3]. In this work, critical technical issues associated with the design of a rugged, compact, "real-time" sampling system using photoconductive switches as the test signal generator and sampler were investigated. The design concept is based upon an optoelectronic equivalent time sampling principle and optical-microwave signal mixing. It involves first phase locking of the periodic input signal to be measured to the periodic optical pulses from a mode-locked laser and subsequent sampling of the locked signal by the optical pulses. A photoconductive (PC) switch is used for the optical-microwave mixer and another photoconductor for the sampler. The optical pulses we use were provided by 100 fs pulses from a Ti-Sapphire laser. The optical-microwave intermixing process generates a low-frequency replica of the high-frequency input signal. The ratio of the repetition rate of the input signal to its low-frequency replica is the time expansion factor. The repetition rate of the low-frequency signal provides the offset frequency for the equivalent time sampling. Since there is no electro-mechanical moving parts required to acquire a waveform, the sampling is done at a fast rate, and acquisition times of 10 ms or less are possible. The

success of this technique depends critically on the stability and reliability of the optical microwave phase locked loop (OMPLL) which locks the phase of the signal generator to the optical pulses.

2. Experimental set up

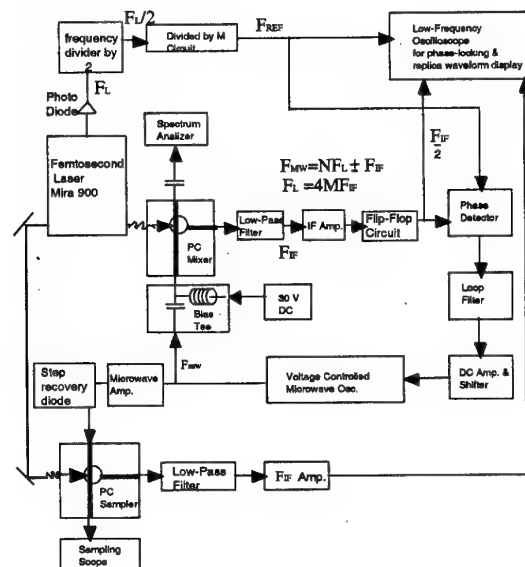


Figure 1. OM sampling system

Figure 1 is the schematic diagram of the OM sampling system. The 100 fs 800 nm laser beam is split into two beams, one for OM phase locking (OMPLL) and the other for waveform sampling. One beam of the laser beams illuminates the GaAs PC mixer (which is used in phase locking the laser and the microwave or pulse source). The laser signal and microwave output are mixed in the PC mixer and the resultant intermixed signal is then amplified through a high gain intermediate frequency (IF, 600 kHz) amplifier. Then the IF signal is sent through a flip-flop circuit and its phase is compared to a reference signal which is obtained by frequency dividing the

output from the laser photo detector. The resulting error signal is then delivered through a loop filter to tune the voltage controlled oscillator (VCO). When OM phase-locking is established, a clear trace around the center frequency of the microwave oscillator will appear and the frequency bandwidth will decrease by two orders of magnitude. Only after phase locking has been established should the high frequency waveform sampling be carried on.

3. Phase locking loop (PLL)

A PLL basically is a feed back system, that synchronizes an oscillator in phase and frequency to an incoming signal. The phase detector measures the phase difference between the input and output signals and produces an error signal proportional to the measured phase difference. The error signal will drive the VCO, changing its frequency so as to minimize the phase difference between the input and output signals. The frequency of the output signal will be identical to that of the input signal and will follow every change of the latter.

There are two type of phase detectors, one is solely phase sensitive, another is frequency sensitive. The later one is sensitive to phase noise, requires signals with a signal to noise ratio of >30 dB, and requires signals with fast transitions (sharp edges). In our case, the F_{if} is from a PC switch which provides a weak signal with high level noise. Consequently, we use a phase sensitive detector in the PLL. To ensure good phase locking, a flip-flop circuit must be used. This makes the OMPLL system very stable.

4. Optical sampling and the replica of the microwave waveform

The working principle of waveform time replica is illustrated in Figure 2.

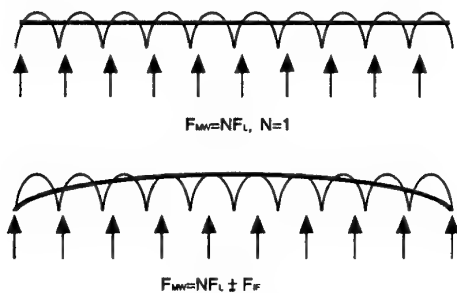


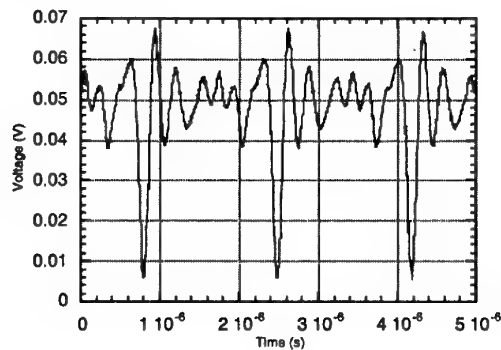
Figure 2. Principle of the time replica

The upper graph shows that the laser pulse will sample the same position of the microwave signal if there is no offset frequency between F_{mw} , the

microwave frequency, and $N F_L$, the multiple laser frequency (N is the multiplier). The sampled output (thick line) will be a flat line. However, if an offset frequency, F_{if} , exists, different mode-locked laser pulse will be sampled at different phases (or delays) on the microwave signal, as shown in the lower graph of Figure 2. The time scale of the OM sampled waveform will be expanded by a factor of $1/F_{if}$ relative to actual time.

In our experiment, the F_{if} was selected to be 600 kHz. The phase locked microwave signal was then used to drive a step recovery diode (SRD) in order to generate high frequency and broadband signals for validating OM sampling systems. The waveform was measured with both a HP 54750A digitizing 20 GHz bandwidth sampling scope and with the present OM sampling system. The results from Figure 3 indicated that excellent agreement was achieved and that OM sampling exhibits a higher bandwidth. The time enlargement factor was 2000 for the waveforms shown in fig. 3. The width of the OM-sampler-measured pulse is approximately 7 ps, which has a bandwidth exceeding the bandwidth of the 20 GHz sampling scope.

The spectrum of the SRD output signal and that of the replica were also measured. The maximum harmonics of the signal from the SRD extend beyond 30 GHz which is beyond the bandwidth of the 20 GHz HP digitizing sampling scope. The low-frequency (OM-sampled) replica, on the other hand, had its harmonics extending only to 18 MHz, which is well within the bandwidth of the 20 GHz sampling scope and most digitizing waveform recorders. It is clear that information above 20 GHz is lost using the 20 GHz sampling oscilloscope while whereas its OM-sampled replica preserves all information. The experimental details and results will be reported.



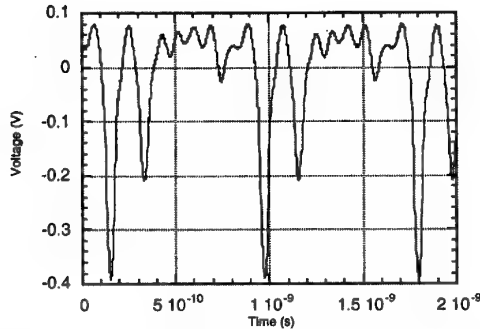


Figure 3. OM sampled replica waveform(top) & scope sampled microwave waveform (bottom)

Figure 4 shows the working principles for high frequency microwave sampling in the frequency domain. The upper graph shows the spectrum of the envelope of the mode-locked laser pulse train and the broadband high frequency microwave signal before intermixing. After intermixing, various sum and difference frequencies are generated, as shown in the lower graph. Any of these sum or difference frequencies from the intermixed signal could be used to perform OM phase locking. However, we have experimentally determined that the F_{if} provides the most stable phase locking. The F_{if} is defined as the frequency of the lowest OM intermixed signal which is the beating frequency between the Nth harmonic of the laser pulse train and the fundamental frequency of the microwave signal. After intermixing, a broadband low frequency replica of the broadband high frequency microwave signal is produced, which is shown on the left-hand side in the bottom panel of figure 4.

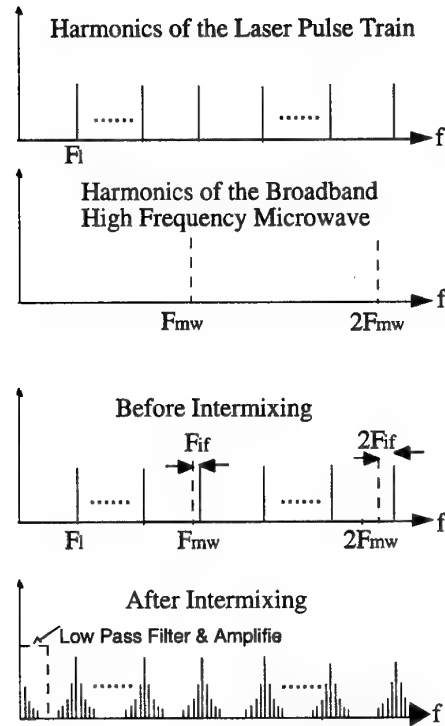


Fig. 4 Working principle for broadband high frequency microwave sampling

5. Conclusion

A flip-flop circuit was used to achieve a stable OMPLL. The flip-flop circuit greatly improved the operational stability and reliability of OMPLL relative to other circuits tried.

Low frequency replication of a high frequency waveform (1 GHz to 30 GHz) was achieved. Results show that the OM sampling system performs better than a 20 GHz digitizing sampling oscilloscope and is also superior to the standard pump and probe systems with orders of magnitude improvement in data acquisition rate.

References

1. CMOS phase-locked loops:74HC(T)4046A/7046A & 74HCT9046A, Page 17 HCMOS Designer's Guide-advance information, Revised edition: June 1995, PHILIPS.
2. S.L.Huang, C.H. Lee, and H-L.A. Hung, "Real-time linear time-domain network analysis using picosecond photoconductive mixer and sampler", IEEE Trans. Microwave Theory and Tech. Vol.43, pp.1281-1289, 1995.
3. N. G. Paulter, "High-speed optoelectronic pulse generation and sampling system", IEEE Trans. Instrumentation and Measurement, Vol. 37, pp.449-453, 1988.

Two-Dimensional Field Mapping of Microstrip Lines with a Band Pass Filter or a Photonic Bandgap Structure by Fiber-Optic EO Spectrum Analysis System

T. Ohara, M. Abe, S. Wakana, M. Kishi, M. Tsuchiya, and S. Kawasaki*

Department of Electronic Engineering, the University of Tokyo

7-3-1 Hongo, Tokyo 113-8656, Japan

Telephone/facsimile: +81-3-5841-6779, E-mail address: tsuchiya@ktl.t.u-tokyo.ac.jp.

*: Department of Communications Engineering, Tokai University

Abstract— An electrooptic spectrum analysis system, containing fiber optics only, was applied for the first time to electric field mapping. DUTs were microstrip lines having a band pass filter or a 2D photonic bandgap structure.

Index Terms—Electrooptic probing, RF spectrum analysis, 2D mapping, photonic bandgap circuit, RF circuit diagnosis

I. INTRODUCTION

New wireless communication services such as the third generation mobile telecommunication systems and/or Intelligent Transport Systems would require RF circuits of higher performance and higher integration as well as shorter turn around time. Techniques for performance evaluation and failure diagnosis are of increasing importance therein, and the internal measurement techniques are expected to be effective from early design stages to final production tests. For this purpose, the electrooptic (EO) probing technique [1]-[3], which is a non-contact internal node measurement method, is attractive because of its high sensitivity, high speed and low invasiveness [4]-[6]. In addition, its application for two-dimensional (2D) mapping of electrical field distribution on RF planar circuits is promising since it provides intuitive visualization of detailed circuit operation. Such 2D RF intensity mapping experiments by the EO probing technique have been performed actively in the last several years [7]-[12]; for instance, near-field measurement of patch antenna [7][8], 2D field mapping of monolithic microwave integrated circuits [9], etc.

Although the EO sampling technique has been utilized exclusively for the 2D mapping, one should note here that a sinusoidal RF signal of a single frequency is usually applied to devices under test (DUT) therein. This fact suggests that the temporal waveform measurement is not necessary and that an alternative method, the frequency-domain spectrum measurement scheme [13], could be more preferred for reducing the data acquisition time. In addition, a continuous wave (CW) laser source and a high-speed photodetector (PD)

are utilized there, which allow the measurement to be free from the synchronization of RF signal source to measurement instruments. We would like to point out thus that the temporal scan free nature and the synchronization free nature of such EO spectrum analysis system (EOSAS) are quite attractive from the 2D mapping application point of view, although such a trial has never been made so far.

In order to confirm those attractive potentials of EOSAS for the 2D mapping application, we attached a 2D-scanning driver to the EOSAS which we had constructed [14][15], and applied it to preliminary mapping of electric field distribution in a microstrip transmission line (MSL) band pass filter (BPF). Furthermore, we extended it to 2D-mapping experiments on an RF circuit with a photonic bandgap structure [16][17] and demonstrated successfully the validity of EOSAS to characterize such a sophisticated RF planar circuit.

II. EXPERIMENTAL SETUP

The configuration of EOSAS we developed is schematically shown in Fig. 1. Although its basic concept is similar to that described in a literature [18], one major difference is that all the optics including its EO probing head is based on fiber optics. This configuration provides that any optical alignment is not necessary except for relatively complex control of the light wave polarization states in the normal single mode fibers. This alignment-free nature is brought by the introduction of fiber-edge EO (FEEO) probe scheme which is described later in detail.

The total optical loss between the polarization controller (PC) and the input of the analyzer is 9.9 dB, which contains 1.5 dB loss at PC, 2.3 dB loss of the optical circulator and 6.1 dB loss of the EO probe. It can be improved up to 4.6 dB since the lowest loss of EO probes that we fabricated so far is 0.8 dB. While such estimation claims that the fiber optic EO probing system is essentially of low loss nature, these losses can be compensated sufficiently by optical fiber amplifiers. Furthermore, a high power and high speed PD can

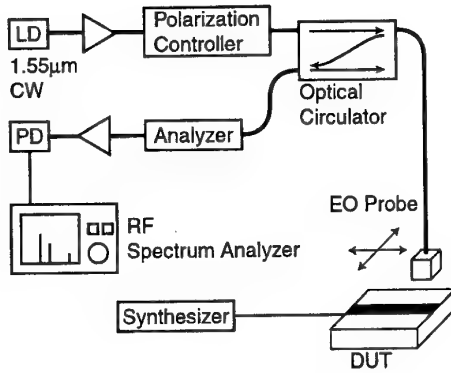


Fig. 1. Schematic illustration of electrooptic RF spectrum analysis system (EOSAS). It consists of fiber optic components only.

provide both sufficient sensitivity and broad bandwidth. We utilized a PD (NEL KEPD2512KPC) which has a bandwidth of 20 GHz, an efficiency of 0.9 A/W, and maximum optical input power of 20 mW. The PD was connected to an RF spectrum analyzer (HP 8564E) through a bias-T. The signal to noise ratio obtained is as high as 35 dB.

We have proposed so-called FEEO-probe [14] in which a small piece of EO crystal is adhered to an edge of optical fiber. We expect and partially confirmed enhanced sensitivity and lowered invasiveness to be brought by the Fabry-Perot enhancement scheme for FEEO-probes [18]-[20], which is to be reported elsewhere. The FEEO-probe we fabricated contains a 50 μm -thick ZnTe crystal glued to a 200 μm -thick glass substrate. The crystal area is 300 μm \times 300 μm . The bottom surface of ZnTe is high-reflection coated by stacks of quarter-wave dielectric layers. The crystal orientation is set so that the electric field along the optical axis is detected (longitudinal EO probing). The EO crystal is attached to the edge of an expanded core fiber (45 μm in diameter) by UV cure adhesive. Here, the expanded core fiber was chosen to reduce the optical loss at the sacrifice of spatial resolution ($\sim 45 \mu\text{m}$). Although the present spatial resolution is larger compared with those in conventional systems ($\sim 10 \mu\text{m}$) [10], we believe it is good enough for the purpose of this paper. Furthermore, this probe structure is symmetric to the optical axis, therefore, the field to be measured is not distorted asymmetrically.

The FEEO-probe was inserted beneath an objective lens of a microscope, and can be moved back and forth by electrically powered micrometers. The position control accuracy is around 1 μm . DUT and the FEEO-probe can be monitored simultaneously by a CCD camera.

III. 2D MAPPING EXPERIMENTS

In order to evaluate the performance of EOSAS setup for the 2D mapping application, we characterized electric field distribution of two kinds of MSLs as

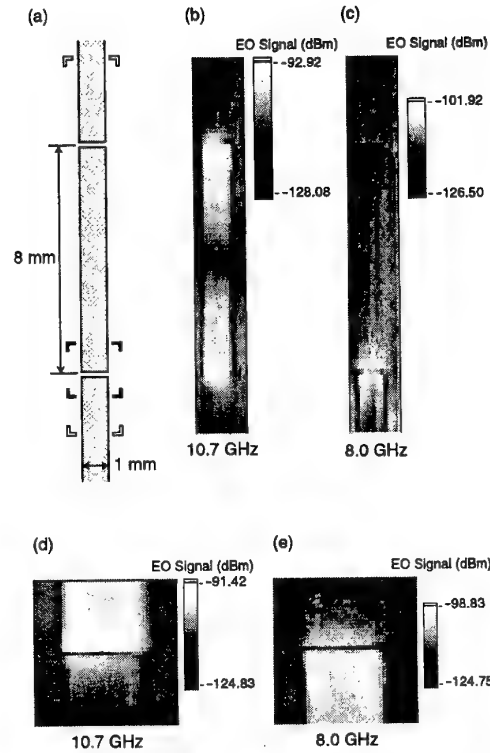


Fig. 2. (a) Schematic drawing of a BPF made of MSL. The area indicated by open rectangular marks corresponds to the maps (b) and (c). That shown by solid rectangular marks corresponds to (d) and (e). The RF signal was fed from the bottom. (b) 2D map of RF intensity at the center frequency of pass band (~ 10.7 GHz). The gray scale is shown by the inset. (c) RF intensity map at 8.0 GHz. (d) (e) RF intensity maps with higher resolution.

follows.

A. Band Pass Filter

The first DUT is a band pass filter (BPF), which is rather conventional and was made by the photolithography technique. Its line width is 1 mm. A schematic of the filter is shown in Fig. 2 (a). The center frequency of its pass band is 10.7 GHz with its Q-factor of 49.2. Figures 2 (b) and (c) indicate measured distribution of RF intensity at 10.7 GHz that is the pass band center frequency and at 8.0 GHz that is out of the pass band, respectively. The measured area is 2 mm \times 14 mm and the size of unit cell is 100 μm \times 200 μm . The total number of measurement points is $21 \times 71 = 1491$. The standing wave formed in the filter cavity of a half wavelength was clearly observed as shown in Fig. 2 (b). On the contrary, the reflection at the incident port is indicated in Fig. 2 (c). Those results suggest that the EOSAS-based 2D mapping measurement is fairly effective to visualize a circuit function (BPF in this case). Figures 2 (d) and (e) show maps with a higher resolution: the cell size is 50 μm \times 50 μm . The images of microwave were obtained more clearly.

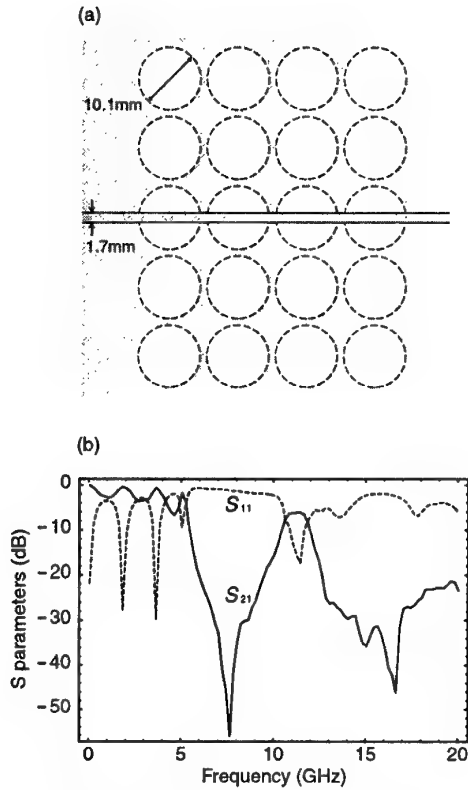


Fig. 3. (a) Schematic drawing of a RF-PBG circuit. (b) S parameters of RF-PBG circuit measured by a network analyzer.

B. Photonic Bandgap Structure

Another DUT to appreciate the performance of EOSAS is the MSL with a photonic bandgap (PBG) structure. It was made on a circuit substrate etched by the photolithography technique. Basically, the PBG structure was proposed as one of the artificial photonic crystals to localize the electromagnetic energy [16]. Therefore, the PBG structure has to be realized with a 2D or 3D structural periodicity as shown in Fig. 3 (a). In this DUT case, the PBG structure was designed within 11.5-12.5 GHz for the TE mode and fabricated two-dimensionally by the etching process. It is expected to work as a two-dimensional BPF or even a two-dimensional band elimination filter (BEF) [17].

In order to confirm the PBG characteristics, the MSL was made on the etched-out hole for the PBG. The band elimination characteristic is expected around 12 GHz and the band pass ones is done in other frequencies. The electrical properties on S-parameters were investigated and shown in Fig. 3 (b). As expected, the BEF characteristic was obtained around 12.5 GHz, while one of the BPF characteristics was observed around 11 GHz. To understand these properties from more intuitive viewpoint, the 2D mapping measurement by EOSAS proposed here was carried out on this DUT. The results were shown in Figs. 4 at 10.8 GHz for the band pass characteristic and at 12.5 GHz for the band

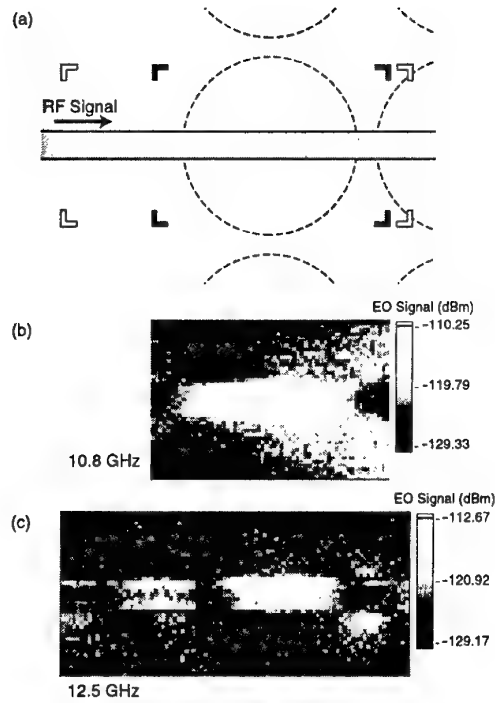


Fig. 4. (a) Structure of RF-PBG circuit and scanning area. (b) 2D map of vertical electric field distribution of an RF-PBG circuit at pass band (10.8 GHz). The scanned area is shown by solid rectangular marks. (c) RF intensity map at stop band (12.5 GHz). The scanned area is shown by open rectangular marks.

elimination characteristic. The measured areas were 10 mm × 15 mm (10.8 GHz) and 10 mm × 22 mm (12.5 GHz), and the stepping pitch was 250 μm.

Although the propagating TEM signal under the MSL was observed in both cases, the difference due to the leaky wave was apparently found in portion of the substrate outside the MSL. The oblique wave propagation found at 10.8 GHz may result from a surface wave or the TM mode in the PBG, which was not taken into account in the design of DUT. On the other hand, prohibition of the wave propagation in the substrate was observed at 12.5 GHz due to the nature of the PBG.

Through the EOSAS measurement, the following significant point was found out; the leaky wave under the PBG structure was clearly measured with the information of the magnitude and the direction of the wave propagation in the circuit substrate which cannot exist in the ordinal MSL. Therefore, the measurement using EOSAS is necessitated for design and analysis of the configuration and periodicity, and the performance of the PBG structure.

IV. CONCLUSIONS

We applied EOSAS to the 2D intensity mapping of RF planar circuits for the first time, and evaluated the system performance by visualizing the internal circuit operations. Standing wave and reflection on the MSL-

BPF, which are rather basic, were observed clearly in a preliminary experiment.

2D mapping experiments provided by EOSAS was applied also to visualization of RF-PBG circuit operation, through which detailed distribution of RF field was clarified. One should note thus that the verification of internal operation state is crucially important in PBG circuit which has 2D periodic structures.

ACKNOWLEDGMENT

The authors would like to thank Mr. H. Takahashi (Hamamatsu Photonics) for providing EO crystals, Mr. N. Ohkubo (Tokai University) for fabrication of RF-PBG circuits, Dr. M. Kato (University of Tokyo) for technical assistance of fabrication of MSL filter and its characterization. Thanks are also due to Prof. T. Kamiya (University of Tokyo) for his continuous support and encouragement.

REFERENCES

- [1] J. A. Valdmanis, and G. Mourou, "Subpicosecond Electrooptic Sampling: Principles and Applications," *IEEE J. Quantum Electron.*, vol. QE-22, pp. 69-78, Jan. 1986.
- [2] B. H. Kolner, D. M. Bloom, "Electrooptic Sampling in GaAs Integrated Circuits," *IEEE J. Quantum Electron.*, vol. QE-22, pp. 79-93, Jan. 1986.
- [3] J. A. Valdmanis, "1THz-Bandwidth Prober for High-Speed Devices and Integrated Circuits," *Electron. Lett.*, vol. 23, pp. 1308-1310, Nov. 1987.
- [4] T. Nagatsuma, "Electro-Optic Testing Technology for High-Speed LSIs," *IEICE Trans. Electron.*, vol. E79-C, pp. 482-488, Apr. 1996.
- [5] M. Shinagawa, and T. Nagatsuma, "An Automated Electro-Optic Probing System for Ultra-High-Speed IC's," *IEEE Trans. Instrum. Meas.*, vol. 43, pp. 843-847, Dec. 1994.
- [6] X. Wu, D. Conn, J. Song, K. Nickerson, "Invasiveness of LiTaO₃ and GaAs Probes in External E-O Sampling," *J. Lightwave Technol.*, vol. 11, pp. 448-454, March 1993.
- [7] Y. Imaizumi, M. Shinagawa, and H. Ogawa, "Electric Field Distribution Measurement of Microstrip Antennas and Arrays Using Electro-Optic Sampling," *IEEE Trans. Microwave Theory Tech.*, vol. 43, pp. 2402-2407, Sep. 1995.
- [8] K. Yang, G. David, J.-G. Yook, I. Papapolymerou, L. P. B. Katehi, and J. F. Whitaker, "Electrooptic Mapping and Finite-Element Modeling of the Near-Field Pattern of a Microstrip Patch Antenna," *IEEE Trans. Microwave Theory Tech.*, vol. 48, pp. 288-294, Feb. 2000.
- [9] W. Martin, "Two-dimensional field mapping of monolithic microwave integrated circuits using electrooptic sampling techniques," *Optical and Quantum Electronics*, vol. 28, pp. 801-817, 1996.
- [10] T. Pfeifer, T. Löffler, H. G. Roskos, H. Kurz, M. Singer, and E. M. Biebl, "Electro-Optic Near-Field Mapping of Planar Resonators," *IEEE Trans. Antennas Prop.*, vol. 46, pp. 284-291, Feb. 1998.
- [11] D. R. Hjelme, M. J. Yadlowsky, and A. R. Mickelson, "Two-Dimensional Mapping of the Microwave Potential on MMIC's Using Electrooptic Sampling," *IEEE Trans. Microwave Theory Tech.*, vol. 41, pp. 1149-1158, June/July 1993.
- [12] W. K. Kuo, S. L. Huang, T. S. Horng, L. C. Chang, "Two-dimensional mapping of electric-field vector by electro-optic prober," *Optics Communications*, pp. 55-60, April 1998.
- [13] D. Le Quang, D. Erasme, and B. Huyart, "MMIC-Calibrated Probing by CW Electrooptic Modulation," *IEEE Trans. Microwave Theory Tech.*, vol. 43, pp. 1031-1036, May 1995.
- [14] S. Wakana, T. Ohara, M. Abe, E. Yamazaki, M. Kishi, and M. Tsuchiya, "Novel Electromagnetic Field Probe using Electro/Magneto-Optical Crystal mounted on an Optical-fiber Facet for Microwave Circuit Diagnosis," for presentation in *International Microwave Symposium (IMS) 2000*.
- [15] T. Ohara, M. Abe, S. Wakana, M. Kishi, M. Tsuchiya and S. Kawasaki, in preparation.
- [16] E. Yablonovitch, "Photonic band-gap structures," *J. Opt. Soc. Am. B*, vol. 10, no. 2, pp. 283-295, Feb. 1993.
- [17] V. Radisic, Y. Qian, R. Coccioli, and T. Itoh, "Novel 2-D Photonic Band Structure for Microstrip Lines," *IEEE Microwave and Guided Wave Lett.*, vol. 8, no. 2, pp. 69-71, Feb. 1998.
- [18] D. Le Quang, D. Erasme, and B. Huyart, "Fabry-Perot Enhanced Real-Time Electro-Optic Probing of MMICs," *Electron. Lett.*, vol. 29, pp. 498-499, Mar. 1993.
- [19] A. J. Vickers, R. Tesser, R. Dudley, M. A. Hassan, "Fabry-Pérot Enhancement of External Electro-optic Sampling," *Optical and Quantum Electronics*, vol. 29, pp. 661-669, 1997.
- [20] P. O. Müller, S. B. Alleston, A. J. Vickers, and D. Erasme, "An External Electrooptic Sampling Technique Based on the Fabry-Perot Effect," *IEEE J. Quantum Electron.*, vol. 35, pp. 7-11, Jan. 1999.

Synthesis of optical transversal filter with tap multiplexing

G. Yu, W. Zhang, J. A. R. Williams

Photonics Research Group, Department of Electronic Engineering and Applied Science, Aston University, Birmingham, B4 7ET, UK

Telephone: +44 121 359 3611 Fax: +44 121 359 0156 email: yug@aston.ac.uk

Abstract: A novel optical transversal filter with tap multiplexing is presented. The performance of a fibre grating based bandpass filter with up to 16 taps is demonstrated.

Introduction: Optical fibre microwave and millimetre wave signal processing is a technique that has seen recent rapid development and is attracting more and more research interest [1-5]. Instead of processing the modulating signal in the electrical domain, this processing is realised in the optical domain, and so is the promising solution for overcoming problems associated with electronic filters. It offers the possibility of a new family of optical fibre microwave devices and circuits with exciting characteristics.

Optical transversal filters are crucial to the desired microwave signal processing in the optical domain. These are based on optical delay lines and therefore the frequency response and performance of an optical transversal filter depends on the number of optical taps used and the way they are distributed in the filter. Increasing the number of taps enables improved performance, for example, increased Q factor and rejection level. Additionally it gives more options in terms of tap apodisation enabling improved suppression of sidelobes in the frequency response. In this paper we present a novel fibre Bragg grating based transversal filter with an easy tap multiplexing technique. Facilitated by this technique, an optical fibre grating based bandpass filter with up to 16 taps has been realised. This is, to our knowledge, the largest number of taps of transversal filter built with fibre Bragg gratings. By using this multiplexing technique, one could make the system more cost effective. It also alleviates the burden of precise grating spacing adjustment, which is critical to the performance of the filter.

Background: For an optical fibre grating based transversal filter with tap weights A_n and effective

unit delay time τ_s , the output signal $S(t)$ is related to the input signal $s(t)$ by

$$S(t) = \sum_{n=1}^N A_n s(t - \tau_s) \quad (1)$$

where the τ_s , associated with the tap spacing, here grating spacing L_0 , can be computed as $\tau_s = n_0 L_0 / c$, n_0 is fibre refractive index. The unit delay time τ_s gives the effective sampling time for the finite impulse response (FIR) filter, the effective sampling frequency $f_s = 1 / \tau_s$. For the case that the tap weights are the same, the microwave signal frequency response $P(f)$ can be predicted to be

$$P(f) = [\sin(N\pi f / f_s) / N \sin(\pi f / f_s)] \quad (2)$$

where f is the modulation frequency. N is tap number.

The grating spacing τ_s and filter tap number N corresponds to the time- and frequency- domain resolution. With a small grating spacing we can get better time domain resolution, but the spacing must be greater than the coherence length of source to ensure incoherent processing. Larger N means enables more control of the frequency characteristics, but also increases the number of components (gratings in this experiment). This invariably, in a fibre Bragg grating gives rises to increased errors in the Bragg grating spacing which generally deteriorates the frequency response of the filter.

A simulated output of $N=8$, and $L_0=2.8$ m is given in Fig. 2(a) (dashed line). Obviously, bandpass filtering is realised at those frequencies where the microwave signals combine constructively.

Experiment: The schematic diagram of the set-up used in the experiment is shown in Fig. 1, where the HP 8703 lightwave component analyser (LCA) is used for the generation of the microwave

modulating signal as well as its detection. A tuneable laser provided the optical carrier. Through the optical circulator (OC) and 1×8 splitter the modulated optical signal reached 8 grating arrays, each with 4 gratings having different Bragg wavelength. This optical signal exiting from the circulator was further split into two beams by a 1×2 coupler, then recombined at the second coupler. One beam passed through directly. The other reflected at an induced grating with the same Bragg wavelength. This grating was placed so that the optical path difference between these two arms is exactly eight times of the unit delay time in the filter. An attenuator was used to compensate the insertion loss from the circulator and the uneven optical coupling coefficients in the coupler.

Looking at the time impulse response of the optical signal exiting from the circulator one can see an eight pulses train which represent the eight reflected signals from the fibre gratings. This impulse response is then split in two and recombined with differential delay between the two copies such that they exactly follow each other. Fig.3 shows the impulse response of the optical signal after the second 1×2 coupler where grating spacing is 2.8m. One can see the pulse number has increased to 16, and all the pulses are equally spaced. This means the taps connecting with that 1×8 splitter has been multiplexed and effective tap number has been doubled. In Fig. 4, the dashed line is the frequency response of the filter consisted of eight taps, which was measured at the output of the circulator. Solid curve corresponds to the frequency response of the optical signal after the second coupler, which is a typical response for 16 taps. As we can see, the bandwidth of passband became smaller while the free spectrum range (FSR) remained the same. A doubling of the filter Q factor has been achieved.

The increasing of tap number improves not only the Q factor, but also the rejection ratio. As we can see from Fig. 4, the sidelobes of 16 taps filter is well below (6dB lower than) that of 8 taps filter. Filter tunability is achieved using grating arrays, as illustrated, and by tuning the carrier wavelength among the Bragg wavelengths of the grating arrays.

Conclusion: A novel configuration of transversal filter with tap-multiplexing has been presented and the improved performance of the filter also

demonstrated. The technique could be further extended to enable further multiplication in the tap number. This reduces the number of gratings required to realise a transversal filter, easing the construction requirements and therefore enabling a reduction in the spacing errors between taps. Further work on apodisation of the tap profile is to be carried out. Further schemes based on this technique are envisaged to greatly improve the performance achievable using fibre Bragg grating based transversal filter designs.

References:

- [1] B. Molsehi, J. Goodman, M. Tur and H. Shaw, "Fiber-optic lattice signal processing," *Proc. Of the IEEE*, vol. 72, No. 7, July 1984
- [2] K. Jackson, S. Newton, B. Moslehi, M. Tur, C. Cutler, J. Goodman, and H. Shaw, "Optical fibre delay line signal processing," *IEEE Microwave Theory Tech.*, Vol. MTT-33, pp. 193-210, 1985
- [3] H. Taylor, S. Gweon, S. Fang, and C. Lee, "Fiber optic delay-lines for wideband signal processing," *Proc. SPIE*, vol. 1562, p. 264, 1991.
- [4] W. Zhang, J. A. R. Williams, and I. Bennion, "Fibre-optic Bandpass Transversal Filter Employing Fibre Grating Arrays", *Electron. Lett.* V.35, No.12, pp. 1010-1011, 1999
- [5] J. Capmany, D. Pastor and B. Ortega, "New and flexible fiber-optic delay-line filters using chirped Bragg gratings and laser arrays," *IEEE trans. On Microwave Theory and Tech.*, vol. 47, No. 7, pp. 1321-1326, 1999

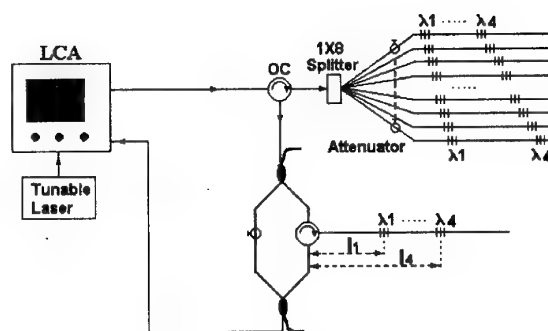


Fig.1. Experimental set-up.

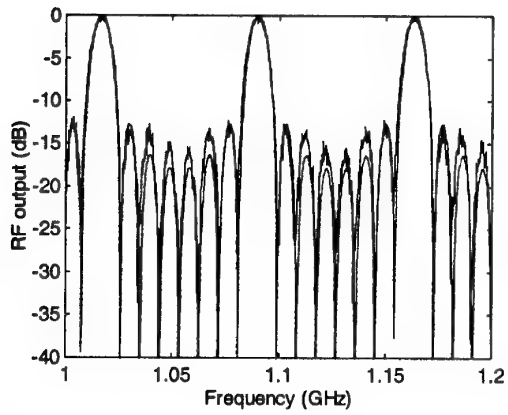


Fig.2. Simulated (dashed) and measured (solid) frequency response of the filter with 8 equal taps.

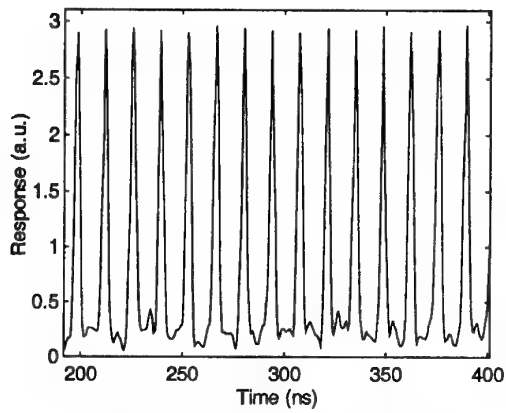


Fig.3. Impulse response with 16 taps

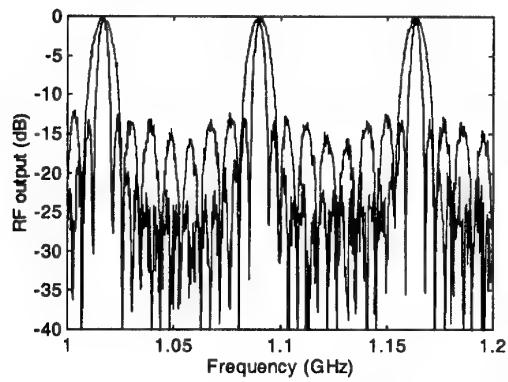


Fig.4. Frequency responses before (dashed) and after (dashed) tap multiplexing.

Velocity-Matched Distributed Photodetectors with p-i-n Photodiodes

M. S. Islam, T. Jung, S. Murthy, T. Itoh, M. C. Wu, D.L. Sivco[†], and A.Y. Cho[†]

University of California, Los Angeles, Dept. of EE, 63128 Engineering IV, Box 951594, Los Angeles CA 90095-1594, USA. Tel: (310) 825-6859, Fax: (310) 794-5513, email: wu@ee.ucla.edu

[†]Lucent Technologies, Bell Laboratories, Murray Hill, NJ 07974, USA

ABSTRACT

We report on the first demonstration of velocity-matched distributed *p-i-n* photodetectors. Record high linear DC photocurrent of 45 mA has been achieved without suffering from thermal damage, thanks to the superior power handling capability of *p-i-n* photodiodes. The frequency response is flat from 1 GHz to 35 GHz.

I. INTRODUCTION

High power, high-speed photodetectors are a key component for microwave fiber optic links and optoelectronic generation of microwave and millimeter-waves [1]. High optical power can greatly enhance the link gain, signal-to-noise-ratio and the spur free dynamic range (SFDR) of externally modulated links. Several approaches have been proposed to increase the maximum linear photocurrent of high-speed photodetectors, including waveguide photodetectors with low confinement factors [2-4], traveling-wave photodetectors [5,6] and phototransistors [7], velocity-matched distributed photodetectors (VMDP) [8,9], and parallel fed VMDP [10]. Using the VMDP with metal-semiconductor-metal (MSM) photodiodes (PDs), we have achieved a saturation photocurrent of 33 mA at 1.55 μm wavelength [8]. Bimberg *et al.* also reported on an MSM-based VMDP with a bandwidth above 78 GHz [9].

The maximum linear photocurrent in our previous MSM-VMDP is limited by the catastrophic damage caused by thermal runaway. *Pi-n* PDs have higher threshold for thermal runaway than MSM photodiodes. It was previously shown that MSM photodiodes fail at junction temperatures of $\sim 700\text{K}$ [11], whereas *p-i-n* can stand junction temperatures above 900K [12]. This is primarily due to the larger barrier height for dark current in *pi-n* photodiodes. Therefore, VMDPs with *p-i-n* photodiodes can achieve even higher photocurrent. Moreover, the uniform electric field distribution in *p-i-n* is also advantageous for linear operation under high power illumination. Moreover, the fabrication of high

bandwidth MSM photodiodes demands sophisticated sub micron e-beam writing and thin MSM fingers are vulnerable to failure caused by high photocurrents. Therefore, VMDP with *pi-n* photodiodes are of great interest for high power photodetection.

In this paper, we report on the first demonstration of the VMDP with *p-i-n* photodiodes. Record-high linear photocurrent of 45mA has been achieved. No thermal runaway was observed for photocurrent above 55 mA. Our VMDP has a flat frequency response up to 35 GHz, though there is an initial drop at low frequency due to slow carrier diffusion. We have also found that the maximum linear photocurrent is dependent on the alignment of input optical fibers. The fiber position for maximum responsivity is different from that for maximum linear photocurrent. A unique technique has been developed to achieve the optimum fiber alignment.

II. DESIGN AND FABRICATION

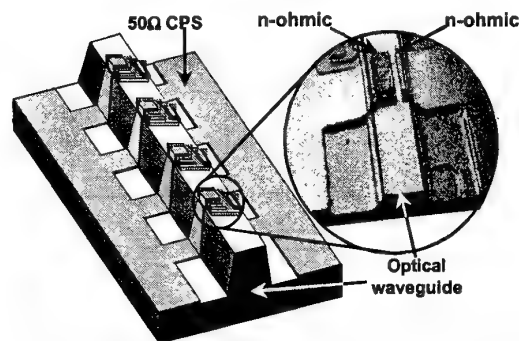


Fig. 1. Schematics of the VMDP with a close-up view of the active *p-i-n* photodiode region.

The schematic structure of the VMDP is illustrated in Fig. 1. A linear array of *pi-n* photodiodes is periodically distributed on top of a passive optical waveguide. Optical signal is evanescently coupled from the passive waveguide to the active *p-i-n* PDs. Photocurrents generated from the individual photodiodes are added in phase through a 50 Ω coplanar strips (CPS) microwave

transmission line that is velocity-matched to the optical waveguide. The photodiodes are kept below saturation by coupling only a small fraction of optical power to each photodiodes.

The active p-i-n PDs consist of a 0.25- μm -thick InGaAs absorption layer and two InGaAlAs ohmic contact layers. One of the main tradeoff in the design of p-i-n VMDP is the placement of ohmic contacts. Fig. 2 shows three different contact schemes: (a) parallel contacts on a continuous waveguide, (b) tandem contacts on a continuous waveguide, and (c) parallel contacts with lower contact outside the waveguide. The contact area for each photodiode is $20 \times 2.5 \mu\text{m}^2$. In our device, the p-ohmic contact is the lower contact, which is close to the core of the passive waveguide. We experimentally investigated the performances of the VMDPs with different contact schemes. Our experimental results show that VMDPs with Scheme (a) contacts have the best performance: they have the lowest loss and more uniform photocurrent distribution along the waveguide. The spacing between the n and p contacts is $2 \mu\text{m}$.

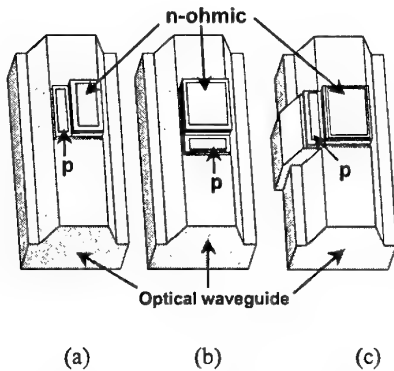


Fig. 2. Schematics of three different contact schemes. (a) parallel on continuous waveguide (b) tandem on continuous waveguide (c) parallel contacts with lower contact outside the waveguide.

A wide horizontally multimode optical waveguide with continuous transitions between passive waveguide and active PD is employed to reduce interface losses. Since the microwave velocity can only be matched to the group velocity of one optical mode, there is some inherent velocity mismatch in multimode devices. However, the mismatch is small ($< 10\%$) and the bandwidth limit due to velocity mismatch is greater than 150 GHz, which is higher than the transit time-limited bandwidth of our current device. Moreover, our BPM simulation shows that more than 97% of the input power is coupled to the fundamental mode during propagation.

III. MEASUREMENTS AND DISCUSSION

The DC responsivity is 0.42 A/W at 1 V bias (without AR coating). This responsivity can be further improved by employing airbridges to connect photodiodes with the microwave transmission line, which prevent direct metal deposition on the sidewalls of the waveguide. The reverse bias breakdown is $\sim 1.5 \text{ V}$. The low breakdown is caused by the diffusion of p-type dopants from the lower contact layers into the InGaAs absorbing layer during the epitaxial growth. The microwave characteristics of the VMDP is measured by HP 8510C network analyzer. The measured characteristic impedance matches very well to 50Ω (within 3%) for a broad frequency range.

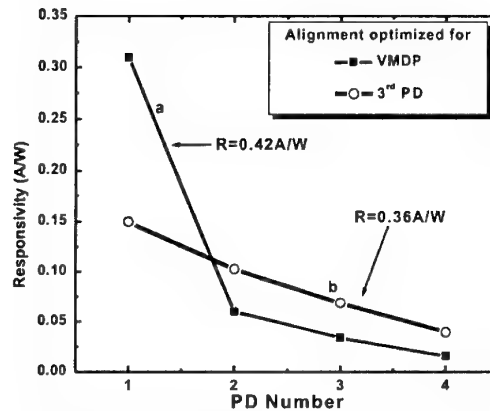


Fig. 3. Measured responsivity of each PDs in the split contact VMDP for focusing the input power to the whole structure and for focusing to the 3rd photodiode.

To characterize the distribution of photocurrents within the VMDP, we have fabricated VMDPs with separate contacts for each photodiodes. We found the photocurrent distribution is sensitive to the alignment of input optical fibers. The measurement results are shown in Fig. 3. When the fiber is positioned to optimize the overall responsivity of the VMDP (0.42 A/W), the photocurrent distribution has a very steep decay (Curve (a) of Fig. 3). The first photodiode contributed 73.8% of the overall photocurrent. The maximum linear photocurrent is 22 mA. If the fiber is positioned to optimize the response of the second photodiode instead of the entire VMDP, more uniform distribution of photocurrent is obtained. The responsivity of the overall VMDP decreased slightly to 0.39 A/W, however, the maximum linear photocurrent increased to 35 mA. This is because more photodiodes are contributing to the total photocurrent when the first photodiode reaches saturation. If we move the fiber again to optimize

response of the *third* photodiode, the maximum linear photocurrent of the VMDP is increased further to 45.5 mA. The overall responsivity became 0.36 A/W. The distribution of photocurrent under this coupling condition is shown in Fig. 3 (line b).

The explanation for the above observation is as follows. Because the first photodiodes is located very close to the facet (100 μm away), the optical field coupled into VMDP has not reached the steady state distribution yet. The transient field can be directly coupled into the photodiodes, resulting in higher photocurrents in the first photodiode. Therefore, when we align the fiber by maximizing the overall response of the VMDP, the fiber-to-waveguide coupling is actually not optimized. Though the absorption of the transient field helps increase the overall quantum efficiency, the extra photocurrent concentrates in the first photodiode and causes it to saturate at lower overall photocurrent. The photocurrents of the photodiodes farther away from the input facet are less influenced by the transient field and, therefore, are better monitors for the fiber alignment.

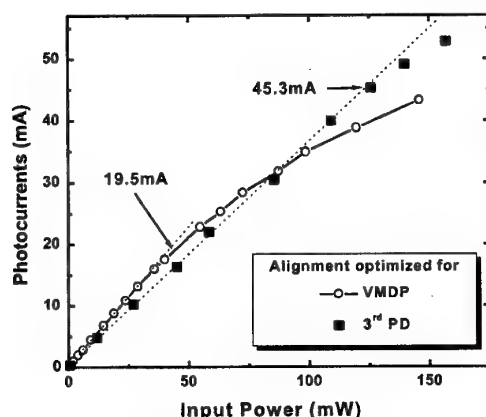


Fig. 4. Measured DC linear photocurrents for two different input fiber positions. The linear current improve greatly when the input power is optimized to a distant photodiode.

This above technique can be used to improve the maximum linear photocurrent of an identical VMDP with the same device geometry but without split contacts. The displacement of the fiber between the optimum responsivity and the maximum photocurrent of a distant (e.g., the 3rd) PD is very reproducible. Therefore, we can calibrate the displacement (ΔX , ΔY , and ΔZ) first using a split-contact VMDP. To align the fiber to a regular VMDP without split contact, it is first aligned to maximize the overall responsivity. This leads to concentration of photocurrent in first PD. We then move the fiber by ΔX , ΔY , and ΔZ using a piezo-controlled micrometer. This reduces the

photocurrent in the first PD and increases the contribution of diodes further down along the array. In all cases, the results are within 5% of that of that obtained from the split-contact test structure. Fig. 4 shows the photocurrents for both optimized coupling to the whole device and for focusing the input power to the 3rd PD using this technique. We achieved more than 45mA of linear photocurrent. To our knowledge, this is the highest linear DC photocurrent reported in high-frequency photodetectors.

Our finding also suggests new VMDP structures with built-in monitor for optimum fiber alignment. In addition to the regular array of PD's of the VMDP, we can add an additional monitoring photodiode in the middle of the waveguide (e.g., between the 4th and the 5th PD's). By optimizing the photocurrent of the monitoring PD, we can achieve high linear photocurrent. Alternatively, we can also employ a much longer passive waveguide to reduce the influence of transient field on the photocurrent of the first PD.

In contrast to the MSM VMDP we reported previously [8], the p-i-n VMDP does not fail at the maximum linear photocurrent. In fact, our device survives at photocurrent as high as 55 mA. If we continue to increase the photocurrent, eventually the facet of the optical waveguide is damaged at 200 mW. Even under this circumstance, the active PD's of the p-i-n VMDP remains alive. In fact, we can reverse the VMDP and couple light in from the undamaged facet, and obtain the same level of maximum linear photocurrent as before.

The responsivity of the VMDP can be improved by employing antireflection (AR) coating. The fiber coupling efficiency can be improved by integrating a spotsize converter for better mode-matching with fiber. Coupling efficiency as high as 90% has been reported [13]. With both AR coating and spot size converter, the responsivity can potentially be increased to 0.9 A/W. The optical power damaging level will also be increased.

We used both frequency and time domain measurements to characterize the AC response of the VMDP. The frequency domain measurement was performed by optical heterodyning method using two external cavity tunable lasers at 1550 nm. The optical signals are combined by a 3dB coupler, and coupled to the VMDP through a fiber pickup head. The output is collected by a 50-GHz probe and monitored by an RF power meter. The calibrated frequency response of the VMDP is shown in Fig. 5. The AC response has a quick rolloff at low frequencies (below 1 GHz) and then remains almost flat. The initial roll off at low frequency is due to the slow carrier diffusion in the active region, which is caused by unintentional migration of p-dopants (Be)

during epitaxial growth. Excluding the low frequency roll-off, the 3-dB frequency is 35GHz.

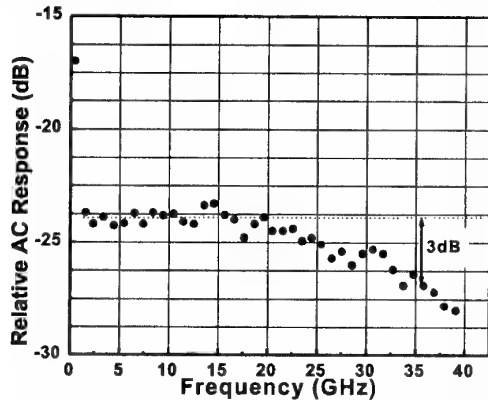


Fig. 5. Measured frequency response of the $p-i-n$ VM DP with optical heterodyning. Except a sharp rolloff below 1GHz, the device has a 3-dB bandwidth >35 GHz.

We have also measured the timedomain pulse response of the VM DP. Short laser pulses with a FWHM pulse width of 1ps, a repetition rate of 25 MHz, and a center wavelength of 1550 nm are employed for the measurement. A VM DP with 8 PDs (each PD has an area of $45\mu\text{m}^2$) was illuminated with an average photocurrent of 0.1mA and the resulting pulses were observed on a 50GHz sampling scope. Fig. 6 shows the measured results. The measured FWHM width is 13ps after deconvolving the response of the 50GHz scope. The measured results also include the losses of the microwave components. In addition to the short pulse, there is a long tail due to dopant migration in to the active region of the photodiode that contributes to slow carrier diffusion. This agrees well with the frequency domain measurement.

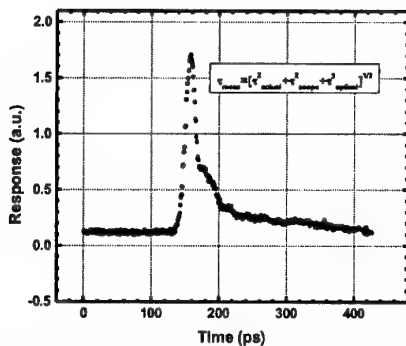


Fig. 6. Measured pulse response of the VM DP. The FWHM is 18ps without including the correction factors. The long tail is caused by the slow carrier diffusion in the dope active region.

A new epi-layer with a setback region is currently being developed to eliminate the low frequency roll off and increase the breakdown voltage. Another issue of our current devices is the

high contact resistance of the lower Ohmic contact, which results in low RC-limited bandwidth. Our current epitaxial layer structure does not have an effective stop etch layer before the lower Ohmic contact layer. As a result, the contact is actually formed on the InGaAlAs layer with low doping concentration. In the new epitaxial layer design, we have also inserted a stop etch layer to improve the contact resistance. The new device should exhibit higher frequency response.

IV. CONCLUSION

We have successfully demonstrated a velocity matched distributed photodetector with $pi-n$ photodiodes. A high linear DC photocurrent of 45 mA has been achieved. In order to increase the DC linear photocurrents a novel alignment technique is demonstrated. The VM DP has a flat frequency response from 1 to 35 GHz. A low frequency roll off due to slow carrier diffusion is also observed. We are now in the process of designing a new epitaxial structure to eliminate the long diffusion tail and improve the contact resistance.

V. ACKNOWLEDGEMENT

The authors would like to acknowledge Allan Hui, Wibool Piyawattanametha and Sagi Mathai of UCLA for their help. This project was supported by ONR MURI on RF photonics, and UC MICRO.

REFERENCE:

- [1] C.H. Cox, III *et al.*, "An analytic and experimental comparison of direct and external modulation in analog fiberoptic links," *IEEE MTT*, vol. 38, no. 5, p 501, May 1991.
- [2] D.C. Scott *et al.*, "Measurement of IP3 in $p-i-n$ photodetectors and proposed performance requirements for RF fiber-optic links," *IEEE Photon. Technol. Lett.*, vol. 12, no 4, p 422, April, 2000.
- [3] S. Jasmin *et al.*, "Diluted and distributed-absorption microwave waveguide photodiodes for high efficiency and high power," *IEEE MTT*, vol.45, no.8, p.1337, 1997.
- [4] A.R. Williams *et al.*, "InGaAs/InP waveguide photodetector with high saturation intensity," *El. Letts*, vol.28, no.24, p.2258, 1992.
- [5] K.S. Giboney, M.J.W. Rodwell, J.E. Bowers, "Traveling-wave photodetector theory," *IEEE MTT*, vol.45, no.8, p.1310, 1997.
- [6] D. Jäger *et al.*, "Distributed velocity-matched $1.55\mu\text{m}$ InP traveling-wave photodetectors for generation of high millimeter-wave signal power," *IEEE MTT-S Digest*, p1233, 1998.
- [7] D.C. Scott *et al.*, "High-power high-frequency travelingwave heterojunction phototransistors integrated polyimide waveguide," *IEEE Micro. and Guided Wave Lett.*, vol.8, no.8, p. 284, Aug. 1998.
- [8] M.S. Islam *et al.*, "High power distributed balanced photodetectors with high linearity", *International Microwave Photonics Conf.*, Melbourne, Australia, 16-19 Nov, 1999.
- [9] Bimberg, *et al.*, "78 GHz distributed InGaAs MSM", *Electronics Letters*, vol.34, no.23, IEE, p.2241-3, 1998.
- [10] S. Murthy *et al.*, "A novel monolithic distributed traveling wave photodetector parallel opt. feed," *IEEE Phot. Tech. Lett.*, June, 2000.
- [11] A. Nespola *et al.*, "Failure analysis of travelling wave MSM distributed photodetectors," *IEDM*, San Francisco, CA, USA, 1998.
- [12] K.J. Williams and R.D. Esman, "Design considerations of high current photodetectors," *IEEE JLT*, vol.17, no.8, p.1443, Aug. 1999.
- [13] A. Umbach *et al.*, "Ultrafast, high-power $1.55\mu\text{m}$ side-illuminated photodetector with integrated spot size converter," *OFC 2000*, Baltimore, MD, March 7-10, 2000.

Photodiode Compression due to Current-Dependent Capacitance

Keith J. Williams and *Peter G. Goetz

Naval Research Laboratory, Code 5650, 4555 Overlook Ave, Washington, DC 20375, USA

TEL: (202) 767-9360 FAX: (202) 404-8645 e-mail: keith.williams@nrl.navy.mil

*Sachs-Freeman Associates, Largo Maryland

Abstract: We present photodetector compression measurements and simulations to demonstrate the consequences of absorption in undepleted regions of *p-i-n* photodiodes. Specifically, this absorption can cause compression when operated above a few milliamps due to a current-dependent capacitance.

As received photocurrents increase above 10 mA in analog and digital systems, the design of linear high-current photodetectors (PDs) which maintain a desirable linear frequency response (not photocurrent dependent) with low nonlinear distortion is crucial. This paper addresses the effects of a nonlinear capacitance component which is shown to be due to an undepleted absorbing region. A number of groups have been studying surface-illuminated [1-5], waveguide [6,7], and traveling-wave [8,9] structures for high photocurrent operation. Undepleted absorbing regions in all these photodetector types arise from unintentional dopants within the InGaAs absorber which can degrade [10] their high current operation. Separately, it has been observed [11-13] that the capacitance of photodiodes can increase under illumination. Here it will be shown that the increase in capacitance at higher currents can be severe and it is sufficient to be the dominant factor in the compression behavior of high-current PDs.

In the measurement system [1,2,5] used to characterize PD frequency response at high average currents, a small portion of a directly-modulated isolated 1313-nm distributed feedback laser (DFB) laser output is combined with a high-power isolated 1319-nm CW laser output. The lasers are separated slightly in wavelength to prohibit generation of RF beatnotes in the PD, but close enough to achieve good overlap of the optical fields in the absorbing layers. The DFB is used to probe the PD frequency response while the average current is controlled with the CW laser. Figure 1 shows the frequency response of a commercial 300 μm diameter PD under low-level illumination (200 μA) from the DFB laser only for applied voltages of 10, 17, and 20V (solid and thin lines). In addition, Fig. 1 shows the PD response when the CW laser is

turned on to yield bias voltage-photocurrent levels of 20V-5mA, 20V-20mA and 15V-10mA (dashed and thick lines). In the figure, the 17 V low-level and the 20V-5mA response curves are indistinguishable. Similarly, the 10 V low-level, the 20V-20 mA, and the 15V-10mA responses are indistinguishable. Thus it appears that the PD capacitance is increasing under illumination.

To quantify this nonlinear capacitance term, dark CV measurements were performed to determine the PD capacitance. To determine the capacitance under high illumination conditions (which the CV meter could not measure), the PD frequency response curves were compared to the PD responses under low-level illumination and assigned the capacitance, determined under dark conditions, that yielded the same frequency response. Figure 2 shows the results for the PD measured in Fig. 1. Note how the capacitance for the 20V-20mA, 15V-10mA and 10V-0mA conditions are equal, as the PD frequency response curves overlap under these conditions (Fig. 1). Note how the capacitance can increase by nearly 40% (@10V) for only 15mA of photocurrent. This will degrade the

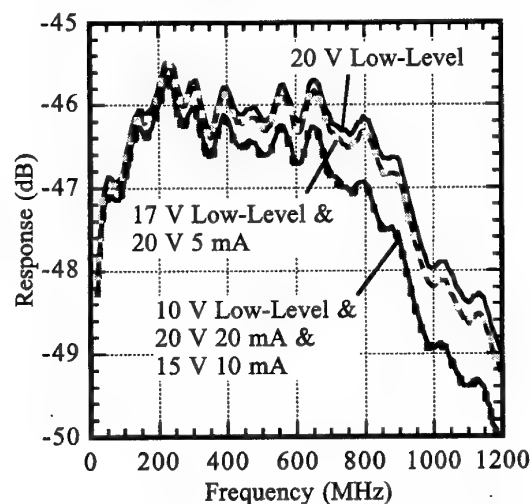


Figure 1. Measured frequency response under 10V, 17V and 20 V low-level (DFB only) conditions (solid thin black lines) and under 20 V-5mA (dashed green), 20 V-20mA (dashed blue), and 15V-10mA (dashed red) conditions.

bandwidth and RF responsivity at higher photocurrents. It appears that the nonlinear capacitance is solely responsible for the RF photoreponse reductions (compression) since the power densities (and space-charge) for these test conditions are insufficient to cause significant compression. Similar results were obtained for 75 μm diameter PDs from the same manufacturer, however, the overlap between various low- and high-level illumination condition responses was not as close. In fact, the overlap varied by a few tenths of a dB, especially at lower frequencies and more moderate currents. This may be due to the influence of emerging space-charge effects.

To investigate the cause(s) for this nonlinear capacitance, simulations were performed on 75 μm diameter PDs. To accurately model these devices, dark CV measurements (Fig. 3) are used to gather information on what possible intrinsic region doping levels may be present. Note how the capacitance gradually decreases with increasing voltage. This suggests that the intrinsic region continues to widen as the bias increases. Allowing 0.1 pF for contact capacitance, two possible doping profiles were modeled (Figs 4a and 4b). For both profiles, it was assumed that an unintentional diffusion (Gaussian profile) of p-type (4a) or n-type (4b) atoms was present in the InGaAs absorber in addition to the background density of n-type atoms ($1 \times 10^{15} \text{cm}^{-3}$). Simulations are then performed to determine the capacitance of these structures under low- and high-level illumina-

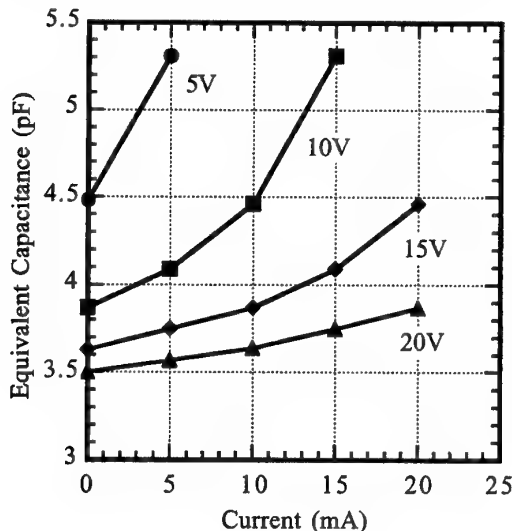


Figure 2. Equivalent capacitance for a 300 μm diameter PD under illumination.

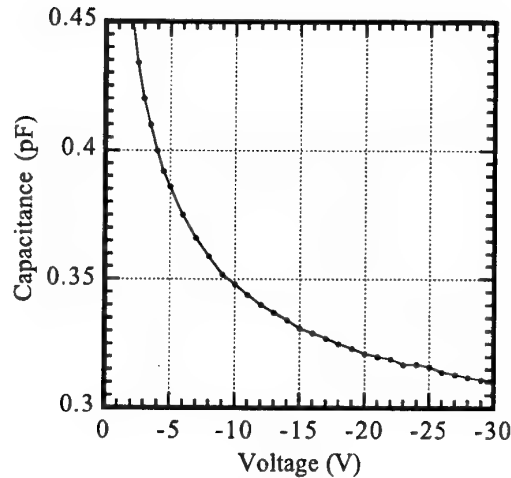


Figure 3. Capacitance-Voltage measurements for a 75- μm diameter photodiode under dark conditions.

tion.

The charge location within the p-i-n structure is calculated using a drift-diffusion simulation [5,10,14] program. The differential capacitance is calculated using $C = dQ/dV$ (definition of capacity), where dQ is the change in charge for a given change in voltage, dV . Figure 5 shows the calculated capacitance under dark conditions for both n-type and p-type i-region doping profiles (from Fig. 4). Note how the trend in capacitance at higher voltages is similar to the CV measurements (Fig. 3) for this PD.

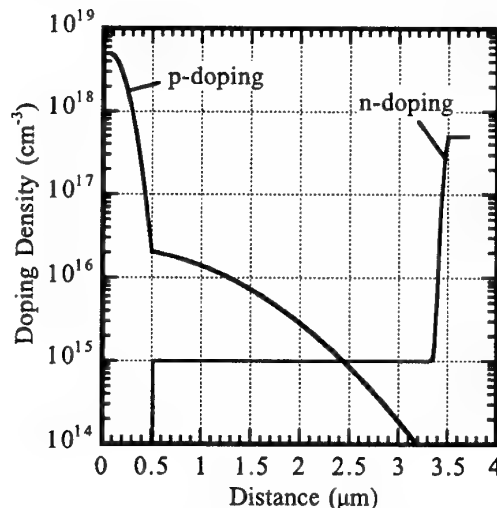


Figure 4a. Modeled doping profile for a p-i-n PD with an unintentional p-type intrinsic region diffusion.

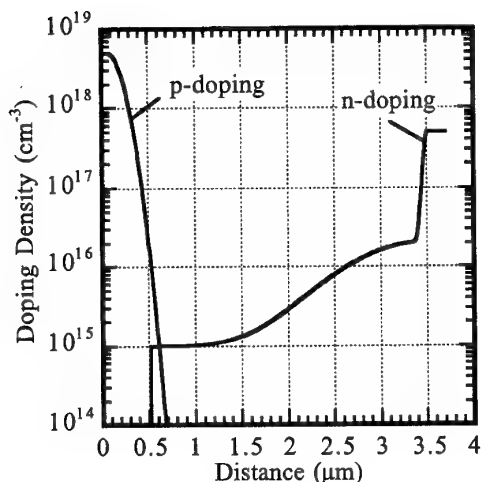


Figure 4b. Modeled doping profile for a p-i-n PD with an unintentional n-type intrinsic region diffusion.

The model is also used to calculate capacitance under uniform illumination conditions and 10 V bias (Fig. 6). Note how the capacitance increases substantially for the n-type diffusion (25%) while for the p-type diffusion, the capacitance peaks before decreasing slightly. A decrease in capacitance would result in an increase in PD RF responsivity and bandwidth. This has been observed in several different PDs [14] where a slight current-dependent increase in RF (not DC) responsivity was measured.

Determining the cause for the increase in capacitance for the unintentional n-type diffusion PD requires a detailed look at the carrier densities within the i-region. Figure 7 shows the calculated electron and hole densities under dark conditions and at 20 mA. Note that under illumination there is an increase in the minority (hole) density in the undepleted InGaAs region (2.6 to 3.5 μm). Minority carrier build-up in this region adds a capacitive term to the overall capacitance which is similar to the diffusion capacitance for a p-n junction under forward bias. Recall that the diffusion capacitance in a p-n junction is the result of minority carrier injection into the quasi-neutral base region of the diode, which varies exponentially with applied voltage. The voltage dependence of the minority carrier build-up in our case does not vary as rapidly with applied voltage (it is more a function of illumination) and thus this term is expected to be less than the diffusion capacitance for p-n junctions. In addition to the hole build-up, the depletion region width is changing slightly. Figure 8 is an expanded view of the n-

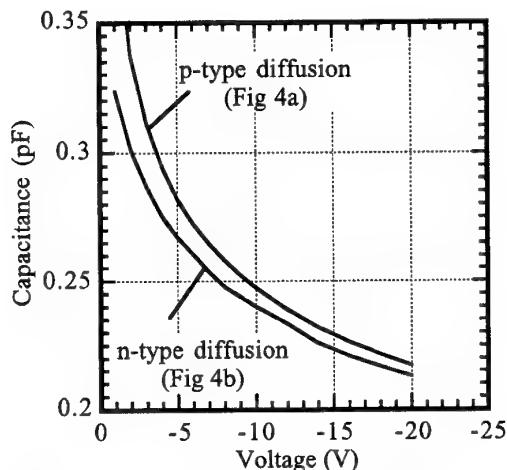


Figure 5. Capacitance calculations for the 75- μm diameter PD doping profiles shown in Fig. 4 under dark conditions.

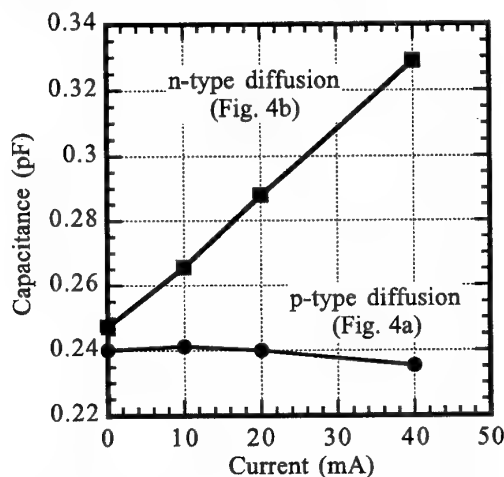


Figure 6. Calculated capacitance for a 75- μm diameter PD under uniform illumination and 10 V bias.

side depletion region edge where it can be seen that the depletion region width is **widening** under high illumination. If capacitance were strictly proportional to Area/distance (A/d), this would suggest that the capacitance were decreasing under illumination and not increasing. However, the capacitance is not strictly A/d when space-charge, nonlinear electron velocity-field relationships, and minority carriers are included in the dQ/dV calculation. Further analysis of these effects will be discussed at the conference.

In conclusion, we have made measurements and simulations to characterize the nonlinear

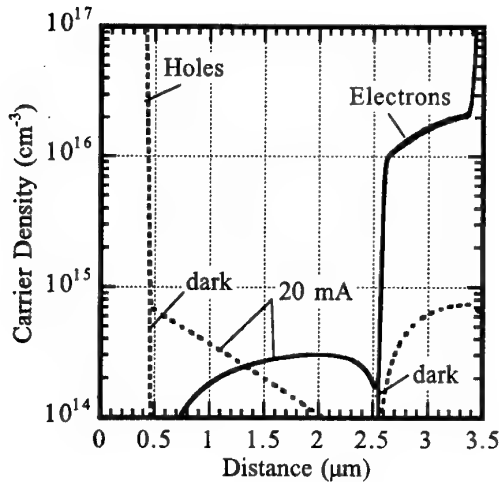


Figure 7. Calculated hole and electron densities under dark conditions and 20 mA uniform illumination. The applied voltage is 10 V.

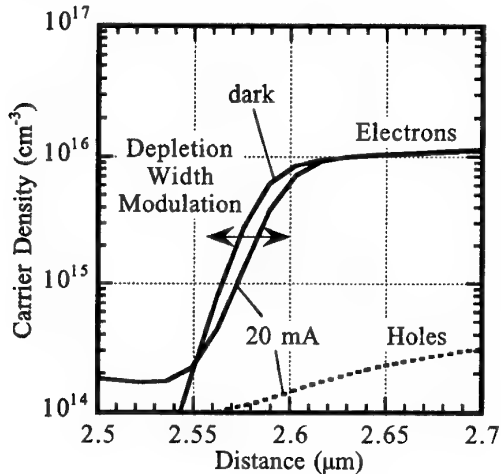


Figure 8. Calculated hole and electron densities near the n-side depletion region edge under dark conditions and 20 mA uniform illumination. The applied voltage is 10 V.

capacitance behavior in p-i-n photodetectors. It appears that an unintentional n-type diffusion into an otherwise depleted absorber can cause the total photodiode capacitance to increase substantially for even moderate current levels. This nonlinear capacitance is shown to dominate the compression behavior in these photodetectors.

This research was supported by the Office of Naval Research.

References

- [1] K.J. Williams, R.D. Esman, and M. Dagenais, "Effects of High Space-Charge Fields on the Response of Microwave Photodetectors," *IEEE Photonics Tech. Lett.*, vol. 6, no. 5, pp. 639, 1994.
- [2] G.A. Davis, R.E. Weiss, R.A. LaRue, K.J. Williams and R.D. Esman, "A 920-1650 nm High-Current Photodetector," *IEEE Photon. Tech. Lett.*, vol. 8, pp. 1373-1375, 1996.
- [3] J. Paslaski, P.C. Chen, J.S. Chen, C.M. Gee, and N. Bar-Chaim, "High-Power Microwave Photodiode for Improving Performance of RF Fiber Optic Links," *Proc. SPIE, Photonics and Radio Frequency*, Vol. 2844, 1996 Denver CO, pp. 110-119.
- [4] N. Shimizu, N. Watanabe, T. Furuta, and T. Ishibashi, "InP-InGaAs Uni-Traveling-Carrier Photodiode With Improved 3-dB Bandwidth of Over 150 GHz," *IEEE Photon. Tech. Lett.*, vol. 10, no. 3, pp. 412-414, 1998.
- [5] K.J. Williams, R.D. Esman, R.B. Wilson, and J.D. Kulick, "Differences in p-side and n-side Illuminated p-i-n Photodiode Nonlinearities," *IEEE Photon. Tech. Lett.*, v. 10, no. 1, pp. 132-135, 1998.
- [6] A.R. Williams, A.L. Kellner, and P.K.L. Yu, "High Frequency Saturation Measurements of an InGaAs/InP Waveguide Photodetector," *Electronics Lett.*, vol. 29, no. 14, pp. 1298-1299, 1993.
- [7] S. Jasmin, N. Vodjdani, J-C. Renaud, and A. Enard, "Diluted- and Distributed-Absorption Microwave Waveguide Photodiodes for High Efficiency and High Power," *IEEE Trans. Microwave Theory and Tech.*, vol. 45, no. 8, pp. 1337-1341, 1997.
- [8] V.M. Hietala, G.A. Vawter, T.M. Brennan, and B.E. Hammons, "Traveling-Wave Photodetectors for High-Power, Large-Bandwidth Applications," *IEEE Trans. Microwave Theory and Tech.*, vol. 43, no. 9, pp. 2291-2298, 1995.
- [9] K.S. Giboney, M.J.W. Rodwell, and J.E. Bowers, "Traveling-Wave Photodetector Design and Measurements," *IEEE J. of Selected Topics in Quantum Electronics*, vol. 2, no. 3, pp. 622, 1996.
- [10] K.J. Williams and R.D. Esman, "Design Consideration for High Current Photodetectors," *IEEE J. of Lightwave Tech.*, vol. 17, no. 8, p. 1443, 1999.
- [11] J.E. Viallet, S. Mottet, L. Le Bjerou and C. Boisrobert, "Photodiode for Coherent Detection: Modeling and Experimental Results," *Journal De Physique Colloque C4*, pp. C4-321, 1988.
- [12] H. Jiang and P.K.L. Yu, "Equivalent Circuit Analysis of Harmonic Distortions in Photodiode," *IEEE Photonics Tech. Lett.*, vol. 10, no. 11, pp. 1608-1610, 1998.
- [13] H. Jiang, D.S. Shin, G.L. Li, J.T. Zhu, T.A. Vang and P.K.L. Yu, "Analysis of IP3 of Photodiode using Equivalent Circuit," 1999 *IEEE Microwave Photonics Conference*, Melbourne, Paper T-5.3 pp. 83-85, 1999.
- [14] K.J. Williams and R.D. Esman, "Photodiode DC and Microwave Nonlinearity at High Currents Due to Carrier Recombination Nonlinearities," *IEEE Photonics Tech. Lett.*, vol. 10, no. 7, pp. 1015-1017, 1998.

A 120-GHz Integrated Photonic Transmitter

T. Nagatsuma, A. Hirata, Y. Royter, M. Shinagawa, T. Furuta*, T. Ishibashi*, and H. Ito*

NTT Telecommunications Energy Laboratories,

** NTT Photonics Laboratories,*

3-1 Morinosato Wakamiya, Atsugi, Kanagawa 243-0198, Japan
Tel. +81 46 240 2252, Fax. +81 46 240 4041, e-mail: ngtm@aecl.ntt.co.jp

Abstract — A photonics-based 120-GHz transmitter has been developed. A photodiode, a planar antenna and a silicon lens were integrated to form a compact millimeter-wave (MMW) emitter. The MMW signal emitted from the transmitter has been detected with a waveguide-mounted Schottky diode. The received power exceeded 100 μW , which is the highest value ever reported for photonic MMW transmitter at frequencies of > 100 GHz.

I. Introduction

Recently, there has been an increasing interest in developing photonics-assisted microwave and millimeter-wave (MMW) generators, where optical microwave and MMW signals are converted to electrical ones with ultrafast optical-to-electrical converters such as photodiodes and photoconductors. In particular, use of 1.55- μm -wavelength-based photonic technology is essential for the application to RF-front-ends in fiber-optic links, fiber-remoting phased array antennas and MMW instrumentation [1-4]. Moreover, most recent progress in wide-bandwidth and high-power photodiodes has made it more realistic to replace conventional purely electronic microwave and MMW generators with those based on photonic technologies, since generation and transmission of MMWs become more difficult as frequencies increase.

In this paper, we demonstrate for the first time generation and transmission of > 100-GHz MMWs based on 1.55- μm photonic techniques. First, the configuration of our fiber-optic transmitter is described. Next, the output-power characteristics of the uni-travelling-carrier photodiode (UTC-PD) chip [5] are measured at 120 GHz. Then, the UTC-PD is integrated with

a slot-antenna made on Si and a Si-lens. Finally, 120-GHz signal from the photonic transmitter is detected with a power of > 100 μW , and used for successful transmission of a video signal.

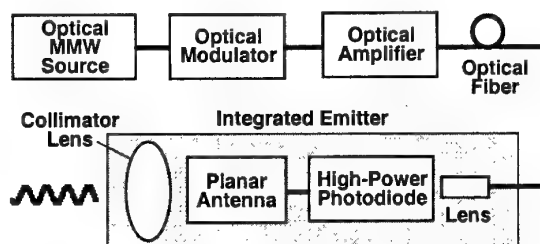


Fig.1. Schematic diagram of millimeter-wave transmitter based on 1.55- μm photonic techniques.

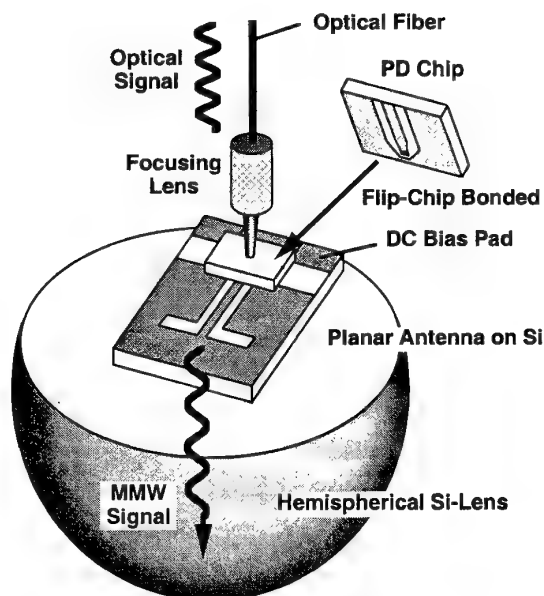


Fig.2. Integrated fiber-optic millimeter-wave emitter.

II. Configuration of photonic transmitter

Figure 1 shows a schematic diagram of millimeter-wave transmitter based on 1.55- μm photonic techniques. Optical MMW signals are generated at specific frequencies and amplified with an optical fiber amplifier.

They are delivered through optical fiber cables to an integrated emitter, where a high-power photodiode, such as UTC-PDs, is integrated with a planar antenna. The configuration of the integrated MMW emitter is shown in Fig. 2. The UTC-PD chip is flip-chip mounted on the antenna made on Si substrate since usual UTC-PDs require backside illumination. The antenna chip is bonded to the hemispherical Si-lens in order to collimate MMW signals in the opposite direction of the optical illumination. This scheme reduces the size of the photonic MMW emitter and simplifies its assembly.

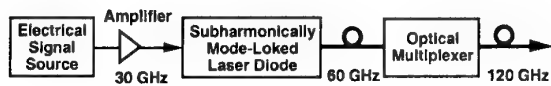


Fig.3. Schematic diagram of the optical 120-GHz millimeter-wave source.

III. Experiment

A. 120-GHz MMW source

Figure 3 shows a schematic diagram of the 120-GHz MMW source used in the experiment. The optical signal is generated with a subharmonically mode-locked laser diode (MLLD) integrated with an electro-absorption modulator [6]. The MLLD is driven at 30 GHz to generate the second harmonic, 60 GHz. The optical signal is frequency-doubled to 120 GHz using optical multiplexer, and boosted with an optical fiber amplifier. Typical pulse width of the optical pulse train is 3-4 ps, and the extinction ratio is > 20 dB when the optical filter is used.

B. Output power from UTC-PD chip

First, we performed an on-wafer measurement of the output power available from the UTC-PD at 120 GHz. The optical MMW signal is focused onto the UTC-PD chip. To detect the MMW signal from the PD, we used GGB Industries' MMW probe, which consists of a coplanar waveguide tip, a coaxial cable, a rectangular

waveguide (WR-10) and a bias-T for the PD. The MMW signal is measured with a calibrated Schottky-diode detector mounted on a rectangular waveguide (WR-8). Taper transition is used to connect the probe and detector waveguides.

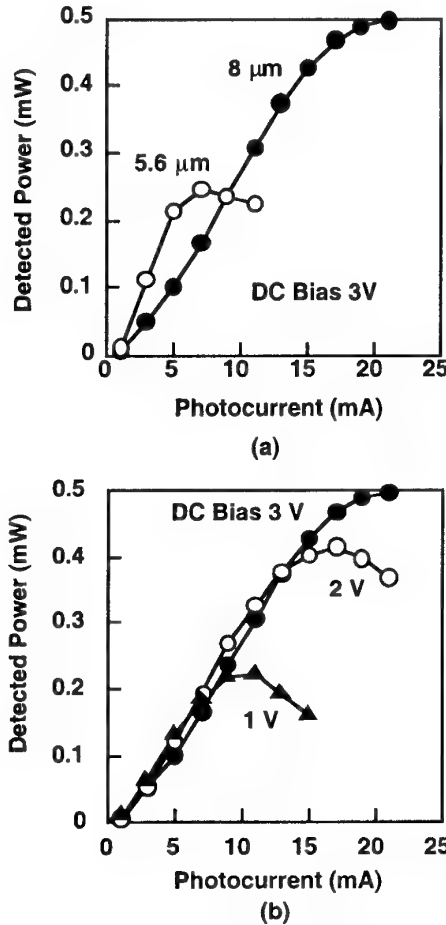


Fig.4. Measured 120-GHz power from the UTC-PD chip using MMW-probe and calibrated Schottky diode detector.

Figure 4 shows the dependence of detected output power at 120 GHz on the DC photocurrent for UTC-PDs of 5.6- μm and 8- μm diameter. Their maximum 3-dB bandwidth, as measured by time-domain pulse response, are 110-115 GHz and 95-100 GHz, respectively. Estimated loss from the pads of the PD chip to the detector is about 3 dB at 120 GHz. So, the actual PD power is higher. The available MMW power is mainly determined by the bandwidth and saturation characteristics of the PD. As shown in Fig. 4(a), the 8- μm diameter PD generates more

power than 5.6- μm one, since its saturation current is much higher. At low power excitation, or low current level, radiation efficiency of the 5.6- μm PD is much higher than 8- μm one due to high bandwidth. As shown in Fig. 4(b), increase of DC bias is effective for lifting up the saturation level at high power excitation. Maximum detected power is 0.5 mW, which indicates that at least 1 mW is generated internal to the UTC-PD chip.

C. Integrated emitter

Photograph of the integrated MMW photonic emitter is depicted in Fig. 5. 120-GHz slot antenna is fabricated with a Si-micromachine process [7]. It is designed and characterized with 3-dimensional electromagnetic simulator and optoelectronic MMW network analyzer [8], respectively. The optimized size of the slot is 774- μm length and 95- μm width [9]. The UTC-PD is mounted to the antenna by a flip-chip bonding. This PD has integrated bias circuitry for externally applying DC voltage. Hemispherical Si lens with a diameter of 10 mm is attached to the antenna chip. From the simulation, > 70-% of the UTC-PD MMW power can be collimated and radiated from the emitter.

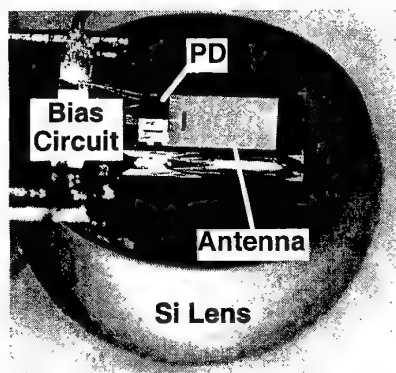


Fig.5. Photograph of the integrated MMW photonic emitter.

D. Transmission experiment

Figure 6 shows a setup for measuring MMW signal from the integrated photonic emitter. Radiated MMW signal is first collimated with a Teflon lens and transmitted in the space. Then, the MMW signal is focused by another Teflon lens to the receiver with a horn antenna. The receiver is an waveguide-mounted Schottky-diode. The power of the received MMW signal is

measured by the calibrated DC voltmeter. In the experiment, we used the 5.6- μm diameter photodiode to show a high-efficiency operation, though the available power is smaller.

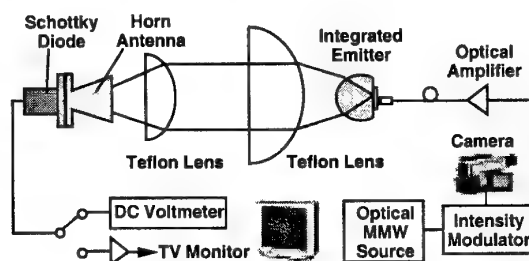


Fig.6. Setup for measuring MMW signal emitted from fiber-optic transmitter.

Dependence of the received power on the photocurrent is plotted as a function of DC bias voltage from 0 to 1.5 V in Fig. 7. The maximum detected MMW power at 120 GHz is 140 μW for a DC bias of as low as 1.5 V, and 15 μW is obtained even for zero-bias operation.

Finally, we applied the video signal from the digital video camera to the optical intensity modulator, and the modulated 120-GHz signal is transmitted and received with the same setup of Fig. 6. The output of the Schottky-diode receiver is amplified and delivered to the video-signal monitor. Even with the zero-bias operating condition, the video signal is successfully demodulated in the TV.

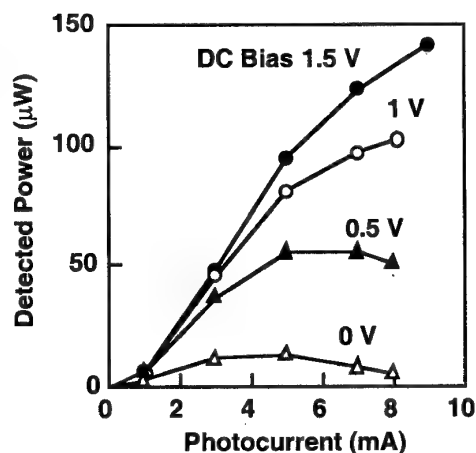


Fig.7. Dependence of detected 120-GHz power on photocurrent of the emitter as a function of DC bias voltage.

IV. Conclusion

We have demonstrated 120-GHz transmitter based on photonic techniques. First, it is shown that the maximum detected power from the UTC-PD is 0.5 mW at 120 GHz, implying that > 1 mW should be generated in the chip. The UTC-PD is integrated with a slot antenna fabricated on Si-substrate, and with a Si-lens. The transmitted 120-GHz signal is received by a Schottky-diode detector. We have obtained > 100 μ W power, even when the photodiode is operated at the battery-operation level of as low as 1-1.5 V.

A video signal is also transmitted and received with 120-GHz MMW signals. These results indicate that the photonics-assisted MMW generation and transmission is possible at frequencies of > 100 GHz for the application in future communication, sensor and measurement systems.

Acknowledgment

The authors would like to thank N. Sahri for the design and characterization of the antenna, K. Sato for the development of the mode-locked laser diode, K. Machida, H. Ishii, S. Yagi, M. Yano, and K. Kudo for the fabrication of the antenna. The authors also express thanks to H. Kyuragi, J. Yamada, S. Mitachi, K. Takeya, and H. Yoshimura for their encouragement and discussion.

References

- [1] C. Cox III, E. Ackerman, R. Helkey, and G. E. Betts, "Techniques and performance of intensity-modulation direct-detection analog optical links," *IEEE Trans. Microwave Theory and Tech.*, vol. 45, pp. 1375-1383, 1997.
- [2] P. J. Matthews, "Practical photonic beamforming," *Tech. Dig. Microwave Photonics 99*, F-11.1, pp. 271-274, 1999.
- [3] T. Nagatsuma, "Progress of instrumentation and measurement toward millimeter-wave photonics," *ibid.*, T-5.5, pp. 91-94, 1999.
- [4] J. M. Payne, B. Shillue, A. Vaccari, *ibid.*, "Photonic techniques for use on the Atacama large millimeter array," T-6.2, pp. 105-108, 1999.
- [5] T. Ishibashi, N. Shimizu, S. Kodama, H. Ito, T. Nagatsuma, and T. Furuta, "Uni-traveling-carrier photodiodes," *Tech. Dig. Ultrafast Electronics and Optoelectronics*, pp. 166-168, 1997.
- [6] K. Sato, I. Kotaka, Y. Kondo, and M. Yamamoto, "Active mode-locking at 50-GHz repetition frequency by half-frequency modulation of monolithic semiconductor lasers integrated with electro-absorption modulators," *Appl. Phys. Lett.*, 69, pp. 2626-2628, 1996.
- [7] H. Ishii, N. Sahri, T. Nagatsuma, K. Machida, K. Saito, S. Yagi, M. Yano, K. Kudo, and H. Kyuragi, "A new fabrication process for low-loss millimeter-wave transmission lines", *Extended Abstract of Intern. Conf. on Solid State Devices and Materials*, A-5-1, pp.126-127, 1999.
- [8] N. Sahri, T. Nagatsuma, T. Furuta, T. Ishibashi, and Y. Umeda, "Integrated millimeter-wave photonic probes for an on-wafer network analyzer," *Tech. Dig. Microwave Photonics 99*, T-5.6, pp. 95-98, 1999.
- [9] A. Hirata, N. Sahri, H. Ishii, K. Machida, S. Yagi, and T. Nagatsuma, "Design and characterization of millimeter-wave antenna for integrated photonic transmitter," submitted to 2000 Asian Pacific Microwave Conf.

Monolithically Integrated Millimeter-Wave Photonic Emitter for 60-GHz Fiber-Radio Applications

Kiyoto Takahata, Yoshifumi Muramoto, Seiji Fukushima,
Tomofumi Furuta, and Hiroshi Ito

NTT Photonics Laboratories

3-1 Morinosato-Wakamiya, Atsugi-shi, Kanagawa-ken, 243-0198 Japan
TEL : +81-46-240-2844, FAX : +81-46-240-4303, E-mail : kiyoto@aecl.ntt.co.jp

Abstract - A uni-traveling-carrier refracting-facet photodiode, a short-stab bias circuit, and a patch antenna were monolithically integrated to make a compact and low-cost millimeter-wave photonic emitter for fiber-radio applications. The device emits the maximum effective radiation power of 17 ± 3 dBm at 60 GHz.

I. Introduction

To meet the rapidly increasing demand for high-bit-rate wireless communication systems, millimeter-wave (MMW) radio has been attracting much interest as the access medium. A fiber radio system is very suitable for such MMW systems not only because fiber has wideband low-loss transmission properties but also because the concentration of modems and controllers in a central station can simplify the antenna base stations [1].

A MMW photonic emitter is one of the key components in base stations. When a conventional p-i-n photodiode (PD) is used as the optical/electrical converter, an electrical high-frequency amplifier is usually needed in order to produce enough MMW power [2, 3]. On the other hand, a high-output-power photodiode makes it possible to construct the MMW photonic emitter without an expensive post amplifier. It has been demonstrated that much higher MMW power can be generated using a uni-traveling-carrier photodiode (UTC-PD) [4, 5], which provides a large 3-dB bandwidth and a high-saturation-output power at the same time. 60-GHz and 40-GHz high-power MMWs have been directly emitted using

UTC-PDs and horn antennas [6, 7]. However, for practical applications, besides the post amplifiers, the costly and bulky external bias-tee circuits and the component interconnections should also be eliminated.

In this paper, we report, to our knowledge, the first monolithically integrated optically-fed MMW photonic emitter consisting of a UTC refracting-facet photodiode (UTC-RFPD) [8], a short-stab bias circuit [5], and a patch antenna. The fabricated device emits 61-GHz MMW with an effective radiation power of 17 ± 3 dBm, which makes it applicable for practical wireless communications.

II. Circuit Design and Device Fabrication

The circuit diagram of the monolithically integrated MMW photonic emitter is shown in Fig. 1. To provide a 3-dB bandwidth large enough for 60-GHz operation, the UTC-RFPD was designed to have a 260-nm thick p-InGaAs

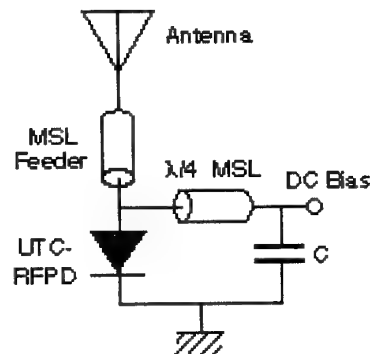


Fig. 1 Circuit diagram of the monolithic millimeter-wave photonic emitter.

photoabsorption layer and a $32\text{-}\mu\text{m}^2$ absorption area. The short-stub bias circuit consists of a $1/4$ -wavelength ($\lambda/4$) microstrip line (MSL) and metal-insulator-metal capacitor [8]. The length of the MSL was designed to be $480\text{ }\mu\text{m}$ for operation at 60 GHz . The $\lambda/4$ MSL bias circuit is better than the widely used spiral inductor for narrow-band applications in terms of device area and process simplicity. The length of the $50\text{-}\Omega$ MSL feeder was set to $\lambda/2$. The 60-GHz patch antenna was designed using a numerical simulator (Agilent Momentum) for a $100\text{-}\mu\text{m}$ thick InP substrate ($\epsilon_r = 12.4$).

The diode epitaxial layers were grown on a semi-insulating InP substrate by low-pressure MOCVD. The fabrication process of the monolithic MMW emitter is almost the same as that of the single UTC-RFPD [7] except for the metalization on the back side for the ground

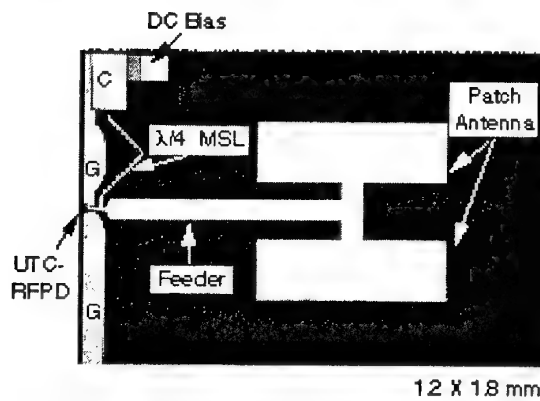


Fig. 2 Photograph of the fabricated monolithic MMW photonic emitter chip.

plane of the microstrip line. Fig. 2 shows a photograph of the fabricated monolithic MMW emitter. The antenna area is $740 \times 656\text{ }\mu\text{m}$ and the chip size is $1.2 \times 1.8\text{ mm}$. The UTC-RFPD has a 3-dB bandwidth of 70 GHz at a DC bias voltage (V_{pd}) of -2 V and a photocurrent of 3 mA and a responsivity of 0.35 A/W for $1.55\text{-}\mu\text{m}$ -wavelength when the incident light is focused on the device through a lensed single-mode fiber.

III. Experiments and Results

The performance of the fabricated photonic emitter was characterized on-wafer using the measurement system shown in Fig. 3. A subcarrier-multiplexing (SCM) light was generated by the carrier suppressed modulation method [9]. A $1.55\text{-}\mu\text{m}$ CW light from a distributed feedback laser diode (DFB-LD) was modulated by a LiNbO₃ Mach-Zehnder (LN-MZ) modulator [10] biased at the transmission null point and driven by an electrical signal with half the desired MMW frequency. The generated 60-GHz SCM light signal with an optical modulation index of over 0.95 was boosted by an EDFA before being focused on the UTC-RFPD. MMW radiation generated by the emitter was transmitted in free space for 0.5 m and received by a horn antenna with a gain of 25 dBi . A spectrum analyzer was used to detect the MMW signal.

Figure 4 shows an electrical spectrum of the received MMW obtained when the LN-MZ was

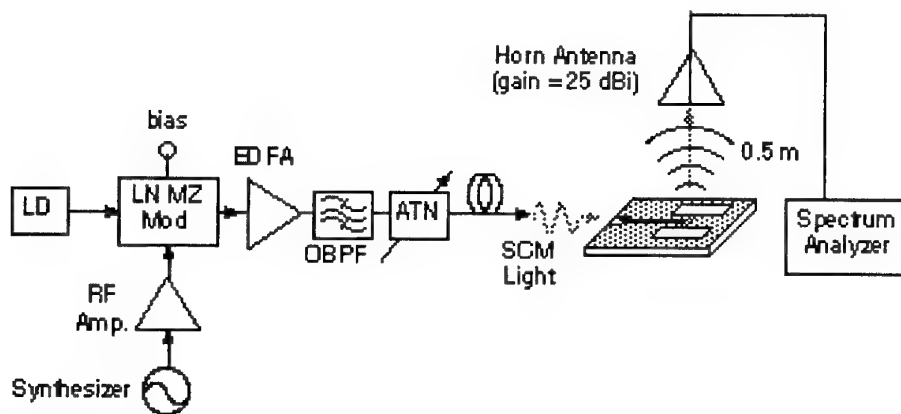


Fig. 3 Experimental setup for measuring MMW signal radiated from the monolithic emitter.

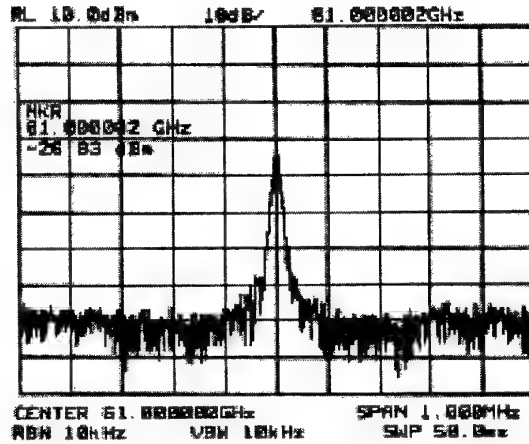


Fig. 4 Measured spectrum for 61-GHz MMW signal.

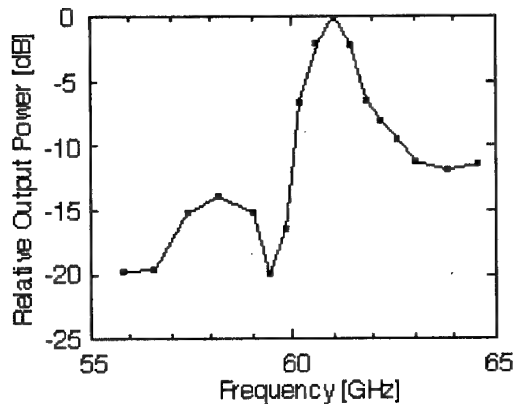


Fig. 5 The MMW output power dependence on the subcarrier frequency.

driven at 30.5 GHz. A sharp 61-GHz MMW signal was observed. Frequency characteristics of the monolithic MMW emitter are shown in Fig. 5. The frequency of the SCM light was varied while keeping V_{pd} and the average photocurrent at -1.5 V and 4 mA, respectively. The output characteristics show a resonant frequency of 61 GHz and a 3-dB bandwidth of 1 GHz. The sidelobe at around 58 GHz and tail at over 62 GHz is probably mainly caused by the frequency dependence of the matching condition between the UTC-RFPD and the antenna.

Fig. 6 shows the dependence of the received MMW power on the average optical input power at 61 GHz for several V_{pd} 's. Here, the optical input power was changed by a variable

optical attenuator. Calibration for the loss due to waveguide/coaxial adapters and the coaxial cable was made in plotting the data. The saturated power increased from -38 to -24 dBm with increasing V_{pd} from 0 V to ~ 1.5 V. The received power shows a good linearity up to the optical input power of 16 dBm for V_{pd} of ~ 2.5 V. The average photocurrent in this condition could be as high as 14 mA (28 mA_{p-p}) because of the UTC-structure of the PD. The maximum received MMW power of ~ 20.5 dBm was obtained for V_{pd} of ~ 2.5 V at an average optical input power of 17 dBm. Considering the basic transmission loss in free space and the gain of the horn antenna, the corresponding effective radiation power of the device was estimated to be 17 ± 3 dBm including the gain of the patch antenna. This indicates that the MMW power of ~ 50 dBm can be received with an antenna with 25-dBi gain even at a distance of 15 m from the MMW emitter. In Fig. 6, the MMW power in the linear response region obtained at $V_{pd} = 0$ V is 3 dB smaller than those for larger negative bias voltages. This is not due to the change in the intrinsic frequency response of the PD. At $V_{pd} = 0$ V, the diode junction capacitance is somewhat larger, which might result in off-matching with the antenna at 61 GHz and cause the output reduction.

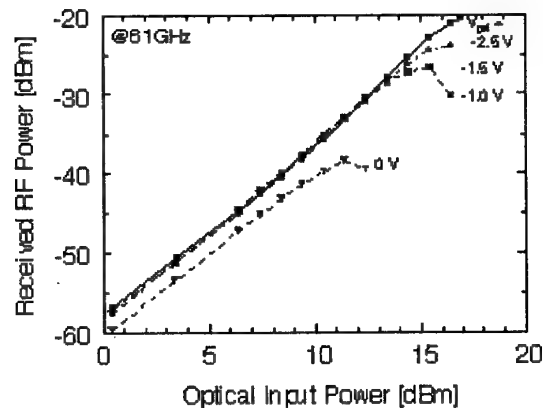


Fig. 6 MMW received power dependence on the optical input power. The emitted MMW was received by the horn antenna with 25-dBi gain after 0.5-m free space transmission.

IV. Conclusion

We have fabricated a monolithically integrated MMW photonic emitter consisting of a UTC-RFPD, a short-stab bias circuit, and a patch antenna for 60 GHz fiber-radio applications. When 61-GHz SCM light was injected into the MMW emitter, the maximum MMW power of -20.5 dBm was received using a horn antenna with 25-dBi gain at a point 0.5-m from the MMW emitter. This indicates that the device has the potential to emit enough MMW power for practical applications. This monolithic device technology enables us to eliminate the electrical high-frequency amplifier and simplify the configuration of the MMW emitter. These merits are very attractive for making compact and low-cost MMW photonic emitter modules.

Acknowledgment

The authors would like to thank Y. Matsuoka and S. Mitachi for their continuous encouragement. We are also grateful to T. Ishibashi for valuable discussions and suggestions throughout this work, K. Yoshino and T. Ohno for their help in experiments, H. Miyazawa for providing the LN-MZ modulator, and S. Iida for technical assistance.

References

- /1/ A. J. Seeds, "Broadband wireless access using millimeter-wave over fibre systems," IEEE Int. Microw. Symp. Dig., vol. 1, TU1B-1, pp. 23-25, 1997.
- /2/ D. Ferling, W. Heinrich, W. Kuebart, G. Luz, and F. Buchali, "Hybrid integrated fibre-amplifier-antenna module for radio applications at 60 GHz," IEEE Int. Microw. Symp. Dig., vol. 1, TU1B-5, pp. 457-460, 1999.
- /3/ D. Wake, L. Noel, D. G. Moodie, D. D. Marcenac, L. D. Westbrook and D. Nessel, "A 60 GHz 120 Mb/s QPSK fibre-radio transmission experiment incorporating an electroabsorption modulator transceiver for a full duplexed optical data path," IEEE Int. Microw. Symp. Dig., vol. 1, TU1B-5, pp. 39-42, 1997.
- /4/ T. Ishibashi, N. Shimizu, S. Kodama, H. Ito, T. Nagatsuma, and T. Furuta, "Uni-traveling-carrier photodiodes," Tech. Dig. Ultrafast Electronics and Optoelectronics, pp. 83-87, 1997.
- /5/ H. Ito, T. Ohno, H. Fushimi, T. Furuta, S. Kodama, and T. Ishibashi, "A 60 GHz high-output-power uni-traveling-carrier photodiodes with an integrated bias circuit," to be printed on Electron. Lett..
- /6/ T. Nagatsuma, N. Sahri, M. Yaita, T. Ishibashi, N. Shimizu, and K. Sato, "All optoelectronic generation and detection of millimeter-wave signals," Tech. Dig. Microwave Photonics, MB1, pp. 5-8, 1998.
- /7/ T. Ohno, S. Fukushima, Y. Dci, Y. Muramoto, and Y. Matsuoka, "Application of uni-traveling-carrier waveguide photodiodes in base stations of a millimeter-wave fiber-radio system," Tech. Dig. Microwave Photonics, F-10.2, pp. 253-256, 1999.
- /8/ H. Fukano, Y. Muramoto, K. Takahata, and Y. Matsuoka, "High efficiency edge-illuminated uni-traveling-carrier-structure refracting-facet photodiode," Electron. Lett., vol. 35, pp. 1164-1165, 1999.
- /9/ J. J. O'Reilly, P. M. Lane, R. Heidemann, and R. Hofstetter, "Optical generation of very narrow linewidth millimeter wave signals," Electron. Lett., vol. 28, pp. 2309-2311, 1992.
- /10/ K. Noguchi, H. Miyazawa, and O. Mitomi, "40-Gbit/s Ti:LiNbO₃ optical modulator with a two-stage electrode," IEICE Trans. Electron., vol. E81-C, No. 8, pp. 1316-1320, 1998.

PHOTONIC MODULES FOR MILLIMETER WAVE COMMUNICATION SYSTEMS

Arthur C. Paoletta, Abhay M. Joshi*, Athena Bauerle

Lockheed Martin Communications & Power Center, 100 Campus Drive, Newtown, PA 18940, USA
Tel: (215) 497-1372, Fax: (215) 497-1370, E-mail: arthur.c.paoletta@lmco.com

*Discovery Semiconductors, Inc., 186 Route 571, Bldg. 3A, Princeton Jct, NJ 08550, USA
Tel: (609) 275-0011, Fax: (609) 275-4848, E-mail: Abhay@chipsat.com

1. Introduction

Photonics for phased array antennas and hybrid / fiber millimeter wave communication systems are being considered. For these systems to be cost effective the integration of photonics with millimeter wave components in a single module that can operate up to Q/V-Band is recommended. To accomplish this high level of integration, opto-electronic monolithic integrated circuits (OEICs) must be developed and housed in low-cost packaging incorporated with antennas.

2. Photoreceivers for millimeter wave systems

The first step in the development path is to demonstrate a high performance photodetector, then integrate it with MMIC amplifiers to form a photoreceiver module. To accomplish this, a new 65 GHz "Dual Depletion, InGaAs/InP Photodetector" was designed, fabricated and tested. A menu-driven program in Visual Basic was compiled which accurately predicts the bandwidth of the InGaAs PIN diode vis-a-vis its transit time, RC time constant, and the effect of packaging parasitics.

For accurate verification of the computer simulation model, several packaged 50 GHz microwave InGaAs PIN diodes were assembled and the experimental results of the bandwidth (any observed resonance and ripple factor) were compared to the computer model. A frequency response of the packaged 10 μ m diameter, fiber pigtailed, microwave InGaAs

PIN diode is shown in Figure 1. From the above frequency response plot it is clear that the ripple factor is less than ± 1 dB for a wide band of frequencies, DC to 50 GHz, which compares with the model. The accurate high frequency InGaAs PIN computer model developed has vastly improved the performance of available microwave InGaAs PIN diodes.

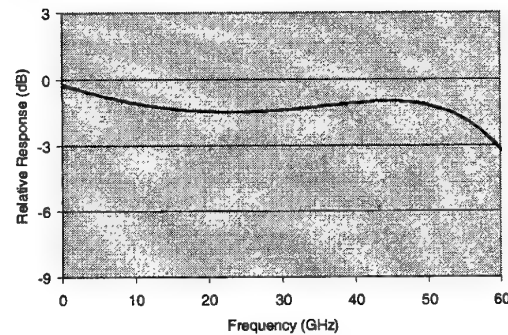


Figure 1. Frequency response of InGaAs co-planar waveguide output microwave PIN diode

Combining these photodetectors with MMICs to form photoreceivers will reduce packaging costs. A photoreceiver module was built using a 40 μ m photodetector, a transimpedance pre-amplifier, and a distributed amplifier. When used as a post photodetector amplifier in high data rate applications, the distributed amplifier has the potential of lower noise when compared to a common source amplifier [1]. The packaged photoreceiver and the frequency response are shown in Figure 2a and Figure 2b, respectively. The next development step is to combine these functions into a single OEIC.



Figure 2a. Packaged photoreceiver

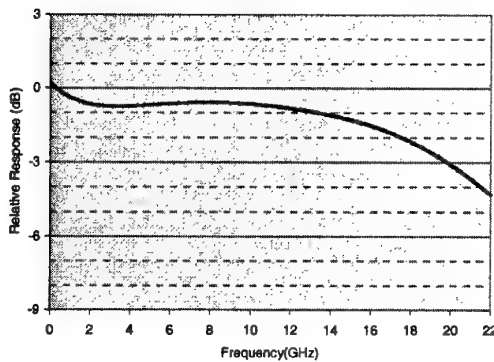


Figure 2b. Frequency response of photoreceiver having 1000 V/W conversion gain at 1.55 micrometer and 30 dB power gain

3. Millimeter Wave Photonic Multi-level Module

As the operating frequency of phased array systems approaches beyond 20 GHz, the antenna size approaches the size of the MMICs. Hence, 'single-layer planar techniques cannot be implemented due to the large module footprint. The most advantageous way to maintain a footprint compatible with Ka-band and higher frequency systems is to reduce the size of the microwave photonics through monolithic integration, and package the modules using commercial multi-level techniques.

A first generation multi-level module was developed consisting of two levels as shown in Figure 3a to demonstrate the concept [2]. The antenna level consists of four planar patch elements. The patch design is $0.49\lambda_g$ by

$0.49\lambda_g$ and the spacing is $0.5\lambda_o$. The antenna dimension is 1.174 by 1.174 sq. mm on a substrate with ϵ_r of 9.8. The transmitter level consists of photodetector and amplifiers. The medium power amplifier selected for the demonstration has 22 dB of gain at 40 GHz. The module was fed by a fiber carrying a millimeter wave signal. The radiated energy was measured as a function of frequency as shown in Figure 3b.

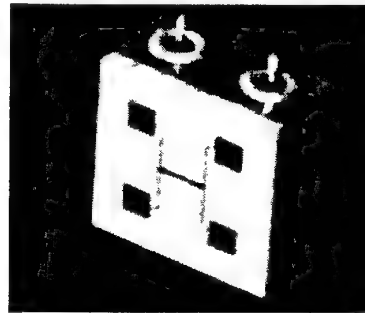


Figure 3a. Millimeter wave photonic module concept (The module dimensions are 7.5 mm x 7.5 mm)

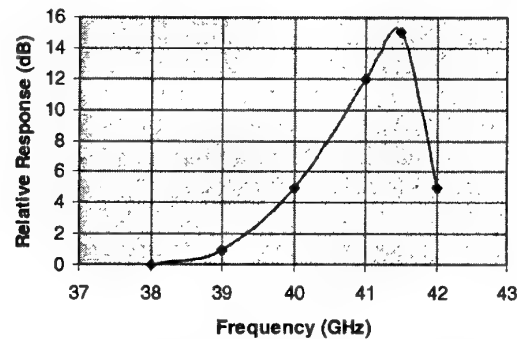


Figure 3b. Measured radiation power of the module as a function of optical modulation frequency

To make these modules cost effective for optically controlled phased arrays, an OEIC has been developed as shown in Figure 4 and a multi-level module that can be manufactured in a high volume batch fabrication process at Ka-Band is shown in Figure 5. The second-generation module is a multi-layer structure utilizing an enhanced circuit processing technique that combines the low cost of thick film technology with the high-resolution etching of thin film technology.

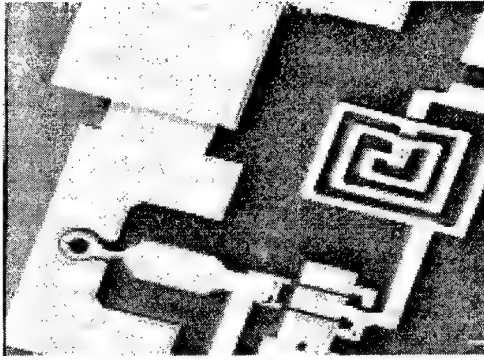


Figure 4. An OEIC consisting of a photodetector and amplifier sections

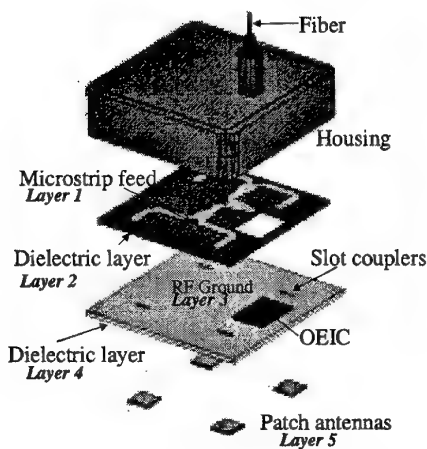


Figure 5. Millimeter wave photonic module for high volume batch fabrication

The layer structure is depicted in Figure 5 and dimensioned in Table 1. The multi-layer module is 11.9 mm square and consists of the microstrip circuit, feed structure, and antenna array. The module uses a planar patch antenna array (Layer 5) to produce a directional radiation pattern. A slot coupler (Layer 3) feeds each patch in the array. The couplers are in turn fed by a microstrip feed network on low loss dielectric containing microstrip power dividers (Layer 1). A 5 mil thick BeO substrate (Layer 4) provides good thermal conductivity to the OEIC and support for the patch antenna. A Kovar housing is brazed onto Layer 3, providing a good RF ground and support for the fiber optic cable and DC power. Since the housing is brazed, the module can be made hermetic.

Table 1. Module layer structure

Layer	Material	Function
1	Gold	Microstrip feed
2	Dielectric	Microstrip circuit
3	Gold	RF ground, Slot couplers
4	Dielectric	Heat sink
5	Gold	Patch antenna

The patch antennas are arrayed in a 2-by-2 configuration having a pitch of $0.8 \lambda_0$, optimizing for module size while maintaining low sidelobe levels. The fields in the microstrip transmission line feed are perturbed by the coupling slot on the ground plane, creating surface currents on the slot which radiate through the dielectric and are directed by the patch as shown in Figure 6. The antenna dimensions and simulated results are given in Table 2. The multi-level microstrip feed, slot and antenna structure is optimized using an electromagnetic simulator, considering ohmic loss, dielectric loss, radiation loss, and surface wave loss. The radiation pattern, in Figure 7, shows the gain is 9.0 dB and the sidelobes are down greater than 10 dB from the main beam.

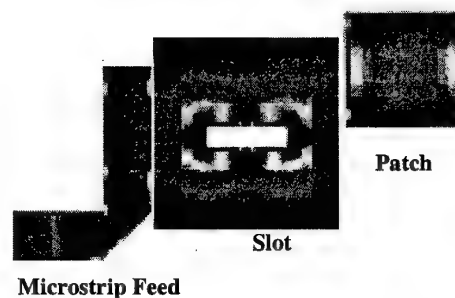


Figure 6. Current density of the multi-level antenna structure

Table 2. Antenna design parameters

Parameter	Dimension (mm)
Slot width	0.20
Slot Length	0.85
Patch Size	1.13
TL width	0.26
Predicted Gain	9.5 dB
Predicted S11	-19.5 dB

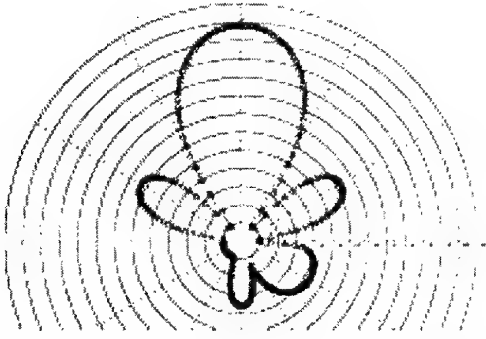


Figure 7. Simulated radiation pattern of the four-element planar patch array at 40 GHz

6. References

1. Aitchison, C., *Electronic Letters*, Vol. 26, No. 20, Sept. 1990.
2. Paoella, A., Joshi, A., Wright, J., Coryell, L., *SPIE Digest*, Vol. 3463, July 1998.
3. Joshi, A., Paoella, A., Mohr, D., Wang, X., "InGaAs/InP based multi-level photonic modules for millimeter wave phased array antennas," Final Report CECOM-TR-98-A504-f, January 2000.

4. Conclusions

Photodetectors with > 50 GHz bandwidths have been developed using a new modeling software. This photodetector technology is used in an initial development of an OEIC. The demonstration of a first generation photonic module was performed using these photodetectors. This work was supported under a Phase I and Phase II Small Business Innovation Research (SBIR) program [3] to demonstrate a multi-level photonic module in a fully monolithic form using advanced packaging techniques with a goal toward cost reduction.

5. Acknowledgements

The authors would like to thank the support of the James Wright and Louis Coryell, US Army CECOM, Ft. Monmouth NJ.

HIGH TEMPERATURE SUPERCONDUCTING MM-WAVE PHOTOMIXERS.

C.J.Stevens¹ & D.J.Edwards²

Oxford University, Department of Engineering Science, Parks Road, Oxford, OX1 3PJ, UK

¹Tel:+44 (0)1865 283272, Fax: +44 (0)1865 273905, christopher.stevens@eng.ox.ac.uk

²Tel:+44 (0)1865 273915, Fax: +44 (0)1865 273905, david.edwards@eng.ox.ac.uk

Introduction

Superconducting mixers are among the most sensitive detectors of radiation built to date. They are becoming widely used in astronomy and remote sensing in the mm and sub-mm wave regions [1]. High T_c superconducting devices are under investigation by a number of laboratories for future instruments and space missions. In particular superconducting hot-electron bolometer mixers are being developed for THz detection [2]. In order to best make use of these devices a compact source of local oscillator signals is vital, and continues to be the subject of considerable research around the world.

Optoelectronic control of mm-wave and potentially of sub-mm wave local oscillator signals for these devices is a very versatile technology which allows the integration of a large number of telescopes into a single coherent receiver [3]. Current approaches to this use fast photodetectors to convert optical signals to electrical signals which are then applied to the mixer devices. As a simple rule of thumb approximately 1 μ W of RF power is required for each superconducting mixer compared to ~1mW for Schottky diode mixers [7].

The subject of this paper is the development of high temperature superconducting devices which are both mixer and fast photodetector in order to realize the direct mixing of electrical and optical signals without the need for a the intermediate optical to electrical conversion stage.

The HTSC photoresponse.

Ultrafast optical spectroscopy [4] and optoelectronic measurements [5] have shown that high temperature superconductors exhibit a very fast sub-picosecond response to optical excitation. In simple current biased microbridges ($\sim 5 \times 10 \mu\text{m}$) two distinct photoresponses were discovered which result in quite different voltage waveforms. Close to T_c a simple *bolometric* signal is observed which converts the rise in electron temperature into a change in the resistance of the device. Somewhat below T_c , where resistance is insignificant, another signal was observed with a very different temporal characteristic which has been identified with the changes in the *kinetic inductance* of the superconductor. The kinetic inductance (referring to the energy stored in the motion of charge carrying particles) is an insignificant contribution to a normal conductor (in comparison to its resistance), but in the case of a superconductor it can be a large contribution to the RF response [6]. In the case of a photoresponse the rapid drop in the density of superconducting charge carriers results in a voltage as the remaining particles accelerate to maintain current continuity. The accelerating voltage arises from the pile up of carriers outside the excited region immediately after the excitation. This response is particularly interesting from the perspective of our work as it produces a fast signal at low temperatures which increases in strength with increasing frequency.

A simple physical model [8] of the response is based on thermal rate equations. Initial photoexcitation of electrons rapidly

(<100fs) produces a hot thermal population of electrons which subsequently relaxes by scattering with phonons and superconducting particles when present. Two rate equations are used to model the cooling of the electrons and the phonons with time constants determined from the literature and ultrafast optical measurements.

$$C_e \frac{dT_e}{dt} = \frac{\alpha P(t)}{V} - \frac{C_e}{\tau_{eph}} (T_e - T_p) \quad (1)$$

$$C_p \frac{dT_p}{dt} = \frac{C_p}{\tau_{phe}} (T_e - T_p) - \frac{C_p}{\tau_{es}} (T_p - T_s) \quad (2)$$

The heat capacities C_e and C_p refer to the electronic and lattice contributions to the total heat capacity.

This model assumes an instantaneous photoexcitation in which the excited particles immediately achieve a thermal distribution. In reality the process of electron-electron scattering which converts photoexcited carriers into a hot thermal population takes some time (~ 50fs) This ultimately limits the range over which the model may be usefully employed. Solving equations 1 and 2 using a modulated optical excitation corresponding to the beat signal between two slightly detuned lasers results in closed form expressions for the electron and lattice temperatures respectively.

$$T_e = T_s + \frac{\varepsilon}{B} \left(1 + \frac{\tau_{phe}}{\tau_{es}} \right) + \varepsilon e^{j\omega t} \left\{ \frac{\left(1 + \frac{\tau_{phe}}{\tau_{es}} \right) + j\omega \tau_{phe}}{(B - \omega^2) + jA\omega} \right\} \quad (3)$$

$$T_p = T_s + \frac{\varepsilon}{B} + \varepsilon e^{j\omega t} \left\{ \frac{1}{(B - \omega^2) + jA\omega} \right\} \quad (4)$$

$$\varepsilon = \frac{\alpha P}{2C_e V \tau_{phe}}, A = \frac{1}{\tau_{es}} + C_p \frac{\tau_{phe} \left(1 + \frac{C_e}{C_p} \right)}{\tau_{phe}^2 C_e}$$

$$B = C_p \frac{1}{\tau_{es} \tau_{phe} C_e}$$

Where P is the optical power incident, τ_{es} is the phonon escape time, τ_{phe} is the phonon-electron scattering time, V the excited volume, α the efficiency of light absorption (~0.8). The bolometric signal (V_{bol}) and kinetic inductance signal (V_{kin}) from the device are given by:

$$V_{bol} = I_{DC} \frac{dR}{dT} T_e(t) - T - T_c \quad (5)$$

$$V_{kin} = I_{DC} \frac{l}{w d \varepsilon_0 \omega_p^2} \frac{2T_e}{\left(1 - \frac{T_e^2}{T_c^2} \right)} \frac{dT_e}{dt} - T < T_c \quad (6)$$

where ω_p is the Drude plasma frequency, the device is of dimensions $l \times w \times d$, ε_0 is the dielectric permittivity of free space, and T_c is the critical temperature of the superconductor. It is important to note that the expression of V_{kin} is only valid for $T < T_c$. Figure 1 shows the response curves described by the above with constants extracted from the literature and from ultrafast optical measurements.

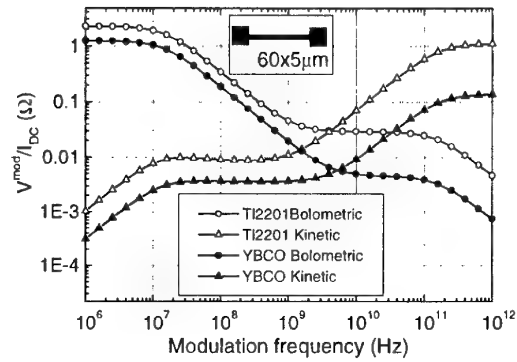


Figure 1: Calculated signals from a 60x5 micron bridge excited using 1mW laser power at 10mA drive current for TI2201 and YBCO.

The data show curves for two materials, YBCO ($\text{YBa}_2\text{Ca}_3\text{Cu}_{6.95}$) and TI2201 ($\text{Ti}_2\text{Ba}_2\text{CuO}_6$) assuming 1mW optical power and 10mA bias current set at the temperature for maximum responsivity. Clearly TI2201 is likely to be a better material for this device, due largely to its much lower electronic heat capacity [$C_e(\text{TI2201}):C_e(\text{YBCO})=1/37$]. The rise in the strength of the kinetic inductance response at high frequencies is caused by the sensitivity to the rate of change in the electron temperature (T_e) rather than T_e itself. At the high end, close to 1THz we expect a rapid fall off in the response as the limiting time to form a thermal electron population begins to limit the electron temperature modulation. The data from optical spectroscopy suggests that this limit is reached above ~1.5THz.

Experimental

Our initial work has focussed on low temperature testing of the model using simple YBCO devices (for which better quality samples are presently available). The samples were obtained from THEVA GmbH and consisted of 100nm of YBCO grown on SrTiO_3 and MgO. The films were patterned using optical lithography via Shipley S1805 photoresist. The device structures tested were 25 micron square bridges located at one end of a gold microstrip waveguide, with a 1mm bond pad forming the earth connection. This microstrip was bonded to an SMA microstrip launcher. Semi rigid coaxial cables were used to connect the device in a cold finger cryostat via a bias T to an RF spectrum analyzer. The samples were biased using Keithley 2400 source measure unit, and a low frequency responsivity was measured using a lockin amplifier. The modulated optical excitation was provided by two 1.53 μm DFB lasers which were temperature and current controlled to provide a tuneable beat frequency from 100MHz to >20GHz (upper limit imposed by the spectrum analyzer, the laser can achieve difference frequencies of >1THz). The maximum useful optical power provided by these lasers was 3mW at the device. Figure 2 shows a simple schematic of the test system.

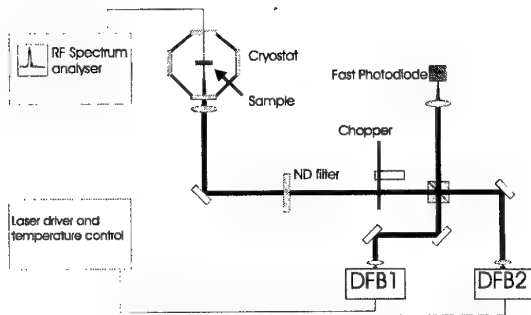


Figure 2: Optical heterodyne test experiment used to measure low frequency signal generation in HTSC devices.

Figure 3 shows an optical micrograph of an YBCO device fabricated as described above. The microstrip line is designed to achieve 50 Ω impedance. The microbridge is 25 microns wide by 30 microns long. The microstrip and

contact pad are evaporated gold patterned using a lift off technique.

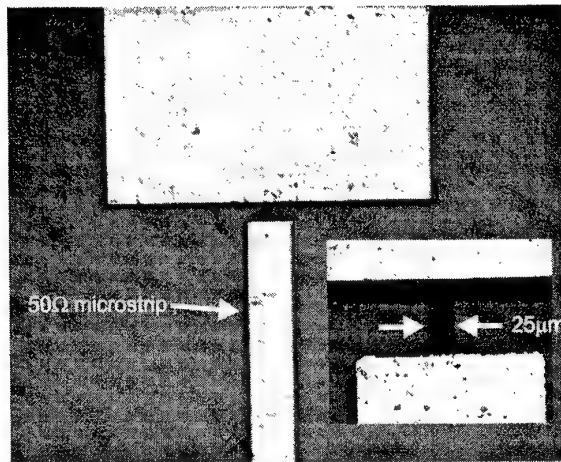


Figure 3. The YBCO microstrip device showing the waveguide and the microbridge dimensions.

Tests were performed by keeping the cryostat at its base temperature of 78K and then biasing the device until its resistance begins to return at which point dR/dT is maximised. At 15mA this resulted in a low frequency response of approximately 10mV from a 1mW optical excitation.

Using the spectrum analyser the output signal from the device was recorded while current tuning one of the two DFB lasers (tuning rate 1.3GHz/mA). Figure 4 shows the results.

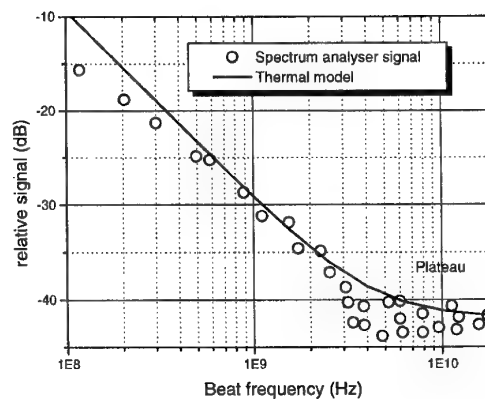


Figure 4. Output signals from the YBCO photomixer compared to the results of the hot electron model assuming coupling to a 50 Ω load.

The fitted line is from the thermal model using the known constants for YBCO with a scaling factor to account for the unknown losses in the waveguide to coaxial transition. The model fit assumes a 50Ω load coupled to the device. The data has been corrected for the losses of the bias T network. At around -40dB the signal shows a flat plateau although this is very close to the noise floor of the equipment. Clearly the plateau present in the model is also shown in the data which implies a nearly flat response up to frequencies of 100GHz and beyond. The present experiment is not able to measure above 18GHz , but future measurements will use quasi-optical techniques to extend the measurements up to and beyond 300GHz . Further measurements in the low frequency regime ($0\text{-}18\text{GHz}$) are planned in order to test the mixing capabilities of the device using free space coupling of mm wave signals directly to the device.

Conclusion

High Temperature superconducting photomixers have been fabricated using simple lithographic techniques. Their performance matches that expected from a hot electron model. These devices may provide the basis

for optoelectronic phase distribution between receivers for astronomy and remote sensing. They may also bring significant benefits to simplify RF imaging technologies by providing a simple route to integrated, optically driven, phased arrays.

1. e.g. KOSMA telescope specifications – 6th international conference on Space Terahertz technology.
2. C.-T.Li, B.S.Deaver et al. Applied Physics Letters Vol73. No12. P1727
3. A.R.Thompson SPIE Proceedings 1998
4. C.J.Stevens et. al. Phys. Rev. Letters 1997, Vol.78, No.11, pp.2212-2215
5. F.A.Hegmann et. al. Applied Physics Letters, 1995, Vol.67, No.2, pp.285-287
6. A.M.Kadin 'Introduction to Superconducting Circuits' Wiley 1999 p 18.
7. G.Beaudin et. al. NATO ASI – Plenum publishers 1996.
8. N.Perrin et.al. Phys. Rev. B vol 28, p5150 (1983)

Optical Processing of Microwave Signals

(Invited paper)

J. Capmany, D. Pastor, B. Ortega and S. Sales

Optical Communications Group
Departamento de Comunicaciones
Universidad Politécnica de Valencia
Camino de Vera s/n, 46022 Valencia, SPAIN

1 Introduction

The processing of radiofrequency, microwave and millimetre wave signals directly in the optical domain by means of waveguide photonic delay lines offers interesting advantages. Among these, the possibility of overcoming the so called electronic bottleneck arises as a fundamental one. This limitation stems from the fact that the sampling speed required to process these signals increases in direct proportion to the bandwidth of the RF signal to be processed. The current state of the art in electronics limits the sampling speeds of electronic devices to a few Gb/s. Being important, the electronic bottleneck it is by no means the only source of limitation, since electromagnetic interference (EMI) and frequency dependent losses can also be sources of important impairments.

An interesting approach to overcome the above limitations involves the use of optical technology and especially fiber and integrated optics circuits to perform signal processing of RF signals conveyed by an optical carrier directly in the optical domain. We will refer to this as OPRFS¹. This approach is shown figure 1.

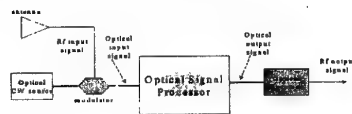


Figure 1

The RF to optical conversion is achieved by direct (or externally) modulating a laser. The RF signal is conveyed by an optical carrier and the composite signal is fed to photonic circuit using optical delay lines for signal processing. At the output/s the resulting signal/s are optical to RF converted by means of an/various optical receiver/s. OPRFS has several advantages: optical

delay lines have very low loss (independent of the RF signal frequency), provide very high time bandwidth products, are immune to EMI, lightweight, can provide very short delays which result in very high speed sampling frequencies (over 100 GHz in comparison with a few GHz with the available electronic technology) and finally but not less important optics provides the possibility of spatial and wavelength parallelism using WDM techniques.

A fundamental distinction must be made on the OPRFS operation regime in terms of the relationship between the coherence time τ_c of the optical transmitter and the basic delay T (time between adjacent temporal samples provided by the structure). If $\tau_c \gg T$ then the processor is said to work under *coherent* regime and its transfer function is linear in terms of the electric field thus depending on the optical phase shifts experienced by the carrier that conveys the RF signals. These are highly dependent on environmental parameters (i.e temperature, ..) and polarization, making their implementation quite difficult under realistic conditions. On the contrary, if $\tau_c \ll T$ the signal processor works under *incoherent* regime and the overall structure transfer function is linear in terms of the optical intensity (i.e power) and the effect of optical phase shifts can be discarded. Although work has been reported on both operation regimes, the majority of contributions focus on incoherent operation, since it is more prone to practical implementation.

This paper aims to review the fundamental concepts, limitations, technologies and major milestones in RF filtering applications of OPRFS. Research contributions within this area extend over the last 25 years.

2. Historical Background

The origin of fiber delay line signal processing can be traced in the seminal paper of Wilner and Van de Heuvel [1] who noted that the low loss and high modulation bandwidth of optical fibers made them suitable for broadband signal processing. Several contributions during the 70s addressed experimental work on OPRFS using

¹ OPRFS: Optical Processing of Radio Frequency Signals

multimode fibers. An intensive theoretical and experimental research work on incoherent OPRFS using singlemode fiber delay lines was carried by researchers at the University of Stanford during the period between 1980 and 1990. Multiple configurations, applications and potential limitations of these structures were considered and the main results of it can be found summarised in [2]-[3]. The technology status regarding optical fiber and integrated components was at the time at its infancy and therefore the OPRFS demonstrated had serious limitations arising from losses and lack of reconfiguration.

The advent of the optical amplifier at the end of the 80s and the development of optical components (variable couplers, modulators, electrooptic switches) and specific purpose instrumentation fueled the activity towards more flexible structures employing these components [4]-[6]. Most of these contributions present filters that still rely on the implementation of time delays by means of fiber strands. Yet, the availability of a novel component, the fiber Bragg grating has opened a new perspective towards the implementation of OPRFSs using this component which can lead to fully reconfigurable and tunable filters [7]-[10]

3 Fundamental Concepts and Limitations

Any filter implemented using OPRFS tries to provide a system function for the RF signal given by:

$$H(z^{-1}) = \frac{\sum_{r=0}^N a_r z^{-r}}{1 - \sum_{k=1}^M b_k z^{-k}} \quad (1)$$

where z^{-1} represents the basic delay between samples. The numerator represents the finite impulse part (i.e non recursive or FIR) of the system function, whereas the denominator accounts for the infinite impulse part (i.e. recursive or IIR) of the system function. N and M stand for the order of the FIR and IIR parts respectively. If $b_k=0$ for all k, the filter is non-recursive and is also known as transversal filter. Otherwise the filter is recursive and it is common to use the term recirculating delay line. Figure 2 illustrates how (1) is implemented for the specific case of an N-order transversal² incoherent filter

² The implementation of a recursive filter is similar but is not considered here due to space restrictions.

using a single optical source. Note that the impulse response corresponding to this situation can be directly derived from (1) yielding:

$$h(t) = \sum_{r=0}^N a_r \delta(t - rT) \quad (2)$$

Which convolved with the input RF signal $s_i(t)$ yields the following output signal $s_o(t)$:

$$s_o(t) = \sum_{r=0}^N a_r s_i(t - rT) \quad (3)$$

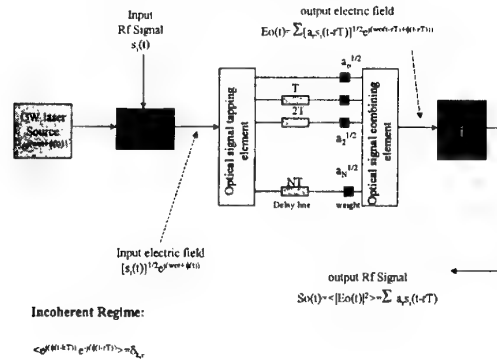


Figure 2

The implementation of the OPRFS requires specific optical components to provide: a) Signal tapping, b) Optical delay lines, c) Optical weights and d) Optical signal combination. 2x2 and 1xN, Nx1 star couplers have been proposed for the implementation of a) and b), variable 2x2 couplers, optical amplifiers (both EDFAs and SOAs), electrooptic and electroabsorption modulators can be used to implement c) Standard, high dispersion singlemode fiber coils and fiber Bragg gratings have been proposed for the implementation of b).

OPRFS must overcome a series of potential limitations prior to their practical realization as pointed out by various researchers. The main limitations arise from source coherence, polarization, positive coefficients, limited Spectral period or FSR (Free Spectral Range, noise: reconfigurability, and tunability.

To date none of the two main approaches that have been followed by most of the research groups throughout the world has been able to address successfully all the above limitations. These main approaches are:

- Implementation of OPRFS using fiber coils as delay lines, single source illumination and signal tapping combination and weighting by means of discrete fiber or integrated optics

components. We will refer to these as FDLFs (Fiber Delay Line Filters)

- b) Implementation of OPRFS using fiber gratings as delay lines and/or weighting elements in conjunction with single or multiple tunable source arrays. We will refer to these as FGDLFs (Fiber Grating Delay Line Filters).

The main activities in FDLFs have been carried during the period 1980-1994, while those of FDLFs have been relevant since 1994 and extend to the present time. In the following we briefly outline the work on FDLFs, focusing more effort in describing the main results obtained in FGDLFs.

4 Fiber Delay Line Filters

Intense research work on passive FDLFs was carried during the period between 1980 and 1990, including the development of special purpose components such as variable 2x2 couplers, star couplers etc. and the experimental demonstration of simple passive structures performing basic signal processing operations such as transversal and notch filtering, correlation, data storage etc [2]-[3]. Both noise and signal analysis methods were developed for these structures. The advent of optical amplifiers (OAs) opened the possibility of overcoming the limitations imposed by the static nature of passive structures both in terms of reconfiguration and loss compensation. The inclusion of OAs provided the structures with enhanced flexibility as sample weighting could be altered. Several contributions proved these advantages both theoretically as well as experimentally [4]-[5]. Synthesis methods were developed and filters with negative coefficients resulting from the application of some of the above methods were experimentally demonstrated. By the middle of the 90s it was thus clear that the main restriction faced by FDLFs was that related to resonance tunability. In 1994 a solution for this problem was proposed by implementing a tunable delay combining of a tunable source and high dispersion fiber delay lines. The concept was extended by Frankel and Esman [6] who demonstrated the implementation of a transversal filter with continuously tunable unit time delays consisting of 8 taps with progressively longer segments of high dispersion fiber, but completed with dispersion-shifted fiber to nominally identical overall lengths. The time delay tuning at each tap was achieved by tuning the wavelength of the optical

carrier. A $Q=30$ bandpass Rf filter tunable over 1 octave was demonstrated.

5 Fiber Grating Delay Line Filters

In 1994 Ball and co-workers [7] proposed the combined use of an externally modulated tunable fiber laser and a 6 element wavelength multiplexed uniform fiber Bragg grating array with the grating spacing set to yield the desired delay to implement a programmable delay line capable of generating 50 ns true time delay in discrete 10 ns intervals. This fueled the research toward the application of the recently available fiber gratings in the implementation of OPRFSs. Uniform Fiber Bragg gratings can be employed both as weighting and delay line elements, since their reflectivity changes with the signal wavelengths and their Bragg wavelength is adjustable. When used as delay elements they can only provide discrete changes in the value of the sampling period. This limitation is removed by the use of linearly chirped gratings.

A simple discretely tunable notch filter was demonstrated by Hunter and Minasian [8] using a michelson interferometer with two uniform fiber gratings placed in series in one of its arms and subsequently continuous tuning was demonstrated replacing the uniform with chirped gratings. In a further step, multitap (29 taps) transversal bandpass filter was demonstrated by spectrally slicing a broadband source with wavelength multiplexed Bragg grating arrays equispaced in time. The reflectivity of the gratings in the array were apodised according to a Kaiser window.

High Q filters have also been demonstrated using fiber Bragg gratings both in fixed and tunable operation by sandwiching an active fiber between two gratings, one of which is partially reflecting while the second one is 100% reflecting. The presence of the internal optical amplifiers allow for the existence of a very high number of signal samples which results in resonances with high selectivity ($Q=325$) [9]. The main drawback is that although the weight of the samples can be reconfigured by changing the amplifier gain, it cannot be done independently sample by sample. Furthermore the length of the active medium severely restricts the filter FSR. A solution has however been proposed for this last inconvenient by placing the former filter in tandem with a Mach-Zehnder lattice filter the period of which is N times larger than that of the former. Q factors over 800 have been demonstrated.

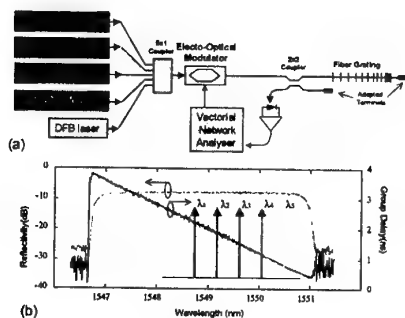


Figure 3

The approaches described above do not usually address dynamic tunability and reconfiguration simultaneously. The dispersive nature of Linearly Chirped Fiber Bragg Gratings (LCFBGs) can be employed to obtain programable RF transversal filters by means of feeding the RF modulated output of an array of sources to the device [10]. The layout of the filter for a specific case of a laser array of 5 elements is shown in figure 3, although in general it is composed of N sources. The advantage of using a laser array as a feeding element to the delay line is twofold: On one hand the wavelengths of the lasers can be independently adjusted. Thus spectrally equispaced signals representing RF signal samples can be fed to the fiber grating suffering different delays, but keeping constant the incremental delay $\Delta\tau$ between two adjacent wavelengths emitted by the array if the delay line is implemented by means of a linearly chirped fiber grating. This means for instance and referring to figure 6 that the delay between the signals at λ_1 and λ_2 , λ_3 , λ_4 , λ_5 , ..., λ_N is respectively $\Delta\tau$, $2\Delta\tau$, $3\Delta\tau$, $4\Delta\tau$ and $(N-1)\Delta\tau$. Hence the configuration can act as a transversal filter, where the basic delay is given by $\Delta\tau$: Furthermore $\Delta\tau$ can be changed by proper variation of the laser central wavelengths in the array. Thus these structure provides the potential for implementing tunable RF filters.

The second advantage stems from the fact that the output powers of the lasers can be adjusted independently and at high speed. This means that the time response of the filter can be apodised or in other words, temporal windowing can be easily implemented and therefore the filter transfer function can be reconfigured at high speed

An additional advantage of employing laser arrays is the possibility of exploiting WDM techniques for parallel signal processing and to provide both a large number of taps and arbitrary coefficients

6 Summary and Conclusions

In this paper we have revised the fundamental concepts and limitations of optical filters for the processing of Rf signals. The main achievements both as far as theoretical as well as practical and experimental work carried by different research groups working on the field have been reviewed.

Acknowledgements

The authors wish to acknowledge the financial support through Spanish government CICYT projects TIC98-0346 and TEL99-0437.

REFERENCES

- [1] K. Wilner and A.P. Van Den Heuvel, 'Fiber-optic delay lines for microwave signal processing', Proc. IEEE, vol 64, pp. 805-807, 1976.
- [2] K. Jackson, S. Newton, B. Moslehi, M. Tur, C. Cutler, J. Goodman and H.J. Shaw, 'Optical fiber delay-line signal processing', IEEE Trans. Microwave Theory Tech, vol 33. Pp. 193-204, 1985.
- [3] B. Moslehi, J. Goodman, M. Tur and H.J. Shaw, 'Fiber-optic lattice signal processing', Proc. IEEE, vol 72, pp. 909-930, 1984.
- [4] M.C. Vázquez, B. Vizoso, M.López-Amo and M.A.Muriel, 'Single and double amplified recirculating delay lines as fibre-optic filters', Electron. Lett., vol 28., pp. 1017-1019.
- [5] J. Capmany and J. Cascón, Discrete-time fiber-optic signal processors using optical amplifiers. IEEE Journal of Lightwave Technology. pp. 106-117, 1994
- [6] M.Y. Frankel and R.D. Esman, 'Fiber-optic tunable transversal filter', IEEE Photon. Tech. Lett., vol 7, pp. 191-193, 1995
- [7] G.A. Ball, W.H. Glenn and W.W. Morey, 'Programmable fiber optic delay line', IEEE Photon. Technol. Lett., vol 6, pp. 741-743, 1994.
- [8] D.B. Hunter and R.A. Minasian, 'Reflectivity tapped fibre-optic transversal filter using in-fibre Bragg gratings', Electron Lett., vol 31, pp. 1010-1012, 1995.
- [9] D.B. Hunter and R.A. Minasian, 'Photonic signal processing of microwave signals using active-fiber Bragg-grating-pair structure', IEEE Trans. Microwave Theory and Techn, vol 8, pp. 1463-1466, 1997.
- [10] J. Capmany, D. Pastor and B. Ortega, 'New and flexible fiber-optic delay line filters using chirped Bragg gratings and laser arrays', IEEE Trans. Microwave Theory Tech., vol 47, pp. 1321-1327, 1999

Optical Transversal Filter Employing High Birefringence Fibre Bragg Gratings

W. Zhang, and J. A. R. Williams

Photonics Research Group, Aston University, Birmingham B4 7ET, UK

Tel.: 44-121-3593611, fax: 44-121-3590156, email: w.zhang@aston.ac.uk

Abstract: Polarisation summing is introduced into optical fibre transversal filter to realise incoherent operation. The Bragg gratings are fabricated on high birefringence fibre, and the resulting filter produces a tuneable microwave frequency response with large free spectral range free of optical coherence.

Introduction: The many advantages of performing microwave signal transmission in the photonic domain using optical fibres has sparked increasing interest in using passive fibre-based structures for also performing signal processing in the photonic domain. A number of filters and signal processing structures have been reported [1,2]. Many of them are based on optical fibre delay lines and their combination to realise various signal-processing functions [3,4]. Therefore the performance of the optical fibre delay line filters is crucial if more advanced processing is to be achieved.

A basic optical fibre delay line filter consists of an optical fibre Mach-Zehnder section where the optical incoherent summing of two beams takes place. In order to meet the requirement of incoherent operation, a low coherence source and a large optical path difference (OPD) are generally needed. This consequently makes the free spectral range (FSR) of the filter limited by the source coherence. A low coherence source could reduce the available bandwidth of an optical fibre microwave system. Moreover, with cascaded optical fibre delay line structures, coherent interference may still take place due to the effect of changing optical coherence as the light traverses the Mach-Zehnder sections in sequence [5] even if a low coherent source and a large OPD are used. A number of techniques have been demonstrated to obtain optical incoherent summing and a large free spectral range, including

using multiple sources or electrically summing. However the former limits the practical application in a wavelength divisions multiplexed optical microwave system, and the latter technique loses some of the merits of optical microwave signal processing. We have previously proposed a novel method to overcome this limitation by constructing an optical delay line filter using high birefringence (Hi-Bi) fibre [6]. Here we present what we believe to be the first optical microwave transversal filter employing fibre gratings constructed in Hi-Bi fibre and demonstrate that we can achieve a device with a large tuneable free spectral range and free of optical coherence interference noise.

The proposed filter consists of two uniform Bragg gratings, each of 1cm length, fabricated on Hi-Bi fibre using the phase mask exposure technique. The result is that the gratings have two reflectivity peaks at different wavelengths corresponding to the differing effective refractive indices for the two orthogonal polarisation modes in the Hi-Bi fibre. The spectral spacing between these two reflections depends on the fibre birefringence. The reflection peak at the shorter wavelength takes place in the fast axis mode, the one at the longer wavelength in the slow axis mode. In our filter the second grating is wavelength shifted by an amount exactly equal to the spectral spacing of the two polarisation reflections. Thus the reflection in the slow axis mode of the first grating operates at the same wavelength as the reflection in the fast axis of the second grating, as illustrated in Fig.1. These two reflections will add incoherently as their polarisation states are linearly orthogonal to each other, and so optical coherence interference will not

arise even under the conditions of high coherence source and small distance between two gratings.

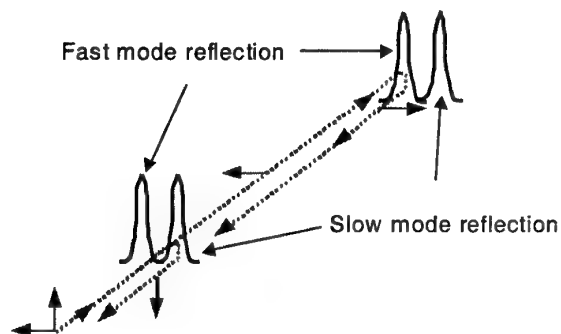


Fig.1 Two reflections from two orthogonal polarisation modes

A schematic of an Hi-Bi fibre grating based filter and experimental arrangement used in this work is as shown in Fig.2.

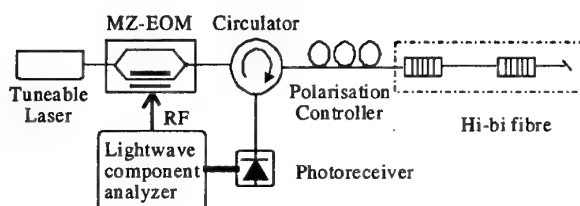


Fig.2 Experimental arrangement for the filter

A tuneable laser (Tunics 1550) was used to launch a beam through an electro-optic modulator into the fibre circulator, then fed into the fibre gratings. The distance between two gratings were first set to ~5cm which was much shorter than the coherence length of the laser (the linewidth of the laser is ~100kHz). The reflected light beams from the slow axis mode of the first grating and the fast axis mode of the second grating passed through the circulator and met at the photoreceiver, analysed by a lightwave component analyser so the microwave frequency response (MFR) of the filter could be measured.

A polarisation controller was used to produce a linear polarised laser beam with 45° azimuth to polarisation axes of the Hi-Bi fibre, or a circular polarised beam so two polarisation modes could be excited equally.

The microwave frequency response (MFRs) was recorded for differing excited polarisation states as

shown in Fig.3. Trace 1 has the maximum notch depth meaning the light intensities reflected from both gratings are almost equal. Trace 2 and 3 show the cases when the two polarisation modes were unequally excited.

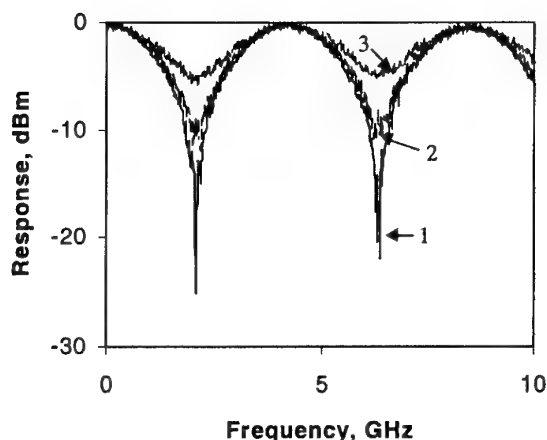


Fig.3 Frequency responses under the different polarisation excitation conditions to Hi-Bi fibre

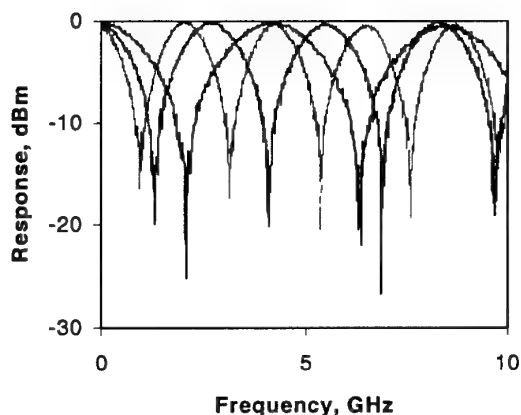


Fig.4 Frequency responses of the tuneable filter

A tuneable free spectral range can be realised by fabricating a series of gratings with different reflection wavelengths on the same piece of Hi-Bi fibre. Changing the operating optical wavelength of the tuneable laser allows selecting a particular pair of gratings with desired distance between them to form the filter.

We constructed such a filter, and the frequency responses were measured while the operating wavelength was set to different values. Fig.4 shows three traces corresponding to the gratings pair separations of 5cm, 7.5cm and 9.5cm, respectively.

In conclusion, a novel filter has been demonstrated. The concept of polarisation summing has been introduced to realise incoherent operation, thus overcoming the limitations imposed by the high optical coherence of the source and increasing the free spectral range of an optical fibre delay line filter. By using a Hi-Bi fibre Bragg grating array, a large, tuneable free spectral range has been obtained. It should be noticed that the experimental frequency responses shown in figures 3 and 4 might not be the results of incoherent summing of the reflections from two polarisation modes. Instead of incoherent summing at the photodetector coherent operation may happen, as the fibre circulator used is not polarisation maintaining and depolarisation in single mode fibre can give rise to coherent summing of two reflections. However, no remarkable coherent noise was observed in the experiments. This is because in both the part of Hi-Bi fibre and the circulator, the two modes travel in nearly identical optical paths providing strong common-mode suppression to the optical coherence noise. The use of polarisation maintaining devices would assure incoherent summing. By overcoming the coherence issue the way is paved to cascade devices to realise a wider range of filtering and processing functions.

References:

- [1] B. Moslehi, J. W. Goodman, M. Tur, and H. J. Shaw, "Fibre-optic Lattice Signal Processing", Proc. IEE V. 72, pp.909-930, 1984
- [2] S. Sales, D. Pastor, J. Capmany, and J. Marti, "Fibre-optic Delay-line Filters Employing Fibre Loops: Signal and Noise Analysis and Experimental Characterization", J. Opt. Soc. Am. A, Vol.12, No.10, pp. 2129-2135, 1995
- [3] T. A. Cusick, et al, *IEEE Trans. Microwave Theory & Techniques*, vol.MTT-45, no.8, pp.1458-1462, 1997
- [4] S. Tedjini, A. Ho-Quoc, and D. A. M. Khalil, "All-optical networks as microwave and millimeter-wave circuits", *IEEE Trans. Microwave Theory & Techniques*, Vol. 43, no.9, pp.2428-2434, 1995
- [5] *Optical Fibre Sensor Technology*, edited by K.

T. V. Grattan and B. T. Meggitt, Chapter 9, Chapman & Hall, 1995

- [6] W. Zhang, J. A. R. Williams, and I. Bennion, "Optical Fibre Delay Line Filter Free of the Limitation Imposed by Optical Coherence", *Electron. Lett.* V.35, No.24, pp. 2133-2134, 1999

A PHOTONIC WIDE-BAND ANALOG TO DIGITAL CONVERTER

Edward N. Toughlian, ENSCO, Inc.

Henry Zmuda, University of Florida
1350 North Poquito Road
Graduate Engineering and Research Center
Shalimar, FL 32579
phone: (850) 833-9350
fax: (850) 833-9366
email: zmuda@gerc.eng.ufl.edu

Abstract—We describe how a tunable laser and common photonic components can perform the process of analog-to-digital conversion. The all-optical processing yields conversion rates orders of magnitude faster than the fastest electronic processor.

I. SYSTEM OVERVIEW

High-speed, high-resolution analog-to-digital converters (ADCs) have been the subject of intense research [1]-[5]. This paper presents the design and initial experimental results for an all-photonic ADC that has the potential to operate at speeds orders of magnitude faster than commercial electronic ADCs. A block diagram for the proposed ADC is shown in Fig. 1. It is seen that the ADC is composed of three major sub-systems. A Sample and Hold (S/H) samples the signal to be digitized and maintains the sample value for a sufficient time such that the correct binary representation of the sample can be established. For the purposes of this paper it is assumed that a S/H is available. Here we focus on the remaining two subsystems, the Tunable Laser (TL) and the ADC Processor (ADCP). Generally any ADC system may include input signal conditioning, path-length equalization, sign-bit extraction, and the like, and although not indicated in Fig. 1, such is the case here as well.

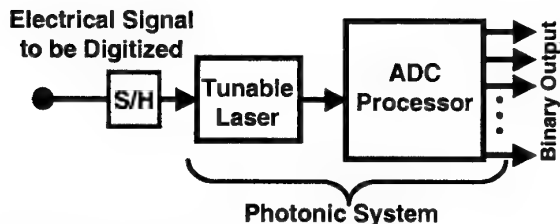


Fig. 1: Photonic ADC System.

II. ADC OPERATION

The analog signal voltage to be digitized, once processed by the S/H, is used to control a high-speed, high-resolution TL. Specifically the TL is designed so that each quantization level corresponds to a unique wavelength. The ADC problem thus becomes one of resolving a wavelength, and this is the function of the ADCP. Since in principle any TL with sufficient tuning speed and resolution can be used, let us first focus our attention on the ADCP portion of the system. Section 3 will present several novel TL architectures that are particularly suited for the present ADC application.

The basic ADCP sub-system architecture is shown in Fig. 2a for the case of a 4-bit ADC. For an N-bit ADC, the output of the TL is split N times and directed to a bank of fixed optical filters with the bit-leg filter designed as follows. Let the quantized input voltage v_i be represented by the binary word $b_{N-1} b_{N-2} \dots b_i \dots b_1 b_0$, and consider the i^{th} bit-leg filter which correspondingly yields the i^{th} binary digit b_i . If the required binary digit is a *logical zero*, then the bit-leg filter is designed to minimize (ideally prevent) the energy from the associated wavelength from appearing at the spectrally broad photodetector. Otherwise the wavelength is passed by the filter resulting in the interpretation of a *logical one* at the detector. Note also that the bit-leg filters have a periodic transfer function in the ADC system passband. This observation greatly reduces the complexity of the bit-leg filters by reducing the potentially large number of discrete narrow-band filters required per bit-leg to a single square-wave-like filter transfer function.

A great deal of versatility exists in the filter implementation. These include, for example; Mach-Zehnder Cascades, Fabry-Perot Etalons, Bragg gratings, and many others. It is possible that a high-resolution system (10 bits or more) might require a hybrid realization that utilizes several types of filters, each optimally suited for a particular bit-leg. Fig. 2b

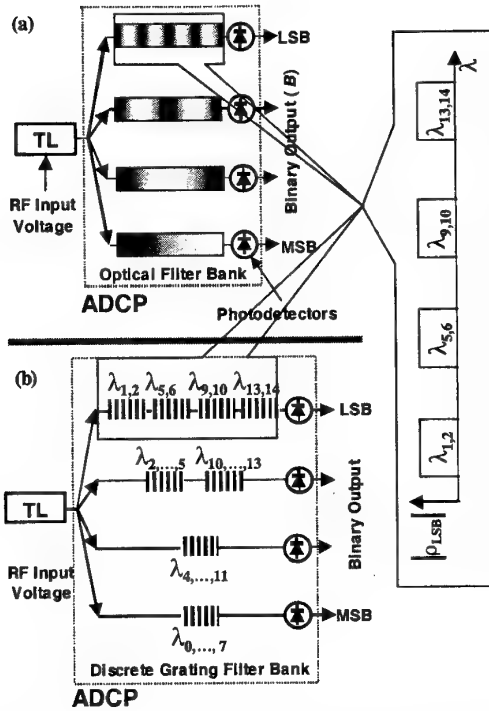


Fig. 2: (a) General architecture for a 4-bit ADCP and (b) a realization using discrete Bragg gratings.

shows a 4-bit ADCP utilizing discrete Bragg gratings to implement each bit leg filter. The realization of Fig. 2b further employs a Gray code that minimizes the ADC quantization error and results in a further simplification of each filters complexity by easing passband/stopband requirements.

The ADCP system of Fig. 2b was constructed using discrete fiber Bragg gratings in a Gray-Coded configuration and a commercial splitter and was designed to resolve 16 wavelengths over a 15nm passband centered at 1550nm. A broadband source was used to characterize each bit-leg filter on an optical spectrum analyzer with the results shown in Fig. 3.

III. TUNABLE LASER ARCHITECTURES

Most commercial tunable lasers are not optimized for tuning speed, a critical attribute for the present application [6], [7]. The tuning speed for the approaches considered here is primarily governed by two parameters, the cavity dynamics and the carrier lifetime. The TL realizations shown below use a Semiconductor Optical Amplifier (SOA) as the laser gain mechanism. These SOAs can have response times exceeding 10 GHz hence making them an attractive candidate for the ADC application. The cavity dynamics are largely dependent on the speed of the components used to construct the cavity as well as the overall cavity length. Implementation of the TL as a photonic integrated circuit can result in a small total cavity length. Also critical for the present application is linear tuning using a single control signal (i.e., the voltage to be digitized) to determine the operating wavelength.

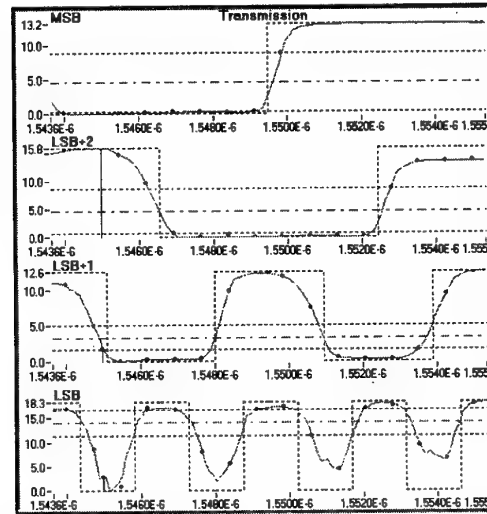


Fig. 3: Measured results for the 4-bit ADCP using discrete Bragg gratings.

A TL with the desired characteristics is presented conceptually in Fig. 4a. Fig. 4a is a representation of a Fabry-Perot laser than can lase at four distinct wavelengths; λ_0 , λ_1 , λ_2 , and λ_3 . The cavity is formed using the mirror (shown on the left of the drawing) as one of the cavity terminations, while discrete Bragg reflection gratings form the other(s). Linear tuning is accomplished by the critical placement of these four gratings shown located at x_i ($i = 0, 1, 2, 3$) with x_i determined by the usual resonance condition, namely $m_i \lambda_i = 2n_i x_i$ for some integer m_i . The refractive index n_i can be rapidly changed by using an electro-optic phase modulator. It is easy to see that Fig. 4b shows an equivalent realization which can be tuned over a continuous wavelength range by replacing the discrete Bragg grating cascade with a chirped grating [8].

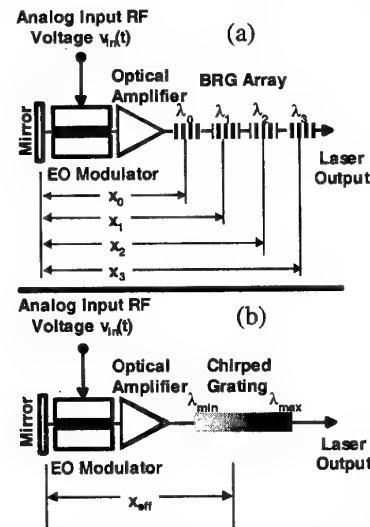


Fig. 4: (a) Tunable laser capable of tuning over discrete wavelength, and (b) a continuously tunable version.

The chirp-grating of the previous configuration effectively introduces dispersion into the cavity in a precisely controlled manner. As Fig. 5 suggests, this dispersion can be accomplished in other ways as well. For example, optical fiber exhibits dispersion and hence a precise length of fiber can be used along with the additional mirror, as shown in Fig. 5a, to form a continuously tunable cavity [9]. The realizations of Figs. 5a and 5b are conceptually equivalent, 5b being a ring cavity while 5a is linear. Fig. 5c shows a laser tunable over discrete wavelengths, accomplished by the inclusion of the Fabry-Perot resonator within the ring configuration.

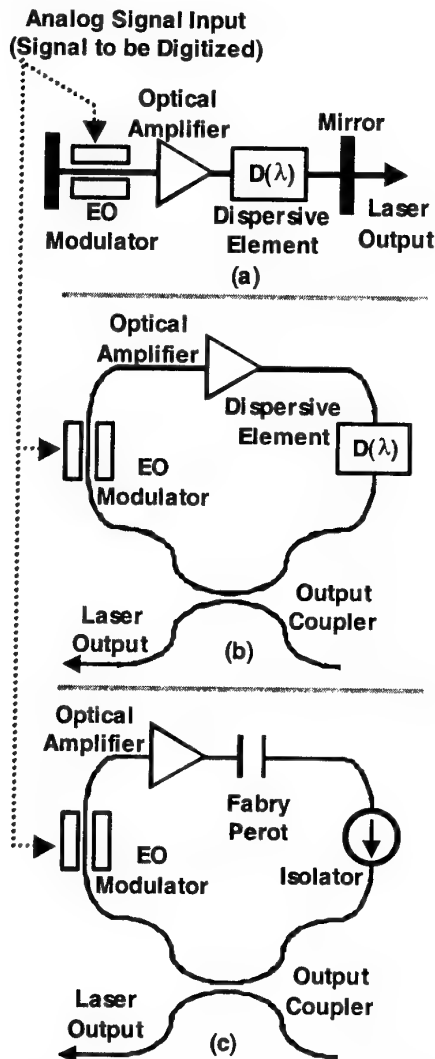


Fig. 5: (a) Continuously tunable laser (linear dispersive cavity), (b) the equivalent ring cavity with dispersion, (c) a discretely tunable laser.

The tunable laser of Fig. 5c was constructed on an optical bench using discrete components. Linear tuning over a 20 nm band was achieved with typical results shown in Fig. 6.

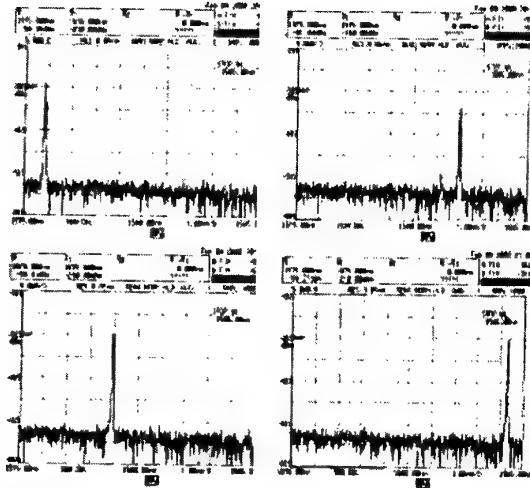


Fig. 6: Linear tuning over a 20 nm band using the discretely tunable laser of Fig. 5c.

REFERENCES

- [1] Jin U. Kang, M.Y. Frankel, and R.D. Esman, "Highly parallel pulsed optoelectronic analog-digital converter", *IEEE Photonics Technology Letters*, Vol. 10, pp. 1626-1628, Nov. 1998.
- [2] M.Y. Frankel, Jin U. Kang, and R.D. Esman, "High-performance photonic analogue-digital converter", *Electronic Letters*, Vol. 33, pp 2096-2097, Dec. 1997.
- [3] B. Jalali and Y.M. Xie, "Optical folding-flash analog-to-digital converter with analog encoding", *Optics Letters*, Vol. 20, Sept. 1995.
- [4] R.G Walker, I. Benian, and A.C. Carter, "Novel GaAs/AlGaAs Guided Wave Analogue/Digital Converter," *Electronics Letters*, Vol. 25, pp. 1443-1444, Oct. 1989.
- [5] H.F. Taylor, "An Optical Analog-to-Digital Converter," *IEEE Journal of Quantum Electronics*, Vol. QE-15, pp. 210-216, 1979.
- [6] Glance, B. U. Koren, R.W. Wilson, D. Chen, and A. Jourdan, "Fast Optical Packet Switching Based on WDM", *IEEE Photonics Technology Letters*, vol. 4, pp. 1186-1188, Oct. 1992.
- [7] E.L. Wooten, R.L. Stone, E.W. Miles, and E.M. Bradley, "Rapidly Tunable Narrowband Wavelength Filter Using LiNbO₃ Unbalanced Mach-Zehnder Interferometers," *IEEE Journal of Lightwave Technology*, vol. 14, Nov. 1996, pp. 2530-2536.
- [8] R. Kashyap, "Fiber Bragg Gratings", New York: Academic Press, 1999.
- [9] F. Ouellette, "Dispersion Cancellation Using Linearly Chirped Bragg Grating Filters in Optical Waveguides," *Optics Letters*, vol. 12, pp. 847-849, Oct. 1987.

Ultra-Low Jitter Mode-Locking of Er-Fiber Laser at 10 GHz and its Application in Photonic Analog-to-Digital Conversion

W. Ng, R. Stephens, D. Persechini and K.V. Reddy*

HRL Laboratories
3011 Malibu Canyon Rd.
Malibu, California 90265
Phone: (310)-317-5704, Fax: (310)-317-5485
Email: wwng@HRL.com

Abstract

We report the 10 GHz mode-locking of a fiber-laser with timing-jitters as low as 16 fsec ($\Delta f=100$ Hz-100 kHz), and amplitude-jitters of 0.058%. From the spur-free-dynamic-range (SFDR) measured for a signal (at 2.49 GHz) sampled with the mode-locked pulse train, we estimate an analog-to-digital conversion resolution of 8 SFDR-bits at 10 GSPS.

I. Introduction

Recently, there has been tremendous interest ⁽¹⁾⁻⁽²⁾ in the application of photonic sampling to help achieve, simultaneously, analog-to-digital conversion (A/D) with high resolution *and* at multi-GHz sampling rates (f_s). Photonics has many attributes that could lead to potential breakthroughs in A/D technology. A recent publication ⁽³⁾ that tracked the advances of A/D technology indicated that, for a given f_s , only 1.5 bits of improvement in resolution were gained between 1989 and 1997. The same reference also attributed the observed limitations in resolution to "effective" timing-jitters (> 0.5 psec) that were present in the sampling apertures of these analog-to-digital converters (ADC). Conceptually, the picosecond pulses generated by a mode-locked laser are ideal vehicles that would enable one to accomplish *impulse sampling* of an analog signal. For example, one can use an electro-optic modulator to impress the analog signal onto the optical pulse train. After photodetection, the received signal due to the modulated pulse train can be fed, in turn, to an electronic quantizer for digitization. An obvious benefit that we gained via the incorporation of photonics in A/D is the added capability to *remote* various elements of the ADC. For instance, several photonic samplers can be remoted from a high-resolution electronic quantizer via an ensemble of photonic links. This is highly desirable in many applications where the analog inputs to an ADC are the received signals of several deployed antenna elements. One can also envisage the

employment of a *remoted* ultra-stable microwave oscillator that would (i) drive a mode-locked laser, and (ii) clock several electronic ADC quantizer via RF-photonic links. Finally, the multi-GHz sampling rates offered by a stable, mode-locked pulse train will reduce the number of mixer-stages that are presently needed to downconvert high frequency signals before digitization.

In this paper, we will report on the ultra-stable mode locking of a fiber laser at the frequency (f_m) of 10 GHz, and its application in a photonic sampling experiment. In particular, we will describe two different approaches for characterizing the timing and amplitude jitter of our actively mode-locked (ML) laser. In the first technique, we measured the phase-noise (ϕ -noise) of the ML laser with the help of a microwave phase-noise test set. In the second approach, we evaluated the spectral densities of its amplitude and timing jitter via a characterization ⁽⁴⁾ of the "noise-pedestals" present in the harmonics of the ML pulse train. Our analysis shows that the stability of our ML pulses will support a photonic sampling accuracy of *~11-bits at 10 GSPS*. Finally, we will report the achievement of 8 spur-free-dynamic-range (SFDR) bits at 10 GSPS in a photonic A/D experiment. The latter result represents the highest bits of resolution reported to date for a photonic A/D experiment performed at GHz sampling rates.

II. Evaluation of the Timing and Amplitude Jitter in a Mode-Locked Fiber Laser

A simple analysis of the sampling procedure shows that the fractional amplitude jitter (σ_A) and timing jitter (σ_t) required to accomplish N bits of resolution are given, respectively, by the conditions: $\sigma_A < 1/2^N$, and $\sigma_t < 1/(\pi 2^N)$. For a sampling rate f_s , the absolute timing jitter (σ_h) must satisfy the condition $\sigma_h < 1/(\pi f_s 2^N)$. We first characterized the timing jitter of the ML fiber laser by measuring, with the help of a

microwave ϕ -noise test-set, the single-sideband phase noise $[L(f) \text{ in dBc/Hz}]$ present in the detected optical pulses. Our experimental arrangement is shown at the inset to Fig. 1.

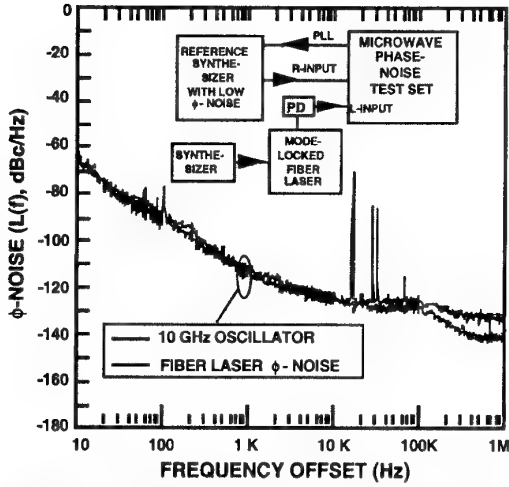


Fig. 1 Single sideband ϕ -noise of ML fiber laser and its driving oscillator.

During the measurement, the ML pulses were typically 3 psec wide. Its corresponding spectral width was $\sim 0.8 \text{ nm}$, giving us a time-bandwidth product that was close to the transform-limited product (for a sech^2 -pulse) of 0.31. Fig.1 shows the result of these measurements. As shown, the $L(f)$ measured for the ML fiber laser tracked that of its driving oscillator at $f_m \sim 10 \text{ GHz}$. By performing an integral for $L(f)$ over our offset frequency range of interest ($\Delta f_L = 100 \text{ Hz}$ to $\Delta f_H = 100 \text{ kHz}$), we can estimate σ_{jt} , the timing jitter of the picosecond pulse train. Specifically, we obtained, after computation of the integral:

$$\sigma_{jt} = \frac{1}{(2\pi f_m)} \sqrt{2 \int_{\Delta f_L}^{\Delta f_H} L(f) df} \quad (1)$$

an absolute timing jitter of σ_{jt} of $\sim 16 \text{ fsec}$, i.e. a $\sigma_j = 0.016\%$ for $T_m \sim 100 \text{ psec}$, where $T_m = f_m^{-1}$.

Next, we applied the technique of harmonic analysis⁽⁴⁾, which examines the noise pedestals present in the detected harmonics of the ML pulse train $G(t)$. To our knowledge, this is a first report on the application of this technique to ML lasers where $f_m > 1 \text{ GHz}$. Specifically, if $\tilde{g}(\omega)$ is the Fourier transform ($\omega = 2\pi f$) of a single pulse in the periodic pulse train $G(t)$, then the power spectrum $S_G(\omega)$ of $G(t)$ is given by:

$$S_G(\omega) = \left| \frac{2\pi \cdot \tilde{g}(\omega)}{T_m} \right|^2 \left\{ \sum_N \delta(\omega - N\omega_m) + S_A(\omega - N\omega_m) + (2\pi N)^2 S_J(\omega - N\omega_m) \right\} \quad (2)$$

where $\omega_m = (2\pi)/T_m$, and N = harmonic number. In the above equation, $S_A(\omega)$ and $S_J(\omega)$ are, respectively, the spectral densities of the amplitude jitter and timing jitter. When we characterize the RF spectrum of the detected harmonics with a microwave spectrum analyzer, the above spectral densities are integrated over the resolution bandwidth (RBW) of the measurement. Therefore, the relative power between the peak ($P_p(0)$) of the "pedestal" for the N th harmonic and its carrier (P_c), the N th harmonic, is given by the following equation:

$$\frac{P_p(0)}{P_c} = \text{RBW} \cdot \{S_A(0) + (2\pi N)^2 S_J(0)\} \quad (3)$$

From Eq.3, we notice that the power (relative to its carrier) for the pedestal of the N th harmonic consists of two components: (i) a component [due to the amplitude jitter ($S_A(\omega)$)] that is invariant with the harmonic number N , and (ii) a second component [due to the timing jitter ($S_J(\omega)$)] that varies as the square of N . Hence, the slope obtained from a plot of $(P_p(0)/P_c)$ vs N^2 gives us an estimation of $S_J(0)$. The square of the fractional timing jitter, σ_j^2 , can be calculated from the product $S_J(0) \times (\text{FWHM of the pedestals})$. Finally, we can evaluate $S_A(0)$ from the noise spectrum measured at low frequencies ($N=0$). Fig. 2 shows the RF spectrum measured for the first four harmonics of our ML laser ($f_m = 10.2 \text{ GHz}$).

We evaluated the ratio $(P_p(0)/P_c)$ from these data, and plotted them (in dBc/Hz) vs the harmonic number N in Fig.3. From the $S_J(0)$ evaluated, we obtained a fractional timing jitter of $\sigma_j \sim 10^{-4}$, which was slightly lower than the measurement obtained from the ϕ -noise test set. Finally, the corresponding ratio for the amplitude jitter was evaluated from the low frequency noise spectrum, and marked as the amplitude noise floor in Fig. 3. The integration of this noise spectrum gave a value of $\sigma_A = 0.058\%$ for the fractional amplitude jitter. Using the criteria given at the beginning of this section, we estimate that the above ML pulse train will support ~ 11 bits of resolution in a photonic sampling experiment.

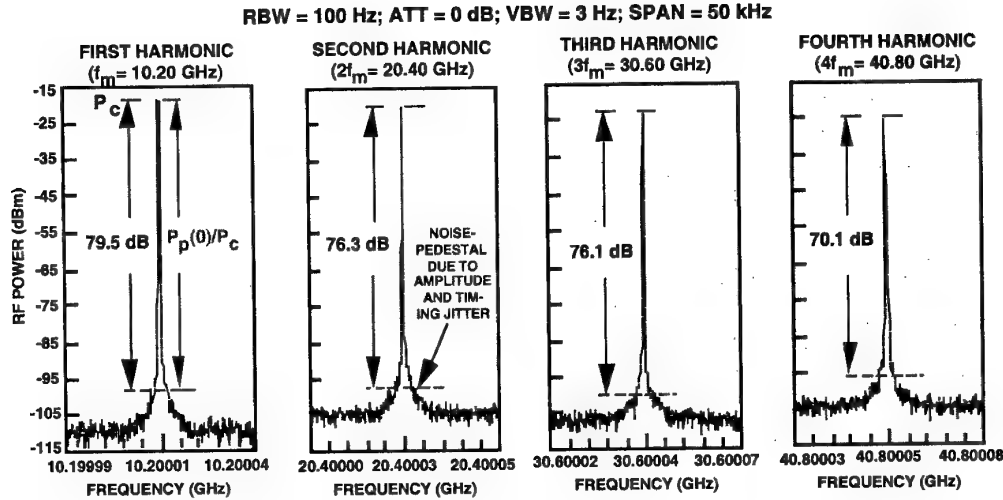


Fig. 2 RF spectrum of the first four harmonics for $f_m = 10.2$ GHz.

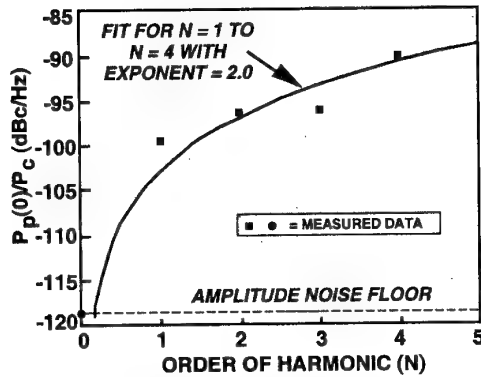


Fig. 3 Relative pedestal power (in dBc/Hz) vs harmonic order.

III. Photonic Analog-to-Digital Conversion at 10 GSPS

Using the above ML laser, we performed a photonic sampling experiment (see Fig. 4) where we fed a modulated pulse train to a commercial digitizer. In particular, the ML pulses were modulated by a 2.49 GHz analog input. The ADC used in our digitizer was specified to possess 8 bits of resolution at $f_s = 10.0$ GSPS. During the experiment, the laser was mode-locked at $f_m = 10.0$ GHz, putting it in synchronism with the digitizer. Since the A/D accuracy of our experiment was limited by the digitizer, we mode-locked the fiber laser with a more versatile synthesizer that offered ~8-9 bits of amplitude and timing stability.

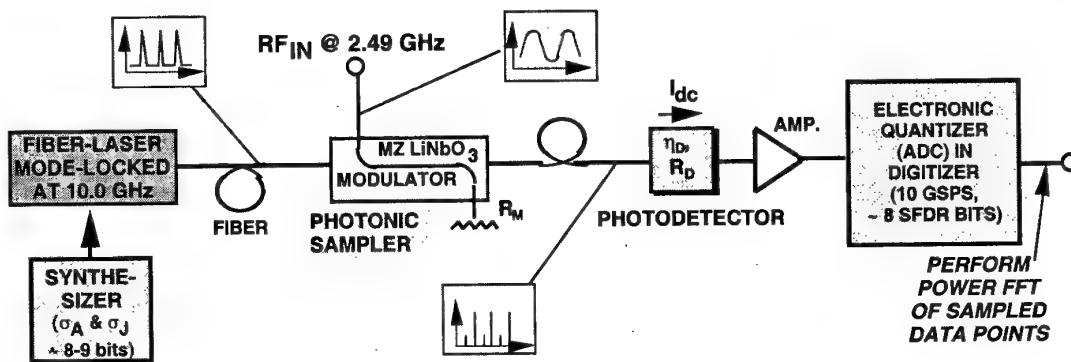


Fig. 4 Schematic of photonic sampling at 10 GSPS with ML laser.

By taking a fast Fourier transform (FFT) of the sampled data points in the digitizer, we can estimate the number of SFDR bits achieved in our photonic A/D experiment. To be specific, the effective number of bits associated with a measured SFDR is given⁽³⁾ by: $\text{SFDR-bits} = \text{SFDR (dBc)} / 6.02$. In the above expression, the SFDR (obtained via FFT) is defined as the ratio of the single-tone signal power to the

highest spur (within the RF-spectrum of interest). We show, in Fig. 5a, the FFT of the analog input to the LiNbO₃ Mach-Zehnder (MZ) modulator. As shown, we obtained a SFDR of ~ 50 dB (at 10 GSPS), which corresponded to ~ 8 SFDR-bits. Next, we show in Fig. 5b, the FFT of the photonic sampled signal after it was digitized by the same ADC at 10 GSPS.

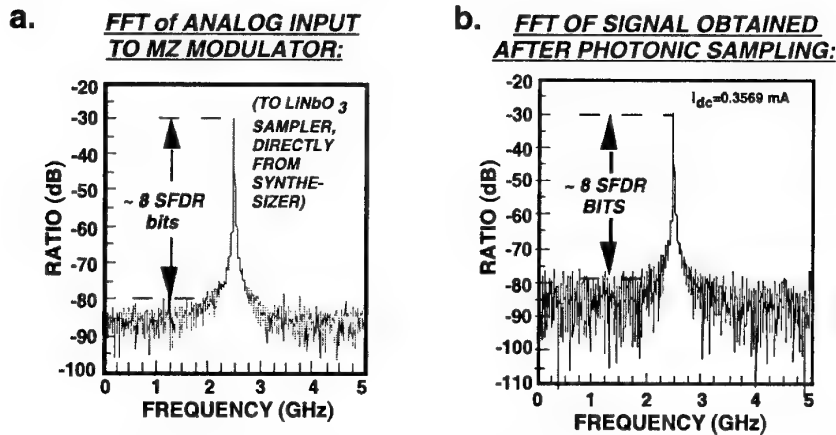


Fig. 5a FFT of analog input to MZ modulator
5b. FFT of photonic sampled signal

Again, we obtained a signal (at 2.49 GHz) with a SFDR of ~50 dB. Hence, we have demonstrated that the photonic frontend of our sampling experiment possessed at least 8 SFDR-bits of resolution (over the Nyquist band of 5 GHz).

IV. Conclusions

In summary, we have characterized the amplitude and timing jitters of a ML Er-fiber laser (at $f_m \sim 10$ GHz) via two approaches. We obtained amplitude (σ_A) and timing (σ_t) jitter values of 0.058% and 0.016% respectively. These jitter values correspond to some⁽⁵⁾ of the lowest reported for ML lasers, and will enable us to achieve ~11 bits of resolution in a photonic sampling experiment. Finally, we demonstrated, for the first time, a 10 GSPS photonic ADC that has a resolution of 8 SFDR bits - a resolution limit set primarily by the electronic quantizer used.

This work is supported by Defense Advanced Research Projects Agency and the Air Force Research Laboratory, Sensors Directorate (Rome Research Site).

*Pritel Inc., P.O. Box 4025, Naperville, IL 60565 - 6102.

REFERENCES:

1. T.R. Clark, J.U. Kang, and R.D. Esman, "Performance of a Time- and Wavelength-Interleaved Photonic Sampler for Analog-Digital Conversion," *IEEE Photonics Technol. Lett.*, Sept.1999, p.1168-1170.
2. F. Coppinger, A.S. Bhushan and B. Jalali, "12 Gsample/s wavelength division sampling analogue-to-digital converter," *Electron. Lett.*, 2000, 36 (4), pp.316-318.
3. R.H. Walden, "Analog-to-Digital Converter Survey and Analysis," *IEEE J. on Selected Areas in Communications*, Vol.17 (4), 1999, pp. 539-550.
4. Van der Linde, D. "Characterization of the noise in continuously operating mode-locked lasers," *Appl. Phys. B*, 1986, 39, pp. 201 - 217.
5. T.R. Clark, T. F. Carruthers, P.J. Matthews and I.N. Duling III, "Phase noise measurements of ultrastable 10 GHz harmonically modelocked fiber laser," *Electron. Lett.*, 1999 (9), pp. 720-721.

Shot-Noise Limited Performance from an EDFA/Brillouin Hybrid Amplified Photonic Link

Shane J. Strutz and Keith J. Williams

Naval Research Laboratory, Building 215, Code 5652
4555 Overlook Avenue, SW, Washington, DC 20375
Phone:(202)404-1514; Fax:(202)404-8645
Strutz@ccs.nrl.navy.mil

Abstract

The performance of a hybrid amplifier composed of Erbium doped fiber and a Brillouin amplifier was investigated experimentally. The relative intensity noise of the amplifier was characterized and compared to the output noise of a shot-noise-limited link. Shot-noise limited performance was achieved within the 500 MHz to 8 GHz frequency band. In addition, low frequency <500 MHz burst noise was reduced by utilizing a phase-modulated signal beam in the Brillouin amplification process.

I. Introduction

The low loss and wide bandwidth of microwave photonic links make them valuable tools for remoting antennas. The photonic links between antennas and control stations can be used to remote local oscillator signals or to relay RF signals from the antenna to a centralized location. However, due to the complexity of the signals received by modern antennas, it has become important not only to efficiently relay information, but also to process the signals at the same time. For example, the need for bandwidth compression

and frequency translation has led to the expanded use of analog fiber-optic links [1-8] which convert RF information into a more manageable intermediate frequency bandwidth[5-9]. Processing RF signals within a photonic link reduces the requirements on the RF electronics and as a result decreases the processing time in many applications.

Though analog photonic links may be used as signal processing tools, the complexity of received RF signals combined with the dynamic range requirements of modern antennas strain the noise figure requirements of photonic links. For example, a typical photonic link composed of a 30 mW DFB laser, a 5 Volt V π Mach-Zehnder Modulator, and an appropriate photodetector, will have an RF noise figure of greater than 30 dB (no microwave preamp). The situation is aggravated when laser sources with high relative intensity noise are used in the link. Higher shot-noise-limited photocurrents reduce the noise figure. Erbium doped fiber amplifiers (EDFA) can increase laser power; however, signal-spontaneous beat noise and excess noise from the amplifier actually degrades the link noise performance. This

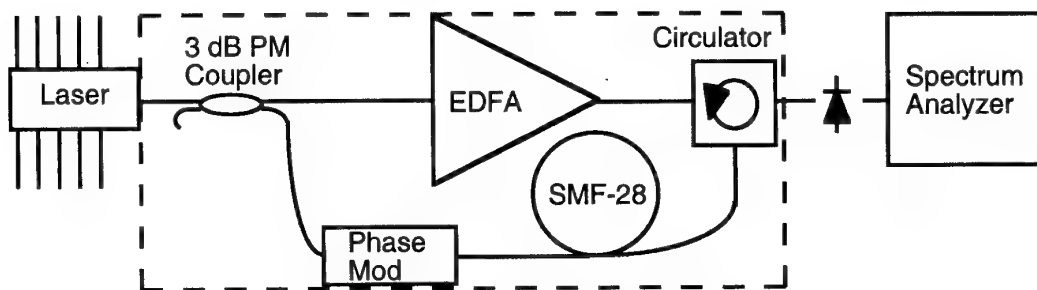


Figure 1. Experimental Configuration

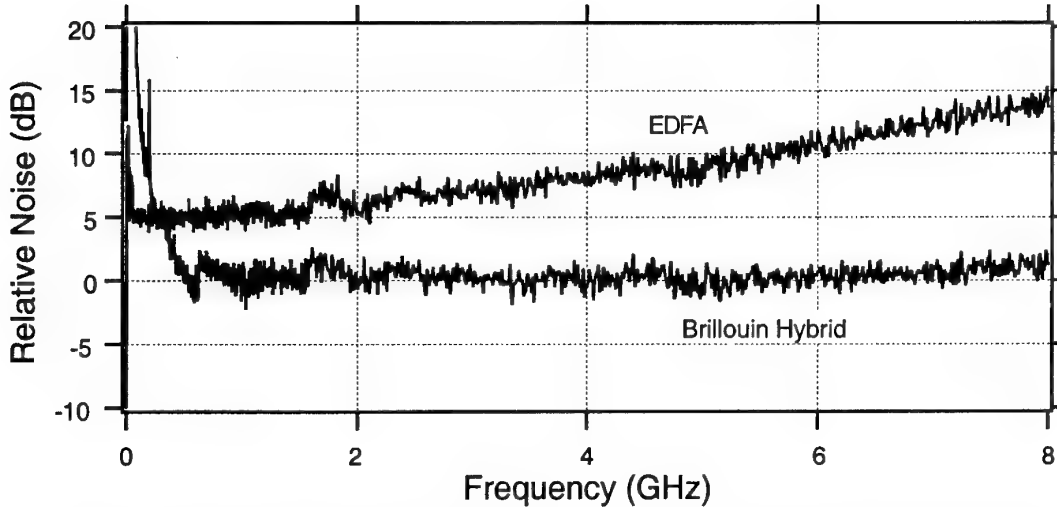


Figure 2. Output Noise Power. 0 dB is equal to the shot-noise level for a 10 mA link.

limits the usefulness of EDFAs for overcoming excessive losses and for distribution purposes. As a result, achieving the high shot-noise limited photocurrent and the noise figure necessary for all optical signal processing requires the use of expensive, high-power solid state lasers. Thus, the development of inexpensive shot-noise limited sources, or amplifiers is essential to the widespread use of photonic links.

In this paper, we attack this noise problem by combining the wide gain bandwidth and low cost of an EDFA, with the relatively narrow gain bandwidth of a Brillouin amplifier. Considerable research has been done on both of these amplifiers [9,10,11] independently, we wish to combine the positive features of each in order to achieve a relatively inexpensive light source for analog photonic links. The system operation, the results of our tests, and a discussion of needed improvements are reported.

II. System Configuration

A diagram of the hybrid EDFA/Brillouin amplifier is contained within the dashed box in Figure 1. The system consists of an EDFA, a fiber-optic circulator, a phase modulator, 25-km of single mode fiber (SMF-28), and a 3 dB coupler. Light emanating from the 30 mW DFB is divided into two paths with a polarization-maintaining

(PM) coupler. Light in one path is amplified by the EDFA, passed through an optical circulator and sent into one end of a 25-km spool of single-mode fiber (SMF-28) to pump the Brillouin acoustic wave. The 200 mW output from the EDFA is well above the 1.4 mW Brillouin threshold for a 25-km spool of SMF-28 at a wavelength of 1556 nm. Light following the second optical path enters a Lithium-Niobate phase modulator ($V_{\pi} = 5.6$ -V). The light is phase-modulated at the Brillouin frequency, which is 10.8 GHz for the combination of SMF-28 fiber and 1556 nm light. The phase-modulated light is used as a signal input (6mW) to the Brillouin Amplifier. The combined effect of the two paths is that light from the EDFA (pump) generates an acoustic wave which creates a scattered light wave (Stokes). The scattered light amplifies the signal beam entering from the opposite end of the fiber spool. The amplified light passes through the circulator and is detected by a photodetector.

In order to compare the performance of the hybrid amplifier link to typical photonic links, we performed measurements on three separate photonic systems. The first link consists of the hybrid amplifier described above with a DFB laser as a pump and a photodetector attached to the output of the hybrid amplifier. In the second link, the hybrid amplifier was replaced with the single 200 mW EDFA. The third link used a low-

noise Nd:YAG laser (1.319 μ m, RIN < -165 dB/Hz). Links utilizing this laser have shown shot-noise limited performance above 100 MHz for photocurrents in excess of 10mA. The third link will be used as a shot-noise limited reference throughout the analyses in this paper.

III. Results and Discussion

Figure 2 shows the output noise power of the hybrid amplifier and the EDFA amplified links relative to the Nd:YAG laser link. Recall that for frequencies above 100MHz the ND:YAG laser (1.319 μ m, RIN < -165 dB/Hz) link exhibits shot-noise limited performance. At a photocurrent of 10 mA the EDFA amplified link was more than 10 dB above the shot-noise limit. As shown in Figure 2, adding a 3dB coupler prior to the EDFA, a circulator, a phase-modulator, and 25 km of SMF-28 to form the Brillouin/EDFA hybrid caused a decrease in the noise of the link. Shot-noise limited performance was achieved between 0.5 and 8 GHz. The noise reduction is due to the narrow gain bandwidth (<20 MHz) of Brillouin amplification. As a result, a portion of the spontaneous emission from the EDFA was filtered out of the optical beam by the Stokes wave. The reduced amplified spontaneous emission noise for frequencies greater than 500 MHz from the carrier decreases signal-spontaneous beat noise at the detector. This is a significant improvement over the noise performance of the EDFA amplified link.

We also examined the effect of the added phase modulator versus no modulation signal in the hybrid amplifier. Figure 3 shows that injecting a phase modulated signal beam into the Brillouin amplifier section of the hybrid amplifier caused an overall reduction in the noise of the amplifier for frequencies below 500 MHz.

In addition to the noise reduction below 500 MHz, the system also showed a reduction in the burst noise caused by the Brillouin amplifier. Large variations in the output noise of the photonic link were observed below 500 MHz when no RF power was applied to the phase modulator. Trace to

trace noise measurements viewed on the spectrum analyzer exhibited more than 10 dB variation. However, when the RF power was turned on (+30 dBm, 10.82 GHz) the burst noise was all but eliminated, the noise level below 500 MHz decreased, and the trace to trace variation in the analyzed spectrum was eliminated.

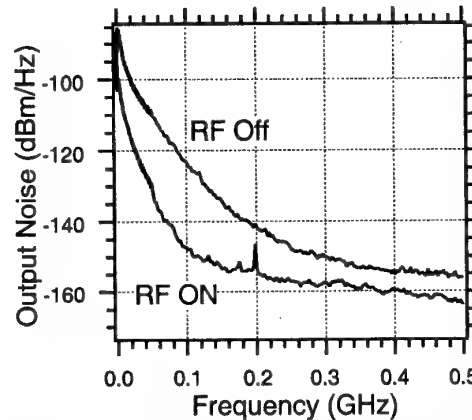


Figure 3. Noise Power with and without Phase Modulation.

To further test the noise reduction we connected a d.c. coupled photodetector to the output of the link and monitored the output with and without phase modulation. Figure 4 shows the power output of the d.c. coupled photodetector versus time. The d.c. output became more stable with phase modulation of the Brillouin signal beam. The increased stability indicates that inserting a phase-modulated signal into the Brillouin amplifier improves the overall performance of the link.

IV. Conclusion

We have presented a new method of achieving shot-noise limited performance at high currents from a 0.5 to 8 GHz analog photonic link without having to resort to expensive solid-state lasers. In our future research, we will continue to examine the effect of phase modulation in our amplifier. In addition, we will investigate the use of feedback to eliminate the need for the phase modulator.

This work was supported by the Office of Naval Research.

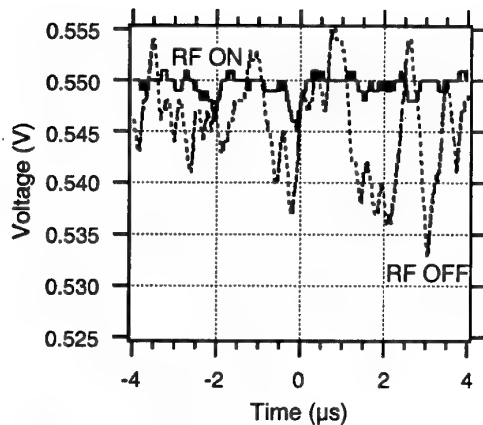


Figure 4. DC Coupled Stability.

[11] N. A. Olsson, and J. P. Van Der Ziel, Fiber Brillouin Amplifier with Electronically Controlled Bandwidth, *Electron. Lett.*, vol. 22, pg. 488-489, 1986.

- [1] L. M. Johnson, and C. H. Cox, "Serrodyne Optical Frequency Translation with High Sideband Suppression," *J. Lightwave Technol.*, vol. 6, pg. 109-112, 1988.
- [2] R. Helkey, J. C. Twichell, and C. Cox III, "A Down-Conversion Optical Link with RF Gain," *J. Lightwave Technol.*, vol. 15, pg. 956-961, 1997.
- [3] C. K. Sun, R. J. Orazi, S. A. Pappert, and W. K. Burns, "A Photonic-Link Millimeter-Wave Mixer Using Cascaded Optical Modulators and Harmonic Carrier Generation," *IEEE Photon. Technol. Lett.*, vol. 8, pg. 1166-1168, 1996.
- [4] G. K. Gopalakrishnan, R. P. Moeller, M. M. Howerton, W. K. Burns, K. J. Williams, and R. D. Esman, "A Low-loss Downconverting Analog Fiber-Optic Link," *IEEE Trans. Microwave Theory Tech.*, vol. 43, pg. 2318-2323, 1995.
- [5] C. K. Sun, R. J. Orazi, and S. A. Pappert, "Efficient Microwave Frequency Conversion Using Photonic Link Signal Mixing," *IEEE Photon. Technol. Lett.*, vol. 8, pg. 154-156, 1996.
- [6] A. C. Lindsay, G. A. Knight, and S. T. Winnall, "Photonic Mixers for Wide Bandwidth RF Receiver Applications," *IEEE Trans. Microwave Theory Tech.*, vol. 43, pg. 2311-2317, 1995.
- [7] T. E. Darcie and B. Glance, "Optical Heterodyne Image-Rejection Mixer," *Electron. Lett.*, vol. 22, pg. 825-826, 1986.
- [8] B.H. Kolner and D. W. Dolfi, "Intermodulation distortion and compression in an integrated electrooptic modulator," *Applied Optics*, vol. 26, pg. 3676-3680, 1987.
- [9] S. H. Lee and S. H. Kim, "All Optical Gain-Clamping in Erbium-Doped Fiber Amplifier Using Stimulated Brillouin Scattering," *IEEE Photon. Technol. Lett.*, vol. 10, pg. 1316-1318, 1998.
- [10] R. W. Tkach, A. R. Chraplyvy, "Fibre Brillouin Amplifiers," *Optical and Quant. Electron.*, vol. 21, pg. 105-112, 1989.

OPTICAL GENERATION OF RAPIDLY TUNABLE MILLIMETER WAVE SUBCARRIER

Y. Li, A. J. C. Vieira, P. Herczfeld, A. Rosen, and W. Janton
 Center for Microwave/Lightwave Eng. Drexel University,
 Philadelphia, PA. 19104 USA
 Phone: (215) 895-2914 Fax: (215) 895-4968
 E-mail: Yifeili@io.ece.drexel.edu

Abstract: This paper concerns an optically generated rapidly tunable millimeter wave source. The millimeter wave signal is generated by beating the output of two Nd:YVO₄ / MgO:LiNbO₃ single mode microchip laser sections realized monolithically in a single composite crystal. The device can be tuned from DC to 100 GHz. The measured tuning sensitivity is 8.8MHz/Volt, and the tuning rate is over 10 THz/sec.

Introduction

Numerous applications like frequency chirped lidar-radar, radio over fiber and biomedical imaging, require optical transmitters that can generate rapidly tunable millimeter wave sub-carriers. Specifically, for accurate range measurements in underwater detection or biomedical probing of tissues [1], a rapidly tunable optical source is required. Semiconductor laser diodes can be tuned rapidly, but their performance is limited due to their inherently high noise. Compact, efficient solid-state microchip lasers, with high spectral quality, show great potential as optical transmitters for these applications. Optical heterodyning of two ring-oscillators for millimeter-wave generation has been reported [2]. However, these approaches employ thermal or PZT tuning, which are essentially very slow processes. To overcome this problem, a monolithic microchip laser system, with electro-optical tenability, was fabricated.

Laser design and characterization

The basic microchip configuration studied is depicted in Fig.1. Two identical optical cavities are formed by depositing dielectric mirrors on opposite ends of a single Nd:YVO₄ /MgO:LiNbO₃ crystal assembly. This configuration is comprised of a 0.3mm long Nd:YVO₄ crystal, which serves as the gain

medium, and a 1.2 mm MgO:LiNbO₃ crystal, which is the tuning section. The two side-by-side lasers are pumped by an 808nm high power laser diode source. Electrodes are deposited on the top and the bottom of the 1.2 mm MgO:LiNbO₃ tuning section. The outputs of the two single mode lasers are combined, coupled into a single mode fiber and transmitted to a high-speed optical detector. By applying an electrical field to one of the lasers, its refractive index is modulated, which shifts its lasing wavelength resulting in a variable millimeter wave signal. In this heterodyned arrangement, the difference in the optical wavelengths, $\Delta\lambda_{opt}$, gives rise to the millimeter wave beat frequency, $f_{mm}=c\Delta\lambda_{opt}/\lambda_{opt}^2$. The monolithic configuration gives the device simplicity, compactness, stability, and reduced sensitivity to external temperature fluctuations. The actual device, mounted on a brass fixture, is depicted in Fig.2.

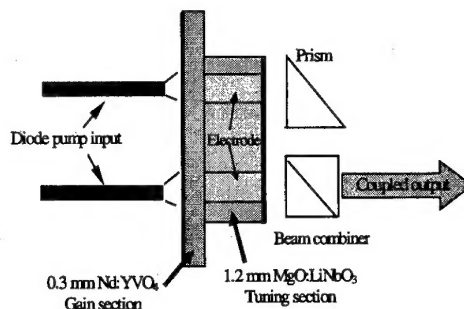


Fig. 1. The microchip laser structure.

Key parameters of the tunable microchip laser are summarized in Table 1. Single mode lasing is assured by positioning the short gain section very close to the reflecting mirror, which greatly reduce spatial hole burning [3]. Simulation, supported by experimental

validation, reveals that the microchip laser operates in single mode regime even when the pump power is raised threefold above the laser threshold. The measured laser output power vs. pump power characteristic is depicted in Fig. 3. The threshold pump power is found to be 160mW, and the overall efficiency at 250mw pump power, where most of the measurements were taken, is approximately 12%.

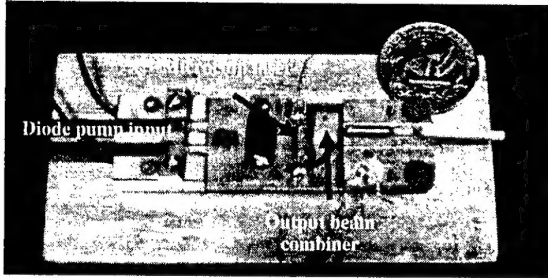


Fig. 2. Picture of the heterodyne transmitter.

Table 1. Key laser parameters.

Symbols	Definition	Values
T	Output coupling	0.02
L	Round trip Loss	0.0016
A	Pump beam cross section	0.045 mm^2
η_{eff}	Overall efficient	0.36
I_s	Saturation power density	$1.275 \times 10^7 \text{ w/m}^2$

The frequency shift of the laser output as a function of temperature is shown in Fig. 4. From this measurement we determined that temperature sensitivity is about 4GHz/°C. Considering the monolithic configuration of the device, it is expected that two laser sections are at the same temperature, and temperature drift will affect both sections similarly. Theoretical analysis shows that if we set the beat signal to 100 GHz, a simultaneous temperature drift of the two lasers will produce a frequency shift of 1.33 MHz /°C, which is acceptable for most applications. Thus the realization of two laser sections in a single crystal assembly dramatically improves the temperature stability.

By varying pump current, the crystal temperature or the applied electric field the beat frequency can be tuned from DC to 100

GHz. The optical spectrum of the two laser outputs is depicted in Fig. 5. To obtain this spectrum first the two lasers were adjusted so that their lasing frequencies were identical, then one of the lasers was tuned until the peak optical powers of the two lasers were 0.3 nm apart, which corresponds to a 90 GHz beat frequency.

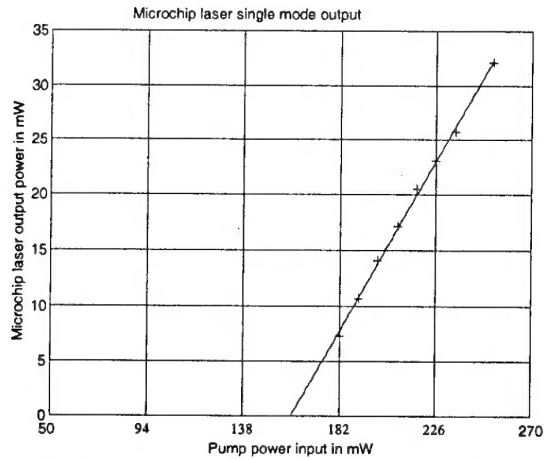


Fig. 3 The laser output power characteristics. The measured threshold pump power is 160mW.

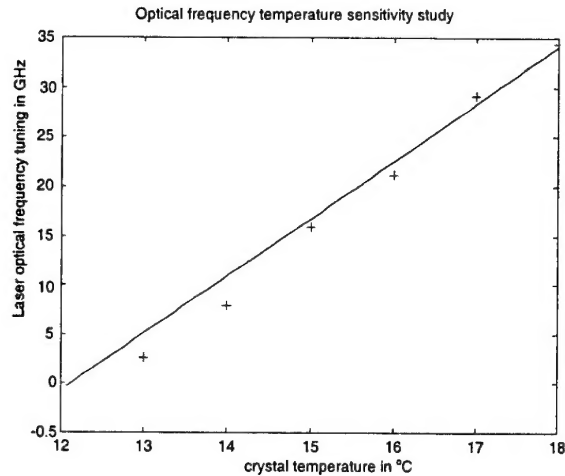


Fig. 4. Optical frequency temperature sensitivity. The optical frequency at 12°C is used as reference.

Chirped heterodyne transmitter

The experimental setup for the characterization of the chirped heterodyne transmitter is shown in Fig. 6. To generate a chirped signal, an electrical ramp voltage signal is applied to one of the two lasers. Since

the applied electrical field shifts the optical frequency of the laser, a chirped beat frequency is generated in the detector.

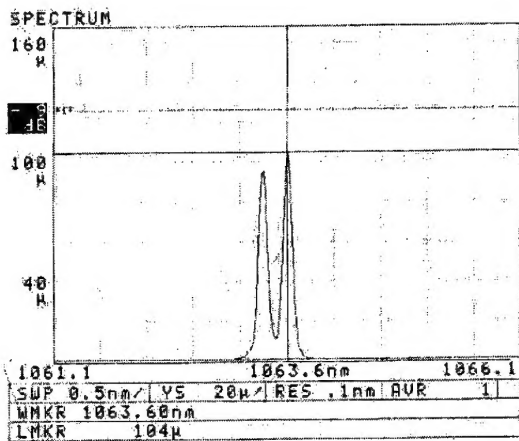


Fig. 5 Optical spectrum of the combined laser outputs. The wavelength separation is 0.3 nm.

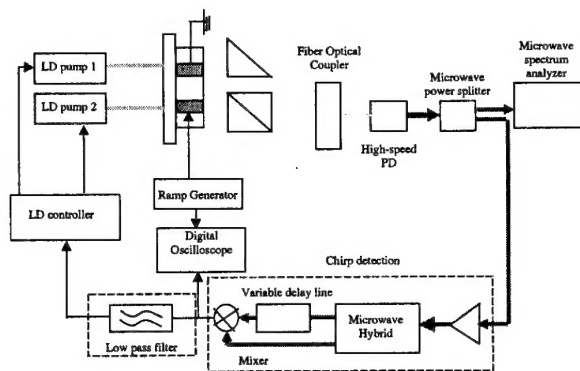


Fig. 6 The transmitter and measurement block diagram.

Although the monolithic laser structure provides for stability, fluctuations of the pump power can result in noise in the beat frequency. To stabilize the signal a feedback scheme using a microwave homodyne discriminator was introduced, which is also used to recover the chirped signal. A low pass filter with stop band of 500 Hz is used to separate the slow, randomly drifting frequency terms from the fast voltage induced FM terms. In this scheme, the feedback only tracks the low frequency drifting, and has not effect on the fast voltage tuning process.

The transmitter was tested with the beat frequency ranging from 7 to 10 GHz. Fig. 7 shows the microwave spectrum with beat

frequency at 7.889GHz. The electrical tuning sensitivity of the transmitter was characterized by subjecting it to a series of ramp signals with a repetition rate of 10KHz, and variable peak-peak voltage, while recording the discriminator output. The result, shown in Fig. 8, indicates a sensitivity of 8.8MHz/volt.

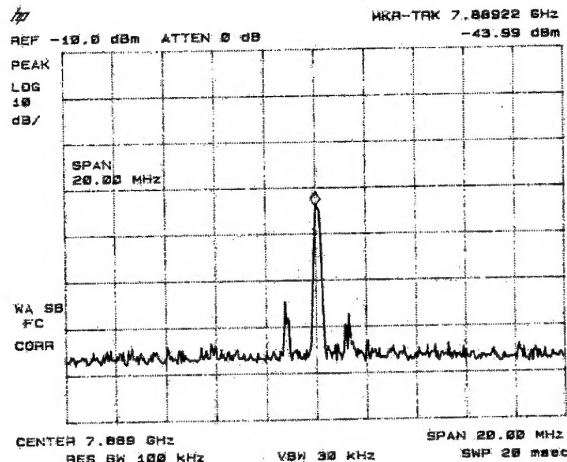


Fig. 7 Microwave spectrum of the beat frequency.

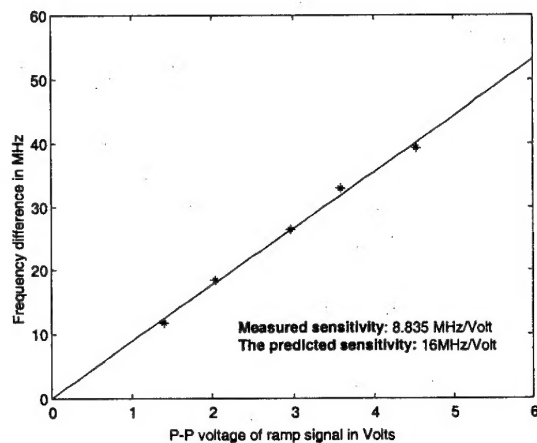


Fig. 8 Transmitter voltage tuning sensitivity.

For the chirping measurement a 1MHz 10 Volt peak-peak ramp signal was applied to one of the lasers. The recovered frequency chirp (top), as well as the applied ramp signal (bottom) were captured by a sampling oscilloscope, as shown in Fig. 9. A frequency sweep of 88.9 MHz over 0.5 μ s time period was obtained, which corresponds to a 177.8GHz/ms tuning rate.

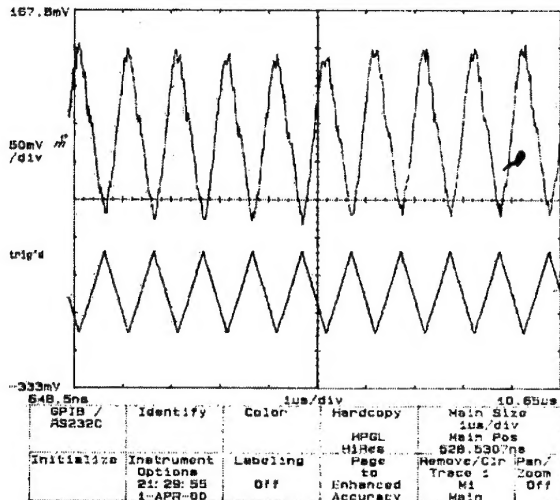


Fig. 9. Applied ramp signal (bottom) and the frequency response (top).

Conclusions

A tunable high-speed optical transmitter was designed, fabricated and characterized. The transmitter consists of two microchip lasers co-located on the same crystal assembly. The outputs of the two lasers are heterodyned to produce a tunable millimeter wave signal. The composite cavity design provides single mode operation, while maintaining excellent efficiency. The monolithic configuration of realizing two lasers within a single microchip crystal makes the transmitter more tolerant to environmental fluctuations. A novel frequency stabilization scheme was introduced. The measured tuning sensitivity is 8.8MHz/Volt and the tuning rate is 10 THz/sec. This tunable optical transmitter provides can be utilized in chirped lidar-radar, radio over fiber and biomedical imaging applications.

References

- [1] L. Mullen, A. Vieira, P.R. Herczfeld, and V.M. Contarino, " Applications of Radar Tech to Aerial Lidar Systems for Enhancement of Shallow Under Water Target Detection", IEEE Trans. Microwave Theory Tech., vol. 43, No. 9, pp. 2370-2378, Sep. 1995.
- [2] G. J. Simonis and K. G. Purchase, "Optical Generation, Distribution, and control of Microwaves Using Laser Heterodyne", IEEE Trans. Microwave Theory Tech., vol. 38, No. 5, pp. 667-669, May, 1990.
- [3] J. J. Zayhowski, "The effects of Spatial Hole Burning and Energy Diffusion on the Single-Mode Operation of Standing-wave Lasers", IEEE Journal of Quantum Electronics, vol. 26, No. 12, pp. 2052-2057.